International Society for Photogrammetry and Remote Sensing

Institute for Photogrammetry and GeoInformation University of Hannover

Joint Workshop of ISPRS Working Groups I/2,I/5 and IV/7

High Resolution Mapping from Space 2001

Sept. 19-21,2001 Hannover,Germany

Content:

T. Andresen, C. Mott, S. Zimmermann, T. Schneider, Limnologische Station der TU München, Germany:
Monitoring of Reed Populations on Bavarian Lakes with High-resolution Satellite Data

E. Baltsavias, M. Pateraki, Li Zhang, Institute of Geodesy and Photogrammetry, ETH Zuerich, Switzerland:
Radiometric and geometric evaluation of Ikonos GEO images and their use for 3D building modelling

A. Baudoin, P. Goudy, M. Rouze, CNES, Paris, France:
The Pleidade Program

A. Buck, R. de Kok, T. Schneider, G. Willhauck, U. Ammer, Lehrstuhl für Landnutzungsplanung und Naturschutz, TUM Freising, Germany:
Topological Rules in Object Oriented Classification

Y.-L. Desnos, Esrin, Frascati, Italy:
The Committee on Earth Observation Satellites Working Group on Calibration and Validation

I. Dowman, University College London, U.K.:
High Resolution Satellite Data: Status and Issues

M. Eineder , N. Adam, H. Breit, S. Suchandt, J. Holzner, B. Rabus, W. Knöpfle, German Aerospace Center (DLR), Wessling, Germany:
Results from the SRTM Calibration Phase

C. S. Fraser, H. Hanley & T. Yamakawa, Dept of Geomatics, University of Melbourne, Australia:
Sub-Metre Geopositioning with Ikonos GEO Imagery

R. Goossens, F. Benoit, University of Gent, Belgium, **M. Schmidt, A. Altmeier, Menz G.,** University of Bonn, Germany:
Extraction of Digital Elevation Models and ortho-images from CORONA KH4B Data

J. Grodecki, G. Dial, Space Imaging, Thornton, CO, USA:
IKONOS Geometric Accuracy

Habib, Y.-R. Lee, M. Morgan, Dept of Civil and Environmental Engineering, Columbus, OH, USA:
Bundle Adjustment with Self-Calibration of Line Cameras using Straigth Lines

Y. Hu, V. Tao, Department of Geomatics Engineering, The University ofCalgary:
3-D Reconstruction Algorithms with the Rational Function Model and their Applications for IKONOS Stereo Imagery

K. Jacobsen, Institute for Photogrammetry and GeoInformation, University of Hannover, Germany:
Automatic Matching and Generation of Orthophotos from Airborne and Spaceborne Line Scanner Images

V.M. Jovanovic, B.Ledeboer , M.Smyth , J.Zong, Jet Propulsion Laboratory, Pasadena, CA, USA:
Georectification of the Airborne Multi-angle Imaging SpectroRadiometer

A. Kandawasvika, M. Hahn, FH Stuttgart, Germany:
Development of Viewers for Interactive 3-D Visualisation of Geodata

M. Khawlie, B. Hansmann, T. Darwish, D. Lichaa El Khoury, G.Faour, C. Abdallah, R. Bou Kheir, National Center for Remote Sensing, Lebanon:
A knowledge-based integrated system to monitor desertification in Lebanon through Remote Sensing

J.-R. Kim, J.-P. Muller, Dept of Geomatic Engineering, University College London, U.K.:
Assessment of automated techniques for extracting vegetation and buildings from 1 m stereo+ multi-spectral IKONOS and 1 m pan-sharpened IKONOS coupled with scanning laser altimetry

G. Konecny, Institute for Photogrammetry and GeoInformation, University of Hannover, Germany:
High Resolution Mapping from Space2001

D. Kosmann, W. Knöpfle, B. Rabus, A. Roth, German Aerospace Center (DLR), Wessling, Germany:
A Large Area Digital Elevation Model from ERS-1/2 Tandem Data

P. Lohmann, Institute for Photogrammetry and GeoInformation, University of Hannover, Germany:
Land Cover Classification using High Resolution IKONOS Data

R. Müller, M. Lehner, R. Müller, German Aerospace Center (DLR), Wessling, Germany:
Verification of Digital Elevation Models from MOMS-2P Data

R. Nóbrega, J. Quintanilha, Escola Politécnica da Universidade de Sao Paulo, Brazil:
Automatic Digital Image Balancing

M. Pausader, CNES, Toulouse, France:
Study of a Processing Chain to Provide Multispectral High Resolution Fused Images for the "Pleiades-HR" System

D. Poli, Institute of Geodesy and Photogrammetry, ETH Zuerich, Switzerland:

Direct georeferencing of multi-line images with a general sensor model

R. Reulke, A. Eckardt, German Aerospace Center (DLR), Berlin, Germany:

Requirements, realisation and results of A Commercial Airborne Digital Sensor (ADS)

H. Runge, M.Werner, M.Eineder, H.Breit, S.Suchandt, German Aerospace Center (DLR), Wessling, Germany, **D. Massonnet,** CNES, Toulouse, France:

Advanced Synthetic Aperture Radar Observations with Clusters of SAR Satellites

S. Scherer, M.Kritschke, RapidEye AG, Munich, Germany:

RAPIDEYE: A Space Based Monitoring System for Agriculture and Cartography

T. Schneider, R. Seitz, B. Förster, Lehrstuhl f. Landnutzungsplanung und Naturschutz, TUM Freising, Germany:, **K. Jacobsen,** Institute for Photogrammetry and Geoinformation, University of Hannover ,Germany:

Remote Sensing Based Parameter Extraction for Erosion Control Purposes in the Loess Plateau of China

F. Scholten, F. Wewel, S. Sujew, German Aerospace Center (DRL) Berlin, Germany:

High Resolution Stereo Camera – Airborne (HRSC-A): 4 Years of Experience in Direct Sensor Orientation of a Multi-Line Pushbroom Scanner

M. Schroeder, W. Mooshuber, R. Müller, P. Reinartz, German Aerospace Center (DLR), Wessling, Germany:

Resolution Tests with a TDI-Camera

H. Schwarzer K.-H. Sümnich, A. Neumann, G. Zimmermann, German Aerospace Center (DLR), Wessling, Germany:

Five Years In-Orbit Calibration of MOS

V. Spreckels, Institute for Photogrammetry and GeoInformation, University of Hannover, Germany, **J. Musiedlak,** DSK, Bottrop, Germany, **U. Wegmüller, T. Strozzi,** Gamma Remote Sensing, Muri Switzerland, **H.-C. Wichlacz,** DSK, Herne, Germany:

Detection and Observation of Underground Coal Mining-Induced Surface Deformation with Differential SAR Interferometry

S. Suchandt, H. Breit, N. Adam, M. Eineder, B. Schättler, H. Runge, A. Roth, E. Mikusch, German Aerospace Center (DLR), Wessling, Germany:

The Shuttle Radar Topography Mission

V. Tao, Y. Hu, Department of Geomatics Engineering, The University of Calgary:

3-D Reconstruction Algorithms with the Rational Function Model and their Applications for IKONOS Stereo Imagery

T. Toutin, Canada Centre for Remote Sensing, Ottawa, Ont., Canada:

Geometric Processing of IKONOS GEO Images with DEM

T. Toutin, R. Chénier, Y.Carbonneau, Canada Centre for Remote Sensing, Ottawa, Ont., Canada:

3D Geometric Modelling of IKONOS GEO Images

T. Toutin, Y.Carbonneau ,R. Chénier, Canada Center for Remote Sensing, Ottawa, Ont., Canada:

Block Adjustment of Landsat-7 ETM+ Images

J.C. Trinder, E.D. Cheng, School of Geomatic Engineering, The University of New South Wales, Sydney, Australia:

Applications of Interferometric SAR for Elevation Determination in Australia

I. Walter, K. Brieß, W. Bärwald, F. Schrandt, W. Skrbek, German Aerospace Center (DLR), Berlin, Germany:

The BIRD Payload Platform

G. Zalmanson, T. Schenk, The Ohio State University, Columbus, OH, USA:

Indirect Orientation of Pushbroom Sensors with 3-D Free-Form Curves

G. Zhou, Old Dominion University, Norfolk, VA, USA:

Architecture of "Intelligent" Earth Observation Satellites

Monitoring of reed populations on Bavarian lakes with high-resolution satellite data

Thorsten ANDRESEN, Claudius MOTT, Stefan ZIMMERMANN, Thomas SCHNEIDER

Abstract

In the past decades a significant decline of aquatic reed populations on Central Europe´s freshwater lakes has been recorded [OSTENDORP (1990)]. In Bavaria, studies have revealed a fall of 50 per cent at lake Chiemsee, while at lakes Ammersee and Starnberg, the decline is as much as 90 per cent over the past 50 years [GROSSER, MELZER (1993)]. Even though water quality has been improving noticeably since the late 1980s [GROSSER, MELZER (1993)], the reed regression is proceeding.
Reed has major functions for the conservation of species, protection of the littoral region and water purification [OSTENDORP (1993)]. In order to counteract current developments, as well in consideration of future European policy guidelines concerning lake water quality, management plans have to be developed to ensure ecological sustainability. This may only be realized with a detailed up-to-date knowledge of the reed extent and the land use in the littoral and lake shore region.
The main objective of this study is to investigate the potential of high-resolution satellite data along with object oriented image analysis to retrieve major aquatic/terrestrial parameters. Monitoring the aquatic reed population is an important aspect in this context. New satellites of the IKONOS-generation offer very high resolution (VHR) data, combined with multispectral information into the infrared region. This attributes are considered to be preconditions to asses the small spatial changes of reed coverage over time. This study should investigate the potential of new sensor generations to substitute the well established but expensive aerial photograph interpretation in an operational environment.

1 Area under investigation

The project area is located about 40 km southward from Munich in the prealpine region of upper Bavaria close to the Alps. It includes the lake Starnberg and the lake area Osterseen, sited south of the lake Starnberg and is a popular recreation area. Main parts of the lake area Osterseen are declared as conservation areas. The core test site, chosen for the development of reed monitoring algorithms, covers a small area at the southern end of the lake Starnberg (Fig. 1).

The genesis of the lake has been discussed controversal. The most likely theory [MUNTHE quoted in ROTHPLETZ (1917)] says that lake Starnberg has been created by erosion from the Isar-Loisach glacier and subglacial spillways during the last ice age (the *Würm-ice age*). Lake Starnberg has been separated from its primary inflowing stream (Loisach). This was an important precondition for further genesis and conservation of the lake system. Therefore almost no siltation of both lake Starnberg and the lake area Osterseen did appear (and still does not appear).

Fig. 1: Project area

1.1 Reed populations at lake Starnberg

In the late 19th century vast stands of common reed (*Phragmites australis*) covered almost the entire lake shore. Today larger stands are situated in the southern region near St. Heinrich and at the western lake shore. Due to the stronger wind stress no or only slight reed stands are found at the eastern shore [GROSSER et al. (1997)].

A significant regression of reed stands at the western lake shore and the Rosensinsel is described for the first time in 1974 [KÖLBING] and 1975 [GOSLICH]. In 1980 and 1989 studies by MELZER and HENSCHEL likewise revealed reed decline in the littoral zone of lake Starnberg. A remarkable absence of Phragmites australis at the north-western lake shore between Starnberg and Possenhofen has also been reported. The overall loss of the reed population in this region is about 90% over the past 50 years [GROSSER et al. (1993)].

1.2 Reed decline

The problem of reed decline predominantly takes place in aquatic reed stands. One must distinguish between aquatic reed, transition reed and reed growing on land. Phenotypic there is hardly any difference between the growth forms, but they differ considerably in their ecological demands. Aquatic reed is partly submersed in water with significant smaller stalk lengths than terrestrial or transitional reed. In consequence there exists a recognizable transition in their horizontal extend.

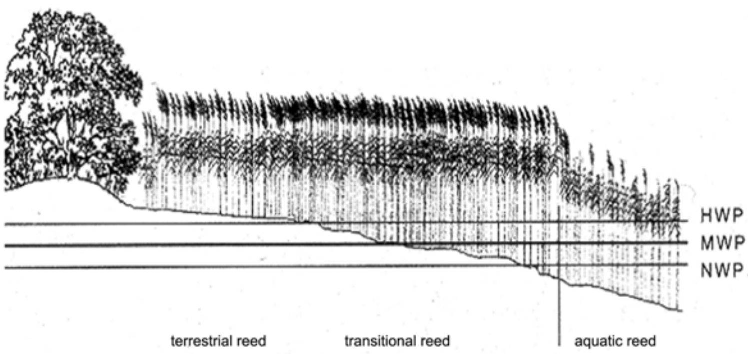

Fig. 2: different reed forms [from GROSSER et al. (1997)]

Slow regression of reed stands is reflected in a remarkable retreat of the aquatic reed boarder, clumped growth patterns, single stalks and overall shorter stalk lengths [VAN DER PUTTEN (1997)].
Immediate and total vanishing of aquatic and terrestrial reed stands also occurs caused by for example building projects.

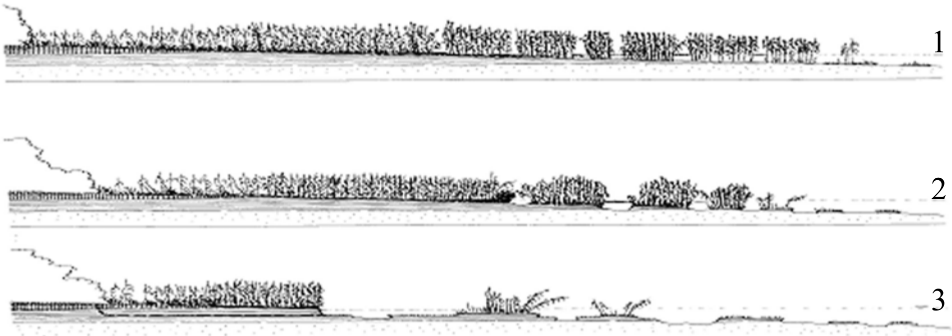

Fig. 3: stadiums of reed regression. 1) slight reed stand, 2) clumped growth patterns, 3) died reed stand [from ISELI, IMHOF (1989)]

Initial causes for reed decline are flood events and persisting high water [OSTENDORP (1991)]. After degradation further damage is caused by browsing and intense usage of lake shores as recreational areas. Embankment, mechanical damage due to wave action, drafted material and eutrophication or waste water stress are further causes [OSTENDORP (1990)].

Major functions of reed stands are conservation of species, protection of the littoral region and water purification [OSTENDORP (1993)]. Therefore aquatic reed regression leads to a multitude of consequences for instance erosion on lake shores, loss of breeding areas and habitats (for rare water birds), decrease of the "self purification" ability of lakes, decline of table fish species.

Regarding the ecological function, the significance of reed populations on lakes and the need of conservation measures becomes obvious. A detailed up to date knowledge derived from modern remote sensing data is a prerequisite for this objective.

2 Monitoring approach

High resolution remote sensing data is expected to be suitable for the observation of certain phases in reed regression. Object-oriented classification approaches can help to develop a system for monitoring lake shore vegetation, especially reed stands and land use near upper Bavarian lakes.

Main objective of this project is the development and verification of basic classification rules, assignable to different VHR remote sensing data at different acquisition dates. A first step is the creation of an object list based on objects of the fauna, flora habitat directive (FFH) and the European water framework directive. This object list has to be revised by verifying the recognizability of the objects in VHR data.

2.1 Materials

The results presented and discussed in this study are based on an IKONOS satellite image acquired in April 2001 with a ground resolution of 1m panchromatic and 4m multispectral. A resolution merge (PCA method) has been applied to ensure the same high resolution in all bands [ERDAS Field Guide (1997)].

At the acqusition date reed stands especially the aquatic reed are not fully developed and dominated by last years reed stalks in their spectral reflection. Therefore we focused on distinguishing only reed stands, litter meadows, pastures, water and forest.

2.2 Conventional monitoring

2.2.1 Ground truth

The state of the art method for thematic investigations in the aquatic domain is mainly the visual interpretation of aerial photographs. Studies conducted by the Limnological Research Station at the Technical University of Munich successfully combined the evaluation of recent and historical aerial photographs with extensive ground truth campaigns for the assessment of reed coverage and land use at several Bavarian Lakes [GROSSER et al. (1997)].

Ground truth campaigns even using aerial photographs are very time and manpower consuming. The costs are high and intervals between topographic surveys are very wide in general.

2.2.2 Airborne data

Interpretation of aerial photographs was generally carried out by visual means [GROSSER et al. (1997)]. The visual analysis of aerial photographs is likewise very time consuming and depends on the experience of the interpreter.

In addition to geometric distortions of aerial photographs, spectral differences in the images because of different viewing angles or different acquisition times provide further problems for automatic analysis. For a continuous monitoring at shorter and regular intervals aerial surveys are required but not feasible due to high costs.

2.3 Very high resolution satellite data

The spatial resolution of satellite data available so far, like Landsat TM, IRS or Spot XS, proofed to be to coarse for a detailed monitoring of lake shore vegetation In comparison the new satellite systems of the IKONOS generation offer very high ground resolution in addition to multispectral data with an improved radiometry. A more differentiated monitoring of vegetation cover seems possible. Whereas compared to aerial photographs we have to consider the multispectral abilities (in the IR spectrum), improved radiometry and particularly the expectations in an increased repetition interval.

Spatial resolutions in the range of 1m or below are preconditions for monitoring aquatic reed stands and allow to distinguish between different reed forms. The spectral variance of land cover classes is significantly increasing. Therefore the classification and generation of homogeneous areas becomes challenging.

2.4 Classification strategies

Various studies demonstrated the limitation of pixel based classification approaches for the analysis of VHR data [BLASCHKE (2000)]. To avoid the disadvantageous effects of VHR data the object-oriented classification system eCognition is used for image analysis.

Object-oriented image analysis consists of two steps, segmentation and (fuzzy) classification of the resulting image-objects.

The multiresolution segmentation algorithm implemented in eCognition extracts homogenous image-objects at different resolutions respectively hierarchy-levels. For each segment (object) object-features are calculated and stored in a database.
Compared to conventional pixel-based classification approaches, utilizing only the spectral response, image objects contain additional information, like object texture, shape, relationship to neighbours and sub-objects among others.

Fuzzy classification is based on the different object-features available. In contrast to pixel-based statistic classifiers, fuzzy classification replaces the strict class definitions of "yes" and "no" by a continuous range where all numbers between 0 and 1 describe a certain state of the class membership [BAATZ et al. (2000)]. Upper and lower border, as well as a membership function are defined to describe the distribution of values within certain features to separate classes.

On the basis of the object-features a basic rule-set is developed in small test areas. Rule-set definitions are based on spectral attributes, relations to neighbour objects and interpretation of deduced information (vegetation indices, leaf area index, band ratios).
Classes separated by object-features but representing parts of a thematic unit, can be combined into semantic groups.

2.4.1 Object hierarchies

One of the most important preconditions is the segmentation of meaningful objects including pixels representing a single semantic class [BAATZ, SCHÄPE (2000)]. As a first step a hierarchy of six layers is created bottom-up by modifying parameters for object size. Lower levels contain small objects such as single trees, bushes or parts of litter meadows. These are included in segments on higher levels where semantic objects like parks, camping sites etc. are represented.

Thus the classification of certain object-classes is done on several layers. Classes derived only on a certain (sub-)level will be just transferred into another (superior) level [BUCK et al. (2001)]. This can be done for example by analysing the fraction of the area of classified sub-objects.

For example classes distinguishable in their mean spectral values such as meadows, water or humid areas are derived on the lowest segment-level. On higher levels length of

segments can be taken into account. Thus roads are classified by using this feature along with spectral attributes of imperious surfaces.
These classes are transferred to the "final" object-level by assigning objects to a certain class if at least 50% of the sub-objects are member of the respective class combined with the membership functions of this level.

Finally a higher level contains all classes and represents the overall-classification result.

2.4.2 Differentiation of objects

Main basis for the development of rule-sets is the distinct differentiation of classes. Following the classification strategy of the eCognition user guide the definition of classes is based on the possibility of distinguishing a class in certain features from others [BAATZ et al. (2000)].
Therefore a class definition for example of aquatic reed contains of a logical description e.g. the spectral response in the IR spectrum, its distance to water among others to get an explicable a class description and additional features like NDVI to avoid an overlapping with objects of other classes

Definitions of semantic classes often become very complex due to the characteristics of VHR data [LILLESAND, KIEFER (2000)]. Hence a definition of water objects just by spectral means consists of six different "sub-"classes from deep water to shallow water/thin reed stand within the group water. Included are classes describing lakes (deep and shallow water), river beds as well as ponds. Very shallow regions with clumped reed stands are subordinated under an aquatic reed group.

2.4.3 Results

In our project area of St. Heinrich in the south of lake Starnberg (Fig. 4 & 5) only a few classes have been derived. Due to the acquisition time at the beginning of the growing season we focused on reed stands, water (lake area), forest (including single trees) and (litter) meadows/pastures (including moor areas). All other objects including settlements, roads and other impervious surfaces remain unclassified for the moment.
Object-oriented classification has been used generate homogenous objects for fuzzy-classification. Object-relations to neighbours such as distance or relative border to water-objects are taken into account for distinguishing reed stands.

The classification result has been compared with a lake shore mapping (SUK[1]) from the year 2000. The SUK was based on visual interpretation of aerial photographs with a resolution of 20 cm/pixel and extensive ground truth campaigns. The interpretation scale was 1:2500. The thematic layer resulting from the classification with eCognition was intersected with the SUK in ArcView 3.2. The result was further analysed by cross tab in MS Excel. Table 1 shows the comparison between object level 5 with an average object size of 0.2 ha and the SUK. The SUK was assumed as correct.

[1] SUK – Seeuferkartierung = lake shore mapping

Fig. 4: Core test site, classification

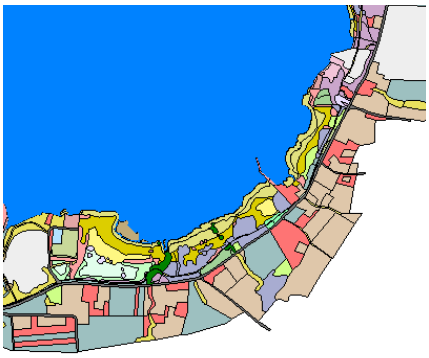

Fig. 5: lake shore mapping

classification	SUK water	reed	(litter) meadow	forest	other	result
water	**96,3%**	13,3%	0,0%	0,4%	1,7%	57,4%
reed	0,3%	**63,0%**	4,4%	10,9%	2,9%	3,9%
(litter) meadow	0,0%	0,8%	**74,2%**	2,6%	12,1%	9,3%
forest	0,2%	6,3%	4,2%	**56,0%**	10,5%	5,1%
other	3,2%	16,6%	17,2%	30,2%	**72,7%**	24,3%
result	100,0%	100,0%	100,0%	100,0%	100,0%	100,0%

Tab. 1: Classification accuracy on object level 5, objects are transferred from various levels and being revised

3 Discussion

The presented classification results show the ability of the so far developed rule-sets to distinguish between objects and to generate semantic classes.
Causes for the obvious "classification" errors are various. First of all the compared datasets are not the same season (IKONOS April 2001, lake shore mapping September 2000 partly based on aerial photographs of September 1999). The reed is at the beginning of its growing season and shows spectral overlaps with litter meadows and some kinds of impervious surface.

For spectral separable classes like **water** we obtain a good recognition rate of 96,3 % only with some overlaps. Water covers approx. one third of the project area containing the lake area and some small canals. Errors result from mapped canals which could not be detected in the satellite image.

The **reed-class** shows a classification accuracy of only 63 % with intense overlaps to water, forest and unclassified. One problem are the different acquisition dates. A comparison of

the IKONOS image from the beginning and the mapping from the end of the growing season apparently reveals a remarkable retreat of the aquatic reed border only caused by the lag and thus explains the strong overlap with the class water (13.3 %).
Another problem are single trees which are not included in the lake shore mapping but classified in the IKONOS image.
In combination with the spectral overlaps of reed stands at this time with litter meadows, lowland moors and sometimes impervious surfaces (unclassified) the classification error of about 37% becomes explainable.

Litter meadows show a good classification result of 74,2 %. Overlaps are caused by spectral similarities between reed, lowland moor, impervious surface and the heterogeneous features of litter meadows.

Forests are very rare in the core test site. The poor classification result of 56 % is caused by the wide class-types of the lake shore map. Single trees classified as forest in the satellite image are often included in impervious surface classes like settlements in the SUK. Overlaps with reed are caused by the detection of single trees in reed stands which are not included in the SUK. On the other hand deciduous trees included in the SUK are difficult to classify in the IKONOS scene at this acquisition time.

Semantic classes of the lake shore mapping are relatively wide and often contain different class-types causing a partly incorrect representation. For example a class for settlement can include trees or grass. Object-oriented classification distinguishes between these objects and classifies trees or grass (as meadow) depending on the object-level.
The semantic classes derived from the satellite data can not exactly fit the classes of the lake shore mapping.

4 Summary and Outlook

Monitoring the reed decline at upper Bavarian lakes is one step in the development of an automatic monitoring system on the basis of the European water framework directive.
Modern satellite data of the IKONOS generation providing ground resolutions of 1m are an important precondition for the change detection of objects with small spatial extents.

Very high resolution satellite data contains significant more information than previous satellites (e.g. Landsat TM) but problems arise from their high spectral variance. The so called "salt & pepper" effect is a handicap for the recognition of semantic classes.
Besides the geometric distortions additional problems are spectral differences in the IKONOS images resulting from IKONOS' ability to sway its sensor. As a result variations in brightness between multi seasonal scenes will probably provide problems for image analysis and should be corrected before evaluation.

Object oriented classification systems enable us to analyse high resolution data and avoid some of the above mentioned problems. Based on a preceding segmentation, a fuzzy approach is used to classify the VHR data. The primary task is the creation of object lists that take the abilities of different remote sensing data into account and meet the requirements of future European guidelines of water pollution control.

Major problems are the generation of meaningful objects that fit to semantic classes of the object lists. Classification rules for all object types and their representation in VHR data from different sensors and on varying acquisition times have to be developed. The next step will be the assignment of the deduced classification rules on more complex scenes.

Another approach is the integration of additional knowledge contained in regional mappings or digital elevation models (DEM).
In the context of reed monitoring it is necessary to distinguish between different reed stands, litter meadows, lowland moors among others to recognize the outer reed border. Consistent classes describing for example impervious surfaces like roads derived from mappings can be logically combined with the features of the image objects.
The integration of GIS-data can lead to a value adding process as well as an easier and more accurate mapping of image objects compared to utilizing only the information from one source [BUCK et al. (1999)]. Information's of high resolution DEMs below 0.5 m are expected to simplify recognition of the transition between terrestrial and aquatic reed.

Additional knowledge from thematic layers has not been used in this study so far but will be included in our future work.

5 Bibliography

Baatz, M. & Schäpe, A. (2000): Multiresolution Segmentation – an optimization approach for high quality multi-scale image segmentation. In: STROBL, J. et al. (Hrsg.): Angewandte Geographische Informationsverarbeitung XII. Beiträge zum AGIT-Symposium Salzburg 2000, Karlsruhe, Herbert Wichmann Verlag: 12–23.

Baatz, M., Heynen, M., Hofmann, P., Lingenfelder, I., Mimler, M., Schäpe, A., Weber, M., Willhauk, G. (2000): eCognition user guide. Defeniens, München.

Blaschke, T. (2000): Objektextraktion und regelbasierte Klassifikation von Fernerkundungsdaten: Neue Möglichkeiten für GIS-Anwender und Planer. In: 5. Symposium „Computergestützte Raumplanung" – CORP2000, S. 153-162.

Blaschke, T. (2000): Ohne Salz und Pfeffer. Objektorientierte Bildanalyse – eine Revolution in der Fernerkundung. In: GeoBIT 2/2000: 30-32.

Buck, A., de Kok, R., Schneider, T. Ammer, U. (1999): Integration von Fernerkundung und GIS zur Beobachtung und Inventur von Schutzwäldern in den Bayerischen Alpen. In: STROBL, J. & BLASCHKE T. (Hrsg): Angewandte Geographische Informationsverarbeitung XI, AGIT 1999.

Buck, A., de Kok, R., Schneider, T., Ammer, U. (2001): Modular project design for simulating topological rules in object oriented analysis. In ZGIS & DGPF (Veranstalter): Fernerkundung und GIS. Neue Sensoren – Innovative Methoden. Workshop im Vorfeld der AGIT 2001. Salzburg, Juli 2001: 16.

ERDAS, Inc. (1997): ERDAS Imagine Field Guide. 4th Ed., Erdas, Inc., Atlanta.

Goslich, C. (1975): Freiflächenplanung für Feldafing und Tutzing am Starnberger See. - Diplomarbeit, TU Weihenstephan.

Grosser, S.; Veit, E.;. Pohl, W & Melzer, A. (1993): Investigations into reed Decline at Bavarian Lakes - The Decline of Reed Stands and its Triggering Causes. Limnological Research Station of the TU Munich.

Grosser, S.; Pohl, W.; Melzer, A. (1997): Untersuchung des Schilfrückgangs an bayerischen Seen. - Bayerisches Landesamt für Umweltschutz, 141, 97.

Iseli, C., Imhof, T. (1989): Bielersee 1987. Schilfschutz. Erhaltung und Förderung der Naturufer. Verein Bielerseeschutz, Nidau.

Kölbing, A. (1974): Der Starnberger See und die seinem Trophiezustand angemessene Bewirtschaftungsweise des Coregonenbestandes. -Veröff. Zool. Staatssamml. München, 71, 1-108.

Lillesand, T.M.; Kiefer, R.W. (2000): Remote sensing and image interpretation. 4th Edition. John Wiley & Sons. New York - Chichester - Weinheim - Brisbane - Singapore - Toronto.

Ostendorp, W. (1990): Röhrichtrückgang in Mitteleuropa. - DGL Tagungsband, Tagung in Essen.

Ostendorp, W. (1991): Damage by episodical flooding to Phragmites-reeds in a prealpine lake: proposal for a model. - Oecologia, 86, 119-124.

Ostendorp, W. (1993): Schilf als Lebensraum. In: Landesanstalt für Umweltschutz Baden-Würtemberg (eds.): Beih. Veröff. Naturschutz Landschaftspflege Bad. Württ. 68, 173-280.

Rothpletz, A. (1917): Die Osterseen und der Isarvorlandgletscher. Mitteilungen der Geographischen Gesellschaft München 12, 99-314.

Van der Putten, W.H. (1997): Die-back of Phragmites Australis in European wetlands: an overview of the European Research Programme on Reed Die-back and Progressuion (1993-1994). In: Aquatic botany 59 (1997), S.263-275.

RADIOMETRIC AND GEOMETRIC EVALUATION OF IKONOS GEO IMAGES AND THEIR USE FOR 3D BUILDING MODELLING

Emmanuel Baltsavias, Maria Pateraki, Li Zhang
Institute of Geodesy and Photogrammetry, ETH-Hoenggerberg, CH-8093, Zurich, Switzerland
(manos, maria, zhangl)@geod.baug.ethz.ch

KEY WORDS: high-resolution satellite imagery, IKONOS, radiometric analysis, image preprocessing, geometric evaluation, orthoimages, building reconstruction, accuracy analysis

ABSTRACT

Investigations on the radiometric and geometric characteristics of IKONOS Geo satellite imagery and its use for orthoimage generation and 3D building reconstruction are reported. The paper first starts with an analysis of the radiometric quality of IKONOS Geo images of varying preprocessing and type, focussing on noise, edge quality and definition, and various artefacts. A noise estimation method is presented and results from various IKONOS Geo images, showing an intensity-dependent noise of 1.5-10.5 grey levels, which is high considering the effectively 8-9 bit data. Methods will be presented that reduce noise, enhance edges and contrast and optimally reduce 11-bit to 8-bit, without leading to loss of small, but still important, image details. Next, the topic of the geometric potential of IKONOS Geo images using the Rational Polynomial Coefficients (RPCs) and a possible improvement will be discussed. The geometric analysis makes use of stereo images and testfield data provided by the University of Melbourne with 28 well defined and distributed GCPs with 1-2 dm accuracy in object and image space. It will be shown that the RPCs have moderate absolute accuracy (large systematic bias, conforming to the Geo product accuracy specifications of 25 m RMS) but sub-metre relative accuracy. With the help of 4-8 accurate and well-distributed GCPs and a simple translation (bias removal), 0.4-0.5 m and 0.6-0.8 m absolute accuracies in planimetry and height can be achieved with the full set of 60 RPCs per image, or reduced RPCs omitting the higher-order terms (down to 22 coefficients). Even when using just one GCP to remove the bias, the accuracy is at worst ca. 2 m. In a related paper (Fraser et al., 2001b), it is shown that other simple sensor models (including affine projection) can produce similar or better accuracy than the RPCs with similar GCP requirements. This is shown also in this work, but with a different 3D spatial resection, using relief-corrected affine transformation and down to just 3 GCPs. Results from generation of orthoimages from three projects using own methods will be shown, including quantitative analysis, and showing how with simple and fast methods the 1-2 m accuracy of the much more expensive IKONOS Precision and Precision Plus can be achieved. With 1-2 dm accurate GCPs and depending on DTM accuracy and sensor elevation, sub-metre planimetric accuracy can be achieved. Buildings of the University of Melbourne Campus were measured manually and stereoscopically. After measuring a point cloud, 3D points were automatically structured and visualised with the system CC-Modeler, including texture mapping. The point accuracy was evaluated using GPS measurements of building corners and was found to be in the meter range. The completeness of the data and their limits regarding modelling roof details were evaluated: (a) qualitatively and (b) quantitatively through a comparison to a 3D model that was generated from aerial images. The results of this assessment are summarised, these highlighting both the high metric potential of IKONOS and difficulties to be anticipated in building reconstruction when the modelling should be complete and detailed.

1. INTRODUCTION

Although IKONOS imagery has been commercially available since early 2000, the use of this imagery and especially the scientific investigations on its potential use in various applications has been restricted due to various reasons, the main ones relating to the closed policy of Space Imaging (SI). Some publications from SI scientists report on the radiometric and geometric characteristics of the sensor (Gerlach, 200), the use of rational polynomial functions as a substitute sensor model (Grodecki, 2001), and the 3D mapping accuracy that can be achieved with this imagery using stereo triangulation (Dial, 2000). Independent investigations on the geopositioning accuracy of IKONOS using 2D transformations and full 3D analysis are reported by Hanley and Fraser (2001) and Fraser et al. (2001a, 2001b), respectively. Li et al. (2000) report 3D point positioning accuracy studies using simulated data. They mention that 4-7 GCPs suffice, but their results are too pessimistic when using GCPs (1.5 – 3 m RMS) and too optimistic when not using any GCPs at all. Generation of accurate orthoimages from IKONOS Geo imagery is reported by Kersten et al. (2000), Toutin and Cheng (2000) and Davis and Wang (2001) with achieved accuracies in the 1-2 m range. Regarding use of high-resolution spaceborne imagery for object detection, recognition and reconstruction, the first investigations using IKONOS imagery appeared only recently, while some research was performed earlier using simulated data or empirical analysis. Ridley et al. (1997) evaluated the potential of 1m-resolution spaceborne imagery for the needs of UK's Ordnance Survey using simulated data. Regarding buildings only 72.9% and 85.6% could be interpreted correctly for monoscopic and stereoscopic evaluation, respectively. Sohn and Dowman (2001) present investigations on building extraction, however the results presented were few and dealing only with large detached buildings without a comprehensive analysis of accuracy, completeness and modelling of details. Dial et al. (2001) present first investigations on automated road extraction, focussing rather on wide suburban roads of expanding US cities. Hofmann (2001) tries to perform a 2D detection of buildings and roads using spectral information, a laser scanner derived DSM, context and form with the commercial package eCognition.

In between, some commercial systems (Erdas Imagine, LHS Socet Set, Z/I Imaging ImageStation, PCI Geomatics OrthoEngine) support to one or the other extent IKONOS imagery for import, stereo viewing and processing, orthoimage generation etc. by using the rational polynomial coefficients (RPCs) provided by SI with some image products (stereo images, Geo Ortho Kit), estimating RPCs from ground control or using alternative (bundle adjustment, DLT) and partly proprietary mathematical models. While estimating RPCs from GCPs is both expensive (high number of GCPs required) and suboptimal, use of bundle adjustment due to the undisclosed IKONOS sensor model is impossible. DLT, as shown in Fraser et al. (2001a) could be used with GCPs, while proprietary sensor models (PCI) are of unknown quality, while raw IKONOS data which would be most appropriate for use with a strict sensor model are not available.

Given the present shortage of information on the photogrammetric performance of the IKONOS system, it has been necessary to examine various salient aspects when evaluating the use of 1m Geo imagery. These comprise the geometric accuracy of geopositioning from mono and stereo image coverage; the radiometric quality, with an emphasis on characteristics to support automatic feature extraction (e.g. noise content, edge quality and contrast); orthoimage generation; and attributes of the imagery for the special application of building extraction and visual reconstruction. In the present paper, we examine these aspects with the aid of three-fold IKONOS coverage of a precisely surveyed testfield covering the city of Melbourne, as well as additional images in the radiometric analysis and orthoimage generation.

Details on IKONOS, including sensor and platform parameters and product description, can be found at Space Imaging (2001). Here, it is only reminded that the field of view is 0.93^0 and the available products include *Geo*, *Reference*, *Pro*, *Precision* and *Precision Plus* with absolute geopositioning accuracies (RMS, 1-sigma)[*] of 25m, 11.8m, 4.8m, 1.9m and 0.9m, respectively. In June, SI introduced the Geo Ortho Kit which provides together with the Geo imagery an Image Geometry Model (IGM) allowing users to generate their own accurate orthoimages, using DTMs and GCPs. However, this product has a substantially higher cost than the normal Geo products (Ortho Kit is currently offered only by SI USA at a 57-78% surcharge and SI Eurasia at a 280% surcharge, while the cheapest Ortho Kit product outside N. America is 62 and 98 USD/km^2 for the two SI companies respectively). In July 2001, SI published new prices and partly new products, e.g. stereo imagery is offered for the reference and precision products only and this not by all SI

[*] It should be kept in mind that when no GCPs are used (as with Geo) these errors refer to a, generally unknown to the image user, reference height plane employed in the image generation and it also does not include displacements due to relief. Thus, checking the accuracy of Geo products, using GCPs, often leads to much higher errors (see Table 9) that the ones specified here.

regional partners. These investigations refer to the Geo product which is a geometrically corrected product that has been rectified to a pre-specified ellipsoid and map projection, re-sampled by cubic convolution to 1m pixels and in the case of a stereopair in addition epipolarly resampled.

2. INPUT DATA

2.1 Image Data

The imagery comprised a stereopair of epipolar-resampled Geo PAN images, and a nadir-looking scene of PAN and multispectral imagery. The latter were also combined to a Pan-Sharpened image. As indicated in Table 1, the sensor and sun elevation angles for the stereopair (imaged in winter) were less than optimal. Apart from the right stereo image, the azimuths of sensor and sun differed considerably, leading to strong shadows in non-occluded areas.

	Left Stereo	**Right Stereo**	**Nadir**
Date, Time (local)	16/7/2000, 09:53	16/7/2000, 09:53	23/3/2000, 09:58
Sensor azimuth (deg)	136.7	71.9	143.0
Sensor elevation (deg)	61.4	60.7	83.4
Sun azimuth (deg)	38.2	38.3	50.0
Sun elevation (deg)	21.1	21.0	38.0

Table 1. Acquisition parameters of IKONOS PAN images.

The overall geometry was close to that of 3-line imagery, with the base/height ratio of the stereopair being B/H = 1.2. Supplied with the stereo imagery were the RPCs which provide a mechanism for object-to-image space transformation and 3D point determination. There were no RPCs for the near-nadir image, since the option of obtaining these coefficients for mono Geo imagery was not available at the time the data was acquired.

2.2 Melbourne IKONOS Testfield

The testfield covered a 7x7 km area over central Melbourne with 32 GCPs (mostly road roundabouts) with 1-2 dm accuarcy in object and image space. The position of the roundabout centres was estimated by using 6 or more GPS measurements along their perimeter and a least squares based ellipse fit. The image coordinates were determined similarly, using manual measurements. To complement the image mensuration via ellipse fitting, least squares template matching was also employed within the stereo imagery, with special care being taken to alleviate problems such as target occlusions from shadowing and the presence of artefacts such as cars. Thus, matching utilised gradient images instead of grey values and the observational weights were determined from the template gradients, i.e. only pixels along the circular template edge were used in matching, thus making the method insensitive to contrast differences and other disturbances. In spite of significant disturbances, and size and shape variations of roundabouts, the matching performed correctly in most cases (in 22% of the points matching failed, and in the rest a few points had slight errors due to disturbances at the roundabout perimeter; in case of failed matching, the coordinates used came from the ellipse fit). A point, that is important also in 1D matching for DSM generation, is the fact that with both pixel coordinate measurement methods the y-pixel coordinates of the stereo pair, although usually very close to few tenths of a pixel, in some cases had differences above 0.5 and up to ca. 1 pixel. This could be due to image measurement errors but also imprecisions in the epipolar resampling.

A second essential component of the Melbourne testfield comprised information on buildings. Building height data for 19 image-identifiable and readily accessible roof corners was provided through precise GPS surveys at the University of Melbourne campus, to 10cm accuracy. This data formed the metric standard by which the 3D triangulation for building extraction would be assessed. Image coordinate observations were carried out by manual recording, both in stereo and monoscopically (for the nadir image), nominally to 0.5-1 pixel precision. However, the definition of corner points was often weak, leading to the possibility of significant errors. An existing stereopair of 1:15,000 scale wide-angle colour aerial photography of the campus was employed in the evaluation of the building extraction potential of IKONOS imagery. This imagery had previously been used to create a reasonably detailed 3D model of the campus, which could be compared to that derived from IKONOS data in terms of recoverable feature content.

3. RADIOMETRIC ASPECTS AND IMAGE PREPROCESSING

3.1 Radiometric Quality Analysis

Prior to discussing radiometric features of the IKONOS imagery, it is worthy of note that operational aspects of the image acquisition are likely to have a more profound effect on the homogeneity, or non-homogeneity, of image quality than specific radiometric characteristics of the sensor system. For example, large changes in image quality and suitability for automated feature extraction are associated with variations in the sensor view angle, the sun angle and shadowing, the seasons, atmospheric conditions, and whether the scene is recorded in mono or stereo. These influences are well-known, but it needs to be appreciated that with the exception of the last aspect, they are largely beyond the control of the image user, at least in most cases. There is limited opportunity for the user to dictate specific imaging dates, times and weather conditions. Of the three images employed, the near-nadir image was superior in terms of both contrast and visual resolution. This can be explained by the higher sensor and sun elevation, though it is uncertain if this fact alone accounted for the modest difference in image quality, or whether differences were in addition due to changes in atmospheric conditions or aspects of the epipolar resampling of the stereo images.

A fact that is not widely known is that the IKONOS linear CCDs employ Time Delay and Integration (TDI) technology, i.e. the line consists of several lines (also called stages) that accumulate the signal received from one scene object by all lines, in applications where either illumination is very low or the dwelling (integration) time of an object is very short due to high object or sensor speed. Due to the high satellite speed over ground of 6.79 km/s and the small pixel footprint, the integration time of each line must be kept small (typically, IKONOS acquires for the PAN 6000 lines/s resulting in an integration time for each line of the TDI of 0.166 ms, and a pixel footprint in flight direction of ca. 1.13 m). This integration time is too short to achieve a sufficiently strong signal and high SNR and to reproduce the high dynamic range of natural scenes. Thus, IKONOS uses TDI technology in 5 different modes, accumulating each time the signal from a different number of TDI lines, up to 32 (Gerlach, 2000), while the TDI mode remains constant during the acquisition of one particular scene (to solve the same problem, the EROS A high-resolution satellites use a so-called nimble imaging technology, whereby the satellite bends backwards at an almost constant predetermined angular speed to image the same scene object with one single line over a longer time period; the EROS B series satellites will employ TDI technology as IKONOS). Typically, IKONOS images with 16 TDI stages, resulting in a total integration time of 2.7 ms. The accumulation of the signal with TDI technology leads to a smoothing of the signal, especially in the flight direction, since the TDI lines can not exactly image the same scene surface and thus a signal mixing occurs (see Fig. 7 in Gerlach (2000)). SI uses a so-called Modulation Transfer Function Compensation (MTFC) to unsmooth the signal. This leads visually to a sharper image, but at the same time to lower contrast and artefacts (ringing, overshoot) that can be seen especially along strong edges parallel to the CCD direction (see again Fig. 7 in Gerlach (2000)). This leads to a worse edge definition for metric purposes, especially by automated procedures. A second preprocessing performed by SI is the Dynamic Range Adjustment (DRA). This, as MTFC, aims at a visual improvement by stretching the grey values to cover more uniformly the available 11-bit, but this destroys the absolute radiometric accuracy of the images (thus, it is not applied to multispectral data) plus it leads to combination (mixing) of grey values that are not frequently occupied.

All Melbourne images were preprocessed by SI with MTFC but no DRA. Although the images were 11-bit data, the number of grey values having a substantial frequency was much less than 2048. For the left, right and nadir PAN images, grey values with a frequency of more than 0.01% were covering only the ranges of 44-343, 56-423 and 61-589, respectively. The corresponding effective grey value ranges of 299, 367 and 528 (37, 46 and 66 grey values for a linear stretch to 8-bit) are quite similar to the effective 8-bit intensity range observed with other spaceborne linear array CCD sensors such as SPOT and MOMS. The peak of the histogram is typically towards the darker values (at 62, 73 and 82 for left, right and nadir, respectively) with the right part of the histogram decreasing smoothly and slowly towards the higher grey values.

To increase the reliability of the results and test images with varying spectral content and different preprocessing and imaging conditions, several additional images apart from the Melbourne images were used. The overall noise characteristics of the images were analysed in both homogeneous (sea and lake surfaces) and nonhomogeneous areas (e.g. whole image, excluding large homogeneous surfaces). The use of nonhomogeneous areas in image noise evaluation is justified as large homogeneous areas do not always exist, plus this allows an analysis of the noise variation as a function of intensity, as noise for CCD-imagers is not additive but intensity-dependent. Both areas are selected manually and as large as possible. A small window is moved within the area with a freely defined spacing and the standard deviation, as an indication of noise, is calculated. Small windows are justified since homogeneous areas (e.g. water) often show low frequency grey value variations, which would lead to higher standard deviation if it were computed from the whole area. For nonhomogeneous areas, a small window is imperative in order to get small homogeneous areas between edges. For homogeneous areas, the standard deviations are sorted and the N% smallest ones are used to calculate a mean standard deviation, which indicates the noise. Typical values for N are 80-95. With nonhomogeneous areas, the grey level range is divided in bins, and the standard deviations are assigned to a bin according to the mean grey value of each window. In each bin, the standard deviations are sorted, and the noise is estimated as the mean of the N% smallest standard deviations. N is chosen small, e.g. 5, using the reasonable assumption that at least some windows will be homogeneous, even in highly textured images. The noise is estimated for a bin only if the N% sample number is sufficiently large (e.g. > 100). For both areas, care should be taken with homogeneous areas that are saturated (at one of the histogram ends), as this will lead to too low estimated noise. This noise estimation method is quite general and could be applied to any type of image, without the need of on-platform calibration devices or special targets in the image.

The results using four PAN images, two MSI and one PAN-MSI and homogeneous areas led to a noise estimate (mean standard deviation) of 4.5-5, 2 and 4.5-5.5 grey levels respectively. All images were preprocessed by SI using MTFC, while one PAN was preprocessed also with DRA, and PAN-MSI was also preprocessed by an unknown projective multispectral algorithm. The results showed a very high consistency, i.e. noise was similar for all PAN and MSI images, in spite of the different image acquisition characteristics. MSI images exhibit lower noise, probably due to larger pixel spacing (48 μm) and electron well capacity of the multispectral line CCDs. As expected, the PAN-MSI images have higher noise, due to the higher noise of PAN which is injected in the sharpened image, and maybe the specific image sharpening algorithm used by SI. The three spectral channels (R, G, B) had similar noise for the MSI images, while for the PAN-MSI (NIR, R, G) the G channel had lower noise by 1 grey value. Using nonhomogeneous regions, the noise relation to the spectral image type remained generally the same, but the noise was intensity dependent being lower for the first bins (at 1.5 grey levels), and increased for higher intensities up to ca. 10.5, which is more than suggested by SI investigations (4 grey values in all 5 channels without MTFC, see Gerlach, 2000). In the multispectral channels, the noise slightly increased from B through to NIR. The Lucern/PAN filled more bins due to the DRA. Although the noise extent was not judged to be of crucial significance for the specific task of building reconstruction, if one considers the fact that the 11-bit data represent actually only 8 to 9-bit, the noise is high, while its negative influence on automated processing becomes even more pronounced, if an often necessary contrast enhancement is performed (see Fig. 2, top right).

Geo images have been found to exhibit artefacts in addition to their noise content, of which a number remain unexplained. Many are visible only in homogeneous areas, especially after contrast enhancement. Although the artefacts often lead to small grey level variations (e.g. 2-4 grey levels in 11-bit images), after contrast enhancement, which is often required for visual interpretation and measurement or automated computer processing, they can lead to erroneous high-contrast texture patterns. Apart from chess pattern noise and dark or bright stripes in the flight direction, which are typical of linear array CCD spaceborne sensors, the following concerns regarding artefacts have been identified: some striping in the stereo images in the flight direction (Fig. 1 e, width of stripes ca. 630 pixels); signal saturation due to strong reflectance and spilling of this bright signal due to read-out to neighbouring lines in flight direction (Fig. 1 f); an apparent MTFC effect similar to the unsharp masking used to sharpen edges (Fig. 1 f, note black contour at the bottom of the white saturated area); a staircase variation of the grey values within homogeneous areas of the epipolar-resampled stereo images (Fig. 1 a shows the right stereo image, Fig. 1 b the left one; note also the white dotted line on water, which is physically nonexisting); jumps in grey value across the flight direction (visible in homogeneous areas, see Fig. 1 c); the ghosting of moving objects leaving colour patterns behind, visible especially for blue, due to the 0.5 s time difference between acquisition of PAN and MSI and partly deficiencies of the image sharpening method (Fig. 1 g and h show a stereo Pan-Sharpened pair; note the blue car in 2 h which is however not visible in 2 g, while the corresponding MSI imagery of 2 h is, at the position of the blue car, only very slightly blueish); physically nonexisting bright lines, neither along or across flight direction; and some striping normal to the flight direction (horizontal bright stripes in Fig. 1 d). These radiometric concerns are not related solely to the sensor imaging parameters but also to the subsequent image processing methods and to image compression. The compression to 2.6 bits leads to some artefacts, which are more visible in homogeneous areas. Some additional problems include shadows and image saturation. The shadow areas in the Melbourne imagery did not have a significant signal variation, and thus in spite of a strong contrast enhancement, feature details in shadow areas were often hardly visible. Saturation occurred routinely, with bright vertical walls, especially those with surface normal approximately in the middle of the illumination-to-sensor angle. This led again to a loss of detail and poor definition or disappearance of edges when two saturated walls were intersecting. Shortcomings in edge definition, partly inherent in 1m imagery, and problems with variability in image quality, often lead to instances where buildings and trees, for example, of nominally sufficient size are almost impossible to identify.

3.2 Image Preprocessing

In order to reduce the effects of the above mentioned radiometric problems and optimise the images for subsequent computer processing (the measurement of GCPs and buildings, and in other IKONOS projects orthoimage generation and mapping), various preprocessing methods were developed, implemented and tested. The first consisted of an anisotropic Gaussian low-pass filtering to reduce noise and stripes in the flight direction (which for non-stereo images are almost vertical), coupled with application of a Wallis filter for contrast enhancement. The filter anisotropy was aimed at filtering more in the line direction in order to reduce vertical striping. In a second preprocessing step, after the low-pass filtering, an unbiased anisotropic diffusion was used to further reduce noise and sharpen edges (Fig. 2). The improvement of the Wallis filter in shadow regions was not as much as previously achieved for aerial and other satellite imagery, possibly due to a low signal variation in these regions. Both these approaches were applied to 8-bit data that were generated by a linear compression of the original 11-bit imagery.

Later, a third, improved approach was adopted. All preprocessing was applied to the 11-bit data. First, two adaptive local filters were developed. They reduced noise, while sharpening edges and preserving even fine detail such as one-pixel wide lines, corners and line end-points. Optionally, salt-and-pepper noise can be eliminated to a certain extent. The effect of the two local filters is generally quite similar, although they use a different number and size of masks, and one employs a fuzzy method. They require as input an estimate of the noise, which may be known or estimated by the methods mentioned above.

Next, a new version of the Wallis filter (Baltsavias, 1991), which estimates automatically some of the filter parameters, is applied, and finally a reduction to 8-bit imagery by histogram equalisation is performed (Figs. 5 and 6). We used histogram equalisation, as it is optimal for general-purpose computer processing, since it preserves more grey values that are more frequently occurring. The histogram equalisation was iterative with the aim being to occupy all 8 bits with similar frequencies. Processing in 11-bit led to slightly better 8-bit images than first transforming to 8-bit and then preprocessing, even though the 11-bit imagery was effectively only 8 to 9 bits. The third preprocessing approach produced sharper edges than the first two ones (see Fig. 2). The histogram equalisation may lead to too strong bright and dark regions for visual interpretation, and thus for this purpose it could be replaced either by a reduction of Gaussian type or an optimisation of a selected target grey level range. A noise estimation of the Melbourne stereo images after the fuzzy noise reduction method (third approach) led to a noise decrease by factor three, while after Wallis the noise increased. However, the images had still slightly lower noise than the original ones, but with better image quality. After reduction to 8-bit the noise increased, with only few bins showing more than 1-3 grey level noise, as encountered in scanned aerial imagery. The noise had a Gaussian form, being lower at the two histogram ends due to compression of grey levels at these histogram positions by the histogram equalisation.

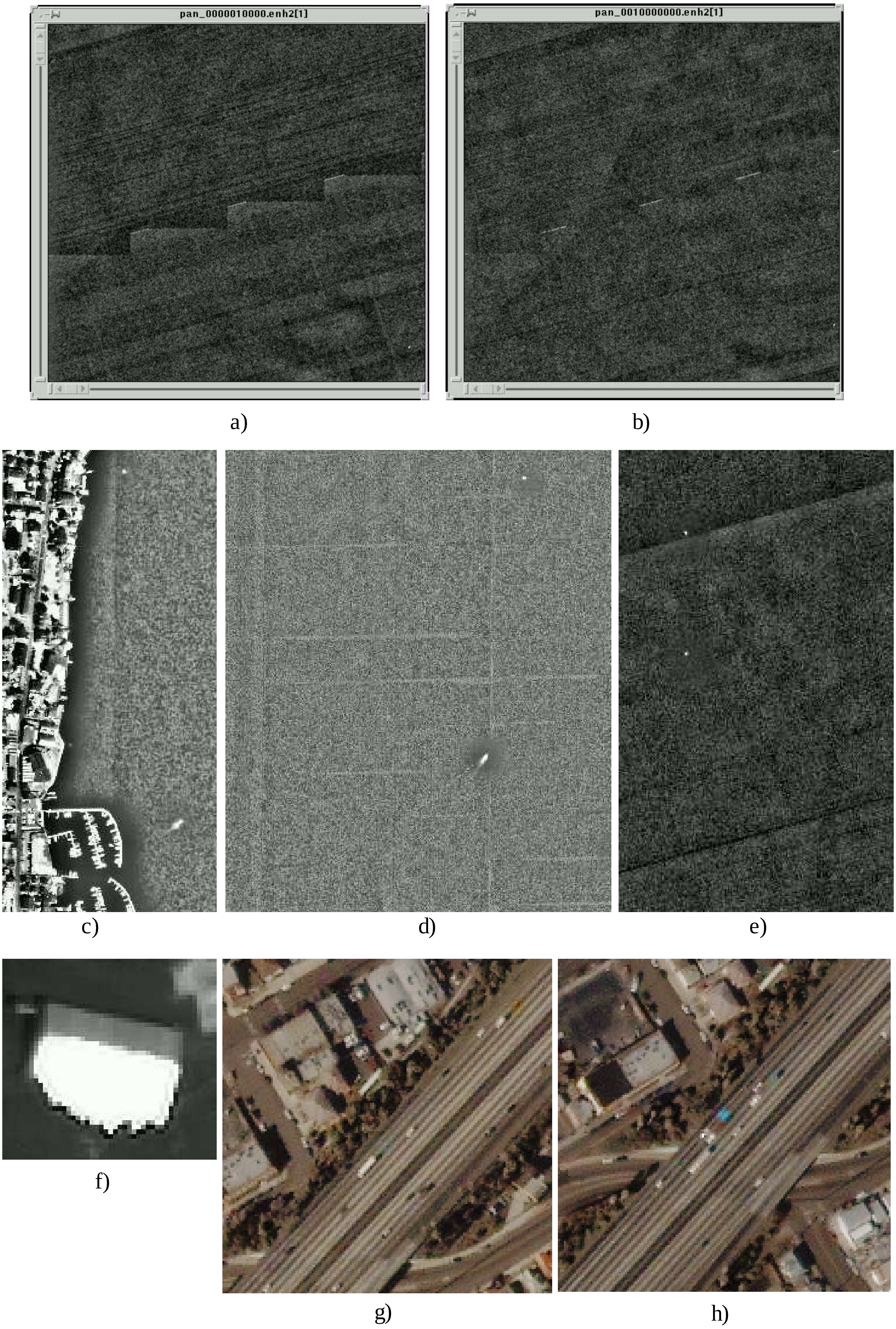

Fig. 1. Artefacts (see explanations in text).

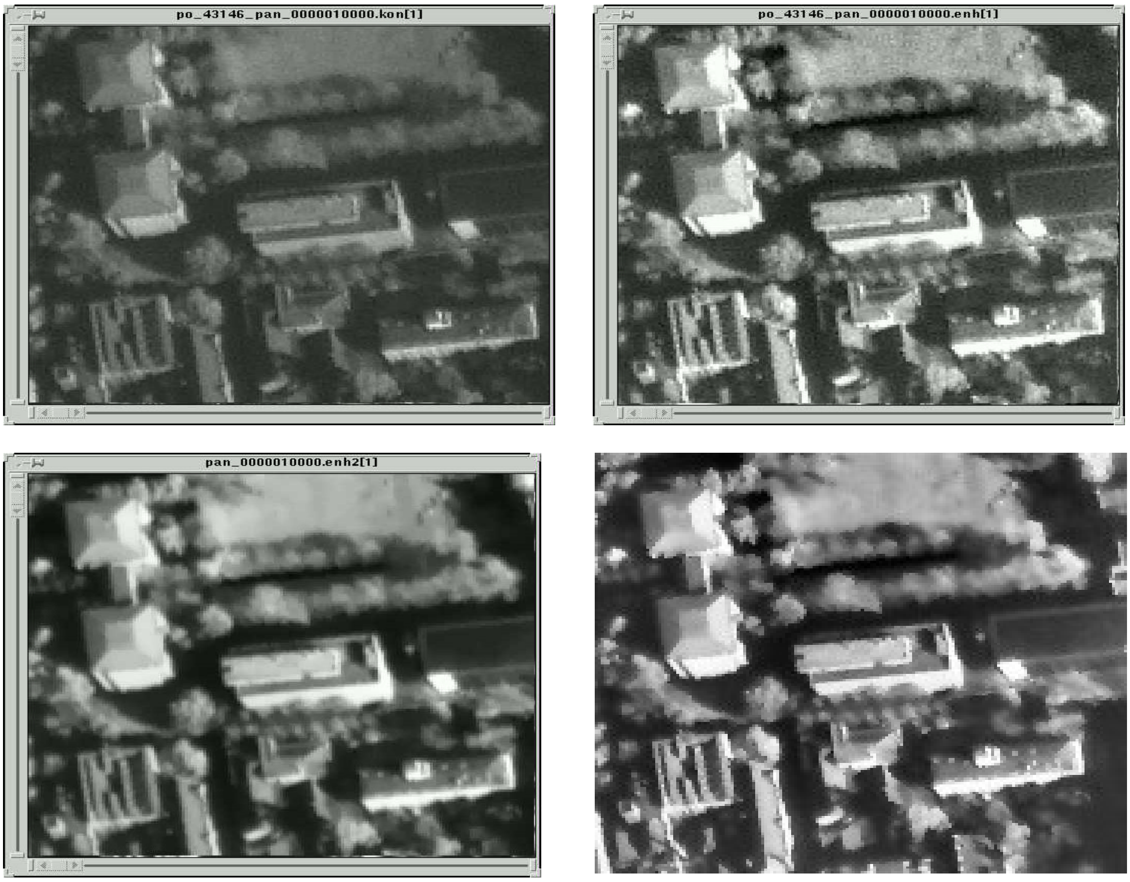

Fig. 2. Top: original image (left) and after Wallis filtering to indicate noise content (right). Bottom: preprocessing by the second (left) and third (right) methods.

4. METRIC QUALITY

4.1 Accuracy Potential and Sensor Orientation Models

The last 15 years various mathematical models have been formulated to derive 3D information and generate orthoimages from spaceborne line CCD sensors, especially SPOT, IRS-1 C/D and MOMS. These models have varying complexity, rigour and accuracy. Strict sensor models have been developed using the known sensor information and modified collinearity equations, in some cases including parameters for modelling errors in the interior orientation or in-flight calibration, or incorporating orbital information and orbital constraints. Several empirical tests have shown that with such models, reasonable B/H ratio and good quality GCPs in both object and image space 3D accuracies in the order of 0.25 – 0.3 pixels can be achieved for well-defined points. It would be reasonable to except that high-resolution imagery as IKONOS would exhibit similar accuracy characteristics. However, for IKONOS strict models can not be used, as both the sensor model and ephemeris data are proprietary information of SI, while raw data are also not commercially available but only one that have been geometrically processed by unknown transformations. Thus, alternative models come into play.

One possibility is the use of RPCs provided with some IKONOS products, like stereo and Geo Ortho Kit (Grodecki, 2001; Yang, 2000). Since the RPCs for Geo products are estimated by using only position and attitude data of the sensor and no GCPs, it is expected that the accuracy in both image and object space that can be achieved by RPCs will not be very high and would correspond to the accuracy specifications of this product). As it will be shown below, this has been verified by tests, while it has been also shown that the positional errors are very systematic due to a large bias and can be reduced to sub-metre errors in the simplest case by just a translation, which can be computed using some GCPs. Other models that do not need sensor and orbit information have been developed and used for spaceborne linear CCDs. RPCs can be estimated by using GCPs and not as an approximation of a strict sensor model as in the case of the RPCs provided by SI. Other nonrational polynomial models (Kratky, 1989; Papapanagiotu and Hatzopoulos, 2000) can be estimated similarly. However, estimating such polynomial coefficients using GCPs needs many GCPs that cover the whole planimetric and height range, which is difficult to impossible and costly, and also leads to extrapolation errors and possible undulations between GCPs, especially with high degree polynomials. DLT has been used by El-Manadili and Novak (1996) and Savopol and Armenakis (1998) with SPOT and IRS-1C images respectively, while Wang (1999) expanded the DLT by adding corrections for self-calibration, and Yang (2001) used it in piece-wise functions. Hattori et al. (2000) present 4 models termed 1D perspective, 1D affine, parallel perspective and 2D affine models based on extensive work of Okamoto (see e.g. Okamoto et al., 1999). For larger FOVs (e.g. SPOT), the affine projection introduces errors, which can be eliminated by a pretransformation of the images from central perspective to affine projection using terrain height information. Hattori et al. (2000) present results with SPOT images which show that both affine models perform better than the perspective ones. Palà and Pons (1995) used similarly a 2D affine model, incorporating terrain relief corrections in image space, however, only for generation of orthoimages, not 3D positioning.

All above models refer mostly to original raw images. However, Geo is rectified to a so-called inflated ellipsoid and map projected without terrain relief corrections. To relate object information to such imagery, the object information could be first corrected by relief displacements using a flat Earth or curved Earth model. Then, a simple affine transformation can relate object and image spaces (see Section 4.3), without the need to apply any image transformation (from central perspective to affine or correction for terrain relief). In fact, since the relative accuracy of Geo images is in the sub-metre level, the major correction needed are shifts between the two spaces. The two scales and shears are needed to model smaller deviations between the two spaces. Using various Geo images with GCPs in different projection systems and affine transformation between the two spaces, showed that the two scales deviate from 1 in the 4^{th} or 5^{th} decimal only, while the rotation is in the order of 1-2 deg (except of course for stereo images which are rotated), and the non-orthogonality of the axes is in the order of 0.003-0.03 deg. This affine transformation can be used not only for object to image transformation, but also 3D point positioning using two or more images, using essentially 6 parameters per image, and not 8, as sensor elevation and azimuth are known (see Eq. (8)). Simple linear models like the DLT and affine projection perform well with IKONOS images that cover a small area, but as the area increases, unmodelled higher-order terms are expected to lead to an accuracy deterioration. However, this also depends on the quality of the unknown methods used by SI to generate Geo images, i.e. to what extend non-linear terms can be modelled in generation of large Geo images.

4.2 Use of RPCs for Object to Image Transformation and 3D Point Positioning

In the rational function model, image pixel coordinates (*px, py*) are expressed as the ratios of polynomials of object coordinates (*X, Y, Z*), which in the case of the SI RPCs correspond to latitude, longitude and height. In order to improve the numerical stability of the operations, the two image and three object coordinates are each offset and scaled to fit the range from -1.0 to 1.0. For an image, the ratios of polynomials have the following form:

$$
\begin{aligned}
px_n &= \frac{f1(X_n, Y_n, Z_n)}{f2(X_n, Y_n, Z_n)} \\
py_n &= \frac{f3(X_n, Y_n, Z_n)}{f4(X_n, Y_n, Z_n)}
\end{aligned}
\qquad (1)
$$

with px_n and py_n normalised pixel coordinates and X_n, Y_n, Z_n normalised object coordinates.

To compute the normalised coordinates, the following equations are used:

$$
\begin{aligned}
&px_n = \frac{px - px_0}{px_s}, \quad py_n = \frac{py - py_0}{py_s} \\
&X_n = \frac{X - X_0}{X_s}, \quad Y_n = \frac{Y - Y_0}{Y_s}, \quad Z_n = \frac{Z - Z_0}{Z_s}
\end{aligned} \tag{2}
$$

with px_0, py_0 and px_s, py_s offset and scale values for the two image coordinates respectively, and similarly X_0, Y_0, Z_0 and X_s, Y_s, Z_s offset and scale values for the object coordinates.

In the RPCs, the maximum power of each object coordinate and the total power of all object coordinates are limited to 3. In such a case and following the SI definition of coefficient sequence, each polynomial has the following form (for convenience, the subscripts are omitted), which leads to the 80 RPCs per IKONOS image:

$$
\begin{aligned}
f(X,Y,Z) = {} & c_1 + c_2 Y + c_3 X + c_4 Z + c_5 XY + c_6 YZ + c_7 XZ + c_8 Y^2 + c_9 X^2 + c_{10} Z^2 + c_{11} ZYX \\
& c_{12} Y^3 + c_{13} X^2 Y + c_{14} Z^2 Y + c_{15} Y^2 X + c_{16} X^3 + c_{17} XZ^2 + c_{18} Y^2 Z + c_{19} X^2 Z + c_{20} Z^3
\end{aligned} \tag{3}
$$

With the SI RPCs, the two polynomials used in denominator are identical, while the first coefficient of the denominator is 1, to avoid the case when the denominator becomes close to zero, leading thus to practically 59 parameters. Using the RPCs, the distortions caused by the optical projection can generally be represented by the ratios of first-order terms. Thus, these terms are used by the space intersection procedure below to derive the initial object coordinate values.

The RPCs can be directly used for the transformation from object to pixel coordinates. However, the transformation from pixel to object coordinates is the inverse procedure and needs an iterative calculation due to the non-linearity of the RPCs:

1) Calculation of initial values for ground coordinates. As mentioned before, the distortions caused by the optical projection can be represented by the ratios of first-order terms in the RPCs. Omitting the higher-order RPCs, the functions which transform the object coordinates into pixel coordinates can be expressed as follows:

$$
px^i = \frac{(a_1 + a_2 Y + a_3 X + a_4 Z)^i}{(b_1 + b_2 Y + b_3 X + b_4 Z)^i}; \qquad py^i = \frac{(c_1 + c_2 Y + c_3 X + c_4 Z)^i}{(d_1 + d_2 Y + d_3 X + d_4 Z)^i} \tag{4}
$$

   where i is the index of the images (i = 2), and $(a_k, b_k, c_k, d_k)_{k=1,\ldots,4}$ are first-order RPCs. After making some changes of these equations, we can get the following equation groups:

$$
\begin{aligned}
&((a_1 - b_1 px) + (a_2 - b_2 px)Y^0 + (a_3 - b_3 px)X^0 + (a_4 - b_4 px)Z^0)^i = 0 \\
&((c_1 - d_1 py) + (c_2 - d_2 py)Y^0 + (c_3 - d_3 py)X^0 + (c_4 - d_4 py)Z^0)^i = 0
\end{aligned} \tag{5}
$$

   Obviously, given two or more images and their first-order RPCs, the initial object coordinates (X^0, Y^0, Z^0) can be derived from all above equations or just 3, two involving px and one py.

2) Derivation of the final object coordinates. By performing a Taylor expansion, the observation equations can be formulated as

$$
\begin{aligned}
&px^i = F(X,Y,Z)^i = \frac{f1(X^0, Y^0, Z^0)}{f2(X^0, Y^0, Z^0)} + \frac{\partial F^0}{\partial X} ?X + \frac{\partial F^0}{\partial Y} ?Y + \frac{\partial F^0}{\partial Z} ?Z \\
&py^i = G(X,Y,Z)^i = \frac{f3(X^0, Y^0, Z^0)}{f4(X^0, Y^0, Z^0)} + \frac{\partial G^0}{\partial X} ?X + \frac{\partial G^0}{\partial Y} ?Y + \frac{\partial G^0}{\partial Z} ?Z
\end{aligned} \tag{6}
$$

   and the final object coordinates can be derived by least square adjustment.

Out of the 32 testfield points, two were not available and another two seemed to be erroneous. Using the pixel coordinates of the remaining 28 GCPs, the corresponding pixel coordinates in left and right IKONOS images were computed using the RPCs and compared to the known pixel coordinates of the two datasets from ellipse fitting and least squares template matching (see Table 2). The differences had a very large systematic component. However, the relative accuracy as shown by the standard deviations is in the subpixel range, so after removing the bias by the use of some GCPs, e.g. 6, the achieved RMS become similar to the standard deviations listed in Table 2. The results with least squares matching are slightly worse than those of the ellipse fitting dataset, since occlusions and especially shadows at the roundabout perimeter influence matching, while with ellipse fitting the perimeter points were selected manually. However, with least squares matching the errors in left and right image are similar (i.e. the parallax errors are less), since for both images the template image and matching parameters were identical, and the shadow disturbances very similar. This consistency leads to better height accuracy as shown in Table 3, although the planimetry is still worse.

The values of the higher order RPCs, especially in the denominator, are very small. Their effect in the resulting pixel coordinates, even after multiplication with scale, is not significant even for the worst case, when the normalised object coordinates have an absolute value of 1. This was observed in various sets of available RPCs. To investigate how many RPCs are really needed, we repeated the computations of Table 2, combining the first 1 and 4 coefficients in the denominator (1 corresponds to nonrational polynomials and 4 include the 1st order terms), with the first 4, 9, 10 and 20 coefficients of the numerator (4, 10 and 20 correspond to 1st, 2nd and 3rd order polynomials, while 9 is like 10 without the quadratic term for the height, which in various RPCs was consistently smaller). Leaving out some coefficients, could change the value of the remaining ones, in presence of correlations between the parameters, which are very probable in the overparametrised RPCs. The correct procedure would be to recompute the RPCs with reduced coefficients, as an approximation to the strict sensor model, but clearly this could not be done. The results for the 20/4, 10/4 and 9/4 RPCs in the numerator/denominator give very similar results to the 20/20 version, which is what we expected from the numerical values of the left-out coefficients, i.e. 9 parameters in the numerator and 4 in the denominator or 21 parameters in total seem to suffice. This could be useful to speed up operations, if RPCs are to be used. The worse relative accuracy of the remaining versions (3-10 pixels standard deviation), combined with the better results of the 4/1 version (ca. 1 pixel), are in our opinion due to correlations between the RPCs and not an indication that more coefficients are needed. Indeed, in this paper and in Fraser et al. (2001b) it is shown that an affine model, computed from 4-6 GCPs gives equal or better accuracy than the full set of RPCs.

	Ellipse fitting				**Least squares matching**			
	Left Image		**Right Image**		**Left Image**		**Right Image**	
	x	y	x	y	x	y	x	y
Mean	28.94	-16.07	28.00	-16.52	28.94	-15.91	27.93	-16.14
Stand. Dev.	0.40	0.35	0.56	0.46	0.51	0.62	0.65	0.62

Table 2. Differences (in pixels) between known pixel coordinates and ones computed via RPCs.

Using the known pixel coordinates of the GCPs measured by ellipse fitting and least square template matching, 3D object coordinates of these points can be computed by the above described space intersection algorithm. Compared with the GPS measured coordinates after transformation of both coordinate sets to UTM, the RMS errors in X, Y and Z were 8.0, -31.3, 1.5 m respectively and the results again show a very large systematic trend (see Table 3). Then, six well-distributed points were selected as control points and other points served as check points. By using the six control points, two correction methods, only removing a positional bias and 3D similarity transformation between the RPC-computed and the known object coordinates, were performed, leading to sub-metre 3D accuracies (Table 3). The results are not sensitive to the selection of the six points as long as they are fairly well distributed. Fig. 3 shows the deviation of the GCP differences from the mean difference (bias). Although this test dataset is limited to be conclusive, it seems that in planimetry, where the bias is higher, the deviations vary within the image and in some cases they are locally systematic. Thus, the use of well-distributed GCPs for bias removal is suggested. The difference between the two corrections (translation and 3D similarity) is small, with the 3D similarity transformation giving slightly better results, especially in Z. Another version that was tried, was the subtraction of the bias in the pixel space, before performing 3D spatial intersection, and the results were similar to the ones with bias subtraction in the object space. Table 4 shows the maximum deviation from the mean bias. This shows that if only one GCP is used to remove the bias, the maximum additional error which will be added to the sub-metre accuracy after bias removal is in the order of 1-2 m.

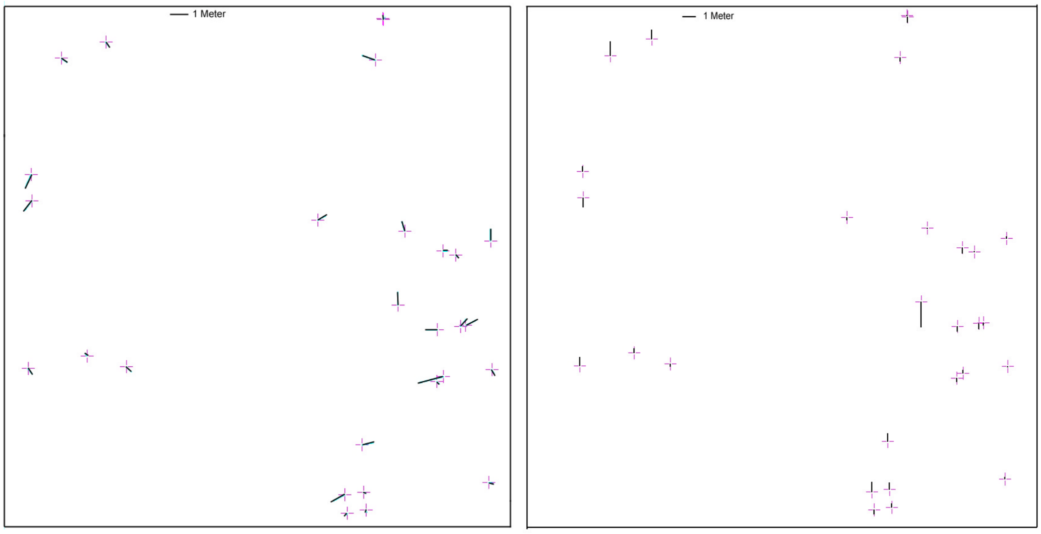

Fig. 3. Plot of the deviations from the mean bias computed from all 28 GCPs for planimetry (left) and height (right).

In a related paper, Fraser et al. (2001b) present results of 2D transformations using similarity, affine and projective models and 3D positioning using DLT and affine models with 2 and 3 image configurations. Their results show that with all these simple models sub-metre accuracy can be achieved, and that the affine model performs the best with 0.3 – 0.4 m planimetric accuracy (RMS) for 2D transformations and 0.25-0.45 m and 0.45-0.70 m planimetric and height accuracy using 2-3 images, 4-8 GCPs and bundle adjustment for 3D spatial resection. This accuracy is higher than the one achieved using the full set of RPCs.

Processing Method	**Least Squares Matching**						**Ellipse Fitting**					
	RMS (m)			**Max. (m)**			**RMS (m)**			**Max. (m)**		
	X	Y	Z	X	Y	Z	X	Y	Z	X	Y	Z
Use of RPCs	8.00	31.37	1.55	8.96	-32.40	-2.18	8.28	31.50	1.78	9.74	-32.40	-3.52
Position Bias Removal	0.65	0.50	0.68	-1.89	1.08	-1.80	0.49	0.43	0.79	1.48	1.21	-1.92
3D similarity	0.65	0.44	0.58	2.07	-1.01	1.10	0.48	0.37	0.74	-1.18	-1.13	-1.82

Table 3. Errors of 3D point determination using RPCs.

Least Squares Matching						**Ellipse Fitting**					
Mean Bias			**Max. Dev. from Bias**			**Mean Bias**			**Max. Dev. from Bias**		
X	Y	Z	X	Y	Z	X	Y	Z	X	Y	Z
7.98	-31.37	-1.42	-2.02	-1.09	-2.09	8.26	-31.49	-1.59	1.48	1.22	-1.92

Table 4. Mean bias computed from all 28 GCPs and maximum deviation of GCP errors from mean bias (in m).

4.3 Use of Relief-Corrected Affine Transform for Object to Image Transformation and 3D Point Positioning

The GCPs in UTM were projected on a reference height of 0m, and then several transformations (affine, bilinear, quadratic and biquadratic) from object to image space were computed with all GCPs. The results (sigma-0 after the least squares adjustment) were practically identical for all transformations. The results for the ellipse fit and matching datasets for the left/right/nadir images were 0.41/0.46/0.36 and 0.60/0.60/0.45 pixels respectively. The nadir image gave better results probably due to better image quality and more accurate relief correction, since height errors influence the relief displacement by factor 5 less than for the stereo images due to the higher sensor elevation. The residuals showed that some image measurements, especially with matching were poor, with more than 1 pixel errors (thus, also the results of the matching dataset are less accurate). The affine transformation was repeated with variable number of GCPs (3, 6, 8, all and “all, cleaned” without few pixel measurements with large errors). The results were very similar to the ones published in Fraser et al. (2001b) and the results form the matching dataset were worse in almost all cases, by ca. 0.1-0.2 pixels. However, it was interesting to note than 3 GCPs gave similar or better results than 6 or 8 (see Table 5). This is a confirmation that the most important factor is the point quality not their number. The 3 GCPs for the stereo and nadir images were points 4, 8, 16 and 9, 26, 29 respectively (see Fig. 1 in Fraser et al. (2001b)), with good but not optimal distribution. The results with 3 GCPs were worse than the ones with all GCPs only by 13-14% and 22-24% for the stereo and nadir images respectively. The conclusion is that even 3 highly accurate GCPs with fair distribution suffice for subpixel accurate transformation from object to image space.

As a next step, we performed 3D spatial resection using the following method. The above affine transformations which were computed for each image independently provided six parameters (see Eq. (8) below). The parameters a_4 and b_4 were computed as explained at Eq. (8). These 8 parameters were used with the same programme for 3D resection using RPCs (see Section 4.2), without bias removal naturally. The results using the ellipse fit dataset are listed in Table 6. Although the affine parameters from the “all, cleaned” version were used, all points were used in the computation of the error statistics. It is very interesting to note that the results with 3 GCPs are very similar to the “all, cleaned” version. In all cases, planimetric accuracy is in the 0.3-0.5 m range and height accuracy in the 0.6-0.8 m range. The results are very similar to the ones in Fraser et al. (2001b), however some significant differences exist. Fraser et al. compute 8 affine parameters (as in Eq. (8)) using GCPs and bundle adjustment. We estimate only 6 parameters (excluding a_4 and b_4 , which are functions of known quantities and other parameters) for each image separately and using relief-corrected planimetric coordinates of GCPs. Thus, we need minimum only 3 GCPs and no image pretransformation from central perspective to affine projection (Hattori et al., 2000) is needed. Later, is time consuming, needs a DTM, interior orientation and approximate exterior orientation and may introduce image errors. A use of bundle adjustment in our estimation of the 6 affine parameters could be favourably used but has not been implemented. Summarising, with our approach 3 accurate GCPs can be used for the computation of 6 affine parameters from relief-corrected object space to image space without any knowledge about the sensor and its orbit, but knowing the sensor elevation and azimuth and assuming they are constant within one scene. These parameters can be used for any transformation between the original object space and image space, including orthoimage generation (see Section 5), as well as 3D spatial resection for point positioning and automatic DSM generation, including its use to constrain matching along a line or perform an epipolar resampling.

Image	Coordinate dataset	# control points	# check points	x-RMS	x-Mean with Sign	x-Max. Abs.	y-RMS	y-Mean with Sign	y-Max. Abs.
Left	Ellipse fit	3	25	0.45	-0.06	1.16	0.43	0.06	0.91
	Matching	3	25	0.51	0.07	1.17	0.75	0.21	1.96
Right	Ellipse fit	3	25	0.47	-0.03	1.46	0.53	0.09	1.27
	Matching	3	25	0.54	-0.01	1.47	0.75	0.19	1.93
Nadir	Ellipse fit	3	25	0.39	0.01	1.31	0.44	-0.18	0.95
	Matching	3	25	0.37	0.17	0.93	0.67	0.16	1.95

Table 5. Error statistics (in pixels) for affine transformation from object to image space for various images and pixel coordinate datasets. The statistics refer to the check points only.

# of images	2				3			
# of GCPs	3	6	8	All, cleaned	3	6	8	All, cleaned
X-RMS	0.49	0.44	0.45	0.42	0.32	0.33	0.33	0.32
Y-RMS	0.38	0.47	0.46	0.38	0.32	0.39	0.37	0.30
Z-RMS	0.76	0.75	0.73	0.71	0.57	0.62	0.60	0.58

Table 6. Error statistics (in m) for 3D resection using relief-corrected affine transform computed from different number of GCPs. The statistics refer to the check points only, except the "all, cleaned" versions. The number of check points is 28 minus the number of GCPs.

5. ORTHOIMAGE GENERATION

5.1 Orthoimage Generation Methods

Our group has been involved in various projects aiming at generation of accurate orthoimages with use of GCPs and DTMs starting from IKONOS Geo. Thereby, two approaches have been used to model the transformation from object to image space. The first approach is using Kratky's polynomial mapping functions (PMFs) (Kratky (1989), Baltsavias and Stallmann (1992)), which include 14-16 terms up to 4th degree. The PMFs, like the RPCs, are a very good approximation of a strict sensor model and are estimated similarly to the RPCs. They have been successfully used for orthorectification of spaceborne imagery (Baltsavias and Stallmann, 1996). In the IKONOS case, with unknown sensor model, the PMFs must be estimated using GCPs, which is suboptimal, as explained in Section 4.1. The second approach is using an affine transformation. At least 3 GCPs are needed, but we have used in our projects 4-6 to have a certain redundancy (although 3 good GCPs suffice as shown in Section 4.3). Before computing the affine transformation from object to image space, the GCPs are projected on a reference plane and the planimetric X and Y coordinates are corrected according to Eq. (7):

$$\Delta X_i = -\Delta Z_i * \sin(a) / \tan(e) \qquad (7)$$
$$\Delta Y_i = -\Delta Z_i * \cos(a) / \tan(e)$$

with $\Delta Z_i = Z_i - Z_o$

Z_i = height of ground point i

Z_o = height of reference plane

a = sensor azimuth

e = sensor elevation

ΔX_i , ΔY_i = planimetric displacement of point i due to projection onto the reference plane

whereby the azimuth and elevation are taken from the metadata file delivered with the images. Eq. (7) shows that the radial planimetric displacement depends only on elevation, while its distribution among the two axes X and Y depends on the azimuth. For scenes imaged away from the orbit footprint, the displacement would be more in the X direction and vice versa. The above equation has been used for the whole Geo scenes, as the variation of azimuth and elevation within a scene, when the satellite is not rotating, is so small, that their influence on the planimetric displacement is negligible. The choice of the reference plane is irrelevant (at least in our implementation, where the affine transformation is computed from centred coordinates), but we use for less computations (no need to compute ΔZ_i) the same reference plane as for the DTM, i.e. at height zero. The GCPs do not have to cover the whole image, i.e. their distribution is not so important, as long as the affine parameters can be determined reliably. This can be achieved, if the range of their coordinates in the 2 directions (in object or image space) covers e.g. ca. 1/3 of the area dimensions. Then, for each orthoimage pixel, knowing the height, we project it onto the same reference plane and then perform the affine transformation and grey value resampling. In our implementation, we combine the projection to the reference plane and the affine transformation to one common operation involving 8 parameters (instead of 6 for the 2D affine transformation) according to Eq. (8), and this operation is applied to the DTM nodes, which are treated as anchor points. An additional advantage of this approach is that the regular DTM structure is preserved, and thus an update philosophy can be used in the computations leading to even faster orthoimage generation.

$$x_i = a_1 + a_2 X_i + a_3 Y_i - a_4 Z_i \quad (8)$$
$$y_i = b_1 + b_2 X_i + b_3 Y_i - b_4 Z_i$$

with x_i , y_i ...pixel coordinates

X_i , Y_i , Z_i ...DTM coordinates without any relief displacement of the planimetric position

a_1 , a_2 , a_3 , b_1 , b_2 , b_3 ...six 2D affine parameters computed from the GCPs after projection to the reference plane

$a_4 = [a_2 * \sin(a) + a_3 * \cos(a)] / \tan(e)$

$b_4 = [b_2 * \sin(a) + b_3 * \cos(a)] / \tan(e)$

The advantage of the second approach over the first one is the need for much less GCPs (which are difficult to get in non-urban regions) and more freedom in their choice (distribution). Furthermore, the computations are less. The accuracy of the second approach can be better since there are no extrapolation effects and possible numerical instabilities. In addition, if GCPs along a water body can be selected, the height must be known only for one GCP. For both approaches, the higher the sensor elevation, the less important the height becomes. In the extreme case of very high elevation, the orthoimage can be produced from planimetric GCPs and respective 2D transformations, without a DTM or with a much less accurate one. The planimetric influence of height errors can be estimated by Eq. (7), e.g. for an elevation of 60, 70, 80 and 85 deg, a height error of 1 m, causes 0.58, 0.36, 0.18 and 0.09 m radial displacement, respectively. Since Geo products usually have elevations larger than 60 deg, height errors always influence planimetry to a lesser extent. The relief corrected affine transformation used in orthoimage generation but also 3D positioning (see Section 4.3) assumes than elevation and azimuth are constant within one scene. As mentioned above, the variation of azimuth and elevation is minimal within a scene, when the satellite does not rotate during scene acquisition, which seems to be the common scanning mode used by Ikonos. However, Ikonos has also other scanning modes, where azimuth and especially elevation may change within a scene, e.g. consider the case when the sensor is looking forward and rotates backwards constantly (i.e. elevation change) to scan a scene backwards. Although such scanning modes seem to be seldom, are more complicated and for flat terrain and non-Lambertian object reflection cause varying imaging conditions (illumination-to-sensor angle changes), caution should be paid that for some scanning modes the constant angle model may be insufficient and should be replaced by ones using higher order (especially linear) terms in the angle variation.

5.2 Influence of DTM and GCPs on Orthoimage Accuracy

The planimetric accuracy of the orthoimage depends on the accuracy of the GCPs and the DTM. For IKONOS compared to other spaceborne sensors, DTM accuracy is less important due to the small FOV, while GCP accuracy becomes more important, due to the small pixel footprint. As shown in Sections 4.2 and 4.3, the planimetric potential of IKONOS Geo lies in ca. 1/3 pixel. Thus, the GCPs should be 1-2 dm accurate in both object and image space. While getting this accuracy with GPS in object space is no problem, finding image points suitable for measurement by image analysis techniques with 0.1-0.2 pixel accuracy and accessible in the scene for GPS measurement can be problematic. This is one more reason in favour of the second orthoimage generation approach. Best GCPs have good contrast, are preferably on the ground and are intersections of straight, long enough lines or centres of gravity of circular/elliptical features. The planimetric accuracy of the orthoimage can be easily estimated by the GCP accuracy and Eq. (7) using as input the DTM accuracy and the known azimuth and elevation. For example, with 1-2 dm GCP accuracy, DTM accuracy of 2 m and elevation larger than 70 deg, a sub-metre planimetric accuracy can be achieved, similar to the much more expensive Precision Plus product.

5.3 Test Results

We have produced orthoimages from IKONOS Geo in three projects. Table 7 shows some characteristics of the images and input data for the orthoimage generation used. In all projects, the aim was to generate more accurate orthoimages, starting from the cheapest product of SI. In the first project described in Kersten et al.

(2000), our first approach was used (see Zug / 1 and Zug / 2 in Table 8) and a second one from another company (Zug / 3 and Zug / 4), similar to our second one but more complicated in estimating the azimuth and elevation. Zug / 1 has check points only within the perimeter of the used control points, while Zug / 2 also outside, showing the extrapolation errors that can occur with our first approach, especially notable in the maximum absolute errors. The achieved accuracy with both methods was 1.5-2.5 m RMS, but in this case the potential of IKONOS was not fully exploited, because the GCPs, as checked with more accurate reference data made available after the project end, had unfortunately the same accuracy as the produced IKONOS orthoimages and a high bias error, close to the RMS error. The orthoimages were not accurate enough, because the DTM used in their production was not a very accurate one and most probably orientation errors causing the bias.

In the second project, a Pan-Sharpened image of a Greek island with little man-made objects was orthorectified. Although 38 GCPs measured with GCPs were available, about half of them were not well-defined in the image. The DTM has a grid spacing of 2 m and was interpolated from 1:5,000 map contours and additionally measured breaklines. Its accuracy, estimated using the GCP points, was ca. 3.3 m RMS. Both approaches were employed with 38 and 28, and 4 GCPs respectively for the geometric transformation (Nisyros / 5, / 4, / 3 and / 2 in Table 9). Version 3 is like 2 but only with the points that were well identifiable and measurable, and shows the accuracy potential with good GCPs. Nisyros / 1 shows the accuracy of the original Geo image. The planimetric accuracy of both approaches was similar, with the second approach being slightly better. The second approach was not more accurate, as we had expected, due to the lack of accurate enough GCPs. This project is dealt with in detail in another publication (Vassilopoulou et al., 2002).

In the third project, a PAN image of Lucerne was processed with the second approach and 6 GCPs covering 1/2 to 1/3 of the image extent for the affine transformation. The GCPs included 5 GPS points, 46 points measured in triangulated aerial imagery and 17 points measured from Swissimage orthoimages (see product generation parameters below). The expected accuracy of these 3 groups was 0.5, 1 and 2-3 m, however, the accuracy of the last two groups seemed to be worse, based on a 2D affine transformation using all GCPs after reduction to a reference height plane (excluding two large blunders, 16 points had residuals more than 3m and up to 8.3m). The GCP accuracy varied a lot, with the orthoimage GCPs being insufficient and most photogrammetric GCPs equally inadequate. The majority of GCPs were not well-defined in the image, including the GPS points. Version Lucerne / 1 in Table 9 shows the accuracy of the original Geo product. Versions 2 to 5 show the accuracy using all GCPs and sequentially reducing their number, deleting the poorer ones. Again, versions 4 and 5 show that with good GCPs, the accuracy can be in meter level or below. Production of the same orthoimage with identical GCPs using the PCI OrthoEngine software which uses a self-developed sensor model for IKONOS led to X and Y RMS of 6.1 and 1.5 m respectively with very systematic residuals.

	Zug	**Lucerne**	**Nisyros**
Date, Time (local)	8/4/2000, 10:11	22/4/2000, 10:21	8/4/2000, 10:35
Sensor azimuth (deg)	266.0	256.3	134.9
Sensor elevation (deg)	85.7	67.7	73.5
Sun azimuth (deg)	151.3	153.6	136.6
Sun elevation (deg)	47.1	53.0	53.4
DTM spacing/accuracy (m)	5 / 0.4 (raw irregular data)	25 / 2.5 in lowland, 10 in Alps	2 / 3.3 *
GCP accuracy (m)	1.5-2	0.5 – 3**	ca. 0.5
GCP definition	Medium to good	Very poor to good	Poor to good
Elevation range (m)	400-990	0-700	400-2100

* Estimated from the GCPs

** See comment on real accuracy in text

Table 8. Acquisition parameters of IKONOS images used in orthoimage generation.

Project / Version	**Image type / Control Points**	**Check Points***	**Mean with sign**		**RMS**		**Maximum absolute**	
			X	**Y**	**X**	**Y**	**X**	**Y**
Zug / 1	PAN / 27	41	0.9	-1.3	1.5	1.6	3.8	3.2
Zug / 2	PAN / 27	69	1.1	-1.5	2.5	2.0	11.3	6.5
Zug / 3	PAN / 34	26	-1.3	-2.5	1.8	2.7	3.4	5.0
Zug / 4	MSI / 39	26	-0.8	-1.5	1.4	1.7	3.6	3.5
Lucerne / 1	PAN	66	-70.9	-15.4	134.2	30.6	501.5	118.1
Lucerne / 2	PAN / 6	65 **	-0.47	0.92	2.6	2.2	9.9	5.9
Lucerne / 3	PAN / 6	47	-0.14	0.86	2.2	2.2	6.7	5.9
Lucerne / 4	PAN / 6	21	-0.23	-0.15	0.8	0.8	1.5	1.5
Lucerne / 5	PAN / 6	14	-0.22	0.07	0.6	0.6	1.0	1.1
Nisyros / 1	PAN-MSI	38	-102.6	70.0	106.1	75.5	153.1	122.8
Nisyros / 2	PAN-MSI / 4	34	-0.7	0.2	1.7	1.0	4.4	2.3
Nisyros / 3	PAN-MSI / 4	15	-0.6	-0.1	0.9	0.6	1.5	1.4
Nisyros / 4	PAN-MSI / 28	10	-0.3	1.0	1.8	1.5	4.4	2.6
Nisyros / 5	PAN- MSI / 38	0	-0.4	0.8	1.5	1.3	3.7	2.3

* Check points in Lucerne include 6 control points ; ** One GCP was outside the produced orthoimage

Table 9. Statistics of planimetric errors (in m) of generated orthoimages (see explanations in text).

The above results are a proof that orthoimages of 1-2 m accuracy can be routinely produced from various Geo products (PAN, MSI, PAN-MSI), with varying image quality and sensor elevation, with DTM and GCPs of rather moderate accuracy, and hilly to steep terrain and without needing a strict sensor model nor RPCs. With better quality GCPs, even sub-metre accuracies can be achieved. Use of the Geo Ortho Kit product results in significantly higher costs and much more mathematical operations, while DTM and GCPs are still needed and probably also transformations from the local map coordinate system to the one supported by the IGM. The accuracy improvement of the produced orthoimages compared to the original Geo images regarding both RMS and maximum absolute errors as shown in Table 9 is enormous.

6. BUILDING EXTRACTION FROM IKONOS

6.1 Accuracy of Building Extraction

Depending on the application, accuracy requirements vary. Regarding the here treated building extraction within the wider application frame of digital city models, metric accuracy expectations again vary. To fulfil requirements for mobile communications, one of the major markets for city models, accuracies in the 1-2 m range are generally needed. This implies the need to use the expensive Precision or Precision Plus imagery (with costs outside N. America 140-180 USD/km^2 and 220-250 USD/km^2 respectively). However, as it will be shown here, 3D positioning at 1-m accuracy level or better can be achieved by using the cheapest product Geo.

Whereas the 3D ground point determination in Section 4 was centred upon ‘high-quality’ targets, accurate positioning of building features, generally corners and edges, involves not only metric factors but also issues of image resolution and feature identification. The approach adopted in the reported investigation to ascertaining the metric quality of building extraction in stereo IKONOS imagery again involved independent checks of photogrammetrically triangulated distinct points against their GPS-surveyed positions. As mentioned, 19 image-identifiable roof corners were precisely surveyed to serve as accuracy checkpoints in the building extraction phase. Within the stereo triangulation, the RPCs produced RMS accuracies of 0.7m in planimetry and 0.9m in height after removal of the bias in object space using the known GCP coordinates. Corresponding accuracy estimates resulting from the 19 checkpoints for the affine and DLT models with 6

GCPs were 0.7m and 0.6m, and 1.0m and 0.8m, respectively, for planimetry and height. Triangulation of the 3-fold image coverage produced results which were not significantly different than those for the stereo restitution. Whereas in practice it may be unlikely that a 3-image coverage would be employed for building extraction, provision of the near-nadir image can prove very useful for subsequent orthoimage generation of built-up urban areas.

6.2 Evaluation of Building Extraction

In order to provide a qualitative and quantitative assessment of the potential of stereo IKONOS imagery for the generation of building models, the University of Melbourne campus was measured manually in stereo with both an in-house developed software tool for the IKONOS stereo images, and using an analytical plotter for the 1:15,000 colour aerial imagery. The resulting plots of extracted building features are shown in Fig. 4. The manual measurements of roof corners and points of detail were topologically structured automatically using the software package CC-Modeler (Gruen and Wang, 1998) and also visualised (Fig. 5).

This process revealed that many building points could neither be identified nor subsequently measured in the IKONOS images. Moreover, in a number of cases, buildings could only be reconstructed in a coarse generalised form (Fig. 6). Measurement and interpretation in stereo is a considerable advantage, as is the use of colour which was unfortunately not available in the IKONOS stereopair. Other influential factors are shadows, occlusions, edge definition (related also to noise and artefacts), saturation of bright surfaces, sun and sensor elevation and azimuth, and atmospheric conditions. The 1m resolution of IKONOS also leads to certain interpretation restrictions. This investigation was aimed in part at quantifying the extent of such limitations.

A comparison of the two models in Fig. 4, one from aerial photography and the other from IKONOS imagery, revealed the following regarding the IKONOS stereo feature extraction: about 15% of the building area as measured in aerial images could not be modelled; a number of both small and large buildings could not be identified and measured; some new buildings could however be reconstructed, even if small; and buildings could be often only generalised with a simplified roof structure and variations to their form and size. It is interesting to note that this 15% fits very well with the findings of Ridley et al. (1997). However, additional tests with different IKONOS imagery are needed in order to draw safer conclusions.

Fig. 4. Buildings of University of Melbourne campus reconstructed from 1:15,000 aerial images (left) and from stereo IKONOS imagery (right). To simplify visualisation, first points and first lines have been omitted in the left figure.

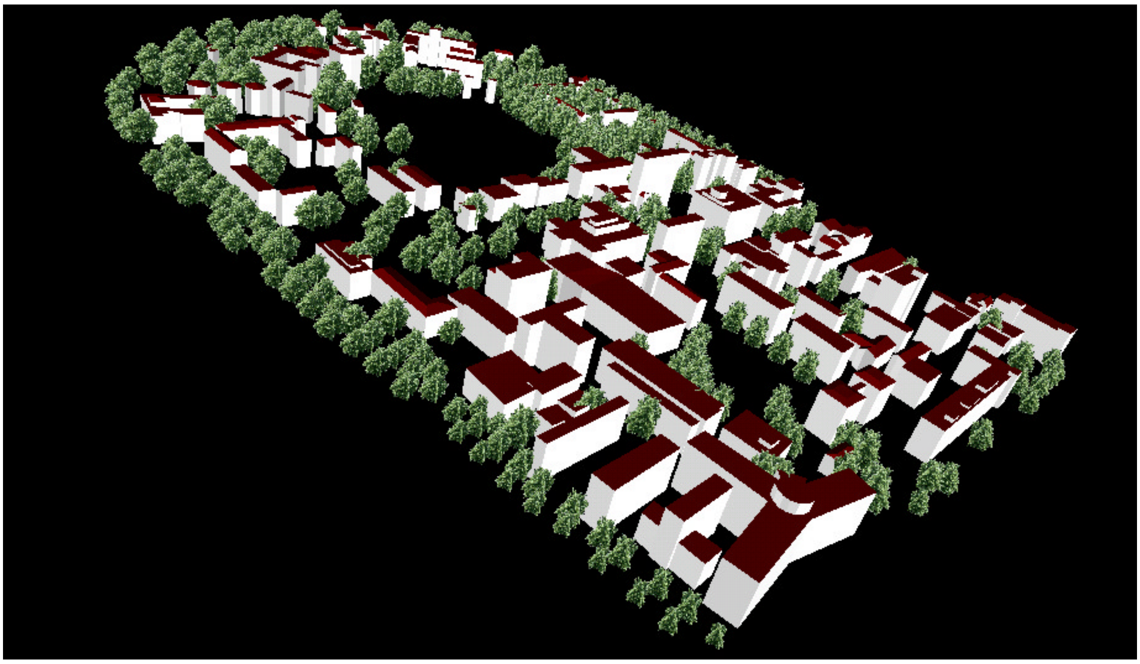

Fig. 5. Visualisation of University of Melbourne campus with buildings and trees extracted from stereo IKONOS images.

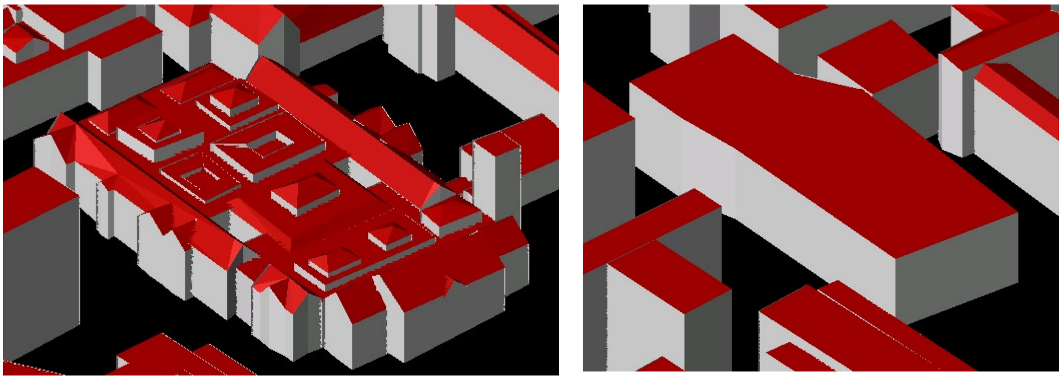

Fig. 6. Building with complicated roof structure as measured from aerial images (left) and IKONOS images (right).

7. CONCLUSIONS

This investigation has shown that IKONOS Geo stereo imagery has high geometric integrity and the potential to yield sub-metre geopositioning accuracies, using either simple geometric models for sensor modelling or provided RPCs and a moderate number (4-8) of accurate GCPs. Similarly, object to image transformations and orthoimage generation can be achieved with 1-2 m accuracy, or even sub-metre one with good GCPs, with a simple and fast 2D affine transformation after relief displacement corrections (or incorporating the later in a 3D affine transform). This affine transformation gives sub-metre results with just 3 good GCPs and can be also employed in 3D spatial resection for point positioning and DSM generation. Building points can be measured with an accuracy of ca. 1m. These results are impressive in the context of building reconstruction, but they must be weighed against some notable shortcomings of 1m satellite imagery for building (or other) feature detection and identification. While the limitations of an image resolution of 1m are well understood, it is more the variability of image quality from scene to scene that will limit application of the imagery to building reconstruction and city modelling. The influence of factors which are largely beyond the current control of the image user, such as date and time of image collection, restriction to favourable sun angles and atmospheric conditions, etc. will likely generate difficulties if one is seeking to exploit the imagery to its full potential. We have witnessed in this investigation problems in trying to comprehensively describe the stereo scene and identify not only all buildings of a certain size, but also to accurately reconstruct their form without excessive generalisation. The shortcomings in radiometric quality, although not a major influence factor for this manual building extraction, do cause problems in both manual and computer mensuration accuracy and interpretability. Noise is relatively high, the applied MTFC destroys to a large extent the edge information, and many artefacts exist. Thus, better radiometric sensor performance is needed to fit the high geometric quality of IKONOS and a better preprocessing needs to be developed by SI, along the lines presented in this work. The issues of radiometric inhomogeneity both within and between IKONOS scenes are unlikely to be affected by the level of IKONOS product purchased and this investigation has demonstrated that very high metric performance is achievable, at least for the small area of single scenes, with the least expensive product offering, namely Geo imagery, and without the need of sensor model information, ephemeris data or RPCs.

ACKNOWLEGEMENTS

The provision of imagery and ground control information by the Department of Geomatics, University of Melbourne and the co-operation with C. Fraser, H. Hanley and T. Yamakawa are gratefully acknowledged. The IKONOS image of Lucerne was kindly provided by the National Point of Contact, Swiss Federal Office of Topography, Wabern, the images of Zug by the company Swissphoto AG, while the IKONOS image of Nisyros was made available by Prof. E. Lagios, University of Athens, Greece within the EU project Geowarn (www.geowarn.org). Gene Dial and Laurie Gibson (Space Imaging) are acknowledged for valuable discussions and suggestions and provision of information.

REFERENCES

Baltsavias, E.P., 1991. Multiphoto geometrically constrained matching. Ph.D. dissertation, Institute of Geodesy and Photogrammetry, ETH Zurich, Report No. 49.

Baltsavias, E.P, Stallmann, D., 1992. Metric information extraction from SPOT images and the role of polynomial mapping functions. International Archives of Photogrammetry and Remote Sensing, Vol. 29, Part B4, pp. 358-364.

Baltsavias, E., Stallmann, D., 1996. Geometric potential of MOMS-02/D2 data for point positioning, DTM and orthoimage generation. International Archives of Photogrammetry and Remote Sensing, Vol. 31, Part B4, pp. 110-116.

Davis, C.H., Wang, W., 2001. Planimetric accuracy of Ikonos 1-m panchromatic image products. Proc. ASPRS Annual Conference, St Louis, 23-27 April 2001, 14 p. (on CD-ROM).

Dial, G., 2000. Ikonos satellite mapping accuracy. Proc. ASPRS Annual Conference, Washington D.C., 22-26 May 2000, 8 p. (on CD-ROM).

Dial, G., Gibson, L., Poulsen, R., 2001. IKONOS satellite imagery and its use in automated road extraction. In: Automated Extraction of Man-Made Objects from Aerial and Space Images (III), E. Baltsavias, A. Gruen, L. Van Gool (Eds.), Balkema Publishers, Lisse, pp. 349-358(in press).

El-Madanili, Y., Novak, K., 1996. Precise rectification of SPOT imagery using the direct linear transformation model. Photogrammetric Engineering and Remote Sensing, 62(1), pp. 67-72.

Fraser, C., Baltsavias, E., Gruen, A., 2001a. 3D building reconstruction from high-resolution IKONOS stereo imagery. In: Automated Extraction of Man-Made Objects from Aerial and Space Images (III), E. Baltsavias, A. Gruen, L. Van Gool (Eds.), Balkema Publishers, Lisse, pp. 325-338(in press).

Fraser, C.S., Hanley, H.B., Yamakawa, T., 2001b. Sub-metre geopositioning with Ikonos GEO imagery. Proc. Joint ISPRS Workshop High Resolution Mapping from Space 2001, Hannover, 19-21 September (on CD-ROM).

Gerlach, F., 2000. Characteristics of Space Imaging's One-Meter Resolution Satellite Imagery Products. International Archives of Photogrammetry and Remote Sensing, Vol. 33, Part B1, pp. 128-135.

Gruen, A., Wang, X., 1998. CC-Modeler: a topology generator for 3-D city models. ISPRS Journal of Photogrammetry and Remote Sensing, 53(5), pp. 286-295.

Grodecki, J., 2001. Ikonos stereo feature extraction - RPC approach. Proc. ASPRS Annual Conference, St. Louis, 23-27 April 2001, 7 p. (on CD-ROM).

Hanley, H.B., Fraser, C.S., 2001. Geopositioning accuracy of Ikonos imagery: indications from 2D transformations. Photogrammetric Record, 17(98), 12 p. (in press).

Hattori, S., Ono, T., Fraser, C., Hasegawa, H., 2000. Orientation of high-resolution satellite images based on affine projection. International Archives of Photogrammetry and Remote Sensing, Vol. 33, Part B3/1, pp. 359-366.

Hofmann, P., 2001. Detecting buildings and roads from IKONOS data using additional elevation information. GIS, (6), pp. 28-33.

Kersten, T., Baltsavias, E., Schwarz, M., Leiss, I., 2000. Ikonos-2 Carterra Geo – Erste geometrische Genauigkeitsuntersuchungen in der Schweiz mit hochaufgeloesten Satellitendaten. Vermessung, Photogrammetrie, Kulturtechnik, 8, pp. 490-497.

Kratky, V., 1989. Rigorous photogrammetric processing of SPOT images at CCM Canada. ISPRS Journal of Photogrammetry and Remote Sensing, 44(2), pp. 53-71.

Li, R., G. Zhou, S. Yang, G. Tuell, N.J. Schmidt and C. Fowler 2000. A Study of the Potential Attainable Geometric Accuracy of IKONOS Satellite Imagery. International Archives of Photogrammetry and Remote Sensing, Vol. 33, Part B4/2, pp. 587-595.

Okamoto, A., Ono, T., Akamatsu, S., Fraser, C.S., Hattori, S., Hasegawa, H., 1999. Geometric characteristics of alternative triangulation models for satellite imagery. Proc. ASPRS Annual Conference, Portland, Oregon, 17-21 May, 12 p. (on CD-ROM).

Palà, V., Pons, X., 1995. Incorporation of relief in polynomial-based geometric corrections. Photogrammetric Engineering and Remote Sensing, 61(7), pp. 935-944.

Papapanagiotu, E.G., Hatzopoulos, J.N., 2000. Automatic extraction of 3D model coordinates using digital stereo images. International Archives of Photogrammetry and Remote Sensing, Vol. 33, Part B4/2, pp. 805-812.

Ridley, H.M., Atkinson, P.M., Aplin, P., Muller, J.P., Dowman, I., 1997. Evaluating the potential of the forthcoming commercial US high-resolution satellite sensor imagery at the Ordnance Survey. Photogrammetric Engineering and Remote Sensing, 63(8), pp. 997-1005.

Savopol, F., Armenakis, C., 1998. Modelling of the IRS-1C satellite pan imagery using the DLT approach. International Archives of Photogrammetry and Remote Sensing, Vol. 32, Part 4, pp. 511-514.

Sohn, G., Dowman, I. Extraction of buildings from high resolution satellite data. In: Automated Extraction of Man-Made Objects from Aerial and Space Images (III), E. Baltsavias, A. Gruen, L. Van Gool (Eds.), Balkema Publishers, Lisse, pp. 339-348 (in press).

Space Imaging, 2001. Company web site. http://www.spaceimaging.com (accessed 10 August 2001).

Toutin, Th. , Cheng, P., 2000. Demystification of IKONOS! EOM , 9(7), pp. 17-21.

Vassilopoulou, S., Hurni, L., Dietrich, V., Baltsavias, E., Pateraki, M., Lagios, E., Parcharidis, I., 2002. Orthophoto Generation Using Ikonos Imagery and High Resolution DEM: Study Case on Volcanic Hazard Monitoring of Nisyros Island (Greece). ISPRS Journal of Photogrammetry and Remote Sensing (submitted for publication).

Wang, Y., 1999. Automated triangulation of linear scanner imagery. Proc. Joint ISPRS Workshop on Sensors and Mapping from Space, Hannover, 27-30 September, 5 p. (on CD-ROM).

Yang, X., 2000. Accuracy of rational function approximation in photogrammetry. Proc. ASPRS Annual Conference, Washington D.C., 22-26 May, 10 p. (on CD-ROM).

Yang, Y., 2001. Piece-wise linear rational function approximation in digital photogrammetry. Proc. ASPRS Annual Conference, St Louis, 23-27 April, 14 p. (on CD-ROM).

THE PLEIADES PROGRAM

Alain BAUDOIN[1], Philippe GOUDY[2], Michel ROUZE[2]

[1] CNES, 2 place Maurice Quentin 75039 Paris Cedex 1, France (alain.baudoin@cnes.fr)

[2] CNES, 18 avenue Edouard Belin 31401 Toulouse Cedex 4, France (michel.rouze@cnes.fr)

KEYWORDS:

Space Imagery, SPOT, Pléiades, High Resolution, Small Satellite, Radar, Multispectral, Superspectral, Dual Use, Interferometry.

SUMMARY:

The new Pléiades concept proposed by CNES is based on a detailed mission analysis taking into account the evolution of the user needs and technical capabilities (smaller satellites), showing the request for 10 space components.

Cooperation with other major European Countries and development of dual systems are two of the main objectives of the program, fulfilled by the agreement between France and Italy to develop a Dual System. Two Optical High Resolution satellites will be developed under the leadership of France and four SAR-X satellites will be developed under the leadership of Italy.

Other components such as the Interferometric Cartwheel for generating high quality DEM, Wide Field and SuperSpectral systems for continuing and enlarging (to precision farming or environmental studies) the SPOT 5 mission are already under study. The remaining components (C band, L band and P band radar, thermal and hyperspectral missions) are envisaged through ESA programs.

1 Introduction

This paper presents a new Earth Observation concept, Pléiades, proposed by CNES. Pléiades is based on the 15-year-old SPOT experience, taking into account the evolution of user requirements, technological capabilities and worldwide offer.

The Pléiades program is a concept defined by CNES between 1998 and 2000. The main objectives and orientations of the program are to fulfill the user needs, which will be described in the first part of the paper (§2 to 4), looking for a larger European cooperation and for a dual exploitation between civilian and defense partners while encouraging technical innovation.

As this concept is very similar to the Italian Cosmo-SkyMed one it was possible to settle a cooperation between France and Italy on a Dual System, which will be then described in the main part of the paper (§ 5 to 7).

Studies on other Pléiades components (§ 8 and 9) will be mentioned before the conclusion of the paper.

2 Overall User Needs and Market Demand

2.1 Mission analysis.

The Pléiades mission analysis has been performed by CNES with the help of a User Committee. The main French actors in Earth Observation have provided their support to this analysis, as user organizations, such as IGN, BRGM, INRA, CNRS, or as services or system providers, such as SPOT IMAGE, SCOT, ACRI, Astrium and Alcatel Space. To access the user needs and their possible evolution within the next years, SPOT experience and many market surveys were used, updated and synthesized.

Results and recommendations from several meetings with the different user communities organized by the Ministry of Education, Research and Technology (MENRT) in the frame of its initiative “Espace et Société” (Ref. 1) were taken into account, as well as those from two dedicated workshops on Pléiades. The GMES initiative (Ref. 2) is also taken into account to assess the evolution of the institutional demand beyond the evolution of the European and worldwide market.

A summary of these users need assessment, which is fully coherent with the ERSIS study (Ref.3) performed for ESA by the European industry, can be described as follows:

For most of the application domains (cartography, agriculture, forest, geology and risk management, defense and security, ocean) it is recognized that the useful information related to thematic parameters should be obtained using several sources of data: ground and airborne surveys are complementary to satellite imagery. Furthermore several types of sensors are needed, either to collect different types of information or to be merged as to extract enhanced information. It is also noted that each sensor could be used for several applications.

The main application domains were identified and for each of them key applications were selected as representative in terms of institutional or economical interest and of data requirements.

2.2 Cartography:

For basic mapping, land use planning, urban surveys or telecommunication the use of space imagery is already mature and well known (Ref. 4), even if the complementarity and competition with aerial photographs are still evolving quickly.

Three types of data are requested: high-resolution (metric or submetric) optical imagery, wide field imagery for medium scale mapping of large areas and radar acquisition when all weather capabilities are needed.

2.3 Agriculture:

Precision farming, agricultural control and crop statistics are application with great potentialities for Earth observation if efficient methodologies could be used to extract useful and accurate end users' information. From current experiments this appears to be feasible but has still to be confirmed and operationally implemented.

Several types of data are needed but the key parameters are the number (6 to 20) and choice of spectral bands with a very good revisit time (to provide weekly information).

2.4 Forest:

Space imagery (SPOT, ERS, Landsat, ..) is already used for forest inventories but new application areas could be envisaged for timber management or ecological surveys. Many Earth Observation data are needed, from very high optical photograph (relevant to airborne sensors) to multi/superspectral data, radar imagery (P or L band) and thermal data (especially for forest fires)

2.5 Hydrology:

Water is considered to be one of the most important issues for the future. Its management, either to provide fresh water or to avoid catastrophic floods could be facilitated using Earth Observation data, such as metric optical or radar imagery and especially accurate Digital Elevation Models derived from stereoscopic or interferometric data. Most of the potential users (insurance companies, water providers, civil protection, ..) are not yet familiar with such remote sensing data and they should be involved as soon as possible in the development of the applications.

2.6 Geological prospects:

Geology was one of the first application domains of Earth Observation and remains an important one, with a very diverse need of data, at several resolutions, with as many spectral bands as possible, and with always stereoscopic and/or interferometric demands.

It is noted that for mining surveys there is a special interest for hyperspectral data.

2.7 Dynamic geology and associated risks:

As for hydrology the potential interest of Earth Observation for dynamic geology and associated risks (earthquakes, volcanoes, landslides, ..) is far to be fully exploited and GMES initiative could help to develop the use of space data, coupled with continuous ground surveys, for such applications. The needs for high resolution, either optical or radar (X band), and for fast services (within few hours or days) have been identified as well as complementary sensors (wide field, thermal, SuperSpectral and C or L SAR).

2.8 Marine applications:

Even if Pléiades has not been designed to fulfil marine applications, some of these applications could be envisaged, either for oceans, sea ice or littoral surveys, especially with wide field imagery and C band data.

2.9 Market analysis.

The analysis of the near future market is given in the following table. Its evolution is more difficult to predict and will depend on the operational capacity for extracting useful information from space data with robust methodologies and accurate physical models. This is particular true for agriculture and hydrology where the demand could increase with the highest rate during the next tens of years.

Application	Agriculture	Forest	Cartography	Hydrology	Geology	Risks	Ocean
Market	15%	15%	50%	5%	7%	6%	2%
Evolution *	++	-	-	++	=	+	=

*: Potential development: -: low =: moderate + : medium ++ : high

Table 1: Market shares and trends

3 Systems to be envisaged

Ten types of system have been identified to fulfil most of the users' needs, as described in Table 2:

Sensor	Resolution (m)	Swath width (km)	Number of bands *	Revisit time (days)	Main applications
Wide Field	2-5	40-100	3-4	3-7	Cartography, Geology, Agriculture, Forest, Hydrology
Optical HR	≤1	10-30	3-4	1-2	Cartography, Risk, Forest, Geology
SuperSpectral	3-10	100-300	6-20	1-2	Agriculture, Forest, Geology
Hyperspectral	5-20	50-300	30-200	2-7	Geology
Thermal	1-40	100	TBD	<1	Forest fires, Geology, Ocean
SAR C	2-4	50-300	1-2	1-5	Geology, Ocean, Hydrology, Geology
SAR X	1-5	10-300	1-4	<1	Hydrology, Risk, Forest, Ocean
SAR L	2-10	50-100	1-4	1-7	Geology, Forest, Hydrology, Ocean
SAR P	5-10	70-100	1-4	1-7	Hydrology, Geology, Forest
Interferometric Cartwheel	1-5	70-100	NA	NA	DEM for Cartography, Risk, Hydrology

* For SAR the number of bands is the number of polarization channels

Table 2: Pléiades component user requirements

SAR and optical sensors are both required for most of the applications, the first one mainly for its all weather capacity, the second one for its better visual interpretation. It is also acknowledged that external data from ground or airborne surveys are in most cases needed to get reliable and accurate information from space imagery.

4 Pléiades implementation

The implementation of these ten possible missions has been envisaged through several programmatic frameworks.

Systems not yet considered as operational in a near future time scale should be studied through ESA R&D programs: P band SAR, thermal and hyperspectral imagery.

When systems are already available or under development in Europe they should be considered as a primary source of data and their continuity should be envisaged in the mid term future: C band SAR (with ERS and ENVISAT) and Wide Field (with SPOT)

Development of dual systems is not envisaged under the responsibility of ESA, due to National Constraints. This is applicable for High-Resolution systems (optical and X band radar), which will be provided through the French-Italian agreement (see below). Nevertheless a minor participation of ESA member States to the development of these systems could be envisaged and users of all Europe could take benefit of these systems.

New operational systems for which there is a great economical interest, such as the superspectral system (and the Wide Field system after SPOT 5), could be envisaged with a Public Private Partnership (PPP). This PPP could be implemented within ESA Earth Watch or through bilateral or other multilateral co-operation schemes.

5 Co-operation between France and Italy on a Dual System

Since beginning 1999 possible co-operations were envisaged and the most fruitful co-operation scheme was found with Italy, as its approach for its COSMO-SkyMed program was very similar to Pléiades, with a possibility to share responsibilities and work between the two Countries.

Both Countries were envisaging dual systems and French and Italian ministries of Research and ministries of Defense agreed in march 2000 to study a possible co-operation on Earth Observation, taking as reference Pléiades and COSMO-SkyMed projects of the French and Italian space agencies.

This possibility was confirmed by the Turin Agreement, signed by Lionel Jospin and Giuliano Amato, the Chiefs of Government of the two Countries, on the 29th of January 2001. This intergovernmental Agreement is an Umbrella Memorandum of Understanding, which gives the overall objectives and implementation rules of the co-operation. Its main purpose is the development and exploitation of a Dual System, with two high resolution components, one with **two optical satellites under the leadership of France**, the other with **four SAR-X satellites under the leadership of Italy**. The extension of the co-operation to other countries can be envisaged, and both France and Italy are proposing such possibility to ESA Member States.

5.1 Overall mission specifications of the Dual System

Pléiades and COSMO-Skymed mission studies have identified the needs for High-Resolution data, both from optical and from radar systems. The Mission Requirements and Technical Performances for the Dual System are now ready and should be used as a reference for the Definition Phase of the Dual System.

Beside specific Defense needs and constraints the Dual System is specified to fulfil a broad spectrum of applications, in the field of cartography, agriculture and forestry, geology and hydrology, marine applications, Earth science, resource management, land use and law enforcement, according to scientific, institutional and commercial users.

The risk management, the monitoring of coastal zones and the control of the sea pollution are considered as important applications to be satisfied.

The system shall have night/daylight and all weather observation capability all over the world.

The system shall provide multi-sensors observation capacities:

- ensuring at lower cost, service continuity of existing optical observation capacities (Spot) and improving these performances (resolution, stereoscopic capacity, image quality, acquisition times, amount of data..).

– giving access to a radar observation capacity with interferometric capabilities.

In order to complement this multi-mission capabilities, the system shall be able to integrate data/products coming from external optical/radar systems (access to catalogue, programmation request, product processing and delivery, ..)

6 The High Resolution Optical component

6.1 Dual System Optical High Resolution Specifications

Taking into account the users' requirements (civilian and defense ones), technical feasibility and cost trade-off the following proposed mission specifications have been agreed between France and Italy, for a constellation of two satellites, to be launched in 2005 and 2006, with the following specifications:

- Bands and Resolution:
- 0.7 m at nadir for Panchromatic band
- 2.8 m at nadir for blue, green, red and near infrared (4 bands)
- Swath: 21 km at nadir
- Revisit time: equal or better than 24 hours
- Coverage capacity: better than 250 images per day and per satellite (20 000 km2 per orbit)

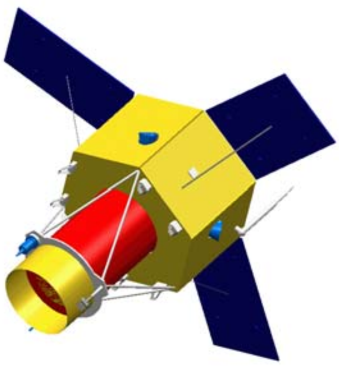

Fig 1 Pléiades HR satellite

6.2 Technological performances and innovations

An Phase A of the Pléiades optical HR system was completed during the year 2000 and beginning of year 2001. The satellite architecture was studied through an industrial contract, with Astrium-F acting has the prime contractor for the satellite, and Alcatel Space Industries responsible for the instrument. The technical feasibility of the satellite, despite its very demanding specifications, was demonstrated with new technological developments among which high performances Fiber Optics Gyroscopes, Control Moment Gyros, TDI, new generation solid state recorder.

For recurring missions, the availability of smaller and less consuming equipment or instruments has allowed to dramatically decrease the size (and cost) of the new generation satellites with respect to the previous generation ones.

More compact telescopes and smaller equipment have allowed to design rigid and agile imagery satellites where the off-nadir pointing is achieved by steering the entire spacecraft body. The absence of tilt mirror, in turns, contributes to render the telescope more compact.

Table 3 shows the evolution of some characteristics and performances from SPOT 1 to Pléiades HR satellites.

Parameter	SPOT 1	SPOT 5	Pléiades HR
Mass	1.8 t	3.0 t	0.9 t
Image resolution	10 m	2.5 m	0.7 m
Data transmission rate	50 Mbit/s	300 Mbit/s	2 Gbit/s
Image compression rate	1.3	2.8	5
Processing rate	8 Mops/s	750 Mops/s	10 Gops/s

Table 3: Characteristics and performances evolution from SPOT 1 to Pléiades HR

7 The SAR-X component

The SAR-X component of the Dual System will be developed under the leadership of Italy. The four satellites should be launched between end of 2003 and end of 2005. With these four satellites the revisit time requirement should be achieved (better than 12 hour)

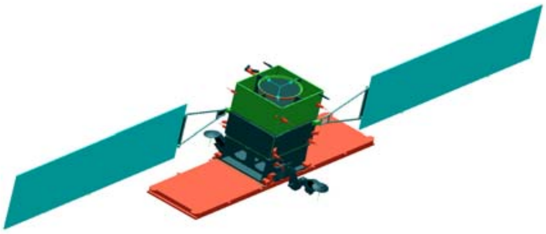

Fig 2: SAR-X Cosmo-Skymed satellite

The fundamental characteristics of the SAR Payload operational modes are summarized as follows:

Modes with one polarization selectable among HH, VV, HV or VH:

- SPOTLIGHT
  - resolution: order of the 1m and less
  - spot area : 10x10 km^2
- HIMAGE (Stripmap)
  - resolution: few meters
  - swath width: several tens of km
- WIDEREGION (ScanSAR)
  - resolution: few tens of meters
  - swath width: hundreds of km
- HUGEREGION (ScanSAR)
  - resolution: several tens of meters
  - swath width: few hundreds of km

Modes with two polarization selectable among HH, VV, HV or VH:

- PING PONG (Stripmap)
  - resolution: few meters
  - swath width: several tens of km

8 The interferometric cartwheel

8.1 Concept

The interferometric cartwheel is an innovative concept, proposed by Didier Massonnet (Ref 5), using several (3 or 4) micro satellites as SAR passive receivers “cooperating” with a main satellite acting as an active SAR emitter. (Fig 3)

The satellites are placed on an orbit very similar to the one of the main satellite, within the same orbital plan and with the same orbital period but with slightly different elliptical shapes. This gives to the micro-satellites a relative motion evoking a wheel with a diameter of few kilometers rotating typically 150 km ahead of the main satellite.

Its main interest is its capability to generate low cost high accuracy DEM (typically 1 m Z accuracy) but it can be used also for many applications, such as ocean current studies.

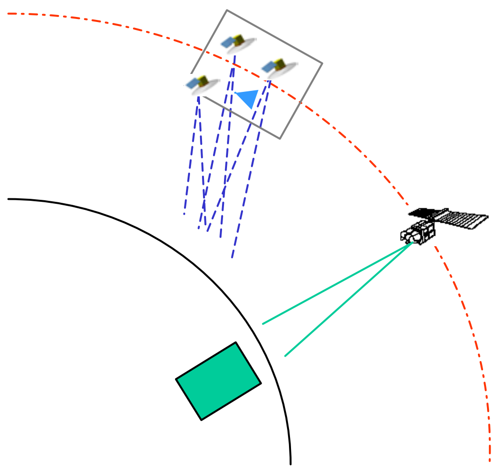

Fig 3: Interferometric cartwheel concept

8.2 Development

Studies on this new concept have been undertaken in CNES in cooperation with NASDA (for using ALOS L band PALSAR), then with ESA and DLR (for using Envisat C band SAR). The definition phase of the project is on progress, while the final decision on the system configuration (using either ALOS or Envisat) is expected next year with an objective to launch the satellite constellation by around 2005.

9 Other components

9.1 The Wide Field

Beyond the use of high (metric) resolution satellite there is, and there will be, still a need for sensors with a wider coverage (typically 50 km) even with a lower resolution (2-3 m). This need has been evaluated by CNES and Spot Image, and confirmed by the ERSIS study performed by Alcatel, Alénia, and Astrium for ESA.

Until 2006-2007 SPOT 5, to be launched within the next months, should fulfil this need. To ensure the mission continuity a new small satellite system, named 3S (Successor of Spot Satellite) has been defined (Ref. 6) and its realization could be decided next year.

9.2 Superspectral components

Since many years CNES, in partnership with industry and research centers, has conducted intensive studies in the domain of superspectral remote sensing, with a particular emphasis on the agricultural and the ecological applications. Theoretical studies have been supported by experimental campaigns with ground, airborne and satellite data. Requirements for such a superspectral system are given in Table 4.

Application	Agriculture	Forest	Land, littoral, urban	Geology and Risks
Resolution (m)	3-20	5-20	2-5	10
Image coverage (km)	50-300	100	50	50
Revisit time (days)	1-2	6-15	/	15-30

Table 4: User requirements for a superspectral component.

Technical studies have shown that this superspectral mission could be achieved either with small satellite (synergies with the previous Wide Field mission could be envisaged) or with micro satellites.

10 Conclusion

Pléiades is not the SPOT follow-on program but more a new concept for Earth Observation, which is proposed, through a wider European cooperation, to satisfy the needs of all scientific, institutional (including Defense) and private users for satellite imagery. Ten types of satellites (space components) have been identified to fulfill almost all these needs, which should be decided and developed step by step, through different cooperation and partnership agreements.

The two first components (Optical High Resolution and SAR-X) have already been decided through an agreement between France and Italy. They will provide high-resolution (metric) imagery with a very short revisit time (24 h for optical, 12 h for SAR) to satisfy dual requirements.

The other components are still under study, among which the Interferometric Wheel is the most innovative project for DEM production. Many works have already been undertaken on Wide Field and SuperSpectral components for which cooperation schemes with Public Private Partnerships are envisaged. Remaining components should be provided through ESA programs.

Beyond the implementation of these space components Pléiades will provide ground facilities for data acquisition, image processing, product generation and user interfaces, in order to provide appropriate data and services to the users. This implies close links with the different user communities, value-added companies and all actors involved in Earth Observation to efficiently prepare the use of Pléiades. The GMES initiative at the European level appears, as far as Risk and Environment are concerned, one of the best frameworks for such preparation.

References:

1: Espace et Société- Actes des rencontres 1998-1999 (French Research Minister – 2000)

2: GMES: (Global Monitoring for Environment and Security) - Joint Working document by the Staff of the European Commission and ESA Executive

3: ERSIS Final report. ESA Contract 13592/99/NL/SF

4: Mapping from Space - Gottfried Konecny - ISPRS Workshop Hanover 1999

5: Capabilities and Limitations of the Interferometric CartWheel, D. Massonnet, *CEOS SAR Workshop,* Oct. 1999, Toulouse, paper 136

6: The current and future SPOT program. A. Baudoin, ISPRS Workshop Hanover 1999

topological rules in object oriented classification

Buck, A., de Kok R. , Schneider, T., Willhauck, G., Ammer, U.
Lehrstuhl für Landnutzungsplanung und Naturschutz
Am Hochanger 13
TUM Freising.
Roeland.deKok@lrz.tum.de

Before classification of VHR data takes place; A modular project design and experimental bitmap classification supports the overall performance of satellite image analysis. A proper analysis of VHR data can be achieved by pre-defining the behaviour of the object primitives and the objects of interest.

The modular design defines the way in which the GIS/Remote sensing information and classification rules are separated. First, a modular design defines the amount of image-/object layers that are needed in the classification process .
To define a module, this study relies on the terminology as described by RUMBAUGH (1991);
1. A *module* is a logical construction for grouping classes, associations and generalisations.
2. A *module* captures one perspective of the situation. An object model consists of one or more modules.
3. *Modules* enables the partition of an object model in manageable pieces.

The artificial bitmap classification is mainly used to clarify and test sets of topological-classification rules. If they function in artificial maps, there should be no problems in applying those rules in real (Ikonos) imagery.
The most simple form is the island-classification or island test.

The set-up of topological rules have to interact with spectral classification levels among the different modules. Therefore, a proper definition of object primitives (spectral dominated) and object of interest (mainly topological defined) needs to be made among GIS and Remote Sensing expertise.

This article shows how a modular project design using the **eCognition** software allows to classify artificial bitmaps and subsequently apply these rules in real (Ikonos) imagery to achieve the desired classification.
The artificial bitmap design allows further theoretical development of object arc-border interaction to allow time-series analysis in multi-temporal imagery. The latter is demonstrated with simulated data.

"The Committee on Earth Observation Satellites Working Group on Calibration and Validation"

by
Yves-Louis DESNOS,

Chair CEOS Working Group on Calibration and Validation
European Space Agency
ESRIN
Via Galileo Galilei
Frascati 00044 ITALY
Tel 00 39 0694180606
Tel 00 39 0694180552
Email Yves-Louis.Desnos@esa.int

The Committee for Earth Observing Satellites (CEOS) was created in 1984, in response to a recommendation from a Panel of Experts on Remote Sensing from Space, under the aegis of the Economic Summit of Industrialised Nations Working Group on Growth, Technology and Employment. This group recognised the multidisciplinary nature of satellite Earth Observation and the value of coordination across the proposed missions. Thus, CEOS combined the previously existing groups for Coordination on Ocean Remote Sensing Satellites (CORSS) and Coordination on Land Observation Satellites (CLOS), and established a broad framework for coordinating all spaceborne Earth Observation missions. The chair of CEOS is held for a one-year term and is currently held by MEXT/NASDA, Japan. ESA will take over the chairmanship in November 2001. In preparation for this hand-over, ESA is taking an active role in CEOS and in the working groups.

CEOS supports four working groups, the Working Group on Calibration and Validation (WGCV), the Working Group on Information Systems and Services (WGISS), the Ad Hoc Working Group on Disaster Management Support (DMSG) and the Ad Hoc Working Group on Education and Training (WGEdu).

The chair of the WGCV was taken over by ESA at the beginning of this year following a number of years of active membership to all the subgroups. The objectives of the WGCV are to enhance technical co-ordination, to promote international co-operation and to focus Earth Observation calibration and validation activities for the benefit of CEOS Members and the international user community.

The WGCV met at their 18th plenary, hosted and chaired by ESA at ESA-ESRIN, Frascati, Italy from 5-7 June 2001. Participants to the WGCV-18 comprise representatives from all the major space agencies. The meeting agenda comprises extensive discussions on setting international terms and standards for the calibration and validation of the world's satellite sensors data.

The importance of integrating activities internationally throughout the various space agencies underpins most of the discussions taking place at the meeting. The relationship that the WGCV has with the ISPRS is also receiving much attention.

A special WGCV/ISPRS session on Geometric and Radiometric Standards was chaired by Prof. Ian Dowman, ISPRS representative. A joint WGCV/ISPRS taskforce profile was defined to tackle issues relating to geometric and radiometric standards, and preparations for the first meeting of this taskforce, in September 2001, were begun.
The working group supports five subgroups:

- Infrared and Visible Optical Sensors (IVOS)

- Land Product Validation (LPV)
- Microwave Sensors
- SAR
- Terrain Mapping

The IVOS subgroup is particularly interested in the importance of intercalibration and intercomparison of the ground-based instruments that are used to validate satellite products. Under the auspices of the Infrared and Visible Observing Sensors subgroup, Dr Ian Barton of CSIRO reported on the very successful Second International Infrared Radiometer Calibration and Intercomparison. This campaign was supported by CSIRO, ESA, EUMETSAT and NOAA and was hosted by the University of Miami, USA, from 27 May – 1 June 2001. A report of the initial results of the campaign will be prepared for the next CEOS Plenary.

The SAR subgroup workshop was jointly organised by NASDA and ESA, and hosted by NASDA-EORC in Tokyo, Japan from 2 – 5 April 2001. During this well attended and fruitful meeting, Dr Masanobu Shimada of NASDA-EORC formally took over the subgroup chair. The CEOS chair, Dr Furuhama from NASDA, addressed the participants, whose numbers averaged 60 per day. A total of 66 presentations and 17 posters spanned 7 sessions. Each session was supported by a round table where prepared seed questions were discussed. At this meeting it was identified that the absence of consistent long-term data sets is an issue that needs addressing. With greater cooperation between the various space agencies this important topic can hopefully be remedied. A CD-ROM containing the proceedings of the workshop is currently being prepared and this will be distributed in September 2001.

The subgroup on Land Product Validation, chaired by Dr. Jeffrey Privette of NASA, met in conjunction with WGCV-18 at ESA-ESRIN from 7 – 8 June 2001 for an LAI intercomparison workshop. This workshop brought together the community involved in LAI field campaigns with the aim of evaluating LAI products from satellites. LAI data collection and analysis procedures and protocols were discussed and defined.

The GOFC Fire Workshop on Satellite Product Validation was held jointly with the CEOS WGCV Land Product Validation subgroup at the Gulbenkian Foundation, Lisbon, Portugal, from 9 – 11 July 2001. Presentations on recent satellite fire product validation activities were given and breakout groups explored opportunities for international collaboration and the development of protocols.

The Terrain Mapping subgroup chair has been handed over to Prof. Jan-Peter Muller from UCL. The last meeting of the group has been held in Banff Canada in July 2001. The Microwave subgroup is now chaired by Dr Manuel Martin-Neira from ESA-ESTEC. Preparations are underway to hold a meeting in conjunction with the specialist Microwave Remote Sensing conference due to be held in Boulder, Colorado, USA, in November 2001.

Noting the recommendations of the WMO/CEOS report number 140 on Strategy for Integrating Satellite and Ground-based Observations of Ozone, the WGCV recommended the formation of a subgroup on Atmospheric Chemistry. At the WGCV-18, terms of reference for such subgroup were defined and this recommendation will be put forward to CEOS plenary.

The 19th WGCV plenary meeting will be hosted by CCRS/CSA in Canada in April 2002.
Thanks to international co-operation and co-ordination, the CEOS Working Group on Calibration and Validation will continue to focus on means to ensure long-term confidence in the accuracy and quality of Earth Observation derived data and products.

Keywords: CEOS, Calibration, Validation

HIGH RESOLUTION MAPPING FROM SPACE: STATUS AND ISSUES

Ian Dowman
University College London
idowman@ge.ucl.ac.uk

KEY WORDS: High resolution data, Mapping, Data integration, Multi-sensor imagery, Education

ABSTRACT
The amount and type of data being acquired from sensors on board Earth observation satellites is increasing along with the range and background of producer and user. The position of high resolution data is particularly interesting because of the role of commercial operators and the rapidly increasing resolution of the data available. This paper looks at the types of data available and the issues that are unresolved in the current situation. These issues include how data can be merged, new processing tools, what products are available and how they can be used in the new competitive market place.

INTRODUCTION

The rate of change in the technology of mapping from space seems very fast when we look over a period of 30 year and see what has been achieved in that time. When Landsat was first launched the thought of sensors with 1m pixel size was almost inconceivable. Yet looking at the year by year activity, change seems very slow: how long have we waited for a choice of 1m commercial sensors? And how long will we still have to wait? In 1982 Konecny et al (1982) showed that 1:50 000 mapping requires an estimated pixel size of 3m. Now, despite the advent of sensors with pixel sizes of less than 3m, there is little evidence that mapping organisations are using the data for topographic mapping. Is aerial photography providing tough competition?

There are many questions still unanswered. This paper will try and address some of them. First the current situation will be assessed and current trends discussed. Then the issues will be summarised and some solutions explored. Finally some conclusions will be tentatively proposed.

NOMENCLATURE

There is a view that discussion of definition of terms is a waste of time. However it does help if everyone means the same thing when they talk about 'High resolution mapping'. Fritz (1997) gave definitions in terms of resolution, which we may assume means pixel size:

Low resolution	≥30 < 300m
Medium resolution	≥3 < 30m
High resolution	≥0.5 < 3m
Very high resolution	<0.5

This nomenclature will be used in this paper and the discussion will include medium and high resolution data.

THE CURRENT POSITION

Table 1 shows the current and future satellites that carry high resolution sensors. The characteristics of the medium resolutions systems such as IRS, SPOT, ASTER and Landsat are well known.

In addition to the optical sensors there are also a number of microwave sensors that are used for mapping.

Satellite/ operator	(Proposed) launch date	Sensors	Bands and stereo capability	Spatial resolution	Swath
IKONOS II Space Imaging (USA)	Sept 24 1999	Pan Multi-spectral	Stereo Fore/Aft B, G, R, NIR	1m 4m	11 * 11 km 11 * 11 km
EROS A1 **EROS B1** ImageSat International (Israel)	Dec 5th 2000 2nd Qtr 2002	Pan Pan		1.8m 0.8m	12.6km/line 16km/line
Orbview 4 Orbital Sciences (USA)	Sept 2001	Pan Multi-spectral	Stereo Fore/Aft B, G, R, NIR Orbview 4 has 200 channel hyperspectral sensor	1m 4m (8m) 20m	8 * 8 km 8 * 8 km
ALOS NASDA (Japan)	2003	PRISM – Pan AVNIR	Stereo Fore/Aft B, G, R, NIR	2.5m 10m	35/70m 70m
SPOT 5 SPOT Image (France)		Pan Multi-spectral	Stereo Fore/Aft SWIR B, G, R	5m, 2.5m (supermode) 20m 10m	60km

Table 1. Characteristics of current and future high resolution optical sensors.

Satellite/ operator	(Proposed) launch date	Sensors	Products	Spatial resolution	Swath
SRTM (JPL)	2000	IfSAR C band	DEM Images		
RADARSAT 1 Canada	1995	C band SAR	Fine Standard	8m 30m	45km 100km
RADARSAT 2 Canada	2003	C band SAR	Ultrafine Standard	3m 28m	20km 100km
ALOS NASDA (Japan)	2003	PALSAR L band	Fine ScanSAR Polarimetric	7-44m 100m 24-89m	
ENVISAT ESA	2001	ASAR C band	Image mode	12.5m	100km
TerraSAR Astrium		X band L band	Polarimetric	1m 9m	

Table 2. Characteristics of microwave sensors suitable for mapping.

The current technical position can be summarised by the following points:

- A wide range of optical sensors are available offering pixel sizes from 1m upwards;
- The technology of existing sensors is fairly stable and reliable, some key points are the use of linear arrays and single, rapidly pointable sensors;

- Positioning devices on board reduce or remove the need for ground control points;
- The main problem in recent years has been failure at launch;
- SAR sensors are continually improving with Radarsat2 having 3m resolution.

In the near future we can expect more high resolution sensors, particularly Orbview 4 and EROS 1B. And these will be followed by higher resolution when 0.5 pixel sizes are introduced. SpotImage is introducing Supermode products, which will have a 2.5m pixel size, generated from two 5m pixel size images acquired simultaneously from 2 arrays which are offset in the focal plane. The two 5m images are interleaved, interpolated and restored to give the 2.5m product. This technology has been used for terrestrial images before, but not for satellite data.

Dedicated mapping missions have been implemented, ERS SAR Tandem Mission and Shuttle Radar topography Mission (SRTM) for example, to generate large area DEMs with SAR Interferometry (IfSAR). Another development that may have significant influence on future acquisition of space data are micro, mini and small satellites. A small satellite weights between 500 and 1000kg, micros and minis less, and several with imaging systems are already in use. Table 3 shows some examples.

Satellite	Launch data	Weight	Sensors
TMSat Thailand	July 1998	50kg	Low resolution synoptic images MSS cameras with 100m pixel size
UoSAT SSTL, UK	April 1999	315kg	10m pan 30m MSS
Topsat UK	Autumn 2003	100-200kg	2.5m pan 5m MSS

Table 3. Examples of micro, mini and small satellites

On the other hand we are seeing multi sensor platforms such as Terra and ENVISAT that have many instruments on board. This trend may be slowing but satellites such as ALOS which will carry three remote sensing instruments designed for mapping: the Panchromatic Remote-sensing Instrument for Stereo Mapping (PRISM) for digital elevation mapping, the Advanced Visible and Near Infrared Radiometer (AVNIR-2) for precise land coverage observation, and the Phased Array type L-band Synthetic Aperture Radar (PALSAR) for day-and-night and all-weather land observation. ALOS was designed with precision spacecraft position and attitude determination capability and it will be possible to acquire AVNIR and PALSAR data simultaneously.

Besides these operational systems data is available from both US and Russian archives. Use is made of these for mapping and a number of groups are working on mapping from the newly released US Corona data.

Sensing techniques other than optical and SAR are also important. VCL will provide unique data sets for understanding important environmental issues using 3 Lasers with footprints 25 m wide. They are near contiguous in the along track direction, and spaced 2 km apart across track. Although primarily designed to study vegetation canopy, VCL will provide elevations along strips over wide areas.

Looking at the technical characteristics of sensors does not tell the whole story. The products which are available and who is producing them is also important. There is now a clear distinction between the scientific sensors and the commercial ones. These issues will be discussed further below.

DATA PRODUCTS

Photogrammetrists have traditionally expected to be provided with image data and the calibration data of the sensor. This allows them to restitute a 3D model and then generate the required products, which could be vector data, digital elevation data (DEM) or orthoimages. This situation has now changed and these products are now being offered directly to the end user by the satellite operator. For example, table 4 shows the products offered by Space Imaging.

IKONOS Product	**Description**	**Accuracy – predicted circular error at 90% probability**
Carterra GEO	Images are radiometrically and geometrically corrected, and map projected with a 1metre map increment.	50m
Carterra Reference	Images are radiometrically and geometrically corrected, and orthorectified using ground control (if available). This imagery is suitable for regional mapping.	25m
Carterra Map	Images are radiometrically and geometrically corrected, and orthorectified using ground control (if available). This imagery is suitable for mapping at 1:24 000 scale.	12m
Carterra Pro	Images are radiometrically and geometrically corrected, and orthorectified using ground control (if available). This imagery is suitable for mapping at 1:12 000 scale.	10m
Carterra Precision	Images are radiometrically and geometrically corrected, and orthorectified using ground control. This imagery is suitable for mapping at 1:4800 scale.	4m
Geo Ortho Kit	Image and Image Geometry Model which can be used in commercial imagery software suites with a DEM to create orthoimages.	

Table 4. Specification of Space Imaging Carterra products.
Source http://www.spaceimaging.com/

Space Imaging also offer stereo pairs but access to this is limited and the specification is not given on the web page. In the case of IKONOS data the situation is different from the traditional one in that neither the sensor calibration data, nor unprocessed data are available. Users can set up there own stereo pairs, and produce orthoimages, but only through the use of rational polynomial co-efficients (rpcs) provided by Space Imaging. Although initially viewed with some concern, tests have shown that rational functions can be used to accurately set up 3D models if used properly, (Dowman and Doloff, 2000, Tao and Hu, 2001). Third party software is needed to set up these models and produce orthoimages, for example provided by LH Systems in SOCETSet or by PCI.

The situation is similar with microwave data and DEMs and orthoimages are often the available product, but here the processing is more complex and beyond the capability of many users. The time and effort that has gone into calibrating the data and generating DEMs from SRTM is an indication of this.

A key requirement of such data is the validation of the product and the provision of understandable data quality information to the user. If more non specialist users are buying data products it is essential that they are told the accuracy and heritage of the data. Some data providers are now giving statistics with the data. USGS, for example, gives production method, standard deviation, slope, aspect and error on control points with the National Elevation Dataset.

A further issue, which has been around for some time, but becomes more acute with the production of these value added products, is common transfer formats. With a much more limited range of processing packages than there were analogue and analytical plotters, interoperability should be an achievable goal.

DATA FUSION

There is now an accepted trend towards fusing different data types to allow more information to be available in a succinct form. The most obvious example of this is the pan-sharpened image generated from high resolution panchromatic data and lower resolution multispectral data. Such images may come from a single sensor (e.g. IKONOS), or from two (e.g. SPOT and Landsat). The use of multi temporal images, combined as colour composites (multi temporal SAR for example) is also widespread. An interesting development for the future is the combination of optical and microwave data. Intermap Technologies and University of Calgary have successfully used rational functions to combine their airborne IfSAR data with IKONOS images. In academia work has been done to combine SAR and SPOT, both geometrically (Renourd and Perlant 1993, Gonçalves and Dowman 2001), and for feature extraction (Dare and Dowman, 2001). New platforms such as ALOS, offer further possibilities in this direction.

There is generally a lack of theory associated with image fusion. Only recently have sensor models been developed and there is work to be done in this area.

IMAGE PROCESSING

The fusion of different types of data makes greater demands on the processing environment. Packages such as LH Systems SOCETSet and ZII Image station SSK generally work with one type of data at one time, and, despite a large degree of integration between photogrammetry and image processing for remote sensing, do not make much use of classification techniques. It is however apparent that the use of DEMs with images is almost essential for feature extraction. The DEFiNiENS eCognition software offers a new concept of image processing based on an object oriented approach which extracts image objects for classification. It build up a hierarchical network of image objects which allows a representation of the image information content at different resolutions simultaneously and classifies objects with local context information.

Feature extraction is of course still the major challenge for photogrammetry and many would say that even operator assisted automation is a long way off. Multi sensor data may play an important part in meeting this challenge but this data may also come from alternative airborne sensors such as LIDAR and IfSAR than from high resolution satellite data.

Another promising trend is the creation of intelligent environments for processing data. The ALFIE system (Automatic Linear Feature Identification and Extraction) in the UK, uses a Geographical Information System built around an Object-Oriented geospatial database. Innovative techniques are employed to extract and classify linear features from imagery using object methods, contextual information and an overarching control strategy. The approach aims to allow a wide variety of image types and feature requirements to be processed in a fully automatic manner, (Wallace et al, 2001). A continuation of the project, ALFIE 2 will introduce the 3rd dimension and allow integration of the SOCETSet software with the LaserScan LAMPS2/Gothic object oriented environment to allow more efficient plotting and database update.

APPLICATIONS

Topographic mapping is still the major application of photogrammetric techniques. This includes the generation of vector data, DEMs and orthoimages, and database revision. At present there is no clear indication that data from space plays a significant role in this. Many studies have been carried out and many trial products have been generated, but at the scales that are most important, larger than 1:10 000, aerial photography is still used. So what are the applications of high resolution satellite data?

There is certainly a demand for global data sets and SRTM will provide a DEM and geo-corrected images of the area between 60˚N to 56˚S from IfSAR data. Similar products have been generated in some countries, for example in UK the Landmap project has created a Digital Elevation Model (DEM) of the British Isles at 1" (~30m) and a set of orthorectified satellite image data products. The DEM has been created from multiple passes of ascending and descending tandem ERS Synthetic Aperture Radar data using commercially available software from Phoenix Systems Ltd., GIS software developed to maximise ERS-tandem strip coverage, and several different COTS Image Processing software packages for the manipulation and visualisation of processed images. In Venezuela a radar orthoimages has been produced from airborne IfSAR. A number of countries are producing an image layer to their national data products. This may be a simply a library of images provided digitally, or a mosaic.

Gopalan (2001) reviews the need high resolution for developmental planning and concludes that '… high resolution satellite imagery will be very useful for working at local scales for big budget applications like site selection for infrastructure development projects…. Apart from these, the emergency response requirements like post disaster relief management could also justify the high cost of using high resolution imagery.' His view is that at present high resolution satellite data is too expensive for developing countries.

There are many new applications of image data. A major growth area at the moment is the provision of geospatial information for a new applications such as telecommunications and location based services (LBS). 3D city models are in demand for planning and environmental control and monitoring. High resolution satellite data may play a role in both of these applications but, as Gopalan stated, the data may be too expensive. Sensors such as ALOS may play an important part is generating landscape models. Another major area is in the monitoring and mitigation of disasters and hazards for which CEOS have established a Disaster Management Support Group. A report from the group (CEOS, 2000) notes that 'Space technology has been demonstrated conceptually, however the viability of operational reliance has generally not been fully demonstrated to the disaster management community', and recommends greater interaction between the space agencies and the applications community. Flood plain mapping for the insurance industry is another new application but work I this area has been mainly done from airborne LIDAR or IfSAR.

AIRBORNE DATA

An issue which has been running through this paper is the increasing synergy between spaceborne and airborne sensors. For the first time since Landsat was launched aerial photography and optical data from space are in competition. A comparison which was frequently made in the past was between the coverage and cost of optical data, such as SPOT, and the higher resolution and higher cost of aerial photographs. Table 5 is taken from Spradley, 1994.

Sensor	**Scale**	**Pixel size**	**Area (sq km)**	**Cost per sq km**
Aerial photography	1:10000	0.15m	5.29	$37.81
Aerial photography	1:40000	0.6m	84.64	$2.36
SPOT		10m	3600	$0.83
KFA-1000	1:270000	4m	6400	$0.47

Table 5. Price of imagery in 1994. (from Spradley, 1994)

Prices today, as quoted by Gopalan (2001) are shown in Table 6. The differential between SPOT and IKONOS data is dramatic and when compared to aerial photography some interesting comparison emerge.

System	**Pixel size (m)**	**Product**	**Price per scene ($)**	**Area of scene km^2**	**Price per sq km ($)**
IKONOS	1	Pan orthorectified	162	2.56	63.28
IRS	5	Master Pan orthorectified	1300	529	2.46
IRS	20	Master pan orthorectified	3000	19600	0.15
Landsat	25	TM terrain corrected	5950	13450	0.19
SPOT	10	US Metro View Pan	550	2560	0.86
SPOT	10	US Statewide Pan orthocorrected	1650	2560	0.64

Table 6. Price of high resolution satellite imagery (from Gopalan, 2001)

The US National Aerial Photography Programme (NAPP) photographs can be purchased on film and scanned at low cost. Orthoquads in the USA are also easily available and inexpensive. Many countries now offer aerial photography and orthoimages off the shelf. So the question must inevitably be asked: what is the advantage of high resolution satellite data? Davis and Wang (2001) have generated high resolution DEMs from NAPP photography and claim that 'Both the horizontal resolution and vertical accuracy of the DEM generated in this study are many times better that that currently available from optical or radar satellite remote sensing systems. In addition, the NAPP imagery represents an inexpensive data source that is readily available throughout the continental US.'

Other airborne sensors are also competitive. IfSAR and LIDAR are particularly significant.

Linked to the price of data is another issue: is it always wise to buy the cheapest product? To the untutored user an aerial photograph may seem as useful as an orthorectified image – it is only when the image is merged with other data that the problems appear.

ISSUES

The issues which have been raised and discussed above can be summarised under a number of headings.

First the technical issues. These relate mainly to the processing of the data. Calibration and validation is very important and correcting the SRTM data, for example, has caused major delays. Calibration data is not available to users of IKONOS data and this creates concern when users must either rely on the products coming from the provider, or carry out their own validation. The user also has to rely on 'black box' software to process IKONOS data and so again user validation is important.

Other technical issues are the need for better theoretical models for data fusion and the need to improve processing algorithms such as editing DEMs, feature extraction and classifying land cover.

The second group of issues relate to accessibility and use. Because of the way in which the data is delivered the user needs to understand how the product was generated, what the level of correction is and what is the final accuracy. (Information about datums and projections must also be provided in an understandable manner.) The user needs to be able to read the data (maybe from the world wide web), onto a number of systems, possibly to merge it with other data, hence standard formats and interoperability are required

It is my view that education of the user is essential. The user must understand the product and hence, besides being given the information listed above, must be educated to understand the importance of accuracy, quality measures and uncertainty measures.

These potential problems mean that there is a vital role for organisations such as ISPRS and CEOS in establishing a framework for calibration and validation, standards and interoperability and presentation of information. CEOS and ISPRS are already working together on these issues. Further collaboration is under discussion in setting up test sites undertaking more comparative tests. These organisations can also promote good practice in the presentation of accuracy of data sets

One final point which cannot be answered at the moment but which will be crucial to the continued development of high resolution mapping from space: can spaceborne data compete with airborne? At present Space Imaging have a monopoly on high resolution satellite data and no doubt their prising policy is set accordingly. What will happen when there is competition?

CONCLUSIONS

We live in interesting times and the development of the market for high resolution data is one of the more interesting issues. For many years the technology and the development of products from the images produced from single sensors preoccupied most scientist in the field. Now we have multiple sensor, multiple resolution, multi temporal data and we have suppliers from government, commercial and hybrid sources. Development of new techniques and new algorithms is still going to be important, but communication between potential users and data suppliers, and the role of institutions as facilitators and promoters of standards and transparency are the activities which may well predominate in the years to come.

REFERENCES

CEOS 2001. The use of Earth Observing Satellites for Hazard Support.

Dare P, Dowman I, 2001. An improved model for automatic feature based registration of SAR and SPOT images. ISPRS Journal of Photogrammetry and Remote Sensing, In press.

Davis C, Wang X, 2001. High resolution DEMs for urban applications from NAPP photography. Photogrammetric Engineering and Remote Sensing, 67(5):585-592.

Dowman I, Doloff J, 2000. An evaluation of rational functions for photogrammetric restitution. International Archives Of Photogrammetry And Remote Sensing, 33(B3):254-266.

Fritz L, 1997. August 1997 status of new commercial earth observation satellite systems. ISPRS Joint Workshop 'Sensors and mapping from space', Hannover, September 1997. Institute of Photogrammetry and Engineering Surveys, University of Hannover. Pages 13-28.

Gonçalves J, Dowman I, 2001. Use of mixed SAR-SPOT pairs for topographic mapping. Proceedings of Conference of Remote Sensing and Photogrammetry Society, London September 2001. In press.

Gopolan A K S, 2001. High resolution Imagery for Developmental Planning. GIS@development, V(4):29-31.

Konecny G, Schur W, Wu J, 1982. Investigations of interpretability of images by different sensors and platforms for small scale mapping. Proceedings of ISPRS Commission I Symposium, Advances in the Quality of Image Data. University of new South Wales. Pages 11-22.

Renouard, L, Perlant F, 1993. "Geocoding SPOT products with ERS-1 geometry," Proceedings of the Second ERS-1, Space at the Service of the Environment, Hamburg: 653-658.

Spradley l, 1994. Cost-effective data for regional GIS bases. International Archives of Photogrammetry and Remote Sensing, 30(4):203-208

Tao C V, Hu Y, 2001. A comprehensive study of the rational function model. Submitted to Photogrammetric Engineering and Remote Sensing.

Wallace S J, Hatcher M J, Priestnall G, Morton R D, 2001. Research into a framework for automatic linear feature identification and extraction. 3rd International Workshop on Automatic Extraction of Man-made Objects from Aerial and Space Images, in Monte Verita Ascona, Switzerland, 10 June 2001 -15 June 2001.

RESULTS FROM THE SRTM CALIBRATION PHASE

M. Eineder, N. Adam, H. Breit, S. Suchandt, J. Holzner,
B. Rabus, W. Knöpfle

German Aerospace Center (DLR), Oberpfaffenhofen, D-82234 Wessling, Germany
Phone: +49-8153-28-1396 Fax: +49-8153-28-1444, e-mail: Michael.Eineder@dlr.de

KEY WORDS: SAR Interferometry, Digital Elevation Model, DEM, Shuttle Radar Topography Mission SRTM, Calibration

1. ABSTRACT

In February 2000 the Shuttle Radar Topography Mission mapped 80% of the earth surface using the first space borne single pass SAR interferometer. On board were two radar systems, a US system operating in C-band and a German/Italian system operating in X-band. At the German Aerospace Center (DLR) the global X-band data set is processed to a global digital elevation model (DEM). Even if the single pass mode provides better coherence than previous dual pass missions, the high complexity of the system poses a challenge on calibration. All electric and geometric subsystems must be calibrated precisely to ensure global homogeneity. The paper deals with clock synchronization, phase dependence on temperature and with motion errors caused by the space shuttle platform. The paper further describes the major error sources and the methods applied for compensation. First results will be shown that predict the global quality of the DEM. The results are illustrated with sample products.

2. INTRODUCTION

At DLR, the first SRTM DEM was generated during the mission only 14 hours after launch using a priori information about the mast, i.e. the nominal interferometric baseline and a rather inaccurate shuttle orbit. This was an early demonstration that the system was working and the mission would be a success. However, due to the inaccurate geometry, the DEM errors were in the orders of 100 meters and more that time. Now we are working to achieve the final DEM quality in the order of 6 meters relative and 16 meters worldwide at a 30 meter pixel spacing. This means to calibrate all the geometric and the electric systems to a small fraction of the X-Band wavelength (3.1 cm). The relative position between both antenna phase centers must be known to better than 0.5 mm, electric phase variations must be compensated by software to residual errors in the order of 1 degree. Here we concentrate on the calibration issues. More detailed information on the mission and on the systems can be found in [10] and [8] and to the data products in [9].

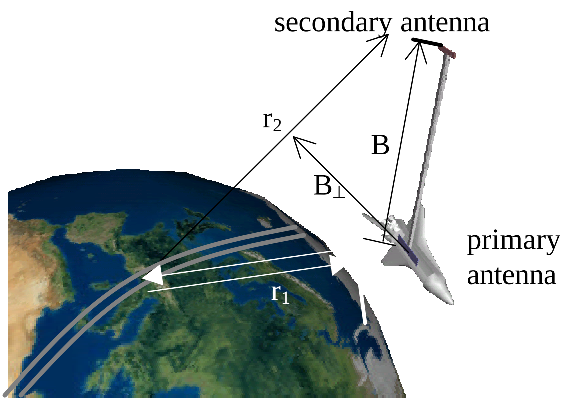

Fig. [1] Imaging geometry of SRTM

interferometric phase: $\phi = \frac{2\pi}{\lambda}(r_2 - r_1)$

height sensitivity: $\Delta z = \Delta\phi \frac{\lambda r \sin\theta}{2\pi B_\perp}$

B : baseline, 60 m for X-SAR

$B_\perp$: baseline component orthogonal to r_2

θ : incidence angle, 54.8° for X-SAR

λ: wavelength of radar, 3.1 cm for X-SAR

r_i: distance between antenna i and object, ca. 400 km

Fig. [1] shows the imaging geometry of SRTM and illustrates the possible sources of errors. The interferometric radar measures the differential distance (r_2-r_1) by means of an electrical phase difference. To triangulate the height z of a ground point, we need a very precise measurement of the interferometric baseline B and the phase φ. Considering the small ratio of the baseline compared to the object distance r and the typical height variation Δz, it becomes clear that we are dealing with very small numbers of (r_2-r_1) and accordingly φ. The baseline error B is influenced by the errors of the attitude and orbit determination avionics (AODA) and the knowledge of the electrical phase center position of the geometrical antenna. The phase measurement error is dominated by thermal noise of the receiver, analog digital converter quantization noise, slow thermal drifts of the receivers, varying delay of cables and processing approximations in the interferometric SAR processor.

3. ORBIT AND TIMING CALIBRATION

Image Location

In contrast to optical sensors, the radar imaging geometry depends little on the orientation of the sensor in space, but very much on the position of the sensor in relation to the imaged object. Thus, for automatic and precise data processing, precise knowledge of the sensor orbit is necessary and sufficient. In flight direction, this requires to synchronize the clock of the radar system with the clock of the GPS system used for orbit measurements. In the SRTM system, the relationship between both clocks is continuously measured with an accuracy of 1 microsecond. This technique greatly enhances the location accuracy of the SAR images down to the accuracy of the GPS derived orbits in the range of 1 meter [3], [2]. Since the radar and metrology systems may have unknown times delays, we calibrated the azimuth timing offsets using sets of corner reflectors located in Germany and in California. We used the zero-Doppler radar imaging geometry equations and calculated where we expected to see the reflectors in the radar image. The differences between the expected and the true position of the reflectors in the image were then converted to time offsets and used to calibrate and control the location accuracy. The results were promising: we could predict the position of 20 corner reflectors with an accuracy of 0.4 meters and a standard deviation of ca. 0.2 meters. From the results, we expect no problems to fulfill the mission requirements of 20 meter circular horizontal location error for 90% of the pixels.

Phase Effects on Image Location

Due to the side looking geometry, not only the DEM height, but also the DEM position depends on the pulse delay and the interferometric phase. Therefore, slow, uncompensated phase variations in the system could cause a slowly varying range offset of the geocoded image. Similarly, high frequent thermal phase noise of the receiver in the order of ca. 4 meters would distort the horizontal image geometry, resulting in blurred images and DEMs on a subpixel level. From the current experiences we know, that both effects are small enough not to violate the above image location specification.

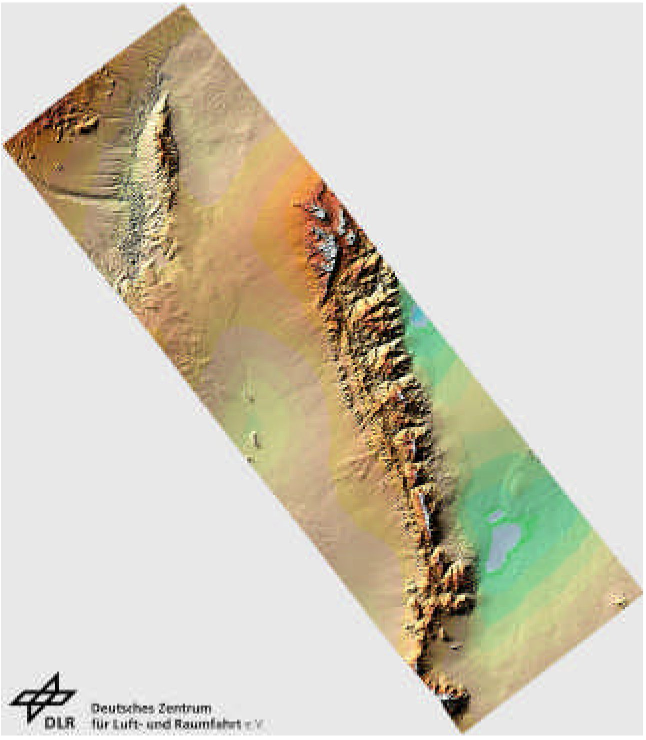

Fig. [2]: First SRTM DEM (New Mexico) produced on Feb. 12th, 2000 - only 16 hours after the shuttle launch. Note the height oscillations along flight direction that origin from mast oscillations that had not been compensated that time.

4. BASELINE STABILITY AND ACCURACY

A critical question before the SRTM mission was, weather the mast could be deployed to its full length and weather it would be stable enough for interferometric measurements. Within the first few hours of the SRTM mission, it could be shown that the 60 meter mast could be fully deployed and was stiffer than specified. We had expected problems due to dynamic range or azimuth misalignments of both antennas due to mast torsion, but fortunately the mechanical system was so stable, that we did not even have to use the dynamic azimuth steering capability of the secondary antenna. Dynamic azimuth steering is done by adjusting phase shifters at the antenna panels and this would have posed additional complexity on the overall phase calibration. The Doppler centroid variation between both channels is a good measure for the torsion of the boom. We measured oscillations in the order of 50 Hz corresponding to ca. 0.006^0 which does not reduce the useable azimuth spectrum significantly and thus makes the products homogenous and the processing more simple.

Some problems still under investigation are caused by the accuracy of the baseline roll angle measurement. While the length knowledge of the baseline is very good and stable due to the mechanical construction and the measurement with a laser distance meter, the baseline angle knowledge is more critical since it is composed from several independent instruments:

- the inertial reference unit (IRU) measures the fast orientation changes of the primary antenna
- the star tracker (STA) measures the slow orientation changes of the primary antenna
- the astros target tracker (ATT) measures the relative position and orientation between the primary and the secondary antenna

Only after thorough alignment of the time and space coordinate systems of the above instruments [3], the errors of the composed baseline angle could be minimized. Even if the absolute precision and the long term stability are within specification, we still observe residual height errors in the DEMs corresponding to very small baseline roll uncertainties of less than 0.001 degrees or 1 millimeter roll error at the end of the mast. The pre-flight SRTM calibration concept foresaw to eliminate slow drifts by using well known ocean surfaces for calibration. However, the fast dynamic properties of the error leaves us with height oscillations in the order of ± 5 to ± 10 meters in geographical scales of 50 km to 800 km. More details on this are given in the ocean calibration section.

5. INSTRUMENT STABILITY

Due to the short mission duration of 11 days the instrument was exposed only to little aging. However, it experienced significant temperature variations within the 90 minute period orbital cycles and even within data takes of up to 40 minutes length. The most significant contribution was identified to be the long cable feeding the down conversion frequency up the mast and feeding back the down converted signal of the secondary antenna [12]. Indeed, we measured phase variations of 50 degrees in phase with the orbital period in a calibration loop. We use the signals of this loop to compensate the interferometric SAR data for the induced error of ca. 25 meters. Other instrument calibration signals show, that another height error of up to 25 meters could be induced by strong temperature changes at the phase locked loop used for demodulation. These errors are of very large spatial scale, occur only under certain geographical conditions and are therefore hard to demonstrate. They are still under investigation and will be compensated as soon as they have been demonstrated.

6. INTERFEROMETRIC COREGISTRATION

The small wavelength of the X-SAR instrument (3.1 cm) together with the small movements of the space shuttle platform poses stringent requirements on the coregistration accuracy between the images of both antennas. The slight non-orthogonal view of the antennas along the flight direction of the shuttle and attitude variations in the order of 0.1^0 cause a Doppler centroid frequency in the order of -2.2 kHz. This in turn corresponds to a linear phase function through any point target in azimuth direction. In consequence, any space varying azimuth misregistration Δaz causes a space variant height error of

$$\Delta h = 180\text{ m} \cdot \Delta az \cdot f_{DC} / PRF,$$

where 180m/cycle is the approximate SRTM phase to height conversion constant. If we allow 1 meter of height error at Doppler centroid frequency of f_{DC}=-2000 Hz and a pulse repetition frequency PRF=1674 Hz, we end up with a coregistation requirement of 0.005 pixel or 2 cm in azimuth. We found, that the conventional image correlation techniques that we had used for interferometric processing of ERS data can hardly meet this requirement, especially under the stringent SRTM requirements of global automatic processing. In consequence, we used the inherent high geometric precision of the baseline and implemented a pure geometrical coregistration approach [6]. This approach does no more image correlation and is thus not only more precise, but also faster.

7. MOTION COMPENSATION

The shuttle and the mast have not only advantages: compared to the smooth baseline formed by two separate satellites, the baseline of SRTM is a coupled mechanical system with more complicated dynamics. It requires special InSAR processing techniques similar to processing air borne data. The track of the primary antenna can be considered smooth compared with the wavelength due to the high mass of the space shuttle and the comparatively low forces from aerodynamic drag and oscillations from the mast. However, the secondary antenna at the end of the 60 meter mast is oscillating significantly due to oscillations of the boom and small rotations round the shuttle center of mass. We therefore implemented a simple, robust and efficient motion compensation procedure by smoothing the effective roll angle of the interferometric baseline [1]. In contrast to airborne interferometry, the motion of both antennas is much smaller than a resolution cell and does not shift or defocus the SAR images [7].

8. COHERENCE AND PHASE NOISE

The coherence is a standard measure for the phase noise between both interferometric channels. Since X-SAR is looking at a flat incidence angle of 54.8°, the reflected energy is low and the receivers operate at full gain setting most of the time. Due to thermal and quantization noise, weak received signals have a lower signal to noise ratio (SNR) and hence lower coherence. The coherence measured in the interferograms is somewhat lower than we had expected before the mission. It varies from γ=0.87 for low backscatter ocean data, over γ=0.93 for typical land data to γ=0.96 for bright land scenes. Using noise measurements from special receive only data takes and a Gaussian model for quantization noise, we can predict the coherence well once we know the average signal levels from both channels. The DEM height noise resulting from the decorrelation noise can be reduced by increasing the number of interferometric looks or by adaptive filtering.

9. OCEAN CALIBRATION

Currently our DEM accuracy knowledge is merely based on ocean areas that provide a large and very precisely known surface. For the comparison, we use geoidal ocean heights provided by the Geoforschungszentrum Potsdam (GFZ) [5], corrected for many effects like barometric pressure, currents and tidal variations. During our tests, we processed many ocean data takes to DEMs, the longest one being 8500 km long. We then took azimuth and range cuts through the DEMs to characterize the linear and quadratic height variations over range and the temporal over azimuth. All the measured height differences were within a ±10 meter band and allow us to assume an excellent long term stability of the X-SAR instrument and the AODA system. We are still concerned by small systematic height errors with an amplitude of ±2.5 meters and 7.1 second period - the frequency of the 1st mode mast oscillation. We also notice other variations with ca. 5 meter amplitude at very large scales of ca. 1000 km. Both errors are quite small compared to the large spatial scale, but since they seem to be coupled with mast motion, we are investigating methods to compensate them.

Fig. [3] demonstrates the current status on a long ocean data take #146.190. We seem to have no problem to fulfill the global accuracy specification: The green lines mark the absolute specification, i.e. a 16 meter (90%) error. Indeed for this very long data take, 99% of the data meet the requirement. The relative specification shown in red requires 90% of the data to be better than 6 meter error. The ocean data shows, that only 84 % of the data meet this requirement due to the residual 2.5 meter oscillations. If the thermal noise is reduced to 3 meters by filtering, even the 90% specification will be met.

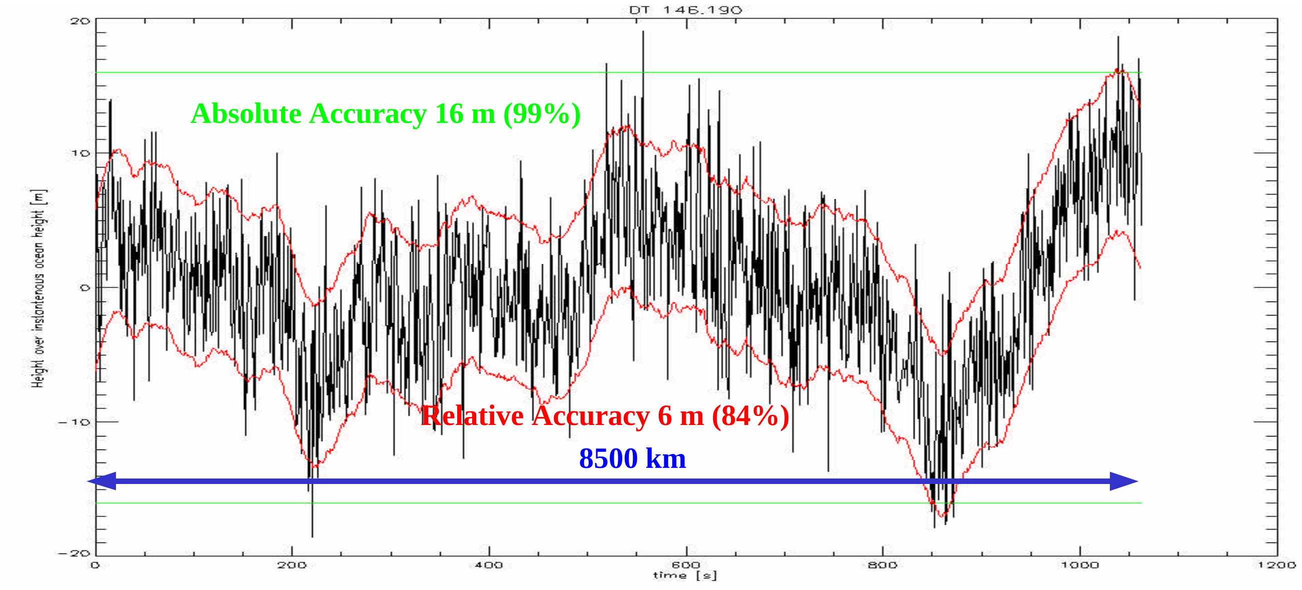

Fig. [3]: SRTM X-SAR ocean height error during a 8000 km data take. The short oscillations are ±2.5 m, the total variations are within a band of ca. 20 m.

10. SPATIAL SCALE OF ERRORS

Fig. [4] shows the error sources of SRTM X-SAR and the corresponding scales. Thermal and quantization noise occures on the pixel scale and can accordingly be controlled by filtering operations. Some aliasing effects of high frequency mast motion components were significant before the sampling of the geometry data was increased from 1 Hz to 4 Hz. Now, it is no more of concern.

The residual mast oscillation effects in the scale of 50 km are often visible at ocean or flat land areas within a typical scene of 170 km x 50 km. We are still investigating methods to suppress this error.

Very low errors occure through thruster firings and thermal drifts on a continental scale (larger than 700 km). These errors are within specification and typically only visible as small offsets within a typical scene. They can partly be eliminated by the ocean calibration procedure.

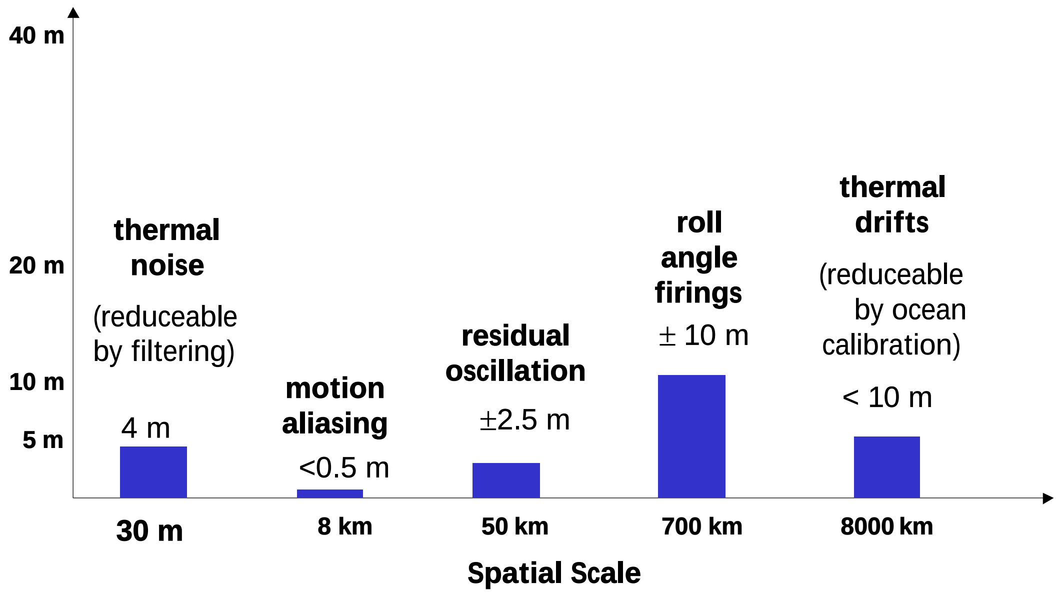

Fig. [4]: SRTM X-SAR errors and spatial scales

11. SUMMARY

During the calibration phase we processed more than thousand scenes to test the system and to determine unknown system parameters. The observed stability of the system makes us confident to meet the mission goals with respect to the absolute height error of ±16 meters (90%). We will also achieve the required 4 m relative error by reducing the thermal noise applying appropriate filtering. Small oscillations in the 50 km scale will need more investigation, however. The excellent timing and positioning concept provides a product localization precision unknown so far. The overall SAR data quality is so good and the geometry so reliable that the processing of the global data set to a global DEM will be an operational production process with a minimum of operator interaction.

12. REFERENCES

[1] N. Adam, M. Eineder, H. Breit, "SRTM X-SAR Motion Compensation: Concept and First Assessment of the Interferometric Observation Geometry", IGARSS 2001, Sydney

[2] W. Bertiger, Y. Bar-Sever, S. Desai, et. al, "Precise Orbit Determination for the Shuttle Radar Topography Mission using a new Generation of GPS Receiver", Proceedings of ION GPS 2000, Salt Lake City, UT

[3] R. Duren, "SRTM Metrology System: Preliminary Flight Results", IGARSS 2000, Honolulu (paper not available)

[4] M. Eineder, H. Breit, N. Adam, J. Holzner, S. Suchandt, B. Rabus, "SRTM X-SAR Calibration Results", IGARSS 2001, Sydney

[5] Helm A., Braun A., Eickschen S., Rentsch M., Schöne T., "Calibration of the Shuttle Radar Topography Mission X-SAR Instrument Using Altimetry Data", Geophysical Research Abstracts, Vol.3, EGS General Assembly Suppl., p404, 2001

[6] J. Holzner, S. Suchandt, M. Eineder, H. Breit, N. Adam, "Co-registration - Geometrical Analysis and Verification for SAR Interferometry Under SRTM Data Conditions", IGARSS 2001, Sydney

[7] G. Franceschetti, A. Iodice, S. Maddaluno, D. Riccio, "Effects of secondary antenna oscillations on X-SAR/SRTM performace", IGARSS 1999, Hamburg

[8] P. Rosen, M. Eineder, H. Breit, E. Gurrola, S. Hensley, W. Knöpfle, B. Rabus, A. Roth, M. Werner, "SRTM-Mission - Cross Comparison of X and C Band Data Properties", IGARSS 2001, Sydney, on CD-ROM

[9] A. Roth, M. Eineder, B. Rabus, E. Mikusch., B. Schättler, "SRTM / X-SAR: Products and Processing Facility", IGARSS 2001, Sydney

[10] S. Suchandt, H.Breit, N. Adam, M.Eineder, B.Schaettler, H.Runge, A.Roth, E. Mikusch, "The Shuttle Radar Topography Mission", ISPRS, Hannover 2001

[11] M. Werner, M. Haeusler, "X-SAR/SRTM Instrument Phase Error Calibration", IGARSS 2001, Sydney

[12] M. Zink, D. Geudtner, "Calibration of the Interferometric X-SAR System on SRTM", IGARSS 1999, Hamburg

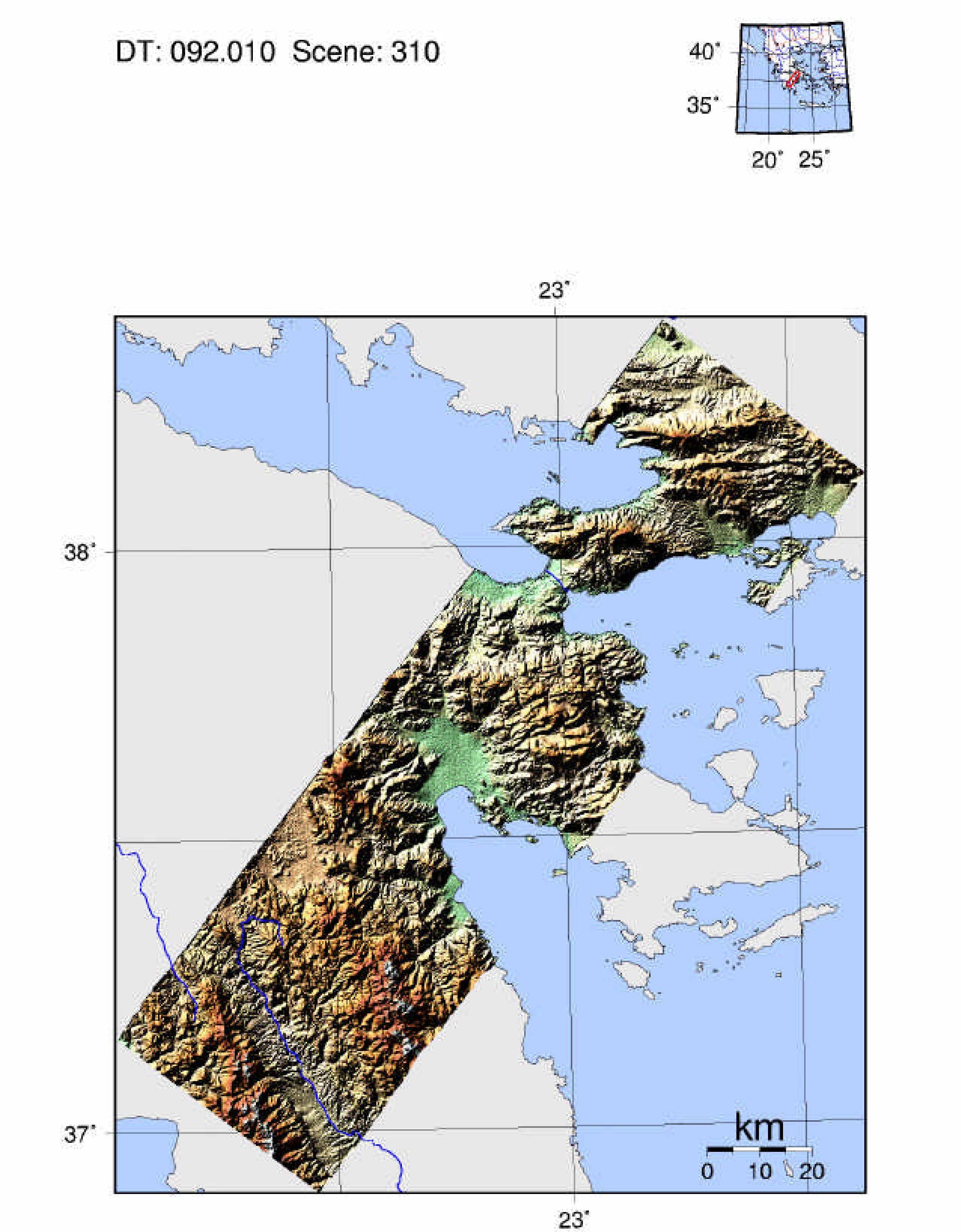

Fig. [5]: An SRTM X-SAR sample image showing the Pelopones and Korinth in Greece, overlaid with a geographical map

SUB-METRE GEOPOSITIONING WITH *IKONOS GEO* IMAGERY

C.S. Fraser, H.B. Hanley & T. Yamakawa
Department of Geomatics
University of Melbourne
Victoria 3010 Australia
(c.fraser@eng.unimelb.edu.au, hanley@sunrise.sli.unimelb.edu.au, yamakawa@sunrise.sli.unimelb.edu.au)

KEY WORDS: *Ikonos* imagery, satellite image orientation, linear triangulation models, high-accuracy geopositioning

ABSTRACT

The *Ikonos* one-metre earth observation satellite system offers the photogrammetric and remote sensing communities a significant new means for geospatial information collection, with the potential of pixel-level geopositioning precision. This paper addresses the subject of the metric accuracy potential of *Ikonos Geo* imagery for both 2D and 3D geopositioning. Photogrammetric approaches to metric accuracy evaluation of line scanner imagery typically involve application of collinearity-based restitution models which require sensor calibration data and possibly also information related to exterior orientation. With *Ikonos* data, however, both the camera model and precise satellite ephemeris data are withheld from the user of *Geo* imagery, leaving only two practical alternatives for multi-image triangulation. The first is use of rational functions and the second involves the employment of sensor orientation models which do not rely on knowledge of the camera model, but do require ground control. Two such candidate approaches are the affine projection model and an extended direct linear transformation (DLT). A test field of precisely measured ground control points within the city of Melbourne has been imaged with 3-fold *Ikonos* 1m *Geo* coverage comprising a stereopair and a near nadir-looking image. In order to quantify the metric potential of this imagery, both 2D and 3D geopositioning have been investigated, the former primarily to verify sensor integrity (linearity) and the latter to ascertain accuracy in the presence of a modest provision of ground control. In both instances sub-pixel accuracy was attained, with planimetric positioning to 0.3m and heighting reaching 0.7m accuracy. The paper describes the Melbourne testfield, discusses the 2D and 3D geopositioning approaches adopted, and reports on the geometric accuracy obtained with the different sensor orientation models.

1. INTRODUCTION

There are basically five image product options for panchromatic and pan-sharpened 1m resolution *Ikonos* satellite imagery. These are *Geo*, *Reference*, *Pro*, *Precision* and *Precision Plus* (Space Imaging, 2001). Except for the *Geo* product, all are orthorectified images, with the *Precision* level products requiring ground control. The absolute positioning accuracies (RMS, 1-sigma) for each product are as follows: *Geo*, 24m; *Reference*, 12m; *Pro*, 5m; *Precision*, 2m and *Precision Plus*, 1m. Between the *Geo* and *Precision* products, there is a substantial price difference, which can exceed four times the *Geo* price, based on published price information. These accuracy specifications would suggest that users of *Ikonos* imagery who are seeking highest metric quality would need to acquire *Precision* or *Precision Plus* imagery. Here we investigate the prospects for obtaining *Precision*-level accuracy from base-level *Geo* imagery.

It is only about 18 months since *Ikonos* imagery first became commercially available and to date there has been relatively little published on the metric quality of this new satellite image data. There have been indications that metre-level accuracy is attainable in ortho-image generation from *Geo* imagery (Kersten et al, 2000; Cheng, 2000; Davis & Wang, 2001). Space Imaging have reported on an evaluation of the geopositioning accuracy of *Ikonos* stereo configurations (Dial, 2000), though while the results were encouraging the investigation did not seek to exploit the full relative accuracy potential of the stereo imagery. One of the reasons that independent assessments have been slow in coming is that the *Ikonos* camera model and precise ephemeris data have been withheld as proprietary information, which precludes to a significant extent 'standard' photogrammetric analysis utilising collinearity equation models.

In this paper the authors report on the results of an ongoing investigation into the 2D and 3D accuracy of *Ikonos Geo* imagery, which considers configurations of single, stereo and three-fold image coverage. This work commenced with 2D evaluation, as reported in Hanley & Fraser (2001), and has progressed into an investigation of 3D feature extraction accuracies. The latter effort has included an assessment of *Ikonos* stereo imagery for building extraction, carried out in conjunction with the Institute of Geodesy and Photogrammetry at ETH-Zurich (Fraser et al., 2001), though it has primarily concentrated on the geopositioning accuracy of well defined ground features via two image orientation approaches. The first of these is the use of Rational Functions, the coefficients of which (often loosely referred to as

RFCs or RPCs) can be supplied with the stereo imagery. The second is the adoption of alternative orientation models, namely the Direct Linear Transformation (DLT) and Affine Projection, which circumvent the need for the *Ikonos* camera model, but do require the provision of a modest number of ground control points (GCPs).

In seeking to experimentally ascertain whether *Ikonos* imagery is capable of sub-metre (sub-pixel) geopositioning accuracy, as is suggested by its design parameters, there is a need to have an object testfield of very high metric quality, with image identifiable GCPs which support sub-pixel image mensuration. Such a testfield has been established to support the current research program. In the following sections this testfield will first be described, after which the results of the 2D accuracy analysis of single *Geo* images will be summarised. The 3D accuracy evaluation for stereo and 3-image networks will then be described, with three image orientation approaches being considered: rational functions, the DLT and an affine projection model.

2. THE MELBOURNE *IKONOS* TESTFIELD

The testfield, which covers a 7 x 7km area of central Melbourne, comprises an array of GPS-surveyed GCPs of which 32 are distinct, image-identifiable road roundabouts. The layout of these GCPs is indicated in Figure 1. Image coverage of the testfield is provided by both an *Ikonos Geo* stereopair of panchromatic images, and a near-nadir looking scene of panchromatic and multispectral imagery. The overall geometric configuration is thus akin to 3-line imagery, with the base-to-height ratio of the convergent stereopair being B/H = 1.2. Supplied with the stereo imagery were RFCs, which provide a mechanism for object-to-image space transformation and 3D point determination. There were initially no RFCs for the near-nadir image, since the option of obtaining these coefficients for single *Geo* images was not available at the time the data was acquired, though they have subsequently been obtained. As will be referred to in later sections, there was a notable difference in quality between the near-nadir imagery, which was recorded in late summer with a sun elevation of 38°, and the stereo imagery, which was recorded in winter with a sun elevation of 21°. An account of the radiometric characteristics of the imagery is given in a companion paper by Baltsavias et al (2001).

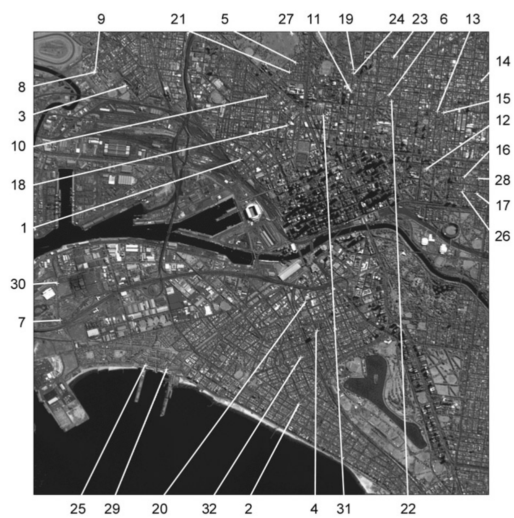

Figure 1. The Melbourne *Ikonos* testfield showing GPS-surveyed object point locations.

A geopositioning accuracy of 1m or better was sought from the stereo *Geo* image data and thus there was a need to measure image-identifiable ground points to sub-pixel accuracy within the imagery, as well as to sub-metre precision on the ground. Road roundabouts were selected as control points since they constituted an elliptical target which was usually well contrasted against its background (the surrounding road) within the image, and which was typically 8 to 25 pixels in diameter. The centroid of each roundabout was measured within the imagery and so the GPS survey also needed to determine the centre point coordinates.

The centroids of each of the 32 roundabouts were determined as described in Hanley & Fraser (2001) by measuring six or more edge points around the circumference of the feature, both in the image and on the ground, and then employing a best-fitting ellipse computed by least-squares to determine the ellipse centres (see Fig. 2). It was possible with this approach to achieve accuracies of image and object point determination in 2D and 3D space, respectively, to better than 0.2 pixels. Figure 2 shows one of the roundabouts as recorded in the nadir-looking *Ikonos* image, along with a best-fitting ellipse to edge points of the same roundabout.

To complement the image mensuration via ellipse fitting, least-squares template matching was employed with the stereo imagery, with special care being taken to alleviate problems such as target occlusions from shadowing and the presence of artefacts such as cars (e.g. Fig. 2). The matching utilised intensity gradients instead of grey values and the observational weights were determined from the template gradients, i.e. only pixels along the circular template edge were used in matching, thus making the method insensitive to contrast differences and other disturbances (Baltsavias et al., 2001; Fraser et al, 2001). All results presented in this paper relate to the image mensuration via ellipse fitting. Although the template matching yielded slightly more consistent height data as a consequence of smaller parallax errors, there was no significant difference in accuracy between the two approaches.

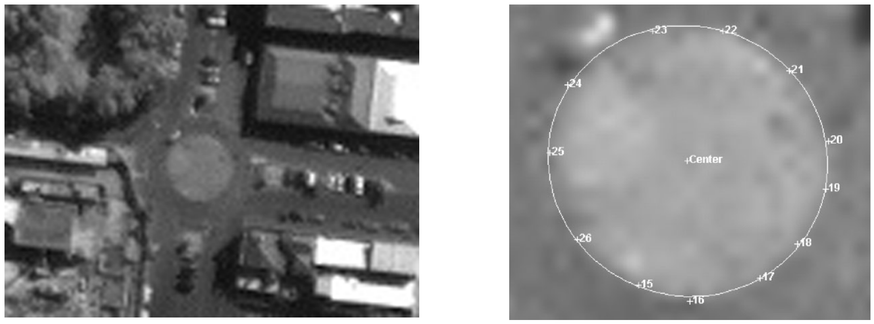

Figure 2. *Ikonos* image of roundabout (left) and recorded edge points and best-fitting ellipse (right).

3. METRIC POTENTIAL

The recovery of 3D cartographic information from satellite line scanner imagery has been the subject of photogrammetric investigation for the last decade and a half. Mathematical models have been formulated to support triangulation of cross-track *SPOT* and *IRS-1C/D* imagery, as well as *MOMS-02* 3-line imagery which is an along-track configuration with similarities to the *Ikonos* coverage of the Melbourne testfield. Fully rigorous mathematical models for orientation and triangulation, which have in turn implied provision of sensor calibration data and, to a degree, prior information on the satellite orbit and sensor attitude data, have been a prerequisite for these developments. In summary, it could be said that under ideal conditions of high-quality image mensuration and ground control/checkpoints, coupled with favourable imaging geometry (e.g. B/H > 0.8) and provision of sensor calibration data, ground point determination to 0.3 pixel accuracy is possible (Ebner et al. 1996) with medium-resolution stereo satellite imagery. However, accuracies of between 0.5 and 2 pixels are more commonly encountered in practical tests.

Through a simple extrapolation of these findings to 1m-resolution imagery, we might anticipate that under similar operational constraints sub-metre 3D geopositioning accuracy should be achievable from stereo *Ikonos* panchromatic and pan-sharpened image data. Consider, for example, a stereo *Ikonos* configuration similar to that covering the Melbourne testfield. Under the assumption of an image measurement accuracy of 0.4 pixel (σ_{xy} = 5μm), the ground point triangulation precision to be anticipated for the stereo configuration is σ_{XY} = 0.3m (planimetry) and σ_Z = 0.7m (height). If this stereo geometry is extended to three along-track images (addition of a nadir-looking image), again as we have for the Melbourne testfield, the triangulation precision in Z remains unchanged (see also Ebner et al. 1992), whereas the planimetric precision is improved to σ_{XY} = 0.25m, or ¼ of the ground sample distance. In order to apply familiar collinearity-based models in this triangulation process, a camera model comprising sensor calibration data must be available. Moreover, for the stereo image restitution, prior knowledge of the satellite exterior orientation is required, though this requirement can be relaxed in the 3-image triangulation.

In the following two sections we evaluate in the 2D and 3D accuracy of *Ikonos* imagery in relation to anticipated object point precision, in the 2D case by examining the application of straightforward conformal, affine and projective image-to-object coordinate transformation models, and in the 3D case through the application of alternative sensor orientation models, namely rational functions, the DLT and affine projection.

4. 2D POSITIONING ACCURACY

In many respects a prerequisite for the application of alternative sensor orientation models is that the imagery itself is of high metric integrity. It should be recalled that the *Geo* product is “a geometrically corrected product that has been rectified to a pre-specified ellipsoid and map projection” (Space Imaging 2001). Moreover, the imagery is re-sampled by cubic convolution to 1m pixels and in the case of a stereopair it is epipolar resampled. As a means of both ascertaining the planimetric positioning accuracy of 1m *Geo* imagery and of evaluating 'sensor linearity', a number of 2D transformations from image to object space were performed. The aim was to examine the accuracy in XY coordinates resulting from mapping the image data to height-corrected 'planes of control' using various ground GCP configurations. This operation was performed separately for each of the three images, with three well-known 2D transformation models being employed: similarity (4 parameter), affine (6 parameter) and projective (8 parameter).

Listed in Table I are the RMS object point discrepancies resulting from the transformations when all available GCPs are included. The most striking feature of the table is that there is relatively little difference in the results between either the three images or the three transformation functions. In all cases the RMS discrepancy values are less than 0.4 pixels and in the case of the near-nadir image the mean XY accuracy surpasses 0.3 m. No individual control point residual exceeded 1 pixel. The expected reduction in RMS values accompanying an increasing number of parameters is apparent, but the minor variations between models indicates that there is no significant systematic error present, at least at first-order. Moreover, application of second- and third-order transformations yielded no significant further reduction in RMS discrepancy values, which again indicated an absence of higher-order systematic errors likely to be of practical consequence. When subsets of 6 GCPs were used, the RMS values of checkpoint residuals (about 25 per image) remained below 0.5m (Hanley & Fraser, 2001).

This straightforward analysis gave a strong indication of the metric integrity of *Ikonos Geo* imagery, which augured well for the use of linear models in 3D geopositioning. The tests also demonstrated that in the presence of good quality control and DTM data (or moderately flat terrain), *Geo* imagery can readily yield an XY positioning accuracy of 0.5 pixels and better in spite of the 1-sigma accuracy specification (admittedly absolute accuracy) of 24m. One of the benefits of the sensor having such a narrow field-of-view of 0.93° is that projective distortions more familiar in wider angle sensors (eg lens distortion) do not amount to significant non-linear image perturbations. It is noteworthy that the two convergent stereo images produced a 10% lower accuracy than the near-nadir image, though it not possible to attribute this minor accuracy fall-off to any one factor. As mentioned, however, the image quality of the stereo pair was noticeably below that of the near-nadir image.

Table I. RMS coordinate discrepancies in transformation from images to 'plane of control'; units are pixels, and metres.

Image; Number of points	Similarity			Affine			Projective		
	X	Y	XY	X	Y	XY	X	Y	XY
1. Near Nadir; 31	0.27	0.33	0.30	0.26	0.32	0.29	0.23	0.30	0.27
2. 'Left' Stereo; 26	0.35	0.39	0.37	0.33	0.37	0.35	0.33	0.36	0.35
3. 'Right' Stereo; 28	0.39	0.37	0.38	0.38	0.36	0.37	0.39	0.35	0.37

5. 3D GEOPOSITIONING

5.1 Rational Functions

Rational functions provide a means of extracting 3D information from stereo satellite imagery without explicit reference to either a camera model or satellite ephemeris information. They are quotients of polynomials which express either image coordinates (line, sample) as a direct function of object space coordinates (typically latitude, longitude and height), or planimetric object point coordinates as a function of image coordinates and ground point height, in much the same way as do collinearity equations. Rational functions, which provide a continuous mapping between image and object space, also defy straightforward geometric interpretation. Indeed, it is said that one reason this sensor orientation model gained popularity for military imaging satellites was that the satellite orbital elements and also the exterior orientation could not be derived from RFCs. In the context of *Ikonos Geo* imagery it is important to note that the RFCs accurately model the rigorously determined exterior orientation (Grodecki, 2001) and they are therefore merely a reparameterisation of the sensor orientation. Thus, object point triangulation via Space Imaging supplied RFCs should yield the same accuracy as the collinearity model (were it available), which would in turn be consistent with *Geo* accuracy specifications.

A general model for rational functions, which is appropriate for mono and stereo imaging configurations, is given as

$$x = \frac{P_1(X,Y,Z)}{P_2(X,Y,Z)}$$

$$y = \frac{P_3(X,Y,Z)}{P_4(X,Y,Z)} \tag{1}$$

where

$$\begin{aligned} P_i(X,Y,Z) = {} & a_1 + a_2 \cdot Y + a_3 \cdot X + a_4 \cdot Z + a_5 \cdot Y \cdot X + a_6 \cdot Y \cdot Z + a_7 \cdot X \cdot Z + a_8 \cdot Y^2 + a_9 \cdot X^2 \\ & + a_{10} \cdot Z^2 + a_{11} X \cdot Y \cdot Z + a_{12} \cdot Y^3 + a_{13} \cdot Y \cdot X^2 + a_{14} \cdot Y \cdot Z^2 + a_{15} \cdot Y^2 \cdot X + a_{16} \cdot X^3 \\ & + a_{17} \cdot X \cdot Z^2 + a_{18} \cdot Y^2 \cdot Z + a_{19} \cdot X^2 \cdot Z + a_{20} \cdot Z^3 \end{aligned}$$

Here, x,y are the normalised (offset and scaled) image coordinates and X,Y,Z the normalised object point coordinates. Typically, the order of the polynomial P_i is three, thus leading to 80 RFCs per image. As can be seen from Eq.1, a number of existing restitution algorithms for line scanner imagery are based on special formulations of the ratio-of-polynomials model (e.g. the DLT and polynomial expressions in which the denominator is reduced to unity).

It is noteworthy that RFCs produced for *Ikonos Geo* imagery are derived solely from the camera model and sensor position and attitude recorded by the on-board GPS receivers and star trackers. We might surmise that the exterior orientation data would be subject to biases which would be unlikely to undergo significant change within the 100 or so seconds between the recording of two images forming an along-track stereo pair. Thus, object point triangulation from a stereopair via the supplied RFCs might be expected to yield higher relative than absolute accuracy. The first step in our investigation of 3D geopositioning from the *Ikonos* stereo imagery of Melbourne was to examine this assumption.

The object space coordinates of all 32 roundabouts were computed from the RFCs via a least-squares spatial intersection model (e.g. Di et al., 2001). The mean discrepancies between the RFC-computed GCP coordinates and the GPS-surveyed values, along with their standard errors, were as follows: Easting, 8.2m bias and 0.50m standard error; Northing: 31.5m and 0.45m; and height 1.7m and 0.78m. Thus, the RFCs yielded a sub-metre relative accuracy, but absolute positions which while exhibiting a bias of only 1.7m in height were in error by in excess of 30m in planimetry. Similar biases can be expected in planimetric geopositioning from single images (eg Baltsavias et al., 2001)

Ground control is required in order to remove such biases. For fewer than 3 GCPs a coordinate translation can be applied, whereas provision of more GCPs will facilitate 3D similarity transformation to account for any rotational error. The triangulated object points in the Melbourne testfield were free of rotational bias and thus the translation and similarity transformation yielded effectively the same results, an absolute accuracy (RMS) of just under 0.5m in planimetry and 0.8m in height. These findings confirm that metre-level accuracy is obtainable from *Geo* stereo imagery with RFCs and a post-triangulation translation/rotation. Our analysis has to date been confined to stereo images obtained from the same orbit. It is anticipated that inclusion of a third image from a different orbit, or triangulation of two images from separate orbits, may not yield such impressive results without modifications to the RFC triangulation model. The issue of spatial intersection via RFCs with different bias characteristics will soon be investigated.

5.2 Direct Linear Transformation

Restitution models based on linear projective equations have already proved practical in photogrammetry, in spite of some well-known shortcomings in comparison to the collinearity equation model. The most widely used of these models is the Direct Linear Transformation (DLT), a variation of which has been proposed by Wang (1999) for the orientation of satellite line scanner imagery. As has been alluded to earlier, the DLT also represents a special case of the rational function model, with the extended form proposed by Wang (1999) being as follows:

$$x = \frac{L_1 X + L_2 Y + L_3 Z + L_4}{L_9 X + L_{10} Y + L_{11} Z + 1} + L_{12}\, xy$$

$$y = \frac{L_5 X + L_6 Y + L_7 Z + L_8}{L_9 X + L_{10} Y + L_{11} Z + 1} \tag{2}$$

where x,y are image space coordinates in the flight and CCD directions, respectively, and X,Y,Z are Cartesian object space coordinates. This model is effectively the 'standard' DLT for frame imagery supplemented by an extra image coordinate correction parameter, L_{12}. Multi-image triangulation based on Eq. 2 does not require knowledge of sensor interior orientation, and nor does it require preliminary estimates of sensor exterior orientation. As a linear approximation to higher-order rational functions the DLT model can be expected to show limitations, especially as the area covered by the *Ikonos* scene becomes large. To overcome such problems Yang (2001) has proposed the use of piece-wise DLTs (without the L_{12} term), which are effectively localised approximations of RFCs. For both the 2- and 3-image orientation/triangulation computations with the DLT for the Melbourne testfield data, all parameters where determined simultaneously in a 'bundle adjustment' approach. Implicit in the formulation of Eq. 2 is the assumption that the dynamic behaviour of the sensor trajectory and attitude can be adequately modelled with variation functions of first-order, which would imply that the DLT approach is most suited to scenes of limited geographical extent.

In an effort to quantify the potential of the DLT, a series of orientation/triangulation computations were performed with both the *Geo* stereopair and the 3-image configuration. Different sets of 6 and 8 GCPs were employed, which yielded very similar accuracy results. We will thus report only one 6-point and one 8-point GCP arrangement in order to indicate representative values, these being shown in Table 2.

Table 2. Accuracy and precision obtained with the DLT for 2- and 3-image *Ikonos* configurations.

Geometric configuration	RMS value of image residuals (μm)	Standard errors (m)		RMS discrepancies at checkpoints (m)	
		σ_{XY}	σ_Z	s_{XY}	s_Z
2-image, 6 GCPs	1.6	0.58	1.10	0.63	0.91
2-image, 8 GCPs	1.7	0.46	0.95	0.45	0.85
3-image, 6 GCPs	2.3	0.42	0.91	0.33	0.51
3-image, 8 GCPs	2.4	0.34	0.76	0.27	0.55

It is noteworthy in Table 2 that the *a posteriori* standard errors are somewhat larger in magnitude than would be anticipated from the collinearity equation model with an image mensuration precision of 0.2 pixels (approximately 2.5 μm). Moreover, the 2-image result also displays an RMS object point accuracy which is somewhat lower than anticipated, though still at sub-pixel level. On the other hand, the results for the 3-image geometry, as indicated by the residuals from 20 or so checkpoints, are close to the optimal anticipated accuracy of 1/3 pixel in planimetry and 2/3 pixel in height, slightly better in fact. Additional computations were also performed using the standard 11-parameter DLT formulation, i.e. without L_{12}, but the results were essentially the same as those listed in the table, which shows that for areas of 50 km^2 or less and moderate terrain, this term may well be neglected.

5.3 Affine Projection Model

A second alternative image orientation approach is a model based on affine as opposed to perspective projection. Under this approach, which is described in Okamoto et al. (1999) and Hattori et al. (2000), an initial transformation of the image from a perspective to an affine projection is first performed, though for areas of moderate size and limited variation in topography this may be neglected. A linear transformation from image to object space then follows, which depending on the particular affine model formulation adopted, may involve the modelling of coefficients as linear functions of time. Formulation of the affine model was motivated by a recognition that as the field of view of the linear array scanner becomes small, high correlations develop between exterior orientation parameters within a perspective projection since the narrow bundle of rays effectively approaches a skew parallel projection. It should be recalled that the field angle of the *Ikonos* sensor is less than 1°. The affine model for 3D analysis of line scanner imagery (affine in both coordinate axes) is given in the form (Okamoto et al., 1999)

$$\begin{aligned} x &= A_1X + A_2Y + A_3Z + A_4 \\ y &= A_5X + A_6Y + A_7Z + A_8 \end{aligned} \qquad (3)$$

where x,y and X,Y,Z are as per Eq. 2 and all parameters, 8 per image, are determined simultaneously in a multi-image orientation/triangulation. As mentioned, application of Eq. 3 may first require an image conversion from central perspective to affine projection, which although needing a prior knowledge of terrain height and approximate sensor exterior orientation, is nevertheless reasonably insensitive to coarse initial estimates of both due to the iterative nature of the conversion (Okamoto et al., 1999).

Listed in Table 3 are the results of the orientation/triangulation computations performed using the affine model for 4-, 6- and 8-GCP configurations, again for two and three images. Whereas the affine and DLT models yield similar accuracy results for the 3-image network, the affine approach produces superior results for the stereo configuration. Beyond this distinction the characteristics seen in Table 2 for the DLT are repeated to a large extent in Table 3. The image coordinate residuals again approach 0.2 pixel for the 3-image network, though they are marginally higher in the affine case as a consequence of the fewer parameters. Also, whereas both models produce equivalent accuracy in planimetry in the 3-image network, the affine model produces more accurate heights. Additional tests were performed to examine the impact of the initial transformation from a perspective to an affine projection, and it was found that although the accuracies were superior with this transformation, the effect was minimal in the Melbourne testfield which displays a height range of only 50m. For larger areas, with significant elevation changes, this transformation is likely to be warranted, and as the area gets larger still additional parameters can be considered to account for non-linearities.

Table 3. Accuracy and precision obtained with the affine model for 2- and 3-image *Ikonos* configurations.

Geometric configuration	RMS value of image residuals (μm)	Standard errors (m)		RMS discrepancies at checkpoints (m)	
		σ_{XY}	σ_Z	s_{XY}	s_Z
2-image, 4 GCPs	1.9	0.57	1.19	0.42	0.68
2-image, 6 GCPs	2.0	0.46	1.00	0.44	0.70
2-image, 8 GCPs	2.2	0.44	0.93	0.37	0.65
3-image, 4 GCPs	2.4	0.41	0.89	0.31	0.48
3-image, 6 GCPs	2.5	0.34	0.78	0.33	0.49
3-image, 8 GCPs	2.6	0.32	0.72	0.26	0.45

In spite of some theoretical shortcomings in the perspective-to-affine image conversion, and in spite of the modelling of coefficients A_i in Eq. 3 as time-invariant, the affine model has provided triangulation accuracies equivalent to the central perspective model. Moreover, the method is equally applicable to along-track and cross-track stereo imaging configurations, and given the narrow view angle of *Ikonos* imagery, the affine approach appears quite well suited to the orientation of 1m resolution imagery.

6. CONCLUDING REMARKS

The findings presented in this paper for 2D and 3D geopositioning from *Ikonos* imagery illustrate, firstly, that sub-pixel object feature point determination is readily achievable, and that high accuracy is possible with the base-level (and least expensive) *Geo* imagery. The investigation has also confirmed that with a straightforward translation or translation/ rotation of the object point coordinates produced via RFCs, accuracies at the 1m level rather than the specified 24m absolute accuracy level can be anticipated. Perhaps of most practical significance is the fact that 2D and 3D geopositioning to sub-metre accuracy can be achieved with relatively straightforward linear models. The cost of applying such models is the need for a modest provision of quality ground control, which appears at this time to be a more economical proposition than acquiring *Precision*-level *Ikonos* imagery. The present work has concentrated upon feature point extraction, though the same empirical model approach is considered equally applicable to DTM extraction and ortho-image generation. The scope of this paper has been confined to consideration of high-quality ground feature points only. As indicated in Fraser et al. (2001) & Baltsavias et al. (2001), however, metre-level accuracy is also attainable for geopositioning operations with less ideal targets, such as in building extraction from *Geo* imagery.

ACKNOWLEDGEMENTS

Components of the *Ikonos* research work, which is supported by the Australian Research Council, are being carried out in collaboration with the Institute of Geodesy and Photogrammetry at ETH-Zurich, where the cooperation of Manos Baltsavias, Maria Pateraki and Li Zhang has proved both productive and beneficial.

REFERENCES

Baltsavias, E., Pateraki, M. & Zhang, L., 2001. Radiometric and geometric evaluation of Ikonos Geo images and their use for 3D building modelling. *Proc. Joint ISPRS Workshop High Resolution Mapping from Space 2001,* Hannover, 19-21 September (on CD ROM).

Cheng, P., 2000. Orthorectification of Ikonos data using rational functions. *ASPRS Annual Conference*, Washington D.C., 22-26 May, abstract only (on CD-ROM).

Davis, C.H. & Wang, W., 2001. Planimetric accuracy of Ikonos 1-m panchromatic image products. *Proc. ASPRS annual* Conference, St Louis, 23-27 April, 14 p. (on CD ROM).

Di, K., Ma, R. & Li, R., 2001. Deriving 3D shorelines from high-resolution Ikonos satellite images with rational functions. *Proc. ASPRS Annual* Conference, St Louis, 23-27 April, 8 p. (on CD ROM).

Dial, G., 2000. Ikonos satellite mapping accuracy. *Proc. ASPRS Annual Conference,* Washington D.C., 22-26 May, 8 p. (on CD ROM).

Ebner, H., Kornus, W. & Ohlhof, T., 1992. A simulation study on point determination for the MOMS-02/D2 space project using an extended functional model. *International Archives of Photogrammetry and Remote Sensing*, vol. 29, part B4, 458-464.

Ebner, H., Ohlhof, T. & Putz, E. 1996. Orientation of MOMS-02/D2 and MOMS-2P imagery. *International Archives of Photogrammetry and Remote Sensing*, vol. 31, part B3, 158-164.

Fraser, C.S., Baltsavias, E & Gruen, A., 2001. 3D building reconstruction from high-resolution Ikonos stereo images. *3rd Int. Symposium on Automated Extraction of Man-Made Objects from Aerial and Space Images*, Ascona, Switzerland, June 10-15, 13 pages.

Grodecki, J., 2001. Ikonos stereo feature extraction - RPC approach. *Proc. ASPRS Annual Conference,* St. Louis, 23-27 April, 7 p. (on CD ROM).

Hanley, H.B. & Fraser, C.S., 2001. Geopositioning accuracy of Ikonos imagery: indications from 2D transformations. *Photogrammetric Record* 17, 12 p. (in press).

Hattori, S., Ono, T., Fraser, C.S. & Hasegawa, H., 2000. Orientation of high-resolution satellite images based on affine projection. *International Archives of Photogrammetry & Remote Sensing*, Amsterdam, 33(4) (on CD-ROM).

Kersten, T., Baltsavias, E., Schwarz, M. & Leiss, I., 2000. Ikonos-2 Carterra Geo – Erste geometrische Genauigkeitsuntersuchungen in der Schweiz mit hochaufgeloesten Satellitendaten. *Vermessung, Photogrammetrie, Kulturtechnik* (8): 490-497.

Okamoto, A., Ono, T., Akamatsu, S., Fraser, C.S., Hattori, S. & Hasegawa, H., 1999. Geometric characteristics of alternative triangulation models for satellite imagery. *Proc. ASPRS Annual Conference*, Portland, Oregon, 17-21 May, 12 p. (on CD ROM).

Space Imaging 2001. Company web site. http://www.spaceimaging.com (accessed 20 June 2001).

Wang, Y. 1999. Automated triangulation of linear scanner imagery. *Proc. Joint ISPRS Workshop on Sensors and Mapping from Space*, Hannover, 27-30 September, 5 p. (on CD ROM).

Yang, Y. 2001. Piece-wise linear rational function approximation in digital photogrammetry. *Proc. ASPRS Annual Conference*, St Louis, 23-27 April, 14 p. (on CD ROM).

Extraction of Digital Elevation Models and ortho-images from CORONA KH4B data.

Goossens, R.[1], Schmidt, M.[2], Altmaier,A.[2], Benoit,F.[1], Menz,G.[2]

rudi.goossens@rug.ac.be, m.schmidt@rsrg.uni-bonn.de, angela@rsrg.uni-bonn.de, f.benoit@rug.ac.be, menz@rsrg.uni-bonn.de

[1]Department of Geography, University of Gent (Belgium)
[2]Remote Sensing Research Group, Department of Geography, University of Bonn (Germany)

KEY WORDS: Corona, Digital Photogrammetry, Digital Elevation Model

Abstract*:*
The satellites used on the CORONA missions carried two cameras on board, enabling the collection of stereo images of the earths surface. During the operational phase (1960-1972), panchromatic images were recorded from many regions of the earth from a flight altitude of 150 km. The resulting data has been available to the public since 1995 and cost $US 18 per strip. Thus this data proves not only affordable for projects with limited budgets, but also for regions where surface information is hard to get or not available. In this paper two methods are described which transform photographic information into digital format and analyse the data with digital photogrammetric software. The first method is applied by performing a high quality scan of the strips directly, the second approach uses a photographic enlargement with a scan of the developed photos. CORONA image strips have no fiducial marks, so this leads to a non metric approach. Modern photogrammetric techniques offer the ability to derive a high resolution digital elevation model (DEM). This requires the collection of sufficient ground control points (GCPs) to produce a DEM with a high level of spatial accuracy. A LEICA 300 Differential Global Positioning System (DGPS) was used for the collection of ground truth data. These GCPs are needed to calculate the external orientation of the Digital Elevation Model (DEM). Two study areas were chosen in the Kingdom of Morocco for this investigation, the first near Zagora and the second near Toundoute. The methodology proposed in this paper has been applied to the first test area, with the second area used as a validation site. The accuracy achieved in the vertical (z) direction is in the order of 20 meters while horizontal (x,y) accuracies in the order of 9 meters were obtained.

1. INTRODUCTION

While CORONA satellite data have been available since 1995, techniques to utilise this data within standard remote sensing software is still not possible (Goossens et al*.*, 2001). The paper proposes a technique to obtain characterise the land surface in areas with little or no topographic information. The photogrammetric software package VirtuoZo 3.1 was used in order to analyse the stereoscopic images and to generate a digital elevation model. The data inherits high image distortions due to the fact that the stereo images are recorded in a converging manner. The purpose of this study is to investigate the utility of this relatively inexpensive data source which is available for many parts of the world, and to deliver a methodology to create a DEM that is suitable for environmental and remote sensing applications e.g. LANDSAT terrain corrections. This would prove useful as it is still not possible to obtain Shuttle Radar Topography Mission (SRTM)-derived DEMs for remote areas. The best available DEM source is currently the GTOPO30 from the U.S. Geological Survey which has a grid resolution of approximately 1 km. An alternative is to digitise topographic maps, but for many regions of the world these maps are of poor quality and do not provide sufficiently detailed information. Hence the aim of this investigation was to establish a methodology to derive DEMs with both less effort and cost, while providing improved accuracy.

2. DATA

The CORONA satellite program was initiated on the demand of the US President Eisenhower at the end of the 1950's after a so called U2 spy-plane was shot down by the former USSR. In the hope of avoiding further

international incidents, the US observational strategy was reorganised. The CORONA program resulted from this and was a cooperative effort between the US Central Intelligence Agency (CIA), the US Air Force and private companies. For the construction of the satellite, only the most state of the art camera-systems of the time were used (Ruffner, 1995).
In June 1959 the first launches of the rockets carrying the CORONA satellites took place, but the first 9 missions failed due to a variety technical problems. The first successful capture of a data capsule that was parachuted from a CORONA satellite was on the 18-th of August, 1960 (MacDonald, 1995).
Aircrafts of the US Air Force had the incredibly difficult task of capturing the ejected CORONA film capsules before they could plunge into the ocean. The capsules were constructed to remain viable for approximately 24 hours, after which they would self-destruct, thereby leaving no chance of being captured by other parties. (Peebles, 1997). This procedure obviously resulted in a loss of much mission data (Ruffner, 1995).
The ground resolution of the first mission data was 40 ft. During the operational phase of the CORONA satellite between 1960 and 1972, the camera systems were improved to a best ground resolution of 6 feet (1.8 meters), which was archived by the KH 4B camera (Table 1). This system had the additional advantage of the facility to take stereo-pictures with one camera looking “forward” and another camera looking “afterward” depending on the flight direction (Figure 1).

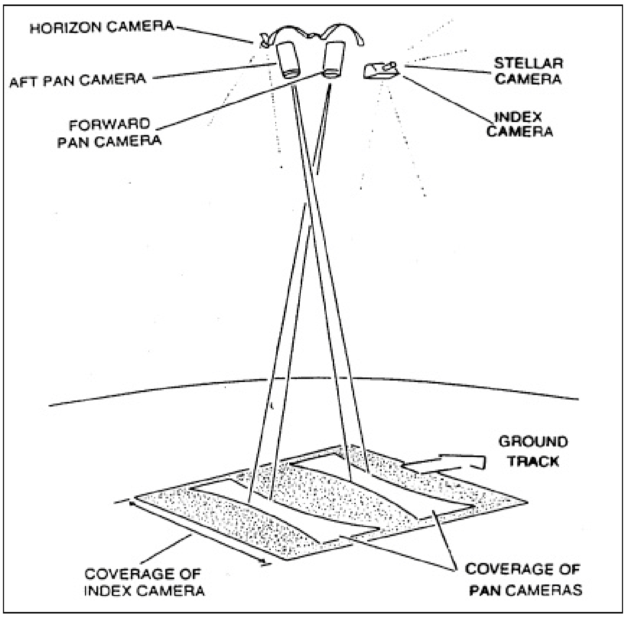

Figure 1: Stereoscopic cameras mounted in the Corona satellites (Campbell, 1996).

The area that is covered by one strip has a size of approximately 14 km x 188 km. In this study strips were used from mission number DS-1117-1.

Table 1: Data properties of the KH 4B cameras.

System	KH-4B
Camera type	Panchromatic
Format of the frame	5.54 cm x 75.69 cm
Best ground resolution	1.83 m (6 ft)
Flight height	150 km
Size of the observed area	14 km x 188 km
Focal length	60.69 cm

An example of a stereo-couple is given in Figure 2, where a different image geometry is already obvious.

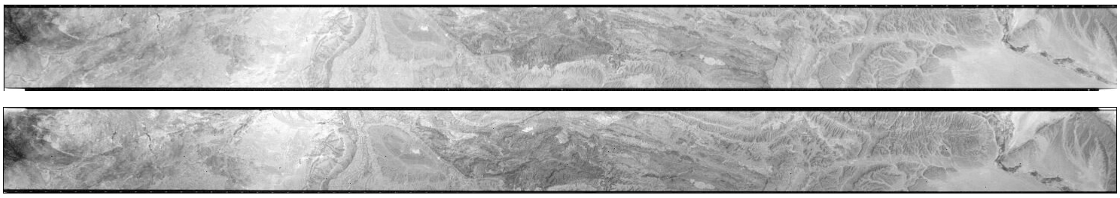

Figure 2: Stereo-couple of the CORONA DS-1117-1 mission of 26-th May 1972. (study region Zagora), the forward strip F-107 and the afterward strip A-113.

3. STUDY REGIONS

Two test areas were chosen to assess the potential application of this methodology. The first, in the vicinity of Zagora, was used to test the proposed method while the second, located near Toundoute, is used to validate the results. Both study areas are located in the south of the Kingdom of Morocco and are characterized by comparable topography and morphology with relatively high mountain ridges, river beds in between with trees (palm trees in the lower parts and mediterrainean vegetation in the higher parts) and extended erosion planes.

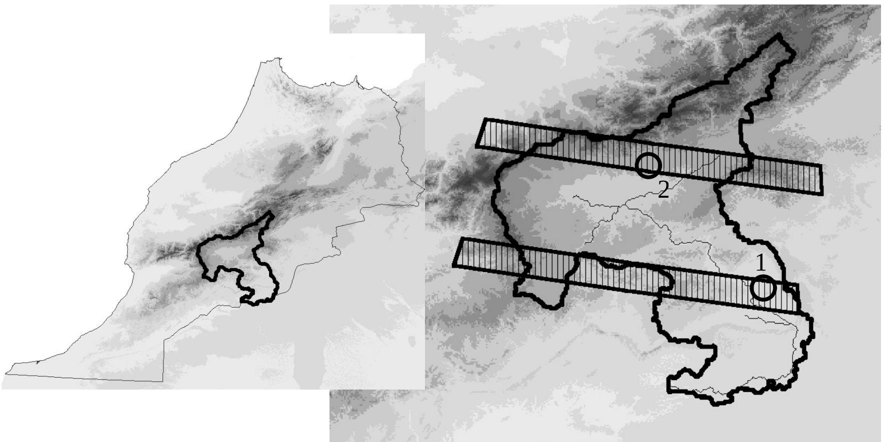

Figure 3: Location of the two study regions, Morocco (CORONA forward strips).

In the background of Figure 3 is the GTOPO30 elevation model where both test areas are indicated; the outlined areas are the River Drâa catchment, and the location of the Forward CORONA strips with the indication of both test zones.

4. FIELD WORK

During the field work, ground control and check points in x, y and z direction were recorded with a LEICA 300 DGPS. The points have a relative accuracy of 5 cm to each other with the absolute position of the base station measured to a precision of approximately 30 cm. This field campaign was conducted in the context of the IMPETUS project (Thamm et al., in press). One set of GCPs were used during the photogrammetrical restitution, the other set for the validation of the DEM. This was done for both test sites. It should be mentioned that for the Toundoute area a much more extended validation data set was available compared with the Zagora test area.

5. METHODS

5.1 Elaboration of the proposed methodology (Zagora test area)

The photographically stored information of the CORONA strips have to be transformed into digital information, in order to benefit from digital photogrammetric methods. This was done in two different ways, as indicated in Figure 4 (Schmidt et al.in press).

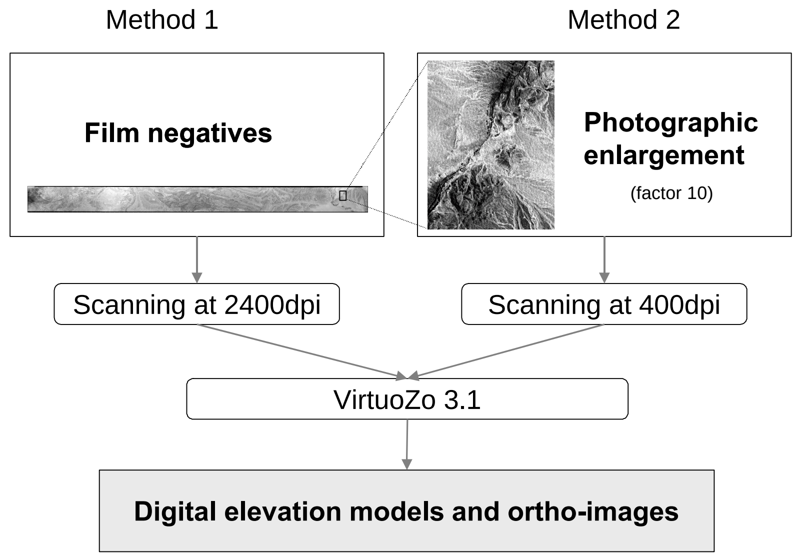

Figure 4 : General methodology.

Within the VirtuoZo 3.1 software it is possible to work on stereo image data using a non metric approach with no further input parameters other than ground control points. The Virtuozo software uses pattern recognition to identify several matching points in both images. From these a calculation of the relative orientation is determined with the orientation parameters kappa (κ), phi (ϕ) and omega (ω) also being defined. Table 2 shows the results of the calculations for both approaches.

Table 2: Parameters of the relative orientation of the image matching procedure. a) for the direct scan: Method 1, b) for the photo-enlarged approach: Method 2.

GCP	dX	dY	dZ	Orientation	Parameters	Paramater	Point accuracy
1	1.918	2.237	0.254	Kappa (1)	0.0245	RMS Error	0.017
2	-5.766	-8.557	-0.577	Kappa (2)	0.0027	mx	6.369
3	4.435	7.940	0.611	Omega (2)	-0.982	my	6.367
4	-7.826	2.658	-0.492	phi (1)	-0.3825	mz	1.521
5	-1.547	-0.331	2.094	phi (2)	-0.1804	mxy	9.000
6	4.073	0.245	-1.581				
7	-1.183	-3.540	-1.065				
8	4.900	1.069	0.464				

GCP	dX	dY	dZ	Orientation	Parameters	Paramater	Point accuracy
1	1.897	-2.315	-0.540	Kappa (1)	0.0068	RMS Error	0.019
2	-11.86	12.478	2.362	Kappa (2)	-0.0064	mx	9.832
3	8.753	-3.909	-0.883	Omega (2)	-0.0953	my	9.174
4	-10.54	2.681	4.889	phi (1)	-9.1219	mz	3.381
5	0.404	-1.659	0.495	phi (2)	-0.2618	mxy	13.449
6	3.337	5.996	-1.780				
7	-0.792	-6.571	-0.733				
8	6.545	8.442	-3.352				

For the calculation of the absolute orientation it was necessary to provide a minimum six GCPs to solve the orientation equation system (Chester, 1980). Eight GCPs were used for the exterior information. Afterwards the y-parallax was removed (Mikhail, et al., 2001) and lines of equal parallax difference and contour-lines were calculated, resulting in a DEM (Maune, 1996). During the processing it is also possible within this software to perform a visual quality check with 3D glasses.

5.2. Validation of the proposed methodology (Toundoute test area)

To validate the proposed methodology in the Toundoute area, the second technique (scanning of the images directly from the film) was used. In order to have an idea of the influence of the scanning resolution on the results of the photogrammetrical restitution, the images were scanned at 1600 dpi. Residuals comparable to those found in the Zagora test area were obtained. For the absolute orientation, seven GCPs were used which also provided acceptable residuals (Table 3).

Table 3: Parameters of the relative orientation of the image matching procedure for the direct scan

GCP	dX	dY	dZ	Orientation Parameters		Parameter	Point accuracy
1	14.371	-6.679	4.635	Kappa (1)	-0.0002	RMS Error	0.02
2	-16.627	5.407	-0.959	Kappa (2)	0.0021	mx	13.29
3	6.830	10.869	1.545	Omega (2)	0.0574	my	11.93
4	-5.063	-16.237	-1.299	phi (1)	-0.8008	mz	3.35
5	-0.047	6.522	-3.285	phi (2)	-0.0657	mxy	17.86
6	-4.628	0.333	-0.888				
7	6.461	0.491	1.112				

6. RESULTS

6.1. Elaboration of the methodology

Based on the DEM, the ortho-image was created and superimposed with contour lines. The residuals on the GCPs and the mean errors are presented in Table 2. It can be seen from this that Method 1 gave more reliable and accurate results than Method 2. A discussion of possible reasons for this are presented below;

1. The phi (ϕ) error is much greater using Method 2 than Method 1, which can be explained by the process of photo enlargement, whereby the projection table of the enlarger was not completely horizontal. This problem is not faced with Method 1.
2. The residuals in x, y and z of the GCP’s are lower with Method 1. These residuals in x, y are a factor of 1.3 better than with Method 2 and in the z direction improved by a factor of more than 2. This is due to the fact that the scanning resolution allows a finer indication of the ground control points.
3. In addition to the above, with Method 1 more ground control points were found automatically; namely sixty-nine (69) as opposed to fifty (50) with method 2. This can be also related to the finer scanning method used in Method 1.

Different products were generated after the restitution of the images: a DEM (Figure 6) which can be inspected using the Nuvision 3D glasses; a file containing the contour lines (labelled or not); the ortho-image and the ortho-image overlaid with the contour lines (Figure 7b). This was done for both methods. All these documents are produced in VirtuoZo 3.1 in a minimum of time. A status report is produced automatically during the process.

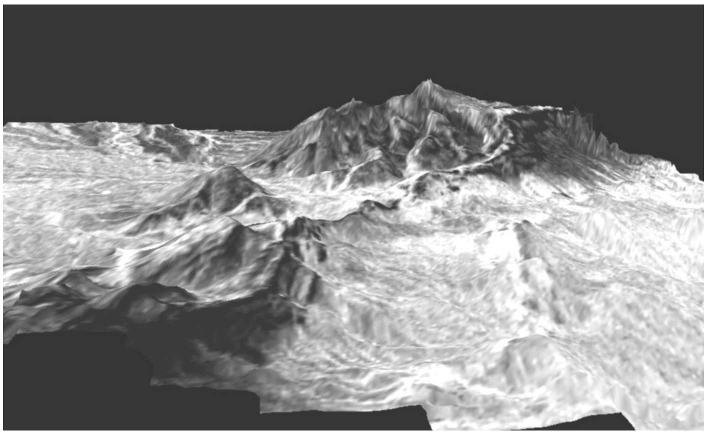

Figure 6: DEM derived from CORONA data .

A first visual comparison of the contour lines from the topographic map and those once generated by the digital photogrammetrical methods show a good resemblance (Figure 7).

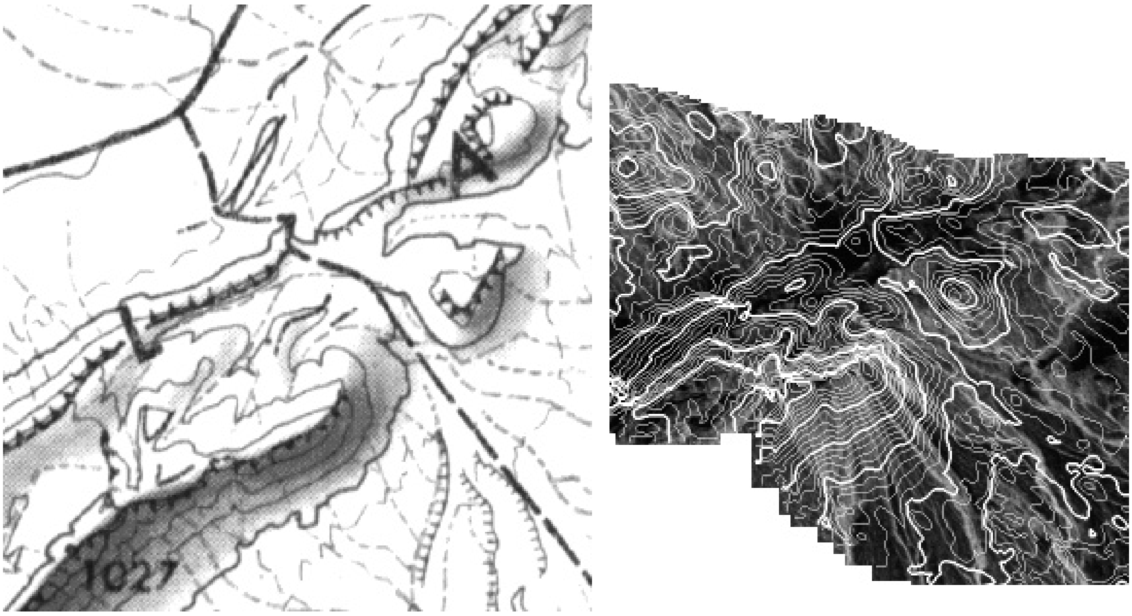

Figure 7:
a) Subset of 1:100.000 Topographic Map – Zagora.

b) Topographic ortho-photomap of the study region derived from CORONA data using the photo-enlargement approach.

The major contour lines indicated on the topographic map can be found on the created contour map, but the detail is much better resulting in a higher resolution DEM. The contour lines were set up at an equidistance of 10 meters, but can be generated more finely if wanted. The option of a 10 m contour interval was selected to correspond with the final scale chosen for the ortho-image (1:50000).

Besides this visual inspection of the contour lines, a more quantitative analysis of the errors on both created DEMs was also made using the validation GCPs measured randomly and distributed throughout the terrain. For the two DEMs all terrain GCPs were chosen that lie in the spacing of the mx, my residuals (Tables 2 and 3) of the DEM points. For Method 2 these values are 9.8 and 9.2 meters and for Method 1 they are both 6.4 meters. This was done in order to calculate an average height difference Δz of the z values from the DEM grid points and the terrain GCPs with results presented in Table 3.

Table 3: Height-deviations of terrain measured points and DEM grid-points.

Method	Residuals (mx,my) [m]		Mean height difference (Δz) [m]	Standard deviation [m]	Number of Points
1 (Scanned)	6.2	6.2	25.13	10.33	30
2 (Photo-enlarged)	9.8	9.2	9.54	13.74	49

With Method 2 Δz is less than 10 meters, but the standard deviation of 13.74 meters is relatively higher than the standard deviation of Method 1 with 10.33 meters. In Method 2 the Δz with 25.13 meters is disproportionally high, but this significant Δz error (20-25 meters) is a systematic underestimation of the real terrain from the generated DEM. No such systematic error is evident for Method 2. A shift of +20 meters to the DEM of method 1 resulted in a very good DEM result. Method 1 also gave better results than method 2 in the flat and sandy plain areas in front of and behind the mountain ridge.

6.2. Validation of the methodology

The DEM created was compared with an extended validation data set, measured in the field with a Leica 300 GPS. The resemblance of the generated DEM and the terrain data is even better here than in the Zagora region. A visual inspection of DEM and validation data set shows a remarkably good fit. A statistical analysis shows that between the two data sets an average difference of 3.5 meters exists (Table 4). The standard deviation of 19.6 on the other hand was quite large, but can be explained by the distorting effects at the edge of the DEM.

Table 4: Height-deviations of terrain measured points and DEM grid-points.

Method	Residuals (mx,my) [m]		Mean height difference (Δz) [m]	Standard deviation [m]	Number of Points
Validation	13.3	12.0	3.46	19.95	1249

It should be mentioned that the relief difference in the Toundoute study area are less than those in the Zagora area, leading to a lower error in z.

7. CONCLUSIONS

It has been shown that the proposed methods provide adequate topographical information when topographic maps and aerial pictures are not available for a test area. It is illustrated that Method 1 using the direct scanning of the films, gives more adequate results with a general underestimation of the real topography. With the proposed approach of method 2 it is still possible to generate a DEM with a relative vertical accuracy of approximately 20 meters, which is provides a reasonable resolution for several applications, e.g. LANDSAT TM/ETM-illumination corrections. This method allows an important reduction of field work because in such a way measurements of the whole terrain with GPS-points is not needed. The proposed method is a cheap way to substitute conventional aerial photos in situations where they may not be available.

8. ACKNOWLEDGEMENTS

The authors would like to thank Dr. Beata De Vliegher, Dennis Devriendt (Geography Department - University of Gent) for their help and advice and Christoph Kany (Geography Department - University of Bonn) for his assistance during the field work. Mary Drobin and Matthew McCabe are acknowledged for helping to edit this text. The work was funded by the BMBF (Project Number: 07GWK02) and MSWF (Project Number: 514 – 21200200).

9. REFERENCES

Campbell J.B, 1996. Introduction to Remote Sensing. The Guilford Press.

Chester,C.S., 1980. Manual of Photogrammetry. Falls Church: American society of photogrammetry.

Day. A., Logsdon J.M. & Latell, B. (1998). Eye in the sky: The history of the Corona spy satellites. Washington D.C.: Smithsonian Institution Press.

Goossens,R., De Man,J. & De Dapper,M., 2001. Research to possibilities of Corona-Satellite-data to replace conventional aerial photographs in geo-archaeological studies, practised on Sai, Sudan. In: Buchroitner,M. (Ed.), A decade of Trans-European Remote Sensing Cooperation, pp. 257-262. Lisse: A.A. Balkema Publishers.

Jensen,J.R., 2000. Remote Sensing of the Environment. London: Prentice-Hall.

Maune D.F., 1996. DEM Extraction, Editing, Matching and Quality Control Techniques. In: Digital Photogrammetry: An Addendum to the Manual of Photogrammetry. Bethesda, Maryland, USA. pp.135-141.

MacDonald,R., 1995. CORONA: success for space reconnaissance, a look into the cold war, and a revolution for intelligence. Photogrammetric Engineering and Remote Sensing, 61**:** pp. 689-720.

Mikhail E.M., Bethel J.S. & McGlone J.C., 2001. Introduction to Modern Photogrammetry. New York: John Wiley & Sons, Inc.

Peebles, C., 1997. The Corona project: America's first spy satellites. Anapolis, Maryland, USA: Naval Institute Press.

Ruffner,K.C., 1995. Americas first satellite Program. Washington: CIA History Staff.

Schmidt,M., Goossens,R., Menz,G: Processing techniques for CORONA satellite images in order to generate high-resolution digital elevation models (DEM). Proceedings of the 21th EARSeL symposium, May 2001, Paris, 8pp., in press.

Thamm, H.-P., Schmidt, M., Mevo Guezo, G., Menz, G.: An Integrative Management Project for Efficient and Sustainable Use of Fresh Water in Western Africa (IMPETUS). In: Proceedings of the 1st Workshop of the EARSeL Special Interest Group on Remote Sensing for Developing Countries, 13-15 September 2000, Gent, 6 pp., in press.

IKONOS GEOMETRIC ACCURACY

J. Grodecki and G. Dial
Space Imaging
12076 Grant Street, Thornton, CO 80241, U.S.A.
jgrodecki@spaceimaging.com
gdial@spaceimaging.com

ABSTRACT

IKONOS, the world's first commercial high-resolution imaging satellite, was successfully launched in September of 1999. From a 680 km sun synchronous orbit, the IKONOS satellite simultaneously collects 1-meter panchromatic and 4-meter multispectral images in 4 bands with 11-bit resolution. Interior and exterior orientation are derived from a sophisticated attitude and ephemeris determination systems, a stable optical assembly, and a solid state focal plane. These features make IKONOS ideally suited for high accuracy mapping applications. The paper describes the IKONOS imaging geometry, sensor model, and the geometric accuracy of IKONOS ortho and stereo products.

INTRODUCTION

Since its launch in September of 1999 IKONOS has been collecting high-resolution images over the entire globe. As shown in this paper the IKONOS images exhibit not only high spatial and radiometric resolution but are also highly accurate in the geometric sense.

SENSOR CHARCTERISTICS

Orbital Geometry

IKONOS circles the earth every 98 minutes at an altitude of 680 km in a sun-synchronous orbit with descending node crossing at about 10:30 am local solar time. The orbital inclination is 98 degrees.

Agility

Unlike Landsat, which only images at nadir, and Spot, which can only roll side-to-side for image acquisition, the IKONOS satellite is agile in that it can be rotated to any angle to acquire an image to the side, forward, or aft of the satellite position.

Exterior Orientation (Attitude and Ephemeris)

The satellite ephemeris is determined from the on-board GPS data, post-processed on the ground with a software incorporating sophisticated filtering / orbital modeling algorithms. The satellite attitude is measured by on-board star trackers and gyroscopes. Post-processing the attitude data in a Kalman smoother results in optimal combination of lower frequency star tracker information exhibiting high absolute accuracy with high frequency gyro data being very accurate over short time interval. The relationship between the satellite attitude coordinate system and the IKONOS camera coordinate system is described by the interlock angles. The initial interlock angles were determined by pre-launch assembly measurements and later refined by in-flight calibration.

Interior Orientation

The interior orientation of the IKONOS camera is described by the Field Angle Map (FAM). The Field Angle Map comprises both the optical distortion parameters and the focal plane array layout. The IKONOS solid state focal plane array consists of multiple panchromatic and multispectral line arrays. The Field Angle Map allows one to determine the line-of-sight vector in the camera coordinate system for each image pixel.

Combining satellite attitude, interlock angles, and the Field Angle Map allows calculation of the pointing direction of every image pixel.

Spectral Resolution

IKONOS collects imagery in four multispectral bands and a single panchromatic band. The IKONOS multispectral bands approximate LANDSAT bands 1 through 4. The relative spectral responsitivity for all five bands is given in Figure 1. Conversion of image DN values to absolute radiance, required for remote sensing analysis, can be accomplished with the radiometric calibration coefficients given in [Space Imaging, 2001].

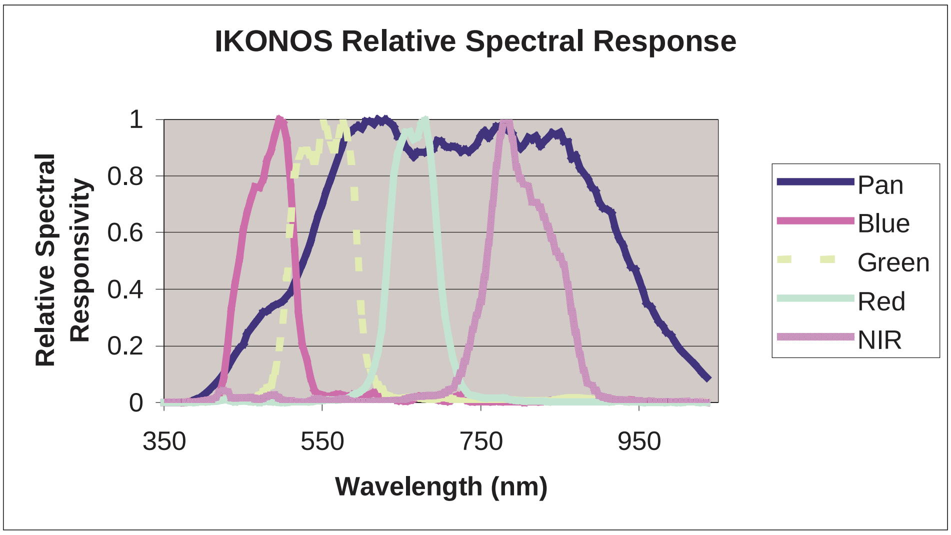

Figure 1. IKONOS Spectral Response Curves.

Radiometric Resolution

Both the panchromatic and all four multispectral bands have 11-bit dynamic range. With 11-bit resolution, details in shadows, highlights, and low contrast scenes can be more easily discerned than in 8-bit images.

Spatial Resolution

The ground sampling distance (GSD) of the IKONOS sensor is 0.82 m (at nadir) for panchromatic images, and 3.28 m (at nadir) for multispectral images. At 30 degrees off nadir the GSD is 1 m for panchromatic and 4 m for multispectral images. Nominal swath width at 1 m GSD is 13 km. All currently offered commercial IKONOS image products are resampled to 1 m GSD, either map projected or epipolar projected. As the width of the Point Spread Function of the IKONOS camera determined mostly by the diffraction limit of the telescope aperture is about 1 m, this does not result in a significant loss of spatial resolution of the final image products.

Temporal Resolution

At 40 degrees latitude the revisit time is 2.9 days at 1 m GSD and 1.5 days at 1.5 m GSD. The revisit times are shorter for higher latitudes and longer for latitudes closer to the equator.

IMAGE COLLECTION

Image Acquisition Geometry

Approximate image acquisition geometry is described by the sensor azimuth and elevation angles contained within the metadata (see Table 1).

Table 1. Sample Image Metadata

```
Acquired Nominal GSD
   Cross Scan: 0.84 meters
   Along Scan: 0.83 meters
Scan Direction: 0 degrees
Nominal Collection Azimuth: 93.7818 degrees
Nominal Collection Elevation: 81.18989 degrees
Sun Angle Azimuth: 151.5820 degrees
Sun Angle Elevation: 29.57948 degrees
```

As shown in Figure 2 below the projection of the line of sight from target to the satellite onto the horizontal plane at the target location defines the sensor azimuth. The sensor azimuth is measured clockwise from the North. The sensor elevation angle is the angle from the horizon up to the satellite.

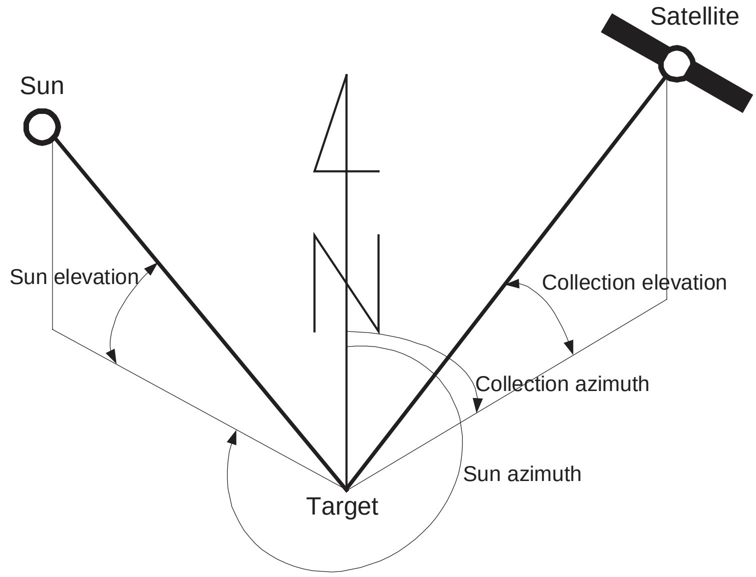

Figure 2. Image Acquisition Geometry

It should be noted that both the sensor azimuth and the sensor elevation angles are not constant for a given image strip and as such should not be used for orthorectification or other geometric corrections. Their accuracy is however sufficient for remote sensing analysis purposes such as topographic normalization.

Mono Collection Geometry

IKONOS mono image strip length typically varies from 10 km to some 200 km. The actual strip length is dictated by the AOI shape and dimensions, weather conditions, collection elevation angle constraints and image scheduling and tasking. Even though in principle IKONOS can collect images at any scan azimuth – as illustrated in Figure 3 – most images are collected in the N-S scan direction. This simplifies collection scheduling and the logistics of the subsequent block adjustment of multiple overlapping images.

Stereo

Unlike e.g. Spot, which takes cross-track stereo images from different orbital passes, IKONOS collects same pass stereo pairs. That is the two images constituting the stereo pair are taken on the same orbital pass. As the satellite approaches the target it yaws, rolls and pitches, as required, to collect the first leg of the stereo pair while pointing in a forward direction. A hundred or so seconds later, after the first image is collected the satellite is maneuvered to again image the same area, this time pointing in a backwards direction. Stereo imaging principle is illustrated in Figure 3 below. Same pass stereo pairs are advantageous for subsequent processing such as feature extraction because the scene content and lighting conditions are virtually the same for the two images.

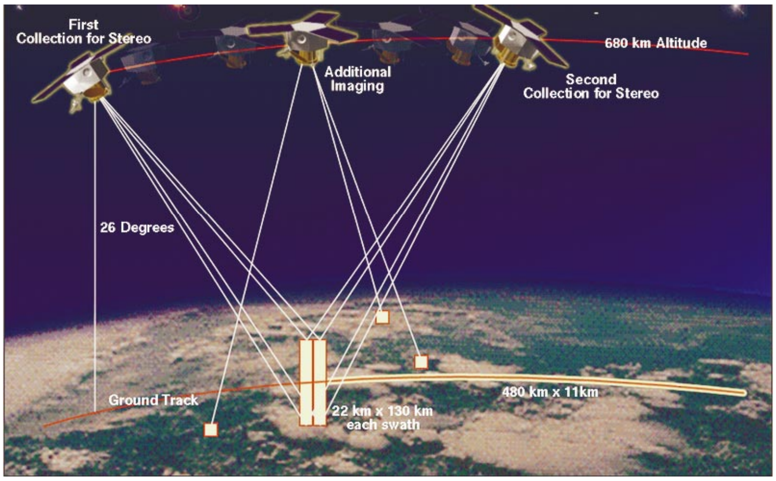

Figure 3. Stereo Image Collection

IMAGE PRODUCTS

Block Adjustment

In order to improve accuracy, multiple overlapping images are block adjusted together. Block adjustment of multiple overlapping images uses least-squares estimation process to estimate the camera model parameters for each image. The images are tied together by tie points whose image coordinates are measured on multiple images. Block adjustment of multiple images without GCP results in minimization of random errors and averaging out of biases affecting geometric accuracy of a single image strip. The ground control, if available, helps to remove the bias errors. Unlike the aerial blocks, the overlap requirement for IKONOS mono or stereo image strips is only about 10%. This is illustrated in Figure 4 below.

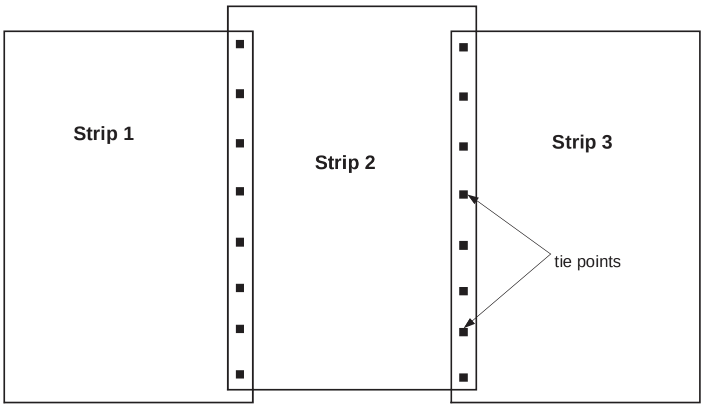

Figure 4. Block Adjustment.

Georectification

Level 2 and Level 3 mono products are georectified, i.e. projected along the line of sight to an inflated ellipsoid, map projected, and resampled to 1 m GSD. Level 2 mono (Geo) and Standard Stereo products are processed without ground control. Level 3 mono and Precision Stereo products are processed with ground control. Georectification is shown conceptually in Figure 5.

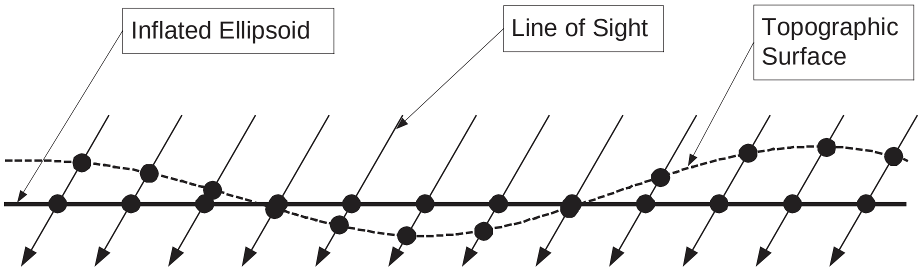

Figure 5. Georectification Process.

Since no terrain model is used in the georectification process, the resulting images are not corrected for terrain displacement. Thus, the horizontal accuracy of a georectified product is determined by both the satellite attitude and ephemeris (and GCP in the case of Level 3) and the terrain displacement. Since the terrain-induced displacement can reach hundreds of meters, the georectified products are not suitable for mapping applications. Accuracy of the Level 2 Geo products is specified as 50m CE90 exclusive of terrain displacement (see Table 2). As demonstrated in this paper the geometric accuracy of the IKONOS satellite without ground control is actually much better than 50m CE90.

Table 2. Georectified Products

Level	Description	Rectification	Accuracy	Mosaic (Level 7)	GCP
2 mono	Geo	Inflated ellipsoid	50m CE90+ terrain displacement	Not recommended (due to shear)	No
3 mono	Adjusted w/ GCPs and georectified	Inflated ellipsoid	2m CE90 + terrain displacement	Not recommended (due to shear)	Yes

Orthorectification

Orthorectification removes distortions in the imagery due to topography. The result is a map accurate product that can be used in GIS and other mapping applications. Depending on the collection geometry, availability of GCPs, and type and accuracy of a DEM used for orthorectification, Space Imaging offers four levels of accuracy for the orthorectified products (see Table 3).

Table 3. Orthorectified Products

Level	Description	Rectification	Accuracy	Mosaic (Level 7)	GCP
4a	Reference	Orthorectified	25m CE90	Yes	No
4a	Pro	Orthorectified	10m CE90	Yes	No
4b	Precision	Orthorectified	4m CE90	Yes	Yes
4b	Precision Plus	Orthorectified	2m CE90	Yes	Yes

Epipolar Resampling

To facilitate working with stereo imagery IKONOS stereo products can be resampled to epipolar geometry. For pushbroom sensors the epipolar geometry deviates from the well-known epipolar geometry of a frame camera. The epipolar lines for pushbroom images are no longer straight lines but complex curves instead. It turns out that, however, over a limited extent straight lines can accurately approximate IKONOS epipolar geometry. Thus, the IKONOS stereo images are divided into segments whose size is dictated by the requirement to minimize epipolar resampling errors.

Table 4. Stereo Products

Level	Description	Projection	Accuracy	Mosaic (Level 7)	GCP
2 stereo	Standard stereo	Epipolar or Map	25m CE90 22m LE90	No – cannot mosaic stereo.	No
3 stereo	Precision Stereo	Epipolar or Map	2m CE90 3m LE90	No – cannot mosaic stereo.	Yes

CAMERA MODEL

In general, a camera model relates object coordinates to image coordinates. Physical camera models are based on the interior and the exterior geometry and other physical properties of the sensor. For 1-meter GSD pushbroom sensors like IKONOS fully parametrized camera models are extremely complex making them enormously difficult to implement. For example the IKONOS System Geometric and Mathematical Model document consists of 183 pages while the accompanying interface control document for the thousands of data items used in the IKONOS camera model is 225 pages. To simplify interface with the end users of IKONOS imagery, Space Imaging uses the Rational Polynomial Camera (RPC) model, also called an Image Geometry Model (IGM),in lieu of the physical IKONOS sensor model to communicate the imaging geometry. RPCs are being distributed with all stereo images and the so called Geo Ortho Kit images. Geo Ortho-Kit images are acquired with a high elevation angle, georectified, and produced with RPC data. As shown in subsequent sections, while being mathematically simple and thus easy to implement, the IKONOS RPC model maintains full accuracy of the physical IKONOS camera model.

Physical Camera Model

For an image taken with a pushbroom camera each image line is taken at a different instance of time (see Figure 6). The exterior orientation parameters, i.e. the attitude angles (roll(t), pitch(t) and yaw(t)) and the position of the perspective center (PC(t)) change from scan line to scan line. The interior orientation parameters, which comprise the focal length, the principal point location, the lens distortion coefficients, and other parameters directly related to the physical design of the sensor, are in general the same for the entire image. A generic pushbroom camera model can be expressed by modified collinearity equations in which all exterior orientation parameters are defined as a function of time (see e.g. [Mikhail et al., 2001]).

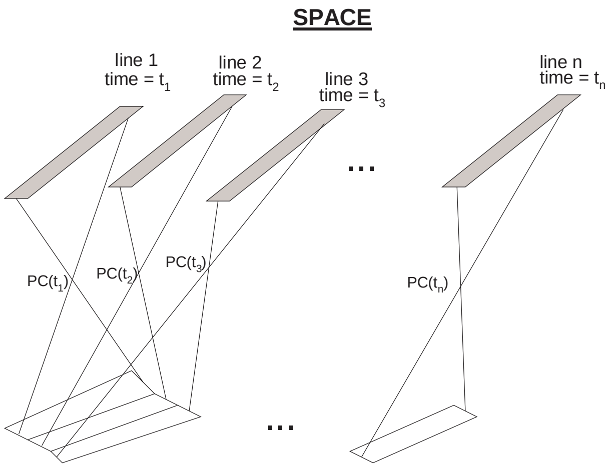

Figure 6. Pushbroom Camera

Rational Polynomial Camera Model

The IKONOS RPC model provides a functional relationship from the object space to the image space. The RPC functional model is of the form of a ratio of two cubic functions of the object space coordinates [Grodecki, 2001]. Separate rational functions are used to express the relationship of the object space to line, and the object space to sample coordinate. The line RPC model is given as

$$l = \frac{Num_L(U,V,W)}{Den_L(U,V,W)},$$

$$\begin{aligned} Num_L(U,V,W) = & \, a_1 + a_2 \cdot V + a_3 \cdot U + a_4 \cdot W + a_5 \cdot V \cdot U + a_6 \cdot V \cdot W + a_7 \cdot U \cdot W + a_8 \cdot V^2 + a_9 \cdot U^2 \\ & + a_{10} \cdot W^2 + a_{11} U \cdot V \cdot W + a_{12} \cdot V^3 + a_{13} \cdot V \cdot U^2 + a_{14} \cdot V \cdot W^2 + a_{15} \cdot V^2 \cdot U + a_{16} \cdot U^3 + a_{17} \cdot U \cdot W^2 \quad \text{and} \\ & + a_{18} \cdot V^2 \cdot W + a_{19} \cdot U^2 \cdot W + a_{20} \cdot W^3 \end{aligned}$$

$$Den_L(U,V,W)=b_1+b_2\cdot V+b_3\cdot U+b_4\cdot W+b_5\cdot V\cdot U+b_6\cdot V\cdot W+b_7\cdot U\cdot W+b_8\cdot V^2+b_9\cdot U^2$$
$$+b_{10}\cdot W^2+b_{11}U\cdot V\cdot W+b_{12}\cdot V^3+b_{13}\cdot V\cdot U^2+b_{14}\cdot V\cdot W^2+b_{15}\cdot V^2\cdot U+b_{16}\cdot U^3+b_{17}\cdot U\cdot W^2 \quad .$$
$$+b_{18}\cdot V^2\cdot W+b_{19}\cdot U^2\cdot W+b_{20}\cdot W^3$$

Likewise, the sample RPC models is expressed as

$$s=\frac{Num_S(U,V,W)}{Den_S(U,V,W)}$$

where again Num_S and Den_S are cubic functions of object space coordinates, *U*, *V*, and *W* are normalized object space coordinates (latitude, longitude, height), and *l* and *s* are normalized image space coordinates (line, sample).

RPC Accuracy Analysis

Accuracy of the RPC model was determined using the approach shown in Figure 7. For a number of imaging scenarios the RPC model was estimated from a 3-dimensional grid of points in the object space generated using the physical IKONOS camera model. In addition, a grid of independent check points was generated which was later used to compute accuracy of the RPC model.

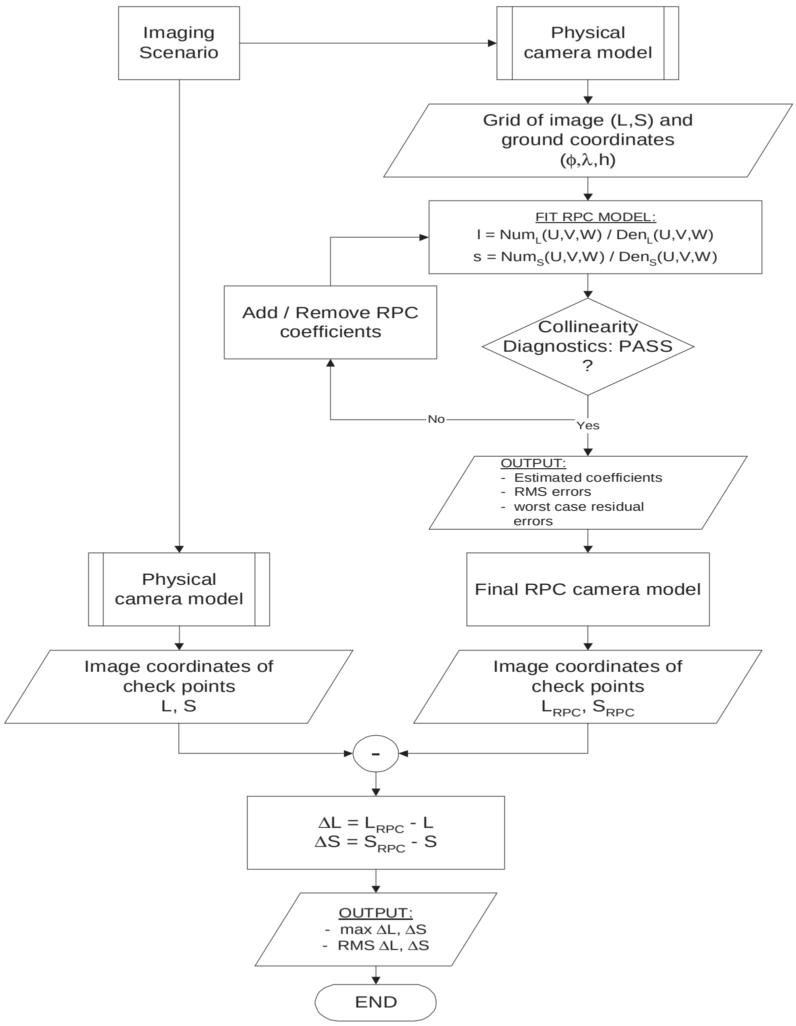

Fig. 7. RPC Accuracy Analysis

RPC Estimation

A least-squares approach was utilized to determine the RPC model coefficients from a 3-dimensional grid of points generated using the physical IKONOS camera model. The 3-D grid of object points was generated by intersecting rays emanating from a 2-D grid of image points – computed using the physical IKONOS camera model – with a number of constant elevation planes (see Figure 8).

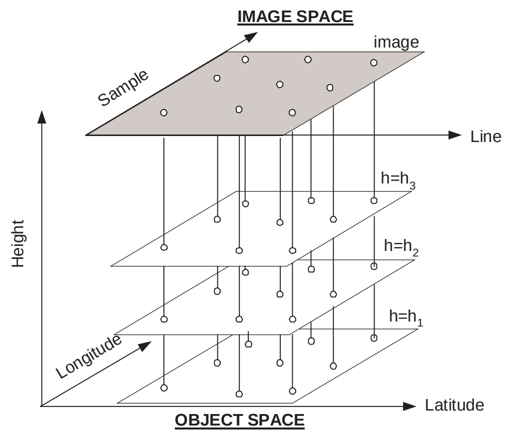

Figure 8. RPC Estimation

RPC Accuracy Results

RPC accuracy (see Table 5) was computed for the following imaging scenarios

- strip length of 100 km,
- roll and pitch angle of the camera ranged from 0^o to 30^o,
- scan azimuth ranged from 0^o through 360^o,
- latitude ranged from $0^o$to 60^o.

Table 5. RPC Accuracy

RPC model	Post-fit RMS error [pixels]	RMS error using independent check points [pixels]	Max error using independent check points [pixels]
line	0.01	0.01	0.04
sample	0.01	0.01	0.03

ON-ORBIT ACCURACY VERIFICATION

RPC Accuracy Verification

The accuracy of the RPC sensor model was verified empirically by comparing a number of IKONOS products generated at Space Imaging with both the physical IKONOS camera model and the RPC camera model, over the past year. As expected, no discernable differences between the products generated with both methods were found.

Geometric Accuracy Verification

The IKONOS geometric accuracy was verified by an On-Orbit Verification program. The geometric accuracy was determined empirically by comparing IKONOS images against the known ground control over the Space Imaging metric test ranges. For stereo images the GCP locations were measured in 3D on a softcopy photogrammetric workstation. This allowed to estimate both the horizontal and the vertical errors. For monoscopic images the horizontal errors were computed by back tracing the known GCPs to the image coordinate space, using the IKONOS camera model, and measuring the offsets between the predicted and the actual locations of the photo-identifiable GCPs on the image. Early accuracy results for georectified and orthorectified products are given in [Dial, 2000]. In this study two Level 2 and two Level 3 stereo pairs, taken over the San Diego metric test range, were compared against a set of well distributed check points. The San Diego test range used in this study consists of 140 GCP over a 22 by 22km area.

As seen in Figure 9 and 10, for uncontrolled stereo images, the horizontal accuracy was found to be 6 m and 4 m for both stereo pairs, while the vertical accuracy was determined to be at 1 m and 6 m level, respectively. It should be noted that in both cases the errors were distributed in a very narrow range, indicating high relative accuracy.

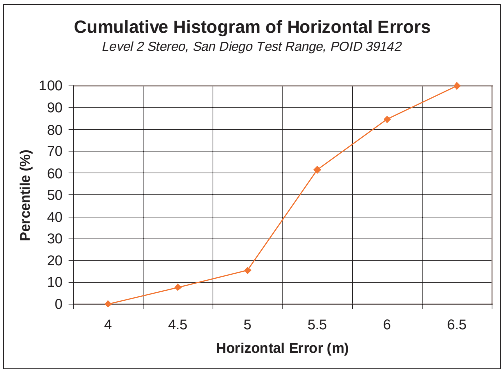

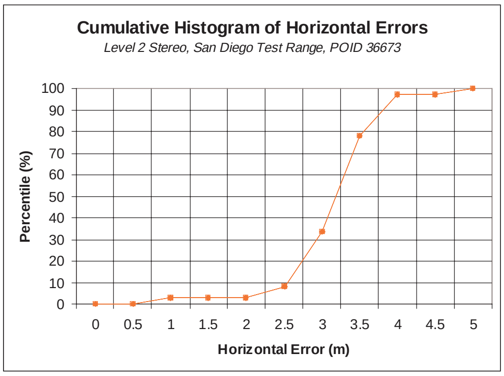

Figure 9. Level 2 Stereo Horizontal Errors

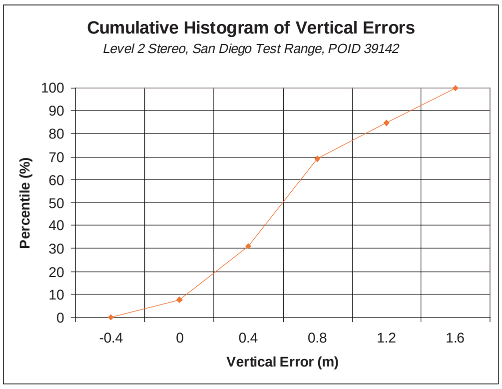

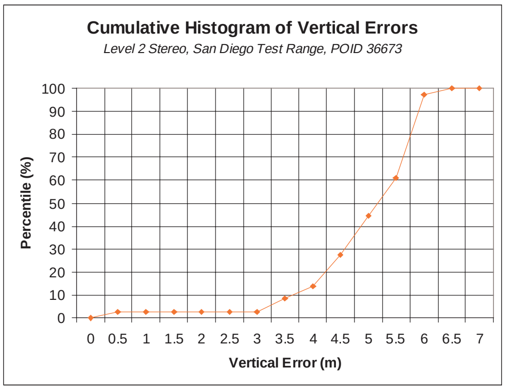

Figure 10. Level 2 Stereo Vertical Errors

The accuracy of GCP controlled stereo images is given in Figure 11 and Figure 12. In both cases the horizontal accuracy was of the order of 1 m while the vertical accuracy was of the order of 2 m.

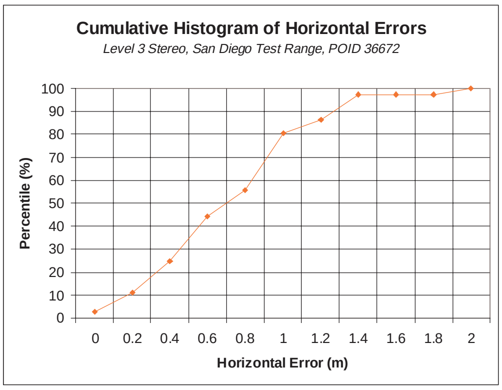

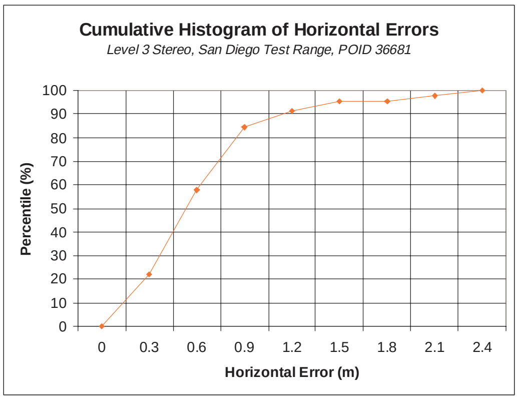

Figure 11. Level 3 Stereo Horizontal Errors

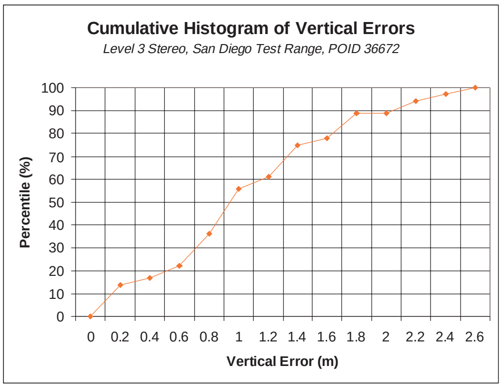

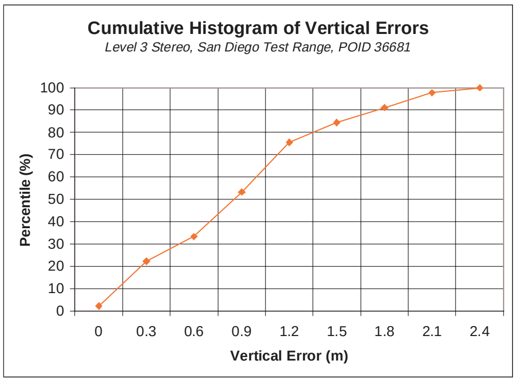

Figure 12. Level 3 Stereo Vertical Errors

CONCLUSIONS

IKONOS is an agile, high resolution, imaging satellite in sun-synchronous orbit. Exterior and interior orientation are determined a-priori by on-board sensors and on-orbit calibration. The 4-band multispectral sensor approximates Landsat bands 1-4 with 4m resolution. The panchromatic sensor provides 1m resolution. While image geometry can be approximated by the sensor azimuth and elevation angles, the physical camera model is precisely described by RPC coefficients. An extensive analysis of RPC accuracy shows worst-case differences below 0.05 pixels when compared to the camera model. The IKONOS RPC camera model provides a simple yet accurate way to communicate IKONOS image geometry to end users. The geometric characteristics and accuracy of Georectified, Orthorectified, and Stereo products have been described. Standard and Precision Stereo accuracy was tested with test range imagery. The high geometric and radiometric accuracy of IKONOS images make them ideally suited for automated classification and mapping applications.

REFERENCES

Dial, G. (2000). IKONOS satellite mapping accuracy. *ASPRS 2000 Proceedings*, Washington DC, 22-26 May 2000.

Grodecki, J. (2001). IKONOS stereo feature extraction - RPC approach. *ASPRS 2001 Proceedings*, St. Louis, MO, 23-27 April 2001.

Mikhail, E.M., Bethel, J.S., McGlone, J.C. (2001). *Introduction to Modern Photogrammetry*. J. Wiley, New York.

Space Imaging (2001). “ IKONOS Relative Spectral Response “, Space Imaging Document http://www.spaceimaging.com/aboutus/satellites/IKONOS/spectral.htm

BUNDLE ADJUSTMENT WITH SELF-CALIBRATION OF LINE CAMERAS USING STRAIGHT LINES

Ayman Habib, Young-ran Lee and Michel Morgan
Department of Civil and Environmental Engineering and Geodetic Science
470 Hitchcock Hall, 2070 Neil Avenue, Columbus, OH 43210, USA
habib.1@osu.edu, lee.1660@osu.edu, morgan.465@osu.edu

KEY WORDS: Linear Features, Linear Array Scanners, Aerial Triangulation, Self-Calibration

ABSTRACT

Increased use of digital imagery has facilitated the opportunity to use features, in addition to points, in photogrammetric applications. Straight lines are often present in object space, and prior research has focused on incorporating straight-line constraints into the bundle adjustment for frame imagery. In this research, we introduce a straight-line constraint in the bundle adjustment for linear array scanners for self-calibration purposes. Prior to incorporating straight lines in the triangulation, one should answer two questions. First, what is the most convenient representation of straight lines in image and object space? Second, how can we establish the perspective transformation between the object and image space for straight lines? In this research, image space lines are represented by a sequence of points along the lines. On the other hand, two points represent object space straight lines. The perspective transformation of straight lines between image and object space is incorporated as a mathematical constraint. The underlying principle in this constraint is that the vector from the perspective center to a scene point on a straight-line feature lies on the plane defined by the perspective center and the two object points defining the straight line. This constraint is particularly important for line cameras. A scene captured by a line scanner is composed of a sequence of images, each of which may be slightly shifted against each other due to slight changes in the system's trajectory. As a result, straight lines in object space do not appear as straight lines in image space. The proposed constraint makes use of straight-line features in object space, and aids in the recovery of the exterior and interior orientation parameters as well as adding to the geometric strength of the bundle adjustment. This constraint has been embedded in a bundle adjustment software application capable of performing aerial triangulation with self-calibration of frame and linear array scanner imagery using point as well as straight line features. Experiments have been conducted to show the effect of using straight-line constraints on the recovery of the Exterior Orientation Parameters (EOP). In addition, we investigated the optimum configuration for the recovery of the Interior Orientation Parameters (IOP). Correlation between the IOP for line cameras has been detected during the course of this research.

1. INTRODUCTION

Most photogrammetric applications are based on the use of distinct points. These points are often obtained through measurements in an analog or digital environment. Recently, more attention has been drawn to linear features. There are several reasons for the utilization of linear features in photogrammetry:

- Points are not as useful as linear features when it comes to higher-level tasks such as object recognition.
- Automation of the map making process is one of the major tasks in digital photogrammetry and cartography. It is easier to automatically extract linear features from the imagery rather than distinct points (Kubik, 1988).
- Images of man made scenes are rich with linear features.
- For line scanner imagery, linear features can be helpful for better recovery of the Exterior and Interior Orientation Parameters (EOP - IOP).

Previous research on linear features in photogrammetry has focused primarily on frame imagery. Straight-line constraints can be incorporated into the bundle adjustment by utilizing the fact that the perspective transformation of a straight line is also a straight line. Mikhail and Weerawong (1994) proposed a straight-line constraint that confines a unit vector defining the object space line, the vector from the perspective center to a point on the object line, and the vector from the perspective center to an image point to one plane. In their approach, the object line is represented as an infinite line. Habib (1999) discussed the various options for straight-line representation in photogrammetric applications. The primary representation considerations are uniqueness and singularities. In this research, we represent a straight line in object space as two points along that line is most convenient for further photogrammetric processing. In this way, the line segment is well localized in the object space. In addition, the coordinates of the points defining the object space lines can be easily introduced to or obtained from a GIS database.
Habib (1999) proposed a straight-line constraint, which forces the image line (represented by the polar parameters ρ and θ) to be coplanar with the plane defined by the perspective center and two object points defining the line. For a more comprehensive review on linear features in photogrammetry the interested reader is referred to Habib et al., 1999.

The techniques discussed so far are concerned with straight lines in frame imagery. In this research, we will extend the use of straight-line constraints to scenes captured by line cameras (e.g., push broom, three-line, and panoramic linear array scanners). The effect of incorporating such a constraint on improving the quality of the recovered EOP and IOP (self-calibration) will be investigated. In section 2, brief background about line cameras and the perspective transformation of distinct points between the scene and object space are presented. The straight-line constraint in scenes captured by line scanner is covered in section 3. Then, the optimum configuration for bundle adjustment with self-calibration using straight lines is investigated in the fourth section. Finally, experimental results, conclusions and recommendations for future work are outlined in sections 5 and 6, respectively.

2. BACKGROUND: Linear array scanner imagery

The increased use of digital photogrammetry, motivates using digital cameras in the image acquisition process to facilitate the automation of various photogrammetric tasks. To attain the same resolution as analogue aerial frame photography, 20K $\times$ 20K 2-D digital array sensors or larger would be necessary. However, at this time, the highest resolution commercially available (at a reasonable cost) is 4K X 4K. Line cameras provide an alternative solution that can produce scenes with acceptable resolution. Linear array scanners simulate 2-D images by using one or more 1-D array of sensors operating with an open shutter on a moving platform.

The electromagnetic energy incident upon these sensors at a given time constitutes an image. Movement of the platform and/or rotation of the lens configuration enable the imaging system to have successive coverage of different areas on the ground. In other words, a scene is defined by a sequence of linear array scanner images. Depending on the number of 1D arrays in the focal plane, the scanning direction and the relation of the sensor with respect to the flight direction, one differentiates between push broom, three-line and panoramic linear array scanners (See Figures 1 and 2).

Previous research at The Ohio State University has focused on modeling the perspective geometry of distinct points in linear array scanners (Habib and Beshah, 1998). The collinearity model used for frame imagery has been modified in such a way that it is also valid for push broom, three-line and panoramic linear array scanners. This model accommodates the most general scenario for line cameras - panoramic linear array scanners. Collinearity models for the other scanner types as well as frame imagery are easily derived from this model, and implemented by fixing some of the parameters of the panoramic model. The perspective transformation model for point features in panoramic linear array scanners is given in Equation 1.

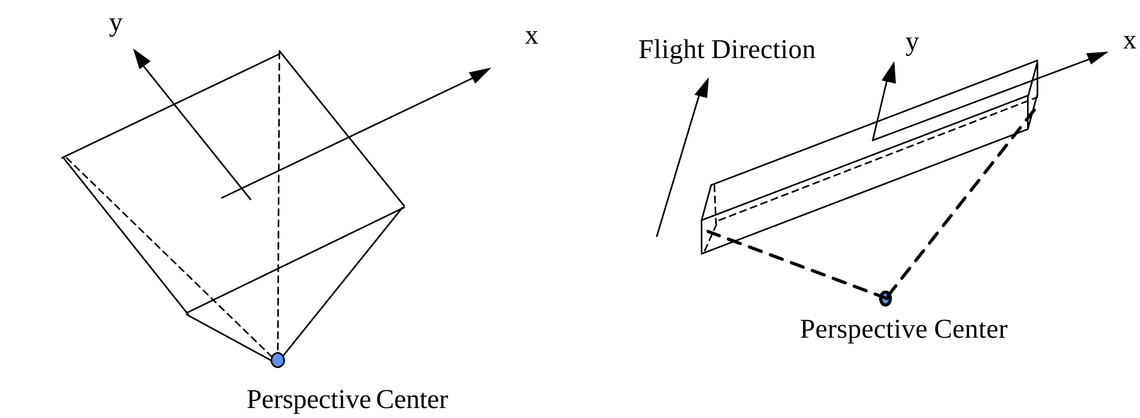

a. Frame Camera b. Push Broom Scanner

Figure 1: Perspective geometry of frame camera (a) and push broom scanners (b).

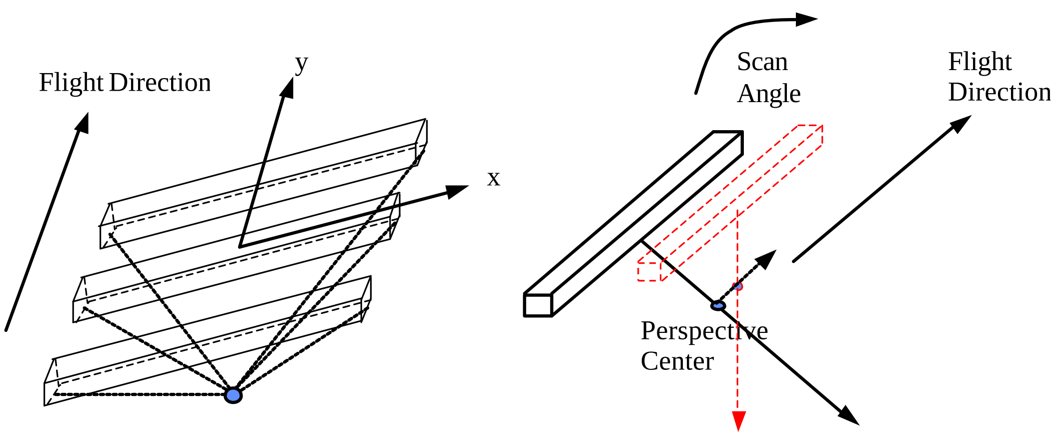

a. Three-line Scanner b. Panoramic Linear Array Scanner

Figure 2: Perspective geometry of three-line scanner (a) and panoramic linear array scanner (b).

$$x_a^t = x_P + imc(t) - c\frac{N_x}{D} + \Delta_x \qquad (1)$$

$$y_a^t = y_P - c\frac{N_y}{D} + \Delta_y$$

where

$$N_x = r_{11}^t(X_A - X_0^t) + r_{21}^t(Y_A - Y_0^t) + r_{31}^t(Z_A - Z_0^t)$$

$$N_y = r_{12}^t(X_A - X_0^t) + r_{22}^t(Y_A - Y_0^t) + r_{32}^t(Z_A - Z_0^t)$$

$$D = r_{13}^t(X_A - X_0^t) + r_{23}^t(Y_A - Y_0^t) + r_{33}^t(Z_A - Z_0^t)$$

x_a^t , y_a^t: Image coordinate measurement of point (a) in the scan line captured at time t

$X_A,\ Y_A, Z_A$: Object coordinates of point (A)

$x_P,\ y_P, c$: Calibrated principal point position and principal distance of the camera

$r_{11}^t, r_{12}^t ... r_{33}^t$: Time dependent elements of the combined rotation matrices $R^T(a_t)R^T(w_t, f_t, k_t)$

α_t : Scan angle for panoramic sensor at time t

$imc(t)$: Image motion compensation at time t

$X_0^t,\ Y_0^t, Z_0^t$: Time dependent object coordinates of the perspective center

$\Delta_x,\ \Delta_y$: Compensate for various distortions in the imaging sensor

Detailed explanation of how to apply this model in push broom and three-line scanners as well as frame imagery is given in Habib and Beshah, 1998.

3. STRAIGHT LINES IN LINEAR ARRAY SCANNER IMAGERY

In this section, we will discuss how to incorporate straight lines in scenes captured by line scanners. Before proceeding with the mathematical model, one first elaborate on the question: What is the most convenient representation for straight lines in the image and object space? The perspective projection of an object space straight line using line scanners might not be a straight line due to the motion of the platform during data acquisition as well as interior orientation deformations. Therefore, image space line features will be represented by a sequence of 2-D points. This representation will allow us to consider the IOP of the imaging sensor as well as the EOP of the platform at different scan lines. As mentioned before, two points will be used to represent object space linear features. Those points are identified monoscopically in one or two scenes containing that line (see Figure 3; the end points are measured in one scene - scene 1). Those points need not be identifiable or even visible in other scenes. The mathematical relationship between the image and ground coordinates of those points is given by the modified collinearity equations (Equation 1).

Now, we need to introduce a mathematical constraint that incorporates intermediate points measured along the line in different scenes. The underlying principal in this constraint is that the vector from the perspective center to a scene point on a straight-line feature lies on the plane defined by the perspective center and the two object points defining the straight line.

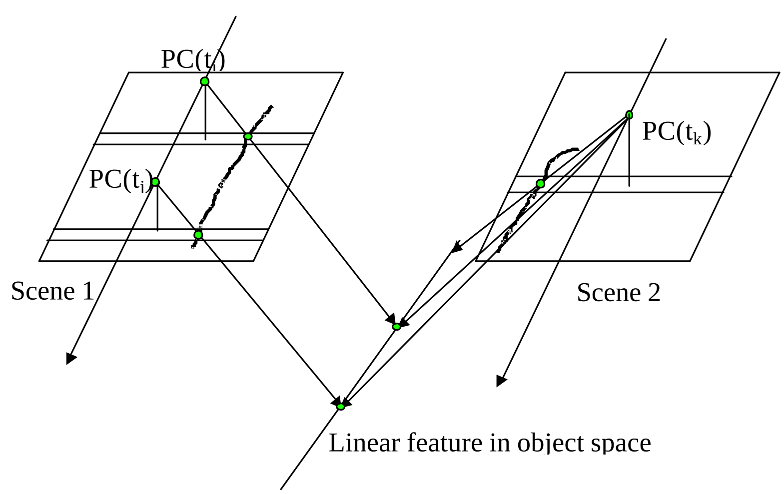

Figure 3: Perspective geometry and straight lines in linear array scanner imagery.

For each image (scan line) containing the linear feature under consideration, the vector from the corresponding perspective center to an image point along the line can be defined with respect to the ground coordinate system as:

$$\vec{V}_1 = R(w^t, f^t, k^t, a^t)\begin{bmatrix} x - x_p - imc(t) - \Delta_x \\ y - y_p - \Delta_y \\ -c \end{bmatrix} \qquad (2)$$

The Δ_x and Δ_y in Equation 2 compensate for various interior distortion parameters (e.g., radial and decentric lens distortions as well as affine deformations). The multiplication with the rotation matrix (R) transforms the vector into the ground coordinate system.
The vector from the same perspective center to the first object point along the line is defined as:

$$\vec{V}_2 = \begin{bmatrix} X_1 - X_O^t \\ Y_1 - Y_O^t \\ Z_1 - Z_O^t \end{bmatrix} \qquad (3)$$

Similarly, the vector from the same perspective center to the second object point along the line is defined as:

$$\vec{V}_3 = \begin{bmatrix} X_2 - X_O^t \\ Y_2 - Y_O^t \\ Z_2 - Z_O^t \end{bmatrix} \qquad (4)$$

Both vectors in Equations 3 and 4 are defined with respect to the ground coordinate system.
As illustrated in Figures 3 and 4, the vectors from the perspective center to each intermediate scene point along the line (Equation 2) should lie on the plane that is defined by the perspective center and the two object points defining the object straight line. This condition can be formulated as:

$$(\vec{V}_2 \times \vec{V}_3) \bullet \vec{V}_1 = 0 \qquad (5)$$

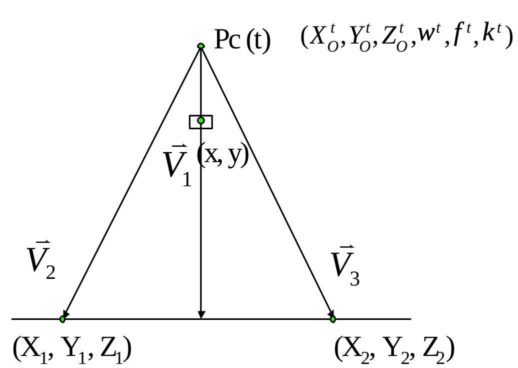

Figure 4: Plane defined by two object points and the perspective center.

This constraint for straight lines in aerial triangulation is a function of the following parameters.

$$f\,(X_1, Y_1, Z_1, X_2, Y_2, Z_2, X_O^t, Y_O^t, Z_O^t, w^t, f^t, k^t, a^t, x, y, IOP) = 0 \quad (6)$$

The unknown parameters are the IOP of the involved scanner, the EOPs of the images (different scan lines) and the ground coordinates of the two points defining the object line. In each scene where the line is visible, the constraint (Equation 5) can be applied to all intermediate points measured along the line, regardless of whether or not the defining points are visible. Those intermediate points are monoscopically measured (i.e., they need not be identifiable or even visible in other scenes). Because the EOPs change from one point to the next, the number of independent constraints will equal the number of measured intermediate points along the line. The ground coordinates of those points along the straight line are not determined during the bundle adjustment. In other words, the constraints do not introduce any new parameters. These intermediate points only contribute to increase the geometric strength of the adjustment. It should be noted that this constraint does not depend on the chosen model dealing with the EOPs for the various scan lines (e.g., modeling the system trajectory with a polynomial, using orientation images, direct observations of the EOPs from GPS/INS or any other model). The constraint can also be applied to frame imagery. In this case, only two independent constraints can be generated per image, due to the fact that there is only one set of EOPs associated with a single image. However, additional constraints will contribute towards a better recovery of the Interior Orientation Parameters (IOP).

4. LINE SCANNER SELF-CALIBRATION

Bundle adjustment with self-calibration aims at simultaneously determining the EOP and IOP of the involved imaging sensor. In this section, we would like to investigate the feasibility of using straight-line constraints to aid in the recovery of the Interior Orientation Parameters (IOP) of line scanner imagery. The effect of various interior orientation parameters on the captured scenes for different straight-line configurations has been simulated using the Multi-Sensor Aerial Triangulation (MSAT) software developed at the Ohio State University. The effects of different IOPs for both x-type (configuration 1) and box-type (configuration 2) in the down and forward looking scanners of a three line scanner can be seen in Figures 5 and 6, respectively. In those figures, the effect of changes in the principal point coordinates (x_p, y_p), the principal distance (c), radial distortion (K_1), decentric distortion (P_1, P_2) and affine deformations (A_1 and A_2) is investigated. The most important criterion influencing the contribution of straight-line constraints is the deviation from straightness in the captured scenes. Those deviations can be attributed to the platform trajectory during the scene capture as well as the distortion parameters. Here, we want to figure out which configuration will cause more deviations from straightness in the captured scenes for various IOP. Observing Figures 5 and 6, one can draw the following conclusions:

1. X-type configuration is more appropriate than the box-type configuration for self-calibration. One can see that the x-type configuration causes more deviations from straightness than the box-type configuration.
2. There is some correlation between the radial coefficient K_1 and the camera principal distance c.
3. For the down looking sensor, there is a perfect correlation between the affine coefficient A_1 and the principal distance c. Also, the affine coefficient A_2 can not be recovered for down ward looking scanner scenes.
4. For the forward-looking sensor, there is a high correlation between A_1, K_1, P_2, C and y_p. In addition there is a high correlation between A_2 and x_p.

5. EXPERIMENTAL RESULTS

In this section, we will demonstrate the feasibility of using the proposed constraint towards the estimation of the IOP and EOP of line scanners by experimental results with synthetic data. The experiments have been conducted using the Multi-Sensor Aerial Triangulation (MSAT) software developed at The Ohio State University. MSAT can perform bundle adjustment with self-calibration for frame and line scanner imagery using point as well as straight-line features.

5.1 Recovery of the EOP

To study the contribution of the straight-line constraints towards the recovery of the EOPs in frame and line scanner imagery, several experiments are conducted with and without linear features. The IOP are available for all these scenarios. Those experiments are identical in the following aspects:

- Sensor specifications.
- Number of images.
- Flight trajectory specifications.
- Number of tie and control points.
- Noise level in the image and object space.

After the bundle adjustment, the quality of the reconstructed object space is checked through Root Mean Square (RMS) error analysis. The imaging specifications with and without linear features as well as the RMS error of the reconstructed object space for frame and line scanner imagery can be seen in Tables 1. Through a closer look at the RMS error values, one can observe that the straight-line constraint is more influential when used in line scanner compared with frame imagery. For the three-line scanner imagery without linear feature constraints, the bundle adjustment did not converge at all. This result was expected since the straight-line constraint allowed for a better estimate for the EOPs (changes in the EOP would cause deviations from straightness in the captured scenes). On the other hand, the straight-line constraint had only minor improvement when applied in frame imagery.

	Frame camera		Line scanner	
	Without Linear Features	With Linear Features	Without Linear Features	With Linear Features
Number of Images	5	5	6	6
Number of Tie points	22	6	22	8
Number of Control Points	3 (± 10cm)	3 (± 10cm)	4 (± 10cm)	4 (± 10cm)
Number of Lines	0	8 (16 points)	0	7 (14 points)
Total Number of Points	25	25	26	26
GPS at the Perspective Center	-	-	(± 1.5m)	(± 1.5m)
RMS-X (m)	±0.117	±0.066	Singular	±0.103
RMS-Y (m)	±0.125	±0.108	Singular	±0.129
RMS-Z (m)	±0.149	±0.089	Singular	±0.434

Table1: Imaging configuration with the RMS error of the reconstructed object space.

5.2 Recovery of the IOP

In this section, we are trying to investigate the feasibility of using the straight-line constraint to perform bundle adjustment with self-calibration of scenes captured by line scanners. Four forward-looking scenes captured by a three-line scanner with eight control points (±10cm) and six tie lines (468 intermediate constraints) have been simulated. The object and image space layouts can be seen in Figures 7 and 8, respectively. Prior knowledge about the EOP are introduced (±10cm & ±10"). In this adjustment, the ground coordinates of the points defining the tie lines as well as the IOP are estimated. The true IOP as well as the obtained results for different experiments can be seen in Table 2. In the first experiment, we tried to solve for all the IOPs. As mentioned before in section 4, there is a high correlation between the y_p, c, K_1 and P_2 elements of the IOP. This correlation is manifested in the wrong estimates for those parameters. In the second experiment, we fixed the y_p and c elements of the IOP. One can see that by fixing those parameters, we obtained better estimates for the remaining parameters.

	True Parameters	Experiment # 1	Experiment # 2
x_p (mm)	0.0	-1.00×10^{-3}	-1.97×10^{-3}
y_p (mm)	0.0	-0.112	-2.66×10^{-3} (FIXED)
c (mm)	300.0	301.473	300.002 (FIXED)
K_1	5.00×10^{-7}	0.0	4.97×10^{-7}
K_2	0.00	0.0	0.0
P_1	5.00×10^{-6}	5.12×10^{-6}	5.10×10^{-6}
P_2	3.00×10^{-5}	3.47×10^{-5}	3.01×10^{-5}

Table 2: Estimated IOP for Line scanner imagery.

6. CONCLUSIONS AND RECOMMENDATIONS FOR FUTURE WORK

A new approach was developed to handle object space straight lines in linear array scanner imagery. Because of the nature of line cameras, straight lines in object space might not appear as straight lines in the scene due to the motion of the platform during scene capture. In addition, IOP might cause some deviations from straightness in the scenes. In the proposed constraint, object space lines are defined by two points, which are monoscopically measured in one or two scenes. Those points need not be identifiable or even visible in overlapping scenes. This representation is advantageous since the object lines are localized and can be introduced to or obtained from a GIS database.

One independent constraint equation is added to the adjustment for each intermediate image point along the image line. The underlying principle in this constraint is that the vector from the perspective center to the intermediate point along the straight-line feature lies on the plane defined by the perspective center and the two object points defining the straight line. Once again, the intermediate points are monoscopically measured. The added constraint aids in the recovery of the many exterior orientation parameters associated with linear array scanner imagery. In addition, it can be used to estimate the IOP of the involved scanner. It is therefore advantageous to evaluate as many intermediate image points along the straight line as possible. This constraint is also valid in the case of frame imagery. In such a case, introduced constraints would contribute towards the determination of the IOP of the imaging system. The incorporation of this constraint into available bundle adjustment software is straightforward. Testing with simulated data proved the superiority of this technique over aerial triangulation with disconnected points when it comes to estimating the IOP and EOP of line scanners.

Future work will concentrate on the following tasks**:**

- More testing with real data. We would like to use an available GIS database and/or data collected by terrestrial mobile mapping systems, e.g. road networks, to provide control for aerial triangulation.
- Automatic extraction and matching of linear features from imagery.
- Expand this constraint to allow for the incorporation of free form linear features.

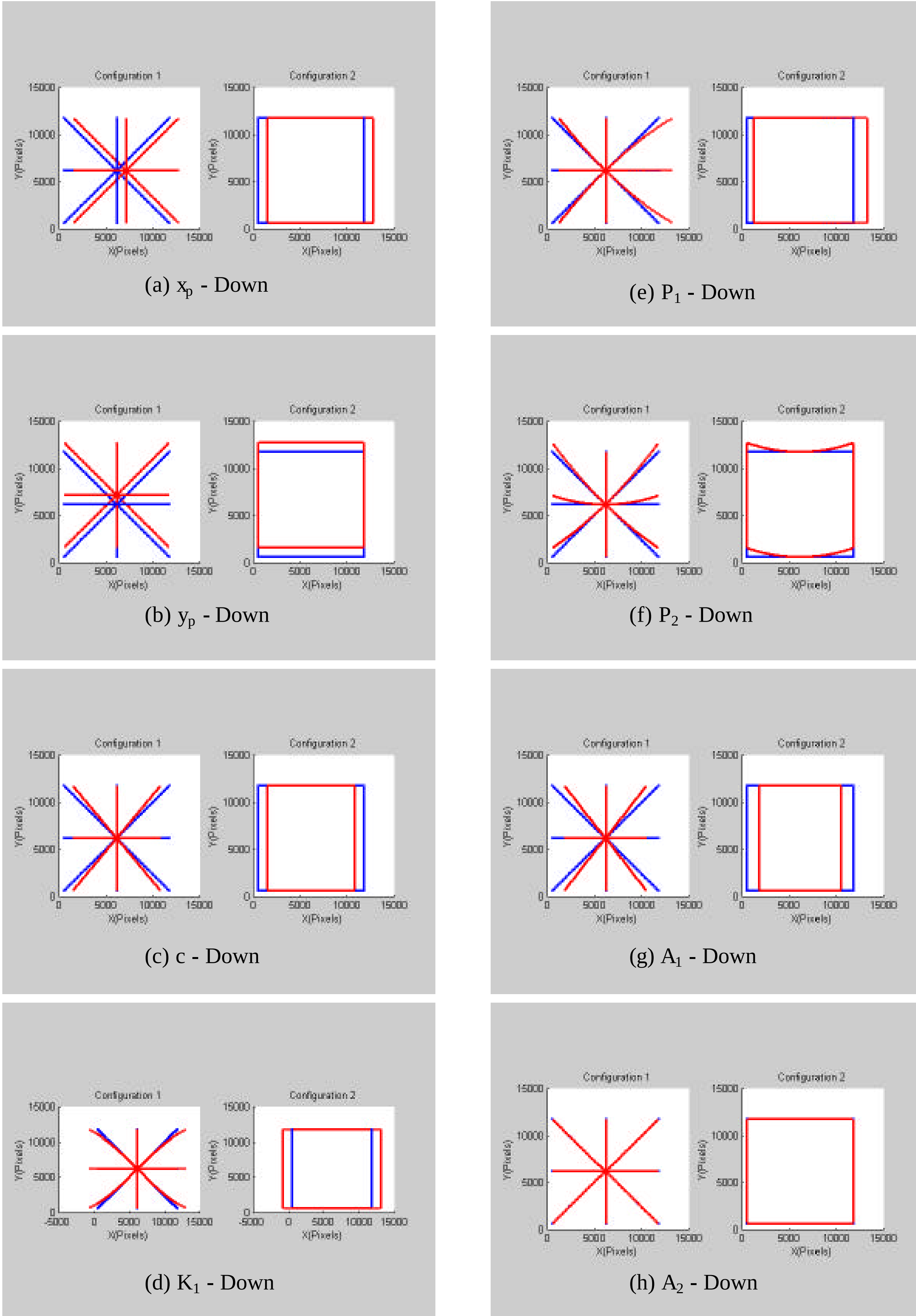

Figure 5: Effect of IOP on X-type (configuration 1) and Box (configuration 2) configurations for the down looking sensor.

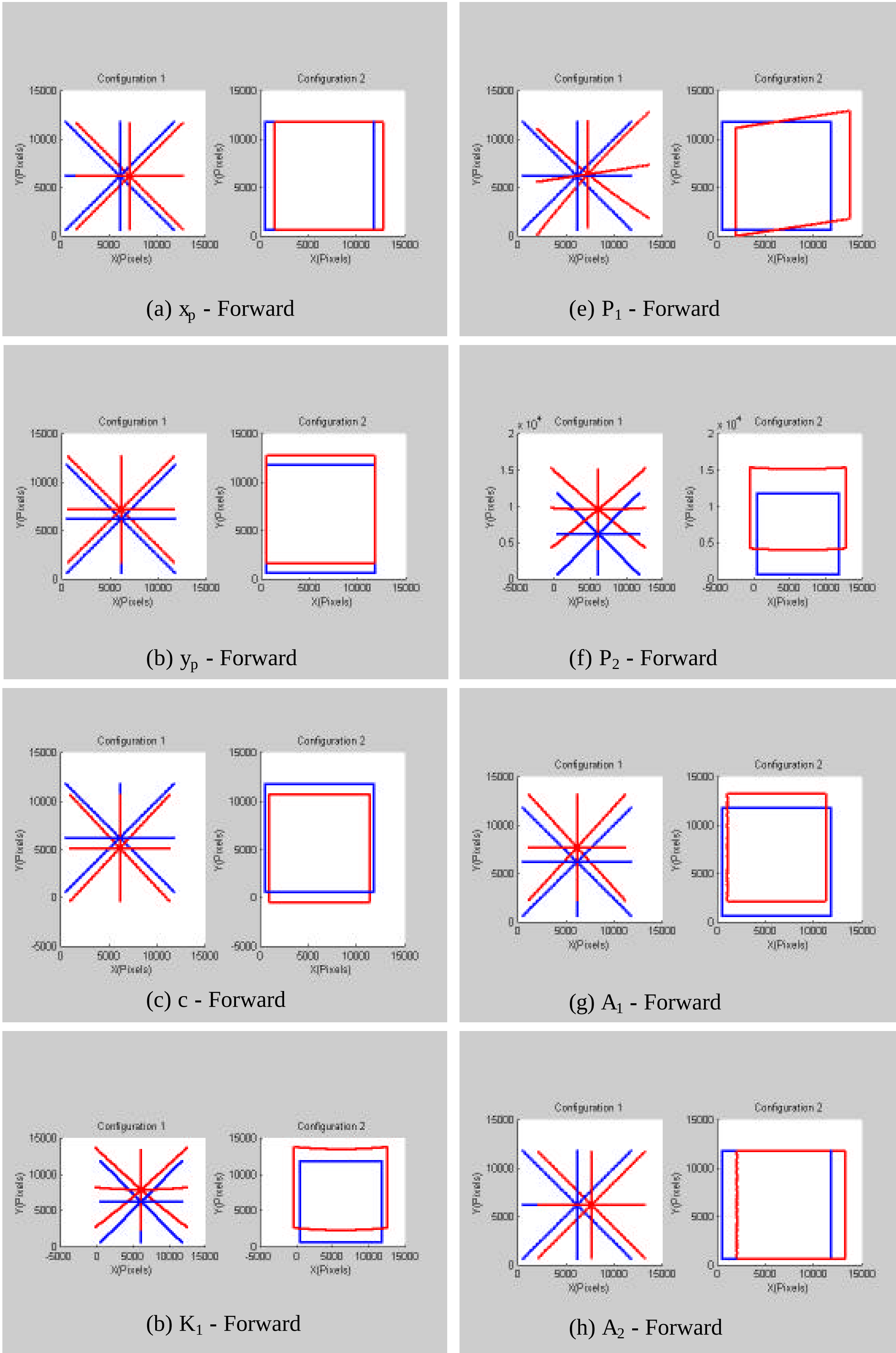

Figure 6: Effect of IOP on X-type (configuration 1) and Box (configuration 2) configurations for the forward looking sensor.

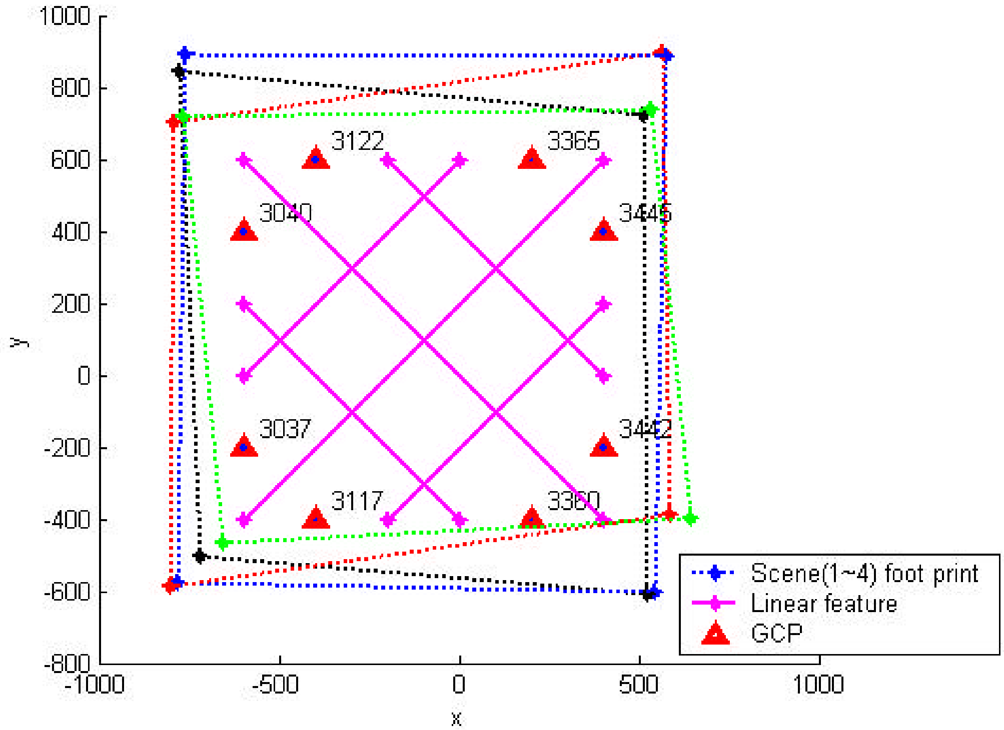

Figure 7: Object space layout for the self-calibration experiment.

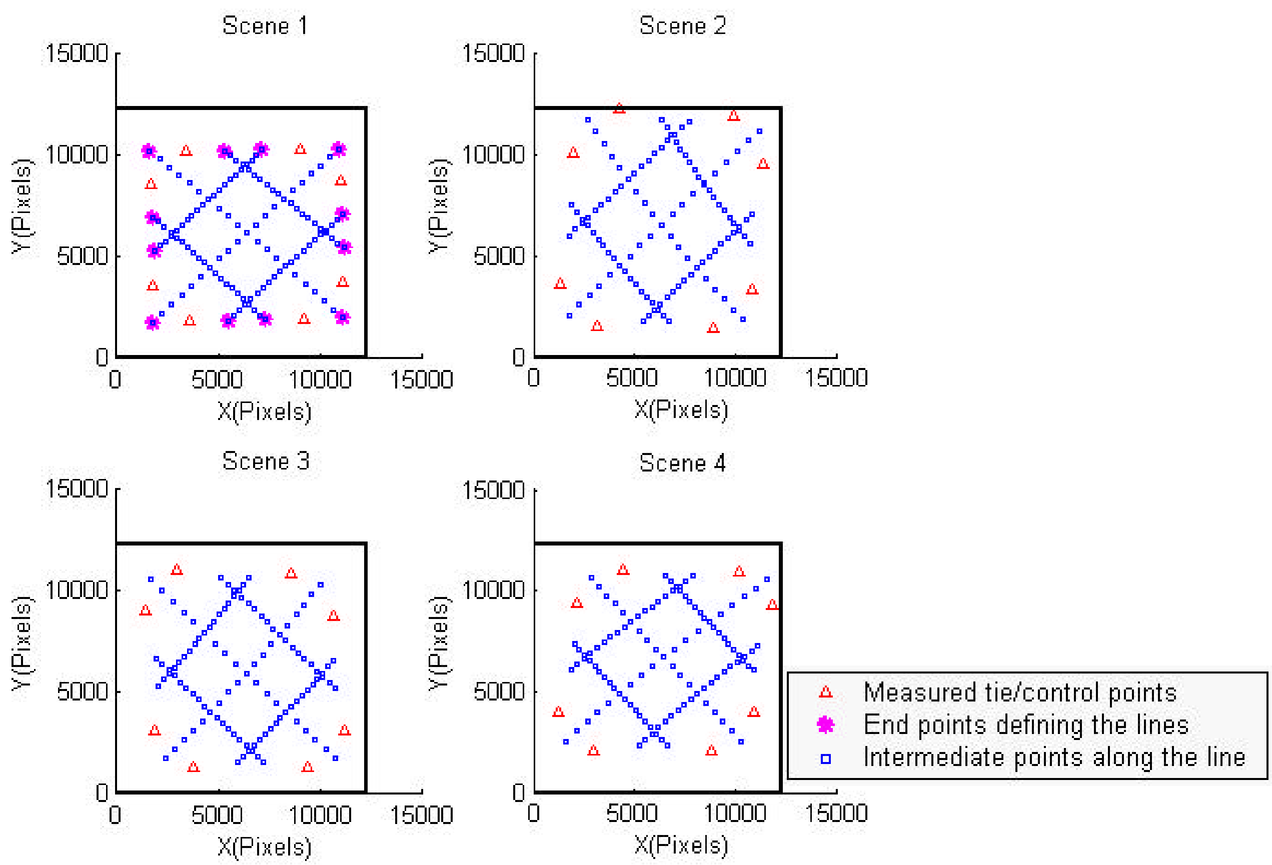

Figure 8: Image space layout for the self-calibration experiment.

REFERENCES

Habib, A., 1999. Aerial Triangulation using Point and Linear Features. In: International Archives of Photogrammetry and Remote Sensing, Munich, Germany, Vol. XXXII, Part 3-2W5pp. 137-142.

Habib, A., Asmamaw, A., May, M., Kelley, D., 1999. Linear Features in Photogrammetry. Departmental Report 450, Geodetic Science and Surveying, Department of Civil and Environment Engineering and Geodetic Science, The Ohio State University, Columbus, Ohio.

Habib, A., Beshah, B., 1998. Modeling Panoramic Linear Array Scanner. Departmental Report No. 443, Geodetic Science and Surveying, Department of Civil and Environment Engineering and Geodetic Science, The Ohio State University, Columbus, Ohio.

Kubik, K., 1988. Relative and Absolute Orientation Based on Linear Features. ISPRS Journal of Photogrammetry and Remote Sensing, Vol. 46, pp.199-204.

Mikhail, Edward M., Weerawong, Kanok, 1994. Feature-Based Photogrammetric Object Construction. 1994 ASPRS/ACSM Annual Convention Technical Papers, pp. 407-417.

AUTOMATIC MATCHING AND GENERATION OF ORTHOPHOTOS FROM AIRBORNE AND SPACEBORNE LINE SCANNER IMAGES

Karsten Jacobsen
Institute for Photogrammetry and Geoinformation
University of Hannover, Germany
karsten@ipi.uni-hannover.de

KEY WORDS: Automatic matching, orthophoto, HRSC, IKONOS

ABSTRACT

Caused by the turbulent atmosphere, the original airborne line scanner images are partially strongly deformed against normal case images and the ground coordinate system. An automatic matching requires a special program which can use the available orientation information from a combination of relative kinematic GPS-positioning and inertial measurement system (IMU). Another possibility is the rectification of the line scanner images to a chosen height level using the camera orientation for every single line. Such rectified images are displaced by the actual ground height and the view direction – especially in the case of inclined lines. The geometry is very close to the geometry of stereo orthophotos, also a stereo view is possible. With these rectified images an automatic image matching is possible by programs based on the region growing method like program DPCOR and with a special program the ground coordinates of digital elevation models (DEM) can be computed with the matched corresponding pixel positions of the rectification's and the sensor orientation. Exactly the same situation is given by the GEO-product of IKONOS-images. They are also rectified to a chosen height level. For the ortho-rectification of IKONOS GEO-products it is not necessary to use the full sensor orientation, the available nominal collection azimuth and elevation is totally sufficient. If control points in different height levels are available, also this information is not required for an optimal geometric correction shown at an example in a mountainous area.

A test block of HRSC-A-images has been rectified and the DEM's are achieved by automatic matching with DPCOR and computation of the ground coordinates by HRINT. Based on overlapping, independent flight strips an accuracy estimation was possible. The height accuracy corresponds to an accuracy of the x-parallax of 0.6 - 0.9 pixel.

1. HRSC – rectification

Original airborne line scanner images may be strongly deformed against the normal case of photogrammetry caused by the turbulent atmosphere, influencing every line in a different way. An automatic image matching in the object space requires the full information of the sensor orientation for every line, so a special software is required for this. An automatic image matching in the image space is usually not possible, but standard matching programs can be used for rectified images, they do have a geometry similar to stereo orthophotos.

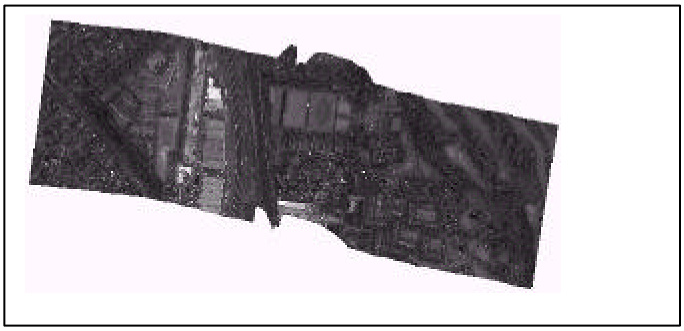

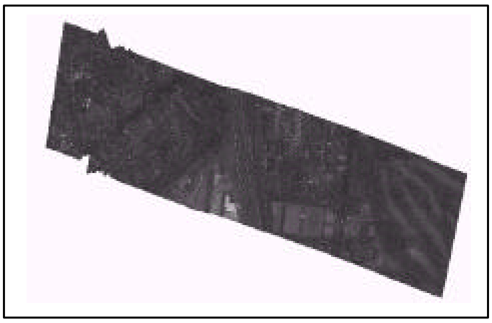

figure 1: rectified HRSC-images taken under turbulent conditions

The investigation of a data set taken with the aerial multiple line scanner sensor HRSC-A (high resolution stereo scanner) of the German Center for Aerial and Space Applications DLR was enabled by the Bundesamt für Kartographie (BKG), Frankfurt. With the program MSC of the BKG the original images have been rectified to a specified horizontal plane using the full sensor orientation, based on the Applanix combination of relative kinematic GPS and an inertial measurement unit (IMU), operating with 200 Hz. Two resulting rectification's are shown in figure 1 and 2. These extreme cases are demonstrating the impossible use of an automatic image matching in the original image space.

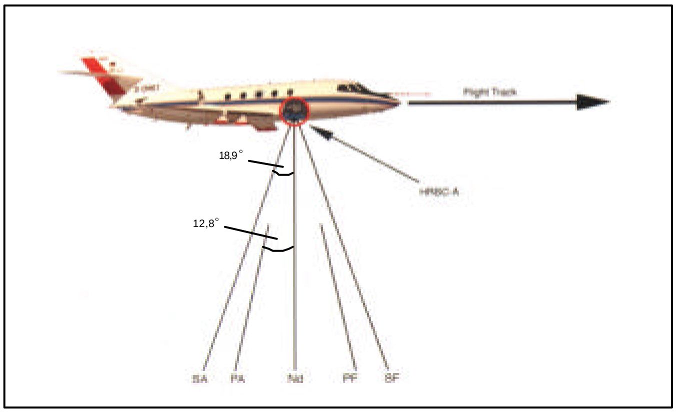

figure 2: geometric distribution of the HRSC-channels

The HRSC-sensor was originally developed by the DLR for mapping the Mars-surface. Based on this camera an airborne version has been constructed. From the available 9 CCD-lines, for the investigations only the nadir view and the most inclined panchromatic lines with a nadir angle of + 18.9° and –18.9° were used. With the flying height of approximately 2500m above ground, an original pixel size in the object space of 15cm has been reached.

The accuracy of the rectification's have been investigated by means of control points and the verification of long straight lines. Between 8 and 12 control points, determined by ground survey with GPS, having only limited differences in the height, are available for every scene. The mean square differences between the rectification's and the control points after affine transformation are shown in table 1. The affine transformation of the rectified HRSC images was necessary because of the limitation of the direct sensor orientation in this accuracy range.

Table 1: mean square differences between control points and affine transformed HRSC-A-rectification's

	flight strip 1		flight strip 2		flight strip 4		flight strip 5	
	SX	SY	SX	SY	SX	SY	SX	SY
nadir view	37mm	37mm	86mm	87mm	77mm	58mm	58mm	32mm
backward 18.9°	141mm	49mm	106mm	93mm	127mm	66mm	51mm	75mm
forward 18.9°	95mm	56mm	135mm	76mm	132mm	82mm	58mm	97mm

The mean square differences for X and Y for all flight strips was for the nadir view +/-72mm, for the backward view +/-109mm and for the forward view +/-110mm. This indicates an influence of the not respected ground height against the height level of the rectification of 83mm, corresponding to a height variation of 24cm for the control points – what is approximately the real height variation of the control points. With the exception of the influence of the height, no other special or systematic errors can be seen at the used control points. The excellent mean square differences of +/-72mm (0.5 pixel) for the nadir view, after fitting by affine transformation to control points, shows the high level of the relative accuracy of the direct sensor orientation.

Another possibility for a geometric evaluation is the analysis of straight lines in the object space. Such straight lines should be also straight lines in the rectification's. This enables the investigation also of possible local influences of a turbulent atmosphere, which may not be represented by the inertial data, operated with 200 Hz, corresponding to an image progress of approximately 2 pixel. Straight lines have been analysed especially in the centre part of the nadir view, where the influence of the limited height variation can be neglected.

Figure 3 shows the deformation of a straight line in the object space, represented in the rectification. This is an extreme case of the flight strip 2 (figure 1, left hand rectification) where the strong lateral acceleration could not completely be covered by the IMU. This is also visible in the image quality showing not sharp parts. In this case, the problem was caused by a rapid change of the yaw (kappa = flight direction) which can be seen in figure 4. The changes of the other rotations and especially the positions have not reached the same size. A similar problem is available in flight strip 4 (figure 2, right hand rectification). Also here the deviations against a straight line have reached the size of 30cm, corresponding to 2 pixel and again it is caused by a rapid change of the yaw.

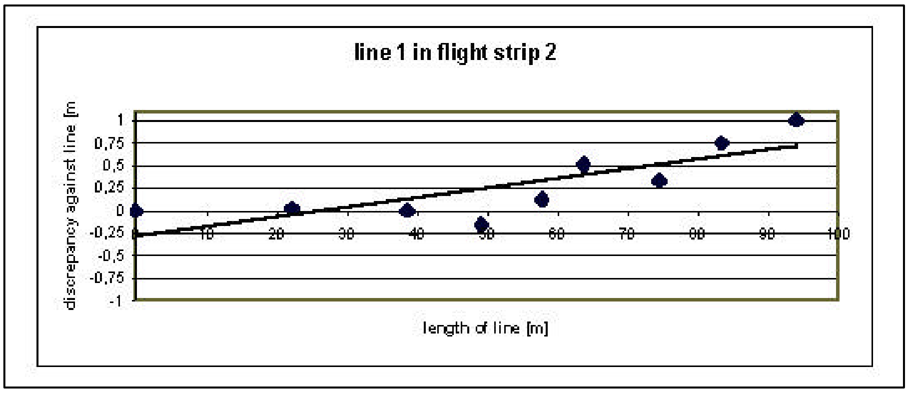

figure 3: deformation of a straight line in flight strip 2

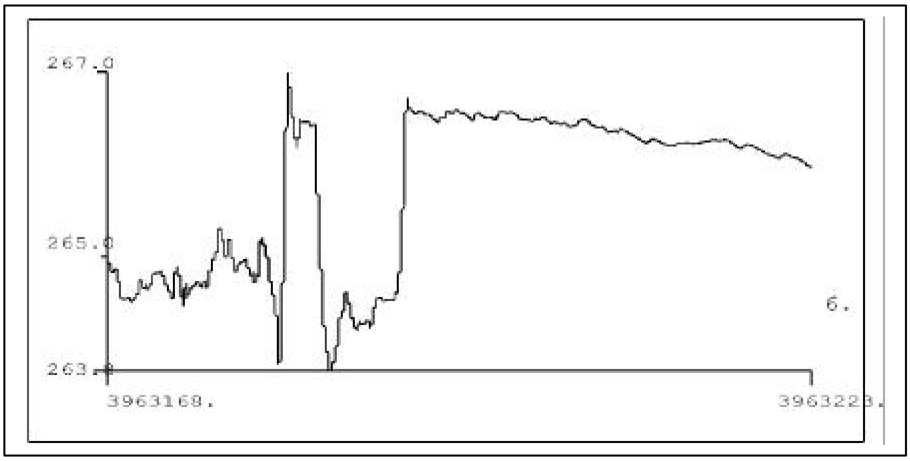

figure 4: change of yaw [°] in flight strip 2

In relation to the accuracy determined with control points of +/-72mm (0.5 pixel), the both extreme deviations in the range of 0.3m (2 pixel) can be accepted.

2. HRSC – automatic image matching

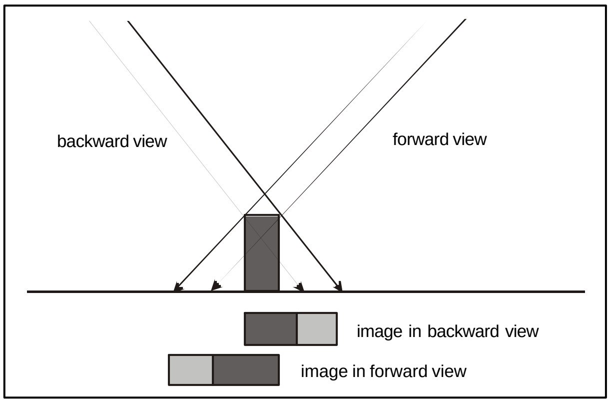

figure 5: geometric situation of rectified HRSC-images

Based on the HRSC rectification's, automatic image matching have been computed by program DPCOR. It is based on the region growing method, using the pixel positions of manual measured control and tie points as start values. The corresponding points are determined by a combination of image correlation and least squares matching. The image matching is handled in the image space. Starting from known corresponding points, other homologue points are identified in the neighbourhood and from these again other points are identified up to the covering of the whole model. This method has the advantage that it is not necessary to modify the matching program for the special image geometry. With the corresponding points, object coordinates have been computed by intersection with the special program HRINT of the University of Hannover using the HRSC rectification's, the direct sensor orientation and control points. Of course a program like HRINT, using the correct geometric model, is required for the determination of object coordinates, but this geometric model is separated from the image matching, so the image matching program DPCOR can be used without changes for several quite different applications like for aerial photos, IKONOS Geo-products and others. The geometric situation of the HRSC-rectification's can be seen in figure 5. The geometry is very close to the stereo-partner of a stereo-orthophoto where we do have exactly the same view direction. In the case of the HRSC, the view direction is changing only slightly corresponding to the recorded attitude data.

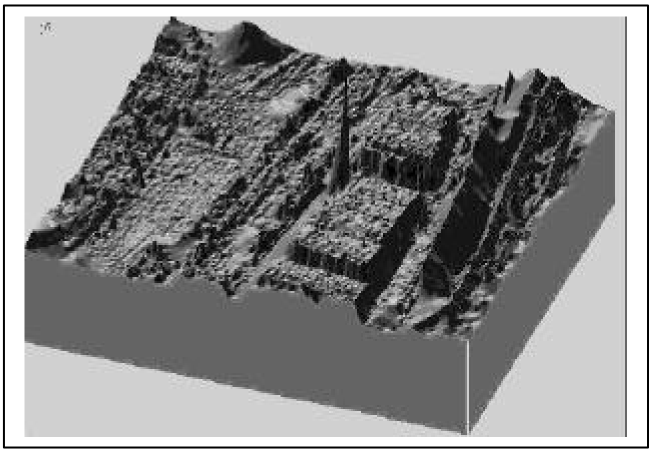

figure 6: sub-area of HRSC-rectification

figure 7: generated DEM

In figure 6 a sub-area of a HRSC-rectification is shown and in figure 7 the DEM of the same area as a 3D-view generated by LISA-Basic. This area has been covered by 4 HRSC-flight-strips. With the combination of backward, nadir and forward view, several DEM can be generated from the same area. Mainly the combination of one inclined view and the nadir view have been used for the automatic image matching because of the fast height variation in this urban area. The combination of the backward with the forward view has caused larger gaps in the DEM. But some gaps can be seen also in the generated 3D-view (figure 7).

The region growing method, used in program DPCOR, is starting from corresponding points like the used control points and it is correlating the neighboured pixel. After correlation a least squares matching will be computed. In the case of a sudden change of the height like at a building, the procedure may not find some corresponding image positions in the neighboured positions. Also from other directions the identification of points located on top of the building may fail and so for example only the ground, but not the top of the buildings may be matched. In the upper left corner (see figure 6 and 7) the region growing method was not able to reach the top of the building and corresponding to this in the DEM there is only 1 point, leading to a 3D-view like a hill. In the region of the highway on the right hand side, the matching failed also because of not sufficient image contrast. In addition there is a mismatching in the centre, creating a steep peak in the 3D-view, but there is only one point causing this. DPCOR is creating only pairs of corresponding points. The object coordinates have been computed with program HRINT using also control points for an optimal location of the DEM.

Beside these problems, the elevations are presenting the area quite well. A lot of noise is caused by the vegetation, but also by parking cars. Finally not a DEM, but a digital surface model (DSM) has been generated, representing the visible surface and not the ground. Such a DSM is useful for several applications, but it can be reduced also to a DEM for example by the automatic method used by the Hannover program RASCOR (Jacobsen 2001). The same area has been matched with several different image combinations. After elimination of blunders, a standard deviation for Z between +/-24cm and +/-34cm has been reached. This corresponds to a standard deviation of the x-parallax between 8.2cm and 12.9cm or 0.6 up to 0.9 pixel. For the rough terrain this is a quite sufficient result.

3. IKONOS-products

Images taken by the space sensor IKONOS do have today the highest resolution available for civilian application. The original images of the line scanner camera are not distributed; only derived products can be bought as different CARTERRA versions. Caused by the lowest price, the CARTERRA Geo – a rectification to a surface with constant height – is mostly used. With the knowledge of the geometric relation it is possible to upgrade the Geo-product to an orthophoto or to determine ground positions with the possible highest accuracy of the mapping system. This requires an expensive stereo pair of images or a DEM. In general the Geo-product has a geometry which is very similar to the HRSC-rectification's.

The imaging system of IKONOS can produce panchromatic (pan) (black and white) with the very high or multispectral (ms) images with a four times lower pixel size. The original pixel size on the ground is depending upon the view direction (nadir angle) which can be changed in the orbit direction, but also across by +/-52°.

original pixel size on ground in view direction $pv = 0.82m / \cos^2 \nu$? ν = nadir angle
original pixel size on ground across view direction $pc = 0.82m / \cos \nu$?

formula 1: original pixel size on ground for panchromatic IKONOS images

nadir angle	0°	10°	20°	30°	40°	50°
pan across view direction	0.82	0.83	0.87	0.95	1.07	1.28
pan in view direction	0.82	0.85	0.93	1.09	1.40	1.98
ms across view direction	3.28	3.32	3.48	3.80	4.28	5.10
ms in view direction	3.28	3.38	3.71	4.37	5.59	7.94

table 2: original pixel size on ground [m] depending upon view direction

The pixel size across the view direction (= in orbit direction) is resulting in an oversampling. The oversampling is not changing the geometry; only the radiometric characteristic will be influenced by a low pass filter effect – that means the contrast will be reduced. A low contrast usually will be more than compensated by a contrast enhancement, named as “MTFC Applied: Yes” in the meta data, but of course the not available information cannot be brought back. Only derived products are available from the company Space Imaging, operating the satellite. The derived products are resampled with a square pixel format – for the pan-images with 1m x 1m and for the multispectral images with 4m x 4m. This is corresponding to a small loss of information for close to nadir images and for images exceeding a nadir angle of 25° the original information is below the used pixel size of 1m or 4m.

The imaging system of IKONOS, build by Kodak, is equipped with a Kodak linear array of 13 816 pixels for pan and 3454 pixels for multispectral, corresponding to a swath width of 11.329 km for a nadir view and up to 29.889km for a nadir angle across the orbit direction of 52°. The flying height varies between 678km and 682km (mean 681km) above mean sea level. The inclination of the satellite orbit against the equator is 98.2°, resulting in a sun-synchronous orbit – the satellite is imaging always at the same local time of the day at approximately 10:30.

CARTERRA -	horizontal accuracy	vertical accuracy	
Geo	50m	-	system corrected to earth ellipsoid and specified map projection
Reference	25m	22m	ortho rectified without control points (DEM with +/-22m required)
Map	12m	10m	ortho rectified without control points (DEM with +/-10m required)
Pro	10m	8m	ortho rectified without control points (DEM with +/-10m required)
Precision	4m	4m	ortho rectified with control points (DEM with +/-4m required)
Precision Plus	2m	3m	ortho rectified with control points (DEM with +/-3m required)

table 3: IKONOS- (CARTERRA-) products with accuracy claimed by Space Imaging

The satellite includes a GPS-receiver and star trackers, allowing a declared stand alone geo-location of +/-12m for X and Y and +/-8m for Z. Of course these are standard deviations which can be exceeded in the individual case and which do require a corresponding height accuracy coming from a stereo scene or an available DEM. The geo-location is present in the WGS84-system, which means, the relation of the national coordinate system to WGS84 (datum) must be known as well as the Geoid undulation. Based on control points, the CARTERRA Precision Plus shall reach a horizontal accuracy of +/-2m and a vertical accuracy of +/-3m.

4. IKONOS-geometry

Satellite line scanner images do have a geometry different from perspective photos. For each line we do have a different exterior orientation – the projection center (X0, Y0, Z0) and also the attitude data (phi, omega, kappa) are changing from line to line. But the satellite orbit is very regular, allowing the determination of the relation of neighboured lines and also the whole scene based on the orbit information.

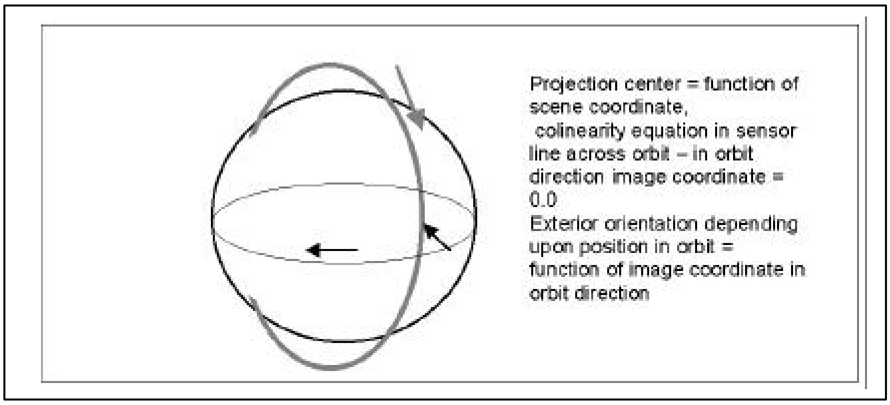

figure 8: geometric condition for satellite line scanner images

Based on a rough information about the satellite orbit, the geometric relation of such satellite line scanner images can be determined based on just 4 control points with the full possible accuracy for example with the Hannover program BLASPO. But like shown in table 3, Space Imaging is not distributing the raw images, only derived products are available. Of course from Space Imaging all the required products are available, but for a very high price and the control points together with the DEM have to be delivered to Space Imaging. If just the most often used CARTERRA Geo shall be upgraded to a higher accuracy level, a special mathematical solution is required.

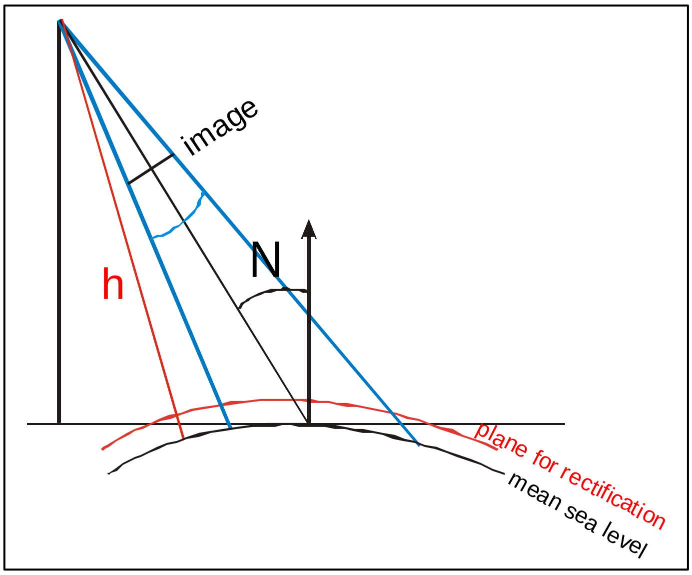

figure 9: : geometric situation of CARTERRA Geo-product

The Geo-product is rectified to a specified plane parallel to the earth ellipsoid. Beside the remaining errors of the image orientation, the geometry of such rectified images is influenced by the local height corresponding to figure 5, the geoid undulation and also the relation of the national coordinate system to WGS84 (datum).

The geometric situation of geo referenced CARTERRA Geo images has been analysed with the data set from the OEEPE-project “Topographic Mapping from High Resolution Space Sensors”. A pan-scene with a displayed pixel size of 1m, located in Switzerland was given together with digital orthophotos and the Swiss DEM of the area as geo reference. The nominal collection elevation of 67.66476° (nadir angle 22.33°) corresponds to an original pixel size of 0,89m * 0.96m, which means the resampled scene includes only a small loss of information against the original image. The tangent of the nadir angle of 0.41 shows the relation between the height difference against the reference plane and the horizontal displacement.

The altitude in the mountainous region goes from 415m to 2197m above mean sea level. The DEM has a grid interval of 25m. The later required interpolation has been made bilinear because even a polynomial fitting of 2nd degree (6 unknowns) based on 3 x 3 points resulted in mean square discrepancies of 9.2m.

Control points have been measured in the available digital orthophotos and the IKONOS-Geo-scene. The available geo-reference of both allowed a direct handling of the coordinates of the IKONOS-scene in UTM (WGS84) and the Swiss orthophotos in the Swiss national coordinate system, an oblique Mercator system. Based on the X,Y-position in the orthophotos, the corresponding height has been interpolated in the DEM (Hannover program DEMINT). The three dimensional coordinates have been transformed from the Swiss national coordinate system to UTM (Hannover program BLTRA). In the UTM-coordinate system the control points determined in the IKONOS-scene could be compared with the transformed points from the orthophotos. Of course the positions directly determined with the CARTERRA-Geo-scene are depending upon the height against the reference plane and also a remaining scene orientation error. The square mean of the difference of in total 128 points reached: MSEX=+/-124.4m MSEY=+/-40.2m with maximal differences in X: -421m and Y: -77m (figure 11).

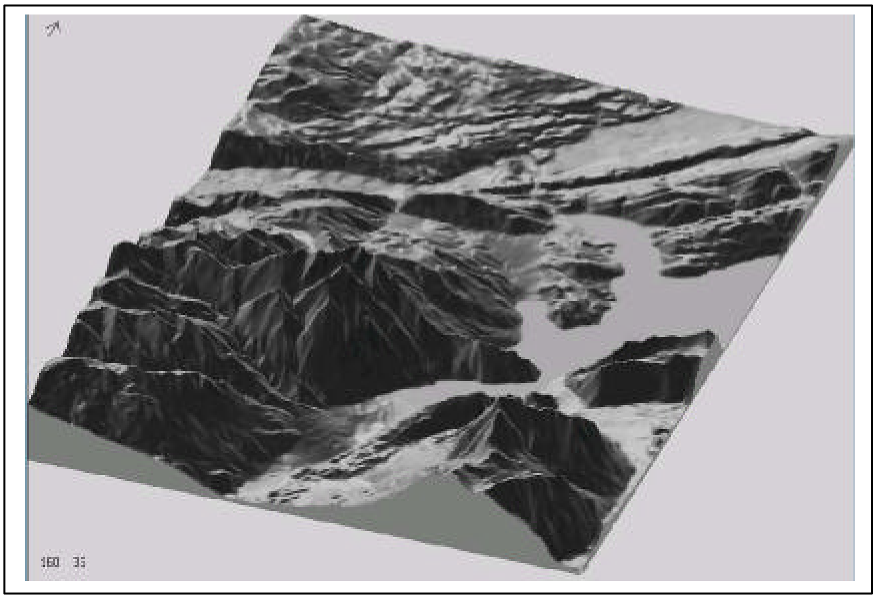

figure 10: DEM of the test area in Switzerland

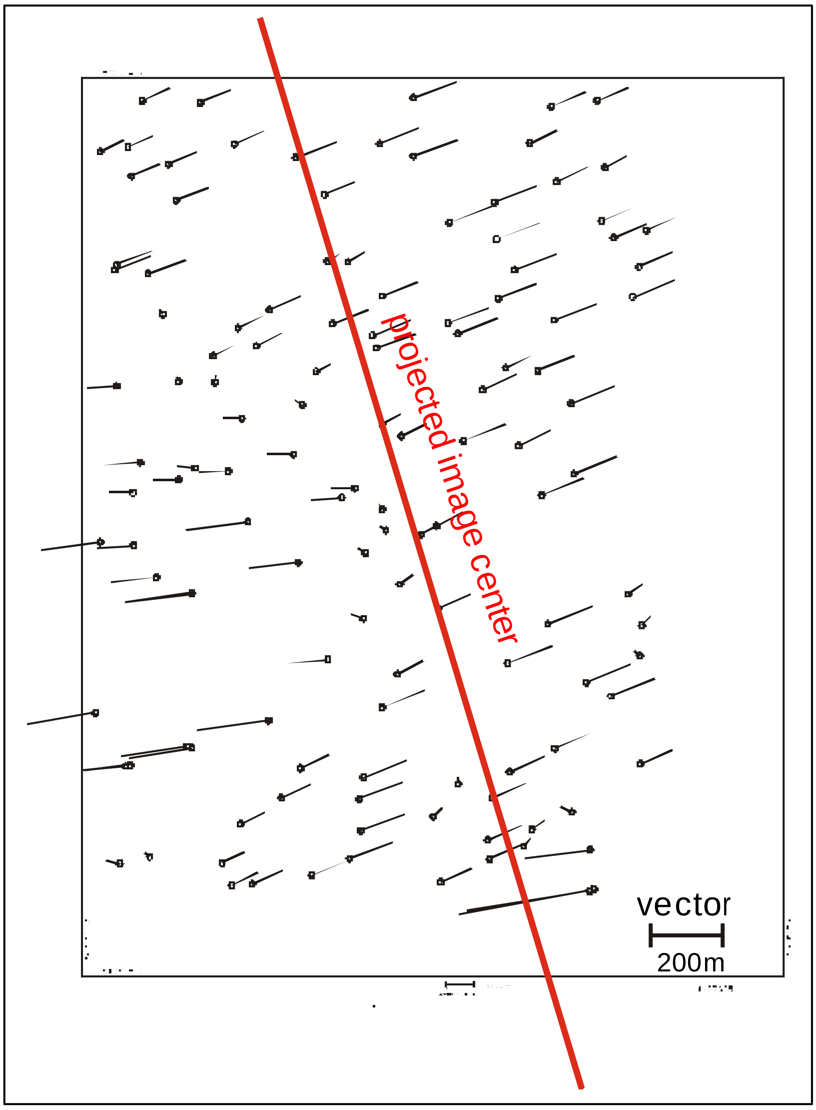

figure 11: geometric differences CARTERRA Geo against control points

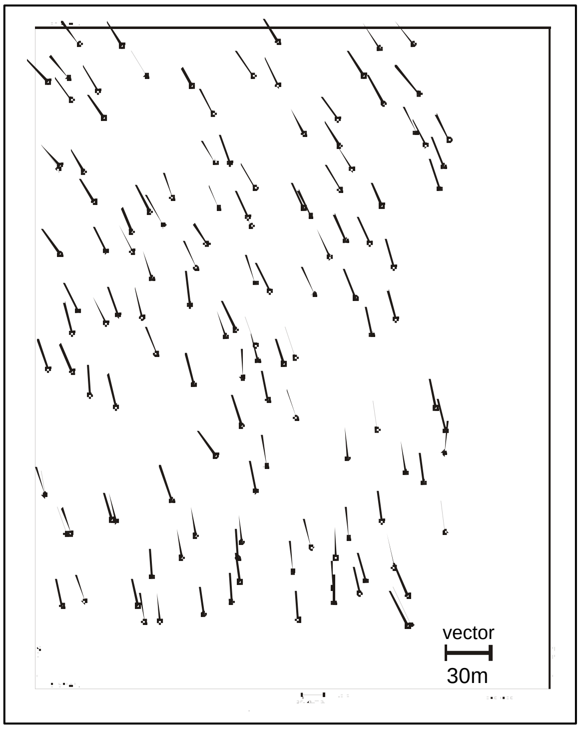

figure 12: differences after correction by the influence of height

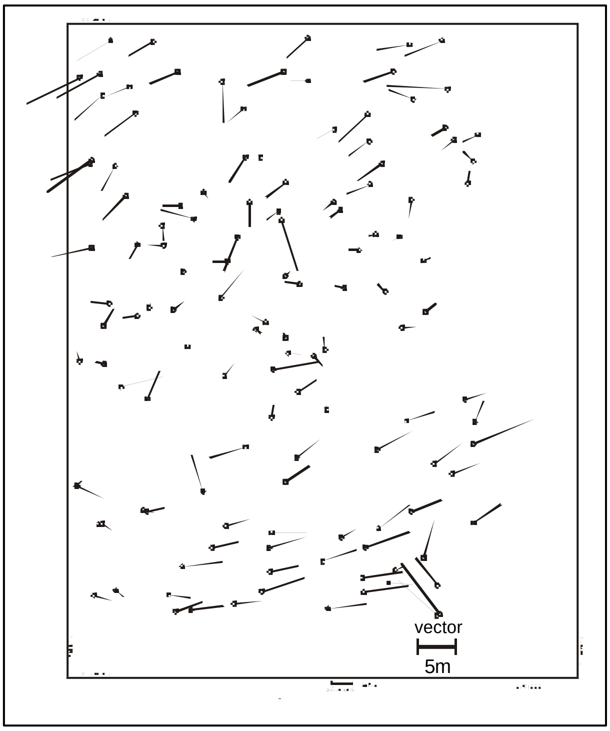

figure 13: differences after correction by influence of height + shift in X and Y

The height level of the plane for rectification in this case is approximately 800m above mean sea level.

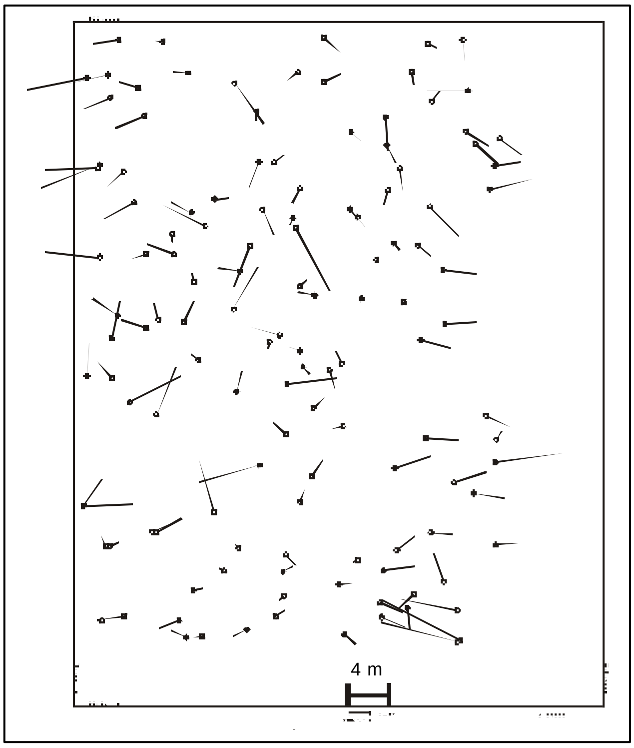

After correcting the influence of the height against the reference plane using the nominal collection elevation and azimuth together with the additionally required geometric model, the mean square differences have been reduced to MSE X=+/-7.5m and MSEY=+/-18.5m (figure 12). The again very obvious systematic errors can be explained by the accuracy of the geo-reference of the IKONOS-scenes without control points. A shift correction (in X: -6.8m, in Y: 18.3m) is reducing the mean square differences to MSE X=+/-3.5m and MSE Y = +/-2.3m. Again there are obvious systematic errors (figure 13) corresponding to a rotation of 0.4°, which means, a shift is not sufficient, a similarity transformation has to be used.

figure 14: differences after correcting the influence of height + affine transformation to control points

After height correction and similarity transformation to the control points the mean square differences are reduced to MSE X=+/-2.57m and MSE Y=+/-1.89m for 128 control points. These values are depending upon the used reference height for the rectification. If the reference height for the rectification has been used not corresponding to the definition used by Space Imaging, larger discrepancies could be seen. Usually the reference height for rectification is not known and has to be estimated. This problem can be solved also by an affine transformation instead of a similarity transformation after the height correction. Based on an affine transformation, the results are independent upon the reference height for transformation and in the case of the OEEPE-data set the mean square discrepancies are reduced to **MSE X=+/-2.52m** and **MSE Y=+/-1.72m** (see figure 14). Nevertheless there are local systematic effects shown by a covariance analysis, the relative accuracy of points neighboured up to a distance of 1km is only RMSEX=+/-1.76m and RMSEY=+/-1.23m. This can be explained by the accuracy of the control points itself, digitised from digital orthophotos – within the same orthophoto the accuracy is better than the absolute accuracy. In addition to this, a separate computation has been made only with control points which have been identified as good during the digitising procedure. For the 79 clearly visible control points the mean square differences are MSEX=+/-1.67m and MESY=+/-1.60m corresponding to approximately 1.6 pixels. Again here we do have an influence of the reference points from the orthophoto and the DEM, that means the final error component coming from the geometric improved IKONOS images is smaller, but here we are at the limit of the required accuracy. Corresponding to the rule of thumb, for mapping a pixel size of 0.05 up to 0.1mm in the map is required. This corresponds to a possible map scale for the panchromatic IKONOS images of 1 : 10 000 up to 1 : 20 000. For a map, the horizontal accuracy requirement is limited to +/-0.2mm or +/-2m for the map scale 1:10000. By this reason, no demand for a higher accuracy exists.

The shown results are based on the full number of control points used in the Hannover program CORIKON. If the nominal collection azimuth and the nominal collection elevation are available, the improvement of the Geo-scene can be made also with a small number of control points. Based on **4 control points**, at the 124 remaining points, root mean square differences of **RMSX = +/- 2.00m** and **RMSY = +/- 1.99m** have been reached – in the mean square of both components just 8% more than in the case of the use of all control points.

5. Conclusion

The geometric handling of rectified HRSC-images and IKONOS-Geo-products is very similar. Based on rectified images an automatic image matching is possible in the rectification's. With a DEM the points located in the rectification's can be transformed into the object space, using the view direction from the sensor to the plane of rectification, so the generation of orthophotos is possible. The geometry of CARTERRA Geo-products can be upgraded without knowledge of the full scene orientation to an accuracy corresponding to the CARTERRA Precision Plus. Only a limited number of control points are required if the nominal collection azimuth and the nominal collection elevation are available. If this is not the case, control points, covering the whole Z-range in the scene have to be used for the determination of these values.

REFERENCES

Jacobsen, K., 2001: New Developments in Digital Elevation Modelling,

Lehmann, F., 2001: The HRSC Digital Airborne Imager, GEO Onformatics, Volume 4, April 2001, pp 22-25

Rosenberg, N., 2001: Geometrische Auswertung von Flugzeug-Zeilenscanneraufnahmen, Diploma thesis, University of Hannover, 2001

Schlüter, M.,1999: Geometrische Auswertung von DPA-Dreizeilenkameradaten. Publication of the DGPF, Bd. 7, pp 391-398, Berlin, 1999

Scholten, F.; Sujew, S.; Wewel, F.; Flohrer, J.; Jaumann, R.; Lehmann, F.; Pischel, R.; Neukum, G.,1999: The high resolution stereo camera (HRSC) – digital 3D-image acquisition, photogrammetric processing and data evaluation. Workshop "Sensors and Mapping from Space", Hannover, 1999

Acknowledgements:

Thanks are going to the Bundesanstalt für Kartographie und Geoinformation (BKG), Frankfurt, Germany, especially to the former collaborator Dr. MartinSchlüter, for the support of the HRSC-image investigation and to the OEEPE for the IKONOS test data.

Georectification of the Airborne Multi-angle Imaging SpectroRadiometer

Veljko Jovanovic, Bill Ledeboer, Mike Smyth, Jia Zong

NASA Jet Propulsion Laboratory
California Institute of Technology
4800 Oak Grove Drive
Pasadena, CA 91109

***Abstract*—An Airborne Multi-angle Imaging SpectroRadiometer (AirMISR) has been developed to assist in validation of the Earth Observing System (EOS) MISR instrument currently flying on the Terra spacecraft. Unlike the EOS MISR, which contains nine individual cameras pointed at discrete look angles, AirMISR utilizes a single camera in a pivoting gimbal mount. A principal requirement for AirMISR is that it must image the same area on the ground from all nine angles. The NASA ER-2 is the preferred platform for AirMISR because its flight altitude of 20 km is above more than 90% of the Earth's atmosphere. Applications of cloud screening, cloud height retrieval, and cirrus detection algorithms require a high-altitude operation. The normal variation in aircraft roll, pitch, and yaw on the ER-2 as well as changes in attitude, track direction and velocity, although small, must be measured. The measured values are used along with post-flight defined corrections in order to georectify and coregister the image data for all angles and spectral bands. This paper provides a description of the algorithm and operational aspects of AirMISR georectification along with examples and results from a recent flight.**

Keywords: Earth Science, Multi-angle, Rectification

I. INTRODUCTION

The MISR instrument was launched into polar Earth orbit aboard the Terra spacecraft on December 18, 1999. Terra is in a 16-day-repeat, 705-km, Sun-synchronous orbit and has approximately a nominal 10:30 am equator crossing time on the descending node. MISR uses nine separate charge coupled device (CCD)-based pushbroom cameras to provide multiple-angle, continuous imagery of the Earth in reflected sunlight [*Diner et al.,* 1998a]. The cameras are oriented in the following configuration: one at nadir plus eight other symmetrically placed cameras that provide fore-aft observations with view angles at the Earth's surface of 26.1°, 45.6°, 60.0°, and 70.5° relative to the local vertical. The imagery is provided in four spectral bands (blue, green, red, and near-infrared) at each angle, yielding a total of 36 image channels (9 angles × 4 bands). MISR measurements are designed to improve our understanding of the Earth's ecology, environment, and climate.

The aircraft version of MISR, called AirMISR, flies on a NASA-owned ER-2 aircraft [*Diner et al.,* 1998b]. Its primary role is to serve as a MISR simulator, providing data useful for: a) validation of MISR geophysical retrieval, b) in-flight radiometric calibration and instrument performances characterization, and c) general scientific research based on a high quality, well calibrated multi-angle imaging data. In order to reach these goals AirMISR data acquisition system must resemble multi-angle geometric attributes of the MISR. Consequently, AirMISR ground data production system must satisfy similar requirements as those defined for MISR geometric processing. More specifically, the image data associated with the nine view angles must be co-registered and geolocated (i.e. georectified) as a part of standard data production.

While there are similar needs for georectification of the images from both instruments, the operational algorithms used to process airborne data are somewhat different than the algorithms applied for the spaceborne data. The theoretical concepts, underlying the design of the MISR science data processing system, responsible for autonomous and continuous georectification have been previously described [*Jovanovic et al.,* 1998]. This paper describes specific algorithm and operational procedure adapted to georectify AirMISR data. The methods selected are designed to deal with particular conditions of the data acquisition system, such us: a) insufficiently accurate ER-2 navigation data, b) impermanent orientation between camera reference frame and INU/GPS reference frame, 3) inaccuracy of the gimbal assembly used to provide multi-angle pointing capability. The next section describes the geometry of the AirMISR imaging event. The following sections describe relevant input data, georectification aspect of data the production system, and format of the final georectified product. The following section also discusses georectification results using data from a recent flight over Steamboat, Colorado.

II. GEOEMTRY OF AIR-MISR IMAGING EVENT

The AirMISR is mounted in the nose of NASA's ER-2, which flies at 20 km altitude. The instrument consists of a single pushbroom camera mounted on a motorized pivot. In a standard operational mode a data run is divided into nine segments, each corresponding to a MISR specific angle. The camera is preprogrammed to pivot aft between segments, thus creating a viewing sequence in which data are first acquired at nominal D-forward (Df) viewing angle of 70.5° of the nadir in the along flight direction. Then consecutively stepping backwards the Cf (60°), Bf (45.6°), Af (26.1°), An (nadir), A-aft (Aa), Ba, Ca, and Da view angles, image data are acquired during a 12 min 141 km flight line. The commanded times of camera rotation and acquisition are coordinated with aircraft velocity and altitude in order to maximize overlap of the targeted ground area (*see Figure 1*).

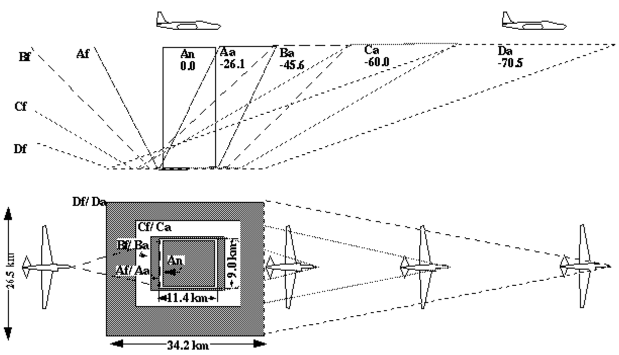

Figure 1: AirMISR image acquisition sequence represents one data run. During a single flight multiple run with different flight azimuths are acquired over one or more ground targets.

The AirMISR camera uses four charge coupled device (CCD) line arrays parallel in a single focal plane The line array contains 1504 photoactive pixels, each 21 x 18 µm. Each line array is filtered to provide one of the four spectral bands. The spectral band shapes are approximately Gausian and centered at 446, 558, 672, and 866 nm. The camera effective focal length was determined to be 58.8 mm. MTF at 20°C. For nominal ER-2 flight conditions, the AirMISR camera has an instantaneous footprint of 7 m cross track x 6 m along track when viewing in the nadir position. For the most oblique D angles coverage increases to 21 m cross track x 55 m along track. Image lines are acquired every 40.8 ms resulting in an along track sample spacing, regardless of view angle, of 8 m for a nominal aircraft ground speed of 200 m/s.

The total image swath width is defined by camera field-of-view and varies from 11 km in the nadir to 32 km at the most oblique angle. The image lengths are controlled by the timings of viewing sequence, which is set so that all nine images are centered over the same ground target. This gives a variable image length of 9 km at nadir up to 26 km at the most oblique angles.

In order to find the geolocation corresponding to pixel's field-of-view, the pixel pointing direction is expressed in the geocentric coordinate system, as follows:

$$\vec{p} = T_1 \vec{r}_{acs} \quad (1)$$

where $\vec{r}_{acs}$ is the pixel pointing direction relative to the aircraft coordinate system (ACS) identical to the INU/GPS body axis reference frame. The vector $\vec{r}_{acs}$ is defined by the observable image coordinates and a set of constants that represent the instrument interior orientation parameters and transformation between instruments, including gimbal position, and aircraft coordinate axes. T_1, defined by the aircraft position and orientation at the time of imaging, represents the transformation between the aircraft and geocentric coordinate system. Equation (1) is the well known photogrammetric model [*Paderes et al*., 1996] used for various image-ground point determinations required for time dependent remote sensing imagery.

III. AIR-MISR GEORECTIFICATION APPROACH

A direct geolocation of AirMISR pixels prior to rectification is not possible due to the insufficient accuracy of ER-2 INU/GPS system and instrument gimbal assembly. For the current system, a collection of ground control points is an unavoidable part of data processing operations. Our approach minimizes human involvement by requiring interactive ground control point collection only over nadir (An) image. Other images are co-rectified to the nadir via automatic tie point collection and a time-dependent trajectory model used to account for system positioning and pointing errors. This section describes input data, georectification algorithm, and output data in more details.

A. Input data

Navigation: ER-2 navigation information, supplied by Litton-92 INU/GPS system, is acquired in-flight by AirMISR as an asynchronous stream of packetized data recorded in a single file. Each packet contains a relative timestamp and a data value for a single navigation parameter. Data processing begins by reading all of the packets, decoding the timestamps and data values and extracting only the parameters needed for georectification. Aircraft attitude is updated 64 times per second. Aircraft position is updated eight times per second. Navigation data are recorded asynchronously with respect to the camera data. The ARINC 429 time stamp included in both data sets is later used to align the navigation and camera time lines during processing. The specified accuracy [*Litton Aero Products*, 1996] for the aircraft attitude and position data along with propagated geolocation error are given in *Table I.*

TABLE I
ER-2, LTN-92 INU/GPS SPECIFIED ACCURACY (2 SIGMA) AN D PROPAGATED GEOLOCATION ERRORS

PARAMETER	ACCURACY	PROPAGETED ERROR
ATTITUDE	0.05 DEG	29 M (NADIR) 170 M (D'S VIEW ANGLES)
HORIZONTAL POSITION	100 M	100 M
VERTICAL POSITION	400 M	130 M (NADIR) 1200 M (D'S VIEW ANGLE)

Digital Elevation Model: The AirMISR georectification relies on the already available Digital Elevation Model (DEM). Almost entire US area is covered with DEM of sufficient resolution ranging from 1 m up to 30 m elevation postings. The maximum geolocation error, resulting from the use of the existing US DEM's is less then 40 m for the most oblique view angles.

Imagery: AirMISR images input to georectification are only radiometrically corrected by radiance conversion and scaling. The red, green, and blue band image of the extreme forward-viewing 70.5º look angle is displayed in *Figure 2*.

Figure 2: Color red/green/blue image of area near Steamboat Springs, Colorado acquired on March 08, 2001 at the Df (70.5ºangle.

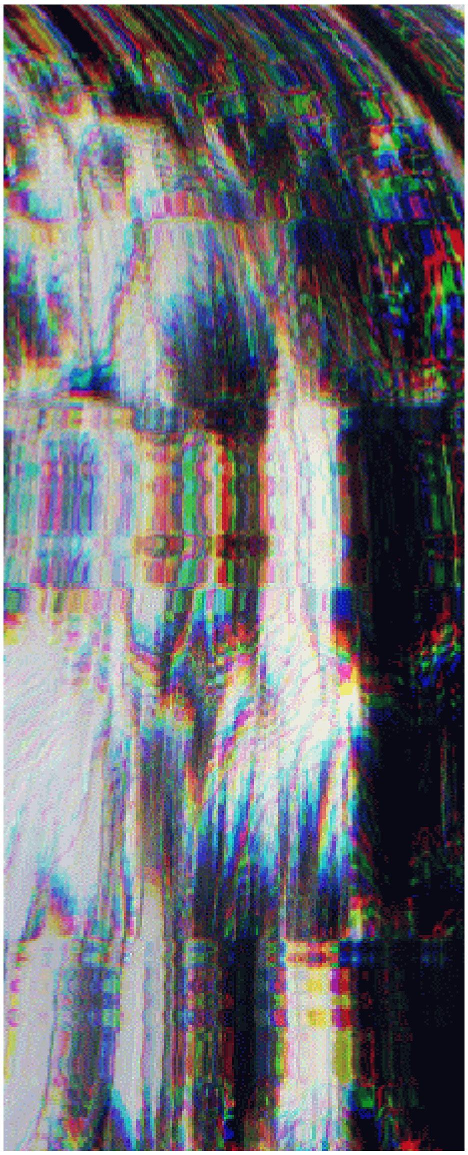

This as acquired image shows several artifacts regarding the geometry of the imaging event. First, the data displayed do not reflect the true along-track/cross-track spatial aspect ratio since at this view the cross-track sample spacing is 21 m while along-track is 8 m. Second, there is an obvious band-to-band misregistration due to the inherent design of the camera. The third artifact is the "smeared " appearance in the along-track direction of some image segments. This kind of effect is a result of the aircraft pitch rate that compensates for the along track motion, being such that the same point on the ground is observed by multiple line times. Also, significant change of the aircraft true heading is evident at the top of the image. Comparison of AirMISR imagery with coincident ER-2 navigation shows, as expected, high correlation between artifacts and aircraft attitude and attitude rate. All of these effects are much less prominent in the imagery acquired at the angle closer to nadir. The *Figure 3* shows red/green/blue image of the same area acquired at the Ba (-26.1º) angle.

Figure 3: Color red/green/blue image of area near Steamboat Springs, Colorado acquired on March 08, 2001 at the Ba (-26.1º) angle.

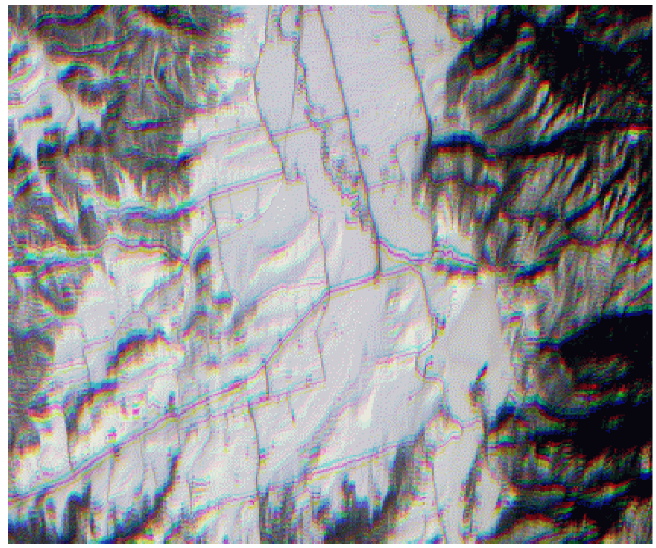

This image shows only band-to-band missregistration to the viewer. All of the artifacts discussed above are corrected during georectification.

Camera Geometric Model: The Camera Geometric Model data set consists of a set of parameters that are used in a mathematical expression that gives the pointing direction of an arbitrary pixel (vector $\vec{r}_{acs}$ in *Equation (1)*). These parameters reflect geometries of the camera system and account for distortions from an ideal optical system [*Korechoff et al.,* 1996]. Namely, the elements of the camera geometric model are:

1. The rotation matrix function of the angles between camera coordinate system and aircraft coordinate system. Nominally, this is the pitch angle commanded to pivot the camera via the gimbal assembly. The angle is accurate only to 0.1º and must be corrected prior to georectification.
2. The rotation matrix function of the angles between camera and detector coordinates system.
3. The separation of a particular band from the intersection of the camera z-axis with focal plane.
4. The pixel number (i.e. boresight pixel) corresponding to the camera x-axis (y=0).
5. The detectors pitch in x direction.
6. The effective focal length.

7. The coefficients of a fifth-order polynomial to account for the nonlinear distortions of the field angle in the cross-track direction.

All of these parameters, except those listed under 1, are calibrated on the ground giving the pointing accuracy corresponding to 0.2 of a pixel when projected on the ground.

Georectification Algorithm: The AirMISR georectification is divided into three parts: 1) initial georectification, 2) determination of sensor attitude and position motion parameters (i.e. exterior orientation), and 3) final georectification. In the first step, the supplied input data are used to project and resample images to the appropriate map projection. This is done on a pixel-by-pixel basis using equation (1) for the ground to image correspondence determination, and bilinear re-sampling for the assignments of the image data to the map projection grid. With this initial georectification, most of the gross image artifacts are removed and imagery as such can be used for tie point identification in order to improve camera / aircraft orientation and position.

In the case of AirMISR, with its very specific imaging sequence, the operations required to estimate exterior orientation must be designed to minimize the human involvement required for the collection of ground control points. In particular, space intersection of nadir image only, including manual collection of GCP's, is done first. Subsequently, the automatic tie points collection and simultaneous bundle adjustment for the remaining eight images are implemented as the final estimation step.

Figure 4a: Tie points collected over initially georectified image acquired at Cf (+60°) viewing angle over the target area near Steamboat Springs, Colorado.

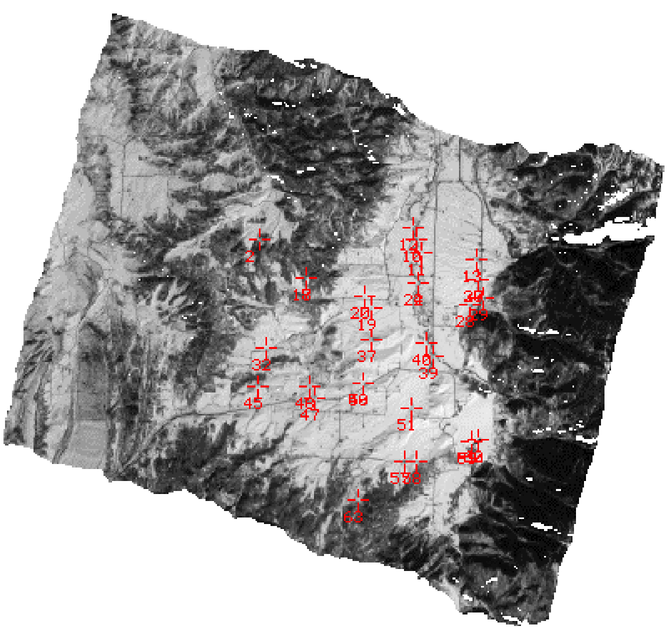

The Landsat-4 and –5 precision geolocated terrain corrected TM scenes are used for the identification of GCP's with expected accuracy of 30 m (2 σ).

Figure 4b: Tie points collected over initially georectified image acquired at An (nadir) viewing angle over the target area near Steamboat Springs, Colorado.

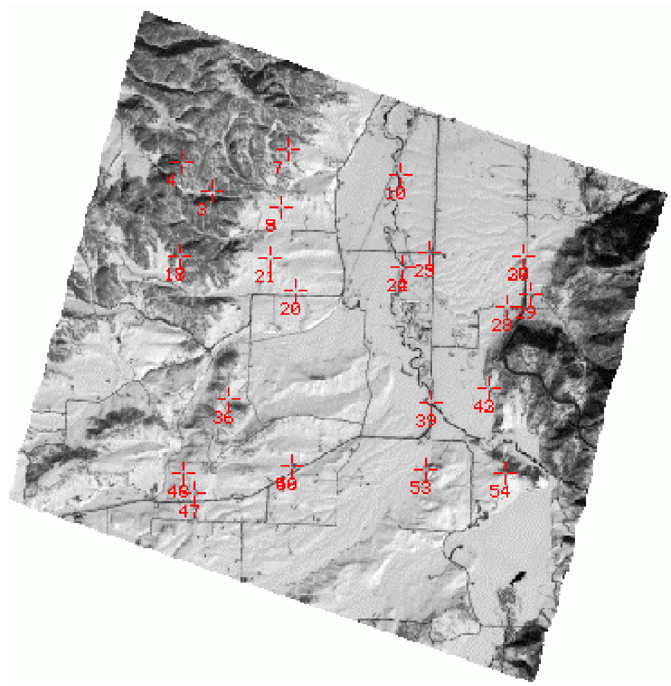

Figure 4c: Tie points collected over initially georectified image acquired at Ba (-45.6°) viewing angle over the target area near Steamboat Springs, Colorado.

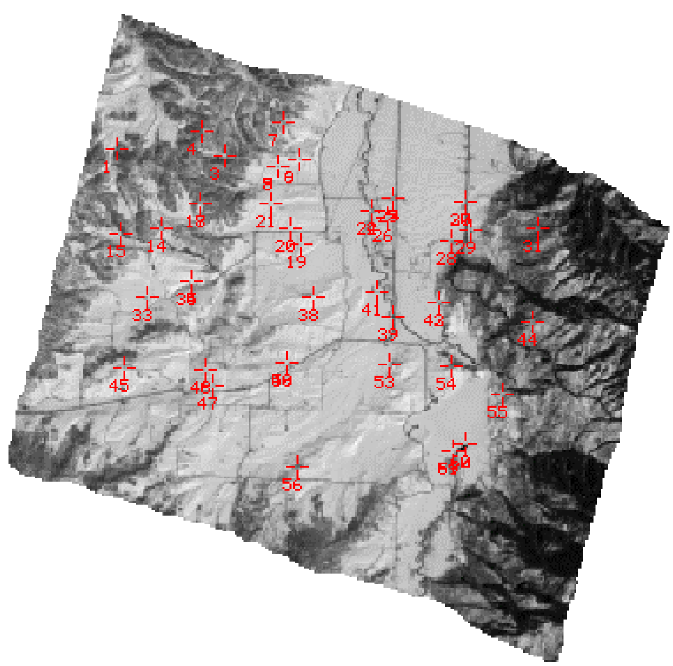

The automatic tie points collection uses a combination of interest point extraction and least-square image matching to identify multi-ray conjugate points for nine AirMISR images.It should be noted that tie point collection is only possible in the initially georectified imagery due to the artifacts in the as acquired data. The figures 4 show distribution of tie points identified over images corresponding to three view angles.

The simultaneous bundle adjustment algorithm, based on Equation (1), processes tie-point measurements so that they are backward projected in *as acquired* image. This is necessary so that measurements can be related to the AirMISR camera system exterior orientation parameters via corresponding time information. The models used to correct exterior orientation parameters are chosen to be time-dependent piecewise linear functions. These functions sufficiently model error behavior in the supplied data and at the same time do not require a large number of conjugate points.

As the last step, estimated corrections to the exterior orientation parameters are used as the input to the final georectification assuring desired subpixel geolocation accuracy across all nine images. It should be pointed out that for the purpose of bundle adjustment only red band data are considered. There is no need for adjustment of the camera geometric model parameters required for band-to-band registration. Their ground calibration is sufficiently accurate and determined values do not change during flight.

Output data: As the georectification output, the 36 layers (4 bands per each of nine view angles) of digital maps are generated. All layers are referenced to the same UTM map projection grid. Common resolution of the output grid is chosen to be 27.5 m. The size of the useful image data varies from view to view as it is shown in *Figure 1*.

IV. GEORECTIFICATION RESULTS FROM A RECENT FLIGHT

On March 8, 2001 AirMISR flew over an area near Steamboat, Colorado, in support of a remote sensing research campaign requiring multi angle data over a predominately snow and ice surface. During the flight, ER-2 made four runs over the same ground target flying along different ground azimuth for each of the runs. Each run completed full image acquisition sequence generating nine images corresponding to nine view angles. The data from run 2 acquired at 205º azimuth are used to show results of AirMISR triangulation and orthorectification.

The orthorectified Landsat TM scene (p035r032) is used to collect 12 ground control points, which are then identified in nadir imagery. As the result of the space resection for nadir image, static corrections to the supplied data are as provided in *Table 2*.

TABLE 2: STATIC CORRECTION TO THE AIR-MISR DURING IMAGING AT NADIR ANGLE

PARAMETER	ROLL	PITCH	YAW	POS (X)	POS (Y)	HEIGHT
CORRECTION	-0.553º	-1.548º	-0.076º	-101	70	263

These corrections provide improvement of georectification accuracy for nadir image from 1000 m down to within the 27.5 m size of output pixel.

The following step, simultaneous bundle adjustment, uses tie point measurements in order to estimate dynamic corrections to the exterior orientation parameters for the entire imaging sequence. During the adjustment, orientation of the nadir camera recovered in the previous step is held fixed, assuring absolute georectification accuracy of the entire image collection. As an example of our estimate in this case, the pitch corrections are given in Figure 5.

Figure 5: Estimated time dependent correction to the AirMISR pitch orientation during 12 min imaging run over the area near Steamboat Springs, Colorado.

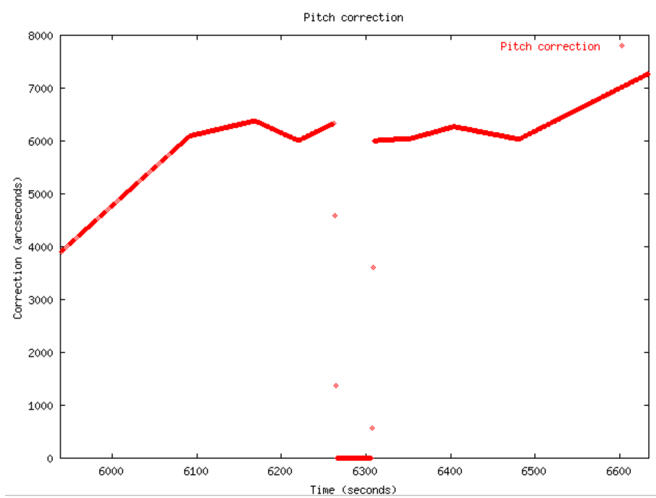

The red line in the middle on the bottom of the graph represents the fact that orientation of the imaging system, corresponding to nadir viewing time, is held fixed during adjustment. The changes in the slope of the graph correspond to the commanded camera-viewing angle. The magnitude of the slope change can be explained with the accuracy of the pivoting mechanism.

Once estimated, the corrections to the exterior orientation are used as the input during final georectification. Figures 6a and 6b can be used to show changes in co-registration accuracy prior to and after the adjustment. Each picture represents a color composite constructed from the red band data layers associated with the three viewing angles. Df layer is color-coded red, An layer is color-coded green, and Da layer is color-coded blue. Only the bottom third of the picture represents the area where layers from all three views overlap. The figure 6a is a composite of image layers prior to adjustment, while figure 6b is a composite of the image layers after adjustment.

The misregistration of the various surface features is obvious when looking at the image in Figure 6a. In comparison, all of the line and other features in figure 6b align within the pixel size of 27.5m.

Figure 6a: Red/Green/Blue color composite of Df, An, and Da image layers prior to adjustment.

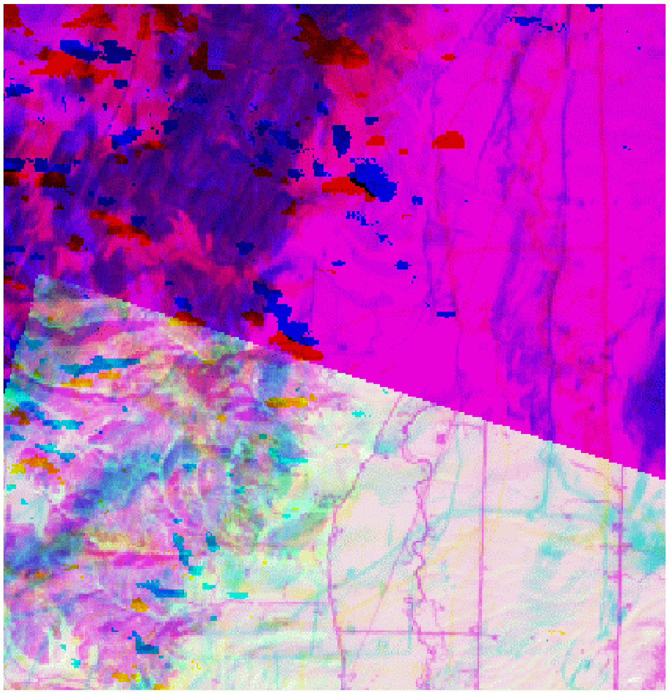

.

Figure 6b: Red/Green/Blue color composite of Df, An, and Da image layers after adjustment.

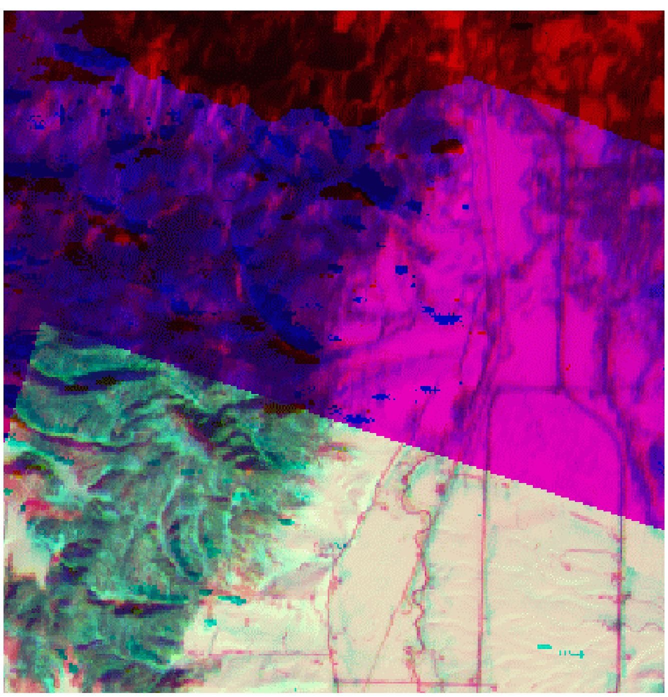

V. SUMMARY

The primary objective of the AirMISR instrument is to acquire image data, which, to the extent possible, match the data acquired by the senior spaceborne instrument. This objective and available budget were two driving forces behind the design of the instrument and the selection of its host airborne platform. The georectifiction objectives are perceived reachable via data production system in spite of not fully adequate pivoting mechanism and the INU/GPS navigation system inherited with NASA ER-2 aircraft. In addition to that, the AirMISR unique image acquisition sequence represents the georectification challenge in its own right. In the approach presented here, the collection of ground control points is reduced to the nadir-viewing image only. It is also shown that successful automatic collection of the remaining eight images tie points is possible only if these images are initially georectified using the supplied navigation. Finally, selection of the time dependent linear piecewise functions for exterior orientation modeling provides results, which meet georectification accuracy requirements for AirMISR imagery.

ACKNOWLEDGEMENTS

The authors gratefully acknowledge the efforts of the MISR / AirMISR Principal Investigator, D. Diner, Instrument Scientist C.Bruegge and the members of the Science Data System Team: M. Bull, S. Adams, and E. Hansen. This work was carried out by the Jet Propulsion Laboratory, California Institute of Technology, under a contract with the National Aeronautics and Space Administration. For further information, see the MISR web site at http://www-misr.jpl.nasa.gov.

REFERENCE

[1] Diner, D. J. et al., "Multi-angle Imaging SpectroRadiometer (MISR) instrument description and experiment overview," IEEE Trans. Geosci. Rem. Sens. 36, pp. 1072-1087, 1998a

[2] Diner, D. J. et al., "The Airborne Multi-angle Imaging SpectroRadiometer (AirMISR): Instrument description and first results," IEEE Trans. Geosci. Remote Sens., 36, 1339-1349, 1998b

[3] Jovanovic, V. M. et al., "MISR photogrammetric data reduction for geophysical retrievals," IEEE Trans. Geosci. Rem. Sens., 36, No. 4, 1998

[4] Korechoff, R. P. et al., "Distortion calibration of the MISR linear detector arrays," in Proc. SPIE, Denver, CO, Aug. 1996, vol. 2820-19

[5] Lee, C. et al, "Rigorous Mathematical Modeling of Airborne Pushbroom Imaging Systems," Photogrammetric Engineering & remote Sensing, Vol. 66, No. 4, April 2000, pp. 385-392

[6] "LTN-92 Inertial Navigation System: Installation / line Maintenance," Litton, Aero Products, Rev. 15, 1996

[7] Mostafa, M.M.R, et al., "A Multi-Sensor System for Airborne Image Capture and Georeferencing," Photogrammetric Engineering & Remote Sensing, Vol. 59, No. 12, December 2000, pp. 1417-1423

[8] Paderes, F. C., et al., "Batch and on-line evaluation of stereo SPOT imagery," in Proc. ASPRS, 1989, vol. 3

DEVELOPMENT OF VIEWERS FOR INTERACTIVE 3-D VISUALISATION OF GEODATA

Admire Kandawasvika and Michael Hahn
m.hahn.fbv@fht-stuttgart.de
Fachhochschule Stuttgart - Hochschule für Technik
- University of Applied Sciences Stuttgart
Department of Surveying and Geoinformatics
Schellingstr. 24
70174 Stuttgart

KEY WORDS: Geodata, 3-D visualisation, interactive, viewer, interface

ABSTRACT

Advancements in three-dimensional (3-D) geospatial data acquisition techniques have led to continuous growth of geographic information. The challenges imposed are how to handle and extract meaningful information from such data in a fast, easy and effective way. The integration and visualisation of these data for the purposes of planning, information-marketing or decision-making are further important research issues of Geoinformatics. This paper tries to address the above issues by means of developing browsers or viewers for visualising geospatial information in their third dimension.

In this paper, some existing visualisation technologies are summarised. General and specific issues of developing 3-D viewers are outlined. For this research, a viewer for visualising places of interest of Stuttgart city model has been developed using an ActiveX control provided by the Skyline Software company. The specifics on this viewer development and the programming part are explained. Focus is given on optimised interface design and functionality.

The future trend in geoinformation science is towards 3-D, real-time, interactive, and realistic visualisations. Most of the viewers or applications will be internet-based. Therefore issues of data streaming and bandwidth have to be handled with care. Marketing of geodata will bloom on the electronic market in the Web. Whether ActiveX technology, Java3D APIs or C++ libraries will be the main tool for 3-D viewer development in future is not yet clear. But, for now, it is quite efficient to develop applications using ActiveX controls.

INTRODUCTION

Advancements in three-dimensional geospatial data acquisition techniques have led to continuous growth of geographic information. A variety of geodata (i.e. data with geographic reference) exists in different format and resolution and from different sources. Particular challenging tasks are the integration of such data under a single environment and the visualisation, for example, for the purposes of planning, information-marketing or decision-making. This paper tries to address the above issues by means of developing browsers or viewers for interactive 3-D visualisation of geospatial information. Reality is three-dimensional and visualising data in 3-D is more effective and more easy to understand for a wider spectrum of users – ranging from a layman to a professional. Currently, three-dimensional visualisation is shoving its way to popularity on the Internet. There will also be a great demand for specific 3-D visualisation applications and this in-turn will increase the need for developing specific viewers for such applications.

It is often argued that data determine the purpose of a visualisation application. In fact, it is data of specific objects or themes that is modelled and that needs to be visualised. In this work the example data are virtual cities or city models. Cities are areas of fast development and the magnitude of their complexity increases geometrically with each major development. Planning of such areas becomes more challenging. A wider range of people have to be involved also in decision-making related to any developments. However, for this research, an existing city model of Stuttgart, Germany, was the sample data to carry out experiments during the development of a new viewer (see section on *development of threedviz viewer*). The used city model comprised a digital terrain model (DTM) with an orthophoto draped over the DTM for texturing and some models of textured buildings.

What should be observed in the development of viewers ?

Since the focal point of any visualisation is the user, the emphasis is placed on simplicity and limited or optimised functionality of such interfaces in order to accommodate the needs of that customer or user. Browsers enhance fast and quick viewing of multi-data under a single environment. The learning-curve required by the user to work with a viewer is far much shorter than that for a full visualisation software. Existing visualisation software which will be discussed in the following section is somehow complex and generically designed in order to supply a number of different applications. This generic type of software does not answer all problems faced by specific applications. Two options may appear: either to customise the existing software or to build viewers for specific applications. For this research, the latter seems to be a promising option depending on the level of sophistication of an application. Viewers are also simple media for communicating ideas and collaborative decision-making can be facilitated easily. Marketing of geodata especially on the electronic market in the Web can greatly be enhanced by means of viewers.

BACKGROUND

There are dozens of commercial terrain visualisation software (see www.tec.army.mil) , and several more freely available (e.g. VRML browsers) on the Internet. However, many of these software are generic or specific to some extent in order to suit their own applications. A project, Pathfinder99 (NIMA 1999), was carried out to analyse and evaluate some of the existing visualisation software. One of the conclusions drawn was that each and every software had some functionality unique to it. Up-to-date, some visualisation companies have produced modelling and visualisation packages (i.e. explorers) separately. The modelling software is used for creating or building models or scenes and the output is usually a proprietary format for their visualisation packages. Integration of geodata is achieved within these modelling packages and data of different format (for example VRML files) can also be imported into such packages. Following are short descriptions of some visualisation software developments.

3-D visualisation technology efforts

VMRL 2.0 : VRML stands for virtual reality modelling language. It is an International Standards Organisation (ISO) standard for describing 3-D objects or worlds on the World Wide Web (shortly named *Web*). VRML can also be seen as a 3-D language for representing complex features with minimal text. VRML browsers are required for reading and interpreting such text into appropriate geometry and motion. Examples of VRML viewers are Netscape’s Live3D, Sony’s CyberPassage and SGI’ Cosmo Player, etc. More recently VRML is being extended to accommodate geo-referencing of data (e.g. GeoVRML).

SGI (Silicon Graphics Inc.) is also active in visualisation technology. It uses its object-oriented 3-D toolkit for developing visualisation applications. *IRIS Explorer* is a viewer developed using IRIS inventor library (now called *Open Inventor library*). SGI’s applications can run on different platforms including Sun, IBM, HP, Windows and Mac (Robert 1995). Photo-realism, high-quality rendering and interactive functionality are further issues addressed by SGI visualisation software.

ViewTec, Germany, has a powerful software *TerrainView* which supports 3-D real-time VR (virtual reality) solution. Visualisation of data interactively and photo-realistically is possible. They have a module METEO for interactive visualisation of realistic weather simulations such as animated clouds, rain and snow fall.

Skyline Software, Israel and USA, provides a pair of software TerraBuilder and TerraExplorer (see http://www.skylinesoft.com) for interactive, photo-realistic, 3-D terrain visualisation. TerraBuilder is a modelling package which integrates data of different resolution, type, and from different sources. The output format is proprietary and can only be read using TerraExplorer. Internet visualisation of geodata is their focus and they provide a powerful data streaming solution. Both the above mentioned software were developed using Skyline’s software development kit (SDK) called *TerraDeveloper*. A first viewer developed for this research was realised using this SDK. Skyline has been working on developing specific applications in sectors such as real estates, military, tourism, sports, and city planning (see their homepage).

G-Graphix, Germany, is a young company whose future seems to be bright. Their products G-Scene (builder) and G-Vista (explorer) were developed using their own library called *G-Render*. The company also focuses on interactive, photo-realistic 3-D visualisation of geodata.

To summarise the above efforts from different vendors, the software are a bit generic and complex. They try to accommodate a number of applications which is to some extent an advantage but not always. However, all the vendors foster issues such as photo-realism, real-time and 3-D interactive visualisation. From this point on, we try to narrow down to technical details on development of viewers for purposes of realising specific applications. We will look at what factors to consider, tools required, and an example of a specific viewer development.

GENERAL DEVELOPMENT CONCEPTS FOR VIEWERS

What are the considerations?

In this paper, three general aspects, in the authors view, which have to be considered when developing viewers are the users or customers, the application (generic or specific) and the geospatial information (generic or specific) to be displayed. However, in our research we are focusing on the specifics.

As mentioned earlier, the users are the focal point of any visualisation. Mariano (2001) went further to say that the browsers should help the people to deal with information overload and organise them in a form that they can easily address and remember. In short, the viewers should give users a clear insight into data. Eick (2001) suggested that when designing and implementing a visualisation system, it is of uttermost importance to consider the perceptual acuity and activities of the end user. Physiological and psychological aspects of humans (refer to Williams et al 1995) are also important issues to consider but they are beyond the scope of this paper. Nevertheless, a viewer should always preserve user context. Another point to consider is the level of sophistication of the users and their wishes. A viewer as a means of communication should facilitate flexible user interaction by means of a mouse or keyboard.

As with data, the type of application and its level of complexity determine the functionality required of a viewer. Note also that some applications may benefit from an immersive environment whilst others do not. Data availability is also a determinant factor for the success of a project or application. Specific data may lead to a specific application.

Some specific aspects to consider in the development of viewers are the functionality provided by the viewers themselves, hardware and software. A summary of functionality of a viewer developed in this research give an insight into basic operations expected of a 3-D viewer (see section on *development of threedviz viewer*). We now look at some software and hardware issues. Software cover mainly the operating system the viewer runs on. Most of the viewers are run on Windows, MacOS, Linux and Unix platforms. Those browsers which run on the Internet require additional software or plug-ins. Microsoft Internet Explorer and Netscape Navigator or Communicator are the commonly used browsers on the Internet. For the hardware, many viewers are run on personal computers (PCs). The trend is PC-based 3-D visualisation (Kennedy et al 1995). As the power of hardware and software increases, Williams et al wrote that the future is where the rendering of scenes is done by the hardware and the software will calculate the objects to pass for rendering. This will result in fast 3-D visualisations.

To summarise, we look at the importance of hardware graphics in the development of viewers. Hardware acceleration may be used for geometry, real-time lighting, clipping, transformation and rendering. In the case of OpenGL, some of the specific effects of hardware acceleration are real-time weather simulations (i.e. fog), anti-aliasing, volume shadows, transparency and reflection calculations, 3-D textures and bump mapping, and volume rendering (see www.opengl.org). Please refer to Watt 2000 for more information on the above concepts. In short, all the fore-mentioned effects are calculated during rendering. Note also that some visualisation applications may be run without hardware acceleration but better results of high quality visualisation are achieved through hardware acceleration – need powerful PC.

What tools are required for developing viewers ?

In order to develop viewers, there are software development kits (SDKs) or application programming interfaces (APIs) available from different software vendors or developers. Some examples are TerraDeveloper (Skyline), G-Render library (G-Graphix), Open Inventor library (SGI), Java3D API (Sun Microsystems), World Toolkit (Sense8), and Intergrator (Evans and Sutherland), etc. Equipped with any of these tools, one needs an interface development environment (IDE) for Visual C++, Visual Basic, Java or Borland C++ for programming the viewers. An IDE helps in designing the viewer graphical interface and assembling of functions (i.e. coding).

Most of the vendors provide libraries and/or ActiveX control for application development (see an example in figure 1). It is easier and faster, from our point of view, to develop applications using an ActiveX control. If an ActiveX control adopts the standards of Microsoft then it can virtually be run on any Windows platform. Another advantage is that many host programming languages can be used to code the control provided the host language can communicate with that control.

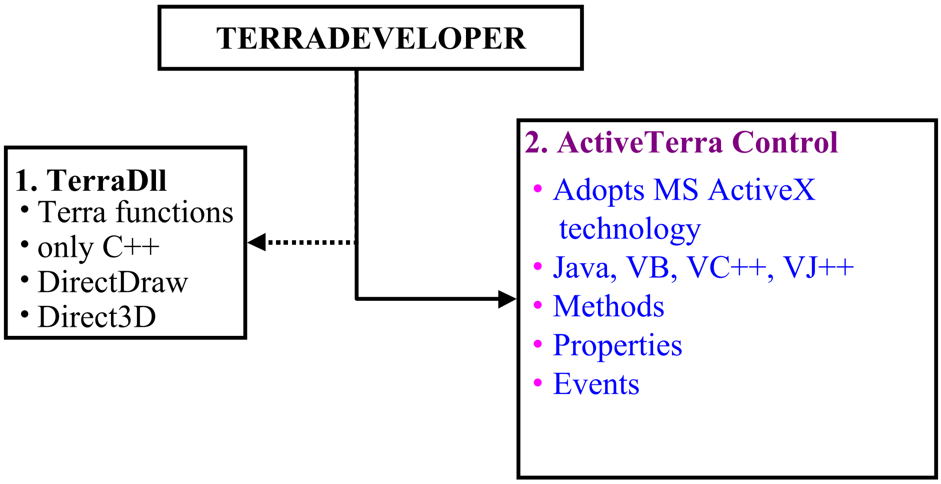

Figure 1. Skyline's SDK containing an ActiveX control and C++ functions

To render a scene, a 3-D engine is required. Low-level APIs like Direct3D or OpenGL are used for developing these 3-D engines. Some libraries provide both APIs (Direct3D/OpenGL) for rendering, for example TerraDeveloper and G-Render library. Figure 2 clearly illustrates a visualisation system architecture. This figure is a generalised version of G-Graphix system (see www.g-graphix.de). Specific applications may be realised in the form of viewers.

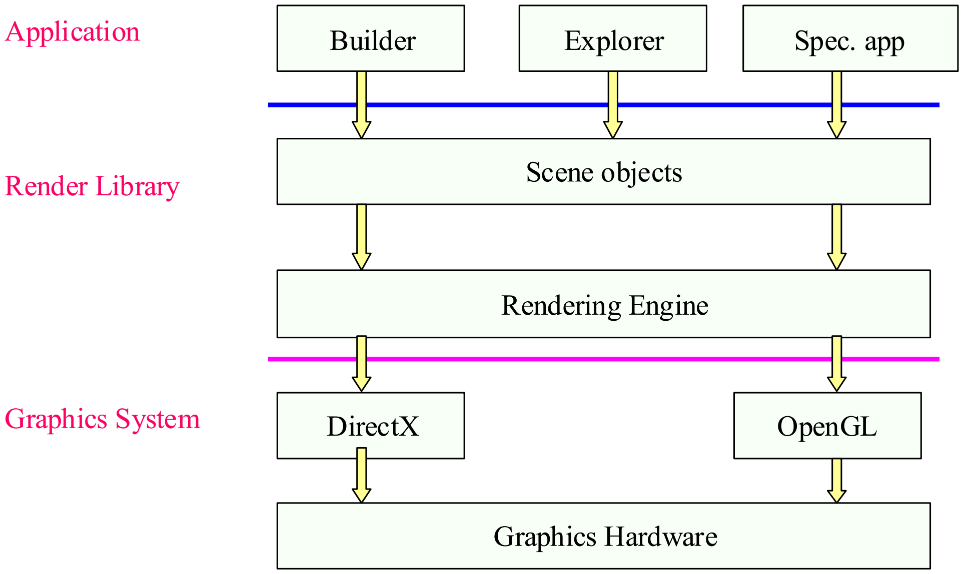

Figure 2. System architecture example of a 3-D visualisation system

DEVELOPMENT OF THREEDVIZ VIEWER

ThreeDViz is a viewer developed as a master thesis project to visualise parts of interests of Stuttgart city model. The viewer was developed using Visual Studio for Visual C++. Figure 3 shows the viewer interface during a design stage.

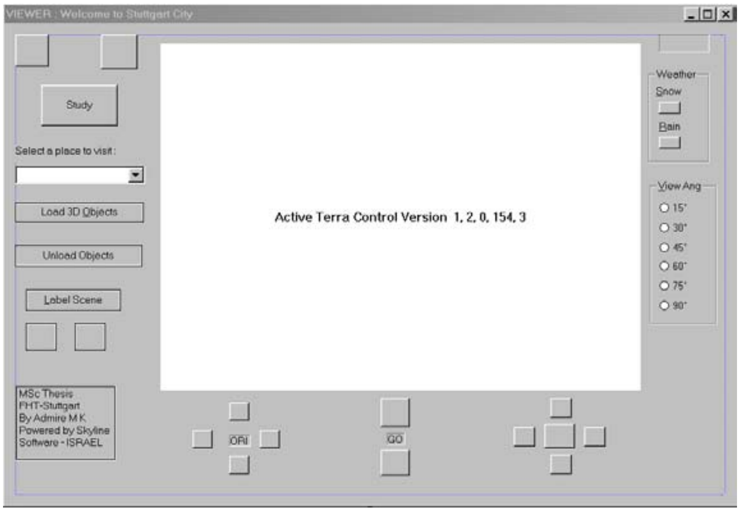

Figure 3. ThreeDViz during a design stage

The interface has control buttons for loading 3-D objects and labels at will from the hard drive, CD or DVD. Weather simulations such snow and rain can be activated at the click of a button. Figure 4 and 5 show a final appearance of the viewer and snow simulations respectively. The bitmaps for navigation buttons on the final interface design were created using Visual Studio for Visual C++ graphics editor and loaded programmatically during program or viewer initialisation. There are also option buttons for changing the viewpoint angle from 15 degrees to 90 degrees (see figure 3). These fixed view angles enables the user to change the perspective angle. At 90 degrees, the user will be observing the terrain in 2-D.

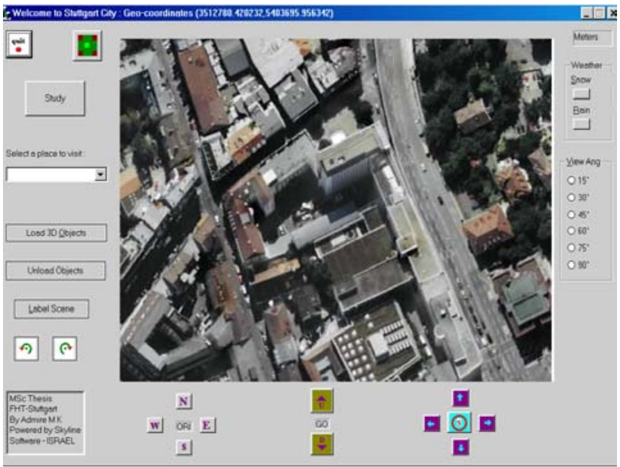

Figure 4. Final interface design

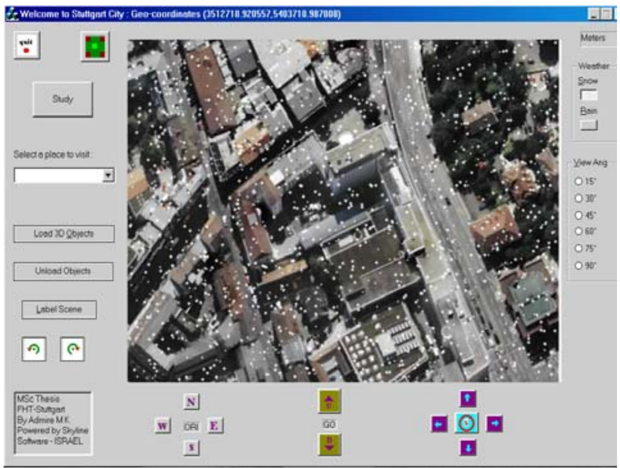

Figure 5. Snow (white spots) simulation

At the bottom of the viewer, there are buttons (N,E,W,S) for observing buildings from north, east, west, and south. There are also buttons for moving up into the sky and down towards the terrain. The user can also move to the left, right, forward, and backward during walkthroughs. It is also possible to rotate the terrain about the viewpoint. Note that dynamic movements are achieved by means of direction prediction calculations. When the user clicks the forward button, the viewpoint is moved dynamically in that direction until the user changes it. Besides labelling places of interest, the user can also select places of interest he or she wants to visit. For this application only a fixed number of places can be selected from the combobox “select a place to visit”. A study button moves the viewpoint to the required place. The viewer displays at the top the geo-coordinates of the current user position in the scene. We now look at some examples of coding ActiveTerra control.

Programming

Coding an ActiveX to life is not that difficult. Here we give two examples, one for loading the terrain with an orthophoto draped on top and the other for loading a building on the terrain.

Loading terrain : Here we will load a textured Stuttgart terrain.

```
void CThreeDVizDlg::InitTerraControl(){
      char  dir[_MAX_PATH] = {0};
       char newdir[_MAX_PATH] = {0};
       GetCurrentDirectory(_MAX_PATH,dir);
       char* pdir = strstr(dir,"ThreeDViz");
       strncpy(newdir,dir,pdir - dir);
       strcat(newdir,"Stuttgart.mpt");
       /***** initilize the control
      m_ctlTerraControl.Init(newdir,0);
      /***** set the render parameters
       /*****initialize weather elements
       /- rain, snow, clouds
       /***** set camera start parameters
       m_ctlTerraControl.Pause(0); }
```

From the above code, the terrain (Stuttgart.mpt) is loaded during initialisation of ActiveTerra control (here named *m_ctlTerraControl*). A system method called *GetCurrentDirectory* is used to locate the terrain file. The extension (*.mpt) is a proprietary format for Skyline from TerraBuilder software. After loading the terrain, the control must be told to render the scene and this is done by *Pause (0)* method. A zero argument tells the system not to pause the render engine which means the scene or object must be rendered. At the time of developing this application, Terra engine used voxel-based rendering technique. To run the viewer, DirectX 5.0 or higher version was required.

Loading a 3-D object : Here we will load a building and position it on its geographical location on the terrain.

```
m_ctlTerraControl.TerraD3DLoad(newdir, "b2.xpc",TERRA_MESH);
m_bau2 = m_ctlTerraControl.GetLastRef();
m_ctlTerraControl.TerraD3DAdd(m_bau2);
m_ibau2 = m_ctlTerraControl.GetLastRef();
// get the ground height
m_ctlTerraControl.TerraMPTGetHeight(bau2_X, bau2_Y, dForceAcc, dSampleSize);
dGroundHeight = m_ctlTerraControl.GetLastDouble();
m_ctlTerraControl.TerraD3DPosition(m_ibau2,bau2_X, dGroundHeight,bau2_Y);
m_ctlTerraControl.TerraD3DScale(m_ibau2, 1.2, 1.5, 1.2);
```

In the code immediately above, the control is told to load a building (i.e. TerraD3Dload) as a mesh object. This method causes memory to be reserved for the object. By calling TerraD3Dadd() method, the building is displayed in the scene. The building is positioned and scaled by using TerraD3Dposition() and TerraD3Dscale() methods. Figure 6 shows a viewer displaying some loaded buildings. Note that before loading any objects, the rendering engine has to be stopped using *Pause (1)* and resumed after loading the objects.

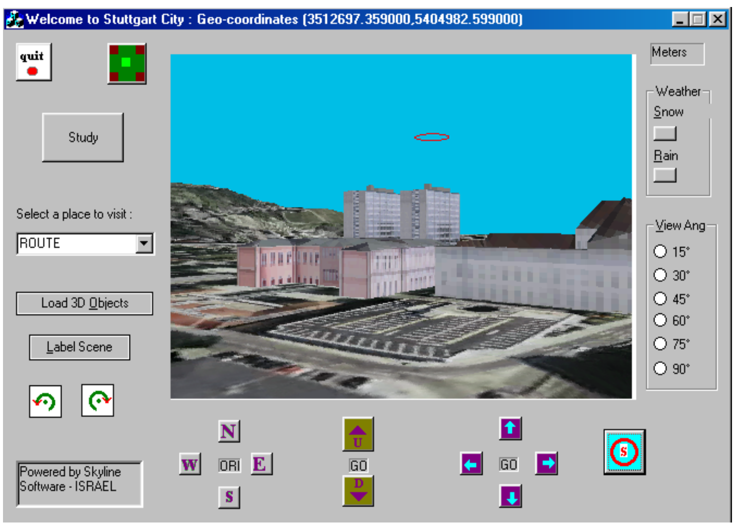

Figure 6. 3-D Objects (buildings) on terrain

Figure 7 shows part of a scene displayed in 3-D. All the buildings are rest assured to be on the terrain. The idea of having buildings floating in the air, as with some systems or viewers, is not pleasing.

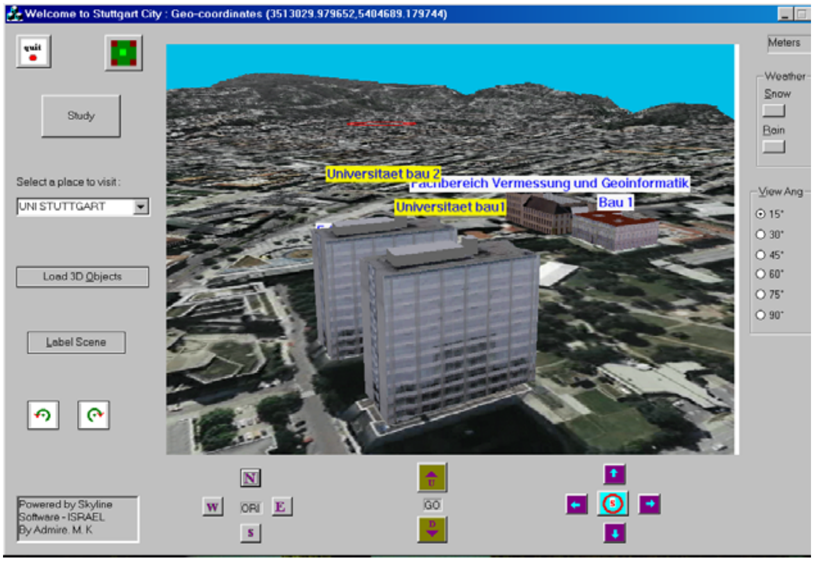

REVIEW AND SUMMARY

Some problems of visibility were faced when simulating snow and rain. The weather elements were sometimes obscured by buildings. This however is a sorting problem of objects within a 3-D scene. Further work is being done to solve the inclusion of weather elements into a scene. Currently, some work is being done to ensure loading of buildings as a layer or single set instead of introducing these objects to the scene individually. When buildings with higher texture resolution were loaded to the scene, the rendering performance was reduced. Increase in PCs power will resolve this problem in the future. Sometimes a heavy textured scene would reduce the fluidity of navigation within the scene. Efforts are being made to see how best can large scale virtual cities be handled and at the same time maintaining high quality photo-realism.

Here is a summary of the functionality realised by our first viewer.

- **Viewpoint** : It is possible to set the viewpoint with respect to the visualized objects or entities in the scene. Dynamic movements are realized through changing the viewpoint position.
- **Navigation controls**: The software recognizes relatively easy navigation controls which can be used to change the viewpoint of the visualized objects or entities.
- **Interaction** : The user can use a mouse for interaction.
- **Speed control** : The user has control over the speed of dynamic movements within the scene.
- **Scene furnishings** : The user can add objects to the scene by clicking buttons on the viewer or by means of an open dialog interface.
- **Selection**: The user is able to make simple selection queries about the data. Selection by coordinates method is used to move the user to a specified point in the scene, for example the viewpoint can jump to any required building object.
- **2D and 3D support** : The 3D viewer supports 2D, 3D, and other volumetric representations and displays.
- **Processing** : Smoothing, filtering, and anti-aliasing techniques are realized.
- **3D Transforms** : It is also possible to perform 3D transforms.
- **Rendering and data streaming** : The visualization software provides good quality rendering and efficient means of data streaming. The visual qualities such as texture, colour, illumination, and shading are also properly handled by the viewer.
- **Geo-coordinates support** : The user can locate him/herself by means of geo-coordinates. The viewer can also support different geo-coordinate systems, i.e. UTM or geographic (lat/long). Different units of measurements are also supported, i.e. metres and feet.
- **Texture mapping** : The viewer handles well textures on objects – photo-realism is maintained.

CONCLUSIONS

This paper has covered issues related to the development of viewers for the purposes of realising specific, interactive 3-D visualisation applications. All the developments of such systems should consider the needs of the end user. The future trend in geoinformation science is towards 3-D, real-time, interactive, and realistic visualisations. Most of the applications will be internet-based provided issues of data streaming and bandwidth are handled with care. Marketing of geodata will bloom on the electronic market the Web.

Furthermore, three-dimensional visualisation will integrate geographic imaging fields such as digital or web photogrammetry, remote sensing, GIS, etc. in solving complex projects. There will be demand in realisation of specific viewers in the fields of tourism, real estates, marketing, forestry, urban planning, and other geo-related fields. Whether ActiveX technology, Java3D APIs or C++ libraries will be the future main or predominant tool for 3-D viewer development, its not yet clear. But, for now, it is easy, in our opinion, to develop applications using ActiveX controls.

BIBLIOGRAPHY

Computer Associates (1998). PLATINUM technology Awareness Industry's First Decision Support Tool to Leverage True 3D Data Visualization Technology. See http://www.platinum.com/products

Csuri, Charles (1989). Visualization Tools. Computer Graphics World. 1989 July;12(7).p.194.

Cuccu, Fabrizio; Moltedo, Laura.(1993). Texture Mapping for Scientific Visualization Environments. Computers & Graphics. 1993; 17(2):pp.131-136.

Eick, Stephen G. 2000. Visual Discovery and Analysis. IEEE Transactions on Visualization and Computer Graphics, vol.6, No.1, Jan-March 2000.

G-Graphix Homepage. www.g-graphix.com

Iles, Robert (1995). Open Invetor, VRML, and Related Technologies. NAG Ltd(1995). Internet reference: http://www.agocg.ac.uk/train/hitch/vr/report.htm.

ISO/IEC 14772-1 : 1997 (1997). The Virtual Reality Modeling Language. December 1997. Available on-line at http://www.web3d.org/specifications.

Kennedy, J., Mitchell, K., Barclay, P.and Marshall, B. 1995. 3D Information Visualisation: Identifying and Measuring Success. Position Paper, University of Glasgow, 2nd FAVIDA Workshop, July 1995.

Mariano, G. 2001. Start-up sees browser's future in 3D. Available on Internet: http://www.news.cnet.com, Feb. 15 2001.

NIMA (1999). National Imagery and Mapping Agency Execute Summary: Pathfinder99: Scene Visualisation. Source : http://www.erdas.co.uk/news/Reviews/NIMA-Report.htm.

OpenGL : the 3D standard. http://www.opengl.org

Skyline Software Systems Ltd.(1999) Terra Programmer´s Reference manual. www.skylinesoft.com.

Mueller Systemtechnic GmbH (2001). ViewTec. http://www.muellersystemtechnik.de

Watt, A.(2000). 3D Computer Graphics. 3rd Edition.

Williams, James G., Sochats, Kenneth M. and Morse, E. (1995). Visualization. A Review of Information Science and Technology. 30(4).pp161-194. Press Release. November, 2, 1998.

Witte, Tom (2000). Commercial Terrain Visualization Software Product Information.US Army Corps of Engineers, www.tec.army.mil/TD/tvd/survey/ZCAP.html, October, 13th , 2000.

A KNOWLEDGE-BASED INTEGRATED SYSTEM TO MONITOR DESERTIFICATION IN LEBANON THROUGH REMOTE SENSING

M. Khawlie*; B. Hansmann; T. Darwish*; D. Lichaa El-Khoury**; G. Faour*; C. Abdallah*, & R. Bou Kheir***
*** National Center for Remote Sensing- Lebanon**
**** GTZ- Beirut Office**
Joint Workshop of ISPRS WG1/2, 1/5 and IV/7
High Resolution Mapping from Space 2001, September 19-21, 2001

INTRODUCTION

Lebanon is considered among those Middle East countries suffering symptoms of desertification, and where human interference is contributing significantly to land degradation (Khawlie, 2000; Masri et al., 2001). As for the natural component, available observational evidence indicates that regional changes in climate have already affected this part of the world among others (IPCC, 2001). Even though Lebanon signed/ratified the United Nations Convention to Combat Desertification UNCCD in 1995, several aspects hinder facing properly the problem of desertification in the country. These include improper management of natural resources, the lack of relevant awareness, the ill financing of priority development projects, and a large gap in upgraded relevant databases or maps.

The latter aspect is very crucial, and the application of advanced information technology on desertification, i.e. remote sensing, constituting the main purpose of this paper, should help fill up this gap. This is important in creating proper databases, in interpreting trends of change, and in implementing an integrated knowledge-based system to approach the problem.

There are several processes, in addition to climate change, which are putting additional pressure on the environment in Lebanon including chaotic urbanization, forest fires, overgrazing, excessive resource exploitation, soil erosion and water depletion (Sadek, 1999). Obviously, these are leading to various environmental impacts that are furthering land degradation and eventual desertification. The effects of the above-mentioned causes can be grouped under three components:

1. Physical degradation, including soil erosion, decreasing fertile land, increase in salinization, reduced water availability etc. (Bou Kheir et al., 2001; Darwish, et al., 1999; Khawlie, 2001)
2. Biological degradation, including degradation of forests, reduction of biodiversity (incl. agro-biodiversity, increase in deleterious species, etc. (Masri, et al., 2001; Sadek, 1999; Safi, 1999)
3. The social fabric including the decrease in available vital resources, land desertion, rural emigration, increased urban stress, etc. (UNDP, 2000; Kallab, 1999; UNESCO, 1997).

Since, as mentioned before, relevant data are not readily available, remote sensing may play a crucial role in the build up of a knowledge-based system, e.g. to assess desertification in Lebanon. In this respect Lebanon is just starting to explore the full potential of Remote Sensing in the field of assessing desertification.

Remote sensing could significantly support studies related to climate instability, human malpractices and resources depletion. Selective data extraction through different and multi-temporal imageries and their analysis would provide relevant information, which are a prerequisite for any further sustainable management and development.

DESERTIFICATION AND REMOTE SENSING IN LEBANON

In the UNCCD desertification is defined as land degradation due to climate change and human activities affecting the terrain, its natural resources, ecosystems and the social fabric. Furthermore, desertification processes potentially threaten the arid, semi-arid and dry sub-humid zones. In Lebanon those areas constitute about 60-70% of the land, and are being exposed to a multitude of stresses from natural causes and human activities (Khawlie, 2000), like soil erosion, decreasing land fertility, deforestation, and salinization.

The Global Circulation Model (GCM) used in the eastern Mediterranean, predicts an average of 1.6°C increase in temperature by the year 2020, and an equivalent average of about 3% less precipitation, consequently this will lead to a change the bioclimatic zones towards more prone to desertification processes. This would expectedly leave a huge impact on the stability of ecosystems and consequently would affect the social fabric. Already, thousands of forest fires flare up every year, adding further deterioration to the chaotic urban sprawl and destroying more productive green land.
Comparing agricultural production (olives, fruits, vineyards, citrus) of the 1960's and late 1990's shows a significant reduction in the productivity of the agricultural sector (Table 1), which is partly due to an advanced stage of degradation in various agricultural areas. The Table shows that the change in the agricultural output is quite serious. It further points out the quick rate of deterioration (notice percentage of forest in the 1980s). But the distinct change is noticeable in barren lands, most of which were rangelands before the last three decades.

Table 1. Change in land use and some land cover over Lebanon between 1960s and 1990s

Land use 1980s			**Hectares**	**% of country**
Arable land			260000	25
Forest (all kinds)			135000	13
Abandoned lands, mostly old terraces			70000	7
Rocky, non-cultivated lands, degraded range lands			515000	52
Urban and constructed areas			27000	3
Land cover change 60s-90s	**Area km^2**		**Change km^2**	**Change %**
	1960s	**1990s**		
Forest	934.3	629.8	-304.5	-32.5
Citrus	268	174	-94	-35
Fruits	544.6	195.6	-349	-72
Olives	437	301	-136	-31
Vinyards	365.8	65.2	-300.6	-82
Barren or deserted	1076.6	4370	+3294	+306

(Adapted from FAO, 1980; Masri et al., 2001)

Several components, which will be considered to assess desertification, can definitely be supported by remote sensing technology and may provide an essential contribution to the development of knowledge-based systems (Table 2). However, as mentioned before, the operationalization of remote sensing, for a sound natural resource management, is lacking behind, and still needs to be incorporated as a tool in the various Ministries and relevant organizations. In fact, some applications of remote sensing to build up a knowledge base have been successfully carried out, like the current production of the first unified 1:50.000 soil map of Lebanon (Darwish, 2000). Both Landsat TM and SPOT were used in evaluating the terrain geomorphology, and help in differentiating soils according to textural variations, profile evaluation and structural identities.
Another important application is the assessment of soil erosion, which is one of the major processes of land degradation in Lebanon and can reach 70t ha^{-1} annually (Bou Kheir, in progress). Such Erosion rates will definitely have serious constraints of any possibility of carrying a healthy vegetal cover. In fact, if this cover is less than 30% of the area of the pixel, the soil spectral character dominates (Girard & Isavwa, 1990). This 30% threshold constitutes an important element of the knowledge base and can be easily used to verify areas vulnerable to erosion. This is especially applicable when linked to spectral soil characteristics, e.g. color, composition and brunification (Weismiller et al., 1984; Altherr et al., 1991).
Furthermore, Forestry is certainly a theme where remote sensing has taken large strides forward, and it is a direct indicator of a healthy plant cover. Land cover/use maps of Lebanon produced from Landsat and Spot in the 1980s give an excellent working base to the knowledge system if compared to satellite imageries in late 1990s and early this millennium. It is this and other comparisons that allowed arrive at estimating the 32% loss in forest cover, standing roughly at the annual 1% as noted before. Moreover, the thousands of fires that are recurring every year between June to November can be easily monitored through remote sensing, but unfortunately they are not. Indeed, remote sensing can contribute to building-up a knowledge-based system that can differentiate spectrally these forests before the fires, during and after the fires. Forest logging and

burning, or the introduction of some diseases that would degrade forests can and should be monitored, and assessed through remote sensing.

Table 2. Use of remote sensing in assessing major aspects of desertification

	Themes / Aspects	Nature-related	Human-induced
Resources	Water (& Climate)	• availability • regime • moisture (in soil) • precipitation/evaporation	• depletion • induce change (plus natural: climate change)
	Soil	• availability • type • erosion (human: bad practice) (natural: slopes & torrential rain)	• depletion • over saturation • salinization (plus natural: salt-water intrusion) • non-fertile
	Rangeland	• availability	• overgrazing • degrading
	Forest	• availability • type • fires	• logging • burning • diseases
	Ecosystems (bio-climatic zones)	• availability • type • modification (due to climate change)	• reduction • modifications • introduce foreign species
Others	NDVI	• seasonality • type	• introduce change • diseases
	Urban Change	• suitable land	• depletion & pollution of all resources including land • destruction

Recently, there is an attempt to make an intensive use of the NDVI, especially of small scale satellite imagery like NOAA, in order to get a better understanding of the dynamic changes of the green cover and to pin point the ‘hot spots’ of fast changing environmental conditions. This approach will help to increase the awareness of decision makers and to visualize the dramatic changes.

A further application of remote sensing in Lebanon is the monitoring of urban change, which has been rather recently carried out (Huybrechts, 2001; Abed, 1999). Urban congregations are expanding in the country replacing green space and agricultural plains, thus increasing the rate of land degradation and decreasing the productive land. Therefore, it is necessary to upgrade the knowledge-based system for understanding the links between demand expansion and resultant degradation. Remote sensing can do that through image interpretation beyond the limits of pixel-based analysis.

Land cover change that has overtaken the Lebanese territory in the second half of the twentieth century is mostly due to chaotic urban expansion at the expense of agriculture, forestry and natural resources (Masri, et al., 2001). In the last three decades this expansion resulted in the estimated following losses: forestry about 32.5%, agricultural lands about 30%-40%, rangelands about 12%, while barren lands, degraded rangelands and urban-constructed areas increased 300%. These data were obtained from comparing multitemporal (1980s and late 1990s) data to older maps. This is still a lacking knowledge system as no proper monitoring, no focused environmental statistics and no implementation of relevant policies is taking place. It is certain that the use of remote sensing can improve the knowledge-base significantly.

It is obvious from the preceding that knowledge gaps abound. Generally speaking, there is no country-wide strategy for environmental monitoring and assessment, and specifically focusing on land degradation (desertification), which is one of the major effects of improper developments that have taken place in the

country. However, some positive signs in terms of sustainable development can be observed, so e.g. the ratification of the UNCCD, in which the country has to establish a NAP (National Action Program to Combat Desertification) which is just starting (see later section in this paper).
Although the application of remote sensing is fairly recent in the country, there are some efforts to foster further application, especially in the field of natural resource management and sustainable development. But, there is still a need for the introduction of an integrated approach, at which the information derived from remote sensing is directly geared to a knowledge-based system which, in itself, is integrated into the decision making process, e.g. for defining proper mitigation measures to combat desertification. Additionally, further development of the remote sensing techniques are required in order to meet the demand of information for small scale planning, like actual erosion assessment. Most national and global scale estimates and assessment of soil erosion have been of erosion hazard, not observed erosion. Existing data on the state of degradation are not answering needs, methods for degradation assessment are not well developed, and methods to monitor the impacts of degradation (e.g. upon crop yields, livestock output, etc.) are not well developed. Thus there are three major components, which should be further developed:

1. Methods for land degradation assessment,
2. Procedures/Methods for basic standardized information (maps, databases, etc.) on land degradation, at national, regional and global levels, and
3. Assessment of the impacts of land degradation on human societies and the environment.

BUILDING A KNOWLEDGE-BASED SYSTEM

The main idea is to use the approaches followed in object-oriented multi-scale image analysis and information about natural, economic and social phenomena simultaneously connected at the time they happen. Satellite imageries are capturing spatial data that a knowledge-based system should link to daily life operations in order to meaningfully extract valuable information for decision-making. A problem that is as serious as desertification must follow such an integrated systematic approach. Knowledge-based systems extract information from complex environments, and are driven by human understanding through use of advanced technology such as image analysis and information management.
Coming back to Table 2, three elements are chosen here to demonstrate how within a knowledge-based integrated system terrain data are transformed into manageable information. The chosen elements are soil erosion, NDVI and urban change. As each stands alone, it supplies data on a single environmental deterioration process. When combined together, however, they give meaningful information on a more “holistic” land degradation level, i.e. desertification. Thus, the 30% threshold, mentioned before, is a vegetal cover but is used to imply the vulnerability of soil. Similarly, eroded soils can often be recognized through typical changes in soil color as they reflect removed topsoil. Altherr et al., (1991) pointed out that there is a distinct spectral difference between brunification of topsoil, identifying pedogenesis, and eroded soils usually dominated by parent rock spectrum.
NDVI, on the other hand, can give information related to vegetal change detection due to forest fires, dryness, agro-cropping, diseased plants, type and intensity of green cover. In several instances forests are removed to give way for agriculture, or for urban sprawls, in others they are burned down (natural or human-made), and NDVI monitoring on weekly basis can imply the trend for increasing dryness, thus giving early warning for possible fires.
The above calls for proper mitigation measures. This is done by modeling used on priority areas together with relevant information on the causes and effects of desertification. The modeling methodology has been developed based on European research projects like MEDALUS and DeMon (CTM-ERS, 1999). The current results are dependent on the available knowledge base, and will be improved and adapted, if further and more updated information are available.
Land degradation involves a complex set of processes or factors that interact in space and time leading to a decrease in land productivity. Thus, it is necessary to identify the various indicators, which will provide the relevant information to define the desertification sensitive zones, and which ultimately will provide information on the proper mitigation measures to be considered (Fig. 1).
The ultimate goal of the modeling is to arrive at identifying Desertification Prone Areas (DPAs). The modeling will be based on a GIS analysis of the various physical, environmental and socio-economic factors shown in Figure 1, many of which are obtained through remote sensing followed by ground truthing. The

dynamics in DPAs will be monitored using remote sensing techniques. Five indices that are crucial in defining DPAs are: climatic, soil, vegetation, land use and demographic pressure index. Each is a resultant of various relevant inputs. Additionally, the procedure to define the DPAs should provide, besides a national zoning, the information on the status of the degradation process, which again will guide the selection of the proper mitigation measures and which can be grouped as follows:

1. degraded land ➡ reclamation needed,
2. in the process of degradation ➡ rehabilitation needed, and
3. threatened but still not degraded ➡ prevention needed.

Dealing with desertification and understanding the dynamics of drought involve a high degree of uncertainty with complex technical, socio-economic and political variables. The current knowledge and understanding of the trends of desertification processes and drought dynamics is a product of a sound field monitoring and space technology applications. The aspects and themes shown in Table 2 identify the major components to be monitored, as there are several indicators on each that can be detected to decide on their status. Some are to be monitored on weekly basis, e.g. NDVI during hot periods, or on daily basis, e.g. climatic data, or on seasonal basis or otherwise, to follow up changes being introduced or observe impacts.

There is still a need for promotional efforts, however, to bring about awareness, knowledge and understanding of space applications in policy making for desertification monitoring and assessment. In the framework of the UNCCD three major components are considered for monitoring, which are:

1. desertification processes,
2. impact monitoring of mitigation measures and
3. the implementation of the UN Convention to Combat Desertification.

These are indeed “phases” in the general approach encountering desertification, and should be built into the “knowledge management” system within the structure of agencies handling desertification in the country.

INTEGRATION OF KNOWLEDGE

Over the past two decades, the problem of land degradation in dry land regions has continued to worsen. The United Nations Convention to Combat Desertification (UNCCD) promotes a new approach to manage dry land ecosystems. Today, overcultivation, overgrazing, deforestation, and poor irrigation practices are degrading dry lands on every continent. Such overexploitation is generally caused by economic and social pressure, ignorance, war, and drought. This is leading to losses in prime resources: fertile topsoil, vegetation cover, and healthy crops, i.e. desertification. The Convention to Combat Desertification will be implemented in Lebanon through the National Action Program (NAP). It will address the underlying causes of desertification and drought, and identify measures to prevent and reverse it. A major component of the NAP is the involvement of the local communities, i.e. a bottom-up approach. The end result should be an evolving program that is “owned” by the very people who most depend on and understand the land.

The preceding points out to the necessity of integration as the inputs, eventually leading to desertification, are multi-sourced, multi-thematic and of different levels. In view of that, a significant reflection of integration and building a knowledge base on desertification is what remote sensing can do best: monitoring indicators.

An indicator is a parameter or an index providing concise and clear-cut information on a process it is sought to characterize, measure and monitor, and this with reference to a specific objective. An indicator contains quantitative information that helps to explain how processes evolve over time and varies in space (Gentile, 1998). There are many potential desertification indicators, they are heterogeneous and could be classified according to various criteria. Indicators are sometimes grouped together according to the objectives for which they have been designed, or subdivided into types and factors. Examples of the former include knowledge and monitoring of desertification and drought processes, and conservation, rehabilitation and sustainable management of natural resources. Examples of the latter include soil erosion (physical), salinization (chemical), plant biomass production or animal population (biological), and land use, urban sprawl, population migration, etc. (socio-economic).

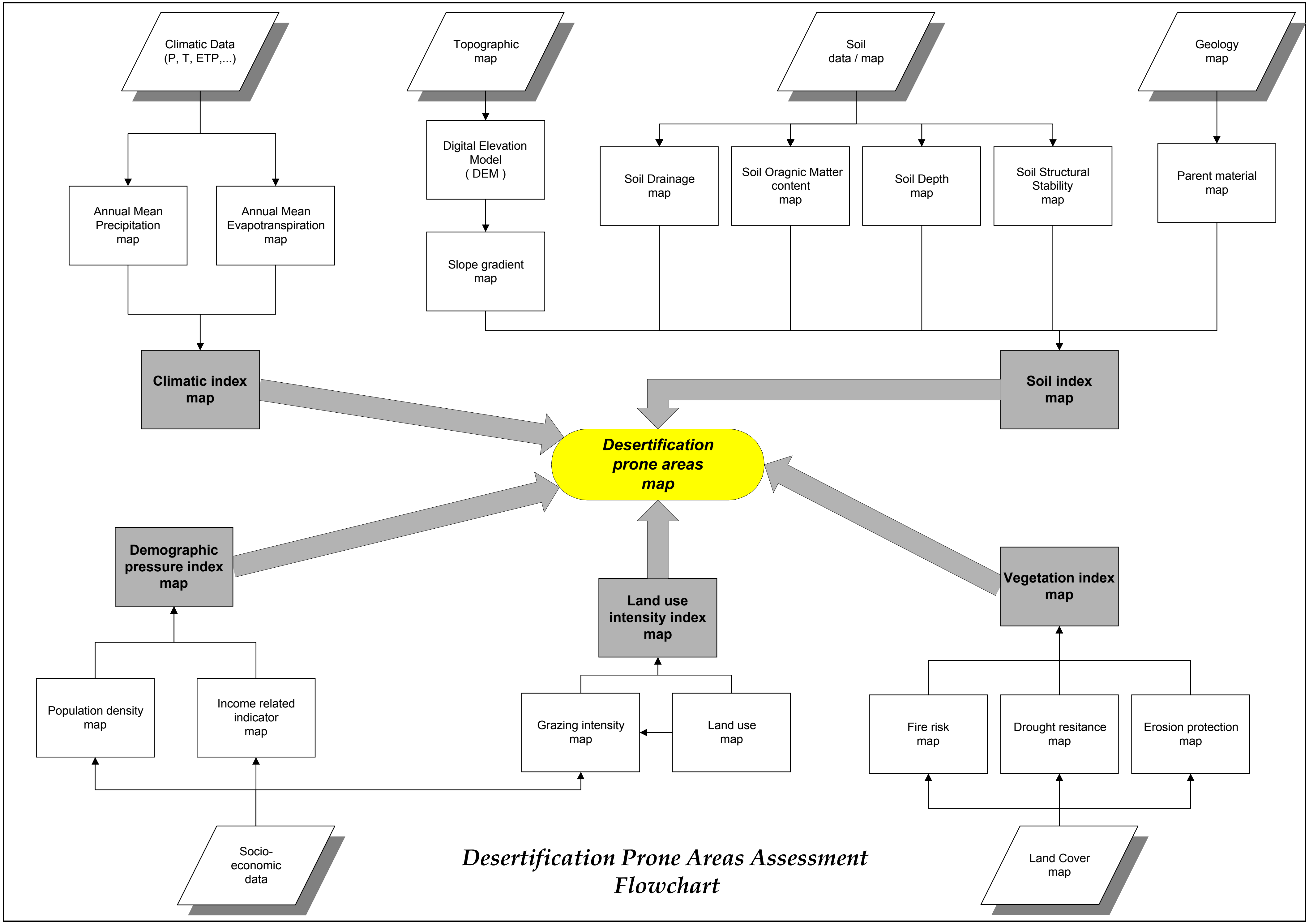

Desertification Prone Areas Assessment Flowchart

The DPSIR (Driving force/ Pressure/ State/ Impact/ Response) model, which follows the indicator-type knowledge analysis introduced by the European Environment Agency (EEA), is widely used for supporting environmental and development policies.

To end up this paper's concern with the knowledge-based approach, it is necessary to realize the importance of "knowledge management". It is handling information about natural, economic or social phenomena simultaneously connected with spatial data. A serious environmental problem like desertification can best be served by remote sensing, together with GIS, through prognostic modeling on all levels. The model in Figure 1 reflects this integrated approach and concern quite clearly. Thus, Lebanon, like many other developing countries, need solutions in integrated databases that concentrate on issues such as: defining spatial data standards, introduce spatial data in the educational program, encourage people's knowledge of and use of spatial data, closely monitor natural resources and the environment, and gear that knowledge to the problem at hand: e.g. desertification. Knowledge management is definitely not only information supplied just on demand. It requires: understanding the background problem, commanding the techniques in observing that problem and analyzing it, presenting the results in an appealing and meaningful manner, and taking the proper decision. Knowledge management is thus itself a process of integration of all the above.

Finally, the information must be navigated and disseminated. Once it becomes static, it will not serve its purpose. Spatial data on a dynamic environmental problem like desertification must be dynamic. Furthermore, any data must be "enriched" (interpreted and analyzed) in order to best serve its purpose. The proper application of remote sensing, and GIS, on desertification is enriching the data because it is extending them with additional information, that the human eye cannot detect. This is what may serve both the decision-maker and the ordinary citizen, and what makes the information well navigated, or properly disseminated.

Therefore, it can be summarized that the provision of any relevant information has to consider the following rules, which are the prerequisite for any successful use of the information. The information has to be:

- in an analyzed and interpreted manner depicting various different options or alternatives.
- provided in an understandable manner to the various different levels (users, decision makers).
- geared towards the need of the users.

REFERENCES

Abed, J., 1999. Mapping the post-war agriculture- urbanization interface in Greater Beirut using change detection of HRV Spot images and GIS. In: Support of Remote Sensing Techniques to Planning and Decision-Making Processes for Sustainable Development in Lebanon. CTM/ERS, NCRS.

Altherr, M.; Hill, J.; Mehl, W.; & Pollicini, P., 1991. NASA multi-sensor airborne campaign: reflectance spectroscopy Ardèche June-July 1991; technical note n°1.91.120: JRC, Ispra establishment, 23 p.

Atallah, T.; Darwish, T.; & Moujabber, M., 1999. Cultural practices and soil salinity in greenhouses in Lebanon. International Conference on Water Management, Salinity and Pollution Control towards Sustainable Irrigation in the Mediterranean Region. CIHEAM/MAI-B and CEC-DGI. Publications of Instituto Agronomico Mediterraneo, Valenzano-Bari. Italy: 115-123.

Bou Kheir, R.; Girard, M-C.; Shaban, A.; Khawlie, M.; Faour, G.; & Darwich, T., 2001. Apport de la télédétection pour la modélisation de l'érosion hydrique des sols dans la région côtière du Liban. Télédétection, 2:1:1-22.

CTM-ERS, 1999. Desertification Monitoring and Control: Analysis of Remote Sensing- Based Projects in the Mediterranean. Centro di Telerilevamento Mediterraneo- UNEP Environmental Remote Sensing Center- Palermo, Italy.

Darwish, T., 2000. Studying surficial resources to obtain a unified soil classification map for Lebanon at 1:50000. NCRS, Beirut.

Gentile, A.R., 1998. From national monitoring to European reporting: the EEA framework for policy relevant environmental indicators. Proceedings of the International Seminar on Indicators for Assessing Desertification in the Mediterranean, Porto Torres, Italy.

Girard, M-C., & Isavwa, A., 1990. L'état de l'art en télédétection sur les zones arides et semi-arides. Natural Resources, 26:1:3-9.

Huybrechts, E., 2001. Les extensions urbaines de la région métropolitaine de Beyrouth. Lettre de l'ORBR n°13, CERMOC, Beirut.

IPCC, 2001. Summary for policy makers- Climate Change 2001: Impacts, adaptation, and vulnerability. IPCC WG2 3rd Assessment Report.
Kallab, F., 1999. Socio-economic impacts. In: Lebanon's National Program for Climate Change (L-NPCC). UNDP, Ministry of Environment, Beirut.
Khawlie, M., 2000. Constraints and challenges of desertification monitoring and assessment in Lebanon. TPN1 Workshop, UNCCD- Asian Regional Thematic Network. Tokyo.
Khawlie, M., 2001. The impacts of climate change on water resources of Lebanon- eastern Mediterranean. RICAMARE Workshop, FEEM Bull. NRM/45.2001, Italy.
Masri, T.; Khawlie, M.; & Faour, G., 2001. Land-use/cover change, water resources and driving forces during 40 years in Lebanon. RICAMARE 1.1. Tunisia.
Sadek, R., 1999. Terrestrial ecosystems, natural habitats and wildlife. In: Lebanon's National Program for Climate Change (L-NPCC). UNDP, Ministry of Environment, Beirut.
Safi, S., 1999. Bioclimatic zones. In: Lebanon's National Program for Climate Change (L-NPCC). UNDP, Ministry of Environment, Beirut.
UNESCO, 1997. Commission Nationale Libanaise pour l'Education, la Science et la Culture. Beirut.
Weismiller, R.A.; Van Scoyoc, G.E.; Pazar, S.E.; Latz, K.; and Baumgardner, M.F., 1984. Use of soil spectral properties for monitoring soil erosion. In: Soil Erosion and Conservation. El Swaify, S.A.; Moldenhauer, W.C.; and Lo, A., (eds). Soil Cons. Soc. of America, Iowa.

Assessment of automated techniques for extracting vegetation and buildings from 1m stereo + multi-spectral IKONOS and 1m pan-sharpened IKONOS coupled with scanning laser altimetry.

Kim, J.-R., Muller, J-P.
Department of Geomatic Engineering
University College London
Gower Street
London, WC1E 6BT, UK

Automated techniques have been developed to extract vegetation and building objects from 1m Digital Surface Models (DSMs) and orthorectified 1m panchromatic and 4m multispectral IKONOS images over an area in rural UK known as Barton Bendish acquired in September 2000. A quantitative assessment is made of the results using Ordnance Survey® Landline (1:2500 digitised data) and presented here.

A 1m panchromatic sharpened multispectral (PSM) IKONOS image of east London was obtained together with a 2m DSM derived from airborne laser altimetry data from Infoterra Limited. The DSM was used to orthorectify the IKONOS 1m PSM and the same automated building and extraction technique applied, albeit that this time the image was acquired in November 2000. A quantitative assessment is made of the results using Landline® data and the results presented here.

High Resolution Mapping from Space 2001

by
Gottfried Konecny
Institute for Photogrammetry and GeoInformation
University of Hannover
Nienburger Str. 1, D-30167 Hannover
Tel.: +49-511-762 2487, Fax: +49-511-762 2483
konecny@ipi.uni-hannover.de, www.ipi.uni-hannover.de

Abstract

The history of optical high resolution from Space starts with the now declassified US Corona program of 1968. On the civilian side it starts from Landsat MSS, TM, the German Metric Camera, the US-LFC, Spot, the Russian cameras KFA 1000, KVR 1000, the German Moms on Space Shuttle and Mir, IRS1 until the 1 to 2 m systems Ikonos 2 and Eros A1 with more to follow in 2001. For the next years governments (France, Japan, China-Brazil, India) have announced high resolution systems. Private contenders have obtained licences for 0.5 m resolution systems.

Present handicaps are not in the obtention of the imagery, but in its pricing, since aerial photographic coverage, if obtainable, is cheaper. Also in radar imaging progress has been made from Seasat via ERS, JERS, Radarsat, Almaz to SRTM with 1 m resolution systems planned in a few years. Another interesting development is the deployment of small satellites such as those by Surrey with ever increasing resolutions. Thus the mapping via high resolution satellites is a realistic challenge for the future years.

A Large Area Digital Elevation Model from ERS-1/2 Tandem Data

D.Kosmann, W.Knöpfle, B.Rabus, A.Roth

DLR, German Aerospace Center, Germany
D-82230 Oberpfaffenhofen

Abstract

DLR's Remote Sensing Data Center implemented a production chain for the operational generation of digital elevation models (DEM) from space borne interferometric Synthetic Aperture Radar (SAR) data. In order to prepare for the preparations of processing of the X-band data set from the Shuttle Radar Topography Mission the software system was tuned by processing a substantial amount of ERS-1/2 tandem pair data sets. Besidse the DEM, a height error map (HEM), a geocoded coherence map (GCM) and two geocoded terrain corrected intensity images (GTC) were produced per tandem pair. Water areas with decorrelated phase information were masked out and filled with reasonable constant height values. The problem of large to medium scale atmospheric distortions was overcome with an automatic phase adjustment approach which allows a significant improvement of the height accuracy. The combination of the individual geocoded data sets to a continuous set - comprising stacked ascending and descending passes - resulted in a large area mosaic covering parts of central Europe. The validation based on large samples of control points shows very good agreement for flat to hilly terrain. It is intended to improve the current DEM data set by including the SRTM data to generate a 'best of' DEM.

Keywords: Interferometrie, Digital Elevation Model, ERS, SRTM

1. Introduction

Today, there is a lack of suitable global height information. The best elevation model showing a global coverage is provided in a 1 km raster size with varying quality. It is available as the GLOBE, GTOPO30 and DTED-0 products. Of course, regionally, better DEMs exist. However, they were acquired with a variety of sensors and many different techniques were employed during the elevation generation process.

Since a few years two radar remote sensing missions offers the possibility to produce the required height information from space with Interferometrie:

- Shuttle Radar Topography Mission (SRTM)
- ERS-1 and ERS-2 tandem mission.

In cooperation between the German Remote Sensing Data Center (DFD) und the Remote Sensing Technology Institute (IMF) that are combined in the Applied Remote Sensing Cluster (CAF) an interferometric processing chain was established. It is capable to produce precise DEMs from both missions.

SRTM provides globally high quality digital elevation models between the latitudes 60° (north) and 57° (south) acquired with the same sensor in one mission operating in C- and X-band. The C-Band covering the whole globe with a reduced accuracy in comparison with the X-band data, but the X-band data sets are consisting of stripes. Both datasets were only available at the fixed time and only in one coverage.

The two ERS satellites operate during various mission tandem mission in a one day shifted repeat cycle. They acquired data from the complete globe. Their datasets covered up to ten times the same area.

2. InSAR processing chain at DLR

DLR-DFD has developed and built an operational interferometric processing facility. It supports ERS tandem and the X-SAR of the Shuttle Radar Topography Mission (SRTM) as input sources. It will also be adapted for ENVISAT ASAR.

The entire processing chain comprises four subsystems, the screening and transcription system, the SAR processor, the generic system for interferometric SAR, and the geocoding and mosaicking system. Within DFD's InSAR production system the interferometric processing comprises spectral shift filtering, slope adaptive filtering, co-registration, multilooking, coherence estimation, flat earth phase removal, and several phase unwrapping procedures.

The geocoding and mosaicking system (GeMos) derives the DEM from the unwrapped phase image. The absolute phase is converted into height values and the slant range heights are geocoded into the DEM. The critical geometric parameters influencing the quality of the DEM are the baseline length and the baseline angle. For ERS tandem these parameters must be derived from the orbit products. The precise orbit product delivers the spacecraft's location within an error box of a few decimeters. As the sensitivity of the SAR interferometry itself is in the order of a few millimeters, the baseline needs to be improved by integrating reference information. In order to avoid time consuming manual tie-pointing, DLR-DFD's interferometric system uses a coarser resolution DEM to estimate the corresponding corrections. This procedure has another benefit against the manual tie-pointing as it provides a huge number of tie-points, distributed over the whole image. As the same DEM is considered for processing adjacent scenes, also the neighboring DEMs fit. Finally the individual DEMs are assembled to a DEM mosaic. Additionally, the system also produces data sets, which are suitable for other applications, such as coherence maps, interferograms, and amplitude images.

3. Interferometric products

GeMos is not only producing DEMs. During the geocoding and mosaiking process following maps are image products were automatically processes:

- Colour shaded DEM
- Geocoded amplitude
- Geocoded coherence
- Initial coverage map
- Mosaiking coverage
- Height error map
- Colour shaded DEM with integrated amplitude
- Reference DEM
- Water area map

Each of these maps has the original resolution of 25m x 25m and is in the same geodetic reference system. The first test area was Bavaria. In a second approach a DEM from Germany in a resolution of 25m x 25m was computed. Fig. 1 represents a quicklook of the DEM.

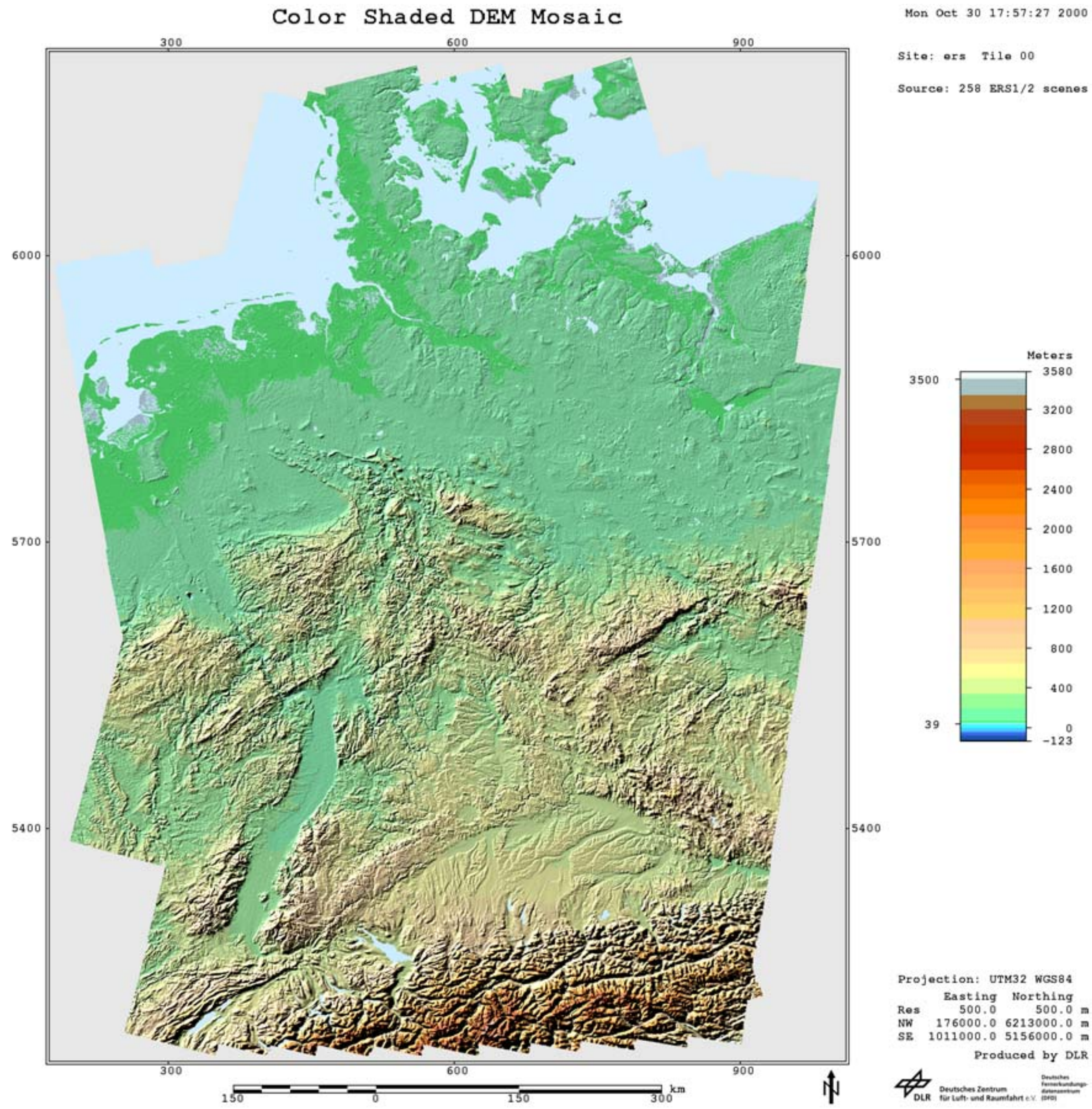

Fig. 1: InSAR DEM from Germany

The DEM from Hannover and the height error map are shown in fig. 3 and 4.

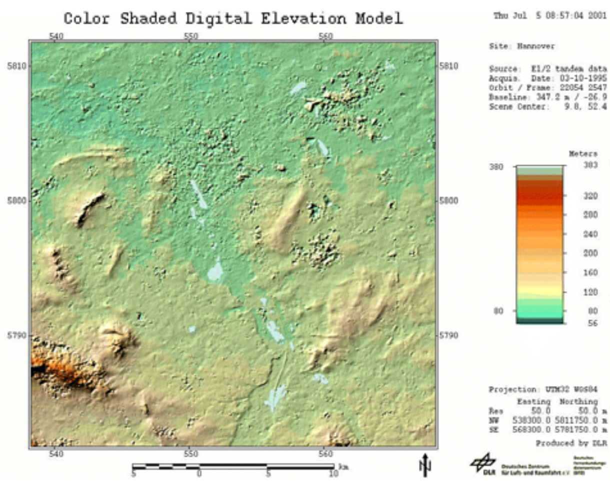

Fig. 3: DEM enlargement HANNOVER

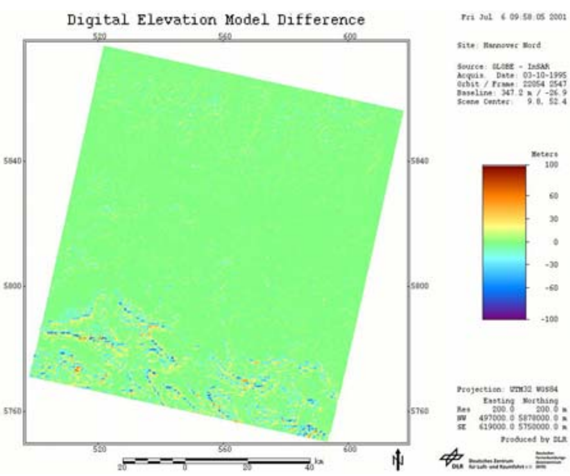

Fig. 4: Height error map Hannover

Besides the DEM also the amplitude of is mosaiced in the defined reference system. Both were combined to a new synergistic product. It offers the user a new information source for various applications. The synergistic product of the same area is shown in fig. 4.

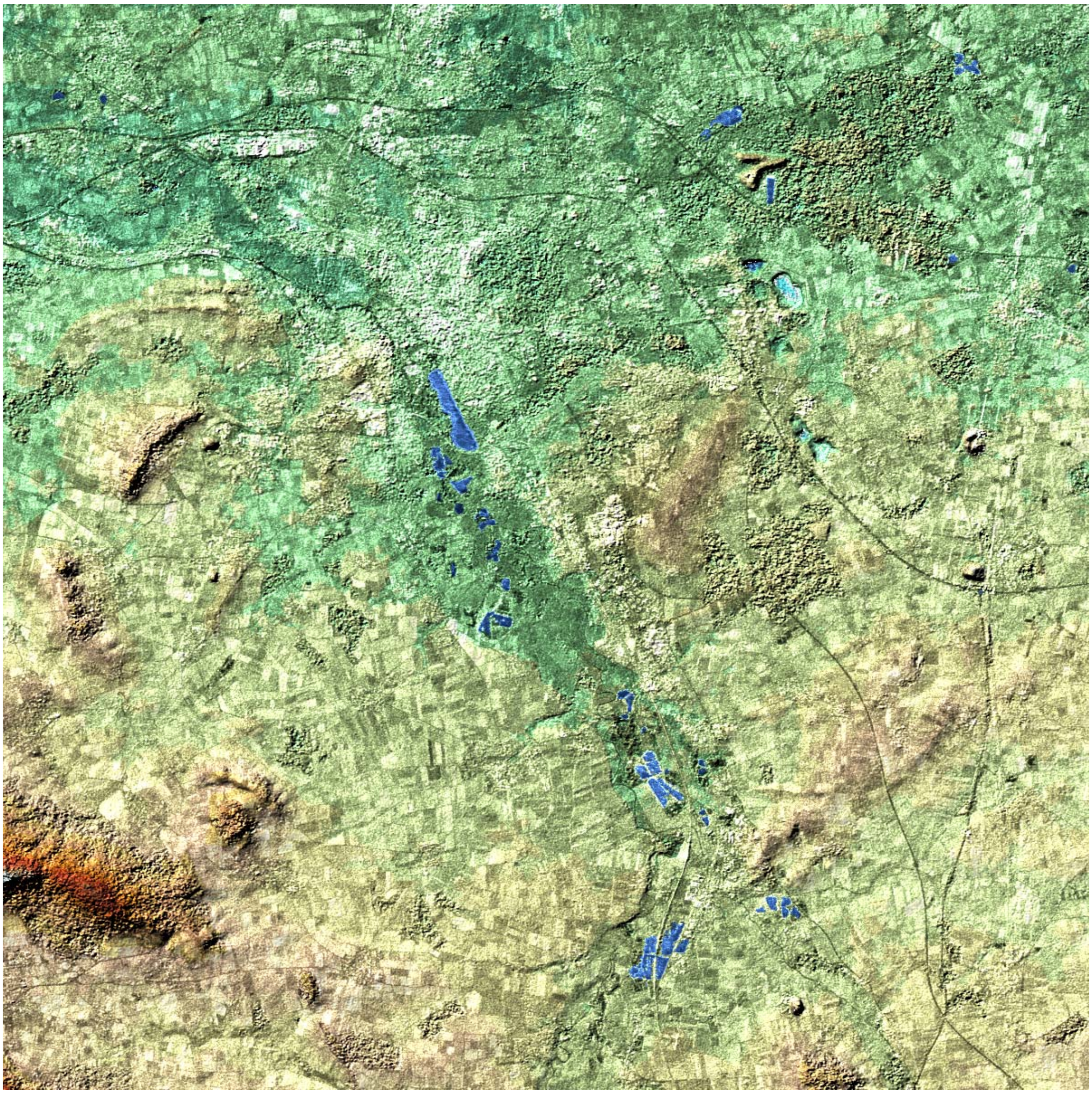

Fig. 4: Combination of DEM and Amplitude from Hannover

4. Water mask

The backscatter of water is an enormous problem during the InSAR processing. The coherence can change from one data set to another, therefore the normal phase unwrapping algorithm didn't produce precise DEMs. To reduce these distortions a water mask for each product was generated. The coherence information is used as input to select water areas. In a second step a visual control is necessary and in undefined areas the amplitude gives the operator the information where he has to define the water mask. Fig. 5a presents an uncorrected amplitude image, fig. 5b presents the result of the water mask generation.

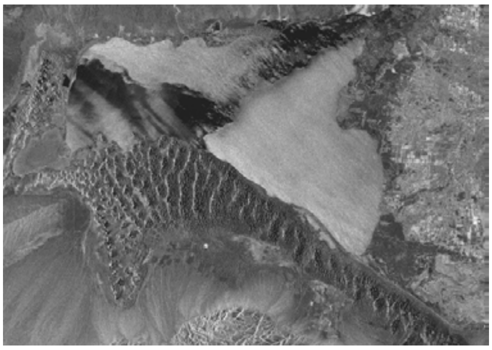

Fig. 5a: Amplitude without water mask

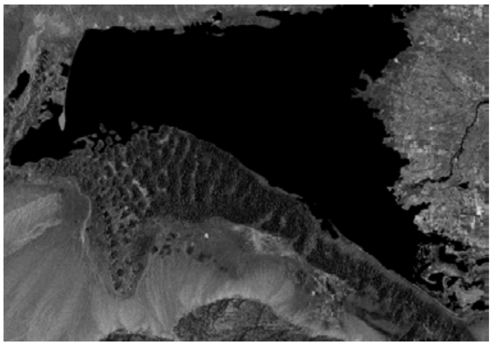

Fig. 5b: Integration of water mask

5. Generation of large area mosaics

Based upon the single DEMS a mosaiking tool especially for DEMs was developed. After the successful proccessing of the Germany DEM, a few hundred ERS tandem pairs covering Europe were used the extent the Deuitschland DEM. During the batch processing up to 444 tandem pairs were mosaiked to a homogenous DEM from central Europe. Both ascending (122) and descending (322) coverages were used. The mosaic covers an area of 1 010 00 km^2. The horizontal resolution is 25m x 25m. As geodetic reference UTM 32 and WGS84 was selected. The height accuracy depends on the local topography. Following classes separated:

Flat terrain (north Germany):	2m – 5m
Moderate relief (Poland):	5m – 10m
Hilly areas (Vogeesen):	8m – 15 m
Alpine regions (Alps):	15m – 25m

These accuracies are valid for 1σ.

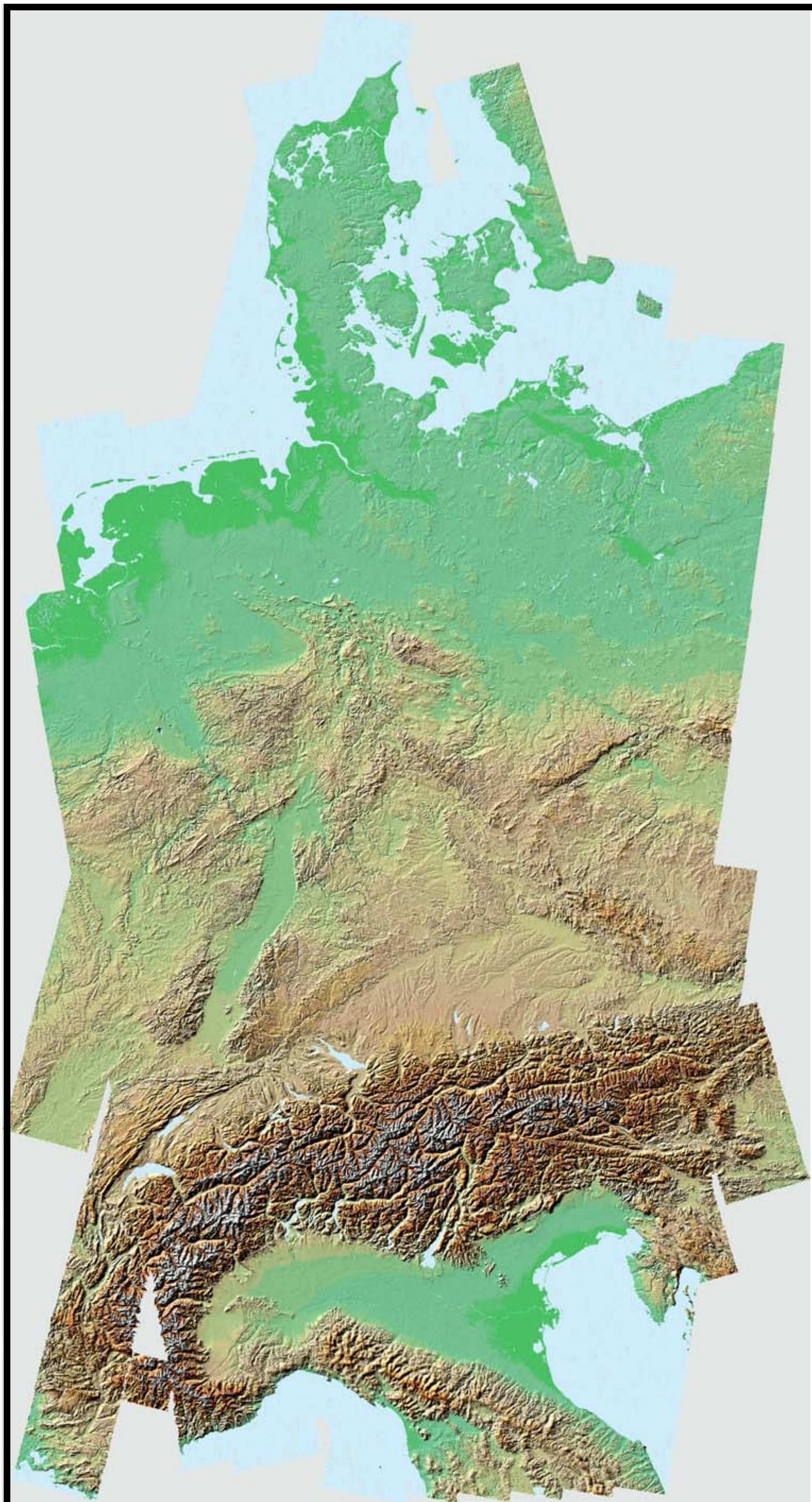

Figure 6: ERS DEM Central Europe

6. Quality Control

The quality control is a very difficult task the processed large areas and causes much problems. Other DEMs with the same resolution are not everywhere available. Reference points height as the best possible quality check could be used only in same regions, were they are accessible for free and in a computer based format. Therefore complete check for the whole DEM with the same approach is not possible. Therefore different procedures were used.
In a region were a relatively good DEM is available, like DTED 3 or Mona Pro profiles were selected in each of them and the differences regarding the InSAR DEM were measured (Fig.e 7a-c). The plot in Fig.8 shows such a profile result.


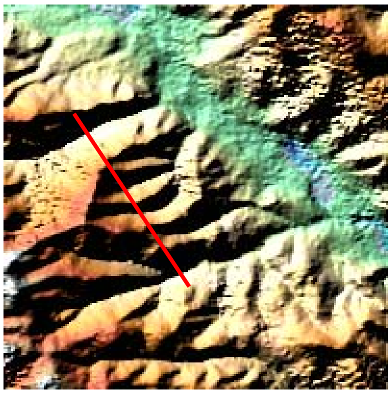
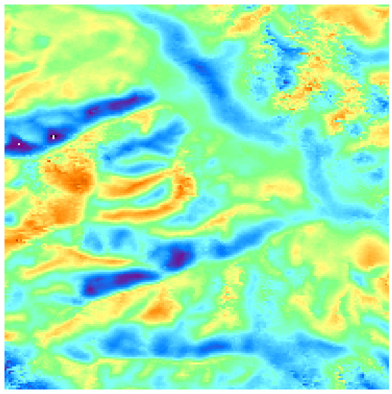

Fig. 7a: Refrence DEM   Fig. 7b : InSAR DEM   Fig. 7c: Error map

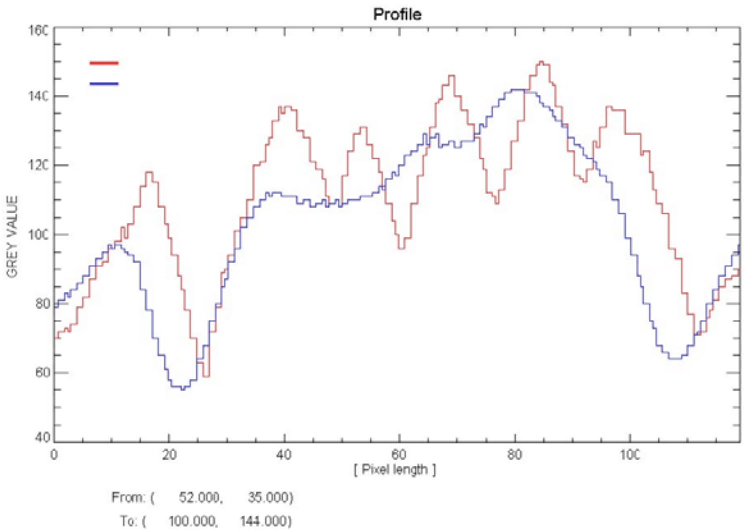

Fig. 8: Profile of errors

An other approach was made in Germany. There a few thousand GPS measured points. The 3-dimensioal points delivers precise height information with an exact location. Due to the fact that the DEM is geocoded only by orbit and system information a check of the quality is possible.

7. Conclusions

The generation large area mosaics from ERS tandem data with a high quality and fine resolution is possible. For most areas the achieved quality is sufficient for typical applications. It was very important to use all available ERS tandem pairs. In areas with a high accuracy up to 9 tandem pairs covering the same area are used. A reduction of the coverage considerably reduces the accuracy.
To handle this amount of data a high performance processing system is an important requirement. The DFD uses two SUN Enterprise 450 servers. Four CPUs and 4 GB RAM guarantees high computing performance. About 500 GB of local disk space are available for storage. The computation of the Europe DEM takes a few days.

8. References

M. Eineder, N. Adam, “A Flexible System for the Generation of Interferometric SAR Products”, Proc. IGARSS’97, Singapore, 1997

W. Knöpfle, G. Strunz, A. Roth, “Mosaicking of Digital Elevation Models derived by SAR Interferometry”, International Archives of Photogrammetry and Remote Sensing, Vol. 32, Part 4, pp. 306-313, 1998

D. Kosmann, N. Adam, S. Dech, S. Gebhardt, W. Knöpfle, U. Marschalk, A. Roth:”INSAR DEM at the DFD”, Proceeddings ISPRS WG IV/4, Hannover, 1998

B. Rabus,. O. Lang, “Ice Motion and Topography in the Siachen Glacier Area, Central Kashmir, derived with an operational processing system for INSAR-DEMs”, Proceedings of Fringe `99, Liège, ESA SP-478

P. Rosen, M. Eineder, M. Werner, A. Roth, ...“SRTM-Mission - Cross Comparison of X and C Band Data Properties”, Proc. of IGARSS’01, Sydney, 2001

A. Roth, W. Knöpfle, B. Rabus, S. Gebhardt, D. Scales: “GeMoS – A System for the Geocoding and Mosaicking of Interferometric Digital Elevation Models”, Proceedings IGARSS’99, Hamburg, 1999

A. Roth, U. Marschalk, W. Knöpfle, B. Rabus, A. Benjes, D. Kosmann, “SRTM/X-SAR Products and Quality”, Proc. of Eusar 2000, Munich, pp. 237-240, 2000

Land Cover Classification using High Resolution IKONOS Data

Peter Lohmann, Bernd Haarmann
Institute for Photogrammetry and GeoInformation
University of Hannover
Nienburger Str. 1, D-30167 Hannover
Tel.: +49-511-762 2486, Fax: +49-511-762 2483
lohmann@ipi.uni-hannover.de, www.ipi.uni-hannover.de

Digital airborne and satellite based multispectral data of high resolution is emerging recently. This development is accompanied by new software developments in the field of multispectral classification including segmentation and rule based attempts. This paper reports on the first results using Definiens eCognition software for automatic multispectral classification. First experience with this software has been made using high resolution airborne digital camera data. This experience and the knowledge gained by the classification of LANDSAT TM data according to the CORINE land cover (CLC) nomenclature will be transferred to IKONOS satellite imagery obtained within an OEEPE test.

VERIFICATION OF DIGITAL ELEVATION MODELS FROM MOMS-2P DATA

Rainer Mueller, Manfred Lehner, Rupert Mueller
DLR Oberpfaffenhofen (German Aerospace Center)
Remote Sensing Technology Institute of Optoelectronics
Image Science - Photogrammetry Group -
82234 Wessling, Germany
E-mail: Rainer.Mueller@dlr.de , Manfred.Lehner@dlr.de , Rupert.Mueller@dlr.de

Joint Workshop of ISPRS Working WG I/2, I/5 and IV/7 on
High Resolution Mapping from Space 2001 September 19-21, 2001 hosted by
Institute for Photogrammetry and Geoinformation (IPI), University of Hanover, Germany

KEYWORDS

Digital Elevation Models, Digital Surface Models, MOMS-2P, Stereo, Image Matching, Multispectral, Accuracy, Orthoimages

ABSTRACT AND INTRODUCTION

The MOMS-2P sensor (**M**odular **O**ptoelectronic **M**ultispectral Stereo **S**canner) is a German stereo camera mounted on the PRIRODA module of the Russian space station MIR. Its main new feature was the along-track three-fold stereo capability. It delivered approx. 65 million km^2 of high quality and high resolution (approx. 18m ground resolution) imagery from 1996 to 1999, which is still subject of ongoing image processing to generate digital elevation models and orthoimages throughout the entire world.

The three-fold along-track stereo principle and multispectral capabilities of the MOMS-2P sensor were highly advantageous for digital elevation model (DEM) generation compared to other satellite systems in orbit. The majority of all data takes of MOMS-2P were imaged in Mode D, which is a combination of the two inclined stereo and two nadir looking multispectral channels (blue and near-infrared) with a swath width of approx. 100km and a ground resolution of 18m. The data of this mode is well applicable for generating digital elevation models and using the multispectral imagery for creating orthoimages, landuse-classification and further evaluations.

This paper describes the latest processing experience in generating high quality digital surface models and orthoimages from MOMS-2P stereo data at DLR. The steps of the processing chain are shortly explained. It is shown that self-calibration via bundle block adjustment is necessary. The quality of the attitude and position data provided by the onboard gyros and the GPS receiver is discussed. It is demonstrated that the highly accurate attitude data is essential for generating precise digital elevation models.

The results of an accuracy analysis using digital surface models (DSMs) produced from Mode D image and orientation data from data takes which cover parts of South Germany. The DSMs are checked against a reference DEM with a mesh size of 25m. For a more detailed height accuracy analysis, classification results using the multispectral part of the Mode D imagery allow a discrimination between various landcover types.

1. Data Processing with the MOMS stereo workstation processing chain

In order to produce digital elevation models and orthoimages from MOMS-2P stereo data a stereo workstation software has been established at DLR. This was done in cooperation with the photogrammetric chairs of several German universities. The main steps of the processing chain are:

- Matching for generating tie points between the 3 looking directions of MOMS stereo data; these tie points are input to photogrammetric bundle adjustment and Otto-Chau region-growing
- Preprocessing of orbit and attitude data
- Photogrammetric bundle adjustment for the estimation of the absolute values of interior and exterior orientation of the camera during imaging of the current data strip
- Matching for a very dense tie point distribution using Otto-Chau region-growing method with mass seed points from previous matching
- Forward intersection to compute the ground coordinates of the tie points based on the reconstructed interior and exterior orientation
- Generation of a regular DEM by two-dimensional interpolation
- Calculation of orthoimages based on the regular DEM and the orientation data

1.1 Processing chain details using sample data

1.1.1 Image data

To fully exploit the 3-fold stereoscopic nature of the MOMS-2P data a sufficiently long strip has to be evaluated in one bundle adjustment. The length and situation of this strip has to be chosen in such a way that the interesting area for DEM generation lies in the region of 3-fold MOMS coverage. In case of data take T08FE the strip was composed of scenes 17 to 23 (40720 image lines - all scenes with acceptable cloud cover – this strip is about 700km long and 100km wide). About 8700 image lines at both ends of this strip are in zones of 2-fold coverage with respect to the modeled exterior orientation interval in bundle block adjustment. A subscene of the area with 3-fold stereoscopic coverage where best DEM accuracy can be achieved is taken for the comparison to an existing reference DEM. The reference DTM used in this analysis was provided by AmilGeo (‘**A**mt für **mil**itärisches **Geo**wesen’ = German Military Surveying Service), has a regular mesh grid size resolution of 25x25 meters and is transformed and projected in the UTM (zone 32) coordinate system with ellipsoidal heights referring to the WGS84 ellipsoid. The accuracy is reported as ±5m in flat terrain, ±9m in hilly terrain and up to ±15m in mountaineous terrain. The accuracy level valid for this particular testsite is to be considered as ±5m to ±9m for the absolute height uncertainty.

The following has to be noted in the use of the reference DTM in this study:

- the data of this reference DTM is to be assumed as the representation of the terrain heights ‘as is’ although knowing the MOMS-2P data is not representing the simultaneous situation of the terrain for this given time. The AmilGeo DTM is dated from 1995, whereas the data was imaged on the 25th June, 1998. No consideration of changes of the terrain/landuse was taken into account.

This subscene contains radiometrically corrected 3-ray-area MOMS-2P data sized 5500 x 5800 pixels which corresponds to an approximate ground coverage of 100 x 100km. The image data contains a subscene from data take T08FE, which was recorded on June 25th 1998, in stereo/multispectral Mode D. The two stereo channels contain the panchromatic, channel 1 the blue and channel 4 the near-infrared reflectance of the earths’ surface and cover an area of Germany in Bavaria of the so called ‘Fünf-Seen-Land’ west of Munich including the lakes ‘Ammersee’ and ‘Starnberger See’ as well as a large part of the city of Munich. A multispectrial classification of this scene was also performed. Figure 1 shows the geographic location of the image datea, DSM coverage and the classification test area

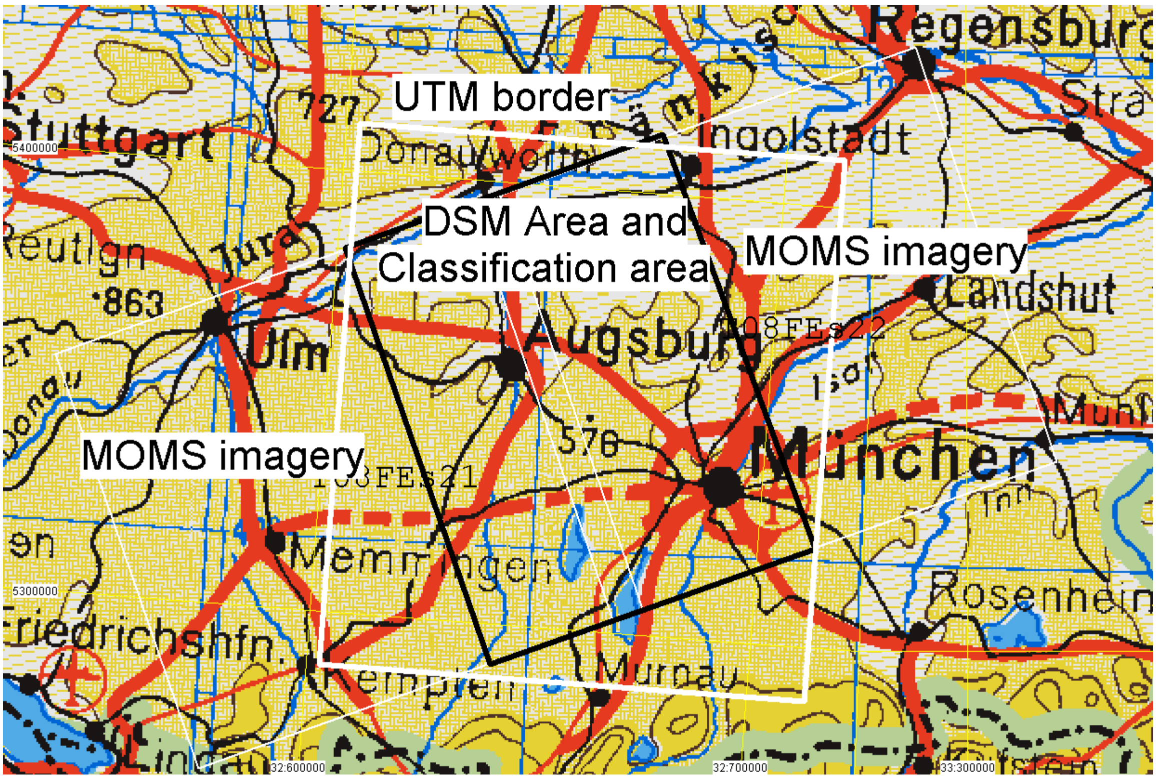

Figure 1: Coverage of DSM and classification area

1.1.2 Matching for tie point generation

This matching is performed purely in image space with DLR software. Details on this software are described in **[Lehner and Gill 1992]**. It relies on a resolution pyramid and applies intensity matching in two forms: normalized correlation coefficient for pixel accuracy and subsequent local least squares matching for refinement to subpixel accuracy. About 1 Million 3-fold homologous points have been found in the strip of T08FE. These enter in the following subtasks:

- Best points in a relatively thin grid are selected for tie points in bundle adjustment
- Image coordinates of GCP are measured in one channel (here channel 6); their coordinates in the images of the other channels are calculated by local least squares matching where the good initial approximations are estimated via a local affine transformation based upon the already found homologous points in the neighborhood
- All points enter as seed points in the Otto-Chau region-growing process for dense matching described below

1.1.3 Preprocessing of navigation data

MOMS-2P has its own navigation system MOMS-NAV consisting of a Motorola Viceroy GPS receiver with dual antennas and LITEF gyro systems in two redundant blocks. Two electronic counters are used to allow the later exact synchronization of image frames and navigation data.

1.1.3.1 Orbit data

Positional data are generated from the GPS data produced by onboard processing. Because of funding problems the option to use GPS raw data for DGPS processing on ground was not available for most of the MOMS-2P data takes. The German Space Operations Center (GSOC) of DLR provides so-called ‘coarse ephemeris files’ by interpolating the relatively inaccurate GPS positions with high-precision orbit models. This results in positional data with a high relative accuracy of 1 m and an absolute accuracy of 30-50 m **[Gill, 1997]**. Thus, a bias has to be estimated via photogrammetric adjustment. Because of the coupling of the six orientation parameters this adds instability to the whole adjustment (normally some of these bias values are not determinable with the necessary accuracy). Therefore, the continuation of the funding for DGPS processing at GeoForschungsZentrum Potsdam would have been of great advantage for the stereo evaluation of MOMS-2P data.

1.1.3.2 Attitude data

The processing of the gyro data including the absolute referencing with INS data of the MIR station is done with software developed by GSOC of DLR. This also comprises the time synchronization of navigation data and image frames which is a very important task as the delay between generation of navigation data and the writing into the data frames is of the order of several hundred image lines. Until the year 1999 the processing was done under the false assumption that the accuracy of the gyro data is in the order of 10’’ (10 arcseconds) only. Therefore, a much too strong filtering was used which led to undulations in the produced digital elevation models **[Kornus et al., 2000]**. With the help of Stuttgart University it was seen later that the filtering removed valuable attitude information and that the accuracy of the gyro data is in the order of 1’’, complying with the level for the white noise given in **[Eissfeller et al, 1996]**. The processing of the gyro data was changed accordingly. The noise level of 1’’ can be seen in **figure 2** where attitude angles (converted to the topocentric coordinate system used in photogrammetric adjustment) are given for data take T08FE for the image line interval used in the adjustment. To visualize the small angular variations in the order of 10’’ which have been suppressed before, a polynomial of 2^{nd} degree is adjusted to and subsequently subtracted from the data. The attitude angles have now been introduced into the adjustment with a relative accuracy of 1’’ with free adjustment of bias, linear and quadratic drift for the three angles.

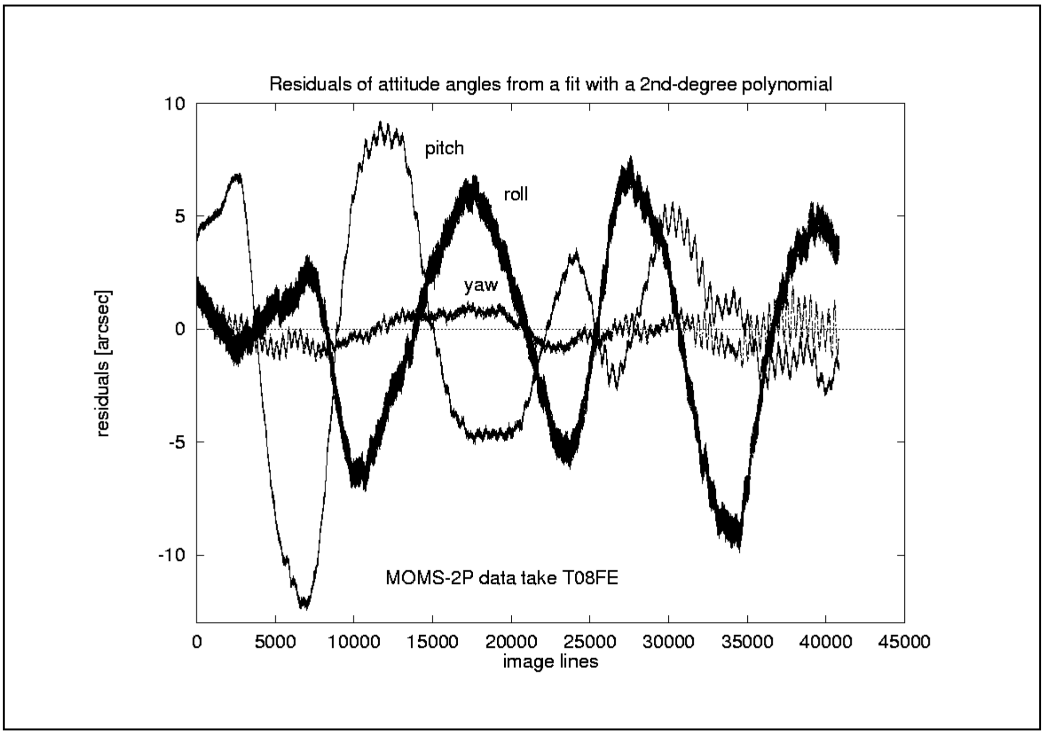

Figure 2: Residuals of attitude angles after fit with 2nd-degree polynomial

1.1.4 Bundle adjustment

The bundle adjustment is done with the software system CLIC of TU Munich which is based on the principle of orientation images **[see Kornus, 1999**]. 15399 tie points have been subselected from the mass tie points found by matching. The subselection is based on a regular grid and on selection of best point per grid cell (with respect to correlation coefficient and stability of matching in both directions for a stereo pair). This results in high quality tie points which are introduced as observations with a standard deviation of 0.2 pixel into the bundle adjustment. The distance of the orientation images (OI) was set to 70 image lines in order to be able to model the behavior of the attitude angles. For each OI the observations of the exterior orientation parameters were introduced into the adjustment. The bias of the positions was set to 0.0 m with a standard deviation of 30 m. No drift parameters for the positions were considered. The standard deviation for the individual orbit measurements (relative accuracy) was set to 1 m. For the attitude angles bias as well as linear and 2^{nd} order drift parameters were introduced as free unknowns. The relative accuracy of the individual measurements for the attitude was set to 1 arcsecond.
212 ground control points (GCP) were introduced. 64 points lie in Switzerland and were measured in 1:50000 topographic maps. Their standard deviation for x and y was set to 20m and for z to 5m. The other 148 points lie in Germany and could be measured in 1:25000 topographic maps. Their standard deviation was set to 15m in x and y and also 5m for z. The points were measured in one channel (MOMS channel 6) and completed to full 3-ray tie points by local least squares matching. The standard deviation of the image coordinates of these special tie points was set to 0.3 pixel. The distribution of tie points and GCP is seen in **figure 3**.

The coordinate system for the adjustment is a local topocentric system (WGS84 ellipsoid). All object space coordinates and attitude angles were converted to this coordinate system.

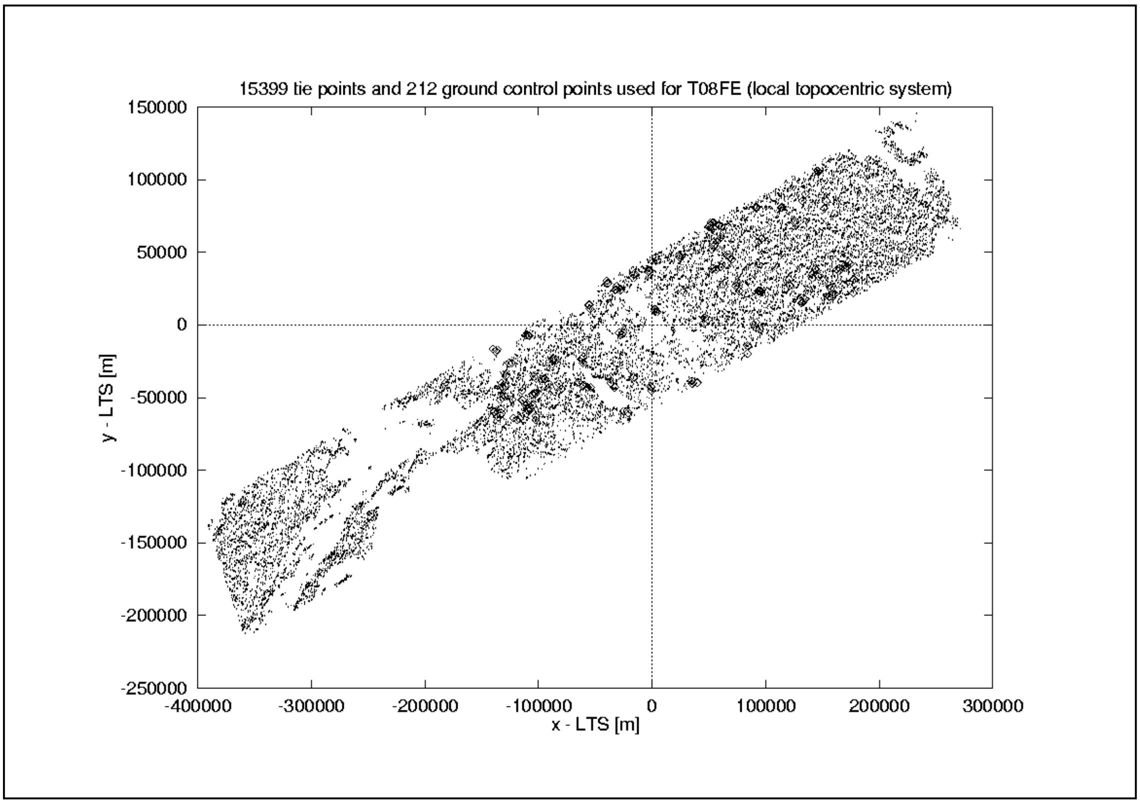

Figure 3: Distribution of tie points and Ground Control Points

1.1.5 Matching for dense tie points for DEM generation

The mass tie points in the previous matching process are by far not sufficient for the derivation of a DEM. They are taken as input seed points of a matching step using Otto-Chau **[Otto und Chau, 1989]** region-growing method (local least squares matching with systematic propagation starting from seed points). The implementation of TU Munich is used [**see Heipke et al, 1996**]. As above three image pairs are used to control the matching in order to reduce the number of blunders. Three subsequent image matching runs for the image combinations back-fore, back-nadir and fore-nadir with a template matrix of 13 x 13 pixels, a step size of 1 pixel and a minimum correlation of 70 % were calculated. From the twice determined differences of the image coordinates in the nadir channel a standard deviation of 0.14 pixel in x and 0.13 pixel in y could be deduced. The originally set of 3-ray points was reduced by points which showed differences higher than 0.5 pixels. A matching with channel 4 (near-infrared) yielded poor results, which is due to the radiometric appearance and is subject of further studies. More than 20 Million homologous points were found by this software for the substrip (5500 x 5800 pixel) of the area of 3-fold stereoscopic coverage for T08FE used later in the DEM comparison.

1.1.6 Forward intersection

Interior and exterior orientation resulting from bundle adjustment and relative calibration information from laboratory calibration are used to calculate ground coordinates for the points found in the previous step. This is done by least squares adjustment for the intersection of the imaging rays with software written at DLR. The results can be controlled via thresholds for the corrections to the observed image coordinates in case of 3-fold homologous points. This is an additional method for reduction of blunders in case of 3-fold stereoscopic imaging. The derived set of points was transformed into UTM (zone32) coordinates with the WGS84 ellipsoidal heights. A total set of over 18 Million coordinates was derived from the process.

1.1.7 Generation of a regular DEM

The irregularly distributed results of approx 18 Million point coordinates from the forward intersection was to be interpolated 2-dimensionally to get a regular DSM of a mesh size of 25x25m with a moving plane algorithm. The software package LISA described in **[Linder,1999]** was used for this purpose.The point distribution of the used data can be observed in **figure 4**. Areas of low variance like the waterbodies of Lake Ammer and Lake Starnberg causing the image matching to fail can clearly be observed.

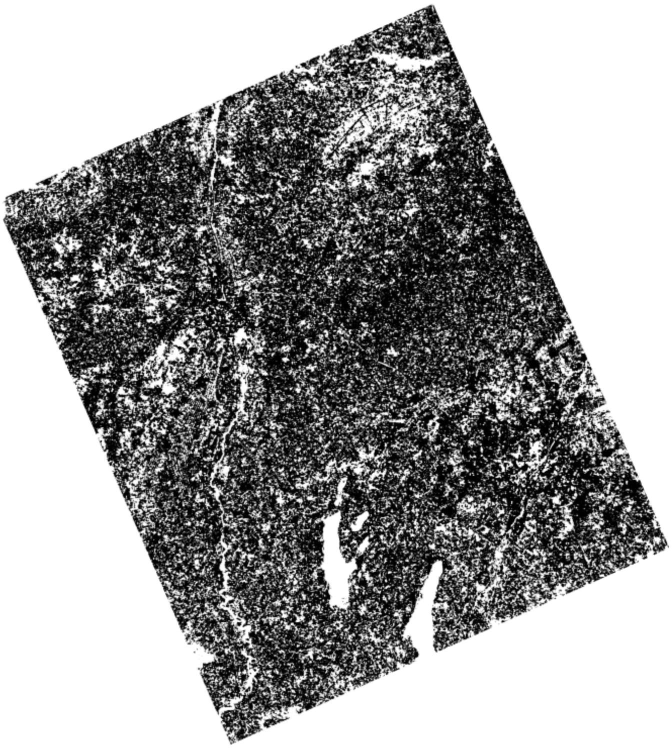

Figure 4: Point distribution of sucessful matching and transformation

1.1.8 Computation of orthoimages

Based on the interior and exterior orientation and relative calibration data of laboratory calibration orthoimages are computed from image strips of the MOMS channels using the regular DEM. The software written at DLR uses the direct method to construct the orthoimages. Starting from DEM in local topocentric coordinate system orthoimages in every defined datums and map projections can be computed.

The inputs for the orthoimage production are the interior orientation (including the geometric calibration values of the CCD lines acquired by laboratory measurements), the six parameters of the exterior orientation for each image line, the regular DSM derived from the MOMS-2P stereo data and the image data itself, which will be transformed to the orthoimage. The exterior orientation as well as the DEM is given in the unique cartesian coordinate system of a local topocentric system (LTS), described by a base point and the geodatic datum. The principle of the orthoimage production is based on the forward intersection of the actual sensor viewing direction (pointing vector) and the DEM using the rigorous collinearity equation.

A set of orthoimages was calculated with the respective image channels in Mode D with a ground pixel reolution of 15m. The map projection and the geodatic datum (earth ellipsoid and 7-parameter transformation) of the orthophoto can be selected using an extended version of the **[GCTP]** (General Cartographic Transformation Package) software.

An iterative procedure is applied to calculate the intersection point of the sensor look direction and the DEM as shown in **figure 5**. Starting with point (1) the corresponding DEM height leads to point (2). The horizontal intersection with the sensor pointing vector results in point (3). This procedure is repeated until the horizontal change Δs_i is lower than half of a pixel size.

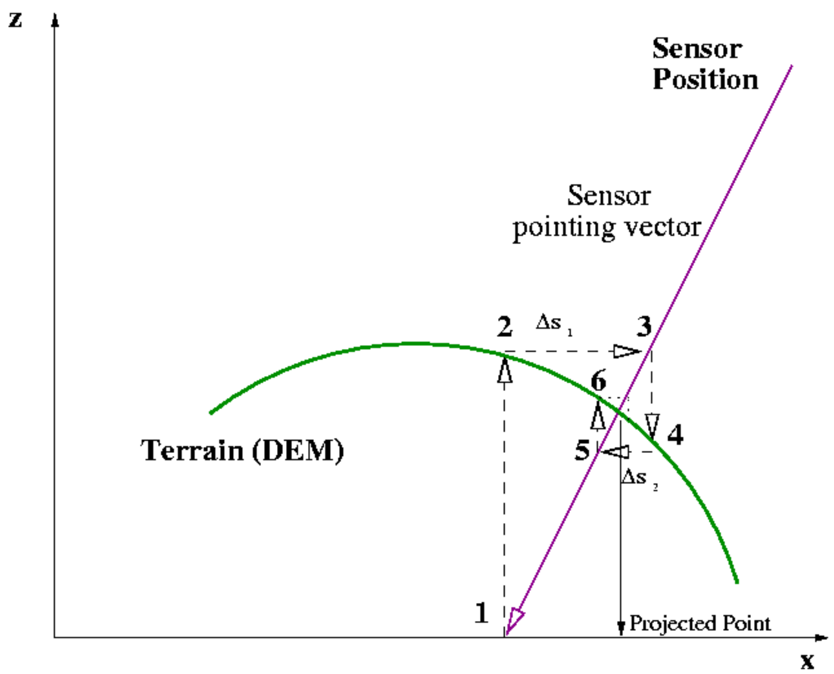

Figure 5 : Iterative calculation of intersection point of the sensor pointing vector with the DEM.

For the resampling technique the direct method, illustrated in **figure 6**, is applied. Polygons, build by the centers of four adjacent pixels of the input image, are transformed to the output image grid and filled, if the pixel center is inside the closed polygon, with the distance weihgted pixel values of the corresponding four gray values or the nearest neighbour pixel value. Skipping to the next four adjacent pixels prevents residual gaps in the orthoimage. This method can be implemented as a fast algorithm.

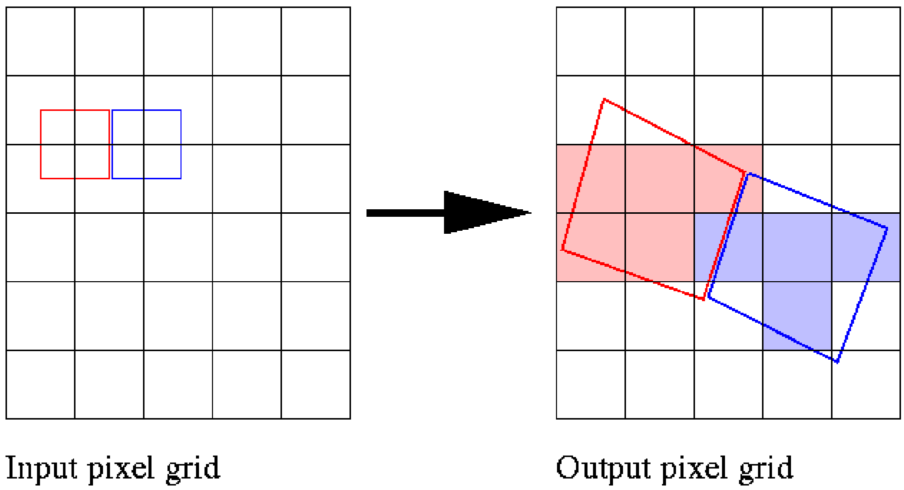

Figure 6: Direct resampling method using polygons. Example for two adjacent polygons (red and blue), which are transformed to the output pixel grid. An output pixel is filled with a grey value, if the center of a pixel is inside the polygon

Figure 7: Sample cut out from ortho image

2. Results

2.1 Statistic of Bundle Block Adjustment

The theoretical standard deviations of the bundle adjustment of all input points (tie and ground control points) yielded to

sX:	**2.225 m**
sY:	**2.552 m**
sZ:	**6.057 m**

The GCP corrections yielded to

sX:	**7.949 m**
sY:	**12.988 m**
sZ:	**1.434 m**

which is well related to the a-priori standard deviations chosen for the GCPs (15-20m in X and Y, 5m in Z).

No check points were introduced because of later comparison of mass points to existing DEM.

2.2 Check of derived object space heights against reference DTM

For the accuracy assessment all single point heights were differenced against the reference DEM by bilinear interpolation of the height from the reference DEM at the particular planimetric point coordinates. The difference dZ is defined by

$$\mathbf{dZ = Z_{ref}\ (height\ of\ reference\ DEM) - Z_{MOMS}\ (MOMS\ DSM\ height)}$$

A negative height difference value is to interpreted as the MOMS height lies above, a positive value the MOMS height lies below the reference DEM.

The statistic analysis leads to the following values:

Total Number of points: 18090559
Minimum difference: -72.6 m
Maximum difference: 72.7 m
Mean difference: 2.6 m
Rms of differences: 10.2 m

Besides some gross errors are still present in the data set, the values confirm a very good height accuracy of 10.2 m for the entire area, its value as to be expected in comparison to other investigations **[Kornus et al., 1999]**.

2.3 Object class related check of derived object space heights against reference DTM

2.3.1 Use of the multispectral classification

The image content description is done by a multispectral classification with the orthoimages derived with a supervised Gaussian-Maximum-Likelihood-Classifier. The selected testsite crosscheck was done with topographic maps to ensure reliability. The accuracy of the classification is asessed with the JEFFREY-MATUSSITA **[Reinartz, 1989]** measure, which represents the separabilty of the classified object classes against each other. A separability measure with a minumum of 94% was achieved between the classes. A set of 30 subclasses was summarized into 4 general classes, for which a height difference measure is the target interest in this study: Open Areas, Woods, Waterbodies, Urban Areas.

However due to inherent spectral variability encountered by a classifier, the data often manifest a salt-and-pepper appearance. It was necessary to use a postclassification smoothing for the classified output to show only the dominant (presumably correct) classification. In this case a Majority-Filter of a size 5x5 was used to replace the central pixel value with the dominant pixel value appearing in the filter-matrix.. Nevertheless the appearance and information of the classification is still somewhat affected by mixed pixel classes as well as wide spreaded small sub classes within classes.

With the help of the classification information the entire set of height points was now subdivided in object-class-height-sets as follows: The multispectral classification was performed with the derived orthoimages of all viewing directions. Each object point coordinate derived from the forward intersection is now directly assigned and sorted to the value of the classification image representing a certain object class found. The result is a set of height-subsets each containing the transformed object height of the point belonging of the (presumably) particular object class. To improve the reliability of the assignment of the points into the certain object class, also a shrink algorithm was used which added a border of two pixels to each classified image region. This ensured a more reliable assignment of points possibly lying on the borders of object classes and resulting a wrong class assignment.

2.3.2 Object-class related height differences

As described in the previous section 4 main object classes were in the main focus. The point sets were now separately differenced against the reference DEM heights and statistically analysed. **Table 1** shows the bias and root –mean-square error of the height differences of each object class.

Class	Mean diffZ (Bias)	RMS of diffZ	No. Of points
Open Areas	5.3 m	10.1 m	9333937
Woods(subset)	-12.8 m	17.2 m	29426
Water	-0.2 m	8.6 m	18881
Urban Areas	1.0 m	7.9 m	1180160

Table 1: Selection of object class related height differences

It has to be noted, that a subset of highly reliable points for the wood class was derived, because the classification result showed a general problem in using the total set of points belonging to the wood class. Not only tree heights, but also clearings were classified as wooden areas. This is sufficient for the thematic information, but dilutes the statistics performed in this manner. This subset was generated by manually choosing areas of dense forest canopy.

The results show some representative and diluted results. For the object class 'Urban Area' the expected mean value of the height difference is actually a negative value of some 5-20m, expecting height of buildings and man made-objects as its the surface of the class which has bee imaged. Also 'Open Areas' show a not expected result: the difference should be actually around 0-3m, for this is the surface of the open terrain.

Nevertheless the classes ‘Woods’ and ‘Water’ showed the expected results. Speaking for the height difference for the ‘Woods’ class the value would well represent the canopy height of 10-15m, as for ‘Water’ a value around zero also would represent the sea level height.

3. Summary and Conclusions

This paper described the well-working processing chain of the stereo processor developed and integrated mainly at DLR for deriving Digital Surface Models from MOMS-2P stereo data. Although the MOMS-2P sensor is no longer providing data, the huge amount of imaged data to be processed and the global need of Digital Elevation Models is still an ongoing task.

It was shown that with a sufficient set of GCPs and navigation data a high quality DSM could be derived. Especially the navigation data had a main focus of interest, as it had shown that the modelling of the yet small attitude variations of 1” arcsecond of the sensor is mandatory to derive the quality achieved.

In theory, an error-free derived object height from optical remote sensing data only deviates in regions where its height is representing the object surface height rather than the terrain height found on i.e. topographic maps or DTM. The bias from the reference height should theoretically reflect its object height e.g. the height of a tree. An area based approach of reconstruction the object space should show regions of surface heights which systematically deviate from the terrain.

The main effects of the deviation of surface to terrain heights and its quantities are:

- systematic undulations introduced by the orientation parameters (3-10m)
- a bias introduced by the particular imaged object surface (depending on object height)
- transformation uncertainties caused by datum shifts (assumed as up to 3m)
- the accuracy level of the reference DEM itself (5-15m depending on terrain)
- terrain changes during the time of derivation and imaging and of the DEM/DSM (up to 10-15m)

Considering all the above mentioned effects causing and influencing a height difference, the results of this study to verify the object-class-dependent bias-part are questionable in terms of a general representativeness. However the statistic values in chapter 2.3.2 are promising.

The results show, that apparently only more precise thematic information, such as a high resolution classification layer or a manual classification of every object height would lead to the expected elevation differences for all classes. It is difficult however to find a good statistical measure and verification of each derived model, lacking a global submeter DTM. In case of this study the accuracy of the reference DTM was in the order of the same magnitude for the expected height differences for especially the class for ‘Open Areas’. Nevertheless the choice of a subset of purely canopy heights led to the expected results, which is promising for further studies and confirms the global reliability and accuracy of the derived DSM.

Because of the mentioned dilution of the assessment of the full accuracy potential, in further studies high resolution Digital Surface Models from Airborne Scanners will be taken into account for a more sophisticated analysis. The years of processing experience with stereo MOMS-2P data are further applied for the inegration of future sensors and the development of new algorithms for the stereo processor, to account for the various appearances of spaceborne stereo data.

REFERENCES

[Eisfeller B., Föckersperger S., Jansche A. and Lemke N] MOMS-NAV – Location of the Russian Space station MIR with Differential GPS, Kayser-Threde GmbH, Munich,
project report not published, 1996

[GCTP] Software Documentation for GCTP General Cartographic Transformation Package: National Mapping Program Technical Instructions, U.S. Geological Survey, National Mapping Division, May 1982

[Heipke, C., Kornus, W., Pfannenstein, A.] “The evaluation of MEOSS airborne 3-line scanner imagery - processing chain and results”, Photogrammetric Engineering and Remote Sensing, Vol.62, No. 3, 293-299, 1996.

[Kornus, W.] “Dreidimensionale Objektrekonstruktion mit digitalen Dreizeilenscannerdaten des Weltraumprojekts MOMS-02/D2”, Forschungsbericht 97-54 (Dissertation), DLR, Institute of Optoelectronics, 1997(b).

[Kornus, W., Lehner, M., Schroeder, M.] “Geometric in-flight calibration by block adjustment using MOMS-2P 3-line-imagery of three intersecting stereo-strips”, Proceedings of ISPRS Workshop on 'Sensors and Mapping from Space 1999', Hannover, 1999.

[Lehner M. and Gill R.S.] “Semi-automatic derivation of digital elevation models from stereoscopic 3-line scanner data”, IAPRS, Vol. 29, Part B4,Washington,USA,pp. 68-75, 1992.

[Lehner, M., Kornus, W.] “Band to Band Registration of MOMS-2P Camera", Proceedings of ISPRS Workshop on 'Sensors and Mapping from Space, 155-162, Hannover, 1997.

[Linder ,W] “Geo-Informationssysteme”, Springer-Verlag Berlin Heidelberg, ISBN 3-540-65276-0, 1999

[Müller, Rainer] “Using Multispectral Information For Accuracy Evaluation Of Digital Elevation Heights From MOMS-2P Data”, Workshop of ISPRS Working Groups I/1, I/3 and IV/4 on Sensors and Mapping from Space**,** Hannover, Germany, 1999

[Otto und Chau, 1989] Otto, G., Chau, T.: Region growing algorithm for matching of terrain images, Image and vision computing, (7)2, pp.83-94.

[Reinartz, 1989] Reinartz, P.: Untersuchungen zur multispektralen Klassifizierung von schwer trennbaren Klassen mit Beispielen aus Waldschadensgebieten, DLR-FB-89-55, München, 1989.

AUTOMATIC DIGITAL IMAGE BALANCING

Rodrigo Affonso de Albuquerque Nóbrega [1,2]
José Alberto Quintanilha [1]
[1] Escola Politécnica da Universidade de São Paulo
Departamento de Engenharia de Transportes – Laboratório de Geoprocessamento
Av. Prof. Almeida Prado, Travessa 2. nº 83
Cidade Universitária – São Paulo – Brazil
CEP: 05508-900
Tel: +55 11 3818 5504
[2] Aerocarta Engenharia de Aerolevantamentos S/A
Rua Michigan, 547 – São Paulo – Brasil
CEP: 04566-000
Tel: +55 11 5543 6466
raanobrega@ig.com.br
jaquinta@usp.br

KEY WORDS: Image Balancing, Local Image Processing, Restoration, Enhancement, Automation, Homogenization, Correlation.

ABSTRACT

Image Balancing is a process able to minimize radiometric divergences at one or several adjacent images. Many factors can cause this divergence and some of them can be explained like chromatic aberrations in different aerial camera positions, hot spots, sun glint and differences in scanner quality, differing film types or images acquired at different times. The effects above usually can be found in aerial photograph, specially in a mosaic composition, turn visible few inconsistencies across images colors, brightness and contrast.

For manual film process, technicians have used different illuminations to distinct regions of image through attenuant light filters to hot spot region and high illumination to dark region, estimating how much light change in color was needed in each part of image to create a perfect balancing. This process was carried over from analogical photographic world to the digital one. Today, the typical image-balancing process requires an operator to load each digital image into a computer to manually or automatically lighten, darken, color-correct and crop each image until it satisfactorily matches adjacent photos, balancing one or all several images together.

The necessity of image balancing in Photogrammetry now is more than visual effects. Correlation process like Automatic DTM generation or Automatic Triangulation have better effects to balanced images than non-balanced images. This paper purpose is show the actual state of the art as well as the main software and hardware solutions to this problem, suggesting suitable methodology to practical works, reporting comparative results and any development implementation methods.

1-INTRODUCTION

Actually, there are many techniques and tools for Digital Image Processing, some of them come from actual technological revolution, substituting almost completely analogical proceedings and tools, used for several decades. The main objective methodological reorganization, to adapt analogical techniques to digital world, is to implement automatic procedures minimizing time and cost and maximizing productivity for any application.

Image Process is a computer based technique which origin with photographs, photographic films and photographic cameras appearing. As well as this photographic product, Image Processing also had developed during the time. Otherwise Digital Image Processing applied in Orbital Remote Sensing, image

balancing techniques have arisen from Photogrammetry necessities, minimizing light exposure in hot spot regions and increasing light in dark regions.
However efficient, analogical procedures consist into manual photographs manipulation, executing unlike enhancement to distinct regions of aerial photo thought color filters, different illumination or local chemical products application, demanding experienced Photogrammetry laboratory technicians.
The actual state of digital technology turn obsolete the most of high precision optical/mechanical photogrammetric instruments that today do not stand out between main photogrammetric systems.
As well as in an analogical instrument, the mathematical concept was preserved in a Digital Photogrammetry. The principal change involved software and hardware implementation to replace stereo-plotters and others mechanical instruments to digital system able to produce maps, orthophotos and digital terrain models, proposing always the automation of the process.
Image balancing, based at digital image enhancement and restoration concepts involves local image processing to calculate statistical parameters locally, automated or manually, for radiometric image benefit.

2-OBJECTIVES

This paper is a part of developing research project by Geoprocessing Laboratory of University of São Paulo, suggesting specific investigation about image balancing techniques, reporting history, and the evolution from photographic to digital process. The project involves real balanced samples produced automatically and manually by different software solutions as well as comparative results and techniques. Otherwise, any image balancing procedures have been tested and implemented using the MatLab® The MathWorks, Inc.
This paper purpose is report the actual state of the art to balancing images, reviewing and compare analogical methods, instruments, results and limitations to computer-based procedures. Furthermore, detailed explanation about digital technique will be showed, including figures, graphics and real samples, relating the local processing function to digital images.

3-METHODOLOGY

There are two specific purposes application to development of Digital Image Processing methods: graphical information processing for human interpretation and graphical information processing for automatic systems (Gonzales and Woods, 1993). The necessity of homogeneity in aerial photographs occur to both purposes application, in a graphical quality of image derived products like orthophotos and mosaics or in an automatic correlation process like triangulation, DTM or pattern recognition.
This research idealization has arisen from practical activities at photogrammetric company projects and from Digital Image Processing academic knowledge, motivating bibliography investigation and solution, consulting Photogrammetry software developer as well as other universities and companies experiences.

3.1-Analogical Procedure

Photogrammetry always have used high geometric and radiometric quality technology in photograph products, though aerial films stability and aerial cameras as well as in a film processing. Analogical aerial film process can be executed manually or automatically (single-frame contact printer and continuous-strip contact printer respectively).
Automated procedures request mechanical systems, without many human interventions. Manual processing, however demands human intervention, have best visual results than most of automatic mechanic systems.

3.1.1-Single-Frame Contact Printer: Human intervention can set exclusive enhancement for each image of roll film, promoting homogeneity in brightness and contrast for different regions of an image. During

manual aerial film processing technicians basically use chemical agents and special filters and illumination, able to customization, for different regions of photographs. Furthermore, only experienced technicians can know how many change in light need to fix photographic imperfections and produce homogeneous aspect.
Single-frame contact printer usually is equipped with many separately low-wattage lamps only for black and white contact prints. The lamps should be regulated independently, this allows the operator to compensate for any unevenness in the negative caused by vignetting by wide-angle lens.
The principal problem is that manual process spends much time, minimizing practical productivity.

3.1.2-Continuous-Strip Contact Printer: Actually, increasing lawsuit for color images had accelerated and transformed this procedure. Manual process, however with best results, are not so fast than mechanical systems. The most of automate systems can adjust temperature, light, time and others linear parameters, i.e. applied equality for all regions of image and all images of roll.
Basically, two types of continuous printers have been used by Photogrammetry, Non-Dodging Printers, manufactured during Word War II, appropriated for large roll films because of high-speed contact printing, but without any light homogenization and Continuous Electronic Dodging, manufactured by LogEtronics, Inc, that can expose the roll film changing scan speed for different regions of image, promoting light balancing for each independent image.

3.2-Digital Procedure

With the instruments revolution to digital world, new techniques have been created, using ancients models to implement procedures suitable to produce results like or better analogical instruments. The great gain involves time and cost. For each new-implemented model tested there are an analogical model result to be compared and this efficiency gain usually can be explained by computer upgrade.
In a recent Photogrammetry, the first revolution involved the introduction of electronic systems, where older stereoplotters using high precision optical and mechanical system was substituted by analytical systems using electronic systems and partially computer resources. Actually these analytical instruments are no more top of high technology. Today stereoplotters uses digital resources, based in a computer system, substituting completely optical/mechanical interactions for mathematics models.
The aerial photograph already can be generated by digital cameras, but it still not so usual because the digital photogrammetric camera technology is recent. The actual digital process need photogrammetric scanner, responsible to analogical/digital conversion.
For any system, aerial photographs always need preprocess. Procedure like digital filters, histogram adjusting or Look Up Table creation, are linear, i.e. the same parameters applied for all images and to produce homogeneity for all images it have to be locally calculated and applied.
The principal objective of enhancement techniques is to process an image so that the result is more suitable than the original image for a specific application (Gonzales and Woods, 1993). Then, we can assume that image balancing can be classified like image enhancement technique, because balanced images have better visual aspect and automatic correlation results than original images.
Otherwise, the same authors entitle to image restoration the process able to reconstruct and recover an image that has been degraded some a priori knowledge of the degradation phenomenon. Thus restoration techniques are oriented toward modeling the degradation and applying the inverse process in order to recover the original image. Thus, image balancing can be assumed like restoration technique too.
For any classed technique, the process has to be personalized for each region of an image and for each image of group. Statistic parameters have to be calculated and applied in a local histogram adjustment.
SCHOWENGERT, 1997 affirms that the essential idea to local processing is based at the partition of an image in several adjacent blocks for pixel-by-pixel benefit using local parameters, called Local Range Modification (LRM).

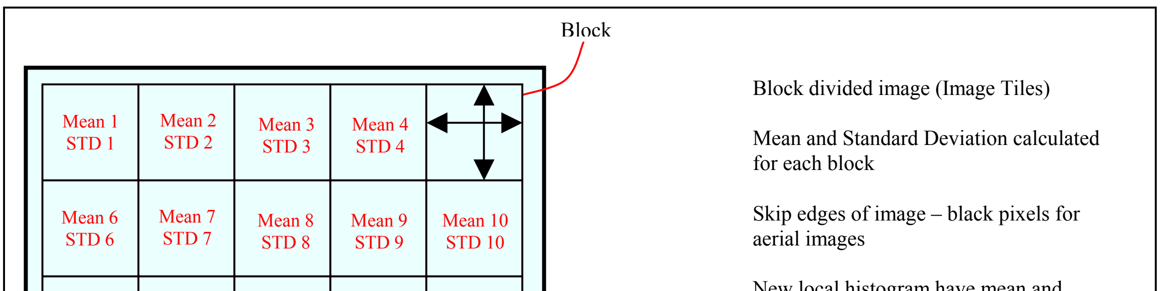

Figure 1: Illustrative sample of Local Range Modification technique (LRM) according SCHOWENGERT, 1997 and adapted at Dodger© software by LH Systems, LLC.

3.2.1-Single Image Balancing: The technique of local processing can be easily explained using one single image first. It consists at calculus of local adaptative parameters. The concept involves basically LRM adaptation to balancing necessities that enables differentiated adjusts for each image adjacent block. The first step is the global parameters extraction, i.e. mean and standard deviation for each color channel. This parameters are used to compare each independent block parameter, estimating witch regions of original image need to be modified, in other words, if the block is darken than image mean, local and global parameters will be help to estimate the perfect bright to this block.
Another important factor to balance images is the color channel decomposition to RGB (Red, Green and Blue respectively). After decomposition, each RGB channel is processed independently, preserving LRM structure. It demands three independents steps, which will need more time and memory to computer system.

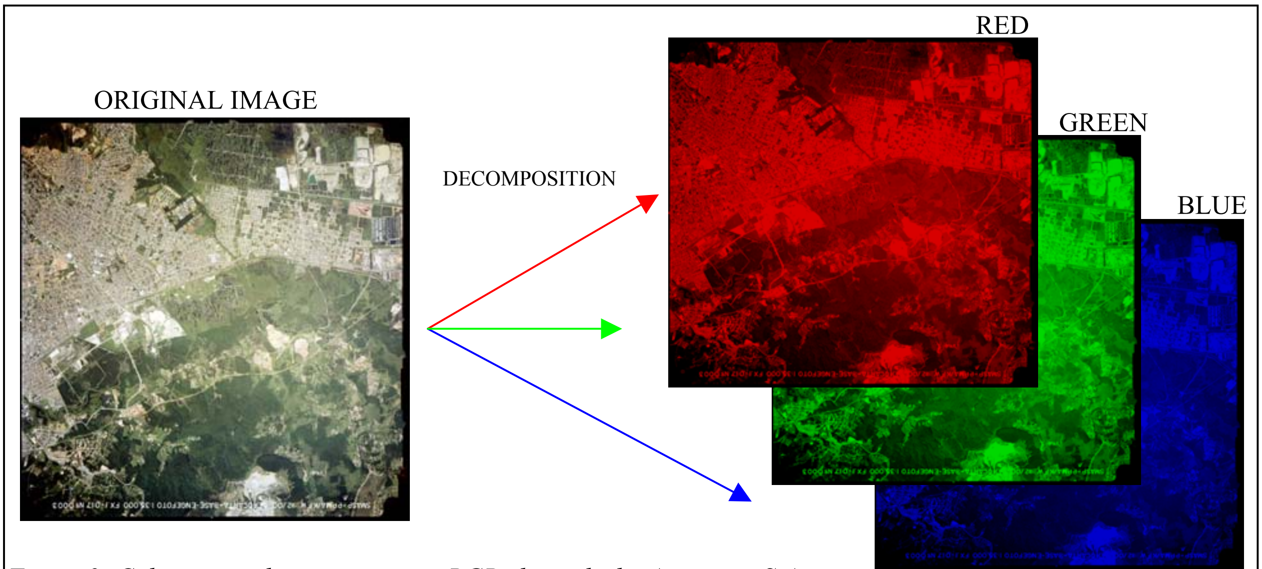

Figure 2: Color image decomposition in RGB channels, by Aerocarta S.A.

Normally dark regions occur near the edges and central region of image is more lighten. However can occur hot spot regions near the border in water features like river, ocean or lakes or the relief can influence drastically images aspect producing large shadow valleys.

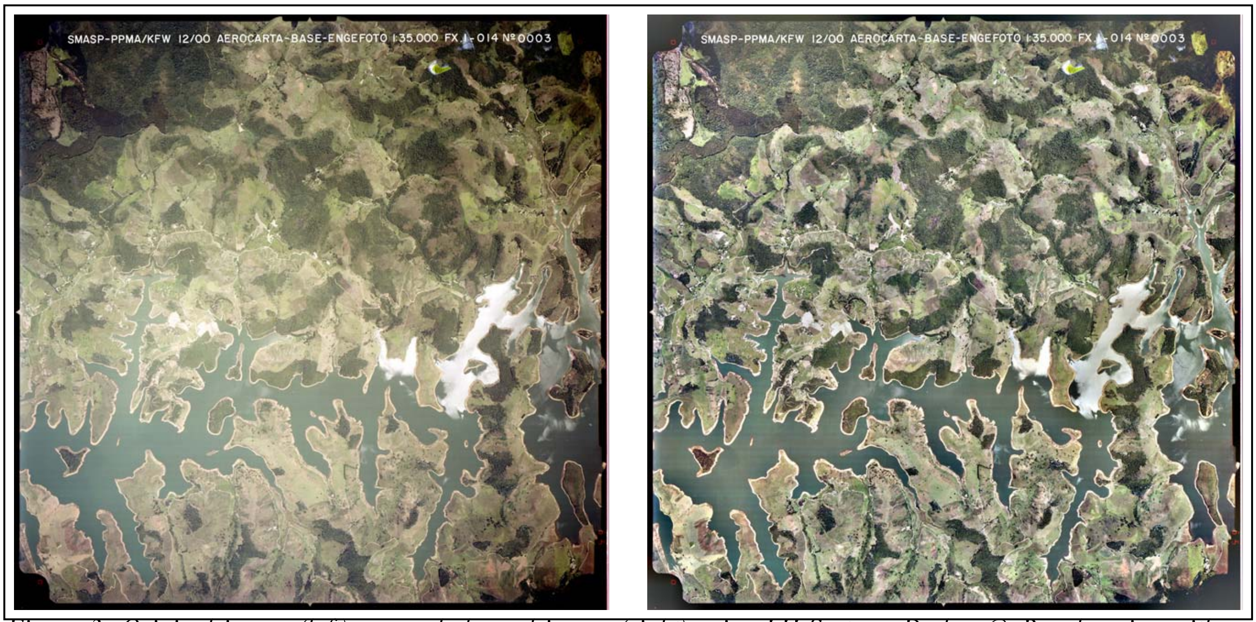

Figure 3: Original image (left) versus balanced image (right) using LH Systems Dodger©. Rural region with intense water presence – Sao Paulo State - Brazil, scale.1: 35000, ceded by: Aerocarta S.A

3.2.2-Multi-Images Balancing: Aerial Photogrammetry always involves several images, distributed per flight strips according project parameters. Sometimes the project needs more than one flight at different time to recover any geographical place. This demands difference at images aspect by different aerial film, atmospheric conditions or sun glint. For any multi-images visualization like mosaics of photo-indexes, the radiometric quality of these images will be compromised. Then, if the same images were balanced, the mosaic or photo-index generated probably will have best visual aspect.

When image balancing is applied for several images together, the principle does not differ of single-image balancing. First all images have to be decomposed to RGB channels, then the program will calculate three independents global values for histogram stretch for each color channel, as showed at following figure:

	Block i			Block ii			Block iii			Block iv			. . .	**IMG 1**		
Mean	120	119	133	127	129	118	125	131	125	138	144	138	. . .	**128**	**131**	**129**
STD	36	39	38	33	37	29	34	39	33	36	36	36	. . .	**35**	**38**	**34**

	Block i			Block ii			Block iii			Block iv			. . .	**IMG 2**		
Mean	132	117	145	143	143	139	139	129	133	145	153	147	. . .	**136**	**133**	**137**
STD	43	31	42	38	35	31	36	32	29	44	45	39	. . .	**39**	**38**	**37**

.
.
.

	Block i			Block ii			Block iii			Block iv			. . .	**IMG n**		
Mean	125	122	131	132	110	136	131	115	121	136	119	132	. . .	**129**	**119**	**129**
STD	37	27	32	35	27	33	36	25	32	32	29	36	. . .	**35**	**26**	**33**

Calculated Parameters		
129	**119**	**129**
35	**26**	**33**

Table 1: Mean and Standard Deviation – single and multiple images sample

According to table 1, different color channel brightness and contrast between images are expresses by mean and standard deviation. Each image histogram is used to automatically estimate ideal color channel parameters. Most of large image balancing applications use this method to estimate the ideal RGB image histograms to be applied to each image.

Base in these desired parameters, the program will calculate how many change in color histograms each image need to seem with ideal image.

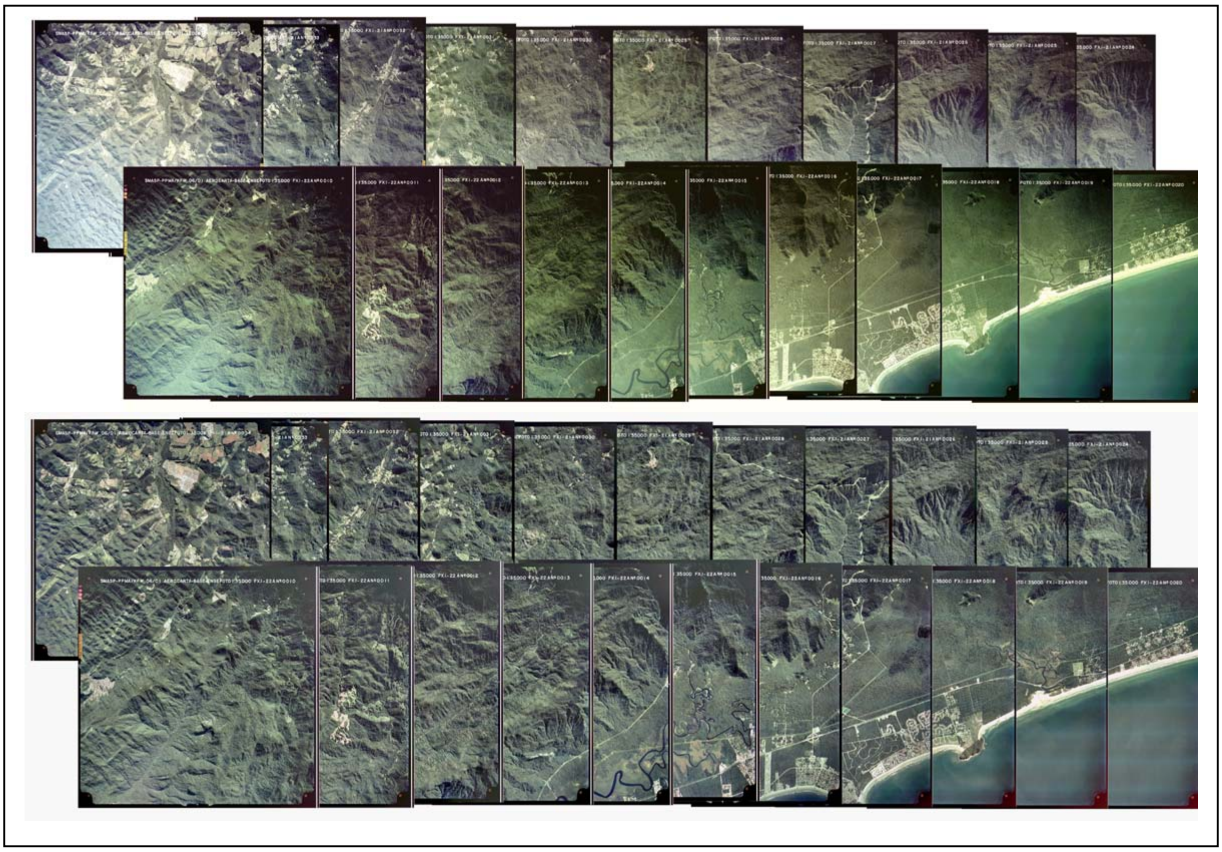

Figure 4: Original Images Photoindex versus Balanced Images Photoindex using LH Systems Dodger©. São Paulo State-Brazil, scale.1:35000, ceded by: Aerocarta S.A

There are some image balancing programs suitable to color parameter extraction, image-by-image, calculating ideal parameters and estimating how many change each channel histogram will need to each image, without process them. These parameters can be reported to posterior detailed process.
Desired histograms already can be manually inputted by operator, based in an ideal image. This method only will produce good results if the operator already knows the corrects parameters to be used for all images.
Look Up Table (LUT) can be used to balance images too. Some image software use LUT to index image color information and generally, each image have an exclusive LUT. The LUT balancing consists in a simple merge of tables to all images, but it is so dangerous process because there are no histograms differences estimation and this modification is applied equally for all regions of image.

4-RESULTS

However this research project still open, any results already can be concluded. About algorithm implementation, the MatLab® program does not run faster then other commercials software, but its tools are efficient and there are many implemented basic digital image processing routines like filters, block processing, format conversion and histogram adjust. Them can easily help the development of advanced procedures.
The use of LRM technique implemented in MatLab® for image balance proposed have obtained good results for single and multi-image processing, confirming the efficiency of local processing method. Complementary study have to consider for soften visual discrepancies between processed blocks therefore simple LRM application can enlighten seamless, damaging visual image quality. Then, any interpolation methods have been tested according to Artero and Tommaselli, 2000 and the results can be showed at Figure 5:

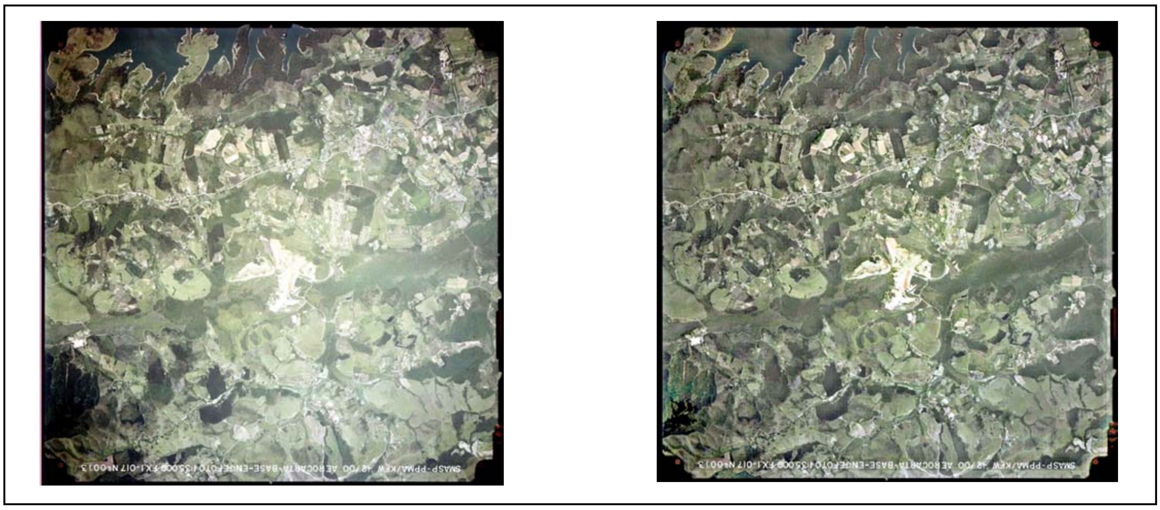

Figure 5: Original Image (left) versus Balanced Image (right) – obtained by implemented procedure using MatLab®.

For practical viewpoint , this results satisfy the expectation because the first idea was research digital techniques to attend only visual aspects of image for mosaic composition, but the research involved correlation results study too. Based in a possible gain during automatic correlation process of images, some tests have been executed using color and black-and-white aerial photographs. The correlation process was the automatic tie point generation using HATS - Helava Automatic Triangulation System core of SocetSet© 4.2 by LH Systems, LLC. After created the project, two subsequent automatic triangulation was processed, first using only non-balanced images and then using balanced images. These two steps was repeated for color and black-and-white projects executed by AEROCARTA S.A for different places during approximately six months, using several large projects size with approximately 100 images distribute in several strips.
The general efficiency of technique results can be reported in the obtained gain that increased from 55% to 67% for color images and from 55% for 79% for black-and-white images.

5-BIBLIOGRAPHY

American Society of Photogrammetry, 1980. Manual of Photogrammetry, Falls Church, VA, USA. Fourth Edition pp. 305-363.

ARTERO, A. O., TOMMASELLI, A. M., 2000. Limiarização Automática de Imagens Digitais, Boletim de Ciências Geodésicas, Curitiba, Brazil, pp 38-48.

AVERY, T. E., 1968. Interpretation of Aerial Photographs, Urbana, Illinois, EUA. Second Edition, pp.86-97.

CORBLEY, K.P., 1996. Color Aerial Photography is Setting Lorain Country, Ohio's Digital Ortho-Based GIS Project Apart from Many Others, Denver, CO, USA.
http://www.eomonline.com/Comon/Arquives/April96/corbley.htm (24 May 2001)
DREW, M. S., WEI, J., LI, Z.N., 1999. Illumination-Invariant Image Retrieval and Video Segmentation, Pattern Recognition Society – 32 pp1369-1388.

GONZALES, R. C., WOODS, R. E., 1993. Digital Image Processing, New York, USA. Chap. 4,5,7.

LATOREE, M., DIAS, A., SHIMABUKURO, Y., CARVALHO, O., 2001. A Influência dos Efeitos da Geometria de Iluminação na Análise de Alvos de Superfície Terrestre Obtidos a Partir de Dados

AVIRIS., Congresso Brasileiro de Sensoriamento Remoto, Foz do Iguaçu – Brazil

LH - Systems, 1998. Socet Set User Manual - Image Balancing: Dodger, San Diego, USA. Chap. 36 pp. 1-10.

NOVO, E. M., 1992. Sensoriamento Remoto Princípios e Aplicações, São José dos Campos, Brazil. Segunda Edição, pp.205-265

SCHOWENGERDT, R. A., 1997. Remote Sensing Models and Methods for Image Processing, San Diego, CA, USA. Second Edition, pp. 202-219.

STRAND, E. J., 1999. It Takes a Wizard to Create Seamless Air Photo Mosaics. Synergetics Inc, Fort Collins, CO, USA.
http://www/geoplace.com/gw/1999/0199/199nuts.asp (25 May 2001)

ZHAO, L., YANG, Y.H., 1999. Mosaic Image Method: A Local and Global Method, Pattern Recognition Society - 32 pp.1421-1433.

Study of a processing chain to provide multispectral high resolution fused images for the "Pleiades-HR" system

Michel Pausader
CNES, Toulouse, France

The imaging Spot satellite series will finish with Spot5 to be launched in 2002. The next generation is named "Pleiades" which is a concept of various dedicated smaller platforms. One of them, dedicated to optical high-resolution observation, is "Pleiades-HR", scheduled for 2006. One satellite will embark an instrument acquiring altogether a panchromatic band at 0.7 meter resolution (at nadir) and four multispectral bands (blue, green, red and near infra-red) at 2.8 meters. The main product delivered by the system should be a high-resolution color image at 2.8 meters obtained by fusion of the panchromatic and the multispectral bands.

The quality of this product will depend on the quality of registration of the five bands. None of these bands are natively registered because there is no beam splitter as on the Spot instrument. The acquisition is made for the panchromatic band by a TDI detector and for the multispectral bands by a dedicated four-band detector. The four-band detector consists in a chip with four detector lines with a different band filter placed over each.

Therefore each of the 5 spectral bands "sees" the ground with a different viewing angle. Nevertheless the difference between this angles will be small : less than 2 milliradians between the pair of most distant bands. The misregistration defaults may then occur from several origins, the main being : uncertity of the digital terrain model used, attitude changes between the different acquisitions (0.2 second at most) and uncertity on the focal plane viewing directions.

To overcome these problems and guarantee a good quality of the image resulting from the fusion, a processing method is under study. The input data are simulated bands computed from higher resolution aircraft acquisitions. During the simulation process, it is possible to inject defaults such as the ones listed above with values corresponding to those assumed to occur on "Pleiades-HR" (resulting also from simulations as the dynamic behavior of the platform and so on …) . Therefore we can obtain perfect data (i.e. without default) which will serve as a reference and data with several levels of degradation. These data are then processed in order to measure and compensate the registration defaults, resample the bands to the final resolution and achieve the fusion process. The processing makes use of a matching process to compute the registration defaults. This study will allow to investigate the type of processing needed according to the level of the defaults and the efficiency of the processing. The study is being achieved for altogether false-color classic image (using green, red and near infra-red bands) and natural color image (using blue, green and red bands) .

The paper will describe the methodology and give some preliminary results.

DIRECT GEOREFERENCING OF MULTI-LINE IMAGES WITH A GENERAL SENSOR MODEL

Daniela Poli
Institute of Geodesy and Photogrammetry
Swiss Federal Institute of Technology, Zurich, Switzerland
daniela@geod.baug.ethz.ch

KEY WORDS: Multi-line sensors, Pushbroom sensors, Sensor orientation, GPS, INS.

ABSTRACT:

A general sensor model for the direct georeferencing of multi-line images acquired by CCD array sensors is under development at our Institute. The model is designed for sensors carried on both spacecraft and aircraft. If the sensor position and attitude are provided by additional observations (GPS/INS), the model computes the approximations of the ground coordinates with a linear forward intersection of two lines and refines them with least squares methods, using all the available lines and according to collinearity equations. For these operations, no GCPs are needed.
This paper describes the mathematical formulation of the model and analyses the results achieved by testing it on stereoimages from the Japanese TLS (Three-Line Sensor), using GPS/INS observations for the external orientation. The ground coordinates of 47 GCPs were available and used as reference data for the results' analysis. These first results from the direct georeferencing showed that a correction of the orientation data for systematic errors was required. The offset vector between GPS antenna and the camera centre of projection was estimated and used to correct the position data. The results improved considerably. Anyway the sensor position and attitude will be improved, by modeling them with polynomial functions depending on time and using GCPs.

1. INTRODUCTION

CCD array sensors often consist of one or more lines of CCD elements that acquire images in a pushbroom mode. Today, a wide class of pushbroom sensors with different characteristics (dimensions, design, stereo-geometry, resolution, etc.) exists and satisfies the requirements for photogrammetric and remote sensing applications.
In particular, a large number of pushbroom scanner systems produce stereo images; some of them are carried on airplane (i.e. ADS40, HRSC, DPA, WAAC, AirMISR) or helicopter (i.e. TLS), others on spacecraft (i.e. SPOT, IRS, JERS, MOMS, MISR, WAOSS, ASTER, IKONOS) and can be used for photogrammetric mapping at different resolutions.
The stereoscopy of the images is achieved across- or along- track with respect to the flight direction. Sensors with across-track stereo capability, usually carried on spacecraft (SPOT, IRS) consist of one line of CCD elements and acquire stereopairs at different times (time delay can be in the order of days or months). On the other hand, sensors with along-track stereo capability consist of two or more CCD-lines viewing with different angles backward and forward the flight direction. The advantage of this geometry is that a larger number of images with a small time delay between their acquisition is available.
Each line in the images is independently acquired with a different exterior orientation, so a classic bundle adjustment is not realistic, because the number of unknowns would be huge.
For this reason, the exterior orientation is usually modeled as a polynomial function depending on time (Zhong, 1992, Lee, 2000). In case of sensors carried on spacecraft, the physical properties of the satellite orbit are used as constraints (Ebner, 1992, Kratky, 1989). Anyway, a sufficient number of well-distributed Ground Control Points (GCPs) is required.
As far as the sensors carried on aircraft are concerned, in most cases the exterior orientation is directly measured with high precision with GPS/INS instruments carried on board and used for the georeferencing and image rectification (Cramer, 2000, Hahn, 1996, Mostafa, 2000, Tempelmann, 2000).

A general sensor model for the georeferencing of stereo images produced by a wide class of CCD array sensors is under development at our Institute. The model is designed for multi-line CCD sensors with along-track stereo capabilities, mounted on spacecraft or aircraft.
If the direct measurement of the sensor position and attitude is available, photogrammetric mapping is performed by direct georeferencing, as described in this paper.
Otherwise, the sensor position and attitude are modelled with polynomial functions depending on time using a sufficient number of well-distributed GCPs.
This paper describes the model for direct georeferencing of images from multi-line CCD array sensors and the results from the test made with the TLS sensor (Section 2). As the external orientation needed an improvement, the algorithm for the position and orientation modeling is presented and first results are shown (Section 3).

2. DIRECT GEOREFERENCING

2.1 Reference systems

The pixel coordinates of corresponding points (column u, row v) are measured in an image reference system with origin at the top-left corner of the image. Then, they are transformed into the body reference system with origin at the center of the sensor, x-axis directed along the flight direction, z-axis looking downwards and y-axis directed along the scan-line, completing a right-hand coordinate system.
The relationship between pixel and body coordinate systems is:

$$\begin{bmatrix} x \\ y \\ z \end{bmatrix} = R_y(\alpha) \cdot \begin{bmatrix} 0 \\ \left(u - \dfrac{n\_col}{2}\right) p_y \\ -c \end{bmatrix} \qquad (1)$$

where α is the off-nadir angle of the current CCD-line, $R_y(\alpha)$ is the rotation matrix around the y-axis, p_y is the pixel size in y direction (in mm) and n_col is the image size in y direction (number of columns).
The coordinates in the body frame can also be available through calibration measurements, if available.
GPS and INS instruments provided the sensor position and attitude. The aircraft position is measured in a geographic coordinate system (latitude λ, longitude φ and height h), with WGS84 as reference ellipsoid.
The attitude (roll r, pitch p, yaw j) are defined in a local Eulerian coordinate system centered at the IMU instrument on the aircraft, with x and y axis tangent to the local parallel and meridian and z completed a right-hand system. The attitude angles represent the rotations between the local and the body frames and define the rotation matrix R^{bl} from the body to the local system:

$$R^{bl} = \begin{bmatrix} \cos p \cos j & -\cos p \sin j & \sin p \\ \cos r \sin j + \sin r \sin p \cos j & \cos r \cos j - \sin r \sin p \sin j & -\sin r \cos p \\ \sin r \sin j - \cos r \sin p \cos j & \sin r \cos j + \cos r \sin p \sin j & \cos r \cos p \end{bmatrix} \qquad (2)$$

In order to simplify the calculations, a local Eulerian coordinate system fixed on the ground is introduced (Figure 1). It is centered at point P placed in the middle of the projection of the aircraft trajectory, at zero height, with X'-axis tangent to the local parallel and looking toward East, Y'-axis tangent to the local meridian and looking toward North and Z'-axis upwards directed.

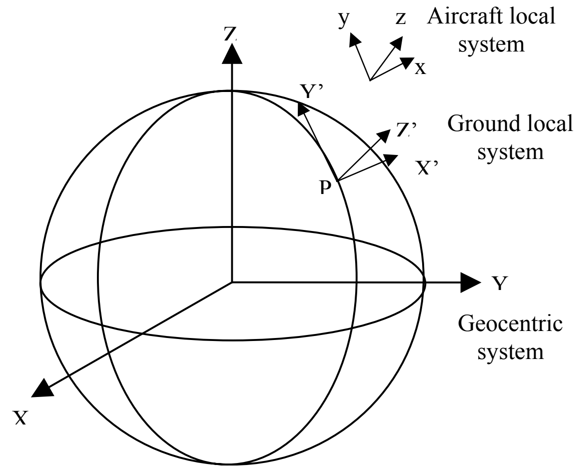

Figure 1. Aircraft and ground local systems and geocentric frame.

For our computations, the matrix that transforms coordinates from the body to the local ground system is required. This matrix is different for each line and can be described as the combination of three rotations: 1) from the body to the aircraft local system (R^{bl}), 2) from the aircraft local system to the geocentric one (R^{GL}) and 3) from the geocentric system to the ground local frame (R^{lG}):

$$R^{bL} = R^{bl} R^{lG} R^{GL} \tag{3}$$

R^{bl} and R^{lG} are time-dependent, while R^{GL} is constant.
Calling X_P, Y_P, Z_P the geocentric coordinates of the origin of the ground local system (point P) and φ_P and λ_P its latitude and longitude, the transformation from the geocentric to the ground local system is (Wang, 1990):

$$\begin{bmatrix} X' \\ Y' \\ Z' \end{bmatrix} = R_x(90-\varphi_P) R_z(90-\lambda_P) \begin{bmatrix} X - X_P \\ Y - Y_P \\ Z - Z_P \end{bmatrix} \tag{4}$$

where (X, Y, Z) are the coordinates in the geocentric system, (X', Y', Z') in the ground local system. In particular,

$$R^{GL} = R_x(90-\varphi_P) R_z(90-\lambda_P) \tag{5}$$

R^{lG} is the transpose (or inverse) of R^{Gl}. According to Eq. 5, it is equal to:

$$R^{Gl} = R_x(90-\varphi) R_z(90-\lambda) \tag{6}$$

where φ and λ are the longitude and latitude of the aircraft.
Finally, R^{bl} is described by Eq. 2.

2.2 Estimation of approximate ground coordinates

A linear forward intersection of two homologous rays is performed in the ground local system in order to estimate the ground coordinates that will be used as initial approximations in the subsequent refinement (Figure 2). For this step, no Ground Control Points (GCPs) are required, because GPS/INS instruments provide the exterior orientation.

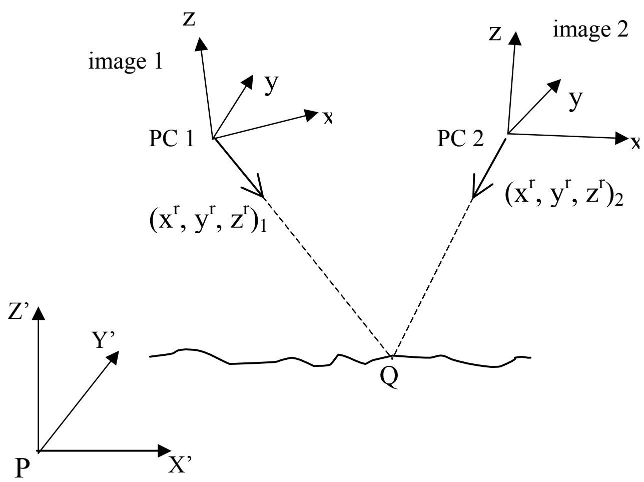

Figure 2. Geometric intersection of two homologous rays from perspective center of image 1 (PC 1) and image 2 (PC 2).

Each homologous ray is written as:

$$\begin{bmatrix} X \\ Y \\ Z \end{bmatrix} = \begin{bmatrix} X_0 \\ Y_0 \\ Z_0 \end{bmatrix} + \lambda \begin{bmatrix} x^r \\ y^r \\ z^r \end{bmatrix} \tag{7}$$

where:
- (x^r, y^r, z^r) is the observation vector in the body system rotated according to R^{bL},
- (X, Y, Z) are the point coordinates and (X_0, Y_0, Z_0) the sensor position for the current line, both in the ground local system,
- λ is the scale factor to be estimated.

Imposing the intersection of two rays, one from image 1 and one from image 2, as shown in Figure 2, yields:

$$\begin{bmatrix} X \\ Y \\ Z \end{bmatrix} = \begin{bmatrix} X_0 \\ Y_0 \\ Z_0 \end{bmatrix}_1 + \lambda_1 \begin{bmatrix} x^r \\ y^r \\ z^r \end{bmatrix}_1 = \begin{bmatrix} X_0 \\ Y_0 \\ Z_0 \end{bmatrix}_2 + \lambda_2 \begin{bmatrix} x^r \\ y^r \\ z^r \end{bmatrix}_2 \tag{8}$$

that gives the system:

$$\begin{aligned} X_{01} + \lambda_1 x_1^r &= X_{02} + \lambda_2 x_2^r \\ Y_{01} + \lambda_1 y_1^r &= Y_{02} + \lambda_2 y_2^r \\ Z_{01} + \lambda_1 z_1^r &= Z_{02} + \lambda_2 z_2^r \end{aligned} \tag{9}$$

In matrix notation, we have:

$$\begin{bmatrix} x_1^r & -x_2^r \\ y_1^r & -y_2^r \\ z_1^r & -z_2^r \end{bmatrix} \cdot \begin{bmatrix} \lambda_1 \\ \lambda_2 \end{bmatrix} = \begin{bmatrix} X_{02} - X_{01} \\ Y_{02} - Y_{01} \\ Z_{02} - Z_{01} \end{bmatrix} \tag{10}$$

that can be written as $A\lambda = b$.

This system is solved with the linear least squares method, with solution $\lambda = (A^T A)^{-1} A^T b$ and gives the two scale factors that minimize the distance between the two intersection rays. Substituting the scale factors into Eq. 8 for both images, two different ground points are obtained. The mean is taken as approximation of the ground coordinates of the current point.

2.3 Forward intersection

The approximations for the ground coordinates previously obtained imposing the intersection of two lines are refined using all the available lines, according to the collinearity equations:

$$\begin{aligned} x &= -c \cdot \frac{r_{11}^{bL}(X - X_0) + r_{21}^{bL}(Y - Y_0) + r_{31}^{bL}(Z - Z_0)}{r_{13}^{bL}(X - X_0) + r_{23}^{bL}(Y - Y_0) + r_{33}^{bL}(Z - Z_0)} \\ y &= -c \cdot \frac{r_{12}^{bL}(X - X_0) + r_{22}^{bL}(Y - Y_0) + r_{32}^{bL}(Z - Z_0)}{r_{13}^{bL}(X - X_0) + r_{23}^{bL}(Y - Y_0) + r_{33}^{bL}(Z - Z_0)} \end{aligned} \tag{11}$$

These equations represent the relationship between the observed coordinates (x, y) in the body coordinate system and the coordinates (X, Y, Z) in the ground local system. (X_0, Y_0, Z_0) is the vector containing the sensor position in the ground local frame and the matrix R^{bL} represents the rotation from the body to the ground local systems. c is the principal distance.
The equations are linearized according to the first-order Taylor decomposition and the system

$$Ad = l \tag{12}$$

is obtained, where:
-A is the design matrix, containing the first derivatives of the two functions with respect to the unknowns, evaluated with the approximations,
- d is the unknown vector (dX, dY, dZ).
- l is the vector of the differences between the observed coordinates and the same coordinates evaluated substituting the approximations in Eq. 11.
Calling P the weight matrix of the observations, the system is solved with the solution:

$$d = (A^T PA)^{-1} A^T Pl \tag{12}$$

The residuals are calculated as:

$$v = Ad - l \tag{13}$$

and the σ a posteriori is equal to:

$$\hat{\sigma}_0 = \sqrt{\frac{v^T Pv}{r}} \tag{14}$$

where r is the redundancy of the system, that is, the difference between number of equations and the number of unknowns.
The iterations are repeated until absolute tests on the solution are satisfied.

2.4 Results

The model has been tested on the Japanese TLS (Three Line Sensor). The sensor consists of one optical system (focal length: 60.36 mm) and three lines of 10200 elements each (pixel size: 7x7 μm), scanning in forward (+21.5°), nadir and backward (-21.5°) directions (Murai, 1995). The internal orientation and the pixels' positions in the focal plane were available from calibration. The sensor was carried on a helicopter that flew at a mean height of about 475 m above ground. A GPS receiver and an INS instrument were mounted on the helicopter too, so the attitude and position for each exposure were available, but without any information about their accuracy.
The image and ground coordinates of 46 well-distributed GCPs were provided and used for our tests. The approximate ground coordinates were computed and refined with the least square forward intersection, as described in Sections 2.2 and 2.3.
The coordinates estimated for the 46 GCPs were transformed in the geocentric coordinate system and compared to the correct ones. Figure 3 shows the differences in XY and Z between the two sets of coordinates.

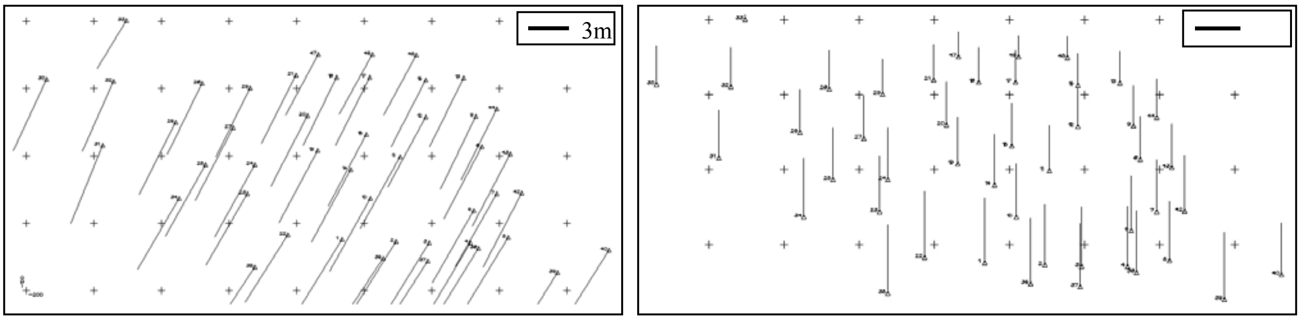

Figure 3. Plot of difference in XY (left) and Z (right) between correct coordinates and computed coordinates of 46 GCPs.

It is evident that the estimated coordinates are shifted by a constant value from the correct ones, probably because the offset vector between the GPS antenna and the camera center of projection was not subtracted.
Therefore, the direct measurement of the sensor exterior orientation using GPS/INS data was not sufficient for an accurate photogrammetric mapping and the use of GCPs for data correction is required.

3. IMPROVEMENT OF EXTERIOR ORIENTATION

3.1 GPS offset estimation

For the estimation of GPS offset, the collinearity equations (Eq. 9) are used and the sensor position for each line (X_0,Y_0,Z_0) is supposed equal to the observed position (X_{GPS},Y_{GPS},Z_{GPS}) plus a constant offset (ΔX, ΔY, ΔZ) to be estimated:

$$X_0 = X_{GPS} + \Delta X \qquad Y_0 = Y_{GPS} + \Delta Y \qquad Z_0 = Z_{GPS} + \Delta Z \tag{15}$$

The collinearity equations are linearized with respect to ΔX, ΔY and ΔZ and, using the same notations as above, the system $Ad = l$ is obtained and solved with least square methods.

The algorithm was applied to TLS data, using 8 well-distributed GCPs, and an offset of –2.87 m in *X*, -5.37 m in *Y* and 3.15 m in *Z* was estimated.
The forward intersection was repeated for 38 check points (CP) including the offset and the results improved, as shown in Figure 4. The mean differences between correct and calculated coordinates were equal to 0.186 m (in *X*), -0.306 m (in *Y*) and 0.081 m (in *Z*) with RMS of 0.549 m (*X*), 0.797 m (*Y*) and 0.462 m (*Z*).

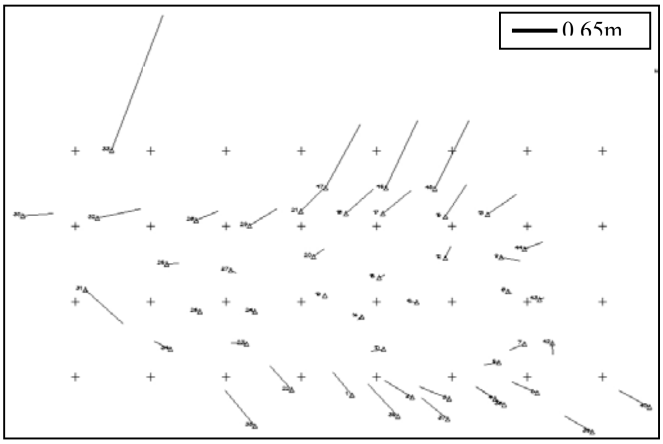

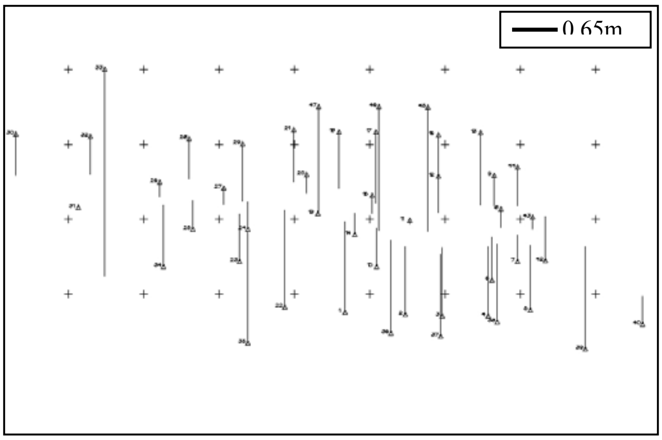

Figure 4 Plot of difference in XY (left) and Z (right) between correct coordinates and calculated coordinates of 38 CPs after correction of sensor position

The results still show a small difference between the correct and estimated ground coordinates, so a further refinement of the GPS and INS data is required for the improvements of the results.

3.2 Position and attitude modelling

The sensor exterior orientation is modeled with time-depending functions. The aircraft trajectory is divided in *N* blocks, according to the number and distribution of GCPs. In each block *i*, which is delimited by an initial and final time t_i^i and t_f^i, the sensor attitude and position are modeled with polynomial function depending on time $\bar{t} = t - t_i^i$, where t is the time of acquisition of the processed line:

$$\begin{aligned} X(\bar{t}) &= p_0^i + p_1^i\bar{t} + p_2^i\bar{t}^2 \\ Y(\bar{t}) &= p_3^i + p_4^i\bar{t} + p_5^i\bar{t}^2 \\ Z(\bar{t}) &= p_6^i + p_7^i\bar{t} + p_8^i\bar{t}^2 \\ \omega(\bar{t}) &= p_9^i + p_{10}^i\bar{t} + p_{11}^i\bar{t}^2 \\ \varphi(\bar{t}) &= p_{12}^i + p_{13}^i\bar{t} + p_{14}^i\bar{t}^2 \\ \kappa(\bar{t}) &= p_{15}^i + p_{16}^i\bar{t} + p_{17}^i\bar{t}^2 \end{aligned} \qquad (16)$$

The unknowns are 18 for each block and are estimated with least square solution. Constraints on the continuity of the functions and of the first derivatives are set on the borders of the block. Currently, the algorithm is under development.

4. CONCLUSIONS

The sensor model developed at our Institute was successfully tested with triplet images acquired by the Japanese TLS sensor. A direct georeferencing, using GPS and INS data for the external orientation and without any GCPs, provided the ground coordinates of 46 points that were measured in the images. After comparing the estimated coordinates to the correct ones, the results showed that an improvement of the exterior orientation data was required. At first, a shift of GPS antenna was estimated using GCPs and subtracted to the position data. The results improved, but a refinement of the attitude data is still required. Currently, the algorithms for the modeling of the sensor attitude (and position) with polynomial functions is under development.

5. ACKNOWLEDGMENTS

Acknowledgments are due to the Japanese Starlabo company, who kindly provided us the data from TLS sensor for our tests and allowed the publication of the results.
I would also like to thank Dr. Livio Pinto, from TU of Milan, for his advice about GPS and INS reference systems.

6. REFERENCES

Cramer, M., Stallmann, D., Haala, N., 2000. Direct georeferencing using GPS/INS exterior orientations for photogrammetric applications. International Archives of Photogrammetry and Remote Sensing, Vol 33, Part B3, pp.198-205.

Ebner, H., Kornus, W., Ohlhof, T., 1992. A simulation study on point determination for the MOMS-027D2 space project using an extended functional model. International Archives of Photogrammetry and Remote Sensing, Vol 29, Part B4, pp.458-464.

Fricker, P., Sandau, R., Walker, A.S., 1995: Airborne Digital Sensors- A New Approach. Proceedings of ISPRS Workshop “Sensors and Mapping from Space”, Hannover, Germany, on CDROM, paper #22.

Hahn, M., Stallmann, D., Staetter, C., Mueller, F., 1996. The DPA-sensor system for topographic and thematic mapping. International Archives of Photogrammetry and Remote Sensing, Vol. 31, Part B2, pp.141-146.

Kratky, V., 1989. Rigorous photogrammetric processing of SPOT images at CCM Canada. ISPRS Journal of Photogrammetry and Remote Sensing, No. 44, pp.53-71.

Lee, C., Theiss, H.J., Bethel, J.S., Mikhail, E.M., 2000. Rigorous mathematical modeling of airborne pushbroom imaging systems. Photogrammetric Engineering & Remote Sensing, Vol. 66, No.4, pp.385-392.

Mostafa, M.M.R., Schwarz, K., 2000. A multi-sensor system for airborne image capture and georeferencing. Photogrammetric Engineering & Remote Sensing, Vol. 66, No.12, pp.1417-1423.

Murai, S., Matsumoto, Y., Li, X., 1995. Stereoscopic imagery with an airborne 3-line scanner (TLS). In: International Archives of Photogrammetry and Remote Sensing, Vol.30, Part 5W1, pp.20-25.

Tempelmann, U., Boerner, A., Chaplin, B., Hinsken, L., Mykhalevych, B., Miller, S., Recke, U., Reulke, R., Uebbing, R., 2000. Photogrammetric software for the LH systems ADS40. International Archives of Photogrammetry and Remote Sensing, Vol.33, Part B2, pp.552-559.

Wang, Z., 1990. Principles of Photogrammetry (with Remote Sensing). Publishing House of Surveying and Mapping, Beijing, China.

REQUIREMENTS, REALISATION AND RESULTS OF A COMMERCIAL AIRBORNE DIGITAL SENSOR (ADS)

Ralf Reulke, Andreas Eckardt
Deutsches Zentrum für Luft- und Raumfahrt (DLR), Germany
Institute of Space Sensor Technology and Planetary Exploration
(Ralf.Reulke, Andreas.Eckardt)@dlr.de

KEY WORDS: Camera, CCD, Photogrammetry, Remote Sensing, Design, Sensors

ABSTRACT

During the past two years the company LH Systems and the German Aerospace Centre (DLR) have developed the commercial airborne digital sensor ADS40. This high-resolution imaging system is able to fulfil both photogrammetric and remote sensing requirements. The new sensor was introduced in mid 2000 and will complete the digital chain for airborne photogrammetric data processing. The design principles for this high-resolution sensor are based on a single optics / single focal plate solution. To meet the requirements, customized CCD-line structures were used. A staggered line arrangement allows a significant spatial resolution enhancement. CCD-line sensors have a linear and reproducible intensity response and are therefore measurement devices in contrast to traditional photo film systems. This has an impact on the instrument design: Digital photogrammetric sensors have also multispectral analysis capabilities. Multispectral CCD-lines can incorporated in the focal plate. The hardware is on the today's technological edge and can handle 120MPixel/s with 14 Bit radiometric dynamic and an SNR better then 8 bits. The data transfer between camera head and camera computer is based on fibre channel connection. The digital realization includes all aspects of real time data normalization, correction and processing. The on board data compression is based on the standard JPEG algorithm. In addition to the technical design, the performances of ADS40 will be shown on application examples to demonstrate the main features of digital sensors: high accuracy, wide field of view, high radiometric dynamics, high signal-to-noise-ratio, in-track stereo capability, multispectral capability.

1. INTRODUCTION

LH Systems, in co-operation with the German Aerospace Center (DLR), has developed a digital airborne stereo sensor, the ADS40 (Sandau et al, 2000). This sensor completes the digital chain, beginning with image acquisition, continuing with stereo processing, and finally leading to digital products (e.g. orthophotos and maps). The new sensor provides imagery suitable for both high precision photogrammetric mapping and thematic data interpretation. This commercial stereo system based on the three-line principle. By assembling additional CCD lines into the same focal plane, the sensor is able to provide true color and multispectral images at the same time.

In the first part we will describe historical background, the second part explains the design principles and the third part gives the hardware concept of the sensor system itself. The last section will focus on the results of test flights. The main attention is focused on the properties of the overall system including the sensor itself, platform, airplane, and inertial measurement unit. The resolution enhancement by using staggered CCD arrays is discussed.

2. HISTORY

DLR was involved in the camera development for Mars 94/96 space mission to Mars with a high resolution and a wide-angle stereo camera. The mission failed in November 1996, but as a result the airborne camera WAAC (Sandau et al, 1996) was derived from this development. The functionality of this camera convinced LHS to establish the joint development of a commercial airborne system. Assessment of a project for the customized development of the first commercial airborne digital sensor started after the OEEPE workshop 1994 in Paris. The main goal of this development was a complete solution to meet the photogrammetric requirements. The whole development focused on a solution that would provide final products automatically to the user. The project was split into four stages to ensure the quality of the digital sensor:

1. The functional model showed the principal SNR relations between the CCD sensor and the cost-optimized electronics.
2. The engineering model - the first complete camera - delivered the first test results of SNR and photogrammetric accuracy (Reulke et al, 1999).
3. The prototype model, which incorporated the 24k CCD line, generated data sets with which to test the accuracy of the staggered CCD arrays.
4. The series model is the final ADS40 product and incorporates the experience derived from the test results of the three previous models. This ensures that the customer will receive a fully tested and proven system.

The delivery of the first systems to the customer starts mid 2001.

3. AIRBORNE DIGITAL SENSORS: REQUIREMENTS

To have a chance of an impact in a market place spoilt for decades by high performance film cameras, an airborne digital sensor must provide a single camera system with

- One lens and one focal plate;
- Large field of view or swath width with a large number of pixels (20 k pixel) for effective image acquisition;
- High geometric resolution and accuracy as well as stereo;
- True color and multispectral capabilities;
- High radiometric resolution and accuracy;
- Reproducible sensor characteristics.

The 20k pixel requirement was formulated from OEEPE in mid 90th and seems to rule out area CCD arrays, because most readily available models in mid 1999 are 4kx4k pixels or less, whereas a linear array of 12,000 pixels is readily available.

A multiple head matrix solution was proposed and partial available from Z/I. DMC (Digital Modular Camera) is the first commercial system, which is based on matrix detectors. This system was first announced at the Photogrammetric Week, September 1999. A prototype was exhibited at the ISPRS 2000 conference. Camera description and data workflow can be found in (Hinz et al, 2000).

The LHS / DLR solution prefers a single head CCD-line solution, because of the availability of large CCD-line. While the geometric relation in a matrix image are fixed and can be simple calibrated, line sensors needs an additional mechanical movement for the second image dimension. This second dimension of airborne image is generated by the aircraft movement and is influenced by attitude disturbances. To overcome this problem and to correct this effect, exact attitude and position measurements are necessary for each image scan line.

3.1 CCD-Line Stereo

CCD-line stereo is based on three different views with a nadir, forward and backward looking line. Considerable research work done in Germany since the 1970s (Hofmann 1986), (Reulke et al, 1992), (Hofmann et all, 1993) has demonstrated the suitability of three panchromatic lines on the focal plane, with additional true color and multispectral lines near the nadir (Wewel et all, 1998). This is a significant advantage of CCD-line cameras and satisfies the one lens and one focal plate requirement. The distance of the true color CCD-lines from nadir in the focal plate gives a minimal stereo views. Therefore uncorrected and overlaid images from the RGB-channels generate perturbing color blurs. A design requirement of this scanner was therefore, to provide RGB-images in uncorrected images.

3.2 Multispectral and True Color

The number of channels desirable in a given spectral region depends on their half-resolution, which limits the energy reaching the detector and therefore also the signal-to-noise ratio. But on the other hand the larger the number of channels used the better defined is the information measured. This describes the situation of a typical optical spectrometer. Because of the limited energy, spectrometers with high spectral resolution cannot reach fine spatial resolution. The ADS40, however, is tailored above all to photogrammetric tasks and needs a very fine spatial resolution. Hence, the channel width should not be smaller than 50 nm and should be spectral rectangular, which is only possible metal interference filter. With this assumption four or a maximum of five channels provide the maximum information. Some of the possible tasks require corrections to the data sets (atmospheric correction, correction with respect to the viewing angles, BRDF effects).

After setting the multispectral characteristics of the system, true color can be derived from this. It is impossible to derive an overall approach to transform multispectral to true color images. Therefore a restriction on the future tasks of this sensor-system is necessary. The optimization criterion during the derivation of the transformation parameters is the color impression of imaged objects. For that purpose 65 spectral surface reflectances where selected. The influence of the atmosphere on the color impression was simulated with a standard atmospheric model. During simulations several parameters - flight altitude, illumination, extinction and aerosol type - were changed. To fill the whole color space an additional standard color test set was used. This approach allows the fine-tuning of the spectral channels and the derivation of transformation parameters for true color representation (Reulke et all, 2000).

3.3 Optics

The resolution requirement is defined by the pixel distance of the staggered CCD-line in the spectral range between 400 nm (blue) and 900 nm (infrared). The use of metal interference filter requires for the digital lens telecentricity at the image side. While the minimization of distortion is of prime interest in the case of the film lens, the most demanding requirement for the digital lens is constant point spread function (PSF).

3.4 Hardware Requirement

Data rate is determined by ground sample distance (GSD) and aircraft speed, to reach square pixel. The calculation of the maximum data rate is done for a GSD of 10cm for the PAN channels and 20cm for the spectral channels. That means that ADS40 works optimal up to a flight speed of 300km/h (83,33m/s). For a single CCD-line the line rate is 833,3Hz by a data rate of 20 MPixels/s or 40 Mbytes/s. The three panchromatic CCD lines create this maximum data rate. The additional 4 spectral channels have a quarter of the data rate because resolution is only a half in each image direction. The total data rate for the system is maximal 160 Mbytes/s, but the output data rate to the mass memory should be lower then 40 Mbytes/s. This large data rate requires also the implementation of data normalization as well as loss less and lossy compression. The lossy compression postulates also data correction before compression. The mean time for a measuring campaign is about 3,5h up to 7h. Therefore the storage capacity of the mass memory system should be in the range of about 0,5-1TByte. To achieve EMC in the airplanes and keep the excellent SNR for the entire system data transfer between camera head and camera computer is based on a fiber connection. This concept guarantees different cable length between 1m up to 500m without any EMC problems. All environmental effects (e.g. temperature and pressure) are compensated inside the ADS. The accuracy of the whole system will be observed and the user get any information via the flight control and management software.

4. AIRBORNE DIGITAL SENSORS: REALIZATION

To achieve stereo and high resolution the ADS40 is based on the tree-line principle. The along-track stereo capability of the ADS40 is achieved by using three staggered CCD-lines with different viewing directions (forward, backward, nadir). Since line scanners are not able to vary the base-to-height ratio the stereo angles between the three lines are set to different values in order to have certain flexibility.

The ADS40 uses nine parallel sensor lines: three panchromatic lines (forward, nadir, backward) and six spectral lines (red, green, blue, 2x new infrared 1 and optional near infrared 2). The three color lines, each equipped with 12000 pixels, are optically superimposed during the flight using special arrangement of trichroitic beam splitter. The near infrared channels are slightly offset with respect to the panchromatic nadir CCD lines.

The interference filters are placed directly on the CCD’s. A telecentric optics provides the optical path required for these filters. The RGB lines are optically superimposed during the flight using a beam splitter consisting of trichroitic beam splitters. Table 1 shows the most important sensor parameters, Figure 1 depicts the ADS40 sensor.

Focal length	62.5 mm
Pixel size	6.5 µm
Panchromatic line	2 × 12.000 pixels
Color lines	12.000 pixels
Field of View (across track)	64 °
Stereo angles	14°, 28°, 42°
Dynamic range	14 bit
Radiometric resolution	8 bit
Ground sampling distance (3000 m altitude)	16 cm
Swath width (3000 m altitude)	3.75 km
Read out frequency per line	1 - 830 Hz
In flight storage capacity	0.5 – 1 Tbyte

Figure 1: ADS40 sensor

Table 1. Parameters of the ADS40 sensor

The ADS40 system has to be understood not only as the sensor itself, it also includes additional modules, like IMU, platform, flight control and management system, camera computer, etc. The following chapter describes each part more in detailed.

4.1 CCD and focal plane module

A single CCD-line is not sufficient to fit image resolution requirements. But the whole Sensor should be mounted behind one optics (in difference to DPA-sensor (7), which use two cameras for the high resolution sensor). Different ways to enlarged the digital sensor are examined:

- Butted arrays
- Overlapping and shift in flight direction
- Staggered arrays

First and second solution causes a gap or an additional stereo angle between both lines. Therefore the decision for a staggered solution is obvious (Figure 2). These detectors consist of two single 12k CCD lines positioned close to each other with an across-track shift of half a pixel. A big advantage of this solution is the smaller size of the image field or the focal plate. But the necessary resolution limit of the optics must be double and be equivalent to the pixel distance.

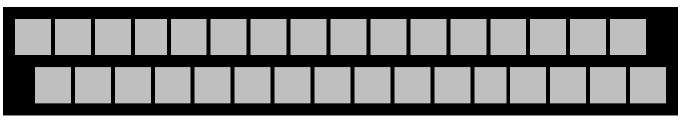

Figure 2. Staggered CCD line

The CCD sensor is a customized design. All the parameters of the CCD, such as dimensions, flatness, conversion factor, electronic interfaces and linearity, fit the requirements of the total system. Figure 3 illustrates the triple sensor device, each sensor consisting of two staggered 12k CCD lines.

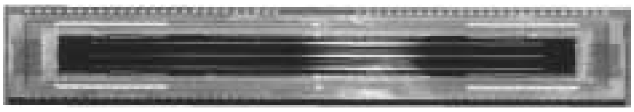

Figure 3. Triple CCD device

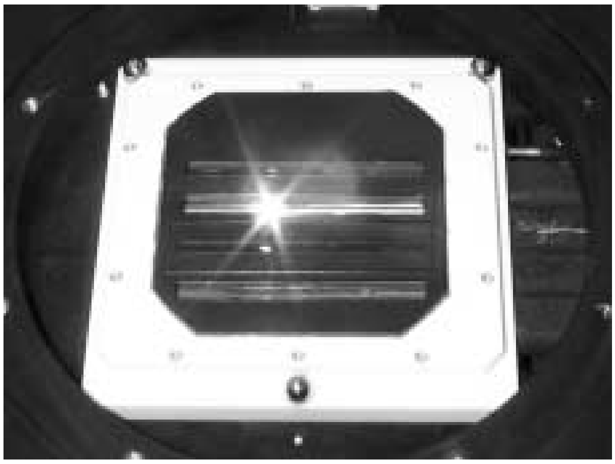

Figure 4. Focal plane

The focal plane (Figure 4) consists of four CCD housings: two of them contain single lines and two contain triple line configurations. All CCD’s have to be placed with a height tolerance of a few micrometers only. To achieve a dynamic range of 14-bit with a radiometric resolution of 8-bit, a temperature stabilization system has been introduced. Furthermore, the focal plane is equipped with a ventilation and air drying system to avoid condensation of water vapor on the cover glass of the CCD packages and focal plane deformations.

4.2 Analog signal processing

The focal plane electronics consist of the CCD lines with only a minimum of electronics necessary to operate the CCD’s. The subsequent CCD signal processing is concentrated in separated sub-units. The panchromatic 24k staggered CCD-line is processed like two independent 12k CCD’s and can also be used only in the 12k mode. Each board includes all the necessary functions for complete analogue signal processing (ASP) of a CCD: input clamping, correlated double sampling, analogue and digital offset correction, 14-bit analogue to digital conversion providing a signal dynamic range of at least 14-bit, dark signal non-uniformity (DSNU) correction and photo response non-uniformity (PRNU) correction. The SNR of photosensitive sensors will be given by the Poisson function. The total SNR is represented by the square root of the full well capacity of a pixel (270000 electrons). Therefore the radiometric radiometric resolution is about 9 bits. The real sensor application includes the RMS noise of the CCD, the A/D noise of the ASP and the analog channel noise. The LH Systems sensor has a real SNR of 8,9 bits in a dynamic range of 14 bits. For the real time prediction of the integration time of the CCD the Digital Processing Controller calculate a 2log histogram of an image block of 8 lines in dependence of the sample time.

4.3 Digital Signal processing

The CCD-related camera head fiber data link has a maximum data rate of 40Mbyte/s. The input pixel interface of the digital processing unit generates block lines (8 image lines) in the first memory of the board controlled by the Head-IO-Controller (HIO). A suited design regarding to the 8 bit input interface of the Camera Head and a 64Bit data interface to a C80 DSP saves processing power for data normalization from 14 to 8 bit. The normalization procedure starts with the search of maximum and minimum for the bock line. If the difference between maximum and minimum is lower then 256 all pixel values will be subtracted with the minimum and store as an 8 bit data set. In the other case the C80 normalized after the minimum subtraction via a linear or non-linear look up table the pixel values to an 8 bit value. After the normalization the next processing step is loss less or lossy data compression in real time. The ZR36053 chip realizes the hardware compression. The output interface (OCTL) to the mass memory (MMS) through the data-recording interface (DRI) is the same like the input interface.

4.4 Attitude Measurement Unit

An Inertial Measurement Unit (IMU) from Applanix mounted directly to the adapter plate holding the focal plane realizes measurements of roll pitch and yaw of the aircraft as well as location in a cm accuracy range.

5. RESULTS OF THE FLIGHT EXPERIMENTS

An important goal of the test flights was to prove the functionality of the entire ADS system including the sensor, the platform and the inertial measurement unit (IMU). A check of the system under real flight conditions was necessary. The main objectives of the ADS test flights were defined as:

- Test of the entire sensor system,
- Radiometry of the sensor,
- Accuracy of the attitude parameters,
- Color imagery,
- Staggered arrays.

First test flight took place end of 1998.

5.1 Radiometry

One of the main advantages in favor of digital sensor systems over film-based cameras is the much higher radiometric dynamics, equivalent to a greater range of gray values within an image. This has a significant impact on the subsequent data processing (e.g. matching). The dynamic range is described by the radiometric resolution and is limited by different noise sources. Both parameters, radiometric dynamics and noise, were main points of our investigations. Figure 5 gives an impression of having 14 bit data instead of 8 bit data at one’s disposal. Depicting either the first 8 or the last 8 bits within the original 14 bit gray level range results in two different images. The first shows the bright parts, but no structure in the dark parts is detectable. The second image inverts the situation: in the dark parts we can see details, the bright pixels look saturated. But again, both images result from the same 14 bit image.

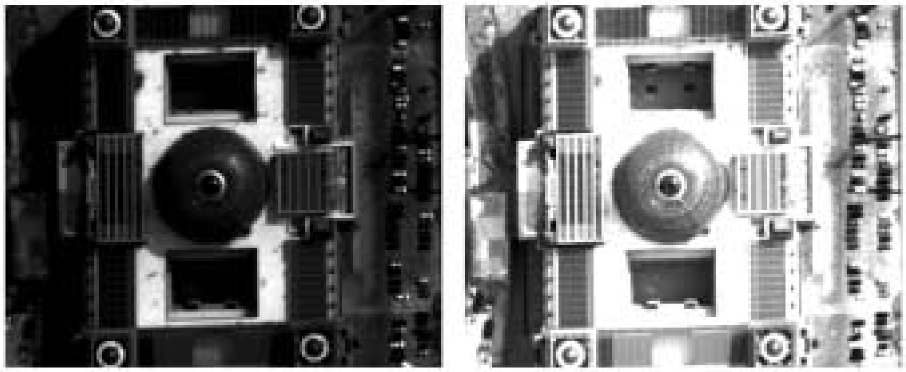

Figure 5. Radiometric zoom, depicting gray values have the first (left) and the last (right) 8 bits within the original 14 bit gray level range

5.2 Accuracy of the attitude parameters

To evaluate the quality of the attitude data we performed a rectification of image data to a reference plane (correction of the flight motions) and the generation of a coarse digital elevation model (DEM). After processing of the IMU data, a simple way to verify the alignment between image scan lines and an appropriate attitude data set can be done by projecting all pixels of the raw image to a reference plane (rectification, see Figure 6). The visual impression of a rectified image is the first, essential indicator of the quality of the attitude data.

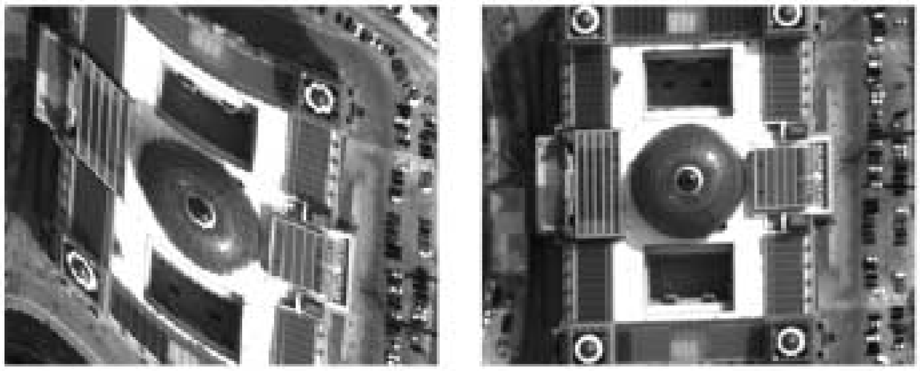

Figure 6. Raw and rectified image

With the help of the position and attitude data we generated digital elevation models. This task is very interesting, because it is the last element in a huge, complex chain, starting with the optics and electronics, including airplane and platform, and ending with data processing. Some errors can only be detected at this final stage. Only when all elements of this chain work together successfully, high quality photogrammetric products can be obtained. Figure 7 shows a part of a terrain model calculated with a tool for automatic DEM generation from line scanner imagery.

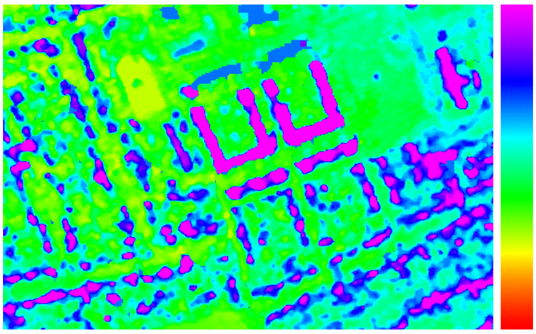

Figure 7. DTM generated from ADS40 image data. Buildings can be recognized easily.

5.3 Color images

The first color ADS40 images were acquired in the middle of 2000. Due to the beam splitter no parallax effects were influencing the color image quality. Visual test showed no color edges. Figure 8 shows a color image from Parma (Italy), which was taken Mai 2001.

Figure 8. Part of an ADS40 color image of Parma, Italy

5.4 Staggered arrays

One of the special points of interest during the test phase was the effect of using staggered arrays instead of linear arrays. The main question was whether or not the theoretical expectations can be fulfilled and the application of such detectors can improve the spatial resolution. Therefore, two special test targets were customized; a Siemens star and different patches with test bars both with a size of 8 m × 8 m.

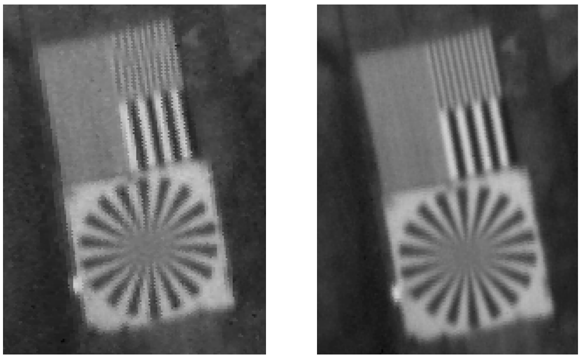

Figure 9. Test pattern scanned with a 12k sensor (left) and a 24k staggered sensor

In order to compare a sensor with a single CCD line (12k) versus a staggered array sensor (24k), a single line sensor was simulated using image data just of one of the two staggered lines with a clock time double as high as the staggered one. The results are shown in Figure 9. The following conclusions could be drawn: Observing the Siemens star in both images lead to similar results. In both cases the modulation transfer function (MTF) of the optics is evaluated. Please note, that actually the optics is too good for a 12k sensor, because spatial frequencies larger than the Nyquist frequency are transmitted. So in worst-case situations aliasing can occur. If the optics were adapted to the 12k sensor, the blurred region would be larger in the 24k image.

The comparison of the bar patterns shows the improvement of using a 24k sensor instead of the 12k sensor. The most interesting part is the upper right patch. The 12k image low contrast and aliasing (non-parallel bars) can be observed. Both, the spatial frequencies and the contrast are better for the staggered arrays. The spatial resolution does not only depend on the system MTF (mainly determined by the optics and the pixel size), but as expected, from the sampling distance (sampling theorem) as well.

6. SUMMARY AND CONCLUSIONS

LH Systems has chosen the three-line scanner approach for photogrammetric imaging. To achieve a high ground resolution with large swath width, the staggered array principle is applied, resulting in the equivalent of up to 24000 pixels. Additional spectral imaging lines (RGB, 2x NIR1 and optional NIR2) with 12000 pixel arrays are used for multispectral imaging. The spectral channels are chosen to allow remote sensing applications also. Both photogrammetric and multispectral imaging occurs simultaneously during a single flight. The ADS40 is optimized for image acquisition with a dynamic range up to 14-bit and a radiometric resolution of 8-bit (including the effects of the Poisson distribution of the incoming light). The compressed data are stored in an on-board mass memory with a storage capacity up to over a half a terabyte.

The imaging process (sensor control and flight guidance) is controlled by an appropriate ADS40 software system implemented in the digital computer system connected to the camera head system via optical fiber links. In addition to the positioning and imaging data ADS40 generate independent on the environment calibrated data sets only. This paper describes also the results of the flights of the ADS test systems. Our main goal was to prove the capabilities of the new sensor system under field conditions. It is the only way to detect error sources at an early stage and can confine the development risks drastically. With the help of the test flights, we were able to solve any hard- and software mistakes and could acquire a lot of know-how dealing with the sensor system. The resolution-enhancing effect of applying staggered arrays could be demonstrated.

7. ACKNOWLEDGMENTS

We acknowledge major contributions from all members of the ADC development team, especially A. Börner, M. Scheele and S. Hilbert.

8. REFERENCES

Sandau,R., Braunecker,B., Driescher,H., Eckardt,A., Hilbert,S., Hutton,J., Kirchhofer,W., Lithopoulos,E., Reulke,R., Wicki,S., 2000. Design Principles of the LH Systems ADS40 Airborne Digital Sensor, International Archives of Photogrammetry and Remote Sensing, Vol. XXXIII, Part B1, Commission I, pp. 258-265.

Sandau R., Eckardt A., 1996. The stereo camera family WAOSS/WAAC for spaceborne/airborne applications, ISPRS Vol.XXXI, Part B1, Commision I, pp. 170-175.

Reulke, R., Börner, A., Michalevich, B., Scheele, M., Scheibe, K., 1999. Flugexperimente mit dem ADC-EM2. 19.Wissenschaftlich-Technische Jahrestagung der DGPF, Essen.

Hinz,A., Dörstel,C., Heier,H., 2000. Digital Modular Camera: System Concept and Data Processing Workflow; International Archives of Photogrammetry and Remote Sensing. Vol. XXXIII, Part B2. Amsterdam 2000; pp. 164.

Hofmann,O., 1986. Dynamische Photogrammetrie, BUL, 54, p.105.

Reulke,R., Scheele,M., Terzibaschian,T., 1992. Optoelektronischer Weitwinkelscanner von MARS-94/96 in der Flugerprobung, Bild & Ton, 9/10, pp. 293-301.

Hofmann,O., Kaltenecker,A., Müller,F., 1993. Das flugzeuggestützte, digtale Dreizeilenaufnahme- und Auswertesystem DPA - erste Erprobungsergebnisse, Photogrammetric Week ’93, ed. D. Fritsch, D. Hobbie, Wichmann, Karlsruhe, p. 97.

Wewel,F., Scholten,F., Neukum,G., Albertz,J., 1998. Digitale Luftbildaufnahme mit der HRSC - Ein Schritt in die Zukunft der Photogrammetrie, PFG, 6, p. 337.

Reulke,R., Franke, K.-H., Fricker,P., Pomierski,T., Sandau,R., Schönermark,M.v., Tornow,C., Wiest,L., 2000. Target Related Multispectral and True Colour Optimization of the Colour Channels of the LH-Systems ADS40, International Archives of Photogrammetry and Remote Sensing. Vol. XXXIII, Part B1, pp. 245.

ADVANCED SYNTHETIC APERTURE RADAR OBSERVATIONS WITH CLUSTERS OF SAR SATELLITES

Hartmut Runge, Marian Werner, Michael Eineder, Helko Breit, Steffen Suchandt
DLR, Oberpfaffenhofen, 82234 Wessling, Germany
Email: hartmut.runge@dlr.de

Didier Massonnet
CNES 18, Avenue E. Belin, 31401 Toulouse, France
Email: didier.massonnet@cnes.fr

KEYWORDS: Synthetic Aperture Radar (SAR), High Resolution SAR, Interferometric CartWheel, Multi-Baseline Interferometry, Along Track Interferometry, Volume Probing, Satellite Formation Flight

ABSTRACT

This paper provides an overview over the advantages and applications of clusters of SAR satellites. It describes the orbit mechanisms for stable configuration flights and how they have evolved from ERS Tandem to the Interferometric CartWheel. The applications, which are described in detail, are superresolution and polarimetric InSAR volume probing for biomass estimation.

Introduction

The first configuration flight between two SAR Satellites was the highly successful ERS Tandem Mission with ERS-1 and ERS–2. Due to technical constraints the two fly-overs were separated in time by exactly one day. Although this mission has pioneered SAR interferometry the large time separation of one day lead to severe decorrelation effects. This problem was overcome with the Shuttle Radar Interferometry Mission SRTM where the two sensors were linked by a 60m long mast (Suchandt, 2001 and www.dfd.dlr.de/srtm).

In this paper we consider light free-flying SAR platforms, which fly in a formation and work in strong cooperation. Such clusters of sensors have several applications and advantages over single, highly advanced, heavy and expensive satellites. The advantages are as follows:

- **Graceful Degradation**
  In case of a significant failure not the overall system will breakdown. The loss of one satellite will cause only 1/n degradation of the overall performance. This situation is similar to a hologram, where a local damage does not cause a hole in the image but only degrades the overall image quality.
  If one microsatellite fails it may be replaced by a new one at any time. Satellites, which are aged, can be replaced by samples of a new generation. On the other hand if an important part of a highly sophisticated satellite fails the overall system has to be replaced, which may interrupt the operations and is much more expensive. The strategy to overcome this problem with expensive satellites is to integrate redundant parts (which makes the satellite even more heavy) and to perform intensive simulations and qualifications and tests prior to launch (which increases the cost significantly).

- **Series Production**
  It can be cheaper to build a series of small, light and simple satellites than to build only one big, heavy and highly sophisticated satellite.

- **Reconfigurable to Different Applications**
  The cluster of SAR microsats could be configured at least for the following applications:
  - high resolution SAR (superresolution) with an along track orientation
  - surface motion measurements (along track interferometry) with an along track orientation
  - multi-incidence angle observations with a cluster distributed in along or across track
  - DEM generation, biomass and ice monitoring with a CartWheel (across track interferometry and polarimetry)

These advantages have led in the United States to the TechSAT21 initiative (AFRL, 1998). In the next chapter of this paper an overview about SAR satellite configuration flight is given. This is followed by a description of the possible applications and missions.

Stable Configuration Flight – From ERS-Tandem To The CartWheel Concept

In order to compare radar images very precisely using the technique of radar interferometry, a relatively small difference of points of view is required. To establish this baseline, many combinations are possible. The most obvious and relatively cheap is to use the same satellite twice, waiting for it to come back in about the same position (i.e. within the requirement of similarity of the points of view). The early development of space borne radar interferometry was based on this method. In this case, the interferometric signal is made of four components that must be discriminated by careful analysis: (1) residual orbital errors which create parallel fringes across the interferogram, (2) topographic signal of which amplitude is modulated by the across-track separation of the spacecrafts, the combined atmospheric delay typical of each scene datum are also contributing (3). Finally (4), any displacement of the ground occurring between the times of the data takes is printed in the interferogram. The time elapsed between the acquisitions, which is responsible for the two last components of the interferometric signal, might cause some loss of signal clarity (loss of coherence) because the elementary targets on the ground have an opportunity to change. This opportunity is generally all the larger that the time elapsed is long. The minimal time elapsed is the orbital cycle of the satellite, which is generally long (35 days for most of the lifetime of the ERS satellites). With the advent of ERS-2, ESA's second radar satellite, identical to ERS-1 as far as the radar is concerned, a new possibility was exploited, **the tandem**.

The principle is very simple, each satellite follows its nominal 35-day cycle orbit, but the two satellites are shifted by one day. From the ground, everybody sees ERS-1, then ERS-2 after one day, then again ERS-1 after 34 additional days. The mission is very interesting because the reduced time separation is a key factor for improving coherence. The elementary targets do not have as much time to evolve. Another great success of this mission was the mapping of relatively quick moving targets such as glaciers. One single day was the ideal time lapse to record the displacement fringes correctly: a full 35-day interval would make them unreadable due to the accumulation of a 35-times larger displacement. Another advantage of the tandem is the ability to maintain a very small difference of point of view. Two factors contribute to this possibility. Firstly, the two satellites face about the same conditions of solar activity and atmospheric braking. Their trajectories evolve in a parallel way and their relative trajectory is very stable. Secondly the orbit corrections can be phased. When a satellite drifts close to the limit (i.e. one kilometer from the nominal track), it is kicked back on track by a corrective impulse. In order to reduce the frequency of the correction, the impulse is strong enough to send the satellite close to the limit on the other side (still one kilometer from the nominal track). The satellite then drifts back slowly. If the second satellite is fired at the same time, regardless on whether it had yet reached the limit, it can remain very close to its companion. Offsets of 50 or 100 meter were achieved routinely in the tandem mission. The offset has sometimes been made greater purposefully in order to increase topographic sensitivity.
Another way of obtaining difference of points of view is formation flying of the two or more radar instruments. Again, the easy way to create it is to put the instruments at the extremities of a mast. This was done in the Shuttle Radar Topography Mission (SRTM). The mast maintained mechanically the baseline and the Shuttle attitude control system maintained the desired viewing angle of the instrument. Another way would be to replace the mast by a propulsion system and to force the second antenna (on a free-flyer) into a parallel orbit. However, such a system would not last long as the fuel consumption would be huge. As an example, assume we want to fly permanently with one kilometer across track apart from a free orbiter. Our spacecraft would then rotate one kilometer off the center of the Earth while being distant of about 7000 km, leaving permanently about 1/7000 of the Earth gravity to compensate. This would correspond to an impulse of more than 100 m/s a day. It can, however, be envisioned that a strong electric propulsion system might maintain a 100-m baseline for a couple of years (10 m/s a day). Similarly, vertical separations can be created with similar costs. However, it is more convenient to analyze the way free-flyers can organize themselves.
We assume a moving frame the origin of which flies a certain orbit, and we consider the relative orbits that can be created with respect to this origin.
Noting Z the vertical axis (positive when sticking up), X the velocity axis and Y the horizontal axis perpendicular to the track, hence oriented to the left as seen from the spacecraft, the equations of the orbit of the micro-satellites, relative to the synchronous orbit are written:

$$X = 2R \sin(\omega t + \phi) \tag{1.1}$$
$$Y = A \cos(\omega t + \psi) \tag{1.2}$$
$$Z = R \cos(\omega t + \phi) \tag{1.3}$$

Where R is the vertical radius of the configuration and A a term liked to a possible change of the orbital plane, corresponding to a change of the Equator crossing time (i.e. a slight change of the ascending node longitude). In the pure cartwheel mode, A = 0 and the relative displacement is contained in the vertical plane including the velocity. Form these equations we conclude that:
1) A configuration where the rotation is restricted to a plane perpendicular to the velocity is impossible.
2) A « flat » displacement (Z=0) is also impossible unless it is reduced to the Y-axis. In the case the micro-satellites collide twice an orbit.

In order to obtain stable differences of point of view as well as of acquisition times all along the orbit, several receivers can be placed with different ϕ or ψ. For instance, if three receivers are given a slightly higher eccentricity than the conventional radar satellite they follow, while keeping the same orbital period, they will feature a non-zero R. Slight changes in the longitude of the ascending node can also be added, creating a non-zero A. They describe an ellipse around the orbital position they would have without the additional eccentricity and longitude change. The even distribution of the perigees results in an even distribution of the receivers along the ellipse, which features a horizontal axis twice as long as the vertical one. The longitude change adds a lateral axis. It can be shown that, with three receivers, the horizontal and vertical baselines vary only by 7.5% along the orbit, with respect to their average value, provided we consider the two satellites best positioned for the purpose among the three.
The main advantage of this "CartWheel" (Massonnet, 2001) concept is the geometric stability of the configuration all along the orbit. In a vertical configuration, this stability is obtained for a left as well as a right viewing. By introducing an inclination of the wheel (non zero A), a given incidence can be privileged, which can be interesting for modifying the ratio between the critical horizontal and vertical baselines, therefore adapting it to the parameters imposed by the companion radar.
However, variations of this concept and other configurations have to be further analysed.

Multiangle SAR Observations

The multistatic observation angles, which can be achieved by a cluster of SAR satellites, are in particular useful to improve scene classification or target identification. The cluster may be distributed in along track or across track. The latter has the special advantage of forward scattering (Mochia, 2001) resulting in a stronger backscatter signal. The difference in the observation angles can be too large for SAR interferometry, but Stereo-SAR techniques may be applied for the generation of topographic maps.

CartWheel Configuration – The DEM Mission

The application of the CartWheel configuration for the generation of a global digital elevation model (DEM) has been studied in detail by a joint team from CNES and DLR (Mittermayer, 2001a,b, Runge 2001). As an illuminator satellite the Envisat and ALOS have been considered. It was shown that a very accurate global topographic model, with vertical accuracy in the range of one meter could be achieved. The CNES developed MYRIADE microsatellites could be used and the earliest possible launch date is fall 2005 (Martinerie, 2001).

CartWheel Configuration – The Biomass Mission

The digital elevation model derived from the X-band SRTM data represents a shape of the earth surface. In densely vegetated areas this elevation model includes the canopy of the trees because the high frequency microwaves are mainly reflected by the top of the trees. For many applications true ground elevation data are required. In order to penetrate the vegetation a long wavelength like the L-band is required. It would be of great interest to measure furthermore the volume and density of the biomass layer on the earth surface. This can be achieved with polarimetric SAR interferometry (Cloude, 2001). A suitable illuminator satellite would be the Japanese ALOS, a European TerraSAR L-band satellite or the proposed US-Echo satellite.

One of the most exciting possibilities of these configurations is the possibility to map volume scattering through the loss of coherence it causes. This is enabled by simultaneous interferometric observations where a temporal loss of coherence does not occur (like in repeat pass systems). However, unlike SRTM, here we can work with much higher level of baseline (i.e. much closer to the critical value of the baseline). The system allows working with a various level of sensitivity using the flexibility in incidence angle permitted by the illuminator and the pointing of the wheel.

Assuming that the system is tuned to a certain fraction of the critical baseline using a given angle of incidence, for instance in the 40° range, it is clear that the equivalent orthogonal baseline will be reduced when working at a lower incidence angle, allowing the exploration of varied percentages of the critical value from the same cartwheel orbital configuration. In reality, volume scattering can be easily understood from a topographic point of view: the elevation of each scatterer creates a topographic phase combined with the strength of the scatterer. As a result, the targets from a volume “disagree” on the phase value because they differ in elevation, which results in a loss of coherence. The coherence depends on the amplitude distribution of the scatterers throughout the depth of the altitude of ambiguity (assuming that the depth of volume does not exceed the latter). Working with lower than nominal incidence angles increases both the penetration depth and the altitude of ambiguity: the change in elevation that creates one additional topographic fringe or “contour line”. A collection of various incidence angles from the same orbital separation is thus likely to provide a very sensitive probing tool for vegetation. As for the DEM application, having a third receiver in an intermediate position can further increase the richness of the data.

A major objective of environment sciences is the determination of the three dimensional structure of the vegetation, especially forests, a major parameter for the monitoring of the biosphere. The evolution of forests, which cover a quarter of the land surfaces, is also a key factor of the evolution of the atmosphere as a carbon sink. The three dimensional structure of the forests can reveal changes in height and species as well as damages caused by thunderstorms and other exceptional atmospheric events.

Similarly, the evolution of the icecaps is one of the keys to the understanding of the trends of the climate. The very cold, thus very dry, ice allows substantial penetration by radar waves, especially at long wavelength.

The penetration in deserts can be assessed by comparison of DEMs made from non-penetrating techniques (optical of short-wave radar) and from long wave radar, or by polarimetric InSAR methods as described above. Much better results for archaeological and paleoclimate research can be expected than from the already remarkable SIR-A and SIR–B L-band missions, where dried out riverbeds and even a lost city (Ubar) were detected under the deserts sand (Holcomb, 1998).

The extension of a biomass mission for ice and desert applications would lead to a general **“volume probing mission”** for climate change research.

Let us assume that the specification of the mission is the mapping of all forests surfaces four times a year under two very different incidence angles, continued all through a three-year long nominal mission. During these three years, the Arctic and Antarctic icecaps could also be mapped twice a year, again using two widely separated incidence angles. In the course of the mission, selected test sites could be observed at any occasion, therefore yielding very frequent observations with many different incidence angles. Assuming that the total activity on the test sites will be similar, in terms of acquired surface, to the systematic mapping of forests and ice caps, we can estimate the volume of data to be acquired:

The global surface of forests is 40 million square kilometers. The global surface of ice caps is 14 million square kilometers. The above requirements represent therefore 2*(40*4+14*2) million square kilometers a year, or 376 million square kilometers. With a swath-width of 100 km, it corresponds to a length of 3.75 million kilometers, or the length of about 94 orbits (40000 km per orbit). Since a satellite typically covers 5250 orbits a year, the duty cycle demanded to the system and therefore to its companion radar is 1.8%. If we assume, for instance, that the radar instrument of the companion (the illuminator) works 18% of the time, the mission would draw 10% of its resource, regardless of some scenes being required anyway by companion’s user community.

Super-Resolution by an Along-Track Formation

The achievable azimuth resolution of a SAR depends on the acquired Doppler- (Azimuth) bandwidth or in other words on the length of the synthetic aperture integration time. This bandwidth has sufficiently be sampeled with a Puls Repetition Frequency (PRF). Furthermore the receiving antenna length must not be longer than double of the desired azimuth resolution. The PRF, however, can not be increased without limits. The higher the PRF the smaller becomes the achievable swath and obviously a higher PRF causes a higher energy consumption.

In order to obtain a larger swath a Scan SAR System can be employed, but this reduces the azimuth resolution. To improve the azimuth resolution (by increase of integration time) a Spotlight SAR can be used, but this configuration does not allow to record a continuous data strip in along-track. Beside these disadvantages Scan SAR and Spotlight SAR require expensive and heavy active phased array antennas. (Spotlight SAR can also be realised by mechanical steering of the satellite, but this technique limits the frequency of observations.)

In order to increase the range resolution chirps with high bandwidth have to be transmitted. (To obtain a 1m range resolution typically a 150 MHz range chirp-bandwidth is necessary.)
The losses in the signal to noise ratio due to the necessary wide-band receiver have to be compensated with a higher radiated power.

The method which is introduced here is aimed to relax the requirements for the PRF and the radiated power. The system uses several (n) receiving platforms which fly in a formation in along track as depicted in Figure 1. All receiving satellites look at the same antenna footprint, but due to their separation in along-track and the squinted antenna look-angles they receive different Doppler frequency bands (Fig.2).

The ground is illuminated by one active SAR system positioned e. g. in the centre of the formation. The distance between the receiving platforms is adjusted that each satellite receives an adjacent Doppler-band. In a processing system these Doppler-bands can be put together in order to form a wide Doppler-band. Without accounting that the Doppler-bands need some overlap the azimuth resolution can be increased by the factor of n. Furthermore the sampling of the Doppler-band (with the PRF) can be reduced by the factor of n for this multiple-platform system in comparison with a system which generates the wide spectrum with only one antenna.
A „Super-Resolution“ SAR processor with aperture synthesis may work in the following sequence:

a.) A complex SAR image is computed from each channel.
b.) From each spectral overlap region an interferogram is formed
c.) The phase offset (which represents the phase difference between the channels) and the co-registration coefficients are extracted.
d.) A pixel co-registration and a phase offset correction for all channels is applied.
e.) A complex summation of the data sets is performed in order to obtain the super-resolution image.

If a higher radiometric resolution is desired, a traditional look summation of the detected data sets can be applied. For target recognition applications it can be helpful to analyse each look
(which is taken from a different aspect angle) separately.

To achieve the same azimuth resolution (Doppler-bandwidth) with the standard and the multiple receiver configuration the azimuth integration time (or the length of the overall synthetic aperture) must be the same for both systems. But the difference is that the antenna footprint of the standard system must be n-times wider than the one of the multiple receiver system. This requires the use of a n-times smaller (shorter in along-track) antenna and results in a n-times longer target illumination time.

The multiple receiver SAR can be seen as a combination of an array antenna and a synthetic aperture antenna.

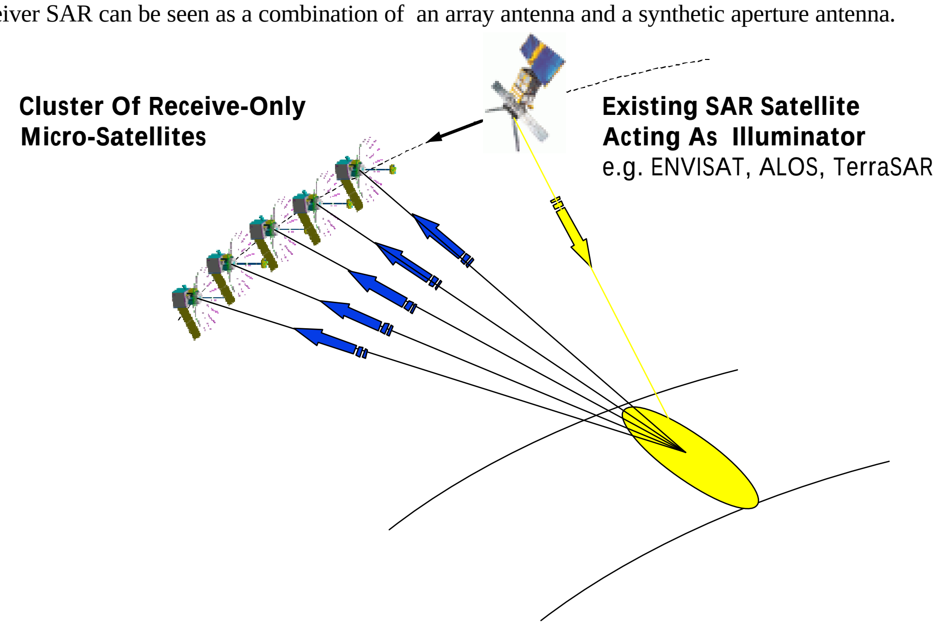

Figure 1: Configuration for superresolution SAR with one illuminator and a cluster of receive only satellites

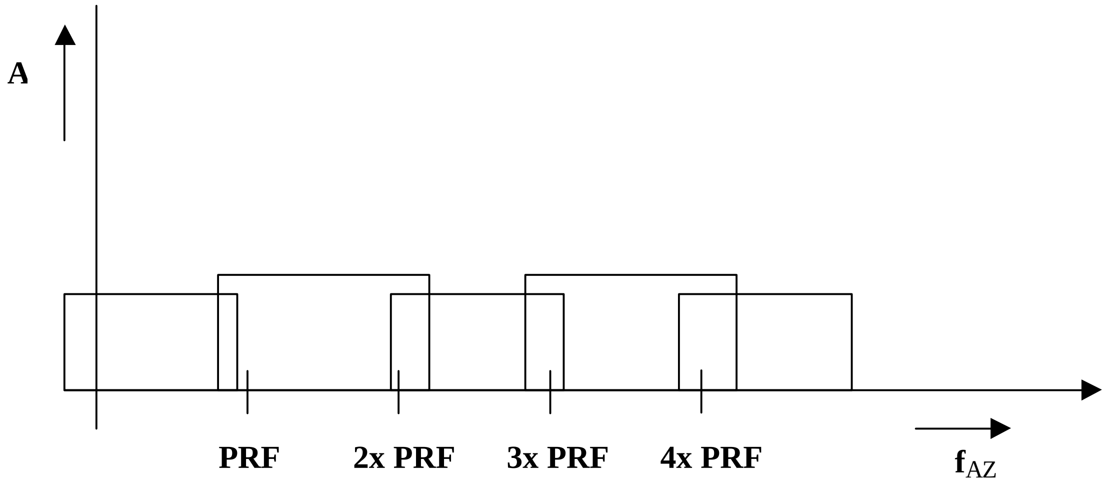

Figure 2: Synthesis of azimuth spectra for superresolution

In summary the **advantages of a multiple-platform system for superresolution** from the radar point of view are:

- **n-times shorter target illumination time**:
  For the imaging of moving scatterer, like the sea surface it is advantageous to use short target illumination times. Long integration times can lead to a blurring of the target. In SAR interferometry a scene decorrelation can appear.
- **n-times lower PRF is possible**
  This is of special importance to wide swath and / or high resolution SARs, because with a standard SAR it is impossible to obtain a wide swath and high resolution at the same time.
- **n-times longer antennas are possible**
  One channel of the multiple-receiver system produces only 1/n of the final azimuth resolution. Therefore, a n-times longer (in along track) antenna can be used. This is a work-around of the fundamental SAR law that the achievable azimuth resolution is limited by half of the antenna length. This is important for the power budget of the radar, because a n-times larger transmit and receive antenna requires a n-times smaller radiated power.
  For the multiple receiver platforms micro-satellites shall be used. Their ability to perfrom attitude control with large along track structures is limited. Therefore a high resolution system with antennas of up to 6m length may be considered.
- **Distributed illuminator is possible**
  In order to make the system redundant and to distribute the burden of power generation and amplification each satellite can be active and can contribute to a joint illumination of the target.
  No longer a single high power illuminator is required. The power requirement for one microsatellite from the cluster is reduced by 1/n in comparison to a single illuminator.

In the following the distributed illuminator concept shall be investigated in more detail. In general with a bi-static system there are **two approaches for the ground illumination:**

a) **The opportunistic approach with an existing illuminator**

Here we take advantage of an already existing (at the time of the mission) SAR satellite which will have proven its capabilities, like Envisat, ALOS, Radarsat or TerraSAR. The main advantage is that one may benefit from investments which are already done and from the infrastructure which already exist. Beside problems with data rights and safety of the master satellite, which can be resolved in practice, it appears the problem of harmonisation of the time schedule of the missions. Furthermore, the design of the microsatellites which fly in formation with the „illuminator“ have to be adapted to the technical constrains (radar bandwidth and frequency, orbits, air drag, etc.) of the master satellite, which will always leads to some sort of compromises.

b) **The cluster of active SAR satellites**

In this concept each platform consists of a complete SAR satellite including a transmitter. Figure 3 shows this cluster of active SAR satellites in comparison with a standard SAR. Please note that the synthetic aperture has the same length for both systems, while the antenna footprint and the transmitted power per satellite can be much smaller for the high resolution SAR with in the cluster configuration.

The chirp generator of each system can be commanded to generate a certain bandwidth, e. g. the first satellite transmit pulses with a spectrum ranging from 0 to 20MHz, the second transmits a pulse spectrum from 20 to 40 Mhz and so on. The receivers are wideband that they can record the echos of all transmitted signals. The separation of the contributions of each transmitter can be performed in the SAR processor by simple bandpass-filtering (Runge, 1999). Figure 4 shows how the 2D-spectra of the received signal is arranged by the SAR processor. The spectrum of the echo signal received by the satellite in the centre of the cluster configuration appears in blue colour.

This active cluster concept avoids the need of a dedicated illuminator and makes a mission self-contained. It is expected that due to the possibility of series production this concept is the cheaper to realize.

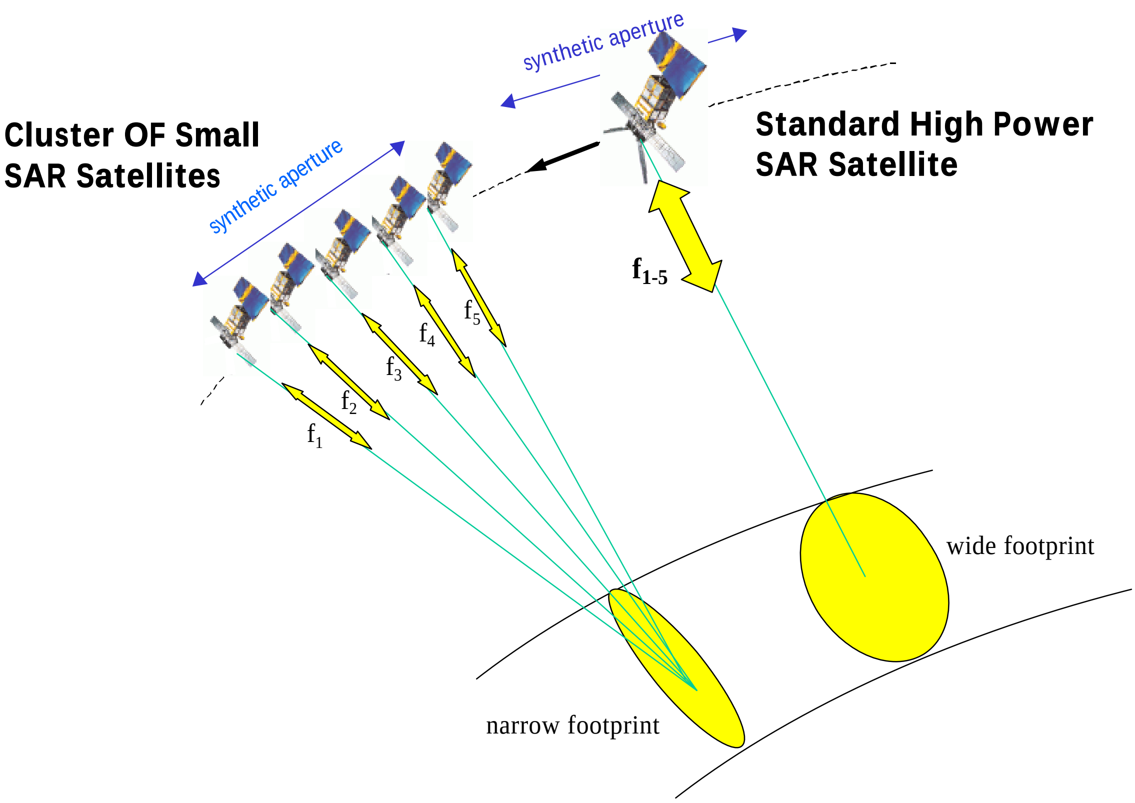

Figure 3: A cluster of active SAR satellites versus a standard high resolution SAR

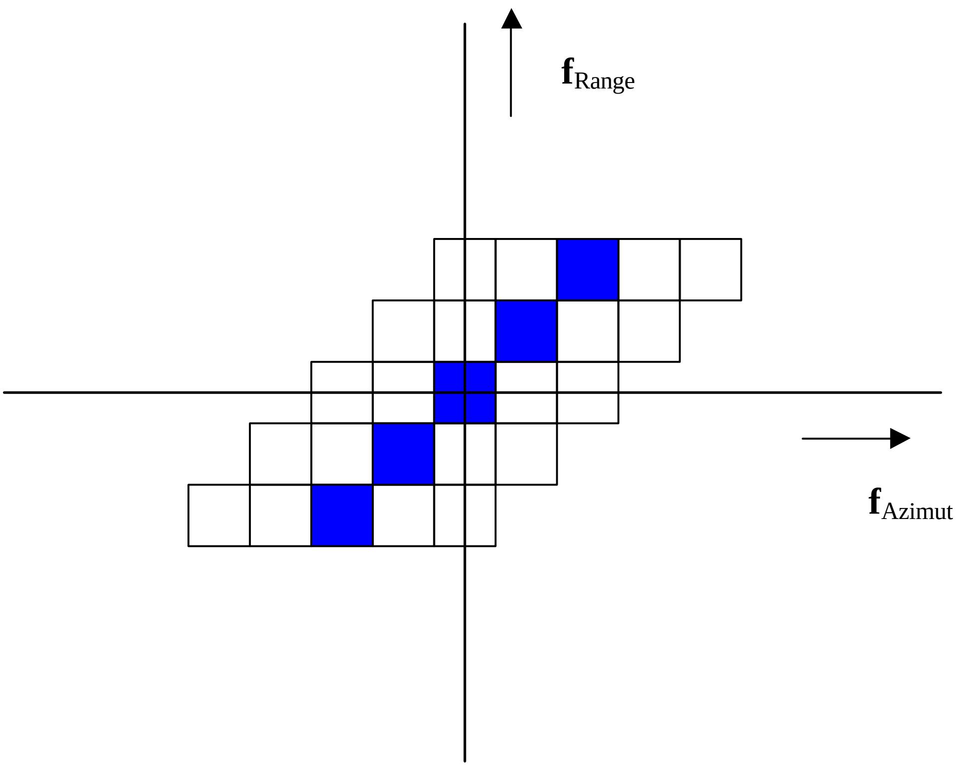

Figure 4: Assembly of 2D-raw data spectra of the active cluster SAR

The Along Track Configuration – The Ocean Currents Mission

The idea to detect and to measure the speed of ocean surface currents with along track interferometry (ATI) dates back to the 80ties of the last century (Goldstein, Zebker 1987). Measurements with aircrafts have been performed by JPL (Carande, 1994) and later by DLR and the Aerosensing company. In comparison with across track interferometry the technique has not become very popular yet because only few results have been published up to now.

The ATI uses two antennas separated in flight direction. Such system acquires two data sets from the same position but with the time lag *Dt.* If the scatterer is stationary the two data sets are identical (save from noise) and the interferometric phase would be zero (Bamler, Hartl 1998). If a scatterer moves in the direction of the line of sight with v_{range} the interferometric phase j_{ATI} will be:

$$j_{ATI} = 360^{\circ} \frac{2 \cdot \Delta t \cdot v_{range}}{l} \tag{2}$$

In order to measure two velocity components a squinted dual beam radar has been proposed (Frasier, et. al. 2001). Care has to be taken at the interpretation of the measurements because corrections for the wave motion have to be applied (Romeiser, Hirsch, 2001). Therefore, the wave height and direction has to be derived from the SAR image first (Bao, Schulz-Stellenfleth, 2001).

The sensitivity of the system is governed by the wavelength λ of the radar, the radar signal to noise ratio and the ATI baseline length. The latter one, however, can not be increased without limits because the ocean surface decorrelates quiet fast! According to (Romeiser, Thompson, 2000) the decorrelation time using the L-band is only 50ms. Therefore, the two satellites in the along-track formation must not be separated further than about 400m and the satellite operators will require very precise position measurements. Probably a sort of distance meter has to be installed on the satellites. For an X-band radar the decorrelation time is even smaller and the two antennas may be connected by a boom or mounted on the International Space Station.

ATI is the only remote sensing technique that has the potential to provide maps of ocean currents at better than 20 km resolution. The principal existing technique is altimetry (like Topex and Jason), which with coarse across-track resolution (typically 250 km) and along-track resolution (about 20 km) is limited to mapping sea level variations resulting from tides, and from mesoscale and large scale geostrophic currents. An additional satellite-based technique consist of using sequences of infrared images to map the advection of frontal features, but this is limited to cloudless areas and to areas where sufficient thermal gradient exist, and therefore is not of general application. Land-based techniques such as HF and VHF doppler radars require heavy infrastructure and have only local coverage.

While these techniques have been used to study several categories of ocean processes, there is a lack of high resolution (i.e. 100-200 m scale) studies of ocean flows, in particular in the fields of air-sea interactions and surface layer circulation and in coastal processes. ATI-SARs are the only instruments capable of advancing studies in these fields. Main applications are:

- mapping of coastal processes, erosion processes, pollution
- ship routing / manoeuvres in high current areas (with strong tides)
- basic studies on air-sea interactions (heat transfer, etc.)
- seasonal weather forecasts
- study of El Nino phenomenas

The following two key requirements may be posed to ATI mission data products:

- spatial resolution: 200 m
- velocity range: from 0.02 m/s up to 4 m/s

Further analysis has to show whether these performance requirements can be reached with illuminator satellites like Envisat or ALOS.

The SRTM Along Track Interferometry Example

In the following the SRTM antenna configuration is taken as an example for a spaceborne ATI. The system was designed for across track interferometry which was performed with a 60m boom. Due to mechanical constrains the canister for the boom and the secondary antenna was mounted with a 7m offset to the main antenna in the Space Shuttle cargo bay. This created a small along track baseline *Dx* which is long enough to detect and measure very fast tidal currents close to coasts. For the special case of SRTM along track interferometry the along track time lag is:

$$\Delta t = \frac{\Delta x / 2}{v_{Shuttle}} = \frac{3.5\,m}{7500\,m/s} = 0.46\,ms \tag{3}$$

(Only half of the antenna separation has been accounted here because of single pass interferometry.) The relation between the measured interferometric phase j_{ATI} and the radial velocity v_{range} is (with λ=3.1 cm):

$$j_{ATI} = 360^{\circ} \cdot 0.030\,\mathrm{s/m} \cdot v_{range} \qquad (4)$$

As an example the motion of a scatterer of 1 m/s corresponds to a phase of 10.8 degrees. (In the DEM a strong target moving with 10 m/s (36 km/h) would produce a 108 degree interferometric phase, which corresponds to a (108/360 * 180 m) 54 m height error due to this motion.)
Strong tidal currents reach up to 10 knots (about 5m/s) and have been detected with the X-SAR / SRTM. Figure 5 shows an example in the Waddenzee at the Dutch coast. Figure 5a depicts the orientation of the data take from southwest to the northeast. The radar look direction was from southeast and the Shuttle heading was northeast.
Figure 5b represents the amplitude image showing in the south the Afsluitdijk of the Ijsselmeer. The islands from left to right are Texel, Vlieland and Terschelling. Also some small islands like Noorderhaaks between Den Helder and Texel and Richel as well as Griend between Vlieland and Terschelling are clearly visible. The image was taken at Feb. 15th 2000 at 12h34 UTC. This was nearly at high tide. In the phase image (Fig. 5c) the strong currents between Den Helder and Texel and Vlieland and Terschelling are clearly visible. It shall be pointed out that only the velocity component in across track is imaged.

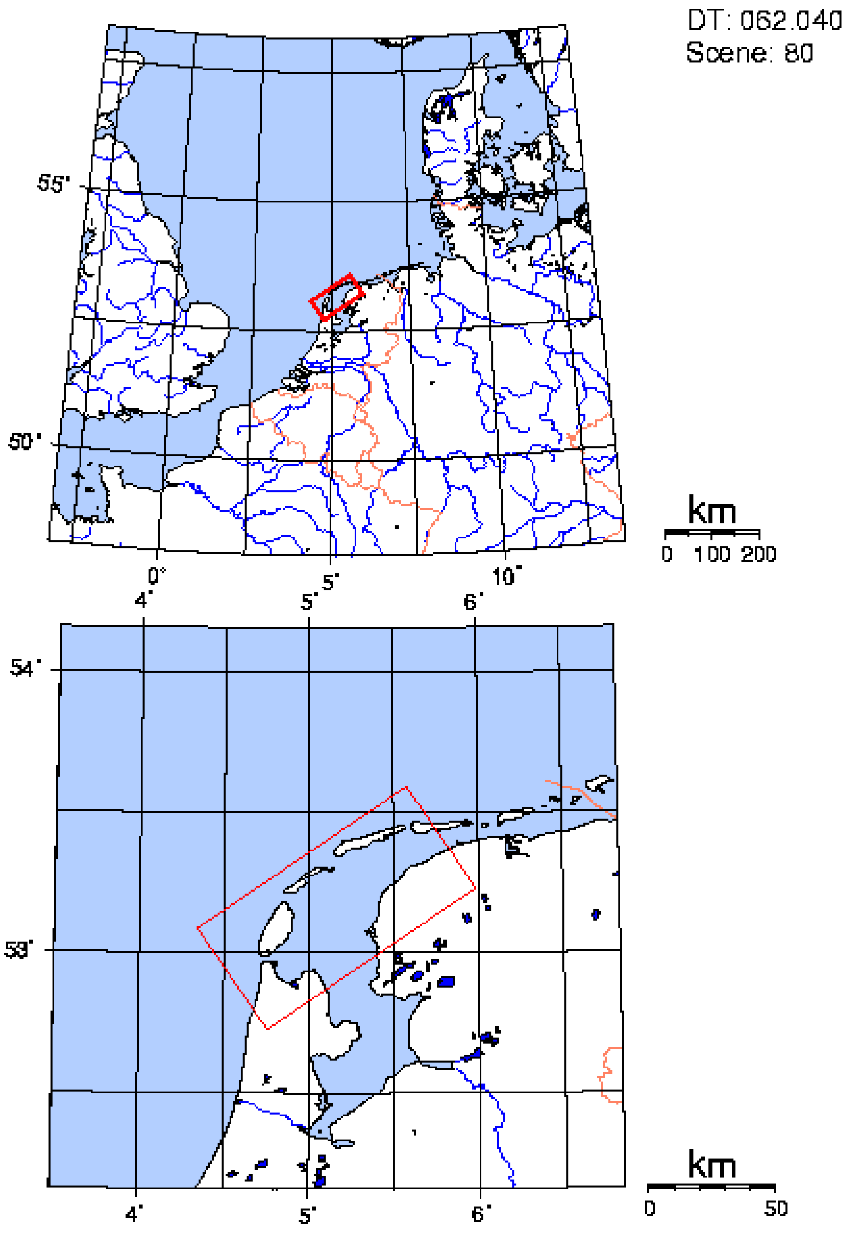

Figure 5a: Orientation and location of the X-SAR / SRTM data take DT062.040.

Figure 5b: X-SAR / SRTM geocoded amplitude image of the Waddenzee in the Netherlands

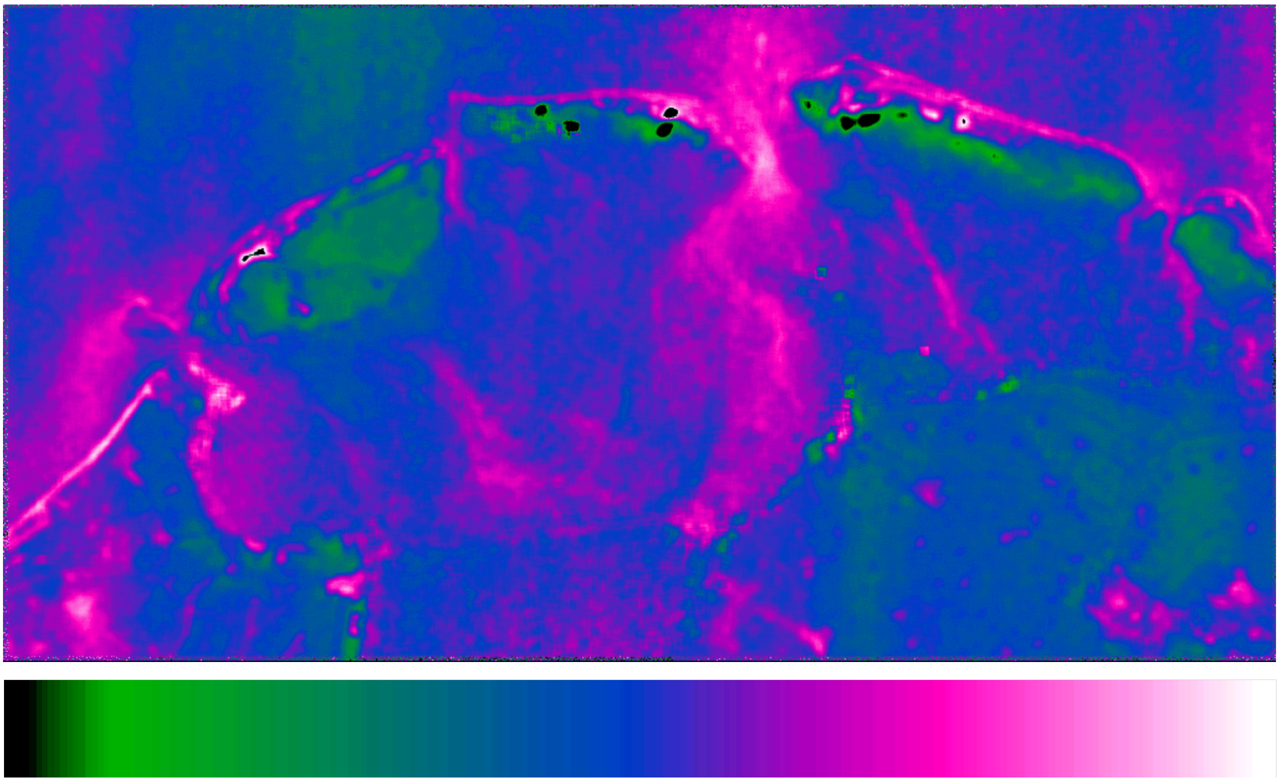

Colour coding:
black: -21°(-2.0 m/s) blue: 0° (0 m/s) white: +21° (+2.0 m/s)

Figure 5c: X-SAR / SRTM phase image of the Waddenzee in the Netherlands

The interpretation of the SRTM interferograms is difficult because due to the additional across track baseline not only motion but also elevation causes a phase shift. In the interferogram shown in Fig5c it was tried to minimize this effect by subtracting an artificial interferogram inversely generated from an existing digital elevation model with a 1km lateral spacing. Therefore, the land in Fig.5c shows some difference between this model and the SRTM elevation model and should not be interpreted here.

References

AFRL Space Vehicles Directorate, June 1998. http://www.vs.afrl.af.mil/Factsheets/techsat21.html.

Bamler, R., Hartl, P., 1998. Synthetic aperture radar interferometry. Inverse Problems, R1-R54.

Bao, M., Schulz-Stellenfleth, J., Lehner, S., Eineder, M., 2001. First results on ocean wave imaging from the Shuttle radar topography mission. Proceedings of IGARSS 2001.

Carande, R. E., 1994. Estimating Ocean Coherence Time Using Dual-baseline InSAR. IEEE TGARS, Vol. 32, No. 4, pp. 846 – 854.

Cloude, S. R., Papathanassiou, K. P., Woodhouse, I., Hope, J., Suarez Minguez, J. C., Osborne, P., Wright, G., 2001. The Glen Affric Project: Forest Mapping Using Polarimetric Radar Interferometry. Proceedings of IGARSS 2001.

Frasier, S. J. et. al., 2001. A Pod-Based Dual-Beam Interferometric Radar for Ocean Surface Current Vector Mapping. Proceedings of IGARSS 2001 .

Goldstein, R. M., Zebker, H. A., 1987. Interferometric radar measurement of ocean surface currents. Nature, 1987, Vol. 328, No. 6132, pp. 707-709.

Holcomb, D. W., 1998. Applications of Imaging Radar to Archaelogical Research. Chapter 16 in Principals & Applications of Imaging Radar, Vol. 2, edited by F. M. Henderson and A. J. Lewis, J. Wiley 1998.

Martinerie, F., Ramongassie, S., Deligny, B., Thouvenot, E., Massonnet, D., 2001. Interferometric CartWheel Payload: Development Status and Current Issues. Proceedings of IGARSS 2001.

Massonnet, D., 2001. Capabilities and Limitations of the Interferometric CartWheel, IEEE TGARS, Vol. 39, No. 3, March 2001.

Mittermayer, J. et al., 2001a. Preliminary Interferometric Performance Estimation for the Interferometric CartWheel in Combination with ENVISAT ASAR. CEOS SAR Workshop, Japan 2001.

Mittermayer, J., Krieger, G., Moreira, A., Wendler, M., 2001b, Interferometric Performance Estimation for the Interferometric CartWheel in Combination with a Transmitting SAR Satellite, updated procceedings of IGARSS 2001

Mochia, 2000. BISSAT: A Bistatic SAR for Earth Observation. NASA / ASI Workshop on “Observing Earth from Space”, Venice, June 2001.

Romeiser, R., Hirsch, O., 2001. Possibilities and Limitations of Current Measurements by Airborne and Spaceborne ATI SAR, Proceedings of IGARSS 2001.

Romeiser, R., Thompson, D. R., 2000. Numerical study on the ATI radar imaging mechanism of oceanic surface currents. IEEE TGARS, vol. 38-II, pp. 446-458.

Runge, H., Bamler, R., Mittermayer, J., Jochim, F., Massonnet, D., Thouvenot, E., 2001. The Interferometric CartWheel For Envisat. IAA Symposium Small Satellites For Earth Observation, Editor H. P. Röser, R. Sandau, A. Valenzuela, Wissenschaft und Technik Verlag, Berlin 2001, pp187 – 190.

Runge, H., 1999. Hochauflösendes Synthetik Apertur Radarsystem. German Patent Application DE 199 29 143 A1, priority date June 26th, 1999.

Suchandt, S. et. al. 2001. The Shuttle Radar Topography Mission. ISPRS Hannover 2001 (in these proceedings).

RapidEye - An Space Based Monitoring System for Agriculture an Cartography

Stefan Scherer, Dr. Manfred Krischke
RapidEye AG, Wolfratshauser Str. 48, 81379 Munich, Germany
Tel.: + 49 89 72495-454, Fax +49 89 72495-291, e-mail: scherer@rapideye.de

ABSTRACT

RapidEye AG, a German venture founded in 1998, intends to establish a global monitoring service for agriculture and cartography. Applications will become operational in 2004. As primary data source RapidEye will operate an innovative space based system. Data will be generated through a constellation of small satellites with significant competitive advantages due to high resolution, quality, availability and capacity. The satellite constellation will have the unique characteristics:

- Frequent monitoring of large areas (large image swath)
- Daily global revisit (4 Satellites)
- High spatial resolution (6.5m) in five spectral bands

RapidEye will provide a range of Earth observation products and services to a global market in the fields of:

- Agriculture: e.g. crop monitoring and mapping, damage assessment, yield prediction
- Cartography: e.g. satellite based maps, change detection services, DEMs
- Other Markets: e.g. spectral data, 3D-visualization, disaster assessment

The RapidEye system will have the capability to provide regular and frequent multispectral high resolution image coverage of all agricultural areas in Europe and the US. The current work concentrates on the generation of agricultural information services based on the multi-temporal data from the satellite system in combination with various other data sources on ground or in space.

1. INTRODUCTION

In spite of rather optimistic growth prognoses, the commercial success of Earth observation is primarily hindered by the fact that required data cannot be generated at the desired time and thus cannot be made available to the customer. This, however, is vital for the establishment of professional applications in the field of agriculture, insurance and cartographic services. A potential customer will change his procedures only if the availability of the alternative is guaranteed.

Consequently, a commercially operated system must primarily aim at offering guaranteed availability of data. A satisfactory availability for optical sensors can only be achieved by minimizing the time between the individual revisits and providing a sufficient capacity to generate frequent image coverage of even large areas of interest. This understanding led to the definition of the RapidEye commercial concept and the RapidEye imaging system.

RapidEye Inc, incorporated in 1998, is a new satellite based GEO-information service company which concentrates on customers in the agricultural and cartographic field. Data will be generated through a

system of small satellites with significant competitive advantages due to high resolution, quality, availability and capacity. To fulfill the customer needs RapidEye will not stop at delivering raw image data. RapidEye's key clients will receive jointly developed geographic information products which are integrated in the client's work processes and therefore offer significant cost advantages and / or new revenue potential.
RapidEye has been selected as key-project for commercialization of space technology by the DLR and part of the German space program.

2. MEETING USERS' NEEDS

The demand for high-quality, current GEO-information is set to grow rapidly during the current decade. Market analyses have identified significant potential in the agricultural and cartography market segments in the European and US market.

RapidEye is targeting a range of information users, which permits the exploitation of its products across a wide customer basis. RapidEye's research demonstrates that the targeted information users have common top-level requirements which are driven by mutual demands.

Information User	User-Specific Information Needs
Farmers, Producers, Food companies, Insurance companies	Generation of statistics of agricultural usage, development and damage assessment
Commodity brokers, Food companies	Determination of agricultural yield predictions
Insurance companies, Disaster relief organizations	Development of crisis management strategies
Commercial, Civil and Military organizations	Creation of cartographic information

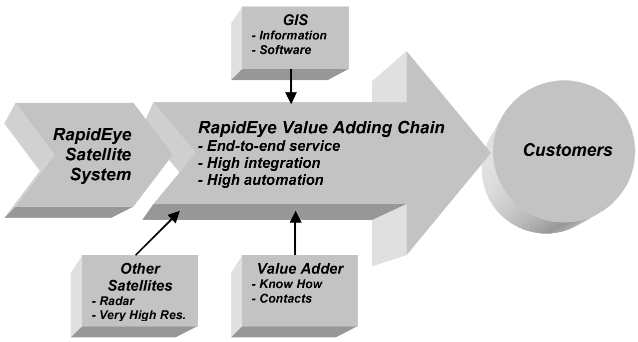

Figure 1: Processing chain

For all users a very high degree of vertical integration is essential. Therefore the RapidEye concept is based on three key elements:

- high resolution Earth monitoring system with guaranteed data availability
- tailored image analysis and information systems
- joint product development with the customer

Since the market focus is on a limited number of key customers the product development can be tailored to the specific users needs.

3. RAPIDEYE HIGH RESOLUTION EARTH MONITORING SYSTEM

The key features of the RapidEye Earth monitoring system are:

- Daily revisit of each point on Earth
- Large imaging capacity
- Multispectral high resolution imager

The RapidEye owned data source comprises a 4-small-satellite constellation, an operations center, ground stations and a data pre-processing and archiving center.

All four satellites are on a sun-synchronous orbit evenly spaced in one orbital plane. The altitude is 600 km and the local equator crossing time is at 12:00 hours (noon).

Figure 2: RapidEye four satellite constellation

Each satellite accommodates a digital optical imager. A regular full repeat coverage can be generated within 3-4 days depending on latitude. A revisit time of one day can be obtained with body-pointing techniques.

The fundamental idea of RapidEye is based on technologies that do -to a large extent- already exist combined with additional innovative detail solutions. RapidEye has signed an agreement with Surrey Satellite Technology (SSTL) in which SSTL will become the prime contractor for the turn-key system and will become an equity investor in RapidEye. The camera is going to be built by SIRA Electro – Optics.

3.1. RAPIDEYE IMAGING INSTRUMENT

The RapdEye imaging instrument is a multispectral pushbroom instrument, providing a swath width of 159 km with continuous observation coverage of up to 1500 km in length. The spatial resolution (GSD) of the imagery is 6.5 m. The camera is based on a dual optical-system design resulting in a dual-swath (both swaths of 79 km are slightly overlapping) observation.

The Earth imaging system captures 6 spectral bands (blue, green, red, red-edge, near infra-red and panchromatic) with 12 bit sampling. The source data are compressed in real-time prior to on-board storage and/or downlink transmission. Loss less (1:2) and/or lossy compression techniques can be selected on command. The design of the imager focuses on high geometric stability and good radiometric sensitivity.

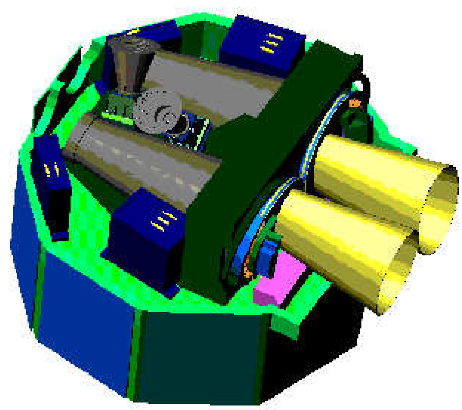

Figure 3: RapidEye optical camera

3.2. RAPIDEYE SATELLITE PLATFORM

The satellite bus is based on Surrey's UoSat12. The wet mass of each RapidEye satellite is approx. 315 kg, the design life is seven years.

Each satellite is three-axis stabilized. The spacecraft uses a redundant GPS receiver for orbit determination and on-board time provision. Attitude sensing is provided by star sensors. The pointing knowledge is expected to be less than +/-50m on ground. A body-pointing capability of the spacecraft exists permits a ±30º FOR (Field of Regard) for camera observations into any direction however, the feature is planned to be used only in the cross-track direction.

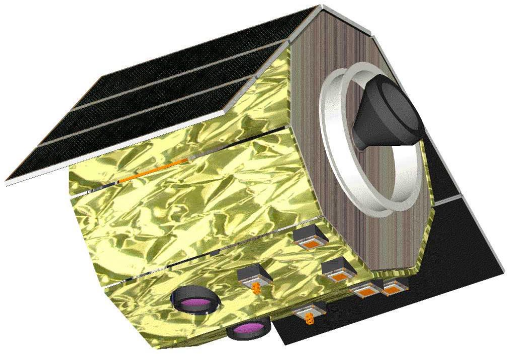

Figure 4: RapidEye satellite based on UoSat12

The X-band downlink will operate at a data rate of 150 Mbit/s and allow to download up to 11 Gbytes of compressed data per ground contact.

The RapidEye constellation is planned to be installed in two separate launches (two S/C each) on a Russian launch vehicle.

3.3. RAPIDEYE GROUND SEGMENT

The ground segment of the data source comprises the space craft operations center, X-band ground stations, and a data pre-processing and archiving facility.

RapidEye's dedicated Spacecraft Operations center will be installed at RapidEye's headquarters and shall form a hub of the RapidEye system. The S-band communication system will allow user requests to be uploaded to the RapidEye satellite constellation on short notice and will permit RapidEye's experts to carry out spacecraft health monitoring and station-keeping. RapidEye's image tasking will make use of short term weather predictions and weather statistics to optimize the performance of the system. RapidEye will use existing X-band ground stations for data reception.

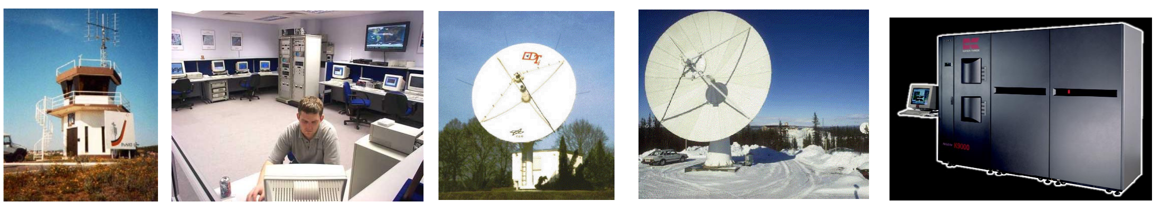

Figure 5: Ground segment facilities

All data received will be processed immediately to ortho-images. The output will be calibrated, terrain corrected data sets with a localization accuracy for most monitoring areas of 1 pixel or better. A extensive image archive and catalogue will be the backbone of the RapidEye data infrastructure. It will hold several hundreds of tera bytes of image data, products and auxiliary data.

4. RAPIDEYE IMAGE ANALYSIS AND INFORMATION SYSTEMS

A key element of RapidEye is the seamless integration of data source, image analysis and the customer information systems. Together with it's key customers RapidEye is currently developing a number of information services. The focus is on agriculture and cartography.

Customer Group and Product	**Product sample**
Agricultural Insurance: Crop map Crop monitoring Damage assessment Risk analysis	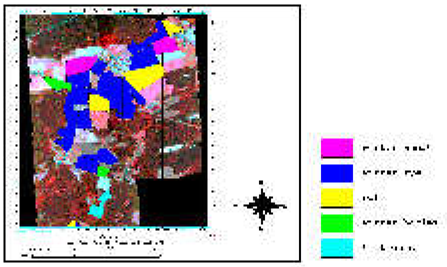
Producers (Farmers): Soil maps Crop vigor maps Crop stress Field management information	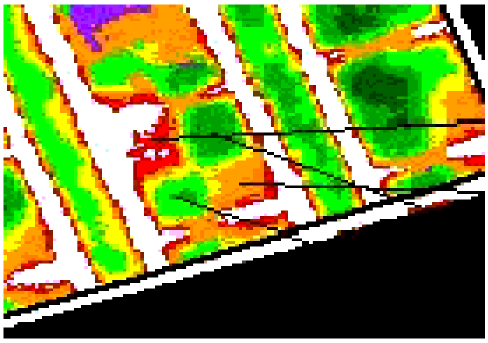
National and International Institutions / Governments: Yield predictions Subsidies Control Damage assessment	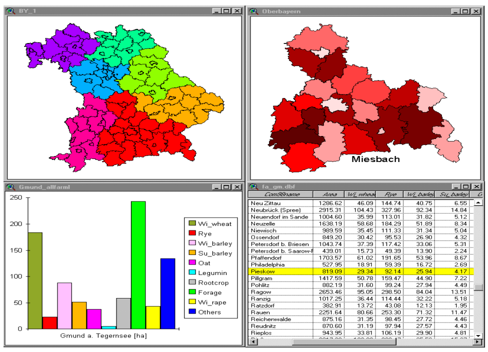

Cartography and Military :
Global image mapping 1:25’000
Continuous map update
Change Detection
DEM

4.1. AGRICULTURAL POTENTIAL OF RAPIDEYE

RapidEye is currently developing a number of services for the agricultural sector. Main partners do operate in the field of:

- Agricultural insurances
- Agricultural consulting services
- Food processing companies
- Agrochemical services
- National and international institutions.

The most advanced is the implementation of an operational service for large scale crop monitoring and damage assessment for the United Hail Insurance in Germany. VH is offering insurance schemes for hail and soon for multiple peril in Germany and its eastern neighbors. The primary aim is to support the monitoring of 1.5 million insured parcels and the assessment of ~65'000 damaged fields per year by the use of remote sensing technology. The successful implementation of such a service requires a careful design and integration of the complete processing chain. This affects all elements from the satellite configuration to the assessment procedure in the field. Key issues considered are:

- Design and integration of the information flow from satellite tasking to information delivery
- Introduction and development of a GIS infrastructure in the insurance process
- Development of operational damage assessment algorithms.

To support the RapidEye development programs continuous research is carried out since the beginning in 1999. The program includes acquisition of multitemporal airborne and satellite based imagery together with extensive ground truthing of more than 10’000 ha. The technology has been investigated to assess damage and yield loss by hail and drought by means of remote sensing.

4.2. CARTOGRAPHIC POTENTIAL OF RAPIDEYE

Although planned as agricultural monitoring system RapidEye has the potential to revolutionize also global cartographic mapping. The system has the capability to generate and maintain a global coverage of

- DEM with 20 grid size and 5m vertical accuracy
- Up-to-date ortho-image maps at a scale of 1:25'000

RapidEye is currently investigating concepts for generating and marketing both potential data sets.

Global DEM coverage:
The capabilities of the RapidEye system to generate global digital elevation models have been investigated together with the Institute For Photogrammetry, Stuttgart.

RapidEye has the ability to acquire off track stereo images with only a time delay of ~24 min. This can be achieved by imaging the same area of interest from two subsequent satellites. The viewing angle varies with the latitude and phasing of the satellites in the orbital plane. The level of coherence of the stereo pairs will be close to the one of in-track stereo pairs. Also the cloud situation will be nearly identical.

The quality of the RapidEye DEM will exceed the DEM generated by the SRTM mission (DTED Level 2). The Grid size will be 20x20m , the absolute vertical accuracy ~5 m. The generation of a global coverage of stereo pairs is estimated to last 1-2 years. The acquisition could be finished by 2004/5.

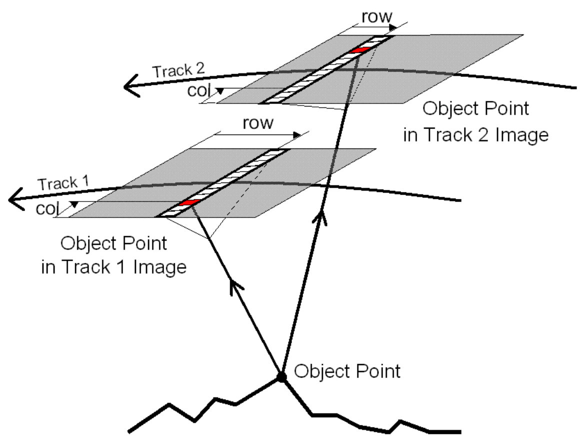

Figure 6: Cross track stereo acquisition (Source: IFP)

Global ortho image map:
Topographic maps at a scale 1:50'000 and 1:25'000 are not available in many areas of the world and if so they are often outdated. Even in the well mapped areas like the USA and Europe the maps are too old to comply with the requirements of commercial users as mobile network planners or car navigation system providers. RapidEye has the capability to generate and maintain an up-to-date global ortho image set at a scale comparable to 1:25'000 maps (6.5m ground resolution) with a potential geo-location accuracy of +/- 5m globally.

To achieve this the imager and the satellite platform are designed for a very high degree of geometric stability. This will enable RapidEye to produce large ortho-corrected image coverages with a very limited number of ground control points. However the provision of the required high accuracy ground control points is critical and has to be investigated. The global image coverage shall be updated every 1-3 years depending on the region.

5. THE COMPETITION

RapidEye's market analysis has identified many shortcomings in current and future systems and can therefore demonstrate the competitive advantages of the RapidEye system. RapidEye's strength lies in its combination of innovative approaches: the supply of high-resolution images of large areas with a daily revisit capability which for the first time allows guaranteed full coverage of large regions within short time.

The value of the information generated by the current competitors (SPOT, LANDSAT, IRS) is limited due to their slow revisit rates resulting in a lack of availability and real-time data delivery. Four new entrants (EarthWatch, OrbView, SpaceImage and ImageSat) are focused on the high-resolution data market and will not offer complete coverage or rapid data availability. A fifth potential new entrant, Boeing's Resource21 system, plans to target a similar market as RapidEye but with a resolution of 10 meters and a revisit rate of 4 days. RapidEye's system demonstrates significant advantages.

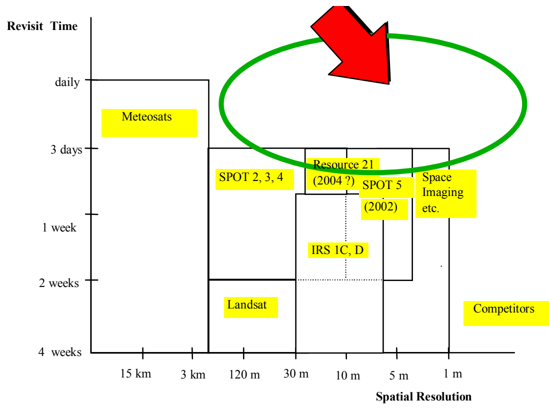

Figure 7:RapidEye targets the decisive gap

6. SCHEDULE

The schedule for RapidEye is tight and leads to a start of the service at beginning of 2004. The satellites will be ordered after financial closing in 2001. During the years 2001-2003, emphasis is primarily placed on the development of customer specific products and their introduction onto the market.

REMOTE SENSING BASED PARAMETER EXTRACTION FOR EROSION CONTROL PURPOSES IN THE LOESS PLATEAU OF CHINA

Schneider, Th*., Jacobsen, K., Seitz, R.*, Förster, B*.**
* Chair for Landuse Planning and Nature Protection, Technical University Munich
** Institute for Photogrammetry and Geoinformation, University of Hannover

ABSTRACT

The loess plateau is one of the poorest regions in China. The massive erosion in this area brings severe ecological but also economical problems on local level, the lack of water storage capacity in the loess plateau at a whole was identified as one of the reasons for the large inundation in the lowland planes of the Yellow River with thousands of victims. Reforestation of the loess plateau should help to solve this problems. Both, socio-economic and ecological values must be taken into account when performing reforestation. To work out reforestation plans and to develop adopted bio engineering erosion control measures, the evaluation of old reforestation programs and the understanding of the current land use and his impact on the erosion processes is very important.
As an important base of information, CORONA-images have been used. The handling of these panoramic space images is described in detail.

1. INTRODUCTION

The project " Erosion Control in Shaanxi Province in P. R. China " is a cooperation project between the faculty of forest sciences, TUM and Northwestern University of Forestry, starting in 1999. The aims of this project are:

- Comprehend erosion situation and land use potential from a regional to a local scale
- Study how to utilise woody plants as the source of reforestation in erosion areas
- Set up nature-near forest stands for the purpose of biodiversity conservation
- Find optimal agricultural systems to control erosion and increase the income of local people at the same time
- Underline the restrictive impact of goat and sheep grazing on self-recovering-ability of the local ecosystems

A three scale approach for the remote sensing support was developed. The investigations on (1) regional scale are based on high resolution satellite data of the Landsat type. They should deliver an estimate about the erosion risk potential and the quantity of soil loss. The (2) local scale investigations are based on very high resolution satellite data and should led to the quantification of soil loss and the identification of areas appropriated for reforestation a s well as for the pre-selection of demonstration sites for bio-engineering measures (level 3).

Both, the identification of erosion risk zones in that highly structured terrain as well as the quantification of erosion processes requires a high precision digital elevation model (DEM) with a raster size as small as possible. Due to the lack of an administrative DEM and the restrictive handling of aerial photographs by the Chinese Authorities the solution was to use declassified Corona data from the early 60th to calculate the required DEM.

For covering the monitoring aspect, mandatory for the quantification of erosion processes, the land use / land cover concerned investigations as well as the detection of erosion processes like the velocity of gully developments and the decrement of plateau area, etc. are planned to

be done by comparison of CORONA with IKONOS data set evaluations. IKONOS data sets are ordered but still not registered.
For erosion risk estimation on local scale a DEM derived from Corona data in combination with Landsat 7 ETM information on land use / land cover can be used. An estimate on the accuracy of the CORONA data derived DEM is given, including a brief comment on effects of the time difference of 38 years until data take as well as on the lack of ground control points.

2. CORONA IMAGES AND BUNDLE ADJUSTMENT

During the Cold War the USA and the USSR developed for military purposes reconnaissance satellites. The USA have created the CORONA camera system with different versions starting in 1960 and ending in 1972, when the film based satellite systems have been replaced by digital cameras.

system	used	cameras	focal length	format	resolution
KH-1	Aug. 60	1	24 inch	2.2 x 30 inch	40 ft
KH-2	12/60 – 7/61	1	24 inch	2.2 x 30 inch	30 ft
KH-3	8/61 – 12/61	1	24 inch	2.2 x 30 inch	25 ft
KH-4	2/62 – 12/63	2	24 inch	2.2 x 30 inch	25 ft
KH-4A	8/63 – 10/69	2	24 inch	2.2 x 30 inch	9 ft
KH-4B	9/62 – 5/72	2	24 inch	2.2 x 30 inch	6 ft
KH-5	5/62 – 7/64	1	3 inch	4.5 x 4.5 inch	460 ft
KH-6	7/63 – 8/63	1	66 inch	4.5 x 25 inch	2 ft

table 1: CORONA camera systems (Doyle, 1996)

In 1995 the CORONA images have been declassified and are now available for a low charge. Of course the more than 30 years old images cannot be used for map updating, but for several applications the generation of digital elevation models (DEM) of the old situation is important. This may be useful in areas with a stable surface, where they can be used together with actual single space images or in areas with strong erosion as reference.

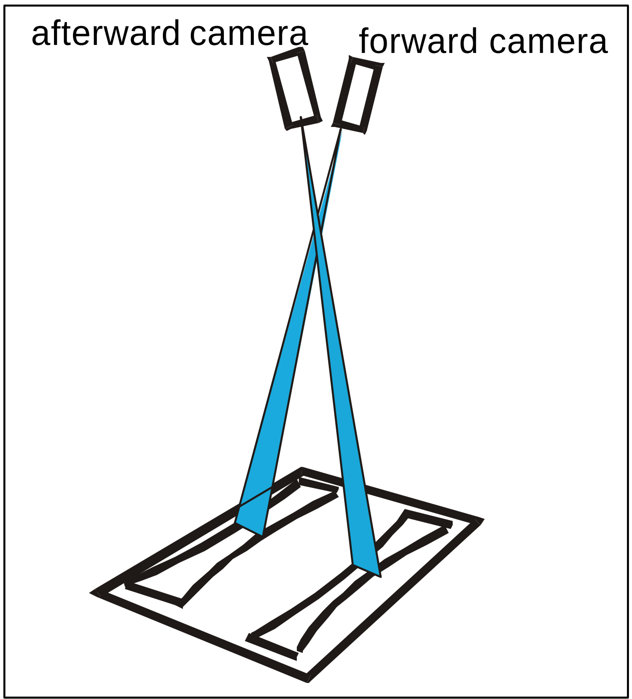

figure 1: configuration of CORONA KH-4-cameras

Like shown in figure 1, the CORONA camera system 4 was equipped with 2 panoramic cameras, scanning the area from one side to the other, and with an index camera as overview. An area of 278km with a width of the individual scenes of 17 km in the center was covered. The convergence angle of 30° between the 2 cameras corresponds to a base to height relation of 0.54, that means the vertical component has twice the standard deviation like the horizontal component. The combination of a forward and an afterward looking camera has the advantage of a stereoscopic coverage within the orbit, which cannot be influenced by seasonal changes of the imaged area.

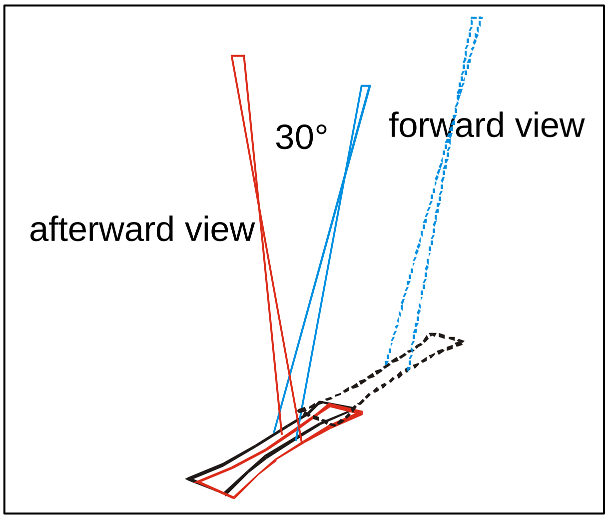

figure 2: possibilities of a stereoscopic coverage

In addition to a stereoscopic coverage within the orbit, of course a stereoscopic coverage of neighboured orbits is possible generating a base to height relation in the range of 1. This is nominal better for the height determination, but it can be affected by seasonal changes of the imaged object.

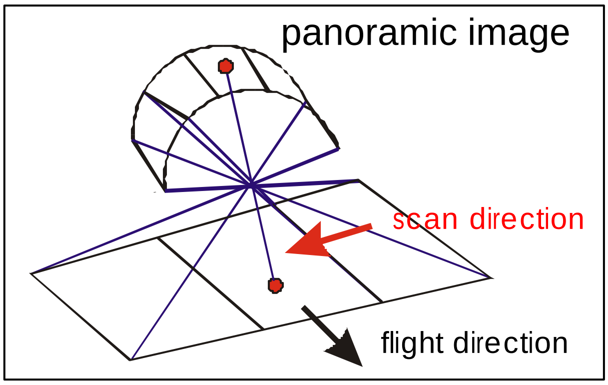

figure 3: geometric principal of panoramic cameras.

The used panoramic cameras are scanning the area from one side to the other. By this reason the image scale is depending upon the nadir angle. For the used flying height of 187km, the scale is varying between 1 : 300 000 in the center up to 1 : 366 000 at a nadir angle of 35°. A second effect is movement of the satellite and the rotation of the earth during scanning. Both are deforming the image geometry against a perspective camera.

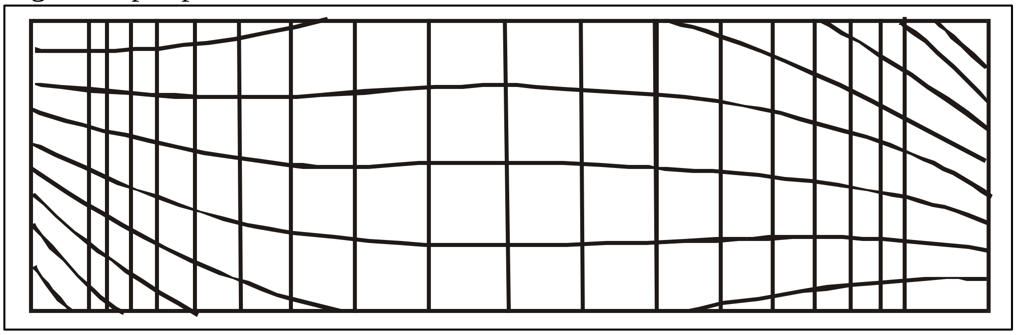

figure 4: geometric difference panoramic – perspective image

A square grid located in the object space will be imaged in a panoramic image like shown in figure 4. Of course this is enlarged, in reality the differences are smaller, but the panoramic images do have in general such a geometry.

In the used program system BLUH, at first the panoramic images are rectified against a tangential plane to the imaging surface, this is equalising the scale. As next step the geometric deformation is handled by additional parameters. This is still required because of the unknown exact imaging parameters like the scan speed. The mathematical model has been proven with KVR1000 images – the corresponding reconnaissance camera of the USSR. In a test area in Germany with accurate control points, an accuracy of +/-3.3m for X and Y has been reached, equivalent to 15µm in the image (Jacobsen 1997).

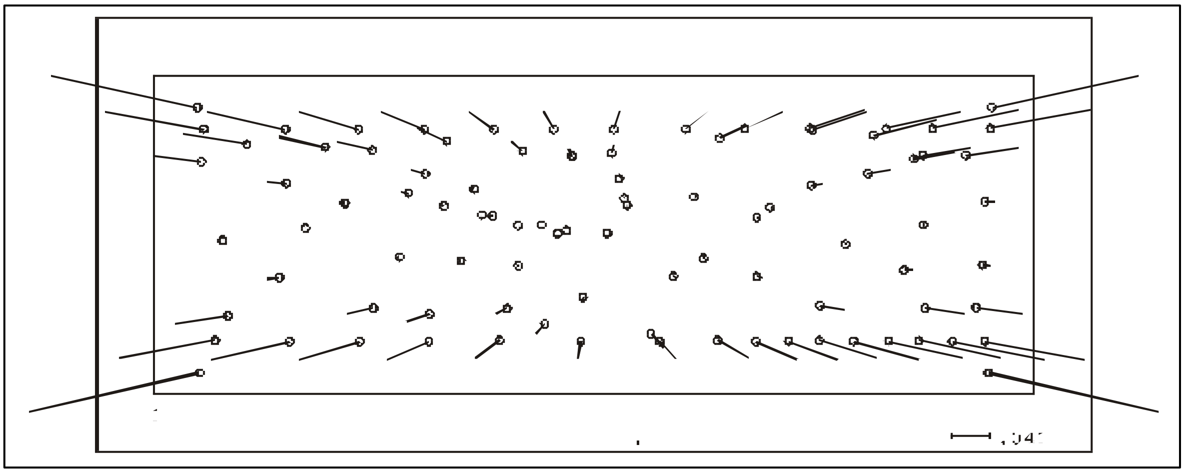

figure 5: geometric correction of KH-4B image (largest vector 185 microns)

Beside the panoramic geometry, the earth curvature has to be respected. The mathematical model, used in photogrammetry is based on an orthogonal coordinate system. In the case of space images, the earth curvature cannot be neglected. The traditional improvement by earth curvature and refraction correction has as a second order effect of flattening the earth surface a change of the base to height relation by the factor flying height / earth radius (187km / 6366km = 3%). This is causing an affine deformation of the model scale with an error in height, but it can be corrected by a change of the used focal length by the same factor, that means the nominal focal length has to be changed from 609.602mm to 627.509mm. The combined correction is improving the sigma0 and the mean square differences at the control points by 6 – 10%.

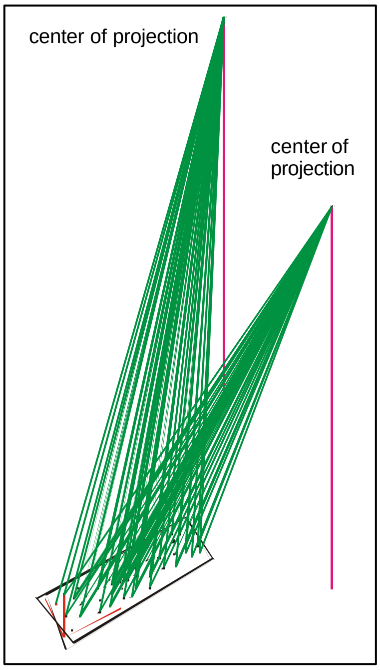

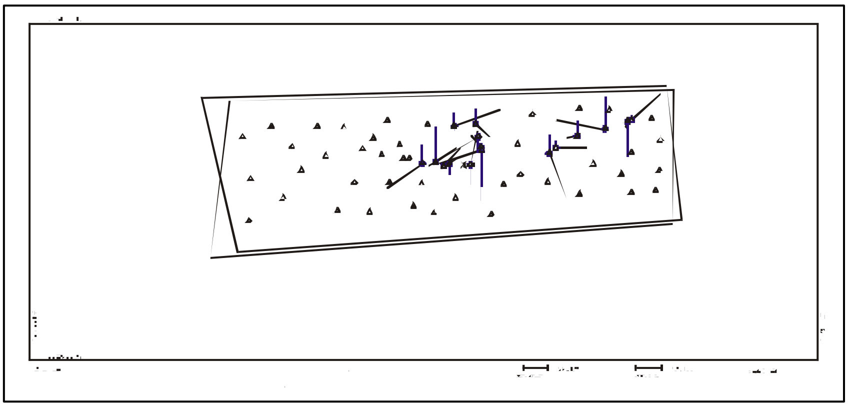

figure 5: distribution and discrepancies at control points

figure 6: 3D-view to configuration of main project area

Not a whole CORONA KH-4B-stereo model has been handled, the project area was limited to a smaller size. In the first model, 16 control points have been available. Finally, like it is often the case, not the quality of the block adjustment, but the quality of the control points has been checked. The root mean square error of the 16 control points in the first model was

RMSEX=27.6m, RMSEY=19.7m and RMSEZ=14.2m. This was within the expectations of the accuracy and the definition of the control points. Of course after more than 30 years, the location of road crossings, used as control points, may have been changed. In the second area only 4 control points are given, so the RMSEX=16.3m, RMSEY=13.6m and RMSEZ=11.8m are not so representative for the object accuracy.

3. DETERMINATION OF DEM

Based on the image orientation, digital elevation models (DEM) have been generated by automatic matching with program DPCOR. DPCOR is using the region growing method - from known corresponding points, points in the neighbourhood are matched and from these again points in the neighbourhood up to a complete coverage of the whole model. For every third pixel a matching was computed. At first an approximation by correlation and after this a least squares matching will be computed. This is the most accurate possibility of image matching. In the average for 71% of the positions, the matching was successful. For the remaining points, usually the contrast was not sufficient.

figure 7: CORONA sub-image of a typical erosion area

The relative accuracy of the DEM's have been estimated to approximately +/-5m. The absolute accuracy is depending the distribution and accuracy of the control points which have not been optimal in this case. But for an analysis of the erosion, one model can be related to the other by corresponding points. The erosion risk can be analysed also without high absolute accuracy, for this also mainly a relative accuracy is required.

CONCLUSION

The IKONOS images have been shown as a very useful tool for the determination of digital elevation models for the analysis of erosions, but also as a reference in areas with stable surface. With no other space images a corresponding accuracy and resolution can be achieved for a limited amount of money.

REFERENCES

Doyle, F.J., 1996: Thirty Years of Mapping from Space, IAPRS, Vol XXXI, Part B4, Vienna 1996

Jacobsen, K., 1997: Geometric Aspects of High Resolution Satellite Sensors for Mapping, ASPRS Annual Convention Seattle, 1997

Jacobsen, K., 1998: Handling of Panoramic and Extreme High Oblique Photographs in Analytical Plotters, IAPRS, Vol XXVII, Part B1, Kyoto 1988

HIGH RESOLUTION STEREO CAMERA - AIRBORNE (HRSC-A): 4 YEARS OF EXPERIENCE IN DIRECT SENSOR ORIENTATION OF A MULTI-LINE PUSHBROOM SCANNER

F. Scholten, F. Wewel, S. Sujew

German Aerospace Center (DLR)
Institute of Space Sensor Technology and Planetary Exploration
Rutherfordstr. 2
D – 12489 Berlin, Germany

email: Frank.Scholten@dlr.de
phone: ++49-30-67055-326
fax: ++49-30-67055-402

KEY WORDS: HRSC-A, Multi-Line Scanner, Direct Sensor Orientation, DGPS/ INS, Boresight Alignment

ABSTRACT

Since 1997 the German Aerospace Center (DLR) is operating the HRSC-A in combination with direct georeferencing methods. Using an APPLANIX DGPS/INS system many scientific and commercial applications could be realized with accuracies in the decimeter range for the standard products, such as true orthoimage mosaics and Digital Surface Models. While traditional aerotriangulation of scanned analog imagery still makes use of ground control for accurate photogrammetric restitution, the multi-stereo capabilities of the HRSC-A, combined with its well defined interior orientation and a high-end DGPS/INS hard- and software system, makes automatic processing of project areas without any planimetric ground control possible for dayly work. Detailed investigations using HRSC-A data have checked that there is no difference in accuracy between using control points or only tiepoints between adjacent image strips (the availability of geodetic datum shift parameters from the WGS84 system to the target reference system is assumed). Only the fact, that the basic GPS measurements are defined in the WGS84 system, generates the requirement for vertical control information in order to transform direct georeferenced DSM height values from heights above the WGS84 ellipsoid to generally requested heights above sea level.

1. INTRODUCTION

The airborne version of the High Resolution Stereo Camera (HRSC-A) is operated by the DLR-Institute of Space Sensor Technology and Planetary Exploration since 1997 (Neukum, 1999; Wewel et al., 1998; Scholten et al., 1999). After first applications in 1997 with standard components for measurements of the sensor position and pointing (3 gyroscopes and independent DGPS, see Chapter 6.) since 1998 the HRSC-A as well as the new HRSC-AX camera generation (Neukum et al., 2001) is adapted with an integrated DGPS/INS system by APPLANIX CORP. for direct georeferencing of HRSC-A image data.

On the one hand the HRSC camera concept using multipli-stereo data acquistions requires permanent and precise orientation data, not only for few moments as it is for aerial frame photography. On the other hand this type of data defines a unique possibility for quality control of the orientation measurements (see Table 1).

	HRSC-AX	HRSC-AXW	HRSC-A
Focal Length	150 mm	47 mm	175 mm
Total Field of View	41° x 29°	30° x 79°	38° x 12°
CCD Lines	9 (4 colors)	5 (2 colors)	9 (4 colors)
Stereo Angles	±20.5°, ±12.0°	±14.5°, ±12.2°	±18.9°, ±12.8°
Color Off-Nadir	-4.6°/-2.3°/2.3°/4.6°	-7.3°/7.3°	-15.9°/-3.3°/3.3°/15.9°
ImagePixels/CCD Line	12000	12000	5184
Pixel Size	6.5 µm	6.5 µm	7 µm
Radiom. Resolution	12 bit	12 bit	8 bit
Max. Scan Rate	1640 lines/s	1640 lines/s	450 lines/s

Table 1: Technical data of HRSC-AX, -AXW, -A

2. GEOMETRIC CALIBRATION

In contrast to analogue frame cameras digital line scanners can be geometrically calibrated for each relevant sensor position in the focal plane. For this purpose the camera is mounted on a special calibration unit, so that parallel light from a collimator passing a slot target hits the focal plane. With 2 rotations about perpendicular axis traversing in the center of the entrance pupil the light can be centered on every pixel of each CCD-line. Precise measurements of these rotations combined with the nominal focal length f yield camera coordinates x_i,y_i,f for the elements of all CCD-lines.

These x_i,y_i values are stored in so called calibration files which will be used during the photogrammetric processing (see also Ohlhof, 1996). Investigation on data of the HRSC-A, which is in permanent operation since 1997 and even has been used checked for space qualification during shock tests, show after re-calibration that the camera geometry is stable since there is no measurable change in the geometric calibration values.

3. ACQUISITION OF ORIENTATION DATA

For direct georeferencing of HRSC-A image data the integrated GPS/INS system *POS/DG 510* of APPLANIX CORP. is used (Hutton & Lithopoulos, 1998). It combines efficiently inertial sensor technology with a GPS receiver. The system consists of three parts, the Inertial Measurement Unit (IMU), a control unit with an integrated GPS receiver and the software package *PosPac*.

The IMU block is seperated from the read-out electronics and is mounted directly on top of the camera head. The IMU sensors (3 gyroscopes and 3 accelerometers) are used for measurements of angular velocities and accelerations of the camera in a frequency of 200 Hz. This allows to measure all movements which are not eliminated by the stabilized shock-damped platform on which the camera is mounted. The GPS antenna ist mounted directly above the camera in order to minimize lever-arm variations due to platform movements. GPS data recording is done with 2 Hz frequency. During the flight the time-synchronized INS and GPS data are stored on a PC card of the control unit for on-ground post-processing. Simultaneously on ground data of one or more DGPS reference stations are recorded with 1 Hz frequency.

4. POST-PROCESSING OF DGPS/INS DATA

The post-processing of the acquired GPS and INS data consists of two steps and is performed using APPLANIX *PosPac* software. The first step is the pure GPS processing, where GPS data recorded in the aircraft combined with GPS data from a reference station are processed to a kinematic GPS trajectory. This GPS solution describes the position of the camera (latitude, longitude, altitude) in the WGS84 reference system in 1 Hz frequency with an absolute accuracy of 5-10 cm and with few cm/s for the velocity. Due to several factors, i.e. bad satellite conditions, disturbances in the ionosphere, and long distances to the reference station, these accuracies can be derogated obviously. For analysis of the quality of the DGPS solution other reference stations beside the station within the target area, i.e. stations with distances of up to several hundred kilometers to the target area, can be incorporated. An important limitation for the use of far away reference stations is the KAR procedure (Kinematic Ambiguity Resolution), which does not perform steadily for distances larger than 30-40 km with losses of satellites and the resulting necessity of re-calculation of the ambiguities. Therefore, far away reference station require a static initialisation of the DGPS trajectory.

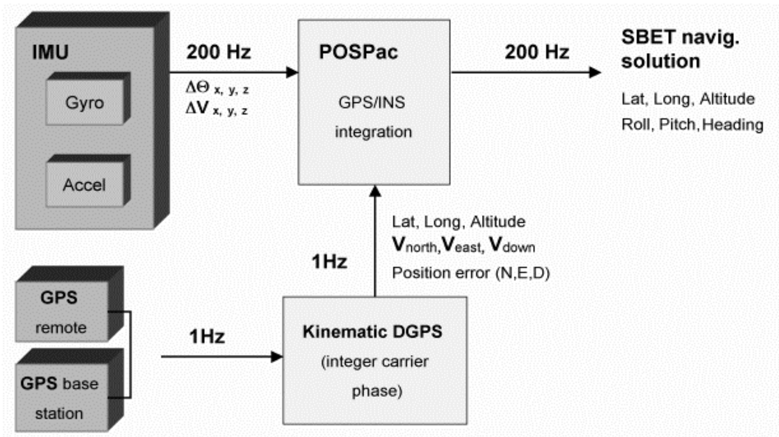

Figure 1: Integrated DGPS/INS post-processing

The second step comprises the GPS/INS-Integration. The inertial navigation algorithm, based on the IMU data, is additionally supported by the GPS position and velocity information. Since typical errors of inertial navigation and GPS measurements are independent and complementary, it is possible to estimate and correct these inertial errors with Kalman filtering very effectively. Thus, the resulting accuracy of the integrated DGPS/INS solution, so called SBET file (Smoothed Best Estimation of Trajectory), is defined by the GPS trajectory concerning position and by the quality of the IMU concerning attitude.

5. PHOTOGRAMMETRIC ADJUSTMENT OF ORIENTATION DATA

After DGPS/INS post-processing the photogrammetric adjustment of the orientation data is performed on the following data basis for the analysis of test flights as well as for operational standard processing of airborne HRSC data:

- Image data of 5 HRSC-A/AX stereo channels (including ancillary information (e.g. time of acqusition for each image line),
- geometric calibration data of each CCD pixel,
- SBET file containing camera position and IMU orientation,
- ground control information (if available).

The process consists of the following steps:

1) interpolation of position and attitude for each image line of all 5 stereo channels

=> actual camera position in the WGS94 system and rotation angles describing the attitude (of the IMU measurement axes !) with respect to a local tangential coordinate system T (X_T,Y_T,Z_T), where X_T is pointing North, Y_T is pointing East and Z_T is pointing in the direction of the WGS84 ellipsoid normal.

2) calculation of additional rotations in order to rotate the local system T to the Earth centered WGS84 system using the position data (X_{WGS84} and Y_{WGS84} pointing in the equator plane to longitude 0 and 90 deg East and Z_{WGS84} pointing to the north pole).

3) Automatic or semi-automatic measurement of image coordinates of IPs (identical points visible in the stereo channels of different overlapping image strips) and, if available, ground control points (GCPs).

4) Common estimation of boresight angles (alignment between the IMU and camera axes), potential systematic position offsets and drifts of the GPS trajectory, and small time offsets between position and pointing information on the one hand and time tags of the image lines on the other hand which might be introduced by filtering procedures during DGPS/INS post-processing .

Step 4 is done within a special heuristic iteration process. At first the boresight angles for pitch and yaw and a possible time offset between image and pointing data are determined by the optimisation of the 3D ray intersection, defined by the calibration and orientation data related to all measured IP's and GCP's image coordinates. Afterwards the boresight angle for roll Boresight-Offset and a possible time offset between image and position data are calculated using IPs (and GCPs). Adjacent image strips should be flown in contrary directions if only IPs are available. Beside this, GPS position offsets and drifts can be determined with the help of GCPs. Thus, this optimisation process yields boresight angles between camera and IMU, time offsets, and offsets and drifts of the GPS trajectory.

During the first year of operation of the HRSC-A a standard navigation constellation, consisting of a block of three dry tuned gyroscopes and a separated L1/L2GPS receiver, was used in order to measure relative pointing and absolute WGS84 positions of the camera. Since an integrated derivation of orientation data is impossible for this constellation, a similar optimisation process developed for the generation of the final absolute orientation of the HRSC data also included the estimation of pointing offsets and drifts for all three orientation angles.

6. GEOMETRIC TESTS AND ANALYSES

The geometric properties of all HRSC airborne cameras, HRSC-A, HRSC-AX, and HRSC-AXW as well as the photogrammetric optimisation procedure used for the estimation of boresight offsets, time offsets, and possible offsets and drifts of the GPS trajectory have been analyzed within different test campaigns. The detailed configuration and results of geometric tests using the high-end APPLANIX navigation system over specific test fields are described in previous publications (Wewel & Brand, 1999; Scholten et al., 2001).

Table 2 shows test results of a HRSC-AX test flown at an altitude of 1,000 m. Orientation data were processed with 4 different DGPS reference stations (SBET 1: reference station within the test field, SBET 2: same as SBET 1 but with additional modelling of lever-arm dynamics to due attitude variations, SBET 3 reference station distance 330 km, SBET 4: reference station distance 480 km, SBET 5: reference station distance 100 km).

	SBET 1	SBET 2	SBET 3	SBET 4	SBET 5
Boresight ω [°]	0.022	0.023	0.022	0.023	0.022
Boresight ϕ [°]	-0.015	-0.014	-0.015	-0.016	-0.016
Boresight κ [°]	0.135	0.134	0.133	0.135	0.135
Δt Position-Image [ms]	0.3	0.9	0.4	-0.3	-0.3
Δt Attitude-Image [ms]	-3.0	-3.0	-3.0	-2.0	-3.0
3D-RMS_rel [cm]	5.8	5.8	5.5	5.6	5.5
3D-RMS_str2str-IP [cm]	8.9	8.9	11.6	11.5	9.2
3D-RMS_abs-GCP [cm]	11.6	11.4	16.7	12.3	10.7

Table 2: HRSC-AX optimisation results using different DGPS reference stations

The slightly reduced absolute accuracy at GCPs with the SBET 3 solution (330 km) of 16.7 cm was improved to 12.9 cm by estimation of a GPS trajectory drift (30 cm/h in the vertical component) during the optimisation process. The DGPS/INS post-processing had already indicated such a behaviour of the trajectory during the one hour flight time.

As expected, results derived with the standard navigation constellation in the early test flights in 1997 are less accurate than results derived with the high-end navigation systems used since 1998. The absolute accuracies derived are 2 - 3 times worse than the actual values presented in 3) but might be sufficient for many applications with reduced requirements.

The test results using the high-end APPLANIX navigation system and statements about the characteristics of HRSC products can be summarized as follows:

1) the values for boresight offsets of a specific HRSC/IMU installation calculated within different tests can be derived with a standard deviation of about 0.002 deg for roll and pitch (0.005 deg for yaw) and range from 0 - 0.2 deg.

2) the SBET solutions include time offsets (introduced by filtering of data) with repect to the image line time tags. These offsets are in the range of 5-10 ms and can be estimated with an accuracy of 2ms.

3) using the optimised orientation values the following mean 3D point errors can be derived from altitudes of 1,000 m to 6,000 m:

   - relative ray intersection (RMS): 5 - 15 cm, (non-signalized significant natural or man-made features, measured within one image strip manually or by multi-image correlation techniques (least squares matching))

   - strip-to-strip accuracy (RMS): 10 - 25 cm, (at identical points in overlapping strips)

   - absolute accuracy at check points (RMS): 10 - 25 cm (defined in WGS84).

4) the accuracy values given above have been derived with the help of DGPS reference stations located in distances of up to 480 km from the test target area. But for stations with distances of more than 30 km, it is recommended to check for drifts in the GPS trajectory with the help of ground control points.

5) if no GPS drift has to be calculated (for standard applications with nearby GPS reference stations) the accuracy of the optimisation process, given in 3), does *not* depend on the availability of ground control. The only restriction is that not only parallel image strips with the same azimuth, but at least one backward or cross strip is flown.

6) for long image strips (> 60 km) there is no evidence of long term drift of SBET orientation, the same accuracies as given in 3) are derived.

7) photogrammetric 3D products (Digital Surface Models) in principal show the same accuracies as given in 3), but especially at steep and tall objects such as buildings, irregularities can occur because of hidden areas or shadowing effects. Image products such as orthoimage mosaics, which are derived using such a DSM might contain aftereffects of these problems, depending on the actual viewing angle.

Another good tool to prove the derived accuracies is the color-orthoimage. With the HRSC cameras objects are imaged with the different color CCDs at different times and under different viewing angles (see Table 1). Therefore the fit of a multispectral orthoimage is very sensitive with respect to the quality of sensor orientation.

Figure 2 shows an example of a true-color orthoimage derived with the new HRSC-AX using red, green, and blue bands combined with high-resolution panchromatic data.

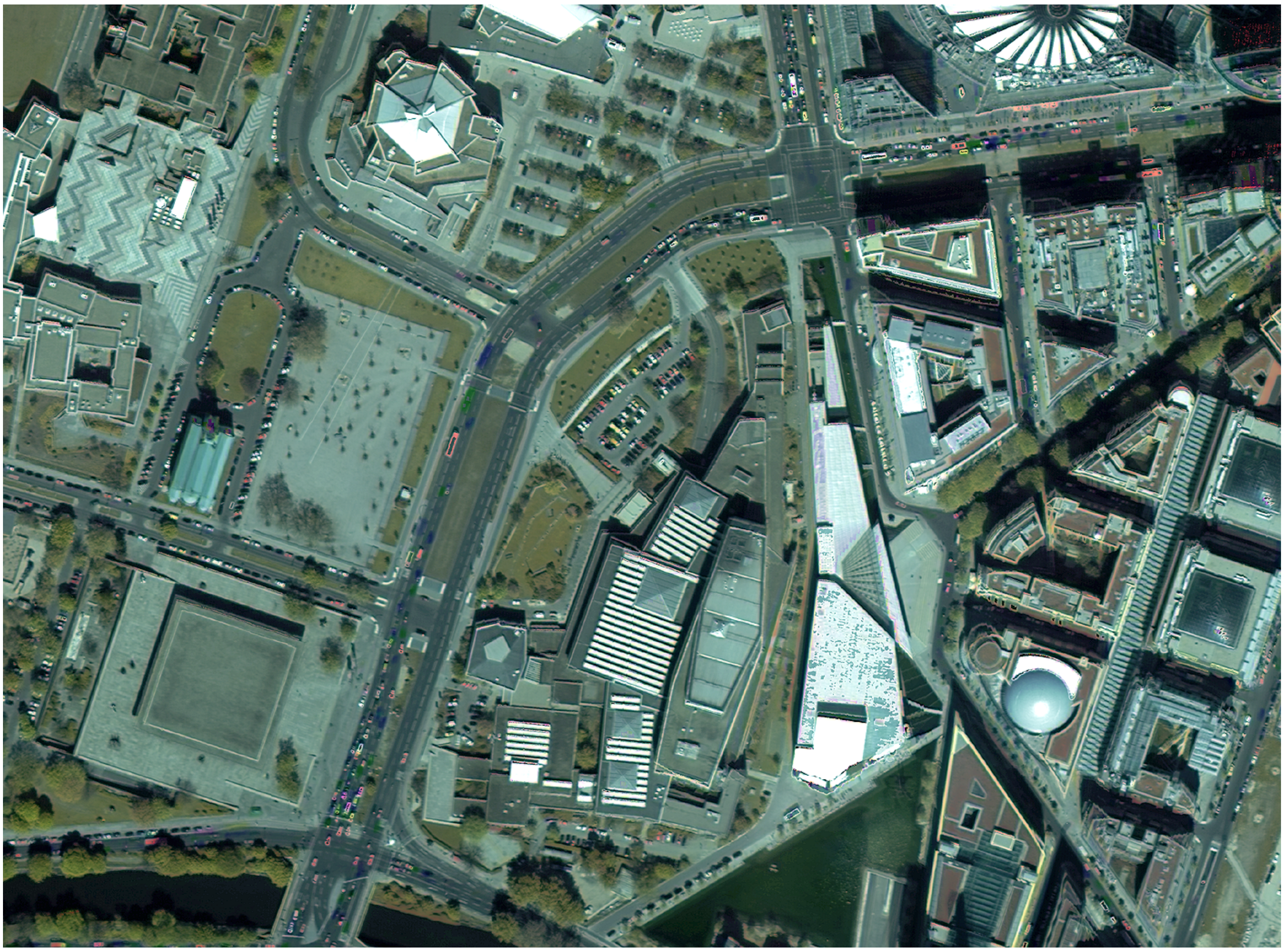

Figure 2: HRSC-AX true-color orthoimage, flight altitude 5,000 m, ground resolution 20 cm
Berlin, Potsdamer Platz, May 3, 2001

7. DATUM TRANSFER FOR PHOTOGRAMMETRIC PRODUCTS

The previously given absolute accuracy values are defined in the reference system of the orientation data, i.e. the WGS84 system. In many cases requested data products have to be generated or transfered to other geodetic reference surfaces and geodetic datums. This can be done without loss of accuracy, if datum shift parameters or sets of ground control coordinates in both systems, WGS84 and the required system, are available.

If 3D information with a not geometrically describable height reference, such as heights above sea level, is required, this can only be done with the help of vertical control in form of one (or more) height control points for which the height above sea level is known. For small areas, the calculated heights (defined above the WGS84 ellipsoid) can be adapted to heights above sea level by simply substracting the geoid height (difference between geoid and ellipsoid) of this area. But, since the shape of the geoid is a function of the planimetric location on the Earth's surface (it can vary up to some meters within 100 km), for large target areas a grid of height control has to be available. Then the height adaption can be done by interpolation within this grid.

8. CONCLUSIONS

Direct georeferencing of image data has been a research field for photogrammetric purposes since many years. But using the best integrated DGPS/INS hard- and software systems, direct sensor orientation without the necessity of ground control has become already operational.

This paper has decribed the apropriate photogrammetric adjustment methods and the high quality of results derived by direct sensor orientation and proved sub-pixel accuracy even for such a high-resolution sensor as the HRSC. Nevertheless, it should be pointed out that the entire system and its products depend on the reliability of the orientation data. The 4 years of experience with direct sensor orientation of HRSC has shown that this dependability can not be taken for granted. Eventually it always depends on the quality of each single hardware unit, especially the Inertial Measurement Unit, which has to fulfil the strong specifications and also on the flexibility of post-processing software with respect to non-standard situations during DGPS/INS integration.

ACKNOWLEDGEMENTS

We would like to acknowledge the scientific and operational contributions of the entire HRSC team of the DLR - Institute of Space Sensor Technology and Planetary Exploration, Berlin-Adlershof.

REFERENCES

J. Hutton, E. Lithopoulos, Airborne Photogrammetry Using Direct Camera Orientation Measurements. Photogrammetrie-Fernerkundung-Geoinformation, 6, E. Schweizerbart'sche Verlagsbuchhandlung, Stuttgart, Germany, pp. 363-370, 1998.

G. Neukum, The Airborne HRSC-A: Performance Results and Application Potential, Photogrammetric Week ´99, Fritsch/Spiller (Eds.), Wichmann Verlag, Heidelberg, Germany, pp. 83-88, 1999.

G. Neukum and the HRSC-Team, The Airborne HRSC-AX Cameras: Evaluation of the Technical Concept and Presentation of Application Results after One Year of Operations, Photogrammetric Week ´01, Fritsch/Spiller (Eds.), Wichmann Verlag, Heidelberg, Germany, 2001 (in press).

T. Ohlhof., Lokale, regionale und globale Punktbestimmung mit Dreizeilenbilddaten und Bahninformationen der Mars96-Mission, In: Deutsche Geodätische Kommission, Reihe C, Heft 445, Munich, Germany, 1996.

F. Scholten, S. Sujew, F. Wewel, J. Flohrer, R. Jaumann, F. Lehmann, R. Pischel, G. Neukum, The High Resolution Stereo Camera (HRSC) - Digital 3D-Image Acquisition, Photogrammetric Processing and Data Evaluation. In: International Society for Photogrammetry and Remote Sensing, Proceedings of Joint Workshop "Sensors and Mapping from Space 1999", Veröffentlichungen des Instituts für Photogrammetrie und Ingenieurvermessungen, Universität Hannover, Nr. 18, 1999.

F. Scholten, S. Sujew, F. Wewel, Einsatz digitaler Kameras im Auflösungsbereich von 5 cm bis 1 m - Die neue HRSC-AX Kamerageneration in der geometrischen Analyse. Publikationen der Deutschen Gesellschaft für Photogrammetrie und Fernerkundung, Band 10, 2001 (in press).

F. Wewel & M. Brand, Geometrische Validierung des hochauflösenden multispektralen Mehrzeilen-Stereoscanners HRSC-A. Publikationen der Deutschen Gesellschaft für Photogrammetrie und Fernerkundung, Band 7, S. 245-252, Berlin, Germany, 1999.

F. Wewel, F. Scholten, G. Neukum, J. Albertz, Digitale Luftbildaufnahme mit der HRSC Ein Schritt in die Zukunft der Photogrammetrie. Photogrammetrie-Fernerkundung-Geoinformation, 6, E. Schweizerbart'sche Verlagsbuchhandlung, Stuttgart, Germany, pp. 337-348, 1998.

RESOLUTION TESTS WITH A TDI - CAMERA

M. Schroeder, W. Mooshuber, R. Müller, P. Reinartz
German Aerospace Center, DLR
Remote Sensing Technology Institute, Image Science
P.O. Box 11 16
82234 Wessling, Germany
e-mail: Manfred.Schroeder@dlr.de

Working Group I/2

KEYWORDS

TDI-Camera, spatial resolution, resolution test pattern, MTF

ABSTRACT

With Time Delay and Integration (TDI) detector arrays, high resolution space camera systems can be developed. The main advantage of TDI-detectors in comparison to conventional CCD-detectors is their very high responsivity which allows extremely short exposure times. This short exposure times on the other hand correspond to very fast data read out rates, e.g. at a ground sampling distance of 0.25 m from orbit height, a line read out frequency of approximately 27 kHz is required. To test the image quality of TDI cameras at these very high data read out frequencies laboratory tests with a “Dalsa TDI-Line Scan Camera CT-E2” were carried out. The TDI-detector array of 2048 elements with a single detector size of 13 x 13 µm², has 96 integrating steps and a radiometric resolution of 8 bit. A moving test pattern simulated the relative motion between space camera and earth surface. The processed images of the test pattern could be used to determine three bar resolving power in across and along flight direction, to derive the MTF curves and to obtain a value for the noise level. Furthermore the influence of slight deviations from the required read out frequency on the resolving power was investigated. The paper describes the laboratory experiment and presents the resolving power results.

1. INTRODUCTION

Today’s High Resolution commercial remote sensing satellite systems have a ground pixel size of approx. 1 m. For the next satellite generation 0.5 m pixel size is foreseen. The question is: can the resolution be further increased? With increasing resolution the exposure times are extremely short and also the line read out frequencies go up linearly with the ground resolution. Table 1 shows the corresponding values for 0.25 m ground pixel size for various orbit heights.

H [**km**]	$\mathbf{V_g}$ [**km/s**]	**Δt** [µs]	**ν** [**kHz**]
400	7.216	34.6	28.864
500	7.059	35.4	28.237
600	6.908	36.2	27.632
650	6.834	36.5	27.336
700	6.762	37.0	27.048
750	6.691	37.4	26.764
800	6.621	37.8	26.484

Table 1: Exposure time (Δt) and scan line frequency (ν) for 0.25 m ground resolution. H: orbit height, V_g: ground velocity for a circular polar orbit.

Due to the very short exposure time only TDI-detector arrays can be used for high resolution purposes. Therefore laboratory tests with a TDI-camera at scan frequencies of about 26.5 kHz were carried out to investigate the image quality at these fast read out frequencies which correspond to 0.25 m ground pixel resolution from approx. 800 km altitude.

TDI is based on the principle of multiple exposure of the same object. This principle is shown in figure 1 for a three stage TDI detector. In the practical tests a 96 stage TDI detector was used.

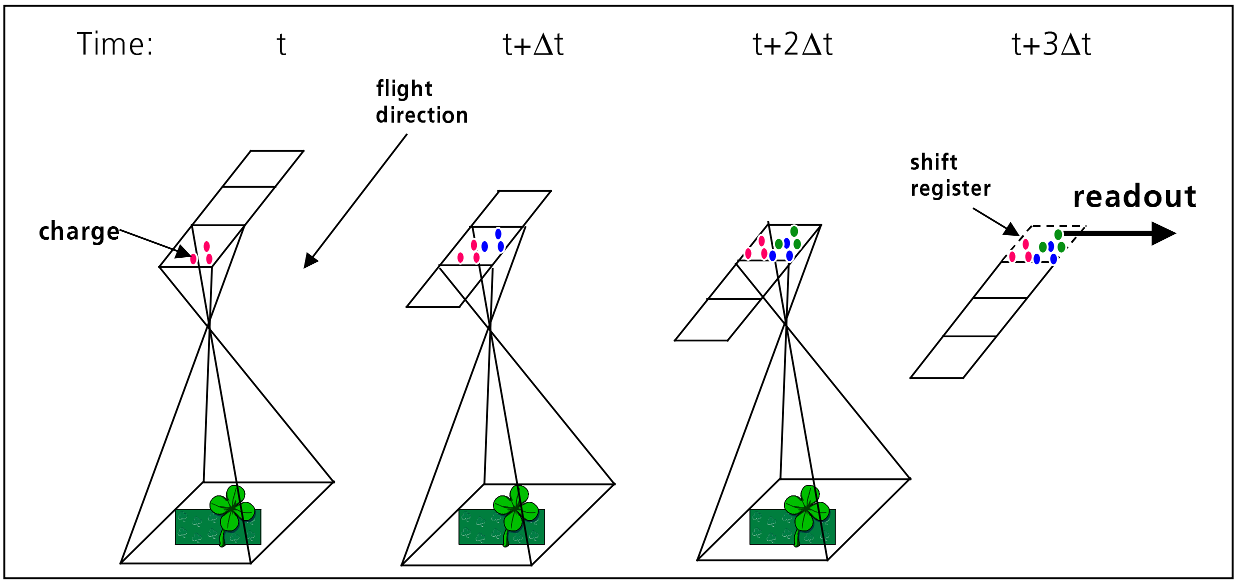

Fig. 1: Exposure Principle of a TDI-detector with three stages. The amount of generated charges is direct proportional to the number of stages.

2. EXPERIMENTAL TESTS

2.1 Laboratory Test Set Up

Fig. 2 shows how the TDI-camera was used in the laboratory to take images of a resolution test pattern. The glass test pattern was moved with constant velocity by a linear motor and was illuminated with a tungsten-halogen lamp through a diffuser screen from the backside. The image scale was 1:6.075. The pixel size in the object space (on the test pattern) was 78.98 µm. For determining the resolving power of the camera system the test pattern was moved with 2.1 m/s, this corresponds to a nominal scan line frequency of 26.591 kHz.

2.2 TDI Camera System

Camera-Type: Dalsa TDI-Line Scan Camera CT-E2, Optics: Tele-Lens APO-TELYT-R 1:5.6 / 800mm from Leica with internal focusing and apochromatic correction with extended spectral range up to 1000 nm; Field of View: 3.1°; Number of lens elements: 11; Aperture: 5.6 to 22; Focusing range: From infinity to 3.9 m; Front lens diameter: 157 mm; Total length: 425 mm; Mass 6.2 kg.

Shutter: The shutter (Type: COMPUR-elektronik-m3) is located between the lens assembly and the TDI Detector array; it is used only to measure the dark signal.

TDI-Detector: The TDI-detector consists of 96 detector lines, each with 2048 detector elements. The size of one detector element is 13 µm x 13 µm. The length of the active sensor array in line direction is (0.013 mm x 2048) 26.624 mm and the width in column direction is (0.013 mm x 96) 1.248 mm. After 96 fold integration of the image line the generated charges are transferred to a shift register. The shift register is then read out with the rate of the corresponding line frequency in 8 parallel channels and serial with 256 pixel elements per channel. After leaving the shift register the voltages are amplified and then converted to digital numbers ranging from 0 to 255 (8 bit).

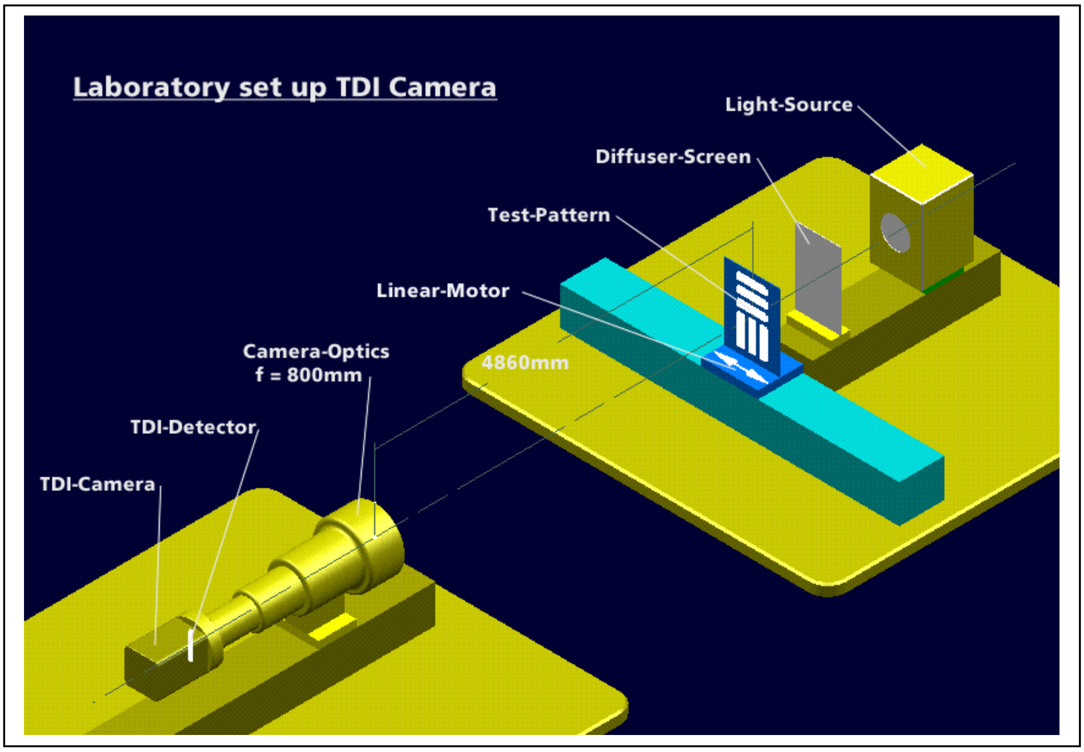

Fig. 2: Laboratory test set up

A minimum image motion blurring respectively a maximum image quality will only be obtained if the line transfer is exactly adjusted to the forward motion rate of the object. This means that due to the constant forward motion each successive image line looks on the same object. For the above mentioned detector this process is repeated 96 times before the integrated charge is read out from the shift register.

Data recording: The maximum line frequency which can be accepted as a continuous data stream by the Data Storage Unit is 28.5 kHz. This value corresponds to a fictive satellite altitude of 458 km and a ground pixel size of 0.25 m. The data rate which has to be recorded is given by:

2048 pixel/line x 1 Byte/pixel x 28500 lines/s = 58.368 MB/s

The processing of such high data rates is accomplished by means of two PCs (Master and Slave) each with dual-processors, 512 MB RAM-storage and three Ultra 2 –SCSI hard discs in multiplex operation mode. The total storage capacity of the hard discs is 108 GB which corresponds to a total recording time of about 30 min.

2.3 The Test Pattern

The three bar test pattern which was used is shown in figure 3. Two versions were used a “positive” target (black bars on white background) and a “negative” target (white bars on black background). The width of the largest bars is 2 mm (group no. -2, element no. 1) and the smallest is 0.0028 mm (group no. 7, element no. 4), which corresponds to 0.33 mm resp. 0.00046 mm in the image plane.

A linear motor (manufacturer: Aerotech) generates the relative motion between object and TDI-camera. It moves the test pattern with a constant velocity of up to 2.1 m/s. The control of the motor is realised with a PC (software program for running the various operation steps), a linear encoder (translating the analog motor motion in digital motor steps), a frequency generator (determination of motor steps per unit time) and a control electronic with power amplifier.

Line Pairs/mm

Element Number	Group Number -2	-1	0	1	2	3	4	5	6	7
1	0.25	0.50	1.00	2.00	4.00	8.00	16.0	32.0	64.0	128
2	0.28	0.56	1.12	2.24	4.49	8.98	17.95	36.0	71.8	144
3	0.31	0.63	1.26	2.52	5.04	10.1	20.16	40.3	80.6	161
4	0.35	0.71	1.41	2.83	5.66	11.3	22.62	45.3	90.5	181
5	0.40	0.79	1.59	3.17	6.35	12.7	25.39	50.8	102.0	203
6	0.44	0.89	1.78	3.56	7.13	14.3	28.51	57.0	114.0	228

Positive targets

Negative targets

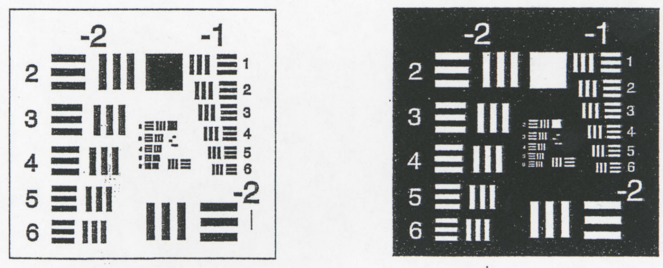

3" square Positive Target from group -2, element 1 to group 7, element 4

3" square Negative Target from group -2, element 1 to group 7, element 2

Fig. 3: Three bar test pattern

3. IMAGE QUALITY ANALYSIS

3.1 Dark Current

The dark current was measured by closing the shutter between the lens assembly and the TDI detector array. The resulting images show that a constant value of about 2 DN can be observed for 7 of the 8 parallel channels, while one had the value of 6 DN. The noise of the dark current can be regarded as very low since the sigma value is in the order of 0.2 – 0.3 DN. This very low sigma shows that due to the averaging procedure, typical for TDI-detectors, the image noise is strongly reduced and is caused mainly by the analog to digital conversion in the last significant bit. A higher bit/pixel value than 8 is therefore recommended.

3.2 Radiometric Responsivity

To test the linearity of the input/output relation an illuminated and reflecting grey wedge from Kodak with reflectance steps from 3% to 80% was imaged. The result is shown in figure 4.

The small deviation from linearity (between 10% and 80% reflectance) may be caused by non homogenous illumination of the grey wedge. For low output-and input signals a deviation from the linearity can be observed. This effect is also known from conventional CCD-detectors, but has to be further investigated for TDI-detectors.

3.3 Noise and Autocorrelation

The noise of the TDI camera was determined over the largest homogeneous square area of the test pattern (fig. 3), using about 3000 pixel values. The analysis shows that the noise for the white object is only slightly higher than for the black object (see table 2).

Object	Number of Pixels	Mean value	standard deviation	SNR
black background: white object	2907	112.03	0.53	211.38
white background: black object	2856	8.57	0.50	17.14

Table 2: Noise level for high and low signal.

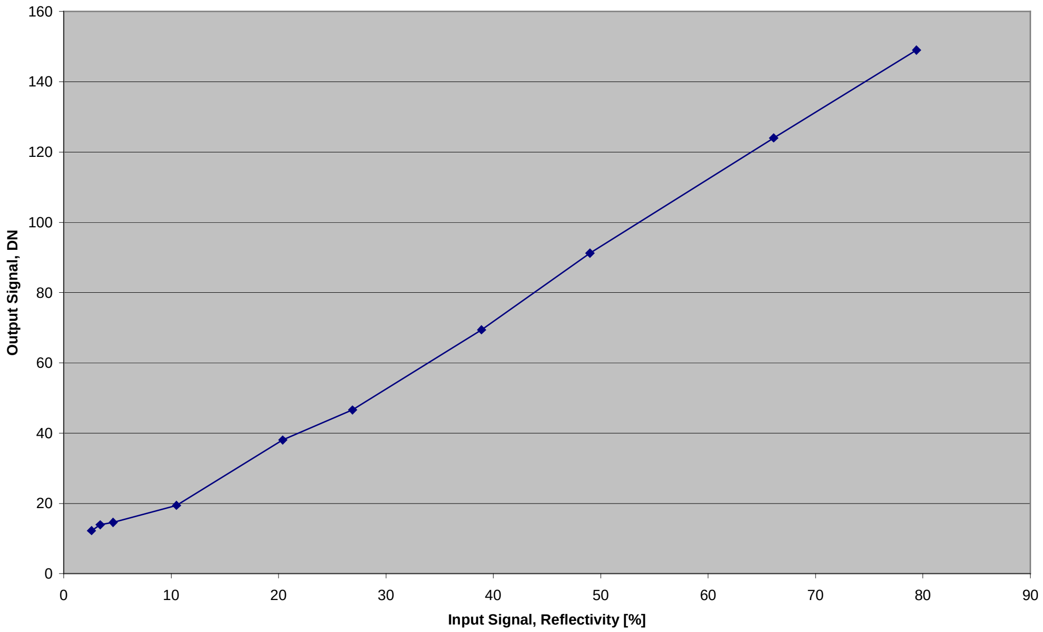

Fig. 4: Signal Output (DN) versus relative input signal (reflectance of grey wedge)

These very low noise values result mainly from the averaging over the 96 stages of the TDI detector.

In order to investigate periodic textures of an image as well as statistical pixel correlations, the autocorrelation function of a homogeneous image area (square in test pattern) was calculated (see fig. 5). Theoretically the autocorrelation function of an image of a homogenous object should produce an autocorrelation image in which only the centre pixel differs from zero. The real autocorrelation image (fig. 5) shows correlation effects in both directions. For the across direction the correlation decreases to 0.3 over 3 pixel, whereas for the along direction it takes 7 pixel to decrease to 0.3. This smearing effect in along direction is probably caused by the forward image motion.

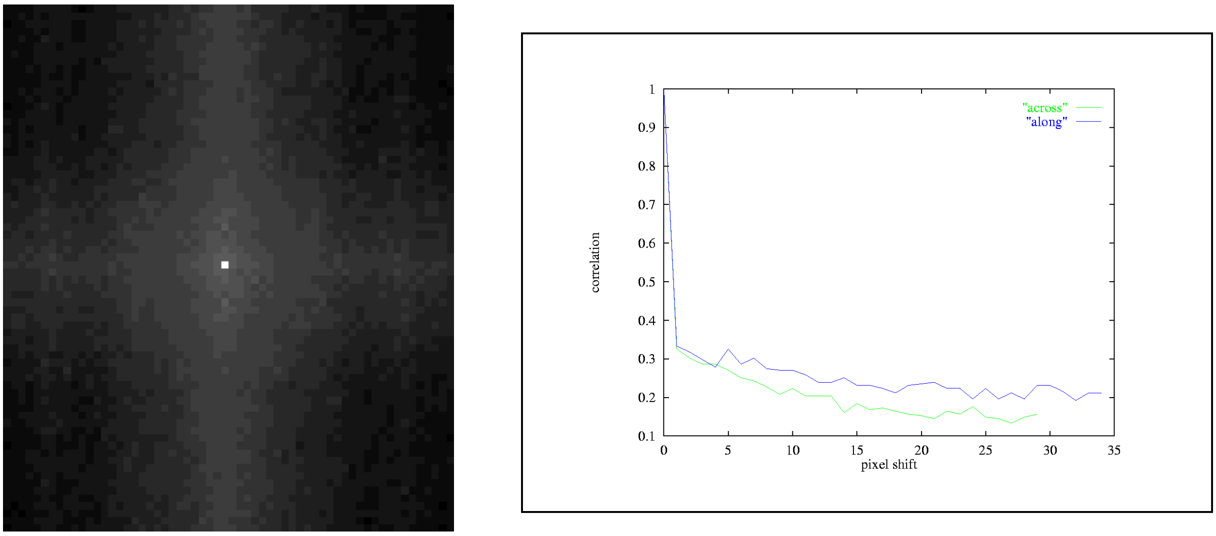

Fig. 5: Autocorrelation function of a homogeneous area of 60 (across) x 70 (along) pixel. In the left image a logarithmic scale of the pixel grey values (corresponding to correlation) is used. In the right image the profiles for the autocorrelation function in along (in flight) and across (in line) direction are shown.

In figure 5 no periodic structure can be detected, which means that „non-uniformity“ effects, common to most of the CCD detectors, are absent.

3.4 Three Bar Resolution

The purpose of this investigation is to find the influence of deviations from the nominal scan frequency (26.591 kHz) on the three bar resolving power. The movement of the test pattern was perpendicular to the detector line direction. The aperture setting of the lens was 5.6. The scan frequency was varied in steps of 250 Hz.

The resolution for the bars parallel to the detector line is called “along” resolution (in flight direction) and the resolution for the bars perpendicular to the detector line is called “across” resolution (in line direction).

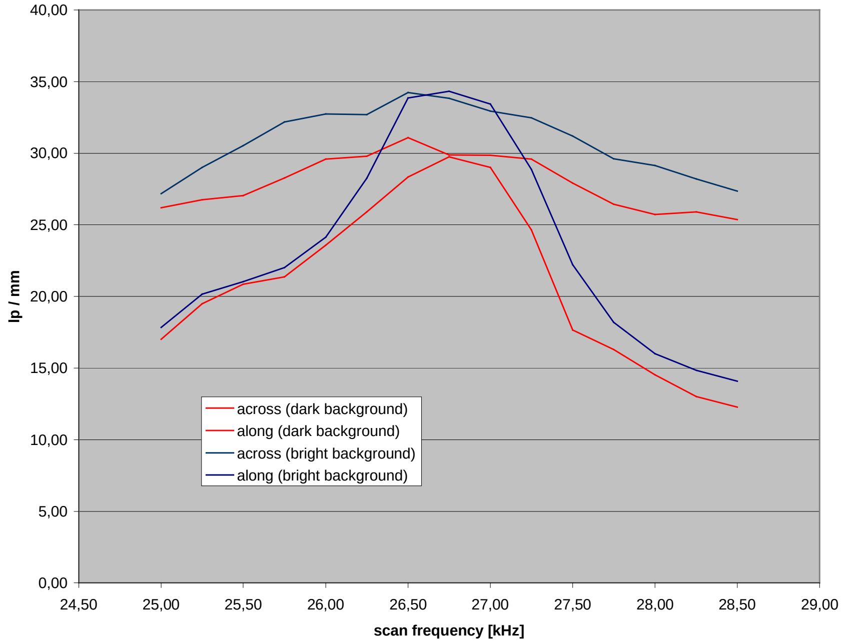

Fig 6: Three bar resolution for various scan line frequencies and for positive and negative test pattern

The imaged test patterns were visually observed by three persons at optimal contrast- and magnification settings on the display screen. The smallest three bar test pattern of which the observer had the subjective impression that he can recognise three separated bars was regarded as resolution limit.

For every scan frequency six images were obtained which were evaluated by each observer. The individual result for each observer is the mean of the six observation. After that the results of all three observers were averaged.

The results are shown in figure 6 for the “positive” and “negative” test pattern. The resolution values for the “positive” pattern are always a little higher than those for the “negative” pattern. As final result the average of “positive”- and “negative” pattern resolution was regarded (s. fig. 7). Figure 7 is an average over 36 observations.

The highest resolution for the “across” direction was found at 26.5 kHz and for the “along” direction at 26.75 kHz; this is in agreement with the expectation that the highest resolution should occur at the nominal scan frequency of 26.591 kHz. The absolute values for “across” and “along” resolution at these frequencies are 33 lp/mm respectively 32 lp/mm. At this high contrast the relation between lp and pixel size is:

1 lp ≙ 2.4 pixel

The across resolution depends only slightly on the scan frequency. Deviations of ± 1 kHz from the nominal scan frequency cause only a 10% degradation in the resolution.

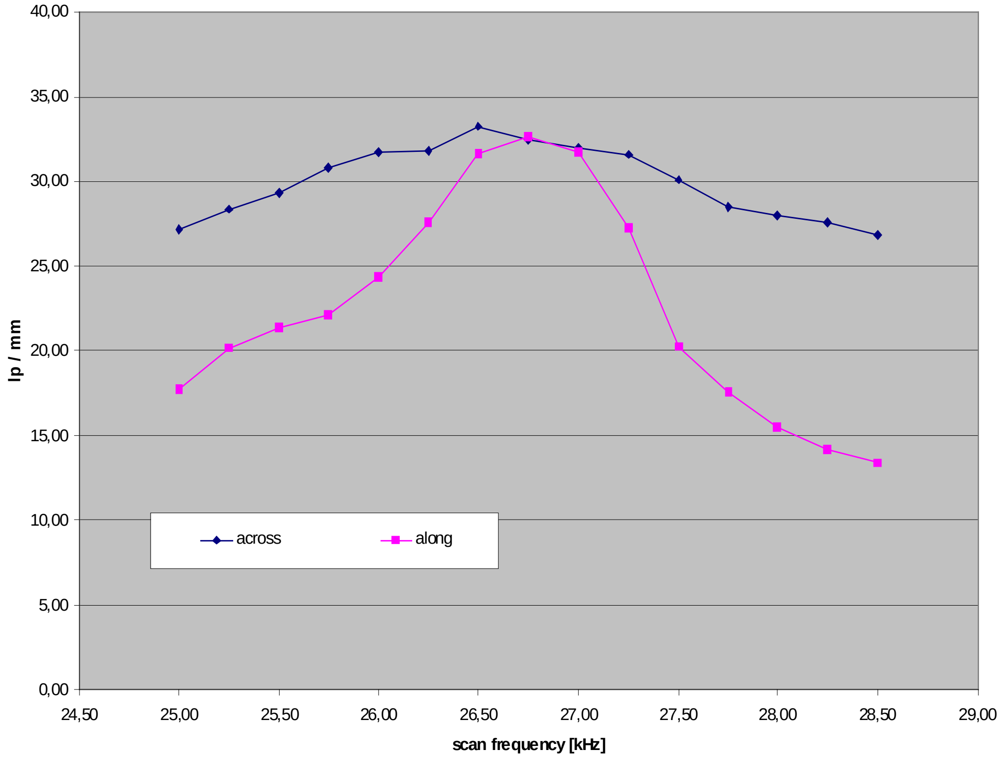

Fig 7: Three bar resolution for various scan line frequencies, average of positive and negative test pattern.

The situation is different for the “along” resolution. Deviations of ± 300 Hz from the nominal scan frequency cause already a resolution degradation of 10%. For higher scan frequency deviations the degradation increases rapidly.

This means in conclusion that if one accepts a 10% degradation in resolution then only 1% deviation from the nominal scan line frequency is allowable.

3.5 Rotation of Detector Line

For optimal operation of a TDI-detector the detector line has to be oriented perpendicular to the motion direction. The question arises how much rotation of the detector line from this nominal orientation can be tolerated without degrading effects on the resolution. To investigate this rotation effect the camera was rotated by some degrees. Fig. 8 shows an image of the test pattern taken with the camera rotated by 2°.

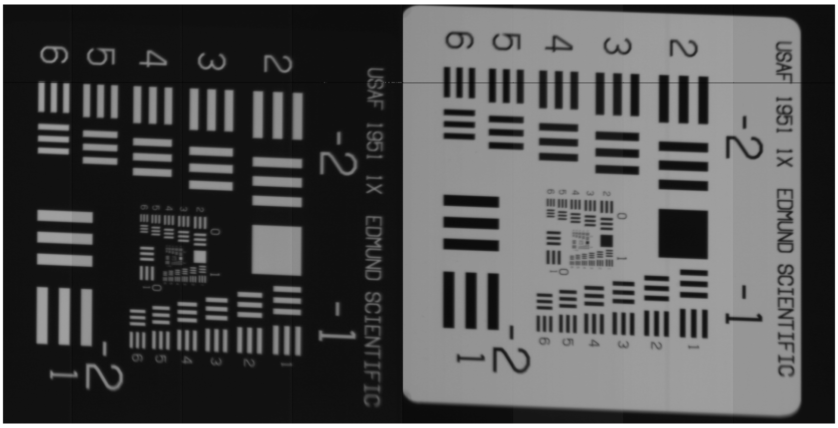

Fig. 8: Image of the three bar test pattern taken with the camera rotated by 2 degrees. Motion direction is from top to bottom.
The influence of the rotation angle on the resolution is shown in figure 9 The influence on the across resolution is much higher than on the along resolution. If a 10% degradation in resolution is accepted then a rotation of only 0.4° is allowable.

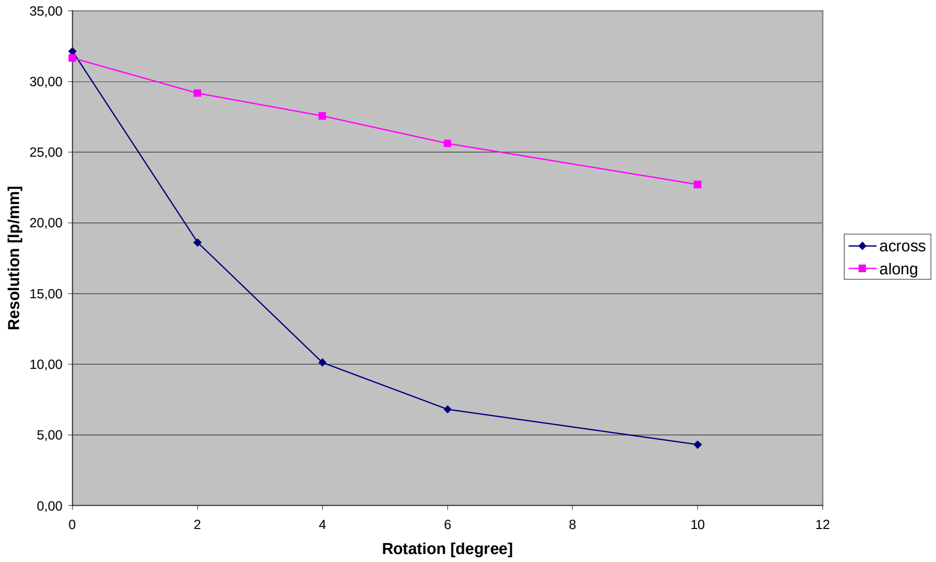

Fig 9: Dependence of resolution on the rotation of the TDI Detector against nominal direction

Due to earth rotation there is always a slight yaw angle κ between satellite flight direction and resulting ground velocity (s. fig. 10) The angle κ depends on the geographical latitude φ. Table 3 shows how κ varies with φ for a 702 km circular orbit of 98.2° inclination; in this case κ varies between 0 and ca. ± 4°.

As only an angle of ± 0.4° is tolerable it can be concluded that for proper operation in space the TDI-camera in the given example has to be rotated by approx. ± 4° during one orbit, to compensate for this yaw angle.

In conventional CCD-images the angle κ causes the skewing effect of satellite images.

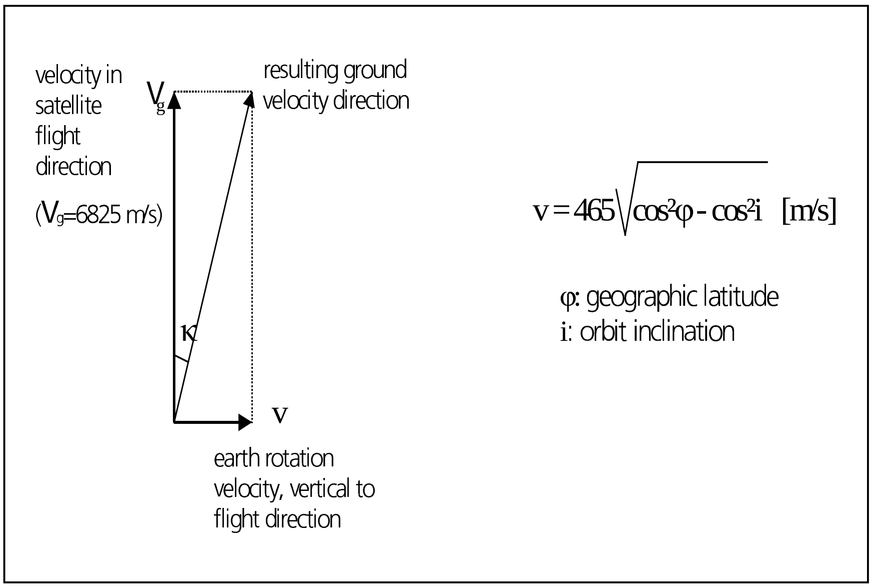

Fig 10: Rotation angle between satellite flight direction and ground speed direction

Geograph. Latitude degree	**κ degree**
0	± 3.86
± 10	± 3.80
± 20	± 3.62
± 30	± 3.33
± 40	± 2.94
± 50	± 2.45
± 60	± 1.87
± 70	± 1.21
± 80	± 0.39
± 81.8	0

Table 3: Rotation angle κ between satellite flight direction (V_g = 6.825 km/s) and ground velocity direction for a 702 km circular orbit with inclination i = 98.2°

3.6 MTF from three bar test pattern

The imaged test pattern with the highest resolution (at 26.5 kHz scan frequency) was used to determine the modulation of the resolved three bar pattern. The Modulation Transfer Function of the camera system is obtained by plotting the three bar modulation versus its spatial frequency. The resulting curves are shown in figure 11.

The MTF for the along direction between 5 and 20 lp/mm is higher than for the across direction.

Theoretically the MTF of the across direction should be higher because it is not effected by forward motion as the along direction.

If one assumes that the resolution is limited by the noise then it can be concluded from figure 11 that this “noise threshold modulation” is at approx. 0.035 (straight line in fig. 11)

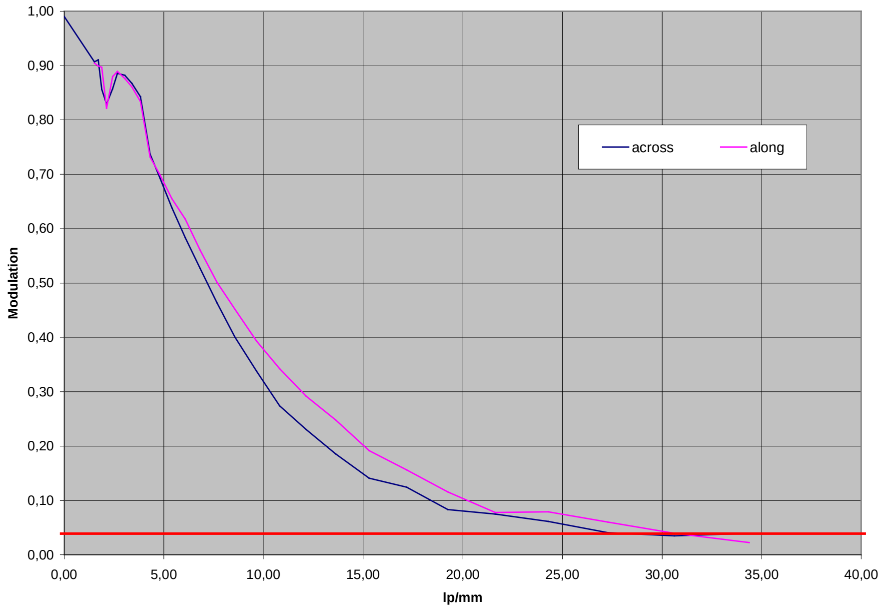

Fig. 11: MTF from three bar test pattern (average of positive and negative test pattern) and „noise threshold modulation“ line.

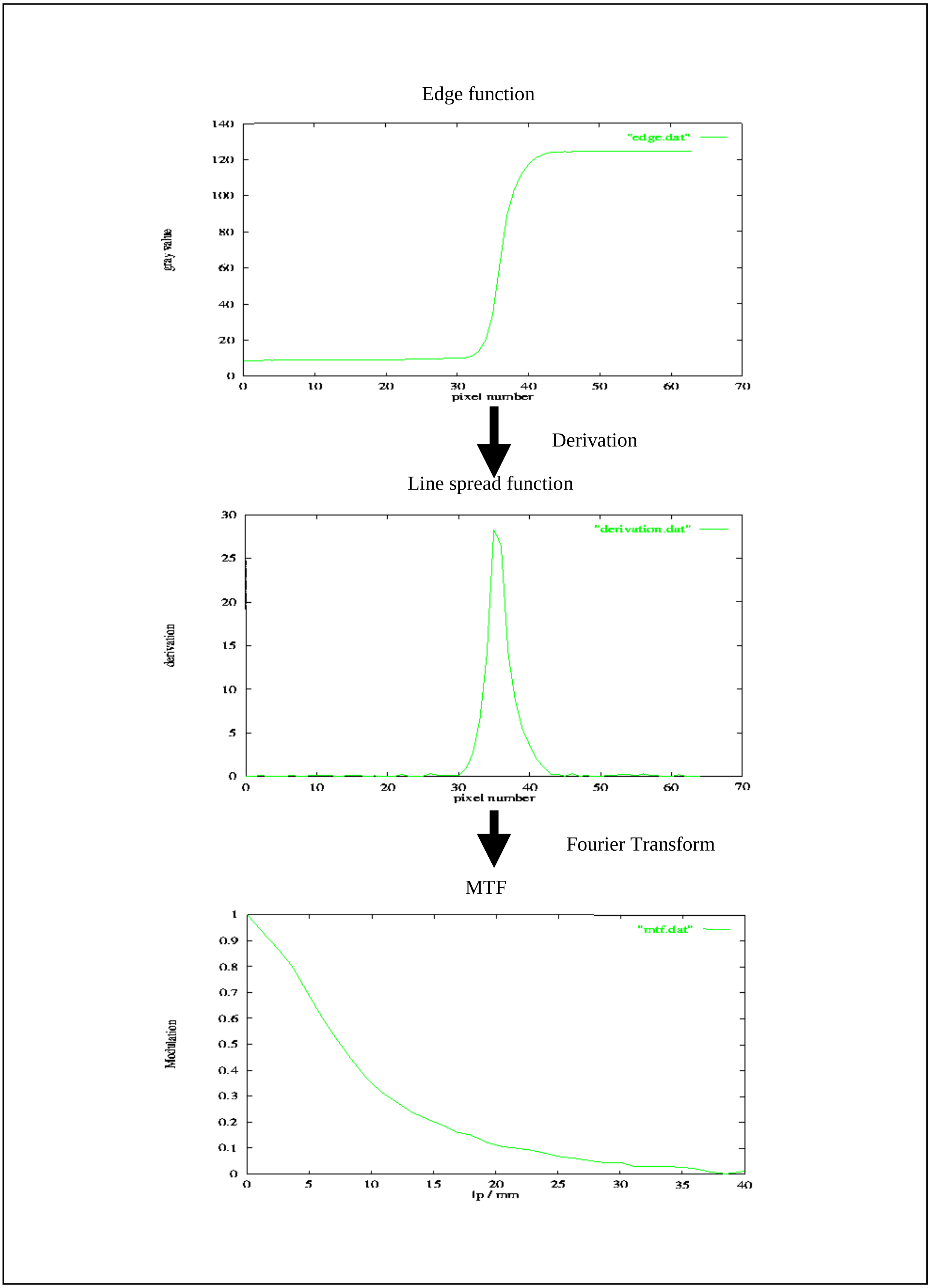

Fig 12: Edge gradient analysis method

3.7 MTF from Edge Gradient Analysis

For edge gradient analysis the edges of the largest square (10mm x 10mm) of the test pattern was used. The method of edge gradient analysis is described in figure 12.

Figure 13 shows the across-MTF. There is nearly no influence of the scan frequency on the MTF. This is in agreement with the three bar across resolution (Fig. 7)

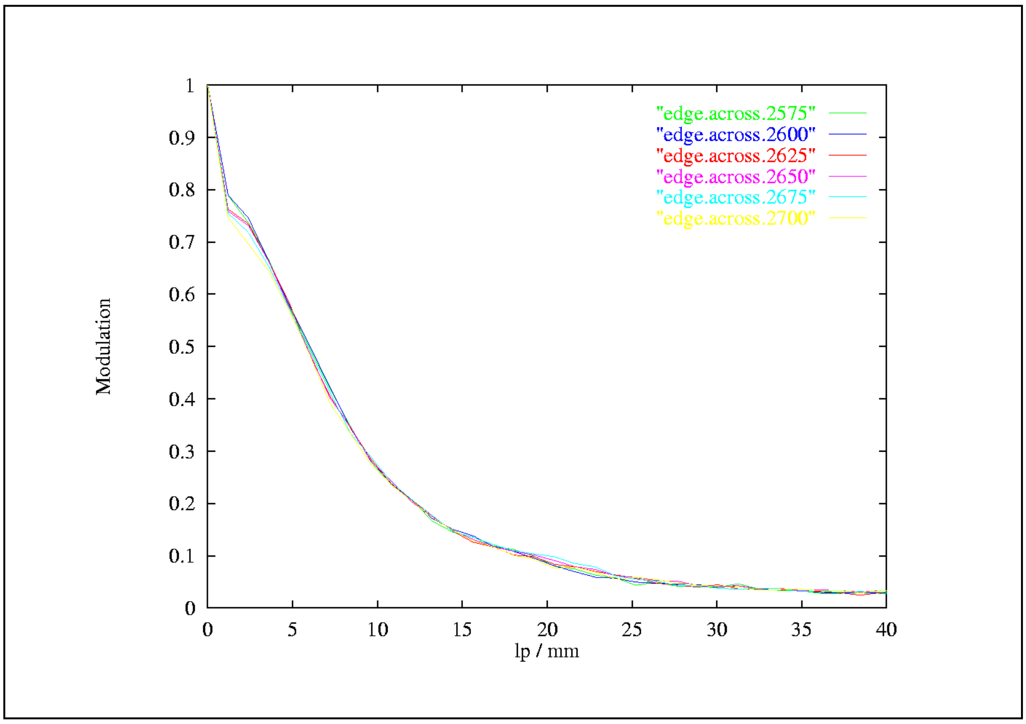

Fig 13: Across-MTF

Figure 14 shows the along-MTF for various scan frequencies. The influence of the mismatch between scan frequency and forward motion velocity can be observed.

Fig. 15 compares across- and along-MTF for the nearly nominal scan frequency of 26.5 kHz. Both curves differ only slightly. Again the along MTF is a little higher than the across-MTF as for the MTF curves from three bar pattern (see fig. 11). From figure 15 and from figure 7 it can be concluded that for nominal scan frequency the three bar resolution and the MTF curves for along and across direction are nearly the same.

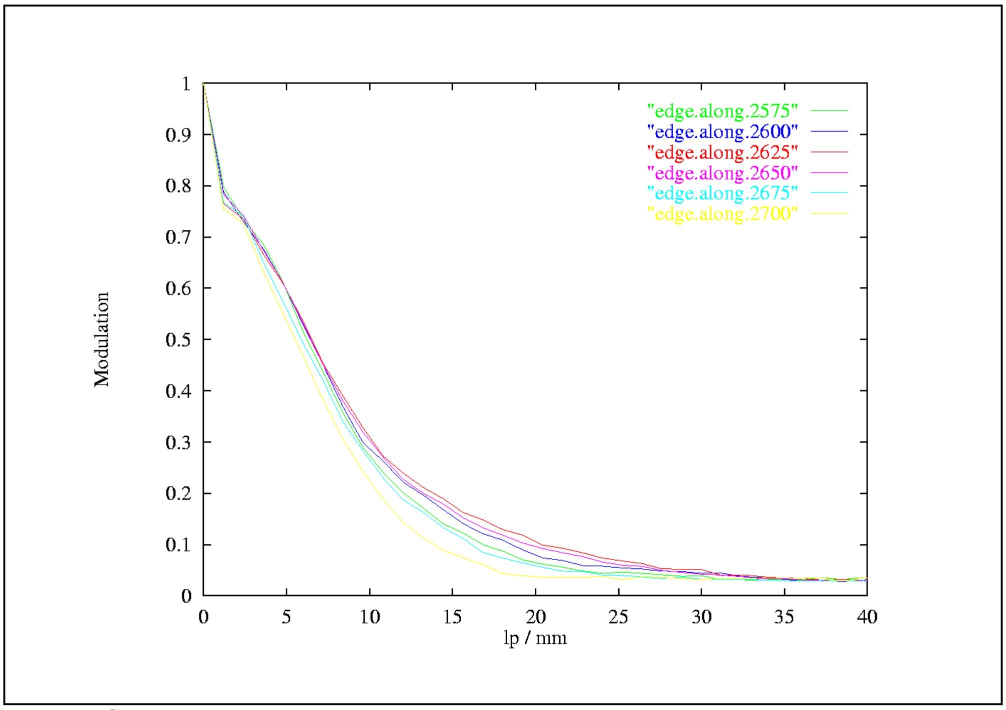

Fig. 14: Along -MTF

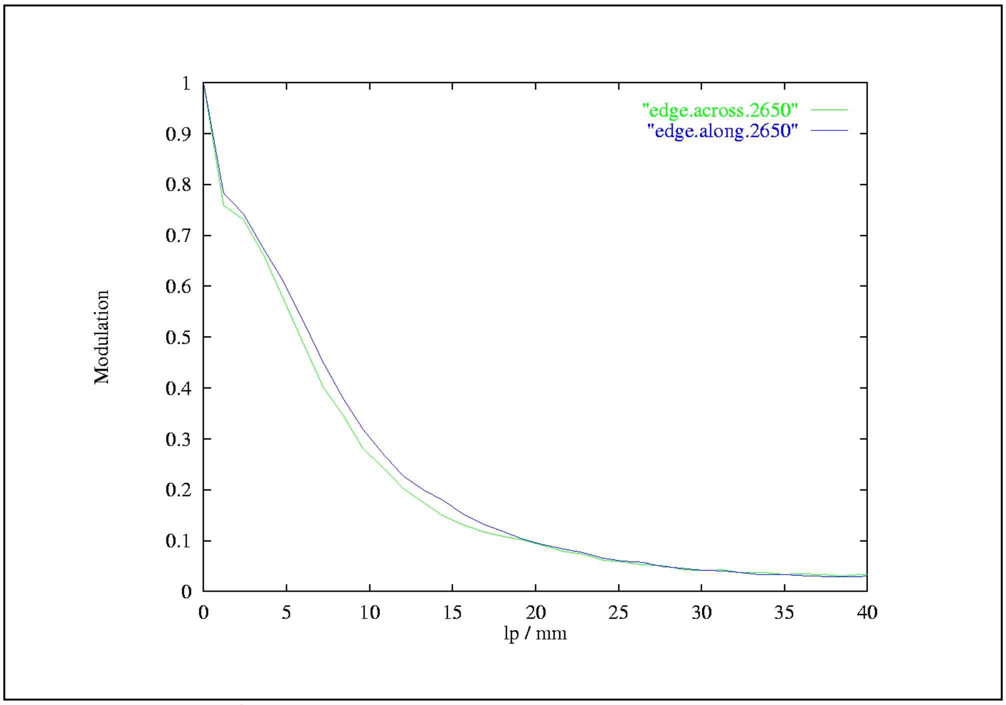

Fig 15: Comparison of along and across-track MTF

3.8 Low Contrast Resolution

The three bar resolution values (s. fig. 7) are only valid for a high contrast target of an input modulation of 1.

To obtain the resolution for a low contrast input of 2:1 corresponding to a modulation of 0.33 the MTF has to be multiplied with 0.33 and intersected with the “noise threshold modulation”. The result is shown in figure16. The low contrast resolution is 19 lp/mm which is equivalent to: 1 lp ≙ 4.0 pixel

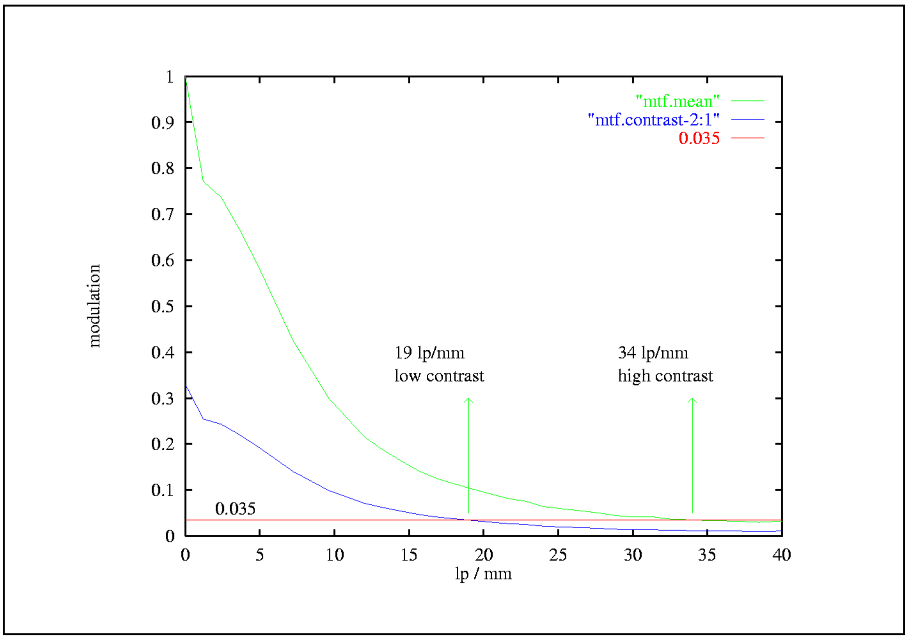

Fig. 16: Low contrast resolution

4. CONCLUSIONS

- Even for high line scan frequencies of 26 – 28 kHz the TDI detector electronics generates a low noise signal. For the 8 bit – digitalisation of the 96 stage TDI-signal the noise equivalent Digital Number was 0.5. This means that higher digitalisation than 8 bit is possible.

- Low noise imaging at scan line frequencies between 26 and 28 kHz – corresponding to 0.25 m ground pixel size from orbit height – is possible with a TDI detector. (The realisation of the 0.25 m ground pixel is only a question of a high quality long focal length optics.)

- The resolution that can be obtained with a TDI-detector of 13 µm x 13 µm size is:

  For high contrast: 32-34 lp/mm equivalent to 1 lp $\triangleq$ 2.3 pixel

  For low contrast: 19 lp/mm equivalent to 1 lp $\triangleq$ 4.0 pixel

- For exact matching of the scan line frequency to the forward motion velocity the across- and along resolution are the same.

- The resolution is very sensitive to mismatching between scan line frequency and forward motion velocity. Only a mismatch of 1% is tolerable.

- Angular misalignment of the TDI-columns with respect to the flight velocity direction degrades the resolution considerably. Only a misalignment of less than 0.4° is tolerable.

- In a space mission a TDI-camera has to be rotated around the optical axis by some degrees to compensate for the angular misalignment caused by the earth rotation.

FIVE YEARS IN-ORBIT CALIBRATION OF MOS

H. Schwarzer, K.-H. Sümnich, DLR-IWP, D, horst.schwarzer@dlr.de; karl-heinz.suemnich@dlr.de
A. Neumann, G. Zimmermann, DLR-IMF, D, andreas.neumann@dlr.de; gerhard.zimmermann@dlr.de

KEY WORDS: imaging spectrometer, calibration, remote sensing

ABSTRACT:
Since April 1996 the Modular Optoelectronic Scanner MOS has been working successful on the Indian Remote Sensing Satellite IRS-P3. Two methods are implemented to check the main parameters of the instrument during the orbit mission: (1) the relative check of instrument sensitivity with minilamps and (2) the absolute recalibration with the sun irradiance. In this paper some experiences with the internal recalibration method to safeguard the reliability and accuracy of the remote data will be considered. A continuous variation of parameters like dark current and sensitivity can be demonstrated as well as some special effects on the lamp data during the mission time.

INTRODUCTION

The Modular Optoelectronic Scanner MOS from German Aerospace Center (DLR) has been working successful now for almost 5 years on the Indian Remote Sensing Satellite IRS-P3. This first imaging spectroradiometer in orbit measures the upwelling spectral radiance of the earth objects in altogether 18 spectral bands of different bandwidths (1,4 nm; 10 nm; 1000 nm) in the spectral region from 400 nm to 1600 nm with a best spatial resolution of 500 m. The main weight beside land and atmospheric scientific investigations has the periodic monitoring (temporary and regionally) of the ocean water quality especially in the costal regions.
To safeguard the reliability of the remote data during the long term mission it was necessary to implement qualified methods to check and/or to recalibrate the instrument sensitivity in the spectral channels. To do that, two independent and complementary methods are implemented.

METHODS OF IN-ORBIT CALIBRATION

The first method has been used the very good reproducible radiance of minilamps for a stability check of the spectrometer and sensor system by comparing the actual response data of the lamp to those from immediately after launch. A second method used the extraterrestrial sun irradiance at a spectralon diffuser in front of the entrance optics to an absolute recalibration of the spectroradiometer.
Both methods have been used in orbit and have been proved for 4 ½ years. The relative check with lamps took place at the beginning of each remote data take for about 6 seconds, while a shutter closes the entrance aperture. The provided lamp response data set U_{ijk} for each pixel i (1 …420), each spectral channel j (1…18) and k (0…4) radiance levels will be compared to a reference data set U^*_{ijk} and indicates the development of the dark signal (for k = 0) as well as the sensitivity (for k = 1…4) in time. The reliability of this procedure is so good as the lamp radiation could be reproduced. Two lamps in each module, which has been used different often, enables to check the lamps among each other.
The recalibration with the sun has been carried out every two or three weeks, when the satellite crosses the terminator near the north pole. The sun irradiance at the diffuser depends on the sun-earth distance, the angle between orbit plane and direction to the sun (both with a yearly variation) and the angle of incidence, which changes corresponding to the satellite motion. The sun response data, normalised to an agreed data of distance (1 AE) and angles (40° declination, 22° azimuth), indicate directly the actual sensitivity.

RESULTS OF IN-ORBIT CALIBRATION

When the shutter closes the entrance aperture and no lamp is switched on, the dark signal of the whole measuring system can be measured. It indicates the state of the optoelectronic system of CCD-lines and the signal electronic up to the analogous-digital converter. The examples in fig.1 und fig.2 show the dark signals of the channels A1 and B8 at the beginning and after 4 ½ years in orbit. The spectral structure is nearly the same, but the values altogether are noticeable increased (namely at all MOS-A channels by a factor 8). MOS-B has a small gain but occasional the uniformity versus the wavelength is for some channels disturbed, extremely in B8.

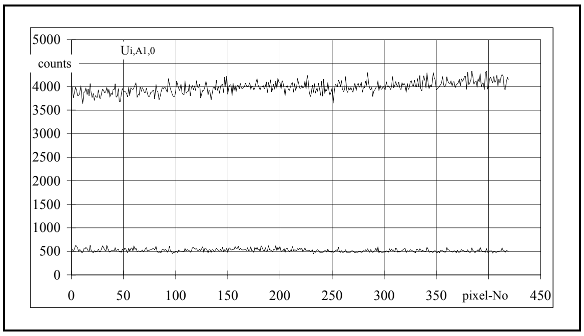

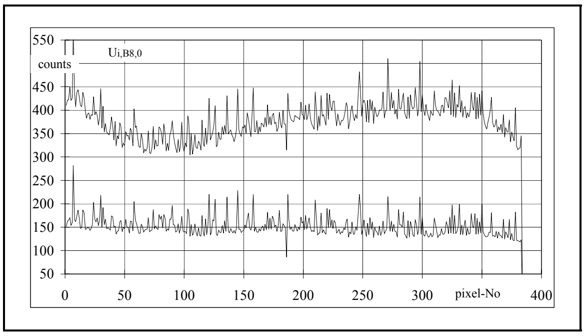

Fig.1 Dark signal of channel A1

Fig.2: Dark signal of channel B8

The averaging the dark signals U_{ijo} over all pixels i leads to a value U_{jo} for each channel, which characterises the behaviour of the CCD-line and electronic altogether. A plot of U_{jo} versus the mission time demonstrates the development of the dark signals, like shown in fig.3 for channel A1 and in fig.4 for channels B1, B8, B12, B13. Compared to the identical quasi linear increase at all MOS-A channels the B channels have different gain and in particular a slight yearly variation. The reason is not clear yet.

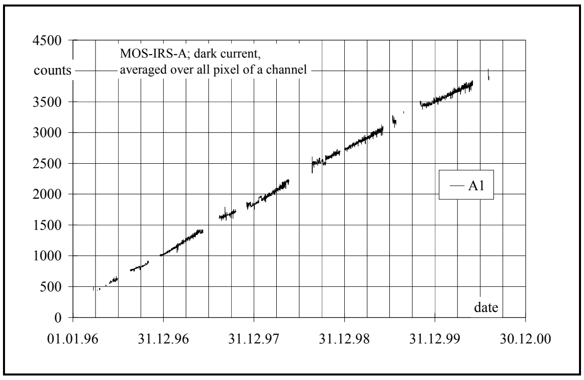

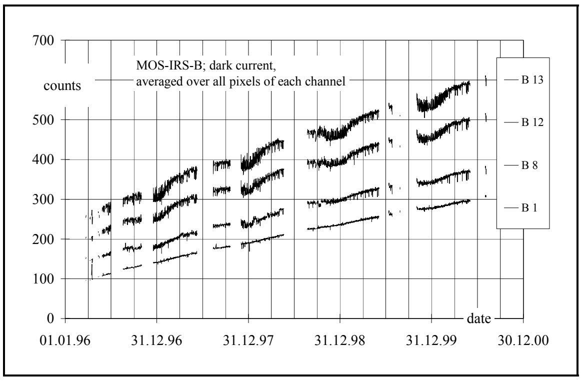

Fig.3: Development of dark signal, channel A1

Fig.4: Development of dark signal, MOS-B

The sensitivity can be estimated by looking at the ratios $R_{ijk} = U_{ijk} / U^*_{ijk}$ of the actual and the reference lamp response data. In fig.5 these ratios for all 18 channels are plotted versus the pixel number, while the different channels are separated by a constant factor, so that the value R_{ijk} = 1,000 starts at different values on the y-axis. The ratios are calculated for the data from both internal lamps in each module; by the way the good agreement indicates the sufficient stability of the lamps in time.

The diagram shows the exiting stability of the sensitivity of all pixels in the different CCD lines. Variations in a 1 % interval and a shift altogether < 6% after such long time under orbit conditions are a very good basis for the reliability of the remote data, provided from the MOS. And the curves demonstrate slight differences in the results of both lamps, a general trend, caused by the different burning time of both lamps and an effect, depending on the channels (or the received wavelengths, which are different for both lamps, positioned left and right beside the main entrance slit of the spectrometer).

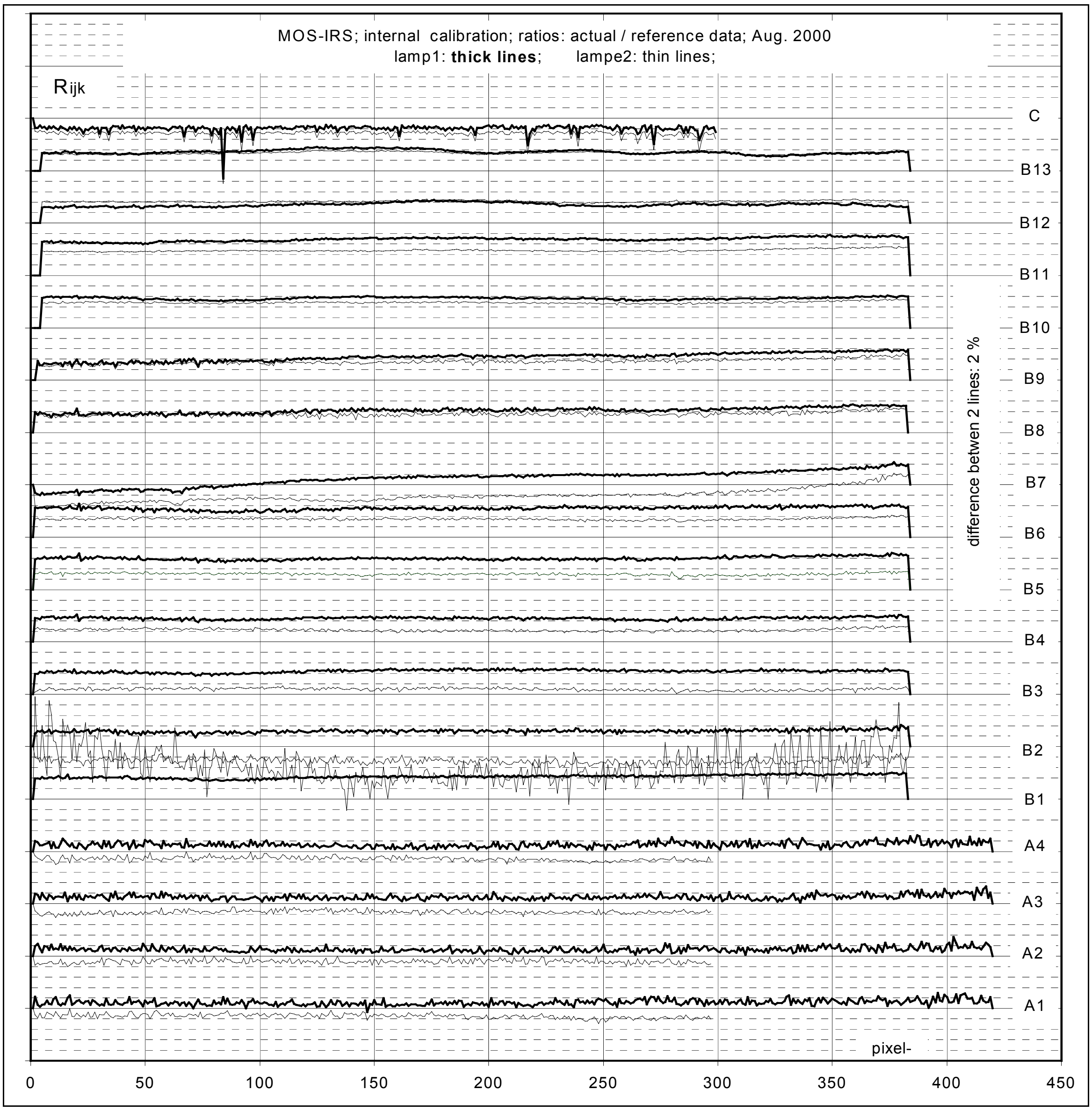

Fig.5: Ratio R_{ijk} of the actual and the reference lamp data after 4 ½ year in orbit

Like in case of dark signals, the averaged values over the pixels of each channel have been plotted versus mission time, showing different behaviour of the MOS modules. While the MOS-A channels remain constant in a ± 1 % interval (see as an example channel A1 in fig.6), the sensitivity of MOS-B channels increases differently up to 5 % (see examples in fig.7) in the first two years. Also shown here, like in the dark signal plot, the yearly periodic variation with different amount in the channels.

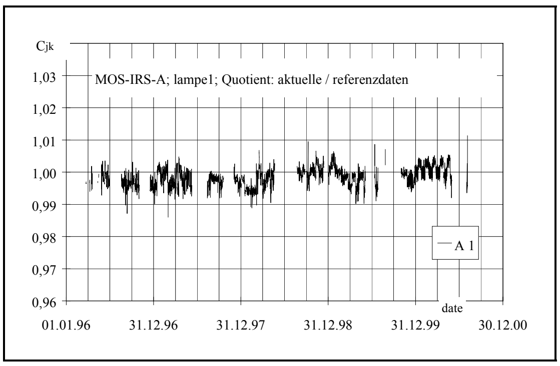

Fig.6: Development of channel sensitivity, MOS-A

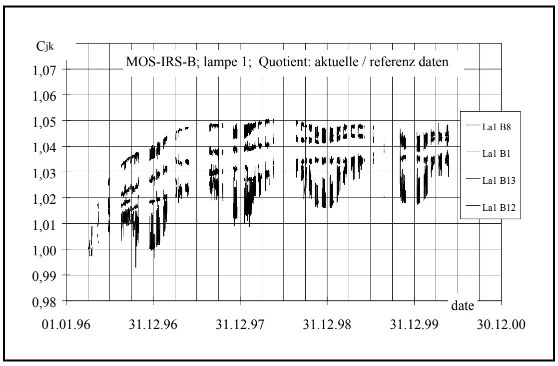

Fig.7: Development of channel sensitivity, MOS-B

The results of the sun calibration method provide substantially the same results as the internal calibration methods. Differences more than 2 % occur first after 3 ½ years in the channels MOS-B in the short wavelength region. Supplementing to the internal check the sun calibration involve also additional optical parts: baffling system, the entrance optics, the entrance slit and the sun diffuser itself. This parts above all can be influenced by hard radiation, and laboratory experiments confirm the suspicion, that it has been caused a decrease of sensitivity in the first 3 MOS-B channels up to 3 %.

The in-orbit calibration system of the MOS instrument has been allowed the verification of important instrument parameters with a sufficient accuracy as a decisive requirement for a reliable interpretation of the remote sounded data of MOS.

REFERENCES

Sümnich, K.-H., Schwarzer, H., 1998. In-flight calibration of the Modular Optoelectronic Scanner (MOS), Int. J. Remote Sensing, Vol.19, No.17, pp 3237 - 3259

Schwarzer, H., Sümnich, K.-H., Neumann, A., Walzel, Th., Zimmermann, G., 2000. Potential of combined in-orbit calibration methods, demonstrated by the MOS-IRS mission, SPIE Vol. 4135, pp 324 - 330

Schwarzer, H., Sümnich, K.-H., Neumann, A., Walzel, Th., Zimmermann, G., Three years in-orbit calibration of Modular Optoelectronic Scanner (MOS), ISPRS-Workshop, 1999, Hannover

DETECTION AND OBSERVATION OF UNDERGROUND COAL MINING-INDUCED SURFACE DEFORMATION WITH DIFFERENTIAL SAR INTERFEROMETRY

Volker Spreckels
Institute for Photogrammetry and GeoInformation, University of Hannover
Nienburger Straße 1, D-30167 Hannover
Tel.: ++49 2041-161310, Fax: ++49 2041-161333, e-mail: spreckels@ipi.uni-hannover.de

Dr. Urs Wegmüller, Dr. Tazio Strozzi
Gamma Remote Sensing AG
Thunstraße 130, CH-3074 Muri b. Bern
Tel.: ++41-31-9517005, Fax: ++41-31-9517008, e-mail: wegmuller@gamma-rs.ch

Jork Musiedlak
Deutsche Steinkohle AG (DSK) – DIG 3.1 Geo-Information
Gleiwitzer Platz 3, D-46236 Bottrop
Tel.: ++49 2041-161335, Fax: ++49 2041-161333, e-mail: jork.musiedlak@deutsche-steinkohle.de

Hans-Christian Wichlacz, Dipl.-Ing.
Deutsche Steinkohle AG (DSK) – TM 1 Deposit Planning
Shamrockring 1, D-44623 Herne
Tel.: ++49 2323-15-3809, e-mail: Hans-Christian.Wichlacz@deutsche-steinkohle.de

KEY WORDS: ERS, SAR, Interferometry, dInSAR, Subsidence, DEM, DTM, Monitoring, Hard Coal Mining.

ABSTRACT: Underground hard coal mining in the German Ruhrgebiet causes significant surface movements. Due to requirements by law, the German coal mining company *Deutsche Steinkohle AG* (DSK) is obligated to assess environmental impacts and to forecast effects of current excavations [1]. Required data are part of the “Geographic Information System” (GIS) and are integrated into the “Geo-Database” (GDZB) set up by DSK. With regard to the increasing demand for extensive information and cost effectiveness, DSK started to evaluate new observation and data processing techniques. It is important to monitor possibly affected areas with a nearly realtime up-to-date surveillance because occurring effects may entail lasting changes and influences on the environment. Especially methods of analytical and digital photogrammetry as well as remote sensing techniques may have the potential to be suitable techniques for a contemporaneous and economic monitoring of large areas [2]. As a rule of thumb, about 90% of the coal mining-induced subsidence will occur within one year of the excavations and movements have to be expected for nearly three years. A combined evaluation of spaceborne differential interferometric SAR (dInSAR) techniques, high accurate terrestrial observations, GPS-measurements and if available digital elevation models (DEM) or digital terrain models (DTM) from aerial imagery, airborne radar or laser imagery are promising for a precise monitoring of surface deformation movements like mining-induced subsidence for large areas.

1. INTRODUCTION

This paper presents the analysis and first results of a current research and development (R&D) project set up by DSK in cooperation with the *Institute for Photogrammetry and GeoInformation* (IPI), University of Hannover. One topic of the evaluations is to determine the potentials and limitations of differential interferometric SAR data collected by ERS satellites to monitor large areas in urban and rural regions. The dInSAR processing was performed by the Swiss company *Gamma Remote Sensing* (*GAMMA*). ERS satellite radar data is mostly uninfluenced by changing weather conditions. The data with relatively high spatial and temporal resolution of 35 days is of interest for monitoring purposes. Linked with terrestrial measurements like line levelling, EDM- and GPS-measurements or GIS data of the GDZB like active mining areas and subsidence models an interdependent evaluation and amendment can iteratively be performed for each data record. Up to date information concerning an ongoing excavation like the migration of the so called “zone of affected ground” can be acquired and documented. Connected with the GIS the combined methods allow to support an economic, independent and actual integration of information available from different sources.

First evaluations using differential InSAR methods for the detection of mining induced surface deformation were performed by *GAMMA* and DSK within the European Space Agency (ESA) Data User Programme: “Differential Interferometric Applications in Urban Areas” [3]. The results were promising and local analyses were performed for three mine sites located in the cities of Gelsenkirchen, Dorsten (1995–1997) and Recklinghausen (2000) with different extraction-, geological and topographic conditions. The satellite data for Recklinghausen will also be used to perform a 3D-analysis based on ascending and descending orbit data.
For these three mining areas levelling lines have been measured during and after the active mining as terrestrial reference. After the parameters of the excavations were available within the GDZB so called “Subsidence Model Calculations” were performed. With this information it is possible to build up and compare a time-series of highly accurate punctual terrestrial data and the subsidence map derived from ERS satellite data. If these independent data takes will contain similar height-change values it will be

possible for the first time to perform a real-time subsidence-monitoring accompanying the current mining activities. For more information about the ERS dInSAR processing see [4, 5, 6, 7].

2. Reference Data

2.1 Photogrammetric Data

Since the 1980s aerial images are used for photogrammetric data capture of topographical surface changes. DSK has developed an archive of digital terrain models (DTM) annually or bi-annually measured by analytical photogrammetric plotters, images matching techniques and, in the latest years, DTM gathered by laser-scanner records. These DTM and the used ground control points (GCP) that are necessary for the triangulation of the aerial images serve as reference data for the present evaluations. Most of the GCP could be retrieved after several years and can therefore serve to combine and connect the available data of the GDZB and the new collected satellite data by using current GPS-measurements. The reference data is originally measured and mapped within the Gauß-Krüger coordinate system so it has to be taken into account that differences between the geodetic datums of terrestrial, air-borne or satellite measurements still have to be expected. To bridge the gaps of time between the different measurements and evaluation periods the photogrammetrically measured DTM can be corrected and subsided using the "Subsidence Model Calculations" [8].

2.2 Terrestrial Measurements

Accompanying the excavations DSK performs extensive terrestrial measurements on levelling lines and ground control points. But according to the improvements the measurement methods changed within the years. Often only the changes in height and extension were recorded for each point but not the accurate position. Mostly the point positions were approximately marked on the maps by hand and had to be re-digitized from large-scale maps or re-measured by GPS-based traverse-lines. Only for the area of Recklinghausen the points of the levelling lines have been exactly determined with GPS-measurements.

2.3 Subsidence Model Calculation

The "Subsidence Model Calculation" is performed in two steps. Before the mining activities start extraction plans are used as model input to receive an overview of the expected environmental impact. After the real mining operation started parameters as the geometry, velocity and the amount of extracted matter are known and the influences can be more precisely estimated (BBVB) [9].
For the comparison with the dInSAR results the terrestrial measurements have to be adjusted to the ERS revisit times. All available information on geology, mining geometry, thickness of the coal seams and further information for each production panel was used to re-calculate the height differences between the moment of the terrestrial measurements to the time the satellite data were recorded.

2.4 Geo-Database (GDZB)

Since 12 years DSK has been using geo-information technologies at several departments for applications dealing with the acquisition, processing, analysis and presentation of all data needed for planning purposes and the daily work. Over the years a complex but well structured archive, the Geo-Database (GDZB), with all data concerning the coal mining activities and the monitoring of environmental impacts has been built up and was handled at the department DIG.
The reference data for the works on the dInSAR data were taken from the GDZB. The radar data, all DTM and subsidence models as well as the derived final results shall be included in the GDZB to be available for future access.

3. Analysis

3.1 Survey Investigation: "Ruhrgebiet"

The use of dInSAR techniques to derive subsidence movements could be recognized after first interferograms covering the whole Ruhrgebiet were processed by *Gamma* without any additional information [10]. Figure 1 presents a subset of an area of 25 km to 25 km wherein the fringes of movement structures can clearly be seen (figure 1, left image).
After the satellite scene was georeferenced to the Topographic Map 1:50.000 (TK50) the interferograms could be overlain with the active production panels at both dates the satellite data was recorded. For less vegetated and urban areas the detected fringes showing subsidence movements are centered to the production panels (figure 1, right image).

These first results were promising and more detailed evaluations for smaller areas were performed. For the years from 1995 to 1997 *Gamma* processed ERS data for the mines of Gelsenkirchen and Dorsten. ERS SAR data for the year 2000 were also processed to survey the city of Recklinghausen. At DSK all available terrestrial and photogrammetrical reference data like DTM, line levelling data, “Subsidence Model Calculation” and geometric mining conditions were taken from the GDZB or re-measured when needed. The height information for the levelling points was then adjusted to the satellite data using the parameters of the BBVB.

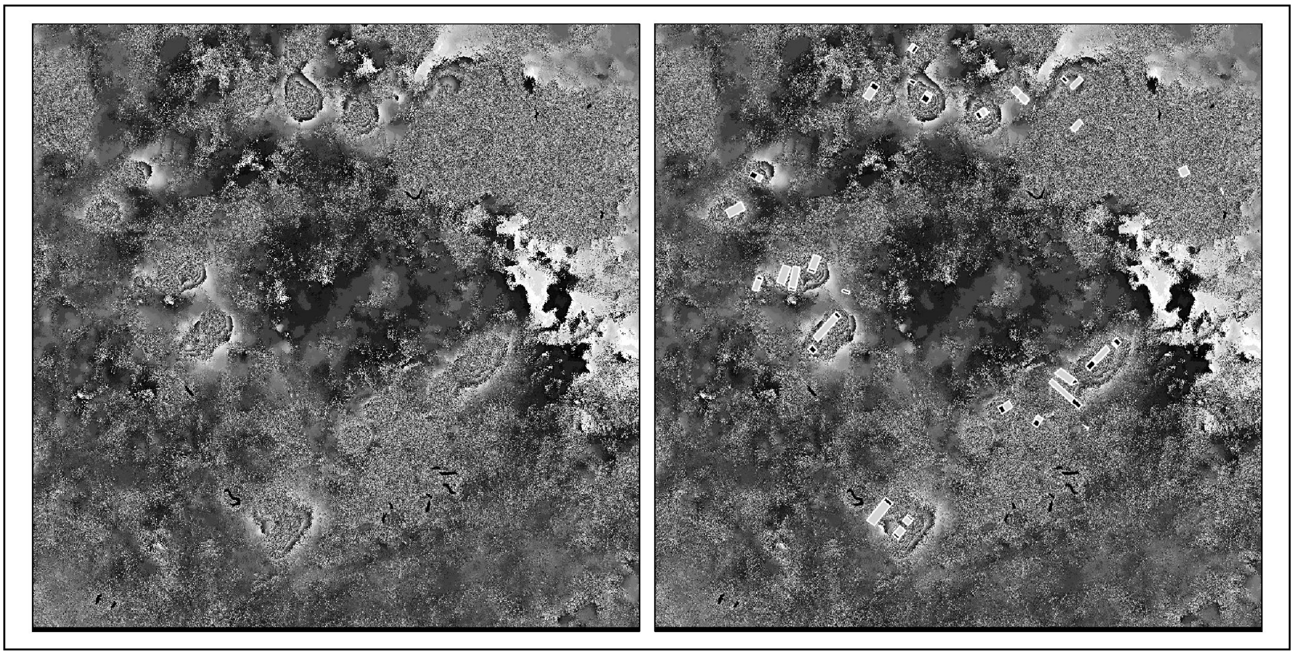

Figure 1: Interferogram: December 12th, 1996 to February 2nd, 1997. Left image without, right image with the overlay of the excavation information at both dates for active production panels. (Gray: December 12th, 1996, black: February 2nd, 1997). Region: 25 km x 25 km.

3.2 Detailed Investigation: “Gelsenkirchen-Erle / Parkstadion”

For this mine site several levelling lines and a DTM measured with analytical photogrammetric plotters were used as reference data for the evaluations. The levelling lines used are shown in figure 2 (upper left image). *GAMMA* processed the dInSAR data and performed the geocoding based on the TK50. Afterwards the subsidence calculated from the interferograms was compared with the adjusted height measurements for each point of the levelling lines.

The DSK subsidence model derived by the “Subsidence Model Calculation” shows parts westward of the “Parkstadion” and in northern Erle that, compared with the terrestrial measurements, include subsidence anomalies (figure 2, upper left image). To reveal the reasons for these anomalies would mean a large effort of subsidence calculations for each production panel because the region was densely mined out within the years 1992 to 1997 (figure 2, upper right). The most probably reason for the subsidence anomaly might be that a production panel mined out in 1993 did not completely collapse after mining ended. When new mining activities started again in the neighborhood in 1995 the old left-over wholes in the ground broke down and caused the additional subsidence observed. Because no reasonably stable subsidence parameters could be derived for a larger area the “Subsidence Model Calculation” were not performed for the adjustment of the levelling-data to the ERS revisits. For this reason the levelling-data was approximately adjusted by linear interpolation.

In figure 2 (lower left) it can be seen that from November 1996 to February 1997 the dInSAR data contains low coherence caused by the long baseline of 323 meter. This is the reason why the solving of the ambiguities (*phase-unwrapping*) [4, 5] could not be properly calculated and the fringes could not be separated as well as for the other interferograms.

Nevertheless the interferograms can precisely represent the location of the so called “zone of affected ground” that separates static areas and dynamic regions with beginning subsidence movements. At these places high tensions occur within the ground and mining-induced subsidence leads to the most heavy impacts on infrastructure. Furthermore the interferograms show an area in the south-east where the “zone of affected ground” does not migrate and seems to be static. This phenomenon depends on the special geotectonic conditions in the underground.

The images in figure 3 present the comparison of movements for the points of three levelling lines. One unit of the vertical axis presents one centimeter of subsidence. The dInSAR profiles are very similar to the measured subsidence just up to an amount of about 8 cm. So the *phase-unwrapping* technique is first of all able to detect subsidence movements within the wavelength (5,6 cm) of the ERS radar system. The subsidence profiles contain a small offset to the levelling profiles. This offset may depend on a reference point for the SAR processing that might not be taken from a static area.

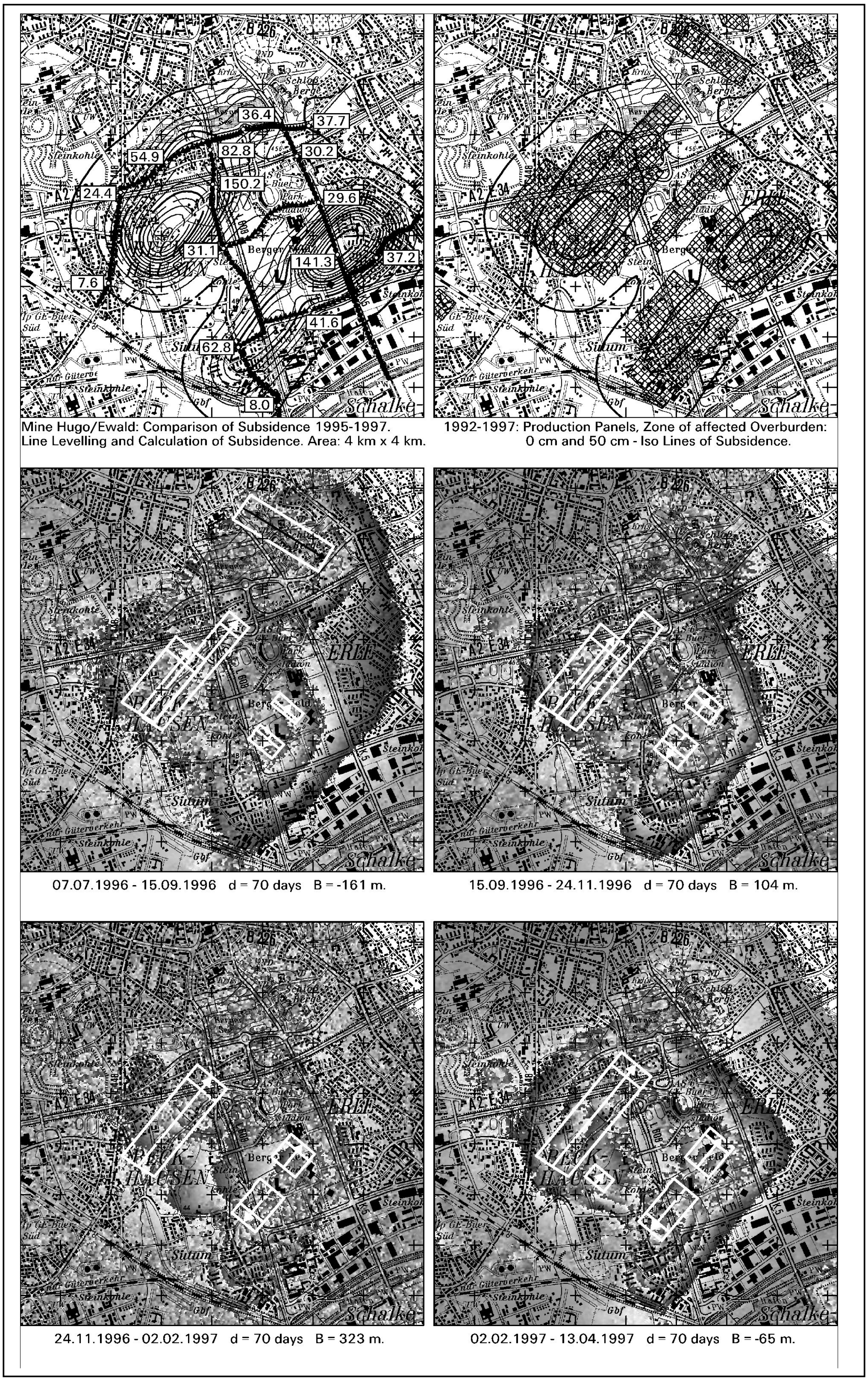

Figure 2: “Subsidence Model Calculation” with 10 cm iso-lines of subsidence compared to selected levelling-points (u.l.). Production panels from 1992 to 1997 overlain with 50 cm iso-lines of subsidence (u.r.). Interferograms from July 7th 1996 to April 4th 1997, ERS revisit: 70 days. Geocoded and superimposed with the TK50 and the current active production panels (mid and lower row). Area: 4 km to 4 km.

The profile of the levelling lines 3-20-19 show at first glance a lower accuracy what depends upon the lower coherence and therefore higher phase-noise in these regions. Such low coherence areas can be detected and masked out from the further processing.
Very good results can be seen on the levelling line 6. Line 5 shows that the limit of the *phase-unwrapping* to detect surface deformation movements is reached at 6 to 8 centimeters. For higher deformation rates the phase gradients became too large to be correctly solved. On the other hand it also has to be taken into account that the reference data may contain inaccuracies that have to be determined. Regarding the levelling profiles, line 5 for example, shows gaps caused by destroyed points (no. 30 to no. 32) or false height measurements like point no. 45.

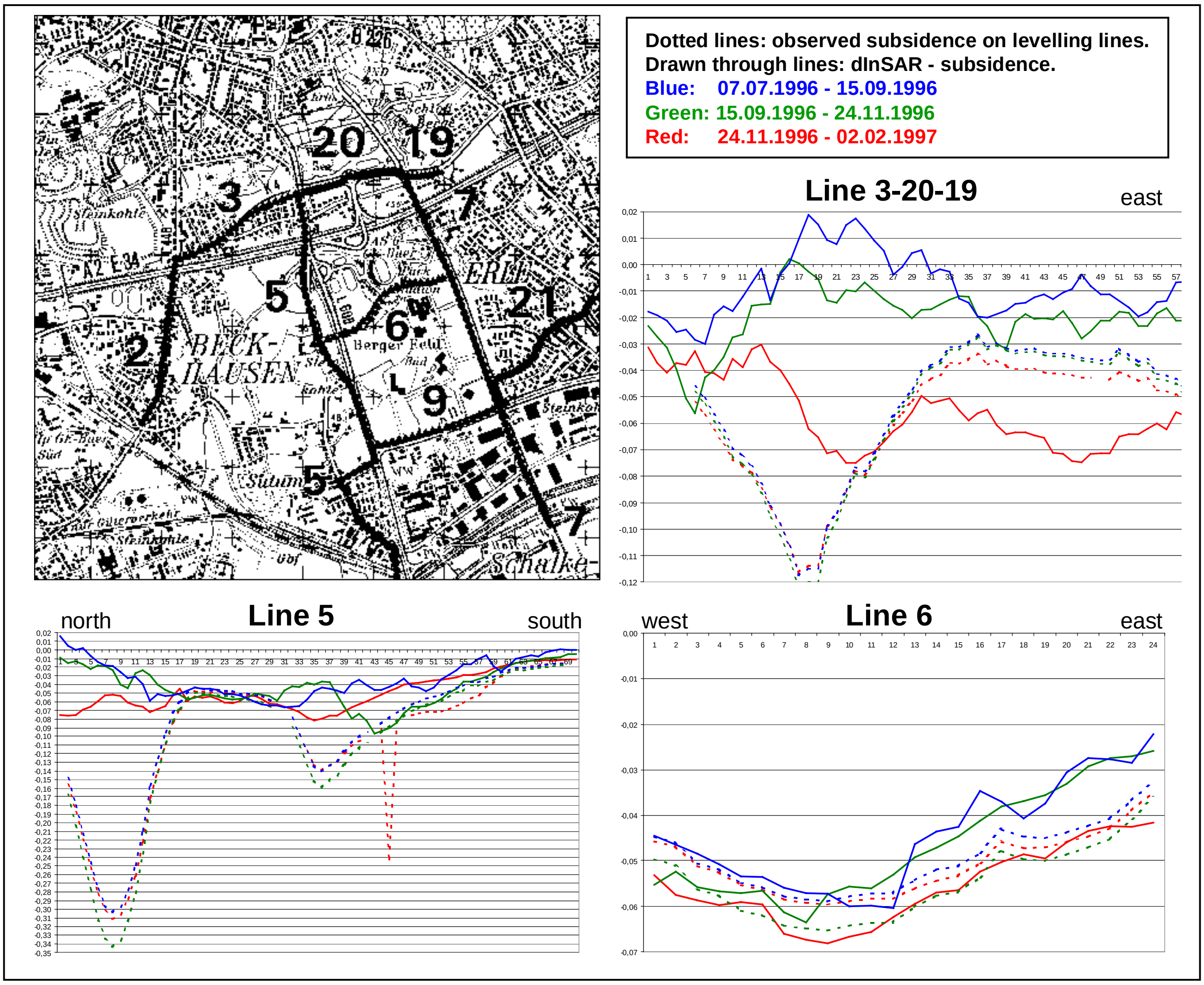

Figure 3: Gelsenkirchen-Erle / Parkstadion: Location of levelling lines (u.l.) and comparison of observed and dInSAR-derived subsidence. Horizontal line unit: 1 cm of subsidence. Image area: 4 km x 4 km.

Once again it should be mentioned that the analysis presents first and preliminary results. It can be assumed that the detection-range might be enlarged, for example if approximate values from the "Subsidence Model Calculation" will be available to improve the phase ambiguity resolution.

3.3 Detailed Investigation: "Recklinghausen"

The dInSAR analysis for Recklinghausen is currently still ongoing so that only first results can be presented. As reference data serves an analytically measured DTM from aerial images and line levelling data collected every three weeks accompanying the mining activities in 2000. About 90 points of the lines were re-measured by GPS in November 2000 and May 2001 close to ERS revisits.
In the city of Recklinghausen three permanent GOCA-GPS [11] receivers recorded three dimensional movements to a reference station located in static parts on a building at the mine site. So this data may serve as reference data for a planned future analysis of 3D-movements from ERS ascending and descending data. First comparisons of levelling and dInSAR subsidence data are presented

in figure 4. This comparison is based on the assumption that only vertical displacements occurred but further analysis will include the combination of ERS SAR data acquired in ascending and descending mode.

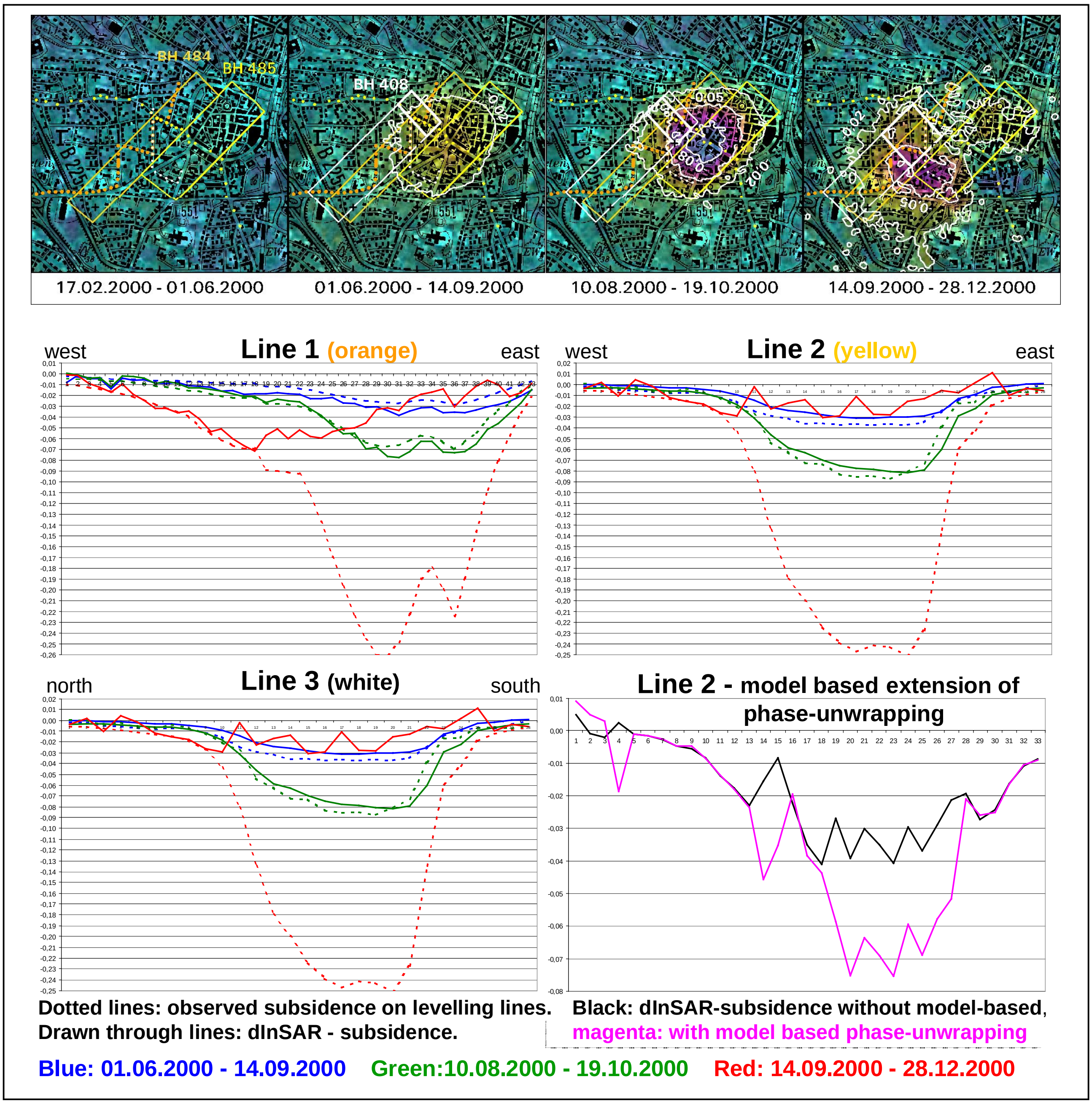

Figure 4: Recklinghausen: Upper row: movements derived by ERS-dInSAR - one color-cycle corresponds to 12,8 cm vertical subsidence, superimposed with 2 cm, 5 cm and 8 cm contour-lines. Image area: 2 km x 2 km. Production panels: BH 484 (Jan. 98–Dec. 98) - orange, BH 485 (Apr. 99 – Nov. 99) – yellow and BH 408 (Jul. 00–Jul. 01) – white; points of levelling lines 1 (orange), 2 (yellow) and 3 (white). Comparison of subsidence movements for levelling and dInSAR data (mid row, lower left). Lower right: comparison of subsidence derived by *phase-unwrapping* techniques without (black) and with model-based approach (magenta).

For a better overview the images present the movements derived by dInSAR techniques (one color-cycle = 12 cm vertical subsidence). They are superimposed with the former production panels: BH 484 (January 1998 to December 1998, orange) and BH 484 (April 1999 to December 1999, yellow). The slight green-yellow colors to be seen in the left image still show little amounts of remnant subsidence caused by BH 485. In July 2000 mining activities started again with BH 408 (July 2000 to July 2001, white). The fat solid white rectangle shows the excavation between the ERS revisits. Within the second and third image it can be seen that the developing subsidence trough follows the mining activities but the center lies southward of the current working field in BH 408, amid the excavated BH 484 and BH 408. This effect depends on the already fractured rock strata in the south caused by BH 484 and BH 485 and the more stable underground northward of BH 408. For these periods with beginning movements up to 10 cm

in maximum for the ERS observation intervals the comparison of the levelling profiles and the dInSAR profiles shows the high similarity with a maximum difference of 2 cm. For the time period of the last image (u.r.) subsidence movements up to 30 cm have been observed with levelling and, as for Gelsenkirchen, again the dInSAR processing worked correctly only for movements up to 8 cm. A first model based attempt to enlarge the detection range of the *phase-unwrapping* with additional height information gained from the levelling lines was processed by *GAMMA*. The profiles in figure 4 (lower right image) show that the model based approach leads to a better representation of the subsidence trough than before but the maximum amount to be detected is still 8 to 10 cm. Further work to enlarge the detection range of subsidence movements with ERS dInSAR techniques with additional information are still going on.
An alternative to avoid this phase-unwrapping problem in the case of high phase gradients as observed for active excavation sites is to use a SAR sensor with a longer wavelength. First interferograms derived from L-band SAR onboard the Japanese JERS satellite for a region in the northern Ruhrgebiet confirms this and leads to the expectation that dInSAR processing with JERS–, or in the future, ALOS-data will be well suited for the detection of the absolute amount of movements caused by underground coal mining even for agricultural land and forested areas [12].

3.4 Integration into the Geo-Database (GDZB)

In chapter 2 it was described that reference data and “Subsidence Model Calculations” were taken from the Geo-Database GDZB. In similar ways new information sources like GPS- and dInSAR derived data sets, as subsidence maps or the position of the “zone of affected ground” shall become part of the GDZB. Thus, this data can be more easily provided to all potential users within the whole company. Figure 5 gives a small overview of how the data can be utilized for different tasks by different internal users.

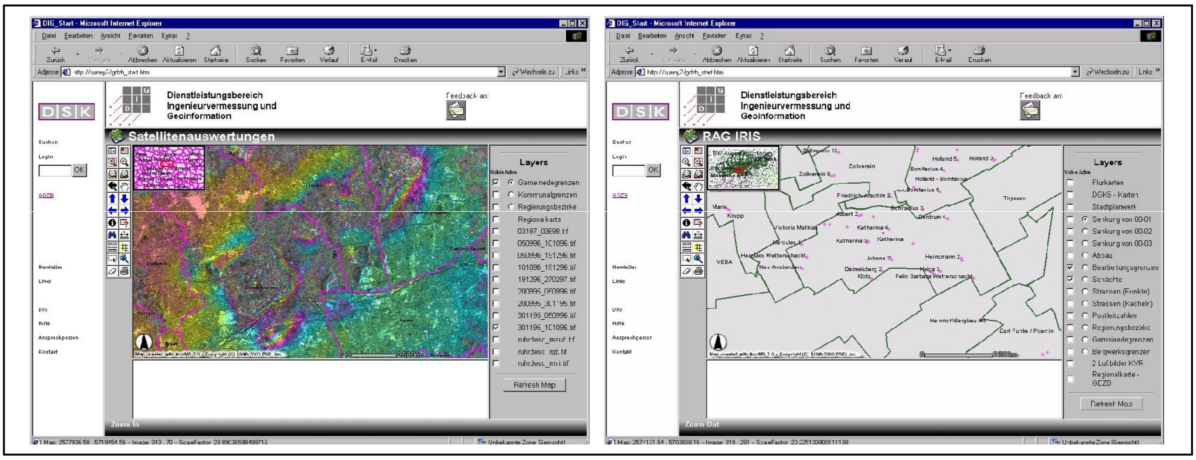

Figure 5: Integration into DSK-GDZB. Left image: overview of dInSAR subsidence and administrative information; right image: geographic operation information - active mine sites, shafts, air-shafts, old mining areas.

4. SUMMARY OF THE FIRST RESULTS AND OUTLOOK

This paper presents first results of an ongoing research and development project (R&D). Further analysis and validation will be performed within the project term.
As yet the comparison of terrestrial measurements and spaceborne dInSAR evaluations already clearly show the high potential to resolve little amounts of subsidence movements up to nearly one decimeter for an acquisition period of two ERS-data sets. For movements larger than 10 cm within an acquisition period the *phase-unwrapping*, even supported by a first model-based approach, can not definitely solve the ambiguities. The model-based *phase-unwrapping* approach will further on be modified an tested.

At the moment the maximal amount of subsidence caused by underground coal mining activities cannot be derived. Nevertheless, the dynamical change of topology and the shape of the migrating subsidence trough can be observed. Especially the position of the so called “zone of affected ground”, the border of static and dynamic areas, can be detected with a high spatial accuracy covering large areas. With the high repetition rate of 35 days ERS-dInSAR methods can be used to back and estimate parameters for the “Subsidence Model Calculations” (BBVB) and in combination with terrestrial and GPS-measurements to correctly derive the absolute amount of subsidence.

The next analyses to be performed in the R&D-project shall examine the potential of a combined evaluation of terrestrial, photogrammetric, as well as airborne and spaceborne InSAR techniques to derive and validate 2D- and 3D-movements caused by underground mining activities, especially to delimit mining-induced subsidence against movements affected by other influences.
Although only some small areas have been processed yet it can be stated that the data processed with dInSAR methods owe the potential to be a perpetual testimony for the whole area of interest. These data sets and knowledge about the accuracy could be very useful against objections of third parties who may use such data sets as well.

The currently operating radar satellite-systems use short wavelengths of about 5 cm so that only areas with high coherence like urban areas, settlements or rural regions with small amounts of changes (from autumn to spring) can be observed. The coal mining activities in the German Ruhrgebiet expand northwards into regions with primarily agricultural use where radar systems with longer wavelengths will lead to better results for the detection of movements. Such a system was the Japanese satellite JERS (1992-1998).
For the year 2002 the launch of ENVISAT is expected. This satellite uses almost the same wavelength as the ERS satellites. Another system will then be the ALOS PALSAR, the successor of JERS, to be launched in 2003.
Because of the promising results DSK will participate as co-investigator of *GAMMA* in an early-on evaluation of the potential of ALOS / JERS and ENVISAT data.

5. LITERATURE

[1] FRANKE, P.: Genehmigungsverfahren im Bergbau und in der Entsorgungswirtschaft. In: Deutscher Markscheider-Verein e.V. (Hrsg.): Wiss. Schriftenreihe im Markscheidewesen, no. 17/1997, pp. 77 - 84.

[2] BENECKE, N.; BRANDT, S.; FISCHER, C.; SPRECKELS, V.; VOSEN, P.: Überwachung der Tagesoberfläche im Gebiet des Steinkohlenbergbaus - Nutzung von GIS, Photogrammetrie und Fernerkundung. In: GIS, no. 1, 1999, pp. 34 - 39.

[3] STROZZI, T.; WEGMÜLLER, U.; WERNER, C.; WIESMANN, A.: ESA-DUP: Differential interferometric Applications in Urban Areas - Final Report to ESA ESRIN/Contract 14502/00/I-IW, 2001.

[4] WERNER, C.; WEGMÜLLER, U.; STROZZI, T.; WIESMANN, A.: Gamma SAR and Interferometric Processing Software. In: Proceedings of ERS-ENVISAT Symposium. Gothenborg, Sweden, 16. - 20. Okt. 2000.

[5] SPRECKELS, V.; WEGMÜLLER, U.; STROZZI, T.; MUSIEDLAK, J.; WICHLACZ, H.-C.: Nutzung von InSAR-Daten zur großflächigen Erfassung von topographischen Veränderungen über Abbaubereichen der Deutschen Steinkohle AG (DSK). Accepted paper: Tagung des Deutschen Markscheider Vereins (DMV) 2001, Trier, Germany, 26. - 28. Sept. 2001.

[6] GENS, R.: Quality assessment of SAR interferometric data. In: Wissenschaftliche Arbeiten der Fachrichtung Vermessungswesen der Universität Hannover, no. 226. Dissertation, 1998. 141 pages.

[7] SCHWÄBISCH, M.: Die SAR-Interferometrie zur Erzeugung digitaler Geländemodelle. Diss., Universität Stuttgart. In: DLR-Forschungsbericht 95-25. 125 pages.

[8] SPRECKELS, V.: Monitoring of Coal Mining Subsidence by HRSC-A Data. In: Proceedings of ISPRS, Vol. XXXIII, Amsterdam, The Netherlands, 16. - 23. July 2000, pp.1452 - 1458, on CD-ROM.

[9] WIELAND, R.: Aspekte zur Wirkungsweise der Modellparameter bei der Vorausberechnung von Gebirgs- und Bodenbewegungen. Vortrag anläßlich der 42. Wissenschaftlichen Tagung des DMV, Cottbus, Germany, 22. - 25. Sept. 1999.

[10] WEGMÜLLER, U.; STROZZI, T.; WERNER, C.; WIESMANN, A.; BENECKE, N.; SPRECKELS, V.: Monitoring of mining-induced surface deformation in the Ruhrgebiet (Germany) with SAR interferometry. In: Proceedings of IGARSS 2000, Honolulu, USA, 24. - 28. July 2000.

[11] JÄGER, R.; KÄLBER, S.; SCHWÄBLE, R. (1999): GPS-based online Control and Alarm Systems (GOCA). Presentation on CD-ROM. Sole distributor: Department of Surveying and Geomatics, FH Karlsruhe, Germany.

[12] STROZZI, T.; WEGMÜLLER, U.; WERNER, C.; WIESMANN, A.: JERS SAR Interferometry for Land Subsidence Monitoring. Accepted paper for the 3rd International Symposium on Retrieval of Bio- and Geophysical Parameters from SAR Data for Land Applications, Sheffield, UK, 11. - 14. Sept. 2001.

THE SHUTTLE RADAR TOPOGRAPHY MISSION

S. Suchandt, H. Breit, N. Adam, M. Eineder, B. Schättler, H. Runge, A. Roth, E. Mikusch
German Aerospace Center (DLR)
Oberpfaffenhofen
D-82234 Wessling, Germany
e-mail: Steffen.Suchandt@dlr.de

KEYWORDS: SRTM, Digital Elevation Model, Single Pass SAR Interferometry

ABSTRACT

The Shuttle Radar Topography Mission (SRTM) flown in February 2000 aimed to map the Earth's topography by the use of spaceborn single pass radar interferometry for the very first time. Two radar instruments carried aboard of Space Shuttle Endeavour, the German/Italian X-SAR (DLR/ASI) and the American SIR-C (NASA/JPL), imaged the Earth's surface between –57 and 60 degrees latitude. One of the most important and also challenging objectives of SRTM is to create a nearly global and homogeneous Digital Elevation Model (DEM) of unprecedented precision. At the German processing and archiving facility the SRTM X-SAR data set is processed within a two years phase using a complex software system. The paper introduces the SRTM project in a brief overview and focuses on the X-SAR data processing as well as on the product specifications and properties.

1. INTRODUCTION

Digital Elevation Models have a large variety of applications ranging from geophysical research over logistics, traffic and telecommunications planning to disaster management and flight support to name only a few. It's true that there already exists a huge amount of digital elevation data for many parts of the world, but on a global scale the available data is either incomplete or not accurate enough. The best available DEM with a global coverage provide height information only on a course raster of e.g. 30 x 30 arcsec for the case of 'GLOBE' (Hastings, 1998). Moreover they have been created by merging different sources of data, which makes them inhomogeneous in quality.

SRTM Objectives and Characteristics

The intention of the SRTM project is to compensate for the lack of global high quality DEM through the use of single pass radar interferometry. As a joint project between NASA/JPL, the Italian Space Agency (ASI) and the German Aerospace Center (DLR), SRTM was designed to produce a nearly global Digital Elevation Model with a homogeneous quality and to make that DEM available to scientific, governmental as well as to commercial users. Moreover, the goal of SRTM is to improve the knowledge in interferometric SAR technology and to gather experience with spaceborne single pass radar interferometry.

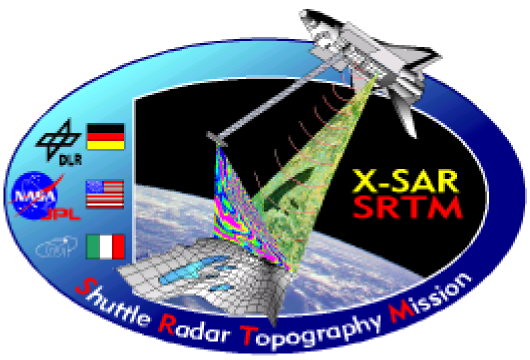

Mission Launch / Duration	11. February 2000 / 11 days	
Orbiter	Space Shuttle Endeavour	
Orbit Height	233 km	
Orbit Inclination	57 degrees	
Orbit Revolutions	159	
Radar Instruments	X-SAR (λ=3.1 cm)	SIR-C (λ=5.6 cm)
Land Coverage	64 Mio km^2	119 Mio km^2
Raw Data Acquisition	3660 GBytes	8590 GBytes
Data Takes	367	764

Figure 1: SRTM X-SAR mission logo and facts

Figure 1 shows some facts about the Shuttle Radar Topography Mission. Two radar interferometers, the German/Italian X-SAR and the American SIR-C instrument, flew aboard the Space Shuttle Endeavour in an eleven-day mission. According to the shuttle orbit having an inclination of 57 degrees, these sensors imaged the earth's topography between 60 degrees north and 57 degrees south, which is about 80 % of the overall landmass. While the SIR-C instrument was operating in ScanSAR mode, thereby obtaining a continuous coverage, the X-SAR instrument was working in strip map mode. The application of the strip map mode with a swath width of 50 km leads to a full and even multiple coverage toward the poles but leaves gaps towards equatorial regions. These gaps will be filled with other high quality DEM. However, although X-SAR does not have a continuous coverage it has a higher accuracy than the C-band data. The coverage for X-SAR SRTM is shown in figure 2.

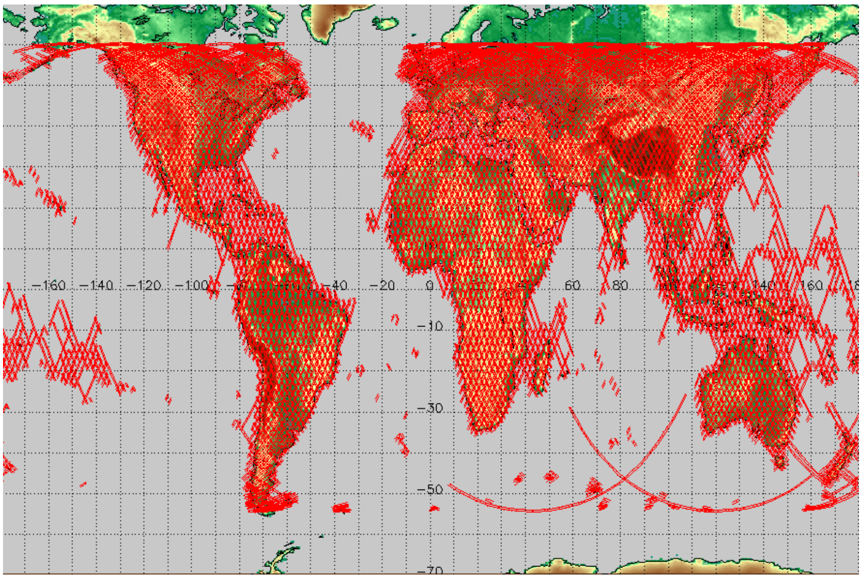

Figure 2: SRTM X-SAR data coverage

Instrument Hardware

The main parts of the instrument hardware and some characteristics of the X-SAR instrument are shown in figure 3. The X-band and C-band transmit/receive antennas, which send the radar pulses toward the earth and receive the echoes respectively, were placed in the shuttle cargo bay. They delivered the SAR images for the primary channel.

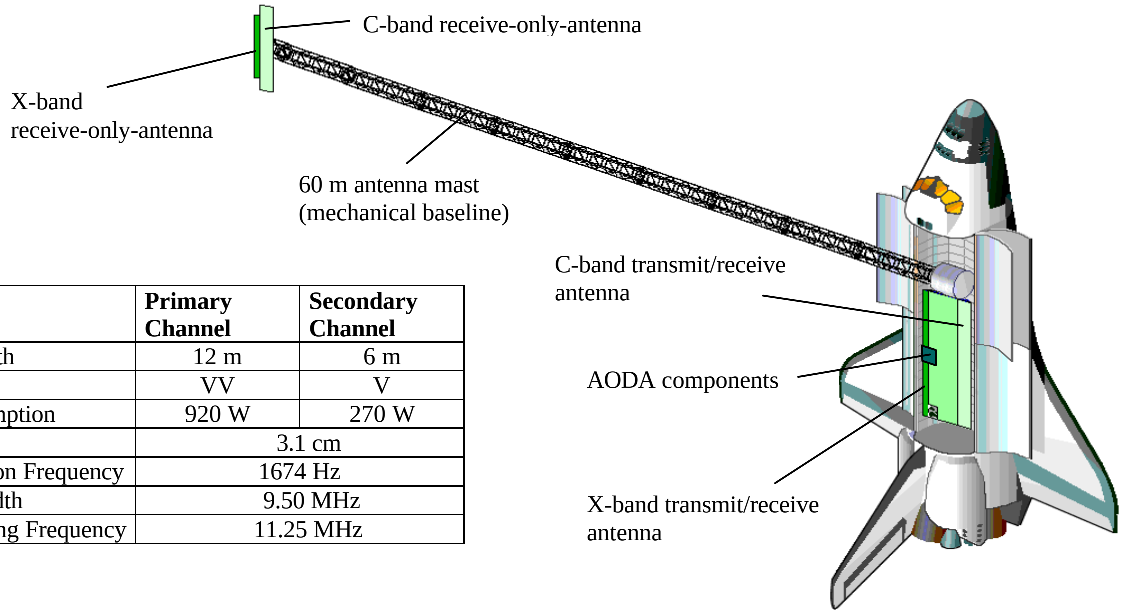

Parameter	Primary Channel	Secondary Channel
Antenna Length	12 m	6 m
Polarization	VV	V
Power Consumption	920 W	270 W
Wavelength	3.1 cm	
Pulse Repetition Frequency	1674 Hz	
Pulse Bandwidth	9.50 MHz	
Range Sampling Frequency	11.25 MHz	

Figure 3: The SRTM interferometer configuration and some characteristics of the X-SAR instrument

To achieve an interferometer configuration, the echoes from the illuminated area on ground must also be acquired from a slightly different position than that of the primary antennas. For this purpose a 60 m long mast carrying X-band and C-band receive-only-antennas on its tip was mounted also in the cargo bay. These antennas provided the SAR images for the secondary channel. During the launch and the landing phase the boom was stowed in a 3 m long canister and was deployed to its full length for mapping operation thus forming the mechanical baseline of the interferometer. During the mapping phase the shuttle flew in a tail-forward configuration and its attitude rolled 59 degrees off from the bay down orientation. This attitude placed the mechanical baseline to the desired optimal tilt angle of 45 degrees from the local nadir. The interferometric configuration used in the Shuttle Radar Topography Mission has three major advantages:

- Due to the use of single pass SAR interferometry, no temporal (atmospheric) decorrelation affects the quality of the interferograms
- Since the same sensor was used throughout SRTM, the DEM will have a homogeneous quality on a global scale
- The Space Shuttle as the interferometer platform enabled a nearly global mapping of the earth's topography within only a few days

For the calculation of such an accurate DEM as in the SRTM case, the precise knowledge of the antenna positions as well as of the baseline attitude, length and dynamics is very essential. A so called Attitude and Orbit Determination Avionics (AODA) mounted at the center of the inboard coordinate system (see also fig. 3) was responsible for the geometry measurements. AODA was combined of several instruments. An Electronic Distance Meter (EDM) measured the baseline length with an accuracy of ±1 mm. The baseline attitude and dynamics were recorded using an Astros Target Tracker (ATT) that tracked the positon of some LEDs at the outboard antennas. Moreover, orbit positions of outboard and inboard antennas were measured using several GPS receivers.

The currently ongoing calibration phase includes geometric and radiometric correction of the SAR data as well as instrument characterization and timing calibration (Eineder, 2001). In the geometric calibration special attention is paid to the analysis and to the compensation of the baseline dynamics because they have a significant influence on the interferogram and on the DEM quality.

2. THE GERMAN PROCESSING FACILTIY FOR SRTM X-SAR DATA

After the calibration phase the SRTM X-SAR data will be processed within 1 ½ years to a global Digital Elevation Model dataset. This is very challenging for at least two reasons. On the one hand the huge amount of raw data requires a complex processing system that has a high throughput with minimum operator interaction and that also schedules and controls the processing and handling of the input/output products automatically. The initial 3660 GBytes of raw data will lead to an amount of interim products of 17 TBytes and to another 0.4 TBytes of final DEM products. On the other hand the desired accuracy of the DEM calls for a very precise orbit, interferometric and geocoding processing including quality control. For this enormous task a processing and archiving facility has been developed at the German Aerospace Center that we introduce in the following.

Overall Processing System

The overall processing system is shown in figure 4. The four subsystems called *Scanner*, *Screener*, *SAR*/*InSAR* and *GeMoS* are the actual sensor data processors. They consist of high performance pipelined software modules of which many are implemented multi-threaded for performance reasons. The sensor data processors are embedded in a so called *Data Information and Management System (DIMS)*. DIMS is a multi-mission, distributed catalogue, storage and scheduling system that uses JAVA/CORBA technology.

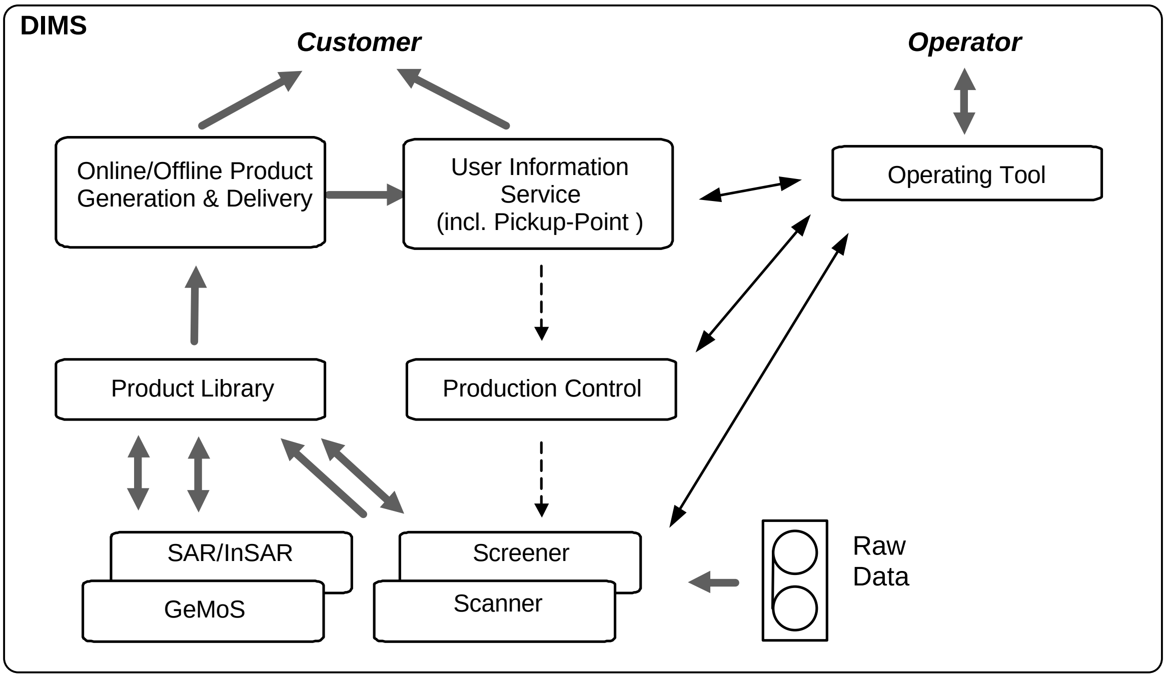

Figure 4: The overall processing system for SRTM X-SAR

The main components of DIMS are the *Product Library*, the *Production Control* and the *Operating Tool*. The Product Library is a twofold software system that on the one hand provides inventory and versioning functionality for all data products and on the other hand controls the storage of these products in a large robot archive. The Production Control component receives production requests (e.g. to produce the DEM of a certain geographical region) and schedules the processing respectively. This means to invoke the required subsystems when necessary and to provide the needed computational resources. With the Operating Tool the PAF operator is able to search the archive for existing products, to generate production requests for new products and to monitor the processing down to module level. Extended information on DIMS is provided in (Mikusch 2000).

Sensor Data Processing Chain

Figure 5 illustrates how the sensor data is processed in the subsystems. At first, the Scanner system reads the data tapes that were recorded during the mission. Its task is to check the quality of the tape data, to analyse the datatake information on it and to convert this information to an archivable format. The datatake information is transferred to the archive as an interim product.

In the second step the Screener/Transcriptor is invoked. This subsystem analyses the SAR raw data and calculates first parameters such as Doppler centroid history and raw data statistics. The Screener/Transcriptor system splits up the raw data physically into tiles, which can be handled more conveniently with respect to archiving as well as to processing in the subsequent systems. Moreover, each tile of raw data is split up logically into scenes. This is necessary to limit the computational requirements for the InSAR and the GeMoS processor.

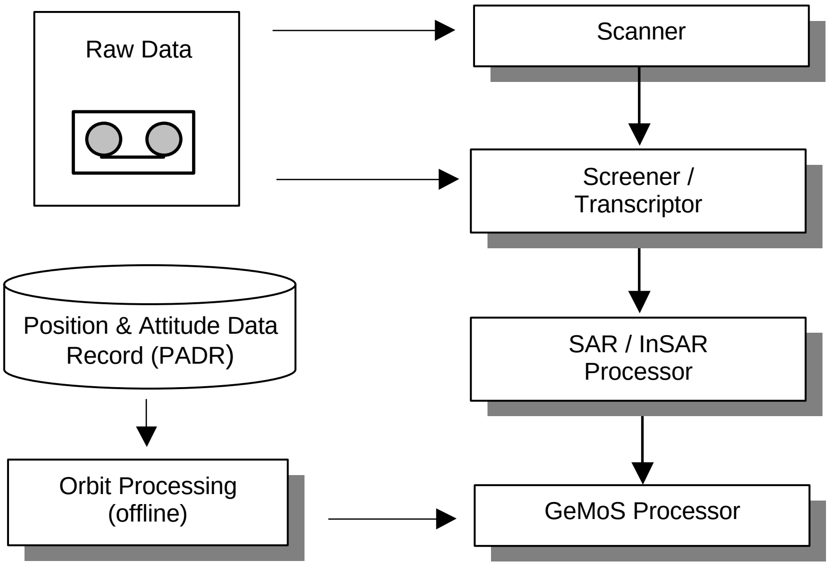

Figure 5: The sensor data processing subsystems

The third subsystem hosts the SAR and interferometric SAR processor. The SAR processor focuses both the primary and secondary SAR image. In addition, the SAR processor does a motion compensation for the secondary channel by adding appropriate phase terms. This is to compensate for a highly varying image shift in azimuth direction caused by an antenna motion in the line of sight. Such an azimuth shift can lead to erroneous interferometric phase terms and thus to height errors in the DEM. While the primary antenna of the SRTM interferometer is very stable due to the high mass of the shuttle, the secondary antenna on the tip of the 60 m mast exhibits fairly strong mechanical oscillations. These are caused by so called thrusters firings, impulses, which serve to correct for the attitude of the mechanical baseline. The corrective firings were necessary since the mast tended to leave its allowed roll angle band of 45.0 ± 0.15 degrees because of a gravity gradient. For detailed information on SRTM X-SAR motion analysis and compensation please refer to (Adam, 2001). Figure 6 shows what an interferogram looks like without motion compensation.

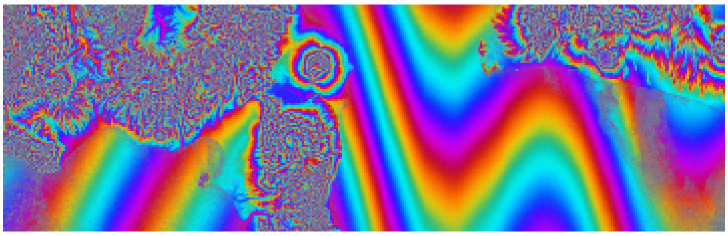

Figure 6: Distorted interferogram phase due to motion of the secondary antenna

The InSAR processor combines the image pairs of the primary and secondary channel to obtain the interferometric phase information, which is exploited for height calculation. It creates a so called interferometric dataset (IFDS), a multi-layer image structure containing e.g. amplitude of primary and secondary channel, coherence between both SAR images and of course the interferometric as well as the unwrapped phase information. The interferometric datasets are transferred to the archive as interim products.

The last system in the sensor data processing chain is the Geocoding and Mosaicking (GeMoS) processor, which the IFDS from InSAR processor are passed to. Here the different IFDS image layers are geocoded. The resulting geocoded IFDS (GIFDS) are then mosaicked to a large digital elevation model (Roth, 1999).

Interferometric SAR (InSAR) Processor

The architecture of the interferometric processor used for the SRTM X-SAR data is shown in figure 7. The input data of the InSAR processor are the primary and secondary single look complex (SLC) images from the SAR processor and the pre-processed position and attitude data records (PADR).

Due to the precise orbit information in SRTM a geometric co-registration algorithm can be applied using zero Doppler iteration and geolocation (Holzner, 2001). The result is a very accurate and stable calculation of the pixel shift between primary and secondary SAR image, even in cases of low coherence. This is very important since the larger the mis-registration the larger the erroneous phase term in the interferogram, especially in the presence of high Doppler centroid values. The geometric co-registration is extensible beyond the scene azimuth limits, which the so called Phase Matching step benefits from.

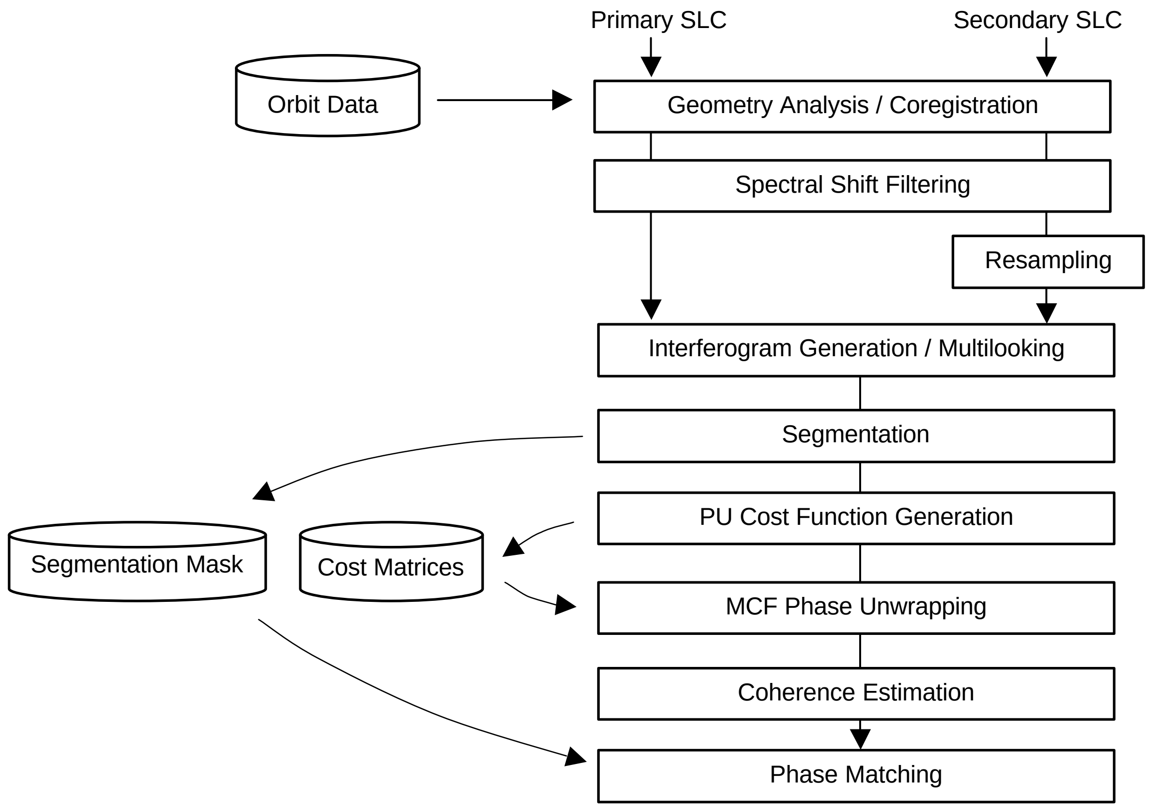

Figure 7: Architecture of the SRTM X-SAR InSAR processor

Phase Matching serves to identify relative phase offsets (integer multiples of 2π) in the overlap area of subsequent scenes. They can occur due to different levels of the absolute phase after phase unwrapping or due to phase unwrapping errors. The reason for this phase offset identification is that, if they are known, all single scenes of a particular datatake can be combined to a phase consistent stripe. It's the geocoding step that benefits from that since only one tie point is needed in the ideal case. Phase matching is done segmentwise. The interferograms are segmented by analysing their local residue density (Hubig, 2000). The phase matching principle is shown in figure 8. Additional information about the InSAR processor can be found in (Adam, 1999).

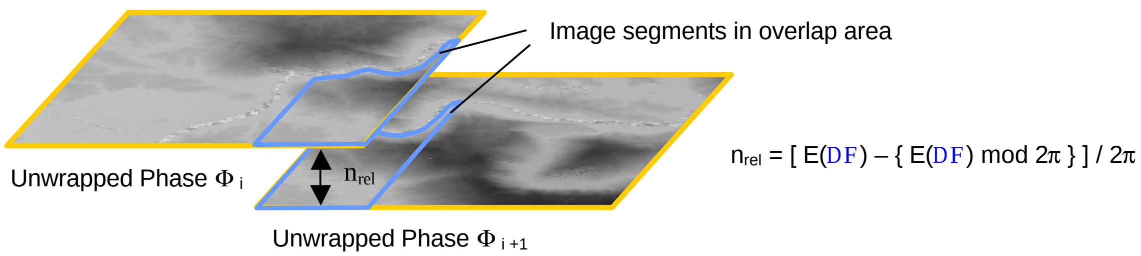

Figure 8: The principle of the InSAR processor phase matching step

Figure 9 is an example of a SRTM X-SAR DEM calculated with the processing chain described above. It has a size of about 170 x 50 km and shows the area of Luxor / Egypt. The course of the Nile is distinctively visible.

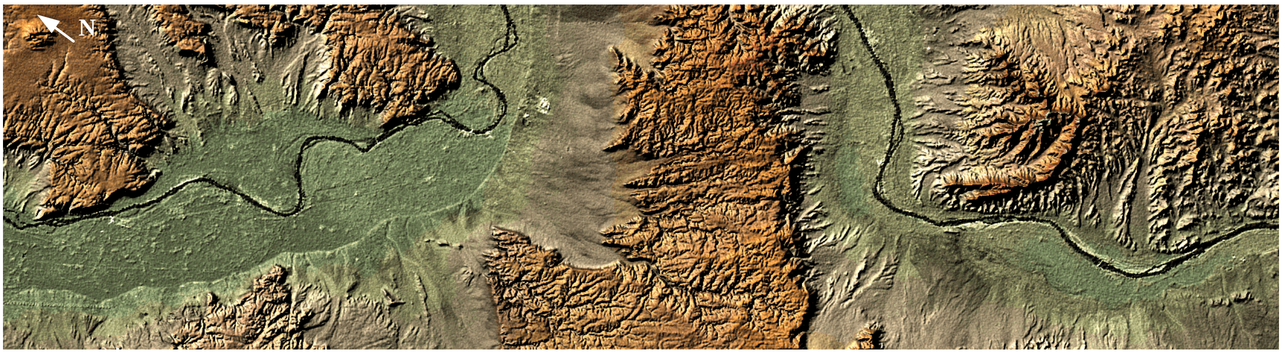

Figure 9: SRTM X-SAR digital elevation model (170 x 50 km) of the area of Luxor / Egypt

3. SRTM X-SAR PRODUCTS

Two different categories of products will be generated from the SRTM X-SAR radar data. The most important of these two are the Digital Elevation Model tiles, which are based on the interferometric data. The other category are the image products that come from the primary SAR channel. This category of products is released for backward compability with the products from the SRL-1 and SRL-2 missions in 1994 when the X-SAR instrument had been in space already with the primary (the inboard) antenna only.

DEM Products

Each of the DEM tiles will have a size of 15’ in both latitude and longitude and will be referenced to the WGS84 ellipsoid. A co-registered Height Error Mask (HEM) accompanies the DEM tiles. The Height Error Mask holds information about the accuracy of each DEM pixel. One pair of a DEM tile and its associated HEM has a data volume of three Mbytes, which enables an easy and fast online delivery of these products to the customer. Table 1 summarizes the product format specifications of the DEM tiles.

SRTM X-SAR DEM tile format specification	
Horizontal Spacing	1’’ latitude x 1’’ longitude
Elevation Intervals	1 m
Horizontal Reference	WGS84
Vertical Reference	WGS84
Tile Size	Fixed, 15’latitude x 15’ longitude
Data Format	16-Bit signed integer
Delivery Format	DTED
Media	CD ROM, ftp

Table 1: Product format specification of SRTM X-SAR DEM tiles

In table 2 the accuracy specifications for the DEM tiles are shown. While the absolute accuracy values refer to the overall Digital Elevation Model dataset, the relative accuracy values refer to sub-areas of 250 km in both azimuth and range. In either case 90 % of the data must lie between the accuracy limits.

SRTM X-SAR DEM accuracy specification	
Horizontal (absolute)	± 20 m (90 % circular)
Horizontal (relative)	± 15 m (90 % circular)
Vertical (absolute)	± 16 m (90 % circular)
Vertical (relative)	± 6 m (90 % circular)

Table 2: Accuracy specification of SRTM X-SAR DEM tiles

Image Products

The image products are compatible with those from the SRL-1 and SRL-2 missions in 1994. They can be used for instance for change detections. Since the elevation is known for each pixel from the SRTM X-SAR Digital Elevation Models, an ortho-rectified SAR image can be provided as standard. Moreover a ground range and a complex slant range image product are released. An overview of the released image products is shown in table 3.

Product Parameter / Product		MGD	SSC	GTC
Equiv. Number of Looks	Azimuth Range	3.5 1.0	1.0 1.0	3.5 1.0
Geometric Representation Ellipsoid Used		Ground Range GEM 6	Slant Range n.a.	UTM WGS84
Data Representation		Detected, Amplitude	Complex	Detected, Amplitude
Pixel Quantization		16 Bit, Signed Integer	16 Bit Real, 16 Bit Imaging	16 Bit, Signed Integer
Spatial Resolution	Azimuth Range	25 m (Mid Swath)	8 –12 m 17 m	25 m (N, E)
Absolute Location Error (σ)	Azimuth Range	< 4 m < 3 km	< 4 m < 4 m	< 30 m (N, E)
Pixel Spacing	x-axis y-axis	12.5 m 12.5 m	4.33 m 13.32 m	25 m 25 m
Product Format		CEOS	CEOS	CEOS

Table 3: SRTM X-SAR image products

Sample Products

First sample products have been released from SRTM X-SAR. These are two digital elevation models both covering the area of Gujarat / India, which was struck by a heavy earthquake in the beginning of 2001. The DEM are shown on the left side of figure 10. One was calculated from an ascending the other one from a descending orbit pass. The right side shows an analysis on the difference height between the ascending and descending pass DEM. For the depicted rectangle the standard deviation is only 3.3 m. This result is very promising because it exemplarily confirms the accuracy of the orbit data as well as the precision of the algorithms that are used throughout the different subsystems.

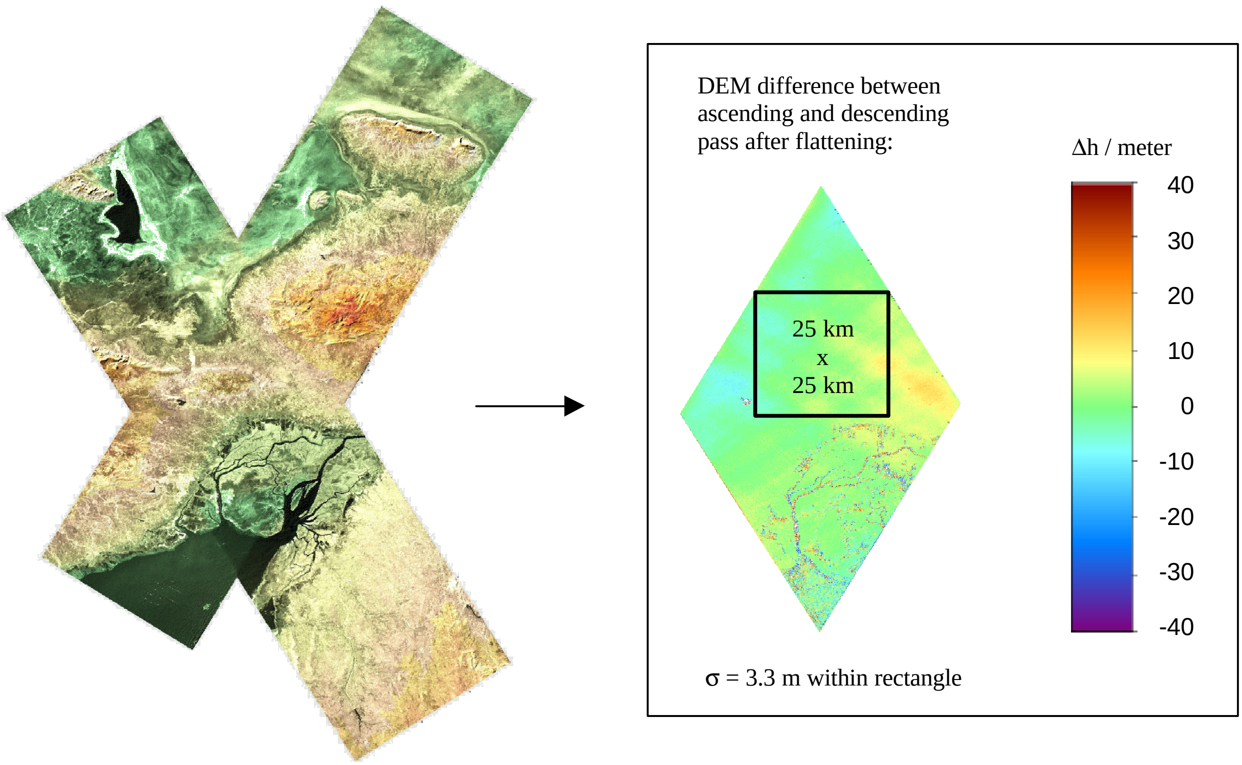

Figure 10: First released DEM from SRTM X-SAR and crossing orbit analysis

4. DATA DISTRIBUTION AND POLICY

The products described above can be delivered to the customer either on CD-ROM or online via ftp. There exists a comfortable user information system based on JAVA / www technology which provides querying and ordering capability for users. This system called EOWEB can be reached under http://www.eoweb.dlr.de. It includes a map browser, which enables the definition of a search area very easily as well as the inspection of the search results.

The data products will usually be made available without any restrictions. Restrictions may become effective by decision of DLR's board of directors due to foreign affairs or due to security reasons. In conjunction with accepted AO proposals the corresponding data is made available free of charge. To all others the "Costs of Fulfilling User Requirements" (COFUR) will be charged.

5. SUMMARY

After a successful and outstanding mission in February 2000 the acquired SRTM X-SAR data will be processed to a homogeneous and global Digital Elevation Model with a very high accuracy. On the one hand the SRTM DEM will fill the gaps in the currently existing global digital elevation models. On the other hand the SRTM DEM will be the most precise DEM on a global scale so far. After the end of the calibration phase, in which we are currently focussing on the elimination of geometric and instrument errors, the X-SAR data will be processed systematically with an advanced processing system allowing for high throughput, quality control and a minimum of operator interaction. Processing will be performed continentwise.

6. REFERENCES

Adam, N., Eineder, M. Breit, H., Suchandt, S., 1999. Shuttle Radar Topography Mission (SRTM): DLR's Interferometric SAR Processor for the Generation of a Global Digital Elevation Model. Second International Workshop on ERS SAR Interferometry FRINGE'99, Liège, Belgium, 1999, http://www.esa.int/fringe99'

Adam, N., Eineder, M., Breit, H., 2001. SRTM X-SAR Motion Compensation: Concept and First Assessment of the Interferometric Observation Geometry. Proceedings of IGARSS 2001, Sydney, Australia.

Eineder, M., Adam, N., Breit, H., Suchandt, S., Holzner, J., Rabus, B., Knöpfle, W., 2001. Results from the SRTM Calibration Phase. International Society for Photogrammetry and Remote Sensing, Workshop "High Resolution Mapping from Space 2001", 19.-21. September 2001, Hannover, Germany.

Holzner, J., Suchandt, S., Eineder, M., Breit, H., Adam, N., 2001. Co-registration – Geometrical Analysis and Verification for SAR Interferometry Under SRTM Data Conditions. Proceedings of IGARSS 2001, Sydney, Australia.

Hastings, D. A., Dunbar, P. K., 1998. Global Land One-kilometer Base Elevation (GLOBE) Digital Elevation Model. Documentation, Version 1.0, National Oceanic and Atmospheric Administration, National Geophysical Data Center, 325 Broadway, Boulder, Colorado 80303, USA. Key to Geophysical Records Documentation (KGRD) 32. 1998.

Hubig, M., Suchandt, S., Eineder, M., 2000. Automatic correction of baseline and phase unwrapping errors in SAR interferograms. Proceedings of EUSAR 2000, 23 – 25 May 2000, Munich, Germany, pp. 131-134.

Mikusch, E., Diedrich, E., Göhmann, M., Kiemle, S., Reck, C., Reissig, R., Schmidt, K., Wildegger, W., Wolfmüller, M., 2000. Data Information and Management System for the Production, Archiving and Distribution of Earth Observation Products. Proceedings of DASIA 2000 – Data Systems in Aerospace, Montreal, Canada, EUROSPACE, ESA, SP-457, pp. 401-406.

Roth, A., Knöpfle, W., Rabus, B., Gebhardt, S., Scales, D., 1999. GeMoS – A System for the Geocoding and Mosaicking of Interferometric Digital Elevation Models. Proceedings of IGARSS 1999, Hamburg, Germany.

Updating Solutions of the Rational Function Model Using Additional Control Points for Enhanced Photogrammetric Processing

Yong Hu, PhD Research Associate and C. Vincent Tao, Associate Professor

Department of Geomatics Engineering, The University of Calgary
2500 University Drive, NW, Calgary, AB, Canada T2N 1N4
Phone (403) 220-5826; Fax: (403) 284-1980; E-mail: yhu@ucalgary.ca and ctao@ucalgary.ca

ABSTRACT

The Rational Function Model (RFM) is treated as a sensor model that allows users to perform ortho-rectification and 3D feature extraction from imagery without knowledge of the physical sensor model. It is a fact that the RFM is determined by the vendor using a proprietary physical sensor model. The accuracy of the RFM solutions is dependent on the availability and the usage of ***ground control points (GCPs).*** In order to obtain a more accurate RFM solution, the user may be asked to supply GCPs to the data vendor. However, control information may not be available at the time of data processing or cannot be supplied due to some reasons (e.g., politics or confidentiality). This paper addresses a means to update or improve the existing RFM solutions when additional GCPs are available, without knowing the physical sensor model. From a linear estimation perspective, the above issue can be tackled using a phased estimation theory. In this paper, two methods are proposed: batch iterative least squares method (BILS) and incremental discrete Kalman filtering (IDKF) method. Detailed descriptions of both of these methods are given. The feasibility of these two methods is validated using an aerial photograph and their performances are evaluated. Some preliminary results concerning the updating of IKONOS imagery were also discussed.

INTRODUCTION

A rational function is a function that can be represented as the quotient of polynomials. Mathematically speaking, all polynomials are rational functions (Newman, 1978). The rational function model (RFM) in this context is a sensor model representing the imaging geometry between the object space and the image space.

The RFM has gained considerable interest recently mainly due to the fact that Space Imaging Inc.(Thornton, CO, USA) has adopted the RFM as a replacement sensor model for image exploitation. The RFM is provided to end users for photogrammetric processing instead of the IKONOS physical sensor model[1]. Such a strategy can serve two purposes. On one hand, the use of an RFM may help keep information about the sensor confidential as it is difficult to derive the physical sensor parameters from the RFM. On the other hand, rational function models facilitate the exploitation of high-resolution satellite imagery by end users. With the RFM provided, users and developers are able to perform photogrammetric processing such as ortho-rectification, 3-D feature extraction and DEM generation from imagery without knowing the complex physical sensor model (Dowman and Dolloff, 2000; Tao and Hu, 2001a). Tests have shown that the RFM can achieve a very high fitting accuracy to the physical sensor model and is capable of replacing the rigorous sensor models for photogrammetric restitution (Madani, 1999; Tao and Hu, 2000a; Yang, 2000). It was reported in Grodecki (2001) that the IKONOS rational model differs by no more than 0.04 pixel from the physical sensor model, with the RMS error below 0.01 pixel.

The RFM solutions are determined by the data vendor using a proprietary physical sensor model. The accuracy of the RFM solutions is dependent on the availability and the usage of the GCPs. If accurate RFM solutions are required, GCPs are needed and are incorporated into the RFM solution process. In this case, the user may be asked to supply the GCPs to the data vendor. However, the GCPs may not be available at the time of processing or can not be supplied due to some reasons (e.g., politics or confidentiality).

If additional GCPs are available, one may ask if it is possible to update or improve the existing RFM solutions (provided, for example, by the vendor). In this paper, we present an approach to update and/or improve the existing RFM solutions when additional GCPs are available, given that the physical sensor model is unknown. In the next section, we briefly describe the RFM by introducing a least squares solution as well as the two computation scenarios for RFM determination. In the following section, we present the two methods for updating the initial RFM solution, namely, batch iterative least squares method (BILS) and incremental discrete Kalman filtering method (IDKF) using additional GCPs. Finally, we show the results computed by both the BILS and IDKF methods to demonstrate the feasibility and the performance of each method. An aerial photograph and an IKONOS stereo pair were used in the experiments. The left and right images of the IKONOS stereo pair were updated and three-dimensional reconstruction was done to check the possibility to update the RFCs without further information about their covariance.

[1] The terms Rational Polynomial Camera (RPC) model and Image Geometry Model (IGM) are used by Space Imaging in its product line. They are the same as the RFM when used in this context.

SOLUTIONS TO THE RATIONAL FUNCTION MODEL

Direct and Iterative Least Squares Solutions

RFM uses a ratio of two polynomial functions of ground coordinates to compute the row image coordinate, and a similar ratio to compute the column image coordinate. The two image coordinates (row and column) and three ground coordinates (e.g., latitude, longitude and height) are each offset and scaled to fit the range from –1.0 to 1.0 over an image or an image section. A detailed description of this normalization process can be found in (OpenGIS Consortium, 1999). For the ground-to-image transformation, the defined ratios of polynomials have the form (Greve, 1992):

$$r_n = \frac{\sum_{i=0}^{m1}\sum_{j=0}^{m2}\sum_{k=0}^{m3} a_{ijk} X_n^i Y_n^j Z_n^k}{\sum_{i=0}^{n1}\sum_{j=0}^{n2}\sum_{k=0}^{n3} b_{ijk} X_n^i Y_n^j Z_n^k} \tag{1}$$

$$c_n = \frac{\sum_{i=0}^{m1}\sum_{j=0}^{m2}\sum_{k=0}^{m3} c_{ijk} X_n^i Y_n^j Z_n^k}{\sum_{i=0}^{n1}\sum_{j=0}^{n2}\sum_{k=0}^{n3} d_{ijk} X_n^i Y_n^j Z_n^k}$$

where r_n and c_n are the normalized row and column indices, respectively, of pixels in the image, X_n, Y_n and Z_n are normalized coordinate values of object points in ground object space, and a_{ijk}, b_{ijk}, c_{ijk}, d_{ijk} are polynomial coefficients called ***rational function coefficients (RFCs)***. The maximum power of each ground coordinate ($m1$, $m2$, $m3$, $n1$, $n2$, and $n3$) is typically limited to 3; and the total power of all ground coordinates is also limited to 3. The unknown RFCs can be solved by using a linear least squares method (Tao and Hu, 2000b). The linearized form of Eq. (1) with respect to RFCs can be written as:

$$v_r = \begin{bmatrix} \frac{1}{B} & \frac{Z}{B} & \frac{Y}{B} & \frac{X}{B} & \cdots & \frac{Y^3}{B} & \frac{X^3}{B} & -\frac{rZ}{B} & -\frac{rY}{B} & \cdots & -\frac{rY^3}{B} & -\frac{rX^3}{B} \end{bmatrix} \cdot J - \frac{r}{B} \tag{2a}$$

$$v_c = \begin{bmatrix} \frac{1}{D} & \frac{Z}{D} & \frac{Y}{D} & \frac{X}{D} & \cdots & \frac{Y^3}{D} & \frac{X^3}{D} & -\frac{cZ}{D} & -\frac{cY}{D} & \cdots & -\frac{cY^3}{D} & -\frac{cX^3}{D} \end{bmatrix} \cdot K - \frac{c}{D} \tag{2b}$$

or

$$\begin{aligned} v_r' = Bv_r = [1 \quad Z \quad Y \quad X \quad \cdots \quad Y^3 \quad X^3 \quad -rZ \\ -rY \quad \cdots \quad -rY^3 \quad -rX^3] \cdot J - r \end{aligned} \tag{3a}$$

$$\begin{aligned} v_c' = Dv_c = [1 \quad Z \quad Y \quad X \quad \cdots \quad Y^3 \quad X^3 \quad -cZ \\ -cY \quad \cdots \quad -cY^3 \quad -cX^3] \cdot K - c \end{aligned} \tag{3b}$$

where

$$B = \left(1 \quad Z \quad Y \quad X \quad \cdots \quad Y^3 \quad X^3\right) \cdot \left(1 \quad b_1 \cdots b_{19}\right)^T$$

$$J = \left(a_0 \quad a_1 \quad \cdots \quad a_{19} \quad b_1 \quad b_2 \quad \cdots \quad b_{19}\right)^T$$

$$D = \left(1 \quad Z \quad Y \quad X \quad \cdots \quad Y^3 \quad X^3\right) \cdot \left(1 \quad d_1 \cdots d_{19}\right)^T$$

$$K = \left(c_0 \quad c_1 \quad \cdots \quad c_{19} \quad d_1 \quad d_2 \quad \cdots \quad d_{19}\right)^T$$

Given n GCPs, the observation error equations can be formed as

$$\begin{bmatrix} V_r \\ -- \\ V_c \end{bmatrix} = \begin{bmatrix} W_r & | & 0 \\ -- & + & -- \\ 0 & | & W_c \end{bmatrix} \cdot \begin{bmatrix} M & | & 0 \\ -- & + & -- \\ 0 & | & N \end{bmatrix} \cdot \begin{bmatrix} J \\ -- \\ K \end{bmatrix} - \begin{bmatrix} W_r & | & 0 \\ -- & + & -- \\ 0 & | & W_c \end{bmatrix} \cdot \begin{bmatrix} R \\ -- \\ C \end{bmatrix} \tag{4a}$$

$$V = WT\,I - WG \tag{4b}$$

where

$$M = \begin{bmatrix} 1 & Z_1 & \cdots & X_1^3 & -r_1Z_1 & \cdots & -r_1X_1^3 \\ 1 & Z_2 & \cdots & X_2^3 & -r_2Z_2 & \cdots & -r_2X_2^3 \\ \vdots & \vdots & \ddots & \vdots & \vdots & \ddots & \vdots \\ 1 & Z_n & \cdots & X_n^3 & -r_nZ_n & \cdots & -r_nX_n^3 \end{bmatrix},$$

$$N = \begin{bmatrix} 1 & Z_1 & \cdots & X_1^3 & -c_1Z_1 & \cdots & -c_1X_1^3 \\ 1 & Z_2 & \cdots & X_2^3 & -c_2Z_2 & \cdots & -c_2X_2^3 \\ \vdots & \vdots & \ddots & \vdots & \vdots & \ddots & \vdots \\ 1 & Z_n & \cdots & X_n^3 & -c_nZ_n & \cdots & -c_nX_n^3 \end{bmatrix},$$

$$R = \begin{bmatrix} r_1 \\ r_2 \\ \vdots \\ r_n \end{bmatrix}, \quad C = \begin{bmatrix} c_1 \\ c_2 \\ \vdots \\ c_n \end{bmatrix}$$

and W can be considered as the weight matrix for the residuals at the left side of Eq. (3):

$$W = \begin{bmatrix} W_r & 0 \\ 0 & W_c \end{bmatrix}, \quad W_r = \begin{bmatrix} \frac{1}{B_1} & 0 & \cdots & 0 \\ 0 & \frac{1}{B_2} & 0 & \vdots \\ \vdots & 0 & \ddots & 0 \\ 0 & \cdots & 0 & \frac{1}{B_n} \end{bmatrix},$$

$$W_c = \begin{bmatrix} \frac{1}{D_1} & 0 & \cdots & 0 \\ 0 & \frac{1}{D_2} & 0 & \vdots \\ \vdots & 0 & \ddots & 0 \\ 0 & \cdots & 0 & \frac{1}{D_n} \end{bmatrix}$$

The normal equation is then

$$T^T W^2 TI - T^T W^2 G = 0 \qquad (5)$$

There are two solutions to Eq. (5), namely, the direct solution and the iterative solution. The direct solution to the RFCs is given by setting W to be the identity matrix. In this case, the normal Eq. (5) can be solved using a standard least square method. As for the iterative solution, the initial value $I^{(0)}$ of the coefficients can be firstly solved using the direct method, then $W^{(i)}$ and $I^{(i)}$ can be calculated by solving the normal equation iteratively until some termination condition is satisfied. The details regarding the two solutions as well as their comparative study results can be found in Tao and Hu (2000a and 2000b).

Assuming that the covariance of error, R_G, associated with image pixel coordinates is known, the covariance matrix P associated with the coefficients I can be computed by (Krakiwsky, 1990)

$$P = \left[T^T R_G^{-1} T\right]^{-1} \qquad (6)$$

The covariance of GCPs in the image after the solution is then given by

$$C = TPT^T + R_G \qquad (7)$$

where TPT^T is introduced by the ground-to-image transformation of the RFM (Eq. 1).

Determination of RFCs

The RFCs can be solved with or without knowing the physical sensor model. With the known physical sensor model, an image grid can be established and its corresponding 3-D object grid can be generated with each grid point's coordinates calculated from its corresponding image point using the physical sensor model. Then the RFCs can be estimated using a least squares solution with an input of the object grid points (X, Y, Z) and the corresponding image grid points (r, c). Tests have shown that the RFM determined using this approach can achieve a very high fitting accuracy to its corresponding physical sensor model, and thus, it can used as a replacement sensor model for photogrammetric restitution (Paderes et al., 1989; Madani, 1999; Tao and Hu, 2000a; Yang, 2000). It is a fact that, in this approach, no actual terrain information is required. RFM performs as a fitting function between the image grid and the object grid. Therefore, if the RFM is used for ortho-rectification and 3-D reconstruction, the achievable accuracy is very much dependent on the physical sensor model used. We call this approach the terrain-independent solution to the RFM (Tao and Hu, 2001a).

Without knowing the physical sensor model, the 3-D object grid cannot be generated. Therefore, the GCPs on the terrain surface have to be collected in a conventional manner (e.g., from maps or a DEM) in order to solve for the RFCs. In this case, the solution is highly dependent on the actual terrain relief, the number of GCPs and their distribution across the scene. We call this approach the terrain-dependent solution to the RFM. Unless a large number of densely distributed GCPs are available, this approach may not provide a sufficiently accurate and robust solution to the RFM (Tao and Hu, 2000b; Toutin and Cheng, 2000). As the RFM that is solved using this approach has no link to the physical sensor, it can not be used as a replacement sensor model. However, this approach can be used as a general tool for image registration with some advantages and unique characteristics compared to regular polynomial based methods (Tao and Hu, 2000c). For a comparison of the terrain-dependent and independent approaches, one can refer to Tao and Hu (2000a).

UPDATE OF SOLUTIONS USING ADDITIONAL GCPS

Two methods are proposed to update the RFM solutions (i.e., the RFC values), given no knowledge of the physical sensor model. Assuming that the values of the RFCs have been pre-determined – when both the original and the additional control points are available – the values of the RFCs can be resolved using the batch iterative least squares method. When only the additional GCPs are available, an incremental discrete Kalman filtering method can be applied.

Batch Iterative Least Squares (BILS) Method

For this method, we use both the original and the new control points to re-calculate the RFCs in a batch manner. This can be fulfilled by simply incorporating all the control points into the normal equation (Eq. 5) with appropriate weighting for the original and new control points. In fact, this method may be used by the vendor when both the original and the new GCPs are known.

Incremental Discrete Kalman Filtering (IDKF) Method

For this method, the existing solution computed using the original GCPs can be updated in an incremental manner, provided that both the RFCs I and the covariance matrix P (Eq. 6) associated with them are known. This method can be used by end-users to update the existing RFM solutions (provided by the vendor) using the newly collected GCPs.

Process Model

Because the true values of the RFCs are constant with respect to time, this static process can be modelled in the form:

$$I_{k+1} = I_k + w_k \qquad (8)$$

with measurements G_k that are

$$G_k = T_k I_k - V_k = T_k I_k + v_k \qquad (9)$$

where the random variables w_k and v_k represent the process and measurement noise, respectively. These white noise random variables are assumed to be independent of each other and demonstrate normal distributions:

$$w_k \sim N(0, Q_k),$$

$$v_k \sim N(0, R_k)$$

where R_k is the covariance matrix associated with the image pixel coordinates of new GCPs, and Q_k is the process noise covariance matrix. Since the true values of the RFCs do not change from step to step, we could let $Q_k = 0$.

Incremental Updating by Discrete Kalman Filtering

To update the initial solution, the static process (Eq. 8) with linearized measurements Eq. (9) can be solved for each group of new control points using an incremental technique based on the discrete Kalman filtering (Brown, and Hwang, 1997):

(1) Predicate the a-priori estimate and its covariance matrix

$$I_k^- = I_{k-1},$$

$$P_k^- = P_{k-1} + Q_{k-1}$$

where the "super minus" indicates that this is the estimate prior to assimilating the new measurements.

(2) Compute the Kalman gain

$$K_k = P_k^- T_k^T [T_k P_k^- T_k^T + R_k]^{-1}$$

(3) Update the a-priori estimate I_k^- by adding weighted residuals from the new measurements

$$I_k = I_k^- + K_k v_k, \quad v_k = G_k - T_k I_k^-$$

(4) Compute the covariance for updated estimate I_k

$$P_k = (E - K_k T_k) P_k^-$$

(5) Compute the covariance of error for new GCPs

$$C_k = T_k P_k T_k^T + R_k \qquad (10)$$

The RFC solution can be updated completely by assimilating all of the new control points, thus running Steps (2) to (5) only once. Alternatively, the new control points can be broken into smaller groups, thereby requiring Steps (2) to (5) to be repeated for each group of new control points. It can be found in this incremental method that the covariance matrix associated with the RFCs of the initial solution is important for controlling the system sensitivity to the new GCPs, and for obtaining correct covariances for the new GCPs.

EXPERIMENTAL RESULTS AND EVALUATION

In order to test the feasibility of the proposed methods, the terrain-dependent approach was used to solve the RFCs. The two methods were also compared in the test.

Test Data Sets

Aerial photograph data

The test data is provided by Intermap Technologies Corp., Calgary, Canada. A raw aerial photograph with 1 meter ground resolution and a DEM with 2.5 meters ground resolution were used to collect control points. The DEM was acquired by Intermap's STAR-3i airborne InSAR system in the Morrison, CO region. Firstly, the raw aerial photograph was ortho-rectified and re-sampled to a ground resolution of 2.5 meters so that it matched the DEM. Then, a set of 50 GCPs well-distributed over the test region was collected from the ortho-rectified aerial image and the corresponding DEM. The measurements in the image are considered to be independent and have an error of zero mean with a standard deviation of 0.75 pixels in the image. The elevation of the selected GCPs varies from 1657.84 meters to 2059.39 meters. In the experiment, this set of 50 GCPs was used to compute the initial values of the RFCs. An independent set of 49 points was collected from the original ortho-rectified aerial image (with 1 meter ground resolution) to serve as additional control points and check points. The standard deviation of image measurements is assumed to be 0.30 pixels in the image. Figure 1 provides a 3-D view of the distribution of the 50 GCPs (marked by dot "•"), and 49 additional control points and check points (marked by cross "+"). In Figure 1, the terrain was generated using a cubic interpolation based on a Delaunay triangulation.

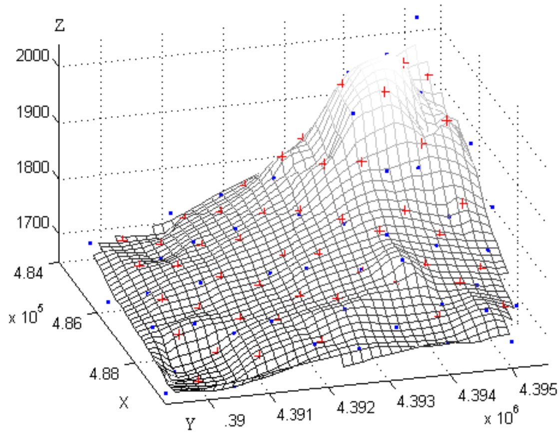

Figure 1. The distribution of control and check points

IKONOS stereo images

The data was collected in the Bruce Nuclear Power Development region near Lake Huron in southern Ontario, Canada. An IKONOS stereo pair was acquired by Space Imaging on July 12, 2001. Both panchromatic 11-bit images were geometrically corrected to the *Geo* level with pixel ground resolution of 1 meter. Each image was supplied together with a set of RFCs and normalization parameters (i.e., offsets and scales), which represent the imaging geometry. The specified accuracy of Geo level IKONOS imagery is was 25 m RMSE (Grodecki, 2001).

We collected 28 ground points from the Canada Data Alignment Layer (CDAL). The CDAL data set consists of many feature points derived from the Canadian National Topographic Database. The feature points were available with longitude and latitude known. We chose the road intersection points among four types of feature points because they are more easily identifiable in the IKONOS images used. The specified horizontal accuracy of the CDAL features is 10 meters CE90. The elevations of the intersection points were derived from the Canadian Digital Elevation Data (CDED) in the same region. The CDED DEM records elevation values referring CVGD28 orthometric heights, which is different from WGS84 ellipsoidal heights used by IKONOS imagery. The exact conversion of elevation values between these two geodetic systems was done using GPS-HT released by Geodetic Survey Division, Natural Resources Canada. GPS-HT allows GPS, DGPS and WADGPS users in Canada to convert NAD83 (CSRS) ellipsoidal heights to CVGD28 orthometric heights. The conversion accuracy was estimated as +/-5 centimetres with 95% confidence. For each intersection object point, the line (row) and sample (column) coordinates of its corresponding image points in the left and right images were collected, and the image line and sample coordinates were assumed to be of a measurement error of 0.3 pixel RMSE.

Results and Evaluation

Test Case 1

For the aerial photograph data set, 9 points among the 49 additional points are selected as additional GCPs, and the other 40 points are used as checkpoints (CKPs). The relief range for these CKPs is 357.07 meters. First, the initial estimates for the RFCs was solved using the iterative least squares method (Tao and Hu, 2000b) with the first set of 50 GCPs. Then, both the BILS and IDKF methods were used to obtain the updated RFC estimates. The IDKF method was applied by adding the 9 additional GCPs one by one assigning higher weight to those new GCPs as they were collected from higher resolution imagery. For the purpose of checking the accuracy of the updated solution, we fixed the process noise covariance at $Q = 10^{-8}$. The 40 CKPs were used to calculate their corresponding positions in the image using the ground-to-image transformation of RFM (Eq. 1) with the new RFC

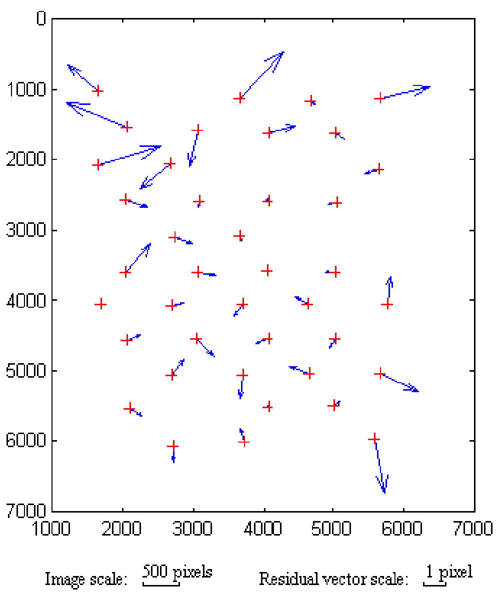

Figure 2a. Residual vectors at CKPs for the initial estimate

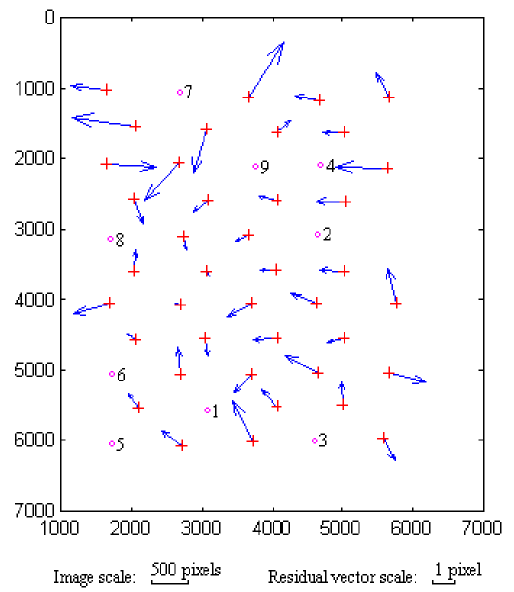

Figure 2b. Residual vectors at CKPs for the final estimate by the IDKF method

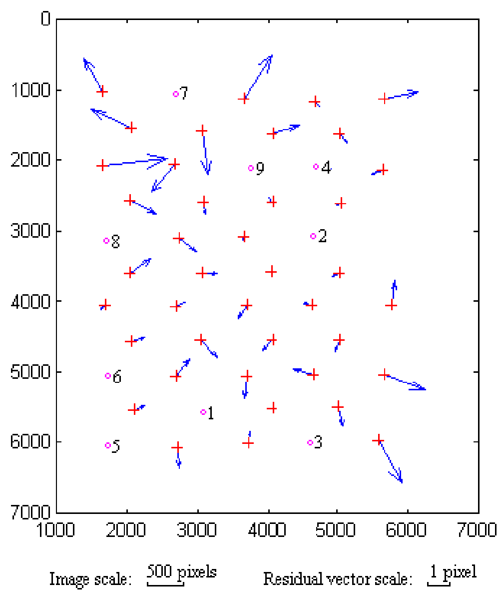

Figure 2c. Residual vectors at CKPs for the final estimate by the BILS method

estimates. The Euclidean distance between the calculated positions and the measured positions was used as an indicator for error residuals.

A part of the experiment results is presented in Table 1, showing results computed by both the BILS and IDKF methods. The root mean square error (RMSE) and the maximum error at CKPs in image row and column directions are listed. The residual vectors at CKPs for the initial estimate are plotted in Figure 2a. The marks with a cross symbol indicate the image positions of the 40 CKPs. The residual vectors at CKPs for the final updated estimate are plotted in Figure 2b. The marks with a small circle indicate the image positions of the 9 additional control points. The residual vectors at CKPs from the BILS solution for all 59 GCPs are shown in Figure 2c. Figures 3a and 3b delineate the total errors (i.e., the residuals combining row and column directions) at CKPs during the updating process by the BILS and IDKF methods, respectively.

To obtain a single term representing the adjustment accuracy at new GCPs, the average standard deviation was used. It is defined as the root mean of the diagonal elements of the covariance matrix (i.e., Eq. (7) for the BILS method, and Eq. (10) for the IDKF method). The computed average standard deviations for the image row and column directions at the new GCPs are listed in Table 2. The first row in Table 2 is the average standard deviation for the initial estimate using the original 50 GCPs.

Before updating, the total RMS error and the maximum error at the CKPs using the 50 GCPs was 1.45 pixels and 3.32 pixels, respectively. For the BILS method after using the 59 GCPs, the total RMS error and the maximum error at the CKPs was 1.23 pixels and 3.10 pixels, respectively. For the final updated solution using the IDKF method, the total RMS error and the maximum error at the CKPs was 1.42 pixels and 2.93 pixels, respectively. An improvement in terms of the final accuracy and the distribution of errors is noticeable after adding nine additional control points.

Although the average standard deviations estimated at the new GCPs are smaller than those at the original 50 GCPs (see Table 2), the final estimate is only slightly superior to the initial estimate at the CKPs. This is due to the fact that only 9 new GCPs were added to the adjustment. The contribution is not significant compared to the large number of GCPs used to obtain the initial estimate for the RFCs. It is also found that a small number of additional GCPs may not always improve the estimation accuracy at the CKPs (see Figures 3a and 3b).

Test Case 2

Among the 49 points of the aerial photograph data set, the 9 points selected as additional GCPs in Test Case 1 were used as CKPs in Test Case 2, and the other 40 points were used as additional GCPs. Similar to Test Case 1, the initial estimate of RFCs was first solved using the 50 GCPs. Then the initial estimate of the RFCs was updated using both the BILS and IDKF methods. For the IDKF method, the results were calculated by adding the additional GCPs one by one and by groups of five points, also assigning higher weight to those new GCPs.

In Table 3, the RMS and maximum errors at CKPs using both BILS and IDKF with groups of five new GCPs (i.e., five GCPs are assimilated each time) are provided. In Table 4, the average standard deviations at the new GCPs are listed, showing results computed by the BILS method, and the IDKF method with new GCPs added one by one and by groups of five.

The total RMS and maximum errors at the CKPs using the 50 GCPs only reach 1.46 pixels and 3.55 pixels, respectively, before updating. For the BILS method, the total RMS and maximum errors at the CKPs using the 90 GCPs were 0.72 pixels and 1.42 pixels, respectively. For the IDKF method, the total RMS and maximum errors at the CKPs for the final updated solution were 1.17 pixels and 2.44 pixels when adding new GCPs one by one, and 0.91 pixels and 2.00 pixels when adding new GCPs by groups of five. The RMS and maximum errors at the CKPs decrease to about half of the initial estimates. It shows that the accuracy is improved quite significantly when a comparable number of additional control points become available.

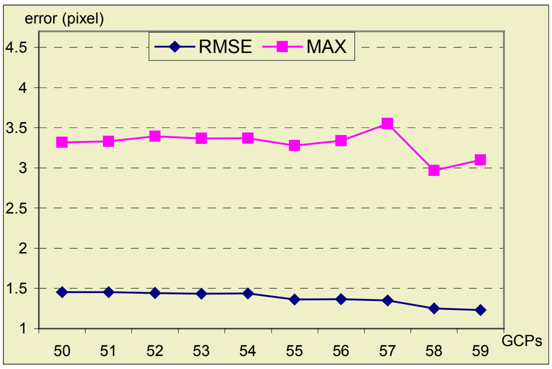

Figure 3a. Total errors at CKPs by the BILS method

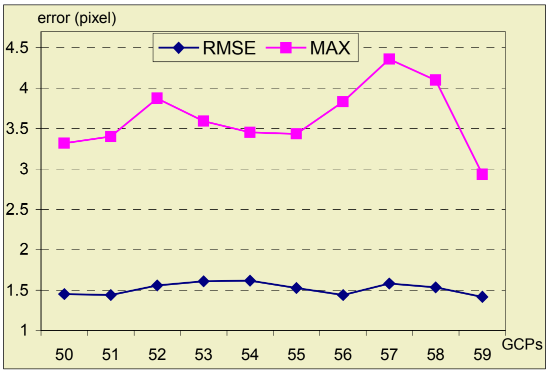

Figure 3b. Total errors at CKPs by the IDKF method

Test Case 3

The IKONOS stereo pair data was used in this test. Among the 28 points collected, 20 points were used as additional GCPs, and the remaining 8 points were used for accuracy checking purpose. Firstly, we evaluated the accuracy of RFCs supplied for each image using the 8 checkpoints. Then, the 20 GCPs with groups of five were used to update the RFCs pertaining to the left image and right image, respectively, using the IDKF method. Because the covariance associated with the RFCs were not provided, we assumed that the RFCs were true values (i.e., let $P = 0$), and set a very small value for the process noise covariance Q to allow for RFCs updating. The accuracy of the new set of RFCs was evaluated at the 8 checkpoints, respectively, for the left and right images. A part of results were listed in Table 5. Finally, the RFCs of the stereo pair before and after updating were used to do 3-D reconstruction with the forward rational function model. The initial ground coordinates were determined by solving the RFM omitting all the 2nd- and 3rd-order terms. The accuracies of 3-D reconstruction results in ground space were compared in Table 6. For more detailed descriptions about the 3-D reconstruction algorithms, one may refer to Tao and Hu (2001b).

Since the covariance P associated with the RFCs was not supplied, we let it be zero, and carefully choosing a process noise covariance Q. Improvements were achieved when the value of Q is between 1e-8 and 1e-12. This range is around the magnitude of the smallest value of the RFCs, which is between 1e-10 and 1e-11 for the IKONOS stereo pair. However, large values for Q (e.g., > 1e-8) will certainly make the 2nd- and 3rd-order terms in the RFM more important. This may be of negative effect to the imaging geometry transferred by original RFCs. Of course, we can reasonably expect that the updating should be more reliable when P is provided for IKONOS imagery.

The numerical results listed in Tables 5 and 6 show that both the ground-to-image transformation and the 3-D reconstruction were improved after assimilating 20 new GCPs. Due to the low accuracy of GCPs used in this test, the improvement was not significant but it did demonstrate that the proposed method can improve the RFCs accompanying the IKONOS Geo level imagery using additional control points.

CONCLUSIONS

When additional control information becomes available, the initial RFM solutions can be updated using the two methods proposed, namely, the BILS and IDKF methods, without knowledge of the physical sensor model. The BILS method incorporates all the control points, including those used to calculate the initial estimate of the RFCs, simultaneously into its estimation process, while the IDKF method is applied incrementally when only the new control points are known. However, it is preferable that the covariance matrices of the RFCs and of the image measurements from the existing RFM solution are known for the Kalman filtering process. End-users can expect good performance if accurate values of the covariance matrices for the RFCs and the image measurements are available.

The accuracy of RFM solutions can be improved using these two methods when a large number of new GCPs are available. However, they may not result in a better accuracy at checkpoints if the additional control points are not sufficient or the covariance matrices provided are not appropriate. The IDKF method is inferior to but still comparable with the BILS method in terms of the accuracy at checkpoints. It was shown that for discrete Kalman filtering, assimilating groups of several control points is more stable and reliable than incorporating only one point at a time. It was also found that assuming a very small but non-zero value for Q_k often obtains better precision at the CKPs in our experiments. This is expected since there are correlations to some extent between RFCs.

In reality, end users often do not have the control points used by the vendor in calculating the initial estimate of the RFCs. In order to facilitate users to update the RFM solutions using additional control information, it is suggested that the covariance matrix of RFCs be included in the image transfer meta-data. This helps to achieve a better updating solution by controlling the system sensitivity to new control information in the Kalman filtering process. Based on the tests using IKONOS imagery, although the covariance of RFCs was not known, we still can expect a satisfactory refinement using the IDKF method proposed.

It is worth noting that the incremental technique can also be used as a quality assurance tool to determine the quality of new control information relative to the original control used to obtain the existing estimates, or verify the existing RFM estimates relative to the obtained high accuracy GCPs.

ACKNOWLEDGEMENTS

The authors wish to thank Mr Steve Schnick, research associate at the University of Calgary for his great assistance in the testing work. We also thank Dr. Bryan Mercer Intermap Technologies Inc., for providing the aerial photography data.

REFERENCES

Brown, R.G., P.Y.C. Hwang, 1997, *Introduction to Random Signal and Applied Kalman Filtering* (3rd Edition), John Wiley & Sons, pp. 190-241.

Dowman, I., Dolloff, J.T., 2000. An evaluation of rational functions for photogrammetric restitution. *Int. Arch. Photogrammetry and Remote Sensing*, 33, 254-266.

Greve, C.W. et al., 1992, Image processing on open systems, *Photogrammetric Engineering & Remote Sensing*, 58(1): 85-89.

Grodecki, J., 2001. IKONOS Geometric Accuracy, *Proceedings of ISPRS Workshop on High Resolution Mapping from Space 2001,* Hannover, September 19-21.

Krakiwsky, E.J., 1990, *The Methods of Least Squares: a Synthesis of Advances*, Dept. of Geomatics Engineering, U of Calgary, UCGE Reports 10003, pp. 21.

Madani, M, 1999. Real-time sensor-independent positioning by rational functions, *Proceedings of ISPRS Workshop on Direct versus indirect methods of sensor orientation*, 25-26 November, Barcelona, pp. 64-75.

Newman, D. J., 1978. Approximation with Rational Functions, *The Conference Board of the Mathematical Sciences by the American Mathematical Society*, Providence, Rhode Island.

OpenGIS Consortium, 1999, *The OpenGIS Abstract Specification - Topic 7: The Earth Imagery Case*, URL: http://www.opengis.org/public/abstract/99-107.pdf.

Paderes, Jr, F.C., E. M. Mikhail, 1989. Batch and on-line evaluation of stereo SPOT imagery, *Proceedings of the ASPRS-ACSM Convention*, Baltimore, US, pp. 31-40.

Tao, C. V., Y. Hu, 2000a, A Comprehensive Study on the Rational Function Model for Photogrammetric Processing, *Photogrammetric Engineering & Remote Sensing (accepted)*.

Tao, C. V., Y. Hu, 2000b. Investigation on the rational function model, *Proceedings of ASPRS Annual Convention*, 22-26 May, Washington D.C..

Tao, C. V., Y. Hu, 2000c. Study of the rational function model for image rectification, *Proceedings of Canadian Conference on Remote Sensing*, 22-25 August, Victoria, BC, pp. 55 – 64.

Tao, C.V., Y. Hu, 2001a, The rational function model - a tool for processing high-resolution imagery, *Earth Observation Magazine*, 10(1): 13-16.

Tao, C.V., Y. Hu, 2001b, 3-D reconstruction algorithms with the rational function model and their applications for IKONOS stereo imagery, *Proc. of ISPRS Workshop on High Resolution Mapping from Space 2001*, 19-21 September, Hanover.

Toutin, T., P. Cheng, 2000, Demystification of IKONOS, *EOM*, 9(7): 17-21.

Yang, X., 2000. Accuracy of rational function approximation in photogrammetry. *Proceedings of ASPRS Annual Convention* (CD-ROM), 22-26 May, Washington D.C..

Table 1. Image row and column residuals at CKPs (unit: pixels)

Number of new GCPs	BILS				IDKF			
	Row		Column		Row		Column	
	RMSE	MAX	RMSE	MAX	RMSE	MAX	RMSE	MAX
0 (initial estimate)	1.134	3.175	0.909	2.700	1.134	3.175	0.909	2.700
1	1.123	3.191	0.909	2.712	1.123	3.205	0.908	2.720
2	1.121	3.253	0.909	2.705	1.258	3.837	0.920	2.945
3	1.122	3.231	0.893	2.575	1.290	3.399	0.863	2.399
4	1.125	3.239	0.893	2.577	1.276	3.322	0.941	2.378
5	1.083	3.238	0.830	2.118	1.241	3.135	0.966	2.399
6	1.078	3.311	0.837	2.175	1.369	3.769	0.857	2.286
7	1.054	3.520	0.842	2.159	1.356	4.315	0.840	2.141
8	0.942	2.950	0.825	2.098	1.274	4.050	0.854	2.177
9 (final estimate)	0.912	3.054	0.824	2.092	1.112	2.827	0.880	2.464

Table 2. Average standard deviations at new GCPs (unit: pixels)

Number of new GCPs	BILS		IDKF	
	Row	Column	Row	Column
0 (initial estimate)	1.001	1.001	1.001	1.001
1	0.408	0.400	0.412	0.410
2	0.406	0.393	0.409	0.405
3	0.404	0.397	0.417	0.420
4	0.399	0.391	0.409	0.411
5	0.401	0.396	0.423	0.423
6	0.402	0.400	0.420	0.421
7	0.404	0.403	0.422	0.423
8	0.405	0.404	0.422	0.420
9	0.402	0.400	0.412	0.415

Table 3. Image row and column residuals at the CKPs (unit: pixels)

Number of new GCPs	BILS				IDKF (groups of five)			
	Row		Column		Row		Column	
	RMSE	MAX	RMSE	MAX	RMSE	MAX	RMSE	MAX
0 (initial estimate)	0.894	1.428	1.151	3.253	0.894	1.428	1.151	3.253
5	0.823	1.931	0.942	2.417	0.668	1.337	1.076	3.047
10	0.757	1.364	0.857	1.552	0.910	1.685	0.913	2.209
15	0.677	1.134	1.059	2.528	0.794	1.875	0.866	2.024
20	0.821	1.824	0.966	2.086	0.646	1.388	0.944	2.170
25	0.627	1.161	0.731	1.585	0.742	1.880	0.786	2.004
30	0.765	1.137	0.951	1.815	0.8115	2.136	0.833	1.925
35	0.442	0.893	0.536	1.146	0.757	1.639	0.679	1.724
40	0.423	0.788	0.579	1.362	0.609	1.098	0.677	1.668

Table 4. Average standard deviations at the new GCPs (unit: pixels)

Number of new GCPs	BILS		IDKF (one by one)		IDKF (groups of five)	
	Row	Column	Row	Column	Row	Column
0 (initial estimate)	1.001	1.001	1.001	1.001	1.001	1.001
5	0.406	0.406	0.410	0.414	0.410	0.411
10	0.402	0.403	0.416	0.419	0.407	0.408
15	0.392	0.393	0.412	0.411	0.396	0.397
20	0.377	0.380	0.406	0.409	0.381	0.384
25	0.375	0.381	0.424	0.424	0.379	0.384
30	0.375	0.381	0.422	0.422	0.379	0.385
35	0.370	0.374	0.417	0.419	0.373	0.377
40	0.369	0.373	0.412	0.413	0.372	0.376

Table 5. Image line and sample residuals at 8 checkpoints (unit: pixels)

image	Number of new GCPs	Updating 1 ($Q = 1e - 10$)				Updating 2 ($Q = 1e - 8$)			
		Line		Sample		Line		Sample	
		RMSE	MAX	RMSE	MAX	RMSE	MAX	RMSE	MAX
left	0 (initial estimate)	2.391	4.418	6.387	9.839	2.391	4.418	6.387	9.839
	5	2.686	5.164	5.542	8.747	2.271	4.159	4.839	8.469
	10	2.139	4.542	5.063	8.393	2.661	5.864	4.157	7.865
	15	2.356	5.029	4.376	7.593	1.879	4.456	3.204	7.195
	20	2.283	4.764	3.611	6.856	2.038	3.156	3.282	6.968
right	0 (initial estimate)	2.339	5.038	8.140	10.722	2.339	5.038	8.140	10.722
	5	2.566	5.561	7.250	9.581	2.300	3.361	7.066	9.447
	10	2.077	4.611	6.240	8.434	2.224	5.272	3.754	5.552
	15	2.604	5.859	5.526	7.590	3.762	7.690	3.228	4.847
	20	2.761	6.058	4.533	6.543	2.780	6.105	3.389	5.999

Table 6. RMS (Max.) errors in 3-D reconstruction with forward RFM (at 8 checkpoints)

3-D reconstruction	Longitude (degrees)		Latitude (degrees)		Height (meters)		
	RMSE	MAX	RMSE	MAX	RMSE	MAX	MEAN
Initial estimate	4.12E-05	7.35E-5	5.96E-05	8.15E-05	3.38E+00	5.440304	-2.69412
Updating 1	3.6E-05	6.29E-05	3.26E-05	5.28E-05	2.420305	4.148788	-1.19204
Updating 2	2.9E-05	5.84E-5	2.85E-05	4.73E-05	2.281873	4.298553	1.023104

3-D Reconstruction Algorithms with the Rational Function Model and their Applications for IKONOS Stereo Imagery

C. Vincent Tao, Professor and Yong Hu, PhD Research Associate
Department of Geomatics Engineering, The University of Calgary
2500 University Drive, NW, Calgary, AB, Canada T2N 1N4
Phone (403) 220-5826; Fax: (403) 284-1980; E-mail: ctao@ucalgary.ca and yhu@ucalgary.ca

Abstract

Rational function model (RFM) is an alternative sensor model allowing users to perform photogrammetric processing without distinguishable loss of accuracy. RFM is considered as a replacement sensor model due to its capability of maintaining full accuracy of the physical sensor models and its generic characteristic of supporting sensor-independent photogrammetric processing. With provided RFM, end users are able to perform photogrammetric processing including ortho-rectification, 3-D reconstruction, and DEM generation with no need to know the physical sensor model, the sensor type and the physical imaging process. In this paper, we investigate two methods for RFM-based 3-D reconstruction, namely, inverse RFM method and forward RFM method. Detailed derivations of the algorithmic procedure are described. A comparison of these two reconstruction methods is conducted. Experimental results based on an aerial stereo pair show that both methods can produce results without accuracy loss compared to the physical senor model, and the forward RFM can achieve better reconstruction accuracy than the inverse RFM. Finally, the forward RFM was used to evaluate the accuracy of 3D reconstruction using IKONOS stereo pairs.

Keywords: senor models; rational functions; 3-D reconstruction; high resolution satellite imagery

Introduction

A sensor model relates 3-D object point positions to their corresponding 2-D image positions. It describes the geometric relationships between the image space and the object space. A well-designed sensor model ensures that 3-D reconstruction (or stereo intersection) and ortho-rectification products generated from imagery are accurate.

The physical sensor models and generalized sensor models are two broad categories of sensor models used (McGlone, 1996). The rational function model (RFM) is essentially a generalized sensor model. Use of the RFM to "replace" the rigorous physical sensor models has been in practice a decade ago (Paderes et al., 1989; Greve et al., 1992). Described in the OpenGIS document (OGC, 1999), there are three main replacement sensor models, namely, grid interpolation model, RFM and universal real-time sensor model. These models are all generalized, i.e., the model parameters do not carry physical meanings of the imaging process. The primary purpose of the use of "replacement sensor models" is their capabilities of sensor independence, high fitting accuracy and real-time calculation (Madani, 1999; Dowman and Dolloff, 2000; Tao and Hu, 2001).

The replacement sensor model should be accurate and robust enough so that it can be used, with no distinguishable loss of accuracy, for photogrammetric processing, e.g., ortho-rectification, stereo feature extraction, DEM generation etc. The name of "replacement sensor model" is sometimes confusing. From an end user perspective, with the replacement sensor model provided, the user can perform photogrammetric processing with no need to know the rigorous physical sensor model, the sensor type and the physical imaging process. However, to be able to replace the rigorous physical sensor model, the rigorous physical sensor model must be known and used for the determination of the unknown coefficients in the replacement sensor model. It is a fact that the achievable accuracy of the photogrammetric processing using the replacement sensor model is mainly affected by the accuracy of the rigorous physical sensor model used for solving the unknown coefficients in the replacement sensor model.

The RFM has gained considerable interest recently in the photogrammetry and remote sensing community, minly due to the fact that some satellite data vendors, for example, Space Imaging, CO, USA, have adopted the RFM[1] as a replacement sensor model for image exploitation. The rational function coefficients (RFCs) of the RFM instead of the physical sensor models are provided to end users for photogrammetric processing. Such a strategy may help keep the confidential information about the sensors as it is difficult to derive the physical sensor parameters from the RFM. On the other hand, RFM facilitates the applications of high-resolution satellite imagery due to its simplicity and generality. It was reported in Grodecki (2001a) that the IKONOS rational model differs by no more than 0.04 pixel from the physical sensor model, with the RMS error below 0.01 pixel.

The RFM was initially used in the US military intelligence community. Therefore, there are few publications available to researchers, developers and users until recent two years (Madani, 1999; Dowman and Dolloff, 2000; Tao and Hu, 2000a; Yang 2000). For this reason, the University of Calgary initiated a research project in early 1999 to investigate various technical issues of RFM. The least squares solution to the nonlinear RFM was derived and described in Tao and Hu (2000b).

[1] The term, Rational Polynomial Camera (RPC) model used by Space Imaging, is essentially the same as the RFM used in this context.

The accuracy assessment of the use of RFM for replacing the rigorous sensor models is provided in Dowman and Dolloff (2000), Tao and Hu (2000b and 2000c) and Yang (2000). The numerical properties of RFM were investigated in Tao and Hu (2000c) and Dowman and Dolloff (2000).

The RFM-based 3-D reconstruction has been implemented in some softcopy photogrammetric software packages (Paderes et al., 1989; Greve et al., 1992; Madani, 1999) but without disclosures of the details regarding their algorithms. Yang (2000) described a RFM-based iterative procedure to compute the object point coordinates from a stereo pair. In his method, an inverse form of RFM, where the planimetric coordinates are represented as rational functions of the image coordinates and the ground elevation, is used to establish the 3-D reconstruction. The method was validated using both aerial and SPOT stereo pairs. Tao and Hu (2000a) developed the software, Rational Mapper, to demonstrate the functionality of RFM-based 3-D reconstruction based on the inverse and forward RFM methods which will be described in this paper. Di et al. (2001) examined the solutions of 3-D reconstruction based on both upward and downward RFM, and provided the reconstruction procedure as well as the testing results using aerial imagery, simulated IKONOS data and HRSC imagery.

In this paper, we provide detailed derivations for the two 3-D reconstruction methods, namely, forward RFM method and inverse RFM method. The basic equations of forward and inverse RFM are given firstly. Solutions to unknown coefficients of the RFM are discussed and the principle of the RFM-based 3-D reconstruction is then described. The two RFM-based 3-D reconstruction methods are described and compared using an aerial photography data. As an application example, the forward RFM is used to perform 3D reconstruction from stereo IKONOS pairs based on RFCs supplied by Space Imaging.

Rational Function Models (RFM)

Forward and inverse RFMs

In the RFM, image pixel coordinates (r,c) are expressed as the ratios of polynomials of object point coordinates (X,Y,Z). The two image coordinates and three object point coordinates are each offset and scaled to fit the range from –1.0 to 1.0 over an image or image section in order to minimize introduction of errors during the computing (NIMA, 2000). A detailed description on this normalization process can be found from OGC (1999). For the ground-to-image transformation, the defined ratios of polynomials have the **forward form** (Greve et al., 1992; OGC, 1999):

$$r = \frac{p1(X,Y,Z)}{p2(X,Y,Z)} \qquad (1)$$
$$c = \frac{p3(X,Y,Z)}{p4(X,Y,Z)}$$

where r and c are the normalized row and column index of pixels in the image respectively, X, Y and Z are normalized coordinate values of points in object space. For the 3rd -order case, the numerators and denominators in Eq. (1) are 20-term polynomials:

$$p = \sum_{i=0}^{m1}\sum_{j=0}^{m2}\sum_{k=0}^{m3} a_{ijk} X^i Y^j Z^k$$

where a_{ijk} are polynomial coefficients called rational function coefficients (RFCs). The order of the terms is trivial and differs in different literature.

The forward form, Eq. (1), defines the ground-to-image transformation. For image-to-ground transformation, an **inverse form** can be used (Yang, 2000):

$$X = \frac{p5(r,c,Z)}{p6(r,c,Z)} \qquad (2)$$
$$Y = \frac{p7(r,c,Z)}{p8(r,c,Z)}$$

It expresses the planar object point coordinates as rational functions of the image coordinates and the vertical object coordinate.

Determination of RFCs

In theory, the RFCs can be solved with or without the physical sensor model. With the known physical sensor model, an image grid can be established and its corresponding 3-D object grid can be generated with each grid point coordinates calculated from its corresponding image point using the physical sensor model. Then the RFCs are estimated using a least square solution (Tao and Hu, 2000b) with an input of the object grid points (X, Y, Z) and the corresponding image grid points (r, c). This approach has been widely used to determine the unknown coefficients of the RFM (Paderes et al., 1989; Madani, 1999; Tao and Hu, 2000c; Yang, 2000). In this approach, no actual terrain information is required. RFM performs as a fitting function between the image grid and the object grid. Therefore, if the RFM is used for ortho-rectification and 3-D reconstruction, the achievable accuracy is very much affected by the physical sensor model used (i.e., the accuracy of the object grid generated using the physical sensor model). We call this approach terrain-independent solution to RFM (Tao and Hu, 2000a, 2001).

Without knowing the physical sensor model, the 3-D object grid cannot be generated. Therefore the ground control points (GCP) on the terrain surface have to be collected by the conventional way (e.g., from maps or the actual DEM) in order to solve for the RFCs. In this case, the solution is highly dependent on the actual terrain relief, the number and the distribution of GCPs. We call this approach terrain-dependent solution to RFM. Unless a large number of densely distributed GCPs are available, this approach can not provide sufficiently accurate and robust solution to RFM. That is, the RFM generated by this approach may not be used as a replacement sensor model if high accuracy is required (Toutin and Cheng, 2000). However, this approach can be used as a general tool for image registration with some advantages and unique characteristics compared to regular polynomial based methods (Tao and Hu, 2000d; Tao et al., 2000). For a comparison of the terrain-dependent and independent approaches, one can refer to Tao and Hu (2000c).

RFM based 3-D reconstruction and ortho-rectification

RFM based ortho-rectification is straight forward. Either the forward form or the inverse form of RFM can be employed. It results in two different rectification approaches: forward rectification, i.e., from the original image space (r, c) with elevation Z to the object space (X, Y); and backward rectification, i.e., from the object space (X, Y, Z) to the original image space (r, c). There is no significant difference between these two approaches in terms of the final results. The advantages and disadvantages of each approach together with the resampling methods can be found in Novak (1992).

After solving the RFM for each image, 3-D reconstruction can be performed using the corresponding points in the stereo pair (the forward form is used herein):

$$r_l = \frac{p1_l\ (X,Y,Z)}{p2_l\ (X,Y,Z)},\quad c_l = \frac{p3_l\ (X,Y,Z)}{p4_l\ (X,Y,Z)}$$
$$r_r = \frac{p1_r\ (X,Y,Z)}{p2_r\ (X,Y,Z)},\quad c_r = \frac{p3_r\ (X,Y,Z)}{p4_r\ (X,Y,Z)} \qquad (3)$$

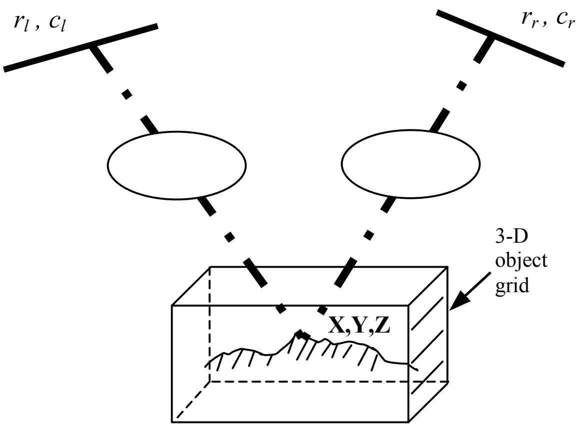

Figure 1. RFM-based 3-D reconstruction and "virtual intersection"

As shown in Figure 1, compared to the conventional stereo intersection, there is no actual intersection of the light rays occurring at the object point. Therefore, we use the term "3-D reconstruction" instead of "stereo intersection" throughout the paper and use dotted line in Figure 1 to represent this virtual intersection. Figure 1 also illustrates the 3-D object grid used for solving the RFCs in Eq. (3). This object cube is established in a way it covers the entire range of the terrain in all three directions. Often very high dense grid points (e.g., 11x11 grid at 5 layers) are used for the determination of RFCs. Therefore, the RFM can fit the physical sensor model very well with this "perfect" control. It is worth noting that Eq. (3) can be extended to the multiple images case where each image with its own RFM is available for 3-D reconstruction.

3-D Reconstruction with Inverse RFM

Algorithm derivation

After the RFCs of Eq. (2) are solved for each image, the 3-D object point coordinates can be iteratively calculated using the corresponding image points in the stereo pair. Applying Taylor expansion of X and Y towards the input variable Z in Eq. (2), we have the first-order approximations:

$$X \approx \hat{X} + \partial X / \partial Z \cdot \Delta Z$$
$$Y \approx \hat{Y} + \partial Y / \partial Z \cdot \Delta Z$$

where

$$\frac{\partial X}{\partial Z} = \frac{\partial p5 / \partial Z \cdot p6 - p5 \cdot \partial p6 / \partial Z}{p6 \cdot p6}$$
$$\frac{\partial Y}{\partial Z} = \frac{\partial p7 / \partial Z \cdot p8 - p7 \cdot \partial p8 / \partial Z}{p8 \cdot p8}$$
$$\partial p / \partial Z = a_1 + a_4 c + a_5 r + 2a_7 Z + a_{10} cr + 2a_{11} cZ + 2a_{12} rZ + a_{13} c^2 + a_{15} r^2 + 3a_{17} Z^2$$

and $\hat{X}$, $\hat{Y}$ are estimated by substituting some approximate values of r, c, Z into Eq. (2).

Given a pair of corresponding image points (r_l, c_l) and (r_r, c_r), and a value of Z, we have

$$X \approx \hat{X}_l + \frac{\partial X_l}{\partial Z} \cdot \Delta Z,\qquad Y \approx \hat{Y}_l + \frac{\partial Y_l}{\partial Z} \cdot \Delta Z$$
$$X \approx \hat{X}_r + \frac{\partial X_r}{\partial Z} \cdot \Delta Z,\qquad Y \approx \hat{Y}_r + \frac{\partial Y_r}{\partial Z} \cdot \Delta Z$$

Eliminating X, Y from above equations, we have the error equations

$$v_X = \left(\frac{\partial X_r}{\partial Z} - \frac{\partial X_l}{\partial Z}\right) \cdot \Delta Z - (\hat{X}_l - \hat{X}_r)$$
$$v_Y = \left(\frac{\partial Y_r}{\partial Z} - \frac{\partial Y_l}{\partial Z}\right) \cdot \Delta Z - (\hat{Y}_l - \hat{Y}_r)$$

Then the least squares solution to ΔZ is

$$\Delta Z = \left(\left(\hat{X}_l - \hat{X}_r\right) \cdot w_X \cdot \left(\frac{\partial X_r}{\partial Z} - \frac{\partial X_l}{\partial Z}\right) + \left(\hat{Y}_l - \hat{Y}_r\right) \cdot w_Y \cdot \left(\frac{\partial Y_r}{\partial Z} - \frac{\partial Y_l}{\partial Z}\right) \right) \Bigg/ \left(w_X \cdot \left(\frac{\partial X_r}{\partial Z} - \frac{\partial X_l}{\partial Z}\right)^2 + w_Y \cdot \left(\frac{\partial Y_r}{\partial Z} - \frac{\partial Y_l}{\partial Z}\right)^2 \right) \tag{4}$$

where w_X and w_Y are weights for X and Y.

Yang (2000) proposed an alternative correction with the form

$$\Delta Z = \left(\hat{X}_l - \hat{X}_r + \hat{Y}_l - \hat{Y}_r\right) \Big/ \left(\frac{\partial X_r}{\partial Z} - \frac{\partial X_l}{\partial Z} + \frac{\partial Y_r}{\partial Z} - \frac{\partial Y_l}{\partial Z}\right) \tag{5}$$

Reconstruction procedure

Now we can sketch the procedure that may be used to compute the object point coordinates from a pair of corresponding points (r_l, c_l) and (r_r, c_r) in the image (see Figure 2).

1) Find an initial approximate value for elevation Z. This can often be specified as the median value of the elevation range (e.g., 0 for the normalized elevation range [-1, 1]).
2) Calculate the quantities:
   ($\hat{X}_l$, $\hat{Y}_l$, $p5_l$, $p6_l$, $p7_l$, $p8_l$, $\partial p5_l / \partial Z$, $\partial p6_l / \partial Z$, $\partial p7_l / \partial Z$, $\partial p8_l / \partial Z$) with r_l, c_l, Z, and ($\hat{X}_r$, $\hat{Y}_r$, $p5_r$, $p6_r$, $p7_r$, $p8_r$, $\partial p5_r / \partial Z$, $\partial p6_r / \partial Z$, $\partial p7_r / \partial Z$, $\partial p8_r / \partial Z$) with r_r, c_r, Z.
3) Calculate the correction ΔZ using Eq. (4), then add ΔZ to Z.
4) Repeat Steps 2 and 3, and update Z each time with ΔZ, until the specified maximum number of iterations (e.g., 10) has been reached, or Z converges (i.e., the absolute value of ΔZ is smaller than a specified threshold, set up based on the elevation error).
5) Substitute the final Z into Eq. (2) together with image point positions (r_l, c_l) and (r_r, c_r) and calculate the mean object point coordinates from $(\hat{X}_l, \hat{Y}_l)$ and $(\hat{X}_r, \hat{Y}_r)$, i.e., $X = (\hat{X}_l + \hat{X}_r)/2$, $Y = (\hat{Y}_l + \hat{Y}_r)/2$.

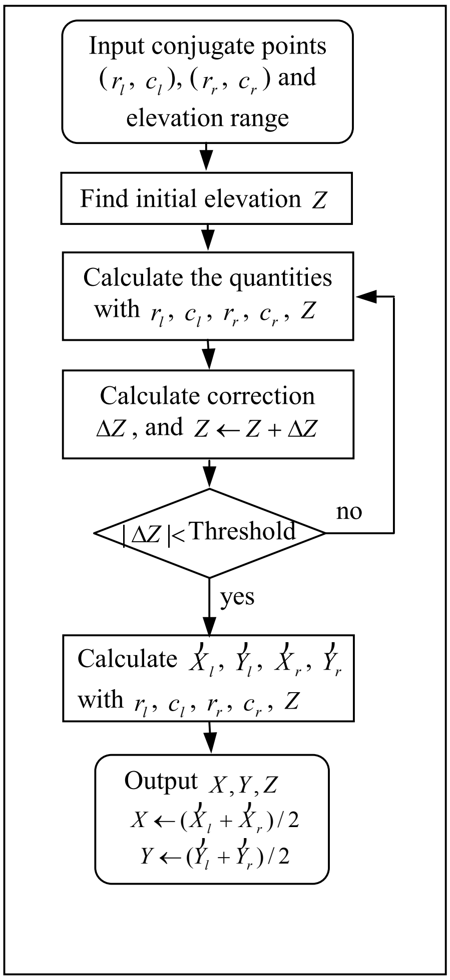

Figure 2. Flowchart of 3-D reconstruction with inverse RFM

Discussions

The above procedure was described in Yang (2000) with the correction Eq. (5) being used in Step 3. We find that the result with improved accuracy can be obtained by using the correction Eq. (4) rather than Eq. (5). However, Eq. (5) is computationally fast. Support results will be shown in section 5.

It should be noted that the object point coordinates for the two images of a stereo pair should be un-normalized or be normalized using the same offset and scale values in the same object coordinate system. If the two images of a stereo pair are normalized separately using different offset and scale values for the object point coordinates, the computation equations should be modified accordingly. The object point coordinates for two images of a stereo pair can also be re-normalized to be in accordance with the condition given above, and then the RFCs would be re-solved so that the equations above could be used without any change.

As with many iterative algorithms, rigorous analytical proof of convergence is very difficult. However, in our experience, the algorithm does always converge fast when the two image points are indeed a pair of corresponding points. Figure 3 plots the absolute value of the correction ΔZ versus the iteration numbers on a logarithmic scale when the 3rd -order inverse form is used with coordinate normalization. The graph shows excellent convergence with the correction value decreasing by many orders of magnitude in just three iterations. No further refinement can be regularly obtainable with more iterations. Therefore, the specified threshold should be strict. In our experiments, three iterations were always sufficient to ensure convergence (a threshold of $1.0e^{-10}$ meter in Z was used in our testing). We have also found that the convergence of the iterative procedure is not dependent on the initial approximate value of Z as long as it falls within the elevation range. For this reason, we start the reconstruction with the initial value of Z set to the median elevation range.

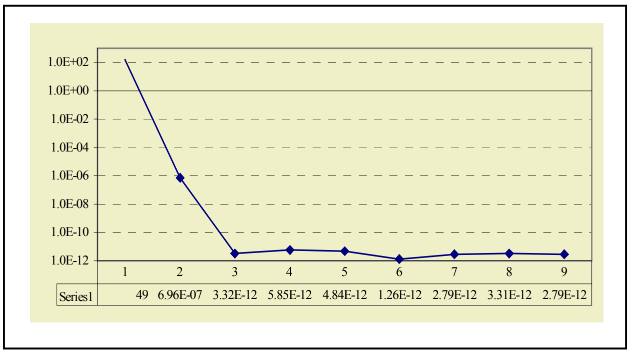

Figure 3. The logarithmic absolute value of correction ΔZ versus iteration

The inverse RFM reconstruction described above may no be able to obtain the best solution since it allows only one explicit least squares solution for Z and discrepancies may occur in the X and Y directions. As we will observe in the next section, the forward RFM allows for a simultaneous least squares adjustment for all three object point coordinates. We will show that a better solution can be expected by treating the result of the inverse RFM as the initial approximate for the forward RFM reconstruction.

3-D Reconstruction with Forward RFM

Algorithm derivation

After the RFCs of the forward RFM form Eq. (1) are solved, the 3-D object position can be iteratively reconstructed from its corresponding image points. Similar to the previous section, we get first-order approximations by applying Taylor expansion of r, c towards the three input variables X, Y, Z in Eq. (1), and reformulate them to the following error equations:

$$v_r = \begin{bmatrix} \frac{\partial r}{\partial Z} & \frac{\partial r}{\partial Y} & \frac{\partial r}{\partial X} \end{bmatrix} \begin{bmatrix} \Delta Z \\ \Delta Y \\ \Delta X \end{bmatrix} - (r - \hat{r})$$

$$v_c = \begin{bmatrix} \frac{\partial c}{\partial Z} & \frac{\partial c}{\partial Y} & \frac{\partial c}{\partial X} \end{bmatrix} \begin{bmatrix} \Delta Z \\ \Delta Y \\ \Delta X \end{bmatrix} - (c - \hat{c})$$

where

$$\frac{\partial r}{\partial Z} = \frac{\partial p1/\partial Z \cdot p2 - p1 \cdot \partial p2/\partial Z}{p2 \cdot p2},$$
$$\frac{\partial r}{\partial Y} = \frac{\partial p1/\partial Y \cdot p2 - p1 \cdot \partial p2/\partial Y}{p2 \cdot p2},$$
$$\frac{\partial r}{\partial X} = \frac{\partial p1/\partial X \cdot p2 - p1 \cdot \partial p2/\partial X}{p2 \cdot p2}$$

$$\frac{\partial c}{\partial Z} = \frac{\partial p3/\partial Z \cdot p4 - p3 \cdot \partial p4/\partial Z}{p4 \cdot p4},$$
$$\frac{\partial c}{\partial Y} = \frac{\partial p3/\partial Y \cdot p4 - p3 \cdot \partial p4/\partial Y}{p4 \cdot p4},$$
$$\frac{\partial c}{\partial X} = \frac{\partial p3/\partial X \cdot p4 - p3 \cdot \partial p4/\partial X}{p4 \cdot p4}$$

and

$$\partial p/\partial Z = a_1 + a_4 Y + a_5 X + 2a_7 Z + a_{10} YX + 2a_{11} ZY + 2a_{12} ZX$$
$$+ a_{13} Y^2 + a_{15} X^2 + 3a_{17} Z^2$$
$$\partial p/\partial Y = a_2 + a_4 Z + a_6 X + 2a_8 Y + a_{10} ZX + a_{11} Z^2 + 2a_{13} ZY$$
$$+ 2a_{14} YX + a_{16} X^2 + 3a_{18} Y^2$$
$$\partial p/\partial X = a_3 + a_5 Z + a_6 Y + 2a_9 X + a_{10} ZY + a_{12} Z^2 + a_{14} Y^2$$
$$+ 2a_{15} ZX + 2a_{16} YX + 3a_{19} X^2$$

Thus, the four error equations for two corresponding image points (r_l, c_l) and (r_r, c_r) are

$$\begin{bmatrix} v_{rl} \\ v_{rr} \\ v_{cl} \\ v_{cr} \end{bmatrix} = \begin{bmatrix} \partial r_l/\partial Z & \partial r_l/\partial Y & \partial r_l/\partial X \\ \partial r_r/\partial Z & \partial r_r/\partial Y & \partial r_r/\partial X \\ \partial c_l/\partial Z & \partial c_l/\partial Y & \partial c_l/\partial X \\ \partial c_r/\partial Z & \partial c_r/\partial Y & \partial c_r/\partial X \end{bmatrix} \begin{bmatrix} \Delta Z \\ \Delta Y \\ \Delta X \end{bmatrix} - \begin{bmatrix} r_l - \hat{r}_l \\ r_r - \hat{r}_r \\ c_l - \hat{c}_l \\ c_r - \hat{c}_r \end{bmatrix}$$

$$v = Ax - l$$

The least squares solution is

$$x = [\Delta Z \;\; \Delta Y \;\; \Delta X]^T = (A^T W A)^{-1} A^T W l \qquad (6)$$

where W is the weight matrix for the image points.

Determination of the initial approximate values

The remaining problem is that initial approximate values of object point coordinates X, Y, Z should be used to start the computation. One method to obtain these initial values is to solve RFM, using only the first-order terms, and omitting the 2nd- and 3rd-order terms, i.e., Eq. (1) is reduced to be

$$r = \frac{a_0 + a_1 Z + a_2 Y + a_3 X}{1 + b_1 Z + b_2 Y + b_3 X}$$

$$c = \frac{c_0 + c_1 Z + c_2 Y + c_3 X}{1 + d_1 Z + d_2 Y + d_3 X}$$

The error equations are

$$v_r = \begin{bmatrix} a_1 - rb_1 & a_2 - rb_2 & a_3 - rb_3 \end{bmatrix} \begin{bmatrix} Z \\ Y \\ X \end{bmatrix} - (r - a_0)$$

$$v_c = \begin{bmatrix} c_1 - cd_1 & c_2 - cd_2 & c_3 - cd_3 \end{bmatrix} \begin{bmatrix} Z \\ Y \\ X \end{bmatrix} - (c - c_0)$$

Then the four error equations for two corresponding image points are

$$\begin{bmatrix} v_{rl} \\ v_{rr} \\ v_{cl} \\ v_{cr} \end{bmatrix} = \begin{bmatrix} a_{1l} - r_l b_{1l} & a_{2l} - r_l b_{2l} & a_{3l} - r_l b_{3l} \\ a_{1r} - r_r b_{1r} & a_{2r} - r_r b_{2r} & a_{3r} - r_r b_{3r} \\ c_{1l} - c_l d_{1l} & c_{2l} - c_l d_{2l} & c_{3l} - c_l d_{3l} \\ c_{1r} - c_r d_{1r} & c_{2l} - c_r d_{2r} & c_{3l} - c_r d_{3r} \end{bmatrix} \begin{bmatrix} Z \\ Y \\ X \end{bmatrix} - \begin{bmatrix} r_l - a_{0l} \\ r_r - a_{0r} \\ c_l - c_{0l} \\ c_r - c_{0r} \end{bmatrix} \tag{7}$$

Thus, the initial approximate values of object point coordinates X, Y, Z can be obtained by solving Eq. (7) using the least squares adjustment. When the coordinates are normalized, it is found that for pushbroom imagery (e.g., IKONOS and SPOT) the coefficient values of the constant and first-order terms in both the numerator and the denominator are larger by many orders of magnitude than those of the second and third-order terms. Therefore, this method may be especially suitable for images acquired by pushbroom-type sensors.

For frame camera imagery, the coefficient values of the constant and first-order terms in both the numerator and the denominator do not dominate when compared with those of the second and third-order terms. As a result, the initial values obtained using this method may often result in divergence of the correction computations with Eq. (6). Based on our experiments, it is found that for the frame camera case, the solution is not sensitive to the initial values of X, Y, Z, and the median values of the three object coordinate ranges may be used to start the reconstruction, for examples, three zeros for normalized coordinate ranges [-1,1].

Another method to obtain the approximate values of object point coordinates is to perform 3-D reconstruction using the inverse RFM form, described in the previous section. The values obtained will then be used as initial approximates for the forward reconstruction.

Reconstruction procedure

Now we sketch the procedure that can be used to compute the object point coordinates from a pair of corresponding points (r_l, c_l) and (r_r, c_r) in the image (see Figure 4).

1) Determine the initial approximate values for the object point coordinates X, Y, Z, by solving Eq. (7), by specifying the median values of the three object coordinate ranges, or by the reconstruction results from the inverse RFM.
2) Compute the following quantities with X, Y, Z:

   ($\hat{r}_l$, $\hat{c}_l$, $p1_l$, $p2_l$, $p3_l$, $p4_l$, $\partial p1_l / \partial Z$, $\partial p1_l / \partial Y$, $\partial p1_l / \partial X$, $\partial p2_l / \partial Z$, $\partial p2_l / \partial Y$, $\partial p2_l / \partial X$, $\partial p3_l / \partial Z$, $\partial p3_l / \partial Y$, $\partial p3_l / \partial X$, $\partial p4_l / \partial Z$, $\partial p4_l / \partial Y$, $\partial p4_l / \partial X$), and

   ($\hat{r}_r$, $\hat{c}_r$, $p1_r$, $p2_r$, $p3_r$, $p4_r$, $\partial p1_r / \partial Z$, $\partial p1_r / \partial Y$, $\partial p1_r / \partial X$, $\partial p2_r / \partial Z$, $\partial p2_r / \partial Y$, $\partial p2_r / \partial X$, $\partial p3_r / \partial Z$, $\partial p3_r / \partial Y$, $\partial p3_r / \partial X$, $\partial p4_r / \partial Z$, $\partial p4_r / \partial Y$, $\partial p4_r / \partial X$)
3) Calculate the corrections $\Delta X, \Delta Y, \Delta Z$ by computing Eq. (6), then add them to X, Y, Z.
4) Repeat Steps 2 and 3 until the specified maximum number of iterations (e.g., 10) has been reached or X, Y, Z all converge.

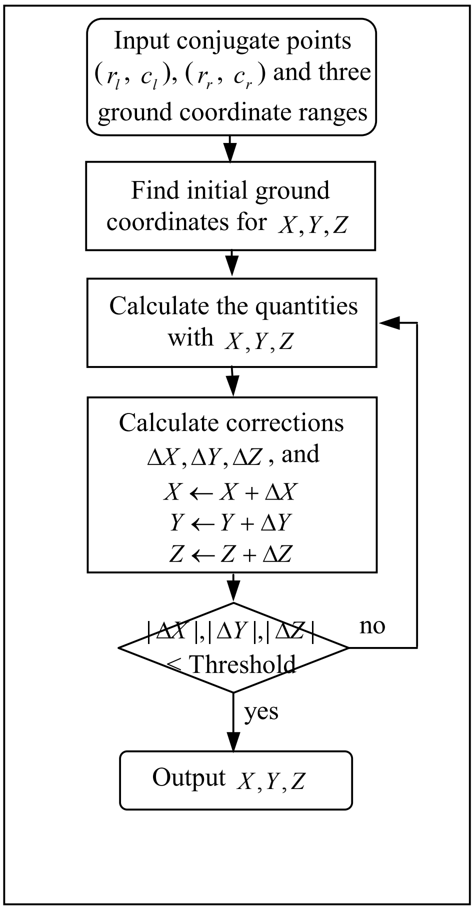

Figure 4. Flowchart of 3-D reconstruction with forward RFM

It should also be noted that the object coordinates for the two images of a stereo pair should be un-normalized or be normalized using the same offset and scale values (in the same object coordinate system) to use the above equations without changes. In our experiments, the above procedure always converged when the appropriate initial values were given. When the initial approximate values for X, Y, Z are obtained by solving Eq. (7) or set to be the median values of the ground coordinate ranges, eight iterations are usually enough to converge (a threshold of $1.0e^{-11}$ meter was used in our testing). When the initial approximate values are obtained from the result of inverse RFM reconstruction, two iterations are usually enough.

Test Results and Evaluation

Aerial Photography Data Test

We tested the two methods using an aerial photography stereo pair provided by ERDAS Inc., USA. The original stereo pair with the scale of 1:40,000 was taken in Colorado Springs, CO and both photos were scanned at 100 microns per pixel. The overlap between the two images was about 68%. The scanned size was 2313x2309 pixels, and the ground pixel size was about 4.5 meters. The relief range was from 1846.5994 meters to 2205.1539 meters. A photogrammetric bundle block adjustment with OrthoBASE was done by ERDAS and the rigorous collinearity equations with orientation parameters for both images were obtained. The average standard deviations after adjustment in object space were $(m_X, m_Y, m_Z) = (1.7008,\ 2.1577,\ 0.2957)$ meters at five control points, and $(m_X, m_Y, m_Z) = (4.2964,\ 0.7726,\ 3.8165)$ meters at one checkpoint. In the overlapping area of the stereo pair, the 3-D coordinates of 7499 object points were intersected using the rigorous collinearity equations. The corresponding 7499 points in both left and right image were also available. Figure 5 shows a 3-D view of the terrain as well as the distribution of these object points on terrain.

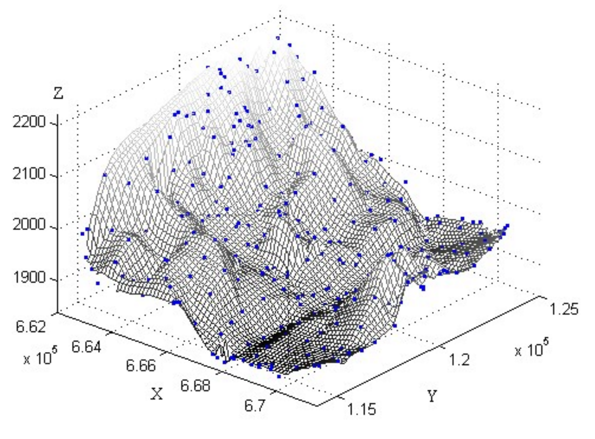

Figure 5. 3-D view of the test data and check points

Accuracy of RFM fitting

To solve the RFCs for each image, the terrain-independent approach (Tao and Hu, 2000a) was used. A 3-D control grid and a check grid in object space, as well as their corresponding image grids were generated using the rigorous collinearity equations. The image grid contained 11x11 points across the full extent of each image. The 3-D control grid contained 5 terrain layers, each with 11x11 points, and the 3-D check grid contained 10 terrain layers, each with 20x20 points. The layers covered the full range of terrain relief. The unknown RFCs in Eq. (1) and Eq. (2) were determined, respectively, using the image grid points and the 3-D object grid points. For the inverse RFM, the accuracy of the solution was checked in the object space, while, for the forward RFM, the accuracy was compared against the check grid in image. Tables 1 and 2 list the RFM accuracy results at the check grid for the left and right images with, respectively, inverse and forward form of RFM. Both RMS errors and maximum errors are given. Only the 3rd-order RFM results are provided. In Table 1, the notion of $p6 = p8$ means that the same denominator is used for X and Y in Eq. (2). In the case of $p6 = p8 \equiv 1$, RFM becomes a regular 3rd -order polynomial form. For the comparison purpose, three cases, $p6 \neq p8$, $p6 = p8$ and $p6 = p8 \equiv 1$ are all provided for the inverse RFM (Table 1) and so do for forward RFM (Table 2).

It is found that both the inverse and the forward RFM provide extremely high fitting accuracy to the collinearity equation model. The rational polynomial form can produce better accuracy than the regular polynomial form. It is also found that the use of the coordinate normalization technique can achieve results with much better accuracy than ones without normalization. As a result, the accuracy loss is hardly distinguishable when the RFM is used to "replace" the collinearity equation model. For the cases with different denominators, the maximum errors at the check grids are 6.55e-07 meters for inverse RFM and 5.52e-08 pixels for forward RFM, respectively. Accuracy of RFM based 3-D reconstruction

The 7499 corresponding points in the left and right images are input to both the inverse RFM and the forward RFM reconstruction. All the 7499 3-D object points were used to check the accuracy of the reconstruction results. The results in Tables 3a and 3b are computed using Eq. (4) and (5), respectively. The results show that use of the correction Eq. (4) can improve the accuracy to some extent. In Table 4, the median values of the three object coordinate ranges were used to start the reconstruction for the cases $p2 \neq p4$ and $p2 = p4$, while the initial values solved with Eq. (7) were used for the case of $p2 = p4 \equiv 1$. Again, use of normalization can obtain much better results than un-normalization for both inverse and forward RFM reconstruction. The results also show that no significant differences are found between the use of different denominators and the same denominator. A very interesting point from the results is that the regular polynomial form ($p2 = p4 \equiv 1$) may obtain better or the same reconstruction accuracy than both the inverse and the forward RFM when normalization is not applied.

The numbers in Tables 3 and 4 demonstrate that both methods can produce the reconstruction results with no distinguishable loss of accuracy compared to the physical sensor model. A comparison of these two reconstruction methods is summarized in Table 5. The reconstruction method with forward RFM obtains higher accuracy than that with inverse RFM except for the regular polynomial case ($p2 = p4 \equiv 1$). However, the inverse RFM can converge fast with less iterations.

Table 1. RMS (Max.) errors at the object check grid with inverse RFM fitting (unit: meters)

	case	Normalization X	Normalization Y	Un-normalization X	Un-normalization Y
Left image	$p6 \neq p8$	5.29e-08 (6.55e-07)	2.19e-08 (1.04e-07)	2.85e-03 (8.48e-03)	6.50e-03 (1.92e-01)
	$p6 = p8$	4.71e-08 (1.54e-06)	3.59e-07 (1.97e-05)	4.13e-03 (2.07e-02)	3.48e-03 (1.89e-02)
	$p6 = p8 \equiv 1$	3.16e-06 (1.91e-05)	2.14e-06 (1.26e-05)	1.06e-04 (1.65e-04)	7.60e-06 (1.88e-05)
Right image	$p6 \neq p8$	1.90e-08 (6.62e-08)	1.81e-08 (1.05e-07)	1.29e-02 (1.85e-01)	1.27e-03 (1.01e-02)
	$p6 = p8$	1.53e-08 (9.01e-08)	1.07e-08 (4.55e-08)	1.69e-03 (7.33e-03)	1.76e-03 (4.11e-03)
	$p6 = p8 \equiv 1$	9.74e-05 (5.56e-04)	6.80e-05 (4.57e-04)	1.45e-04 (5.83e-04)	6.84e-05 (4.56e-04)

Table 2. RMS (Max.) errors at the image check grid with forward RFM fitting (unit: pixels)

	case	Normalization Column	Normalization row	Un-normalization column	Un-normalization row
Left image	$p2 \neq p4$	1.16e-11 (5.73e-10)	4.40e-12 (1.11e-11)	3.64e-04 (1.12e-03)	1.26e-04 (4.89e-04)
	$p2 = p4$	1.02e-09 (6.38e-08)	2.44e-10 (1.34e-08)	1.98e-04 (1.25e-03)	2.62e-04 (1.16e-03)
	$p2 = p4 \equiv 1$	9.44e-04 (2.37e-03)	1.39e-03 (3.53e-03)	1.01e-03 (3.63e-03)	2.59e-03 (1.04e-02)
Right image	$p2 \neq p4$	3.34e-10 (1.98e-08)	1.03e-09 (5.52e-08)	2.25e-04 (7.52e-04)	1.35e-04 (3.19e-04)
	$p2 = p4$	4.07e-11 (1.38e-09)	1.92e-10 (7.52e-09)	4.96e-04 (1.96e-03)	4.17e-04 (1.42e-03)
	$p2 = p4 \equiv 1$	1.01e-03 (2.8e-03)	1.48e-03 (4.26e-03)	1.03e-03 (3.35e-03)	2.54e-03 (7.75e-03)

Table 3a. RMS (Max.) errors at 7499 check points with inverse RFM reconstruction (1) (unit: meters)

case	Normalization X	Normalization Y	Normalization Z	Un-normalization X	Un-normalization Y	Un-normalization Z
$p6 \neq p8$	4.05e-08 (3.28e-07)	1.96e-08 (1.60e-07)	6.54e-08 (3.47e-07)	1.11e-02 (2.69e-01)	3.73e-03 (1.65e-01)	1.32e-02 (3.93e-01)
$p6 = p8$	3.31e-08 (1.20e-06)	1.53e-07 (6.47e-06)	6.65e-07 (3.90e-05)	4.10e-03 (2.89e-02)	2.66e-03 (1.62e-02)	9.31e-03 (4.97e-02)
$p6 = p8 \equiv 1$	9.20e-05 (1.33e-03)	6.23e-05 (9.46e-04)	1.42e-04 (1.27e-03)	1.37e-04 (1.25e-03)	6.33e-05 (9.50e-04)	1.42e-04 (1.27e-03)

Table 3b. RMS (Max.) errors at 7499 check points with inverse RFM reconstruction (2) (unit: meters)

case	Normalization X	Normalization Y	Normalization Z	Un-normalization X	Un-normalization Y	Un-normalization Z
$p6 \neq p8$	4.37e-08 (3.58e-07)	2.96e-08 (4.39e-07)	9.86e-08 (9.42e-07)	1.62e-02 (3.18e-01)	1.29e-02 (2.80e-01)	3.32e-02 (5.61e-01)
$p6 = p8$	3.46e-08 (1.24e-06)	1.65e-07 (6.85e-06)	6.77e-07 (3.99e-05)	6.27e-03 (6.75e-02)	4.22e-03 (4.62e-02)	1.22e-02 (7.95e-02)
$p6 = p8 \equiv 1$	7.94e-05 (5.54e-04)	5.37e-05 (4.35e-04)	1.10e-04 (5.68e-04)	1.47e-04 (8.21e-04)	6.38e-05 (4.97e-04)	1.45e-04 (7.26e-04)

Table 4. RMS (Max.) errors at 7499 check points with forward RFM reconstruction (unit: meters)

case	Normalization			Un-normalization		
	X	Y	Z	X	Y	Z
$p2 \neq p4$	2.47e-09 (1.19e-07)	1.89e-09 (1.24e-07)	2.88e-09 (1.83e-07)	1.19e-03 (1.35e-02)	1.52e-03 (1.23e-02)	2.40e-03 (2.00e-02)
$p2 = p4$	3.41e-09 (2.25e-07)	2.35e-09 (1.17e-07)	8.88e-09 (5.67e-07)	2.33e-03 (1.65e-02)	2.25e-03 (1.58e-02)	4.12e-03 (1.54e-02)
$p2 = p4 \equiv 1$	6.60e-03 (2.73e-02)	4.50e-03 (1.91e-02)	2.63e-03 (1.69e-02)	1.07e-02 (5.08e-02)	4.72e-03 (2.16e-02)	3.02e-03 (1.64e-02)

Table 5. A comparison between two reconstruction methods

Comparison items	**Inverse RFM**	**Forward RFM**
Fitting accuracy (RMS in pixel)*	10^{-8}~10^{-7}	10^{-12}~10^{-9}
Reconstruction accuracy (RMS in meters)*	10^{-8}~10^{-7}	10^{-9}
Initial values required	Z	X, Y, Z
Method to obtain initial values	Set a-priori	Linear solution or set a-priori
Sensitivity to initial values	No	No
Corrections computed	ΔZ	$\Delta X, \Delta Y, \Delta Z$
Need matrix inversion	No	Yes
Need iteration	Yes	Yes
Convergence speed	Fast, ≤ 3 iterations	Slow, 8 or more iterations
* for the rational function case with normalization		

IKONOS Data Test

As an application example, the forward RFM algorithm is tested using IKONOS stereo pairs. The test work was done in the region surrounding the Bruce Nuclear Power Development near Lake Huron in southern Ontario, Canada (see Figure 6). Two IKONOS stereo pairs (referred to as Scene 1 and Scene 2) were acquired, each consisting of panchromatic 11-bit imagery that had been geocorrected to the Space Imaging *Geo* level. As a result, the specified stereo accuracy for these images is 25 m CE 90 (Circular Error 90%) horizontally, and 22 m LE 90 (Linear Error 90%), respectively (Dial, 2000). The RFCs that were supplied by Space Imaging with the imagery represented the imaging geometry to an equal accuracy level.

Evaluation of Absolute Accuracy

To measure the horizontal absolute accuracy of the RFM 3D reconstruction, a vector data set was obtained from the Canada Data Alignment Layer (CDAL). The CDAL data set consists of points that were derived from the National Topographic Database (NTDB) topographic maps. For the absolute accuracy analysis, the CDAL points derived from road intersections were used because it was hoped that the road intersections could be identified more easily than other features on the IKONOS imagery (see Figure 6). The CDAL points have a stated accuracy of 10 m CE 90% which is roughly equivalent to 4.5 m RMSE.

The pixel (column) and line (row) coordinates for 29 conjugate points were acquired for both images (Left and Right) in Scene 1. The conjugate points were selected such that they would correspond with the CDAL road intersection points. Any road intersections that seemed ambiguous (i.e., an accurate position could not be established) were discarded. The pixel and line coordinates were passed into an RFM to generate points with latitude, longitude and height coordinates. To facilitate accurate distance measurements, the CDAL points and the RFM output points were both projected into the UTM map projection. The horizontal distances between the two respective data sets was calculated and the statistics are summarized in Table 6. The result derived by the forward RFM shows the consistency to the specification from Space Imaging (Grodecki, 2001b).

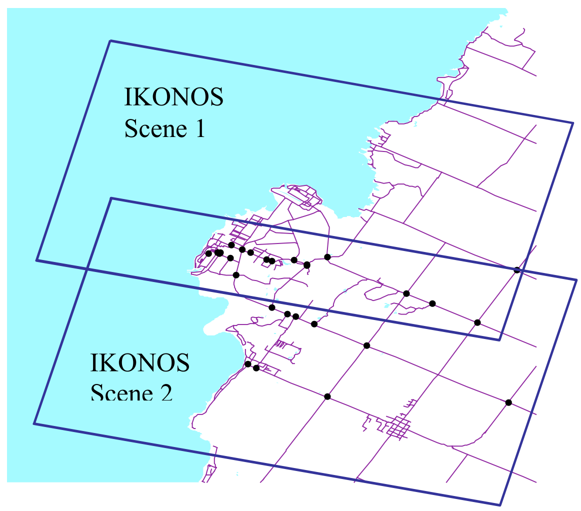

Figure 6. The testing area and the coverage of the IKONOS stereo pairs (black dots are CDAL feature points used as control points)

For the vertical absolute accuracy analysis, a DEM from the Canadian Digital Elevation Data (CDED) was obtained for the area. The product specification states that the vertical accuracy is dependent on the accuracy of the original NTDB topographic map contours that were scanned to produce the DEM. The CDAL intersection points were overlaid on the DEM to obtain orthometric heights (relative to the Canadian Geodetic Vertical Datum 1928) at each of these points. Using the software supplied by the Canadian Geodetic Survey Division, the heights were converted into ellipsoidal heights relative to the WGS84 ellipsoid. A comparison was done between these heights and those computed by the RFM and the statistics are shown in Table 7.

Table 6: Statistics for calculated horizontal distances between CDAL and RFM road intersection points (m)

Mean	6.83
RMSE	7.15
Standard Deviation	2.15
Minimum	2.37
Maximum	10.78

Table 7. Statistics for calculated elevation differences between CDAL and RFM road intersection points (m)

Mean	-3.79
RMS	4.23
Standard Deviation	1.91
Minimum	0.97

Table 8. Statistics for building points (m)

	Scene 1	Scene 2
Standard Deviation of Height Measurements	0.72	1.07
RMS of Plane-Fitting Residuals	0.68	0.68

Figure 7. Left image from Scene 1 with building rooftop points overlaid.

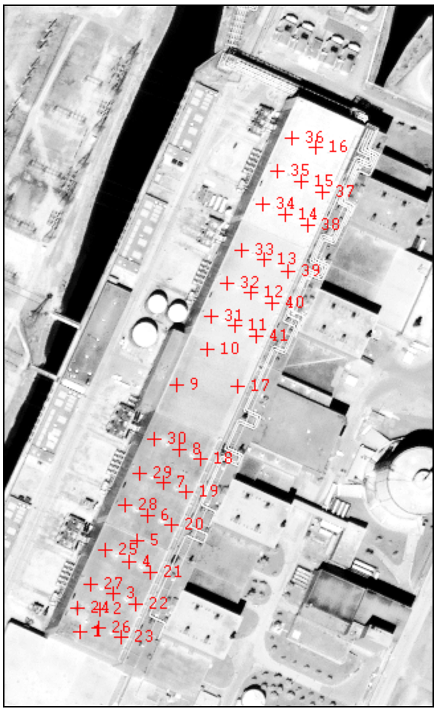

Figure 8. Left image from Scene 2 with building rooftop points overlaid.

Evaluation of Relative Accuracy

The relative horizontal accuracy assessment was done by computing the dimensions of a building using the RFM calculated corner coordinates and comparing them to the actual known distances. The dimension of the building (from the engineering design) is 54.86 m in width and 445.00m in length. The difference between the RFM calculated dimension and the given values is 0.50 m in width and 0.14 m in length.

To obtain a measure of the relative vertical accuracy of the RFM 3D reconstruction, conjugate points were collected on the roof tops of one building in each scene. The distribution of the points are shown in Figures 7 and 8 and the standard deviations of the Z-coordinates calculated by the RFM are shown in Table 8. Under the assumption that the building roof tops were planar surfaces, a plane function was fit to the point data using a least-squares method. The RMS values of the surface-fitting residuals for the two buildings are also shown in Table 8. The tests show that the relative accuracy in both horizontal and vertical directions of IKONOS Geo level images is high.

Concluding Remarks

This study investigated two methods for RFM-based 3-D reconstruction, inverse RFM method and forward RFM method. Experiments using a real aerial stereo pair validated the feasibility of the two reconstruction methods. Each method was shown to have its own strengths and weaknesses. Both methods can obtain reconstruction results with no distinguishable loss of accuracy compared to the physical sensor model. The forward RFM can expect better results. They both can converge well with the threshold set to be one or two magnitudes smaller than the RFM approximating accuracy and are not sensitive to their initial approximate values, provided the initial values are set reasonably. Additionally, the reconstruction result from the inverse RFM can be input to the forward RFM to speed the convergence of the latter method and also to reduce the number of iterations needed.

Despite the fact that different transformation directions are employed, both methods are based on the same rational functions. Our experimental results show that both methods basically perform identically. This demonstrates that the ability of 3-D reconstruction lies in the geometry of the rational functions rather than the method used. The achievable accuracy of the RFM-based 3-D reconstruction is mainly affected by the fitting accuracy of the RFM and eventually affected by the physical sensor model used for the determination of the RFCs in the RFM. If the accuracy of the RFCs solution provided is not good enough, are we able to use additional control information (e.g., GCPs) to update the values of RFCs? We have proposed a Kalman filtering based incremental method to address this issue (Hu and Tao, 2001).

RFM has also been considered by the OpenGIS Consortium (OGC, 1999) as a part of the standard image transfer format due to its characteristic of sensor independence. We feel that use of RFM would be a key driving force towards the interoperability between the image exploitation software (Tao and Hu, 2001). In fact, one can develop a software package with a generic interface to handle the RFM for various sensors, provided that the RFM and its RFCs are supplied. This is very beneficial in terms of making photogrammetric processing interoperable. If each sensory image comes with a set of RFCs (solved or supplied by the data vendor), end users and developers will be able to perform the subsequent photogrammetric processing without knowing the sophisticated physical sensor model. Driven by this fact, we have developed a software package, Rational Mapper, which utilizes the RFM for image exploitation including ortho-rectification and 3-D reconstruction. Figure 9 shows a web-based interface on 3-D reconstruction of Rational Mapper.

Acknowledgements

The testing work for IKONOS stereo pairs was done by Mr. Steve Schnick, research associate at the University of Calgary. Special thanks go to Dr. Xinghe Yang, ERDAS, Inc. for providing his valuable comments and Dr. Yongnian Wang, ERDAS, Inc. for providing the aerial stereo pair with orientation parameters for this research. We also would like to thank Dr. Philip Cheng from PCI Geomatics; Dr. Thierry Toutin from Canada Remote Sensing Centre; Dr. Clive Fraser, University of Melbourne; Dr. J. Bryan Mercer, Intermap Technologies Corp.; Dr. Mostafa Madani from Z/I Imaging, Mr. Brian Robertson from MDA, and Prof. Gordon Petrie from University of Glasgow for the comments and information exchange.

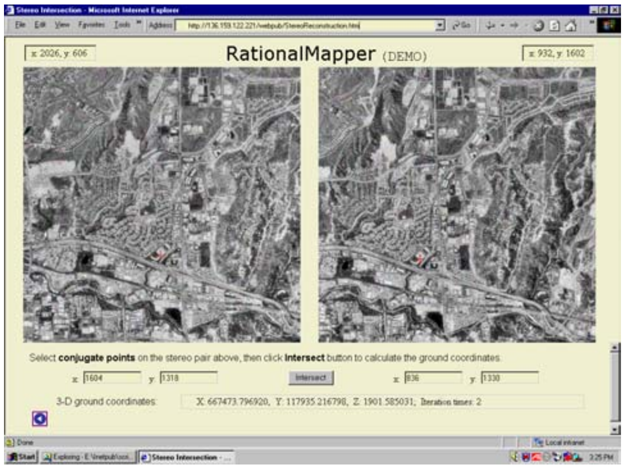

Figure 9. The web interface of Rational Mapper on 3-D reconstruction

References

Di, K., Ma, R., Li, R., 2001. Deriving 3-D shorelines from high resolution IKONOS satellite images with rational functions. *Proceedings of 2001 ASPRS Annual convention,* St. Louis., April 24-27.

Dial, G., 2000. IKONOS satellite mapping accuracy. *Proceedings of 2000 ASPRS Annual convention*, Washington DC, 22-26, May 2000.

Dowman, I., Dolloff, J.T., 2000. An evaluation of rational functions for photogrammetric restitution. *Int. Arch. Photogrammetry and Remote Sensing*, 33, 254-266.

Greve, C. W., Molander, C. W., Gordon, D. K., 1992. Image processing on open systems. *Photogrammetric Engineering & Remote Sensing*, 85-89.

Grodecki, J., 2001a. IKONOS stereo feature extraction - RPC approach. *Proceedings of 2001 ASPRS Annual Conference*, St. Louis., April 24-27.

Grodecki, J., 2001b. IKONOS Geometric Accuracy, *Proceedings of ISPRS Workshop on High Resolution Mapping from Space 2001,* Hannover, September 19-21.

Hu, Y., Tao, C.V., 2001. Updating Solutions of the Rational Function Model Using Additional Control Information, *Proceedings of ISPRS Workshop on High Resolution Mapping from Space 2001,* Hannover, September 19-21.

Madani, M., 1999. Real-time sensor-independent positioning by rational functions. *Proceedings of ISPRS Workshop on "Direct versus indirect methods of sensor orientation"*, Barcelona, November 25-26, 64-75.

McGlone, C., 1996. Sensor modeling in image registration, In: Greve C. W. *Digital Photogrammetry: an addendum*, published by ASPRS, 115-123.

NIMA., 2000. The compendium of controlled extensions (CE) for the national imagery transmission format (NITF), version 2.1, URL: http://www.ismc.nima.mil/ntb/superceded/STDI-0002_v2.1.pdf.

Novak, K., 1992. Rectification of digital imagery. *Photogrammetry and Remote Sensing*, 58(3): 339-344.

OpenGIS Consortium, 1999. *The OpenGIS Abstract Specification - Topic 7: The Earth Imagery Case*, http://www.opengis.org/public/abstract/99-107.pdf.

Paderes, Jr., F. C., Mikhail, E. M., Fagerman, J. A., 1989. Batch and on-line evaluation of stereo SPOT imagery, *Proceedings of the ASPRS-ACSM Convention*, Baltimore, April, pp. 31-40.

Tao, C. V., Hu, Y., 2000a. Rational Function Model and Its applications for Photogrammetric Processing [on-line]. URL: http://geomaci.geomatics.ucalhary.ca

Tao, C. V., Hu, Y., 2000b. Investigation on the rational function model. *Proceedings of ASPRS Annual Convention*, Washington D.C., May 22-26.

Tao, C. V., Hu, Y., 2000c. A Comprehensive Study on the Rational Function Model for Photogrammetric Processing, *Photogrammetric Engineering & Remote Sensing (accepted)*

Tao, C. V., Hu, Y., 2000d. Study of the rational function model for image rectification. In: *Proc. of Canadian Conference on Remote Sensing*, August 22-25, Victoria, BC, pp. 55 – 64.

Tao, C.V., Hu, Y., Mercer, B., Zhang, Y., 2000. Image Rectification Using A Generic Sensor Model – Rational Function Model, *Int. Arch. Photogrammetry and Remote Sensing,* 33 (Part B3), 874-881.

Tao, C. V., Hu, Y., 2001. The rational function model - a tool for processing high-resolution imagery. *Earth Observation Magazine (EOM)*, 10(1): 13-16.

Toutin, T., Cheng, P., 2000. Demystification of IKONOS, *Earth Observation Magazine (EOM)*, 9(7): 17-21.

Yang, X., 2000. Accuracy of rational function approximation in photogrammetry. *Proceedings of ASPRS Annual Convention*, Washington D.C., May 22-26.

GEOMETRIC PROCESSING OF IKONOS GEO IMAGES WITH DEM

Thierry Toutin
Natural Resources Canada, Canada Centre for Remote Sensing
588 Booth Street, Ottawa, Ontario, Canada, K1A 0Y7
thierry.toutin@CCRS.Nrcan.gc.ca

KEY WORDS

Geometric evaluation, Error propagation, IKONOS

ABSTRACT

Thirteen Pan or XS IKONOS Geo-product images over seven study sites with various environments and terrain were tested using different cartographic data and accuracies using a parametric modelling developed at the Canada Centre for Remote Sensing. The objectives were to track the error propagation during the full geometric correction process (bundle adjustment and ortho-rectification). When ground control points (GCPs) are less than 3-m accurate, 20 GCPs over the full image is a good compromise to obtain 3-4 m accuracy in the bundle adjustment. When cartographic co-ordinates are better than 1-m, 10 GCPs are then enough to increase to 2-3 m accuracy with either panchromatic or multiband images. The remaining error is due to GCP definition and plotting. Quantitative and qualitative evaluations of ortho-images were performed with independent check points or digital vector files. Positioning accuracy of 2-4 m is achieved for the ortho-images depending of the elevation accuracy (DEM and grid spacing). To achieve a better final positioning accuracy, such as 1 m, 1-2 m accurate DEM with fine grid spacing is required in addition to well-defined GCPs benchmarked on the ground.

1. INTRODUCTION

IKONOS, launched September 24 1999, orbits the Earth once every 98 minutes at an altitude of approximately 680 kilometres in a sun-synchronous path. The sensor is capable of viewing up-to-60º in any azimuth (in-track and cross-track pointing). The satellite's sensor generates 1-m panchromatic (Pan) and 4-m multi-band (XS) images if they are acquired with a viewing angle between 0º and 26º. Over 26º viewing angles Space Imaging insures 2-m resolution for the panchromatic images (Space Imaging, 2001). Only map georeferenced and a range of orthorectified products with applied geometric correction and oriented to the North are delivered by Space Imaging. The Geo product, which is the most affordable but offers the lowest positioning accuracy, is not corrected for terrain distortions. It has an accuracy of 50m with 90% level of confidence. Accuracy becomes worse in mountainous areas if the images are acquired with off-nadir viewing, which commonly occur for the IKONOS data. Hence, the product will only meet the geometric requirements of mapping scale at 1:250,000 in flat area or less in mountainous areas.

Preliminary accuracy tests with real images using a parametric geometric correction model were performed with few precise GCPs (Toutin and Cheng, 2000; Kersten *et al.*, 2000; Davies and Wang, 2001). Their results demonstrated accuracy in planimetry of around 2-3 m and then confirmed that IKONOS images have a high potential for mapping.

The objectives of this paper are to expand on these preliminary results with a larger data set of IKONOS images: 1-m Pan and 4-m XS, acquired with 10º-30º viewing angles at different azimuth angles. The study sites span low-to-high relief in urban, semi-rural and rural areas of North America and Europe with different topographic data and accuracy. Using a multi-sensor geometric model developed at the Canada Centre for Remote Sensing (CCRS) (Toutin, 1995) and adapted to IKONOS images (Toutin and Cheng, 2000), the paper will track the error propagation from the input data to the final ortho-image. Different cartographic parameters affecting the accuracy are also evaluated.

2. STUDY SITES and DATA SET

Seven study sites with different environments and relief are used in this research. IKONOS Geo-product data (some acquired by international collaborators), covering an area of approximately 10 km by 10 km, have been acquired either in Pan mode and/or XS (Table 1):

1. Toronto, Ontario, Canada is a sub-urban environment and a flat topography with 60-m elevation range. Pan image was acquired April 23, 2000 with collection and azimuth angles of 51º and 21º, respectively. 30 GCPs were collected and their map coordinates were obtained from 20-cm pixel ortho-photos with 0.5-m accuracy and 2-m grid spacing DEM with 5-m accuracy;
2. Beauport, Quebec, Canada is a residential and semi-rural environment and a hilly topography with 500-m elevation range. Two Pan images were acquired January 3, 2001 with collection and azimuth angles for each image of 63º and 322º, 63º and 252º, respectively. 56 GCPs were collected and their map coordinates were obtained from six 1-m pixel ortho-photos with 3-m accuracy and 5-m grid spacing DEM with 5-m accuracy. However, a mean positioning error of 5-7 m in the X direction was found between the different ortho-photos; this error is mainly due to 5-m DEM error during the ortho-photo generation;
3. Toulouse, France is an sub-urban environment and a flat topography with 100-m elevation range. Pan and XS images simultaneously were acquired May 14, 2000 with collection and azimuth angles of 70º and 138º, respectively. 33 GCPs were collected and their map coordinates were obtained from 0.5-m pixel ortho-photo mosaic with 1-m accuracy and 10-m grid spacing DEM with 5-m accuracy;
4. Trier, Germany is an urban and semi-rural environment and a rolling topography with 300-m elevation range. XS image was acquired June 13, 2000 with collection and azimuth angles of 65º and 177º, respectively. 23 GCPs were collected and their map coordinates were obtained from differential GPS with 0.5-m accuracy and 20-m grid spacing DEM with 5-m accuracy;
5. Dresden, Germany is a rural environment and a rolling topography with 300-m elevation range (Meinel *et al.*, 2001). Pan and XS co-registred images were simultaneously acquired August 1, 2000 with collection and azimuth angles of 71º and 335º, respectively. 112 GCPs were collected and their map coordinates were obtained from 1:10,000 topographic maps

with 4-m accuracy and 1-m grid spacing laserscanning DEM with 1-m accuracy. In addition, a second set of map coordinates (118 GCPs) were obtained from 0.4-m pixel ortho-photo mosaic with 1-m accuracy;

6. Caracas, Venezuela is a urban and rural environment and a mountainous topography with 2200-m elevation range (Arismendi *et al.*, 2000). Four Pan in-track images were acquired from the same orbit December 30, 1999 with collection and azimuth angles for each image of 59º and 12º, 65º and 46º, 73º and 71º, 76º and 122º, respectively. Around 30 GCPs were collected for each image and their map coordinates were obtained from 2.5-m pixel ortho-photos with 5-m accuracy and 5-m grid spacing DEM with 5-m accuracy; and
7. Luzern, Switzerland is an urban and rural environment and a mountainous topography with 2000-m elevation range. Pan image was acquired April 22, 2000 with collection and azimuth angles of 68º and 256º, respectively. 70 GCPs were collected and their map coordinates were obtained from 1.25-m pixel images of scanned 1:25,000 topographic maps with 5-m accuracy in the three axes.

Table 1: Description of study sites with environment types, relief and elevation variation (Δelevation), of IKONOS images with mode, collection (Coll.) and azimuth (Az.) angles and of cartographic data with number of GCPs, accuracy of the planimetry (Plani.) and DEM. For Dresden study site, different GCPs were collected twice with different cartographic accuracies.

Study Site	Environment Type	Relief Δelevation	IKONOS Image			Cartographic Data		
			Mode	Coll.	Az.	GCP	Plani.	DEM
Toronto Canada	Sub-urban	Flat 60 m	Pan	51º	21º	30	0.5 m	5 m
Beauport Canada	Residential Semi-rural	Hilly 500 m	Pan Pan	63º 63º	322º 252º	56	3-7 m	5 m
Toulouse France	Sub-urban Rural	Flat 100 m	Pan XS	70º	138º	33	1 m	5 m
Trier Germany	Urban Semi-rural	Rolling 300 m	XS	65º	177º	23	0.5 m	5 m
Dresden Germany	Rural	Rolling 300 m	Pan XS	71º	335º	115	1) 4 m 2) 1 m	1 m
Caracas Venezuela	Urban Rural	Mountains 2200 m	4 Pan	59º to 76º	12º to 122º	30	5 m	5 m
Luzern Switzerland	Urban Rural	Mountains 1800 m	Pan	68º	256º	35	5 m	

Since the processing is performed on the full image area, GCPs cover the total surface (100 km^2) with also points at the lowest and highest elevation to avoid extrapolations, both in planimetry and altimetry. In general, the plotting accuracy for Pan images is about 1-2 pixels in the urban and sub-urban areas and 2-3 pixels in the rural and mountainous areas due to the difficulty to find and locate 1-m precise ground elements. For XS images, the plotting accuracy depends of the method used to evaluate different possibilities and the environment:

- in the Trier site, GCPs have been plotted on the XS image, most of them in the urban environment with an accuracy of half-pixel (about 2 m);
- in the Dresden site, GCP coordinates have been imported and computed by dividing by four

from Pan image coordinates with the same accuracy, 2-3 m in rural environment; and

- in the Toulouse site, GCPs collected on the Pan image have been re-plotted on the XS image with an accuracy better than one pixel. However, these points are not necessarily the best defined in the XS image.

3. RESULTS AND DISCUSSIONS

The error propagation can be tracked along the geometric processing steps with bundle adjustment results on independent check points (ICPs) as a function of GCP numbers, location and accuracies and with the ortho-images as a function of DEM accuracy and spacing. It should be noted that the processing is performed on the full image size (about 100 km^2) and not only on small sub-area.

Bundle Adjustment Results

The first test is performed using different GCPs/ICPs configurations using the Dresden site, which has the most complete data set, were thus evaluated to find the optimal number of GCPs in relation with the error of the cartographic co-ordinates. With Dresden_Pan1 data set, the number of GCPs varies from 112 to 6 and the results (Figure 1, left) are evaluated on the 118 1-m accurate ICPs from the second set of coordinates (Dresden_Pan2). With Dresden_Pan2 data set, the number of GCPs varies from 70 to 6 and the results (Figure 1, right) are evaluated on the remaining ICPs (from 48 to 112, respectively).

In Figure 1 (left), the RMS error on ICPs is always more than 3 m whatever the number of GCPs (even 112), and 15-20 GCPs are a good compromise to keep 3-4 m accuracy. The combination of cartographic and plotting errors (4 m and 2-3 m, respectively) avoid a better accuracy to be obtained, even with a large degree of freedom in the least square adjustment. On the other hand (Figure 1, right), the RMS error consistently decreases to 2-3 m when using the 1-m accurate second set of GCP coordinates (Dresden_Pan2), with slightly better results in the Y-coordinate. Ten precisely located GCPs are then a good compromise to achieve this 2-3 m accuracy. For this test, the RMS error reflects the major source of error, which is the plotting error (2-3 m).

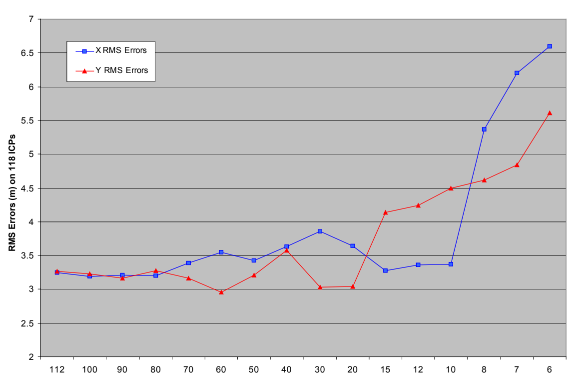

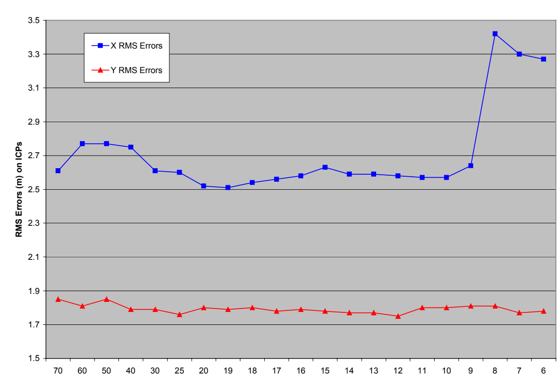

Figure 1.Left: Root mean square (RMS) errors (in metres) on 118 1-m accurate ICPs from the least-square bundle adjustment computed with GCPs varying from 112 to 6 for the Dresden

study site. Right: RMS errors (in metres) on 1-m accurate ICPs from the least-square bundle adjustment computed with GCPs varying from 70 to 6 for the Dresden study site.
By applying these values (25 GCPs for 5-m accurate coordinates and 10 GCPs for 1-m accurate coordinates) on the other data set, Table 2 shows statistical results of the bundle adjustment: number of GCPs/ICPs and the RMS and minimum/maximum errors on the ICPs. For some data sets (Toronto, Caracas), a smaller number of GCPs is used to keep enough ICPs for the statistical evaluation. When the cartographic coordinates are 1-m precise (Toronto, Toulouse, Trier, Dresden_2), RMS errors are always around 2-3 m with slightly worse results for Toulouse. The accuracies for these data sets are due to the plotting errors for each image depending of the environment. When the cartographic coordinates are 5-m precise (Beauport, Dresden_1, Caracas, Luzern), the RMS errors are a little worse than 3-5 m with slightly worse results for Beauport in the X-direction due to the ortho-photo X-error. The slightly worse results for Caracas are partly related to the reduced number of GCPs in the least square adjustment: 12 instead of 20 reducing the advantages of least square adjustment. Consequently, the errors for these data sets result from the map coordinate errors for each study site. These results then confirm the first results on Dresden. Finally, the RMS errors on ICPs are 10-15% higher than the RMS residuals on GCPs, and are in the order of magnitude of the input data errors. Consequently, the results of the bundle adjustment reflect the cartographic error and this cartographic error does not propagate through the modelling but through the residuals.

Table 2: Bundle adjustment results for all study sites with the number of GCPs and ICPs, the root mean square (RMS) and min./max errors (in metres) on the ICPs. For Dresden study site, there are two sets of results as a function of different GCP numbers and accuracies. For Beauport and Caracas study sites, results are given for the different Pan images (A, B, C, D).

Study Site	GCP Number	ICP Number	RMS Errors		Min./Max Errors	
			X	Y	X	Y
Toronto	7	23	1.3	1.3	-3/3	-3/2
Beauport_A	20	36	7.5	2.7	-16/6	-2/6
Beauport_B	20	36	7.6	2.6	-16/11	-4/7
Toulouse_Pan	10	23	3.9	1.8	-8/3	-3/5
Toulouse_XS	10	23	4.9	3.3	-5/11	-6/5
Trier	10	12	2.3	1.8	-3/5	-2/4
Dresden_Pan1	20	118	4.1	2.7	-8/4	-5/8
Dresden_XS1	20	118	4.1	2.7	-8/4	-5/8
Dresden_Pan2	10	108	2.9	1.7	-7/7	-4/5
Dresden_XS2	10	108	2.9	1.7	-7/7	-4/5
Caracas_A	12	15	2.9	3.9	-6/4	-6/7
Caracas_B	12	23	6.4	4.4	-11/12	-9/14
Caracas_C	12	26	6.9	4.4	-13/8	-4/4
Caracas_D	12	12	3.4	4.4	-5/5	-9/7
Luzern	20	56	5.8	3.0	-10/11	-8/9

Refining this analysis demonstrates that the RMS errors are slightly larger than the ICP planimetric error when the input coordinates are 1-m or less precise (Toronto, Toulouse, Trier, Dresden_2). It is the reverse when the input coordinates are 5-m precise (Beauport, Dresden_1, Caracas, Luzern). In fact, the plotting error is the major source of error in the first case (2-3 m versus 1 m) while the map coordinate error is the major source in the second case (5 m versus 2-3 m). When the plotting error is the major source of error, it thus explains that:

- the RMS error differences between Pan and XS images (Toulouse) are not proportional to pixel spacing because the plotting accuracy is about the same (2-3 m);
- the RMS errors in urban environment (Toronto, Trier) are better than the RMS errors in rural environment (Toulouse, Dresden_2) because the GCP definition and plotting are more accurate in urban environment; and
- The RMS errors for XS images are correlated with the plotting error: the best results for Trier (RMS and plotting error of 1.4 m and 2 m, respectively) and the worse for Toulouse (RMS and plotting error of 3 m and 4 m, respectively). In Toulouse the GCPs firstly collected from the Pan image were not necessarily the best-defined points in the XS image.

The last test on bundle adjustment is related to the location of GCPs. It is well known that extrapolation in planimetry outside of the GCP boundary is not recommended. However, it is not well recognized that large extrapolation should also not be applied in the elevation direction. To test the impact of elevation extrapolation, Caracas and Luzern study sites are used because they have more than 2000-m elevation difference. When the highest GCP used in the bundle adjustment is 1000-m lower than the mountain summit (generating 1000-m extrapolation) the largest planimetric errors on the highest ICPs are around 20-30 m. This error reduced to 10 m when the elevation extrapolation is reduced to 500 m.

These tests demonstrate that the CCRS-developed model and method are both stable and robust for IKONOS Geo-product images without generating local errors, and filter random or systematic errors. The input GCP error does not propagate through the rigorous model, but is reflected in the residual. It then gives a good level of confidence of the applicability and robustness of the CCRS parametric model applied to IKONOS Geo-product data in operational environments.

Ortho-images Results

Evaluations of ortho-images of three study sites are performed (Beauport_A, Trier and Dresden). These sites were chosen because digital vector files with 1-3 m accuracy were available. Figure 2 shows the ortho images with vector lines overlaid: Trier (top left), Dresden (top right) and Beauport (top right) compared to otho-photo (bottom right). For Beauport_A, a first quantitative comparison of the panchromatic ortho-image (1-m pixel) was realized with 31 ICPs extracted both from 3-m accurate vector lines. RMS errors of 5 m and 3 m with 1.5-m and –0.5-m bias for X and Y, respectively were computed with no errors larger than 10 m when compared to the vector lines. In a second step, qualitative analysis is performed on the ortho-image (Figure 2, top right) and the ortho-photo (Figure 2, bottom right). The road vector lines are always inside the IKONOS roads: considering 10-m width for the main road, 4-m error can be estimated. These two estimated errors from checkpoints and vector lines are better than a circular error of 8 m directly computed from the ICP errors (Table 2) (the 5-m elevation error has only 2.5-m error impact in the error budget). However, the 5-7 m X-error of the ortho-photos is included in the 8-m circular error, which then biased the predicted error. Furthermore, when comparing the same roads overlaid on the 1-m ortho-photo the same deviations can be noticed: it could mean that part of errors comes from the 3-m error vector lines. Evaluation on other features, such as secondary roads, rivers and even private houses confirms the 4-m error.

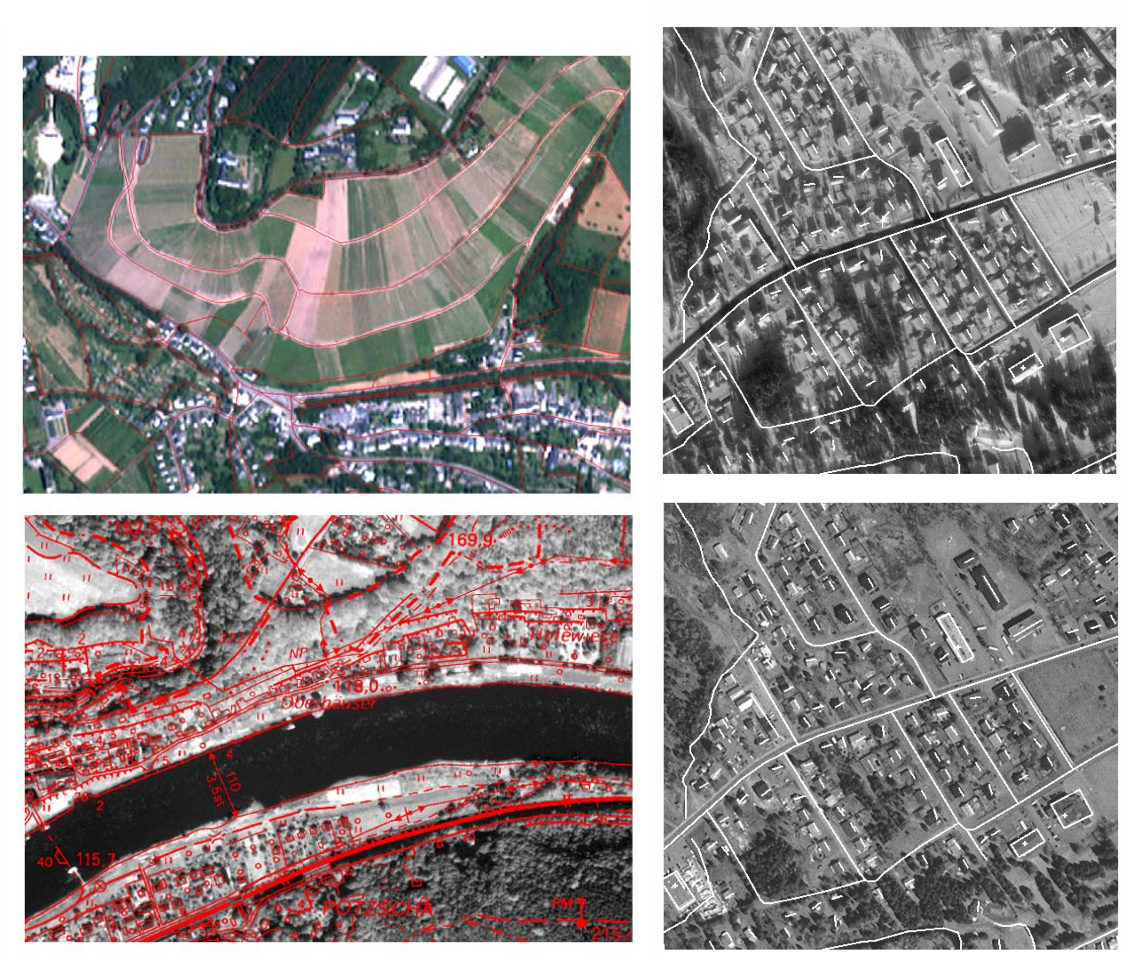

Figure 2. Top-left: sub-area of the Trier ortho-image (2-m pixel spacing, 640 pixels by 440 lines) with 2-m accurate vector lines overlaid. Bottom-right: Dresden ortho-image (1-m pixel spacing, 940 pixels by 660 lines) with 2-m accurate vector lines overlaid. Top-right: sub-area of the Beauport_A ortho-image (1-m pixel spacing, 512 pixels by 512 lines). Bottom-right: Beauport ortho-photo (1-m pixel spacing, 512 pixels by 512 lines) with 1:25,000 3-m accurate vector lines overlaid.

For Dresden, the quantitative comparison of the Pan ortho-image (1-m pixel) was independently realized at Dresden using 31 independent check points extracted from the 0.4-m pixel ortho-photo mosaic with 1-m accuracy. RMS errors of 2 m with 0.5-m bias in both axes were computed with no errors larger than 5 m. It is consistent with a circular error of 3 m directly computed from the ICP errors (Table 2) because the 1-m elevation error has a minor impact in the ortho-rectification process and in the error budget.

Trier and Dresden images with the vector files were evaluated both in Canada and Germany: there is in general a good superposition between the vectors on the appropriate image features. The Trier sub-area (640 pixels by 440 lines) is the most pronounced relief area of the full image with 150-m elevation variation along a steep vineyard. The cartographic lines along the slope, such as in the villages appear to exactly conform to ortho-image geometry with one pixel error

(2 m). It is more evident in 3-m wide vineyard tracks. This approximate error evaluation is consistent and even better than the predicted error of 4 m, previously computed. For Dresden sub-area (940 pixels by 660 lines), the coastlines of the river show errors no more than 2-3 pixels (2-3 m). Other well-defined features, such as roads or city streets visually show the same accurate superposition with the ortho-image in accordance with the check point accuracy evaluation previously done. More results on the other study sites will be given at the Workshop.

4. CONCLUSIONS

To expand on the applicability of CCRS-developed geometric model for IKONOS Geo-product images, 13 Pan or XS images from five international collaborators over seven study sites with various environments and terrain were tested. Cartographic data (maps, ortho-photos, GCPs, DEM, digital vector files) were acquired from different sources, methods and accuracy. The objective of the paper was to track the error propagation during the full geometric correction process (bundle adjustment and ortho-rectification).

When GCPs are less than 3-m accurate, 20 GCPs is a good compromise to obtain 3-4 m accuracy in the bundle adjustment. When they are better than 1-m, 10 GCPs are then enough to achieve 2-3 m accuracy. In the first result, map coordinates is the major source of error while it is the GCP definition and plotting error in the second result. With good GCPs (1-2 pixel accurate for the definition and plotting; 1-m accurate for the map coordinates), 2-m accuracy can be achieved in the bundle adjustment of both Pan and XS images (Toronto and Trier, respectively). Since definition and plotting error of GCPs becomes a key aspect with IKONOS images to increase the final accuracy (to 1-2 m), future research at CCRS will address this point with benchmark on the ground for defining 1-m precise GCP, as done in photogrammetry.

To track the error during the ortho-rectification, quantitative and qualitative evaluations of relative and absolute errors in the ortho-images were performed with either independent check points or digital vector files overlaid. Generally, the measured errors confirm the predicted errors or even were slightly better: 2-m accuracy was achieved for some ortho-images when the cartographic data was of good quality and 4-m accuracy for the others. To achieve a better positioning accuracy, such as 1 m, 1-2 m accurate DEM with fine grid spacing is required in addition to precise GCPs (definition, plotting and map).

Acknowledgements

The author wants to thank his international collaborators for the IKONOS and/or cartographic data in the different study sites: Dr. Philip Cheng of PCI Geomatics, Canada for Toronto; Mr. Réjean Matte of Ministère des Ressources naturelles du Québec, Canada for Beauport; Mr. Didier Giacobbo of GDTA, France for Toulouse; Prof. Joachim Hill of Trier University, Germany, for Trier; Dr. Gotthard Meinel of Institut für ökologische Raumentwicklung, Germany for Dresden; Lic. Ramiro Salcedo of Instituto de Ingenieria, Venezula for Caracas; Mr. Jean-Pierre Perret of the Federal Office of Topography, Switzerland for Luzern. He also thanks MM. René Chénier and Yves Carbonneau of Consultants TGIS inc., Canada for the data processing.

References

Arismendi, J., R. Salcedo, y D. Varela, 2000. Geomorfologia Actual y Cobertura Natural de la Vertiente Norte de la Cordillera de la Costa Afectada por el Evento Hidrometeorologico de Diciembre 99, A Partir de la Interpretacion de Imagenes de Satelite, In: IX International Symposium of the LatinAmerican Society of Remote Sensing (SELPER*),* Puerto Iguazu, Misiones, Argentina, 6-10 Novembre 2000, pp. 505-516.

Davies C. H., and X. Wang, 2001. Planimetric Accuracy of IKONOS 1-m Panchromatic Image Products, In: 2001 ASPRS Annual Conference, St. Louis, MI, USA, April 23 - 27, CD-ROM.

Kersten, Th., E. Baltsavias, M. Schwarz und I. Leiss, 2000. IKONOS-2 Carterra™ Geo: Erste geometrische Genauigkeits-untersuchungen in der Schweiz mit hochauflösenden Satellitendate. Photogrammetrie, Fernerkundung, Kulturtechnik, Vol. 98, No. 8, pp. 490-497.

Meinel, G., M. Neubert and J. Reder, 2001, Pixelorientierte versus segmentorientierte Klassification von IKONOS-Satellitenbildendaten – ein Methodenvergleich. Photogrammetrie Fernerkundung Geoinformation, Heft 3:157-170.

Space Imaging, 2001, www.spaceimaging.com.

Toutin, Th., and P. Cheng, 2000. Demystification of IKONOS. Earth Observation Magazine, Vol. 9, No. 7, pp. 17-21. http://www.ccrs.nrcan.gc.ca/ccrs/eduref/ref/bibpdf/4807.pdf.

Toutin, Th., 1995. Multisource data fusion with an integrated and unified geometric modelling. EARSeL Journal Advances in Remote Sensing, Vol. 4, No. 2, pp. 118-129. http://www.ccrs.nrcan.gc.ca/ccrs/eduref/ref/bibpdf/1223.pdf.

3D GEOMETRIC MODELLING OF IKONOS GEO IMAGES

Thierry Toutin, René Chénier* and Yves Carbonneau*
Natural Resources Canada, Canada Centre for Remote Sensing
588 Booth Street, Ottawa, Ontario, Canada, K1A 0Y7
thierry.toutin@ccrs.nrcan.gc.ca

KEY WORDS

3D modelling, DEM, 3D accuracy analysis, Error propagation, IKONOS

ABSTRACT

Digital elevation model (DEM) extracted from IKONOS along-track stereo images with photogrammetric method is evaluated. As few as 12 GCPs are enough for the stereo photogrammetric bundle adjustment, which also filters the errors of the input data. With an area-based image matching users may produce high resolution DEMs with LE68 errors of 1 m to 4 m depending on the land covers. The best results (1.1 m-2.6 m) are obtained in bare soils, lakes, residential areas and sparse forests. The surface elevation of some of the areas (residential/ forests) did not affect too much the errors because the 1-2-storey houses in residential areas are sparse or because the images were acquired when there is no leave in the deciduous forests. An error evaluation as a function of the slope azimuths shows that the DEM error in sun-facing slopes is 1-m smaller than the DEM error in slopes away from the sun. 5-10 m contour lines could thus be derived with the highest topographic standard.

1. IKONOS STEREO DATA

Three main attributes of IKONOS imagery for stereoscopic capabilities are 360º pointing capability, a base-to-height (B/H) ratio of 0.6 and greater, which is similar to aerial photographs, and the highest resolution available to civilian remote sensing and mapping communities. The 360º pointing capability enables the generation of across-track stereoscopy from two different orbits, such as with SPOT-HRV, as well as, along-track stereoscopy from the same orbit, such as with JERS-1's Optical Sensor. The across-track solution has been used more since 1980; however the along-track solution as applied to space frame cameras has received renewed popularity in the past 10 years. In fact, same-date along-track stereo-data acquisition gives a strong advantage to multi-date across-track stereo-data acquisition because it reduces radiometric image variations (temporal changes, sun illumination, etc.), and thus increases the correlation success rate in any image matching process.

This along-track solution to acquire stereo data is generally chosen by Space Imaging not only for scientific, but also for operational reasons. These stereo data are only available for governmental administrations as long as they are not used for commercial purposes (marketing, selling and distributing). Since Space Imaging does not provide the raw data with their ancillary data, preferred by the photogrammetrist community, only one quite similar to the GEO product can be ordered for stereo data. IKONOS stereo images are distributed in a quasi epipolar-geometry reference where only the elevation parallax in the scanner direction remains. For along-track stereoscopy with the IKONOS orbit, it approximately corresponds to a North-South direction, with few degrees in azimuth depending of the across-track component of the total collection angle. They are distributed in 8-bit or 11-bit GeoTiff format with an ASCII metadata file (including order parameters, source image and products file descriptions), however, detailed orbital information is not included. Since archive orders are generally not available for stereo-images, newly collected data is typically delivered in two or more weeks, depending upon order size, weather, and accuracy.

---

* Under contract with Consultants TGIS inc., 7667 Curé Clermont (Québec) H1K 1X2, Canada

Largely extrapolated on results from similar systems mounted on aircraft platforms or from scanned aerial photos, IKONOS stereo-images should have a potential for creating DEMs with about 2m accuracy for use in national mapping (Ridley *et al.*, 1997). This accuracy can be consistently achieved only if photogrammetric processing is employed (Li., 1998) and if the DEM is manually edited with 3D capability for surface elevation. Work still need to be carried out to evaluate the possibility for automating some processing steps and for using existing cartographic data, such as breaklines, hydrographic features and buildings. The objectives of this paper are to expand on these preliminary results with real IKONOS stereo images acquired from same orbit. Using a photogrammetric-based stereo-model developed at the Canada Centre for Remote Sensing (CCRS) (Toutin, 1995) and adapted to IKONOS images (Toutin and Cheng, 2000), the paper will evaluate DEM error when compared to ground truth, and track the error propagation from the input data to the final DEM. Different cartographic parameters affecting the accuracy are also evaluated.

2. PROCESSING OF IKONOS STEREO DATA

The photogrammetric method of stereo data processing uses a parametric model that reflects the physical reality of the complete viewing geometry, and that corrects distortions due to the platform, sensor, Earth and deformations as a result of cartographic projection. Even though detailed sensor information for the IKONOS satellite is not released, such photogrammetric method was developed at CCRS for IKONOS stereo data using basic information available from the metadata and image files. For example, approximate sensor viewing angles can be computed using the nominal collection elevation and azimuth in addition with the nominal ground resolution.

The CCRS model based upon principles related to orbitography, photogrammetry, geodesy and cartography was adapted for the specificity of IKONOS images. For stereo-images, both collinearity and coplanarity conditions are used to simultaneously compute the interior and exterior orientation parameters in a least-square bundle adjustment process (Toutin, 1995). The CCRS model has been previously applied with only a few ground control points (GCPs) (3 to 6) to VIR stereo data (SPOT, IRS, ASTER and KOMPSAT), as well as stereo SAR data (ERS and RADARSAT). Based on good quality GCPs, the DEM accuracy of this model was proven to be better than one pixel for medium-resolution VIR images, and one resolution cell for SAR images.

The CCRS method is now fully ported into PCI OrthoEngine Satellite Edition V8.0 software. The software supports the reading of satellite data, metadata, GCP and tie points collection, bundle adjustment, ortho-rectification and mosaicking, stereo-model computation, image matching and DEM generation with either manual or automatic editing. After the stereo-model (colinearity and coplanarity equations) are computed using a minimum of six GCPs, an automated image matching procedure is used through a comparison of the respective grey values of the images (PCI, 2001). This procedure utilizes a hierarchical sub-pixel normalized cross-correlation matching method to find the corresponding pixels in the left and right quasi-epipolar images. The difference in location between the images gives the disparity or parallax arising from the terrain relief, which is converted to X, Y, Z map co-ordinates using a 3D space intersection solution. Automatic and 3D-manual editing tools are finally used for the last step to improve DEM quality and coherency.

3. DATA SET

To test the stereo capability of the photogrammetric method, IKONOS stereo product was ordered in autumn 2000 for a area north of Québec City, Québec, Canada (N 47º, W 71º 30’). Figure 1 is the left (backward) image of the stereo pair: one can notice sand/gravel pits (A), frozen lakes with snow (B) and snow over bare soils (C). This study is a residential and semi-rural environment (Figure 2) and has a hilly topography with 500-m elevation range (Figure 3). Unfortunately, the along-track stereo-data was acquired on January 3, 2001 with a

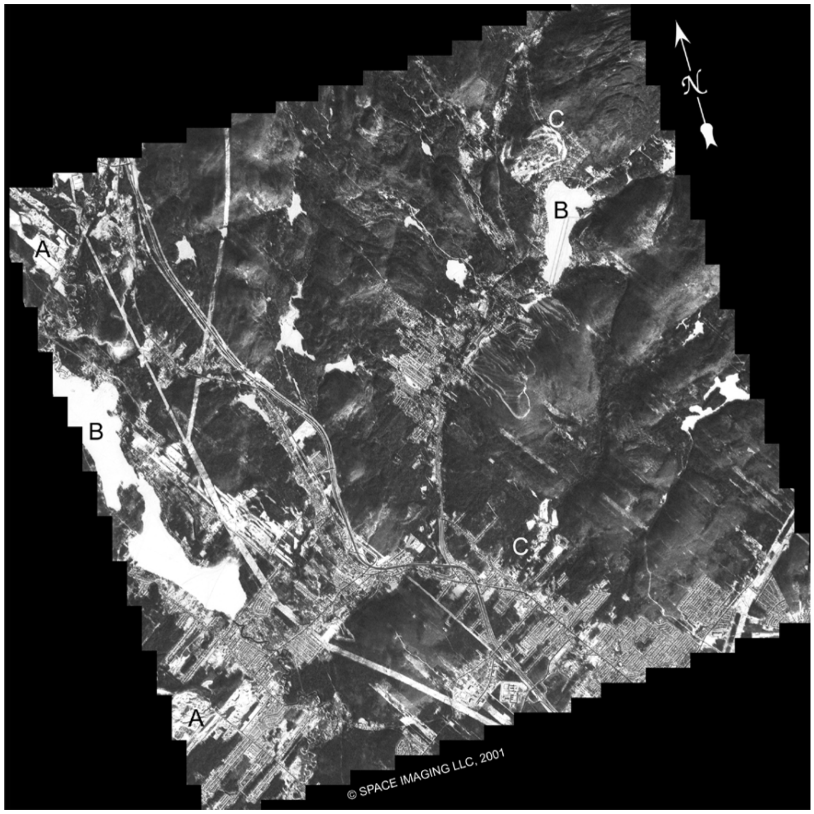

Figure 1: Left (backward) image of the IKONOS stereo pair, north of Québec City, Quebec, Canada acquired January 3, 2001. Note (A) sand/gravel pits, (B) frozen lakes with snow and (C) snow over bare soils.
IKONOS Image © Space Imaging LLC, 2001

Figure 2: Sub-image of left IKONOS stereo pair, north of Québec City, Quebec, Canada. Note (A) sand /gravel pits in operation and (B) residential and urban areas.
IKONOS Image © Space Imaging LLC, 2001

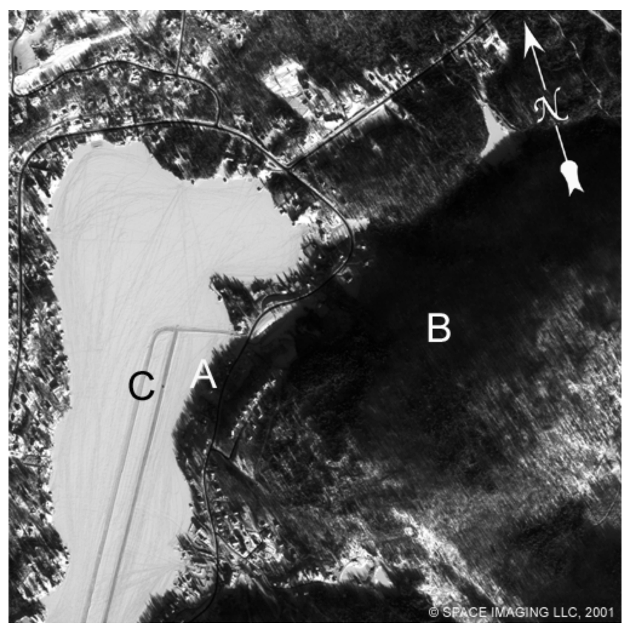

Figure 3: Sub-image of left IKONOS stereo pair, north of Québec City, Quebec, Canada. Note (A) tree shadows on the lake, (B) mountain shadows due19° and 166° solar elevation and azimuth angles and (C) the skater!
IKONOS Image © Space Imaging LLC, 2001

sun illumination angle as low as 19º, generating long shadows due to trees: one can notice the tree shadow on the lake (A) and the mountain shadow (B) (Figure 3). The two panchromatic images with a resolution of a little less than one metre (Note the skater (C) on Figure 3) have collection and azimuth angles 63º and 322º, 63º and 252º, respectively generating 54º stereo-intersection angle (base-to-height ratio B/H, of 1.0) were delivered within thirty days of acquisition. Each image of the stereo pair was delivered in two tiles, and stitching them was necessary to re-generate the quasi-epipolar image geometry. The metadata file was processed to compute the satellite and sensor parameters needed for the photogrammetric stereo model.

The cartographic data (six one-metre pixel ortho-photos, a 5-m accurate DEM, and digital vector lines) was provided by the Ministère des Ressources naturelles du Québec, Canada. While only six GCPs are enough with the rigorous method, 56 GCPs were collected in stereoscopy from the stereo-images for the different tests. Their map coordinates (X, Y, Z) were obtained from six 1-m ortho-photos with 3-m accuracy and 5-m grid spacing DEM with 5-m accuracy. However, a mean positioning error of 5 m in the X direction was found between the different ortho-photos; this error is mainly due to 5-m DEM error during the ortho-photo generation.

4. RESULTS AND ANALYSIS

The first results are given with the root mean square (RMS) and maximum residuals/errors for three different tests performed on stereo IKONOS images to evaluate the robustness of the photogrammetric model:

1. All 56 GCPs are used to compute the stereo-model;
2. All 56GCPs are used to compute the stereo-model with an erroneous point (20-m error in the Y direction); and
3. Only 12 GCPs are used to compute the stereo-model and 34 independent check points (ICPs) are used to check the stereo-model.

Table 1: Comparison of residual/error results (in metres) over GCPs/ICPs for the three tests.

Test Number	**RMS GCPs Residuals**			**Maximum Residuals**		
	X	**Y**	**Z**	**X**	**Y**	**Z**
#1: 55 GCPs	6.0	2.3	2.8	11.6	5.1	6.8
	RMS GCPs Residuals			**Erroneous Point Residuals**		
#2: 55 GCPs/1 error Point	6.4	5.9	3.1	11.6	-17.4	-4.8
	RMS GCPs Residuals			**RMS ICPs Errors**		
#3: 12 GCPs/34 ICPs	5.7	2.5	3.6	7.0	2.4	3.6

The three tests show that the 5-m error in the GCP X-coordinate, as mentioned previously, did not propagate through the rigorous model but is reflected in all X-residuals and in the RMS X-error of Test #3. Test #1 shows that the maximum residual is around two times the RMS residuals, demonstrating stability over the entire stereo-images. Test #2 shows that the Y-residual of the erroneous point is three times higher than the RMS Y-residual. Consequently, the systematic error is immediately detected with its approximate value and direction. Since part of the 7-m X-error on ICPs (Test #3) includes the 5m random error of the ground X-coordinate, Test #3 shows that 12 GCPs are enough to achieve a stereo-model accuracy around 3 to 4m, both in horizontal and vertical directions.

These three tests demonstrate that the photogrammetric method is both stable and robust without generating local errors and filters random or systematic errors. The input GCP error does not propagate through the rigorous model, but is reflected in the residual. Since errors always occur in operational environments, it is thus important to detect all potential errors in the GCPs before starting the extraction of the DEM.

The second result is the qualitative and quantitative comparisons of the stereo-extracted DEM (2-m pixel spacing) using the automatic matching and editing process. Figure 4 is a 3D representation of the extracted DEM: it well reproduces the terrain relief and its specific features visible on the IKONOS images. Different planimetric features are clearly identifiable: sand/gravel pits in A; some repetitive patterns in B, which first look like noise, and linear features in C, related to main roads and power-line clear-cut in the forest environment.

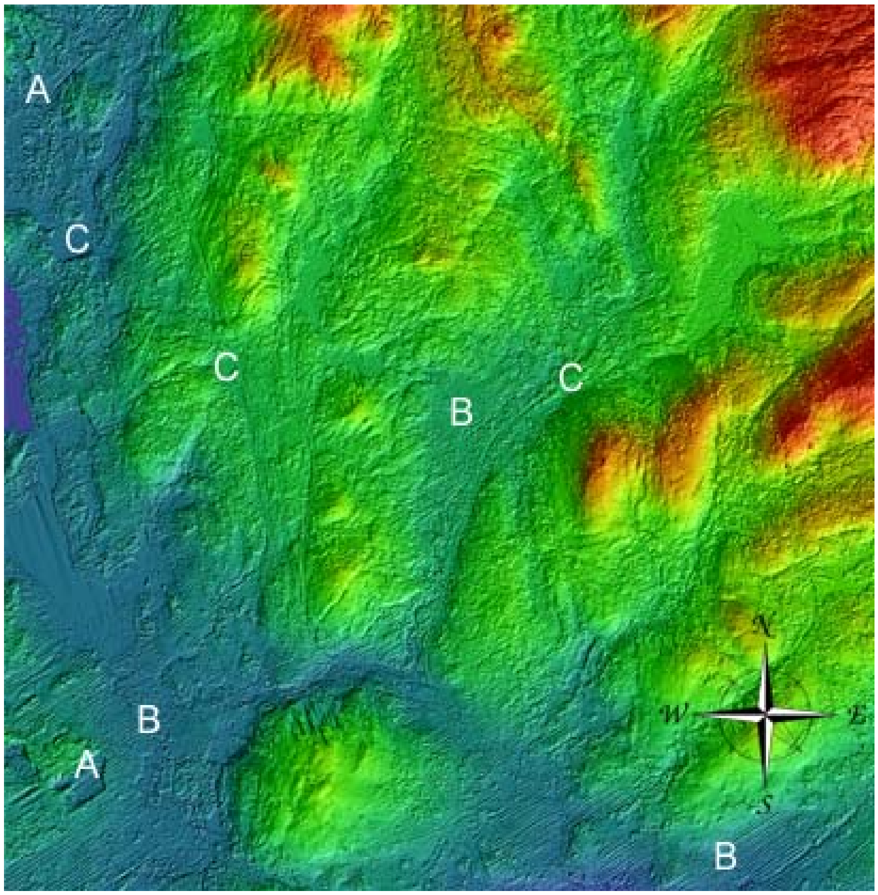

Figure 4: Chromo-stereoscopic image of the IKONOS stereo-extracted DEM. Note (A) sand/gravel pits, (B) repetitive pattern and (C) linear features (power lines and roads).

Looking at the repetitive patterns in more details, they are attributed to the street/house patterns in the residential areas (Figure 5): the matching process worked on the houses and the method then extracted the elevation and shape of the 1-2-storey residential houses. A closer-look comparison (Figure 6) of the IKONOS image (left) and the DEM (right) confirms "the shape extraction" of a large 3-storey commercial building. With some post-processing of the DEM, IKONOS DEM could then be used for 3D building modelling.

For quantitative evaluation, the generated DEM was compared with the topographic DEM (5-m grid spacing and 5-m accuracy) using 4 400 000 points in the statistical evaluation. Even though the images were acquired in January with snow cover, frozen lakes and tree/mountain shadows there is only 5% mismatched areas over the entire stereo-images, of which includes 2.5% for lakes. The remaining 2.5% mismatched areas are mainly located in the northwest slopes of mountains (Figure 1) and are due to the solar shadow (elevation angle of 19º and azimuth of 166º) (Figure 3). These first mismatched results confirm that multi-scale matching well performed with 1m high-spatial resolution data in semi-rural areas.

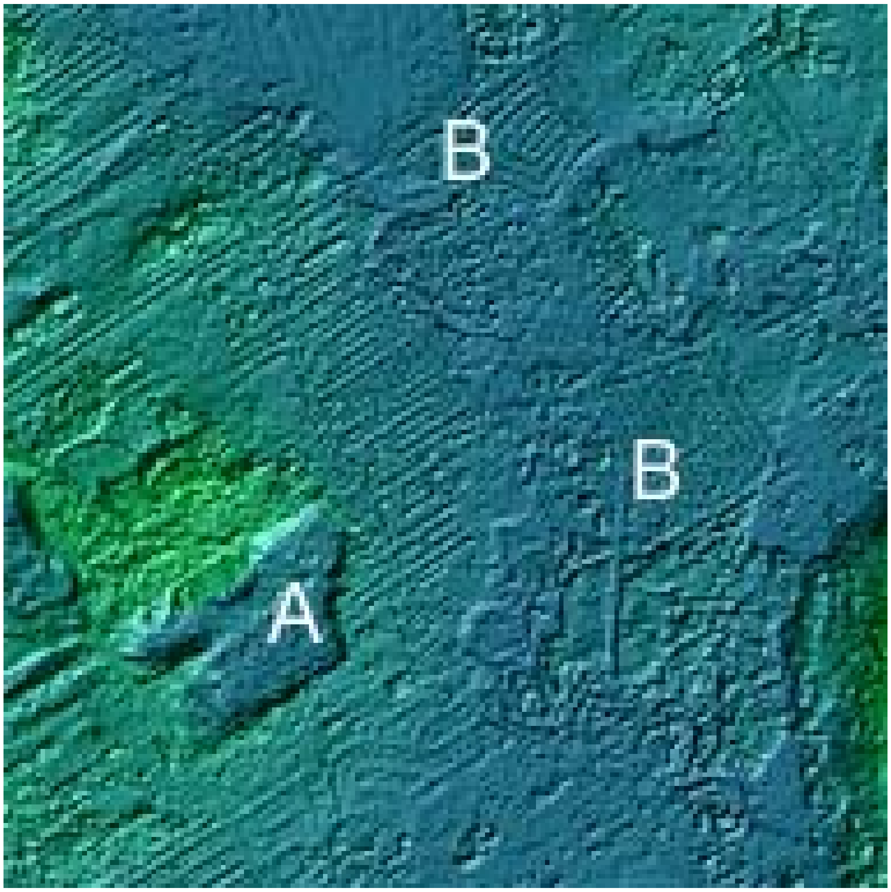

Figure 5: Sub-area of the chromo-stereoscopic image of the IKONOS stereo-extracted DEM. (A) sand/gravel pits and (B) street and building pattern in the residential areas. IKONOS Image © Space Imaging LLC, 2001

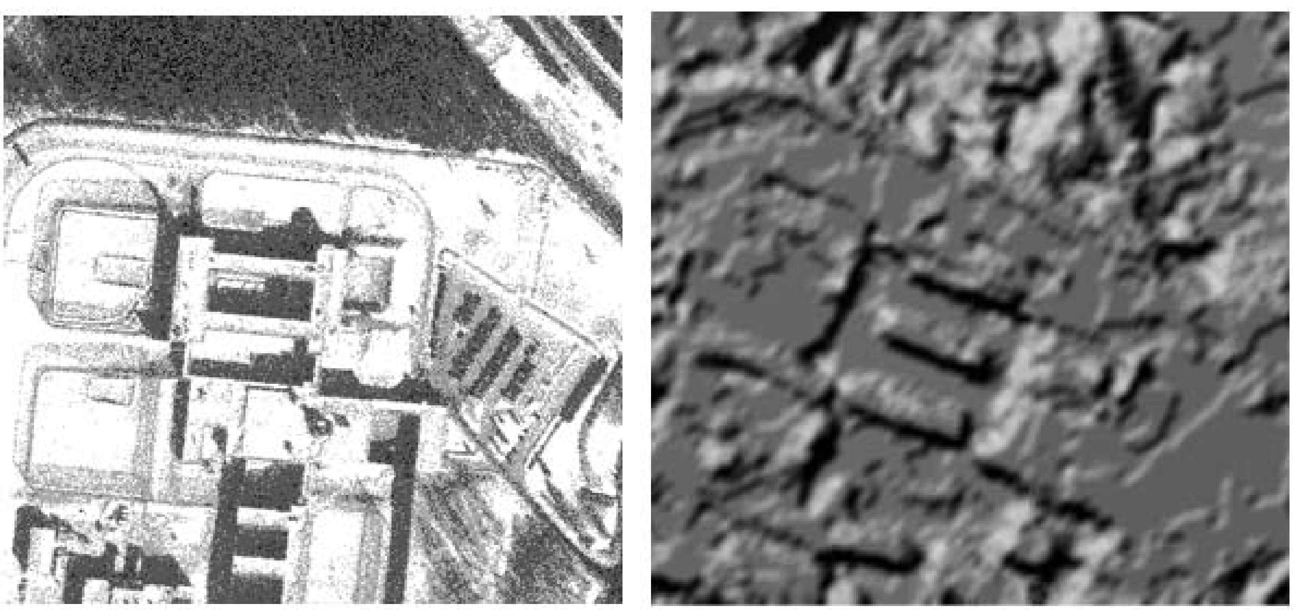

Figure 6: Comparison of the IKONOS image (left) with the stereo-extracted DEM (right). IKONOS Image © Space Imaging LLC, 2001

Table 2 gives the statistical results for different areas of the study sites, the linear error with 68% and 90% levels of confidence (LE68 & LE90, respectively), the bias and the maximum/minimum errors (in metres). The 3.8-m LE68 and 7.7-m LE90 with almost no bias for the entire study site are a good result because not only does it includes the 5-m error of the topographic checked DEM but also includes the canopy/building heights as mentioned previously. It then enables 10 m to 15 m contour lines to be derived with the highest mapping standard. However, the largest errors (-50/37 m) are out of tolerance and cannot be acceptable for DEM in a topographic sense. In order to understand and locate these largest errors, the errors have been colour coded (from blue for the lowest and red the highest) and draped over the DEM in a southwest-northeast perspective view (Figure 7): orange and red colours correspond to 9 m and 15 m errors, respectively. The largest errors are located in the sand/gravel pits (A) and in the northwest slopes of the mountains where solar shadows occur (B) due to solar elevation and azimuth angles of 19º and 166º, respectively. An error evaluation as a function of the slope azimuths shows that the DEM errors in the sun-facing slopes (azimuths from 76º to 256º) is 1-m smaller than the DEM errors in the slopes away from the sun (azimuths from 256º to 76º). These more-than-9-m errors are then representative of our study site and stereo-images, but are not representative of the general IKONOS stereo-performance for DEM generation.

Table 2: Statistical DEM results (linear errors with 68% and 90% confidence levels, LE68 and LE90 respectively, bias and minimum/maximum errors in metres) for the entire study site and different land covers.

Area	**Percentage**	**LE68**	**LE90**	**Bias**	**Min./Max.**
Entire	100%	3.8 m	7.7 m	-0.9 m	-50/37 m
Dense forests	61%	4.4 m	8 m	-2.1 m	-37/29 m
Sparse forests	11.5%	2.4 m	5 m	1.1 m	-34/31 m
Bare soils	6.5%	2.6 m	5.6 m	2.0 m	-33/28 m
Lakes	4%	1.1 m	2.7 m	2.5 m	-29/20 m
Urban/Residential	15.5%	2.4 m	5 m	0.2 m	-26/18 m
Sand/gravel Pits	1.5%	8.5 m	18 m	0.5 m	-50/37 m

For these different reasons: sensibility to the land covers, no digital surface model (DSM) available and many fine details in the stereo extracted DEM, its error evaluation must be realized for different land covers: dense forests, sparse forests, bare soils, lakes, urban/residential areas and sand/gravel pits (Table 2). The best results (around 1.1-2.6 m LE68) are obtained for four classes of no- or low-elevation cover (bare soils, lakes, sparse forest, and urban/residential areas). Even if house elevations are extracted in the method, the 1-2-storey houses in the residential and urban areas, not very dense (10-15% of the residential areas) and high (4-6 m), do not affect too much the statistics for this land cover. Furthermore, since the images were acquired on January, there was not leave in deciduous trees and the rays went through the canopy. It explains the small bias for the sparse and dense forests and the 2.4-m LE68 for the sparse forests. 5-10 m contour lines could thus be derived in these areas. Finally, the largest errors (8.5-m LE68 and –50m/37-m min./max.) are in the sand/gravel pits, located northwest and southwest of the images, where elevations changed over time.

4. CONCLUSIONS

One major drawback of the efficient and appropriate use of IKONOS stereo-data was the difficulty by the users to geometrically process and to extract 3D information using photogrammetric method. The CCRS-developed model that is available in the PCI operational environment can now be used for 3D modelling. As few as 12 GCPs are enough for the stereo photogrammetric bundle adjustment, which also filters the errors of the input data. With area-based image matching users may produce high resolution DEMs with LE68 errors of 1 m to 4 m depending on the land covers. The best results (1.1 m-2.6 m) are obtained in bare soils, lakes, residential areas and sparse forests. 5-m contour lines could thus be derived in these areas. The surface elevation of some of the areas did not affect too much the errors because the 1-2-storey houses are sparse or because the images were acquired when there is no leave in the deciduous forests. An error evaluation as a function of the slope azimuths shows that the DEM error in sun-facing slopes is 1-m smaller than the DEM error in slopes away from the sun.

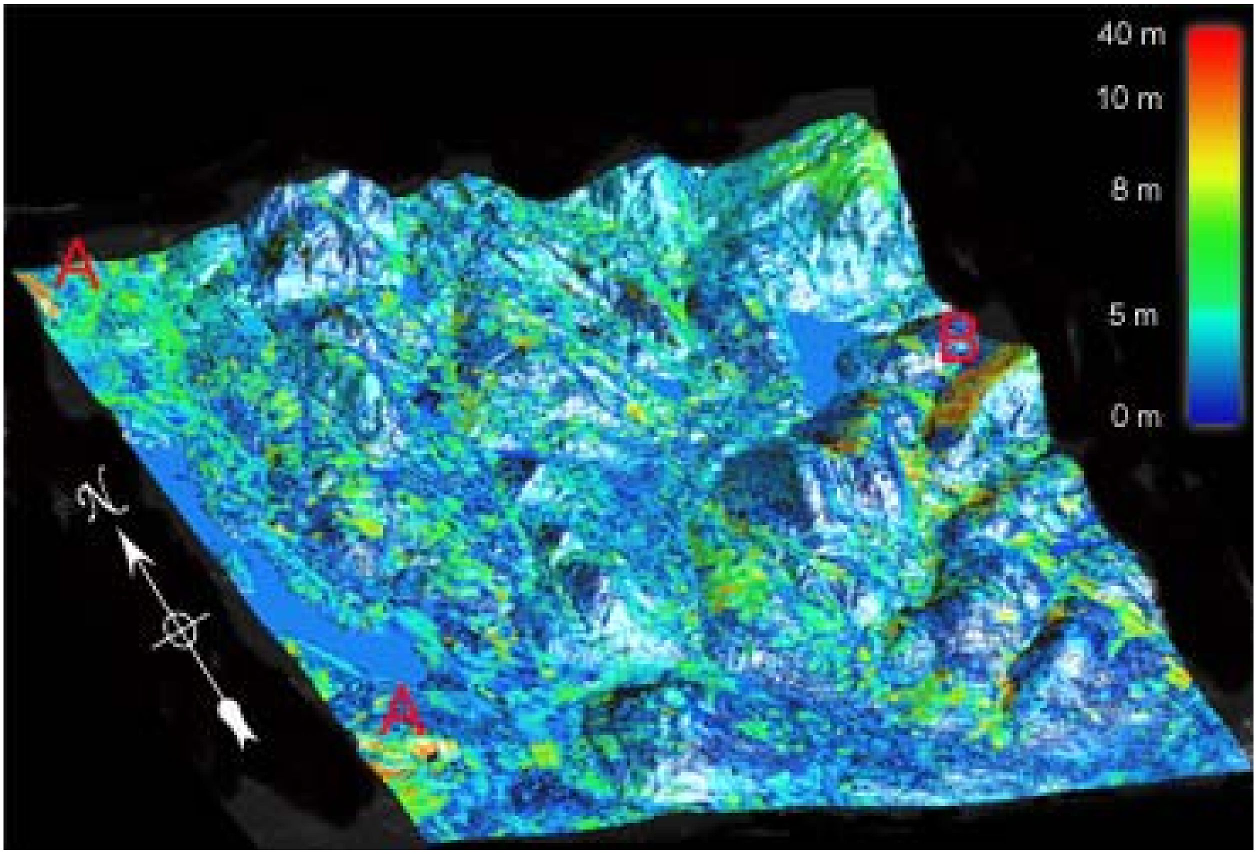

Figure 7: Perspective view of the DEM error (Topographic DEM minus IKONOS DEM) draped over the IKONOS DEM. Note the errors larger than 9m (orange to red) are located in (A) sand/gravel pits (NW and SW) and (B) the northwest slopes of mountains.

Since many cartographic features and fine topographic details are present in the stereo IKONOS DEM, the DEM is in fact a DSM, which includes house elevations and part of canopy heights of dense forests. It can be thus be used as a complementary tool to ortho-images for automatically classifying planimetric features (roads, power lines), urban areas (streets and houses), and for extracting house or canopy heights.

Work still needs to be carried out to evaluate the possibility of integrating some existing cartographic data, such as buildings in urban areas or hydrographic features and canopy heights in rural areas in the post-processing procedures, as well as, extracting cartographic features from the DEM. Evaluation is still ongoing at CCRS using more precise GCPs and topographic DSM, including canopy and building heights. More results on these evaluations as a function of inter-dependent parameters (precise GCPs and DSM, slopes, aspects, land covers) will be presented at the ISPRS Workshop.

Acknowledgements

The authors want to thank Dr. Philip Cheng of PCI Geomatics for the software adaptation to IKONOS and Mr. Réjean Matte of Ministère des Ressources naturelles du Québec, Canada for the cartographic data.

References

Li, R., 1998. Potential of High-Resolution Satellite Imagery for National Mapping Products. Photogrammetric Engineering and Remote Sensing, Vol. 64, No. 12, pp. 1165-1170.

PCI Geomatics, 2001. OrthoEngine Satellite Edition version 8.0. www.pcigeomatics.com.

Ridley, H. M., P. M. Atkinson, P. Aplin, J.-P. Muller and I. Dowman, 1997. Evaluating the Potential of the Forthcoming Commercial U.S. High-Resolution Satellite Sensor Imagery at the Ordnance Survey®. Photogrammetric Engineering and Remote Sensing, Vol. 63, No. 8, pp. 997-1005.

Space Imaging, 2001, www.spaceimaging.com.

Toutin, Th., and P. Cheng. 2000. Demystification of IKONOS. Earth Observation Magazine, Vol. 9, No. 7, pp. 17-21. http://www.ccrs.nrcan.gc.ca/ccrs/eduref/ref/bibpdf/4807.pdf.

Toutin, Th., 1995. Generating DEM from Stereo Images with a Photogrammetric Approach: Examples with VIR and SAR Data. EARSeL Journal Advances in Remote Sensing, Vol. 4, No. 2, pp. 111-117.

BLOCK ADJUSTEMENT OF LANDSAT-7 ETM+ IMAGES

Thierry Toutin, Yves Carbonneau* and René Chénier*
Natural Resources Canada, Canada Centre for Remote Sensing
588 Booth Street, Ottawa, Ontario, Canada, K1A 0Y7
thierry.toutin@ccts.nrcan.gc.ca

KEY WORDS

Bundle block adjustment, Geometric evaluation, Error propagation, Landsat-7

ABSTRACT

This research study shows the potential of large image-block adjustment with nadir viewing sensor images. The method uses the geometric correction system developed for multi-source images at the Canada Centre for Remote Sensing. The results with 15 Landsat-7 ETM+ images show that the same accuracy can be obtained with a large image block than with a single image using the same number of ground control points (GCPs). The number of GCPs depends on cartographic data accuracy to reduce the propagation of GCP error in the least-square block adjustment. To insure consistency and convergence in the block adjustment, strips of same-path and date images has to be generated. Furthermore, elevation tie points (with known elevation value) are used in the overlaps (North-South and East-West) because the viewing-angle differences of overlapping images are small: less than 1º in North-South overlaps and less than 10º in East-West overlaps.

1. INTRODUCTION

Such as in photogrammetry where strips and block of aerial photos are processed together, it seems normal to perform the same process with satellite images from same and/or adjacent orbits. The geometric processing is realized with an image block adjustment instead of a single image adjustment. This spatio-triangulation process was first developed and tested with off-nadir viewing SPOT images (Toutin, 1985; Veillet, 1991) and with along-track stereo MOMS images (Kornus *et al.*, 2000), and generally in a research context or by governmental agencies. Few results were presented neither with nadir viewing images or in an operational environment. Due to new and low-cost Landsat-7 data, it seems interesting to adapt the method for this data and to develop operational strategies in an user-friendly and robust system.

There are different advantages to block adjustment:

- To reduce the number of ground control points (GCPs);
- To obtain a better relative accuracy between the images;
- To obtain a more homogeneous and precise mosaic over large areas; and
- To generate homogeneous GCP network for future geometric processing.

The spatio-triangulation process is based on a bundle adjustment of all images combined with ground control and orbit information. With the spatio-triangulation, the same number of GCPs is theoretically needed to correct a single image, an image strip or a block: 6 GCPs are enough for Landsat-7 (Cheng *et al.*, 2000). However, in operational context, it is better to use twice more when they are precise due to potential error in their identification and plotting, and more when they are less precise. The least-square block adjustment will thus reduce their error propagation.

---

* Under contract with Consultants TGIS inc., 7667 Curé Clermont, Anjou (Québec) H1K 1X2, Canada

This paper will present the method to generate and process image strips and block from Landsat-7 ETM^+ images. Comparative results between the processing of a single image, image strip(s) or block are presented to validate the stability and robustness of the system. The mathematical tool used is the geometric correction developed at the Canada Centre for Remote Sensing (CCRS) for multi-source images (Toutin, 1995) and adapted to Landsat-7 ETM^+ images (Cheng *et al.*, 2000). Different strategies are also presented for operational uses.

2. GENERATION OF STRIPS AND BLOCK

Image-strip generation

Since satellite data are acquired in a continuous strip the data should be delivered in such long strip. However, they are "artificially" cut into square images, the images from a same orbit and from a same acquisition date has to be stitched to re-create the continuous strip in the North-South direction (Sakaino *et al.*, 2000). However, the 1G images are geo-referenced, e.g., projected along the ground orbit track at the image centre, there is a different azimuth for each image, and the lines in the overlap area do not superimpose any more. A matching technique (visual or automatic) has then to be used in the overlap area to compute the rotation-translation in order to stitch the images.

Theoretically, there is no limit to the number of images to be stitched when they are acquired the same date, but practically due to the 1G pre-processing and the cloud coverage, no more than 5 images can be stitched together in about 900-km strip. When the images are acquired from different dates then from different physical orbits, they cannot be stitched in a same strip. Another method with tie points (TP) must be applied to create a link between the images in the North-South direction. However, the stereo-geometry will be weak with base-to-height (B/H) ratio less than 10^{-3}.

Image-block generation

Finally, blocks are generated from images or strips in the East-West direction acquired from adjacent paths. The link between images/strips is realised with TP Since Landsat ETM^+ images are acquired at nadir the intersection angles are 10°-15° depending of the latitude, generating B/H ratios of 0.13-0.25. Consequently, it is necessary to use TP with a known elevation in both directions (North-South, East-West) in order to strength the intersection geometry between the two images and the ground. In operational conditions, use of elevation TP becomes mandatory to avoid error propagation and to obtain a better stability in this weak stereo-geometry. However, some TPs can also be added in East-West directions only. For this block, there are 12 and 10 overlaps in the East/West and North/South directions respectively, when the block is formed with separate images, are 11 and 5 overlaps in the East/West and North/South directions, respectively when the block is formed with strips.

3. DATA SET

15 ETM^+ panchromatic images with 15-m pixel spacing were acquired over the Rocky Mountains, Canada from Vancouver in the south-west to Calgary at the north-east. They are level 1G systematically georeferenced and oriented along the orbit track. They generate a block with five paths and three rows (Figure 1). Some paths have two or three images of the same date (outlined in Figure 1) and one path has images from three dates. It enables different images/strips/block configurations to be tested. The North/South and East/West overlaps are around 10% and 40%, respectively. The images cover an area of 600 km by 500 km, and the elevation variation is 2 500 m. Cartographic data are 350 topographic maps at 1:50 000 with 25-50 m accuracy. About 55 ground points per image were collected. A DEM (50-m grid spacing) was generated from the contour lines of 1:250 000 maps with an error of 50 m. This 50-m error will generate less than 10-m positioning error in the geocoding process of each image (view angle less than 7.5º at the image border).

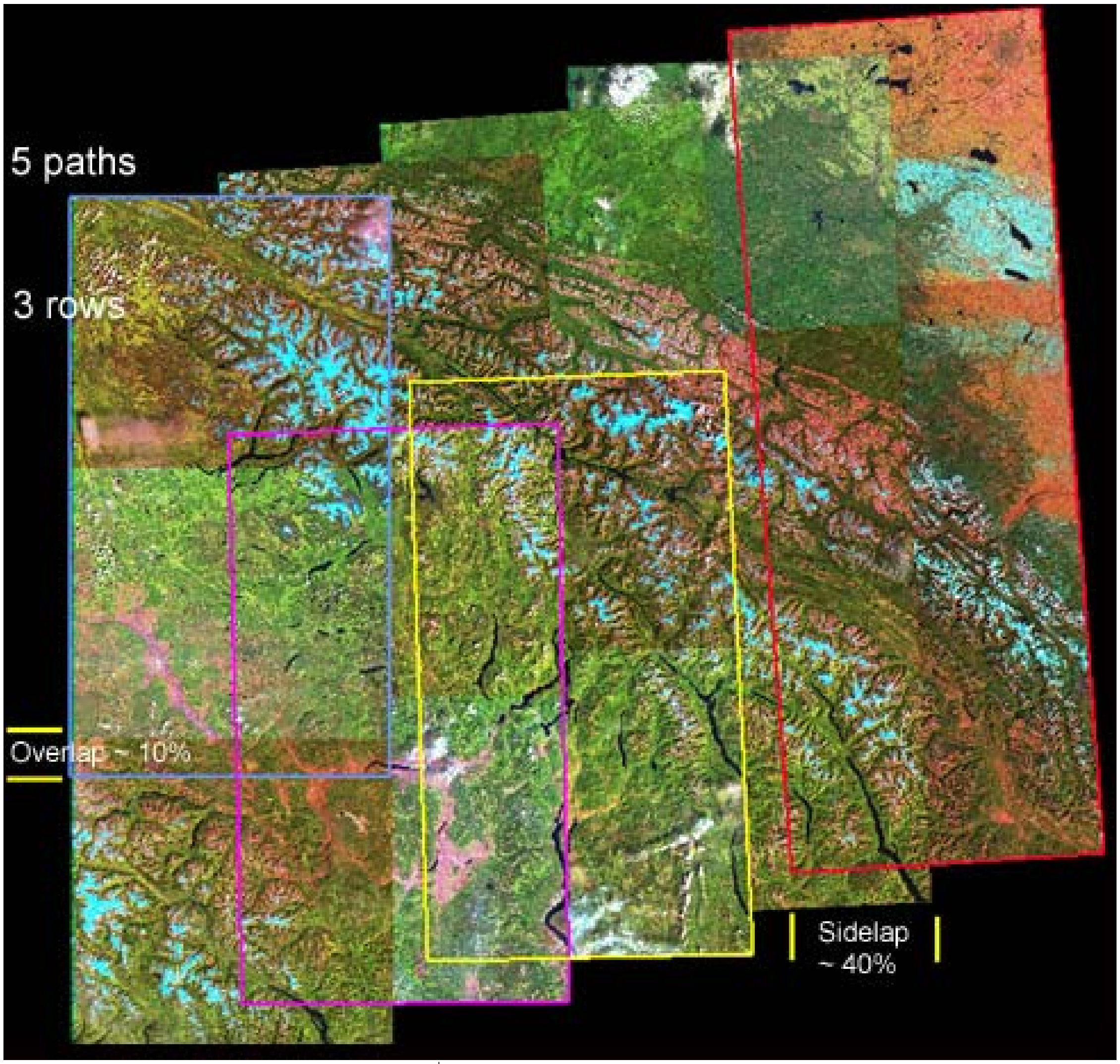

Figure 1: Study site and Landsat-7 ETM+ images over the Canadian Rocky Mountains, Canada. The coloured outlines determinates the 2- or 3 image strips from same path and date.

4. RESULTS AND INTERPRETATION

The first results are given with the least-square bundle adjustment with all GCPs for different numbers and configuration of image(s) and strip(s): a single image, two or three images, two or three image strip and the whole image bloc. Table 1 gives the root mean square (RMS) and minimum/maximum residuals on these different configurations. The results for each configuration (image(s) or strips) correspond to the mean of results for all possibilities for this configuration (e.g., the result for a single image is the mean of results of 15 single images). In the block adjustment, GCPs belonging to more than one image is also used as TP.

These coherent results demonstrate the applicability of the geometric model and of the system to Landsat-7 block adjustment, but also a good stability and robustness of the method, whatever the image/strip/block configuration because all residuals are equivalent. Since they are in the same order than the cartographic data error (25 m), the GCP error did not propagate through the geometric model but in the residuals, due to the redundancy in the least-square adjustment.

Tableau 1: Root mean square (RMS) and minimum/maximum residuals on GCPs (in metres) of the least-square adjustments for different image/strip configurations

Least-square adjustment	GCPs	RMS Residuals X	RMS Residuals Y	Min/Max Residuals X	Min/Max Residuals Y
1 image single	55	20.8	18.9	-59/49	-45/47
2 images N/S	110	21.5	19.8	-41/52	-41/43
3 images N/S	165	20.0	19.2	-43/48	-49/44
3 images E/W	165	19.8	19.5	-45/46	-50/48
2-image strip	110	23.2	22.5	-35/45	-49/37
3-image strip	165	23.0	20.6	-41/48	-41/44
15-image block	800	22.6	21.2	-59/52	-49/47

To find the appropriate number of GCPs as a function of their cartographic errors, different tests are performed by varying the GCP number. A 3-image strip was used because it has the largest number of GCPs (148). Points not used as GCP are used as independent check points (ICPs) to verify the model error. Figure 2 gives the RMS X-Y residuals (in metres) on GCPs varying from 148 to 10 in the least-square strip adjustment, and RMS X-Y errors (in metres) on ICPs varying from 0 to 138, respectively. From 148 to 30-35 GCPs the RMS errors are equivalent with only 2-3 m variations, while 10 GCPs give RMS errors 20% worse. 25-30 GCPs are then a good compromise to avoid the propagation of GCP errors and to keep about 25-m error for the bundle adjustment.

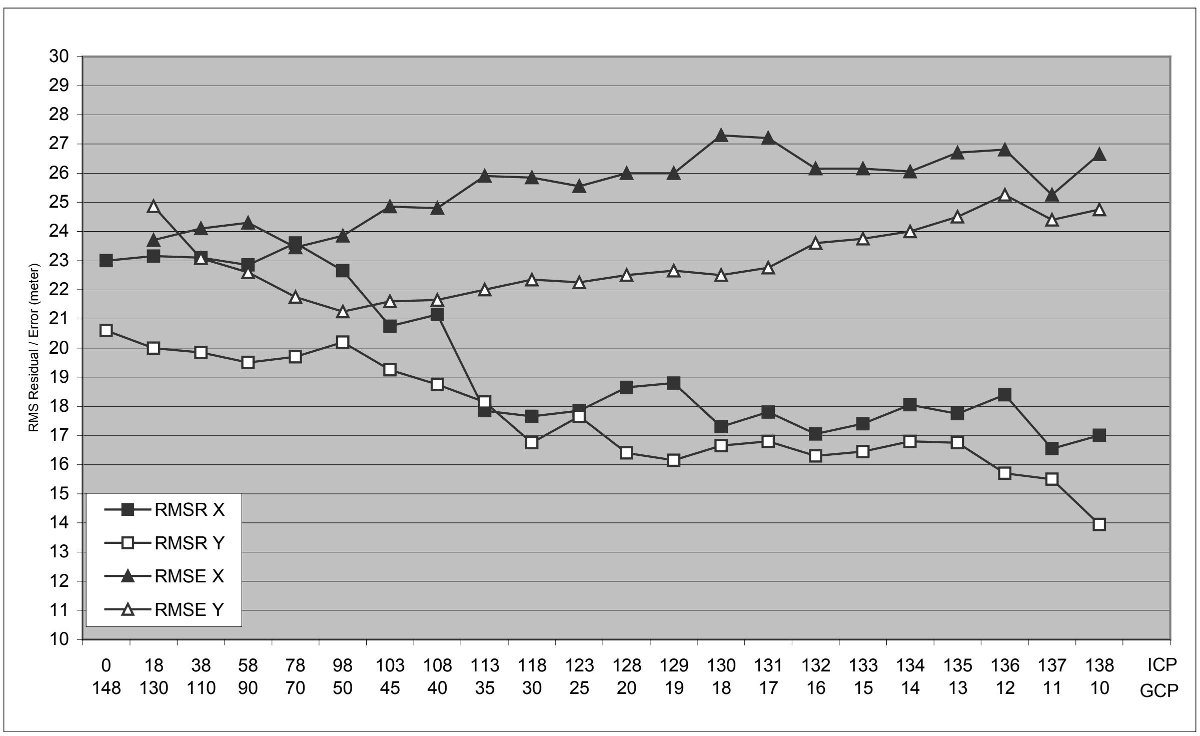

Figure 2: RMS X-Y residuals (in metres) on GCPs varying from 148 to 10 in the least-square strip adjustment, and RMS X-Y errors (in metres) on ICPs varying from 0 to 138, respectively

This result of 25 GCPs is then applied to tests different block adjustment combined with images and/or strips:

1. Three separate images in the North/South or East/West directions with 25 GCPs on the 2 outer images and 10-20 elevation TPs in the overlap areas (Figures 3 and 4, respectively);
2. Block with 15 images linked with 10-15 elevation TPs (Figures 5 and 6); and
3. Block with images and 2/3-image strips linked with 10-15 elevation TPs (Figures 7 and 8, respectively).

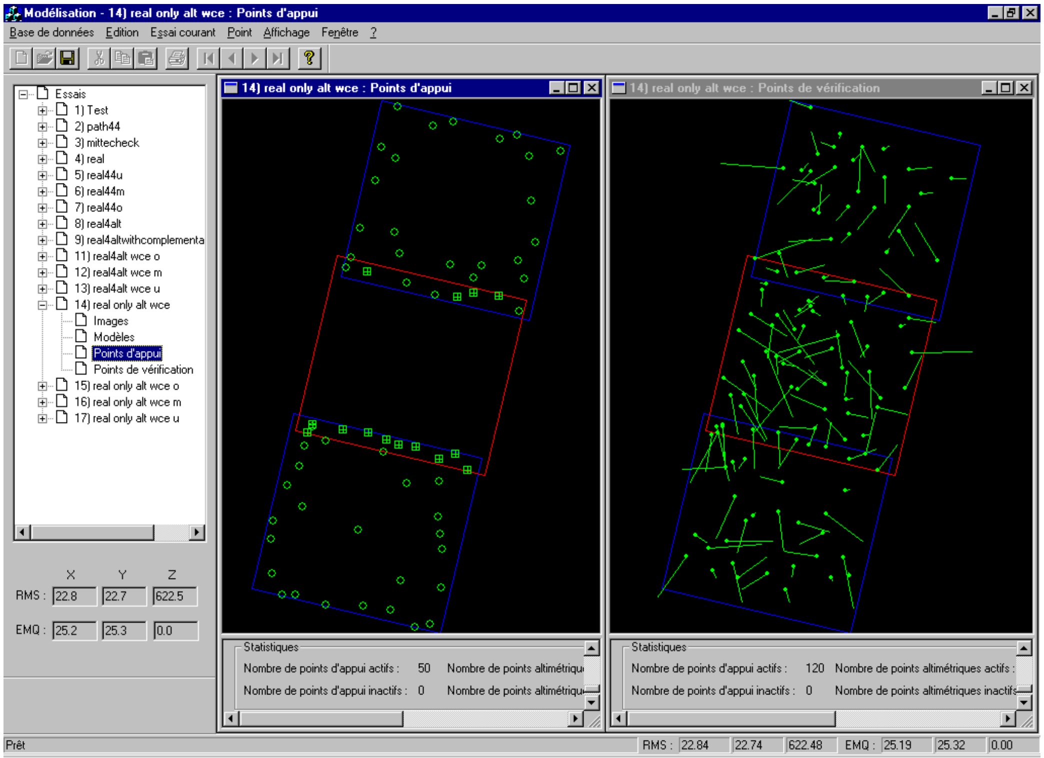

Figure 3: GCPs distribution (left window) and ICP error vectors (right window) of the block adjustment of 3 images in North/South direction with 25 GCPs on the outer images and 10 elevation TP in each overlap

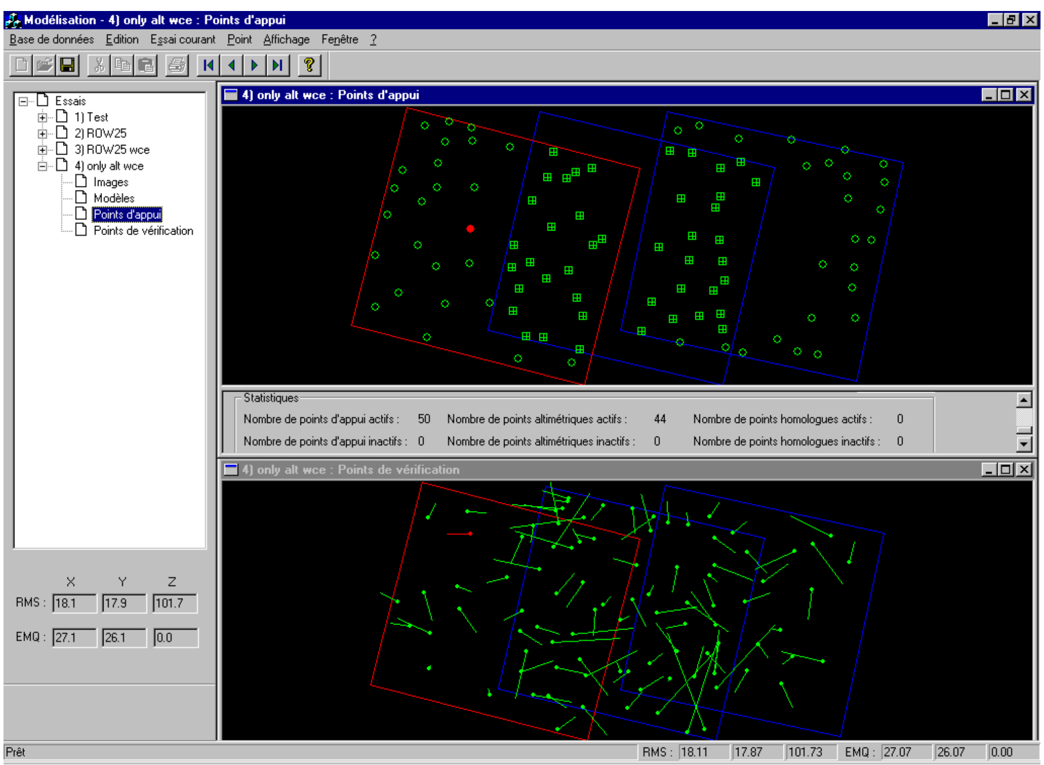

Figure 4: CPs distribution (top window) and ICP error vectors (bottom window) of the block adjustment of three images in East/West direction with 25 GCPs on the outer images and 20 elevation TP in each overlap

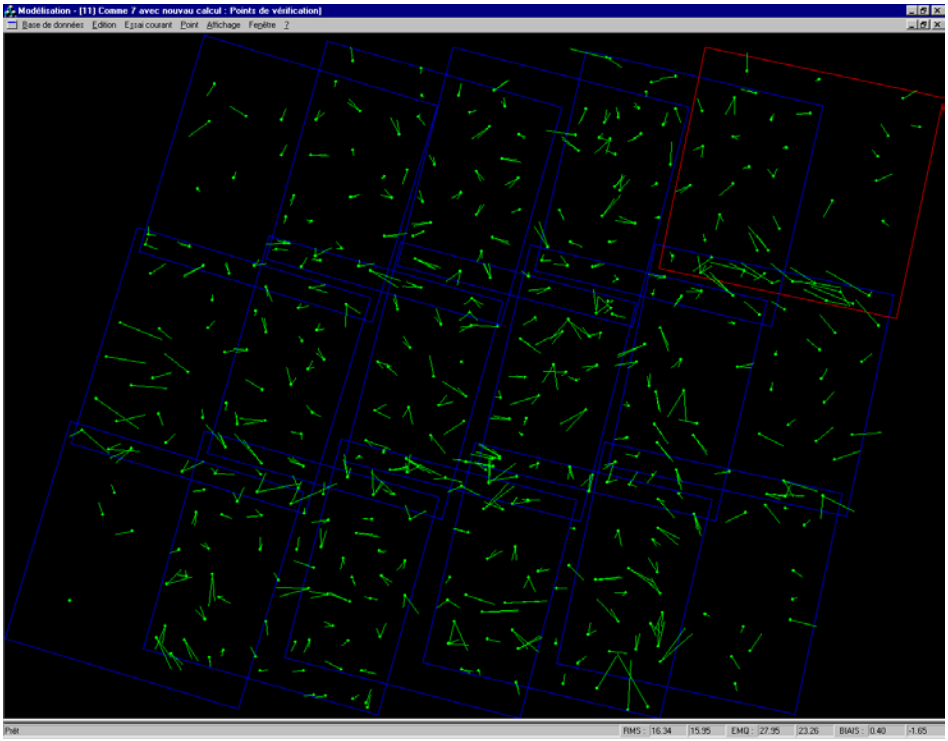

Figure 5: ICP error vectors of the 15-image block adjustment (a) with 25 GCPs every two images and with 10 elevation TP and 5-10 TPs in each overlap

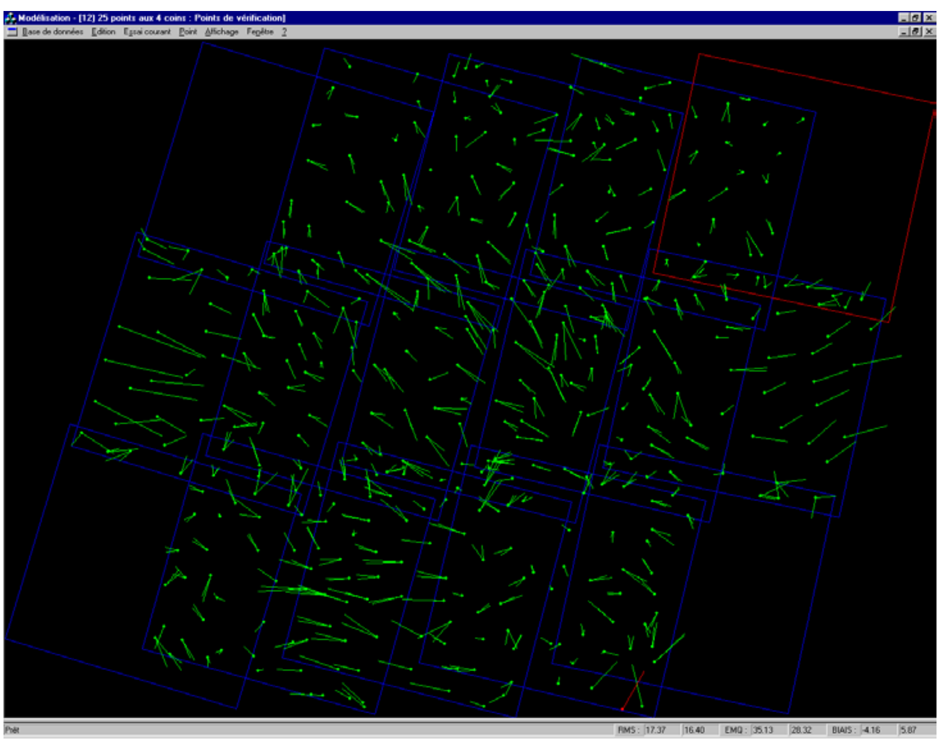

Figure 6: ICP error vectors of the 15-image block adjustment (b) with 25 GCPs in the 4 outer images and with 15 elevation TP in each overlap

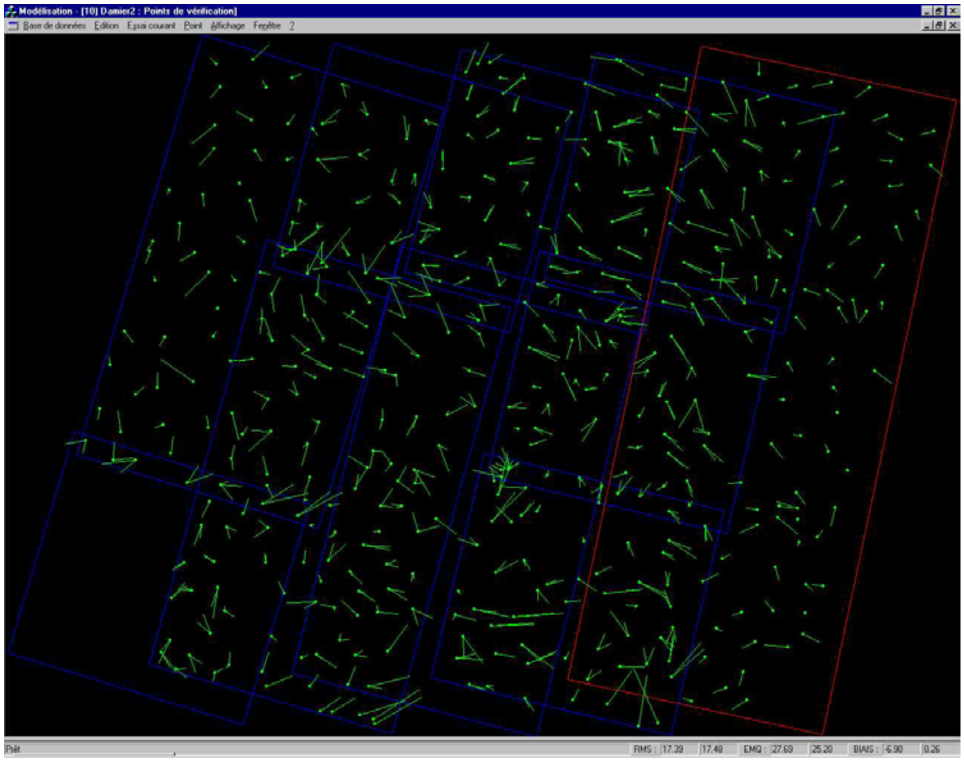

Figure 7: ICP error vectors of the image/strip block adjustment (a) with 25 GCPs every two images/strips, and with 10 elevation TP and 5-10 TPs in each overlap

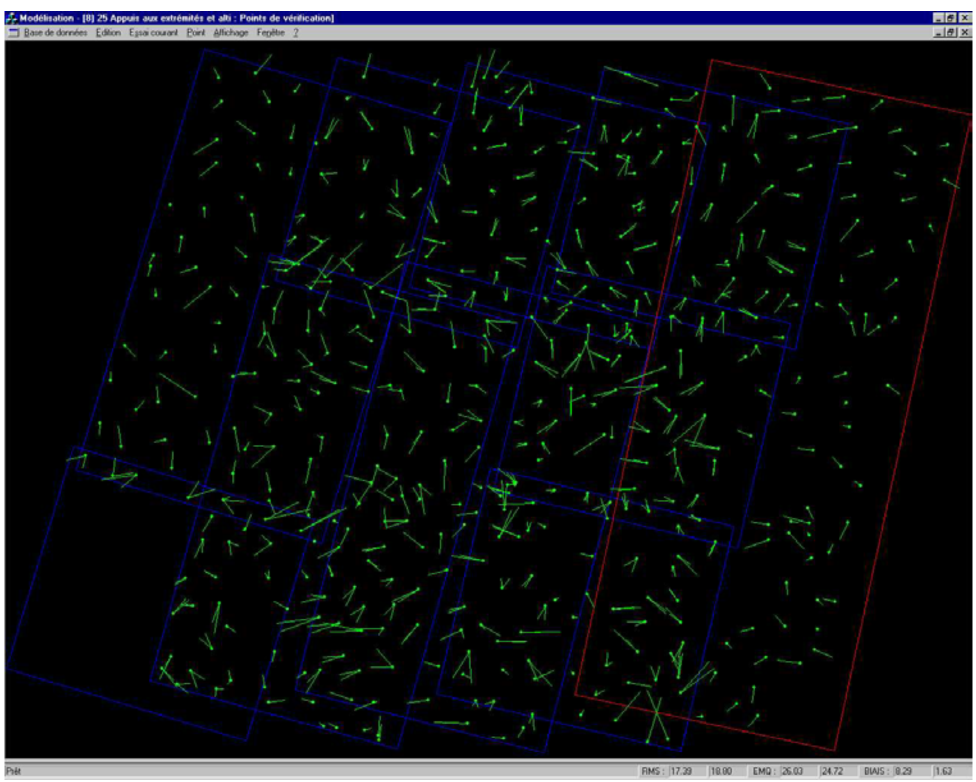

Figure 8: ICP error vectors of the image/strip block adjustment (b) with 25 GCPs in the 3 outer image/strips and 15 elevation TP in each overlap

Figures 3 and 4 show two main windows: one with the GCPs (circle), elevation TPs (square) and TPs (triangle) distribution and the second with the ICP vector errors. For clarity due to the large number of points, Figures 5 to 8 only show the ICP vector errors. In addition for the block adjustment, two tests were performed using 25 GCPs (a) every two images (Figures 5 and 7) or (b) in the outer images/strips (Figures 6 and 8). For every test, the images without GCP are linked with about 10-20 elevation TPs on each overlap. However, since the block test (b) is the most extreme configuration, a little more elevation TPs are used. Conversely, few TPs (5-10) are added in the block test (a) to obtain the same number of "links" between images, but only in the East/West overlaps because the North/South overlaps display a weak stereo-geometry (B/H$\approx 10^{-3}$ or 10^{-5}). The RMS GCP residuals and RMS ICP errors are synthesised in Table 2 for the five bundle adjustments.

Table 2: RMS residuals (in metres) on GCPs and RMS errors (in metres) on about ICPs of the least-square adjustments for different image/strip configurations. Tests (a) and (b) correspond to two different GCP distributions in the block: (a) with GCPs every two images/strips and (b) with GCPs on the outer images/strips.

Least-square adjustment	Figure Number	Number of GCP/ETP/TP	RMS Residuals X	RMS Residuals Y	Number of ICPs	RMS Errors X	RMS Errors Y
3 images North/South	3	50/20/0	22.8	22.7	120	25.2	25.3
3 images East/West	4	50/44/10	18.1	17.9	100	27.1	26.1
15-image block (a)	5	200/160/80	16.3	16.0	600	28.0	23.3
15-image block (b)	6	100/200/0	17.4	16.4	700	35.1	28.3
Image/strip block (a)	7	150/160/80	17.4	17.5	650	27.6	25.1
Image/strip block (b)	8	75/265/0	17.4	18.8	725	26.0	24.7

Table-2 results show a general coherency and confirm Table-1 results and interpretation: applicability of the model, stability and robustness of the method whatever the image/strip configurations, but also now whatever the GCP/TP distributions. A general error of 25-30 m is obtained, but which included the cartographic error of GCPs/ICPs. The two 15-image block adjustments with "weaker links" between the North/South images of same path and date (B/H $\approx 10^{-5}$) give the "worse" results (30-35 m), and especially the block (b) where only GCPs on the outer images/strips are used (no GCP in-between 360-400 km). The different Figures (3 to 8) demonstrate there is no bias/systematic error in any strip/block adjustment, and that the vector errors are similar for all images/strips with or without GCPs. Statistical evaluations for each image independently confirm this last statement. Furthermore, ICP error-vector for points belonging to two images or more are in the same direction, demonstrating a good superposition between the images. Since better results are not obtained for the images with GCPs, the block adjustment method performs well in term of relative and absolute accuracy.

5. CONCLUSIONS

A method of spatio-triangulation using a block bundle adjustment has been tested with 15 Landsat-7 ETM$^+$ panchromatic level-1G images over the Canadian Rocky Mountains. Firstly, the method to create strips and block from images of same path but from same or different dates was given. The bundle adjustment was then tested with single or multiple images and strips. Same results were obtained with a single image or 15-image block, and they were on the same order than the cartographic data accuracy (25-30 m). Other test shows that 25-30 GCPs are a good compromise to not propagate the GCP error in the image/strip adjustment. Different block/bundle adjustments were then performed with 25 GCPs, but with different distributions in the block. The whole results demonstrate the applicability of the bundle adjustment model as well as the stability and robustness of the method with nadir viewing images, whatever the number of images, the overlap directions (North/South or East/West), the image/strip configurations, and the GCP/TP distributions. A general error of 25-30 m is obtained, but which included the cartographic error of ICPs. In operational environment, it is a requisite to generate strips from images of the same path and date, and to exclusively use elevation TPs in overlapping areas in both directions (North/South and East/West) for a greater stability and robustness. Furthermore, less GCPs are required with strips block than with images block.

Acknowledgements

The authors thank Mr. Alexander Berger and Ms. Alexandra Koch of Technische Universität Dresden, Germany for the Landsat-7 ETM^+ image processing. The Centre for Topographic Information Sherbrooke, Natural Resources Canada provided the topographic maps.

References

Kornus W., Lehner M., and Schroeder M., 2000. Geometric in-flight calibration of the stereoscopic line-CCD scanner MOMS-2P. ISPRS Journal of Photogrammetry and Remote Sensing, Vol. 55, No. 1, pp. 59-71

Sakaino S., Suzuki H., Cheng P., and Toutin Th., 2000. "Updating maps of Kazakhstan using stitched SPOT images", Earth Observation Magazine, Vol. 9, No. 3, pp. 11-13.

Toutin, Th., 1985. Analyse mathématique des capacités stéréoscopiques du système SPOT. Thèse de Docteur-ingénieur, Ecole Nationale des Sciences Géodésiques, Paris, France, 163 pages.

Toutin, Th., 1995. Multisource data fusion with an integrated and unified geometric model. EARSeL Journal Advances in Remote Sensing, Vol. 4, pp. 118-129. ww.ccrs.nrcan.gc.ca/ccrs/eduref/ref/bibpdf/1223.pdf.

Cheng Ph., Toutin, Th., and Tom V., 2000. Unlocking the Potential of Landsat 7 Data. Earth Observation Magazine, Vol. 9, No. 2, pp. 28-31. www.ccrs.nrcan.gc.ca/ccrs/eduref/ref/bibpdf/4769.pdf.

Veillet, I., 1991. Triangulation spatiale de blocs d'images SPOT. Thèse de Doctorat, Observatoire de Paris, Paris, France, 101 pages.

APPLICATIONS OF INTERFEROMETRIC SAR FOR ELEVATION DETERMINATION IN AUSTRALIA

John C. Trinder
and
Eric D. Cheng

School of Surveying and Spatial Information Systems
The University of New South Wales
Sydney, Australia

KEY WORDS: Digital Elevation Models, Interferometric SAR, Phase Unwrapping

ABSTRACT

The paper describes tests carried out on extracting elevations from ERS1/2 Tandem synthetic aperture radar interferometry (InSAR) data over Australia. Since there is substantial repeat coverage over Australia by the ERS1/2 Tandem data, it is an appropriate data set for upgrading the elevation data over Australia, providing adequate elevation accuracies can be achieved from the data. The purpose of the tests is to determine the accuracy of the elevations derived from this data by interferometry. The study has involved the use of several software packages for the processing of the data, two of which require the input of identifiable ground control points. The tests have used two of these packages to determine the accuracy of the extracted elevations, based on comparisons with identifiable features on maps and existing DEMs.

1. INTRODUCTION

Synthetic Aperture Radar (SAR) images are routinely collected for remote sensing purposes on a number of Earth observation satellites. SAR images can be used for the determination of elevations, and small variations in elevations over time, as described in Graham (1974) and Gabriel et al (1989), by the process of interferometry, (abbreviated to InSAR) by using the phase information in the return signals recorded by the antenna. In InSAR two images of the same reflected radiation of a scene are recorded by two separated antennas. After registering the two images, the phases corresponding to each pixel in the two images are calculated and differenced, resulting in a phase difference image, called an interferogram. The antennas may be installed on the same platform (single-pass InSAR) or the same antenna may be flown twice over a scene (repeat-pass InSAR). If the antennas are separated in the direction parallel to the line of flight or azimuth direction, motions of the surface such as ocean currents can be measured, while if the antennas are separated perpendicular to the line of flight or range direction, elevation information can be derived.

The European Space Agency (ESA) has launched two satellites ERS1 (in 1991) and ERS2 (in 1995) which include C-band SAR systems. They are single antenna systems and were not designed for interferometry, since the repeat cycle was 35 days. This would lead to insufficient coherence between successive SAR acquisitions in many cases, which would not allow the generation of interferograms. The launch of ERS-2, however, enabled the operation of the two platforms in tandem in 1995-6, the so-called Tandem Mission, which reduced the time between data acquisitions of the two passes to one or two days, thus ensuring adequate correlation between most successive pairs of SAR scenes. The Tandem Mission, which lasted for a period of 9 months, enable the acquisition of pairs of ERS-1 and ERS-2 SAR images over large parts of the global land surfaces including Australia, which are suitable for the derivation of medium to high resolution DEMs.

Australia has a land mass of over 8 million square kilometres. The determination and maintenance of topographic information over the country is a major and expensive undertaking. Currently elevation information is available nationally at an interval of 9 arc seconds, and some areas at 3 arc seconds. Elevations with a higher frequency are available in densely populated areas. The Tandem Mission has resulted in the availability of a large number of pairs of SAR images that are potentially suitable for interferometric applications. The purpose of this study is to test the suitability of using these data for upgrading the DEM database over Australia and to determine other potential applications of this data. In particular, the study aimed to determine the accuracies of elevation extracted from the InSAR data, and the factors influencing these accuracies.

2. PRINCIPLES OF ELEVATION DETERMINATION BY INTERFEROMETRY SAR

Consider two radar antennas which simultaneously view the same region from two positions A_1 and A_2 respectively, as shown in Figure 1, where the distance between two antennas is referred to as the baseline. The range distance between A_1 and an illuminated point on the ground is r, while $r + \delta r$ is the distance between A_2 and the same point. In this example, the radar wave is transmitted from antenna A_1, and after interaction with the terrain, the backscattered return is recorded by both antennas A_1 and A_2. These signals are then processed to complex SAR images, and phases measured in each image are differenced on a pixel by pixel basis. The phase differences are sensitive to both viewing geometry and the height of the illuminated point with respect to reference surface.

From the imaging geometry shown in Figure 1 the elevation h is given by:

$$h = H - r\cos\theta \qquad (1)$$

The phase difference between the two returns signals can be modelled as the corresponding distance δr in terms of wavelength of the emitted signal, which expressed in radians, is:

$$\varphi = \frac{2\pi\delta r}{\lambda} \qquad (2)$$

The phase φ in equation (2) is the fractional phase (value $0\text{-}2\pi$ radians). This leads to an ambiguity in determining the range, which must be solved by phase unwrapping techniques (Goldstein et al 1988). Hence the phase information can be converted to an image, displaying variations in height, provided the viewing geometry is known to sufficient accuracy.

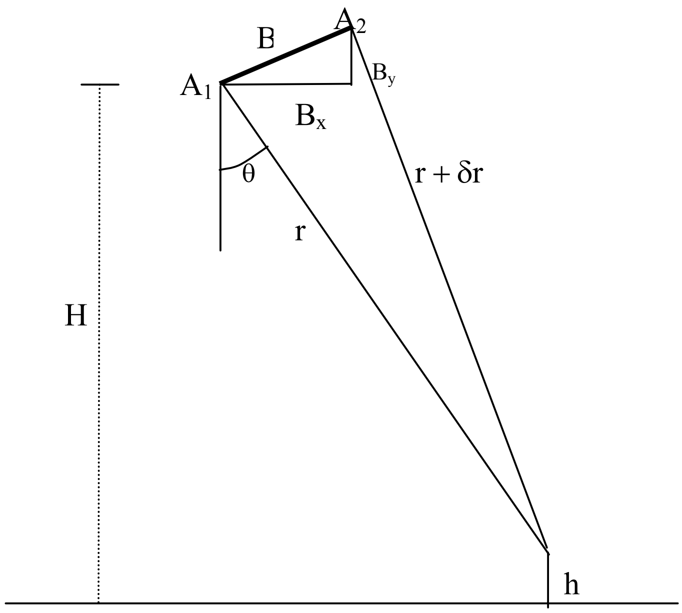

Figure 1: A schematic diagram of InSAR

For repeat pass interferometry SAR, since on each pass the antenna acts as both transmitter and receiver, the total path difference for each observation to an illuminated point on the ground is twice what would be expected in a single pass imaging geometry with two physical antennas. Therefore, the equation for repeat pass geometry is:

$$\varphi = \frac{4\pi\delta r}{\lambda} \qquad (3)$$

The path difference δr is related to baseline and viewing angle θ by:

$$\delta r = B_x \sin\theta - B_y \cos\theta \qquad (4)$$

Where, B_x and B_y are components of baseline as shown in Figure 1.

This study is based on the above formulae for the ERS1/2 Tandem Mission data, together with the necessary equations for phase unwrapping and computations of elevations, using three commercial software packages as described below.

3. TESTS OF THE ELEVATIONS DETERMINED BY INSAR

3.1 Test Procedures

The study commenced with the assumption that the characteristics of the pairs of images that would be suitable for InSAR applications over Australia should have the following characteristics:

- The perpendicular baseline between the orbits of the two data passes should be less than 300 metres, preferably 100-200 metres
- Ground control points should be available with an accuracy compatible with the expected accuracy of the elevations being determined by InSAR processing
- Adequate coherence between the pairs of images should be achievable with the InSAR software being used for the project
- The terrain conditions for the two acquisition should not vary significantly, otherwise temporal decorrelation between the images will occur, thus rendering them unsuitable for InSAR applications.

It was originally proposed that the test sites chosen should cover a range of areas in Australia, and include mountains, rivers, and townships, in which good details are available for the choice of ground control and check points. So far five pairs of data have been tested using a range of software. Three software packages are available for this study, Atlantis EarthView™, Phoenix Systems' PulSAR ™ (Muller et al 2000) at UNSW and Vexcel Synthetic Aperture Radar Processor FOCUS™ at AUSLIG. Atlantis and Vexcel require the input of identifiable ground control points, whereas PulSAR uses the satellite ephemeris information only to position the DEM. Also, the PulSAR software uses two different phase unwrappers, the standard process, referred to as the 'InSAR' and the ESA minimum cost flow phase unwrapper, referred to as 'MCFU'. The results reported in this paper are based on processing with Atlantis and PulSAR.

The procedure for computation of DEMs involves the determination of the coherence between the pairs of images, referred to as master and slave images, the computation of the interferograms from the phase information of the pixels, phase unwrapping to convert the interferogram values to elevations, and the input of Ground Control Points to reduce the elevations to the height datum. The mean errors and estimated accuracy of DEMs in this study have been determined by comparing the computed elevations of the Ground Control Points (GCP) and check points located manually on existing topographic maps with their known values, and by overlaying the derived DEM onto a known DEM. The known DEM available is the AUSLIG

9” DEM national database of Australia with an estimated accuracy of 10 m. In all cases in these tests, accuracies are quoted as the RMS of the differences between the elevations derived from topographic maps of the area, or the known DEM of the area, and the computed elevations by interferometry.

3.2 Images Tested

All the test areas cover rural parts in the states of New South Wales and Victoria in Australia. The base lengths for all image pairs are given in Table 1. All scenes typically comprise details that were chosen for GCPs and check points, such as a railways, highways, features in small townships of several thousand people and large townships comprising up the 40,000 residents, major roads, rivers, lakes, and small waterways. The heights of the terrain in the areas generally vary between 200 to 600 metres, but the scene in Victoria includes mountainous areas that caused problems in image correlation. The first test area comprises one image pair collected on January 12/13, 1996, located in New South Wales. The area is covered by five 1:100 000 maps with the 20 metre contour. Hence the accuracy (standard error) of the positions of the ground control points (GCPs) is about 30 metres while for the elevations the standard error is 7 metres. The second area in New South Wales comprises three pairs of data of the same area, collected on different dates, November 24/25, 1995, December 29/30, 1995 and May 17/18, 1996. For the location of ground control points and check points, nine 1:50,000 maps with the 10 metre contour were available. The standard error of the positions of the ground control points (GCPs) is about 15 metres while for the elevations the standard error is about 4 metres.

The third test pair of ERS-1/2 Tandem images was collected on December 11/12, 1995 (ERS-1/ERS-2), located in Victoria, the area being covered by more than 60 1:25,000 scale maps with 10 metre contours. The standard error of the positions of the ground control points (GCPs) and check points is about 8 metres while for the elevations the standard error is about 4 metres. Because of the low coherence of the images in the mountainous area in this test case, most mountain areas was masked out, but elevations in these areas can be determined by lowering the coherence threshold. However, it was difficult to find suitable GCPs in this area.

Table 1 ERS-1/2 InSAR satellite base lengths

Data Collected Dates	Mode of acquisition	Perpend. Base (m)	Parallel Base (m)
NSW Jan 12/13,96	Ascending	111	45
NSW Nov. 24/25, 95	Descending	129	49
NSW Dec. 29/30, 95	Descending	292	122
NSW May 17/18, 96	Descending	119	60
Vict Dec 11/12 95	Ascending	186	69

3.3 Analysis of Accuracies of Computed Elevations

The initial images tested with Atlantis software were based on full scenes of 110 by 40 kms with a range resolution of approximately 8 to 9 metres and azimuth resolution of approximately 4 to 5 metres. However, the errors in elevations after processing these scenes were larger than 30 metres in some cases. Hence the input image was further processed by dividing them into four sub-images of approximately ¼ scene, each image being about 55 km in azimuth direction and 20 km in range direction. The five image pairs in NSW and Victoria were processed with the Atlantis software, based on full scenes and sub-scenes comprising ¼ of the images. The Victoria scene has also been processed by PulSAR.

The comparisons with the GCPs and check points if available, are shown in Table 2. While the PulSAR DEM was not computed using GCPs, the locations of the GCPs used for the Atlantis software were interpolated onto the results from the PulSAR processing and used as an accuracy check. The comparisons with the 9” AUSLIG DEM are shown in Table 3. In Table 4 a comparison of the elevations computed from the three multiple scenes of the same area are given.

Table 2 Results of InSAR Processing with two software packages

Row	Test Cases	No of GCP/ Check Pts	Source of GCPs, Acc Plan/Ht m	Mean difference m	Elevation RMS differences m
1	**Atlantis NSW Jan 11/12 96**				
2	Full scene - GCPs	75	Maps Plan 30/Ht 7	0	33
3	Upper-left - GCPs	24	Maps Plan 30/Ht 7	0	10
4	Upper-right - GCPs	24	Maps Plan 30/Ht 7	0	9
5	Lower-left - GCPs	21	Maps Plan 30/Ht 7	0	6
6	Lower-right - GCPs	10	Maps Plan 30/Ht 7	0	8
7	**Atlantis NSW Nov 24/25 95**				
8	Full scene - GCPs	94	Maps Plan 15/Ht 4	0	11
9	Small area - GCPs	42	Maps Plan 15/Ht 4	-	8
10	**Atlantis NSW Dec 28/29 95**				
11	Full scene - GCPs	131	Maps Plan 15/Ht 4	0	19
12	Lower left - GCPs	50	Maps Plan 15/Ht 4	0	7
13	Lower right - GCPs	33	Maps Plan 15/Ht 4	0	5
14	Upper left - GCPs	33	Maps Plan 15/Ht 4	0	7
15	Upper right - GCPs	28	Maps Plan 15/Ht 4	0	6
16	**Atlantis NSW May 17/18 96**				
17	Full scene - GCPs	68	Maps Plan 15/Ht 4	0	35
18	Small area - GCPs	23	Maps Plan 15/Ht 4	0	9
19	**Atlantis Vict Dec 11/12 95**				
20	Full scene - GCPs	171	Maps Plan 8/Ht 4	-	9
21	Upper left - GCPs	118	Maps Plan 8/Ht 4	0	7
22	Upper right - GCPs	43	Maps Plan 8/Ht 4	0	9/6
23	Upper right- check points	61	Maps Plan 8/Ht 4	2	6
24	**PulSAR Vict Dec 11/12 95**				
25	Full scene – Check Points	61	Maps Plan 8/Ht 4	-6	10

Figure 3 Comparisons of derived DEMs with national DEM

Row		Mean m	RMS m
1	**Atlantis NSW Jan 11/12 - 9" DEM**		
2	Full scene	1	40
3	Sub-scene	6	15
4	**Atlantis NSW Nov 24/25 - 9" DEM**		
5	Full scene	4	20
6	Sub-scene	3	59
7	**Atlantis NSW Dec 28/29 95 - 9" DEM**		
8	Full scene	14	31
9	Sub-scene	3	14
10	Sub-scene	3	16
11	**Atlantis NSW May 17/18 95 - 9" DEM**		
12	Full scene	11	57
13	Sub-scene	3	27
14	Atlantis - Mean of Nov/Dec/May DEM – 9" DEM	1	17
15	**Vict Dec 11/12 95 - 9" DEM**		
16	Atlantis - Full scene	3	31
17	PulSAR MCFU- Vict Dec 11/12 95 - 9" DEM	-2	11
18	PulSAR – InSAR Vict Dec 11/12 95 - 9" DEM	-2	17
19	Atlantis & PulSAR - Vict Dec 11/12 95	0	23

Table 4. Comparison of multiple scenes

Atlantis – Multiple scene comparison		
Master scene NSW Nov 24/25 95	Mean m	RMS m
NSW Dec 28/29 95	18	39
NSW May 17/18 95	5	53

The selection of GCPs was a difficult task, since the identification of map features on the radar images, where their appearance depended on the reflectance characteristics of the terrain surface, presented problems. A maximum of 100-200 GCPs were usually identifiable on the maps and an image pair. It is believe that these points should result in the best measure of the accuracy of the elevations, since they all represent individual points that were all manually identified on the images. The RMS errors of the full scene DEMs computed by Atlantis (shown in Rows 2, 8, 11, 17, 20, and 21 in Table 2) compared with the GCP elevations varied significantly, being more than 30 metres in some cases. This is also the case for the repeat scenes of the same area, where the accuracies are 11m, 19 m and 35m. For the sub-image tests, the RMS errors of the computed elevations based on the GCPs were between 6 to 10 metres, which approaches the accuracies of the GCPs. The poor accuracy for the full scenes may be due to the inadequacy of the polynomial used to transform the DEM to the terrain surface in Atlantis software and correct for distortions in the DEM with respect to the control.

The comparison of the accuracies of the computed DEMs against the AUSLIG DEM, with an estimated accuracy of 10 m, show much greater variations. In these cases there are over 1 million DEM data points derived from the full scenes used for the comparison, covering the whole area, including areas of trees, mountainous areas, water etc. It could therefore be assumed that there would be areas in the scenes where the coherence of the pairs of images will be poor and therefore the computed elevations would be subject to significant errors. Table 3 shows that the means and RMS of the differences between the computed elevations for full scenes and known DEMs, are generally 5-10 m and 30-40m respectively, while for the sub-scenes, the means and RMS are somewhat better in most cases. The elevations derived from the 17/18 May 96 scene are generally worse than those for the two other scenes of the same area, ie 24/25 Nov 95 and 28/29 Dec 95. The comparison of the 28/29 Dec 95 and 17/18 May 96 scenes with the 24/25 Nov 95 scenes in Table 4 show the variations in the accuracies of the multiple scenes. Hence the three scenes of the same area were meaned and compared with the AUSLIG DEM in Row 14 of Table 3. In this case the mean and RMS are significantly better than the results obtained for the individual scenes.

Results of computations using the PulSAR software are given in Rows 17 and 18 of Table 3. In this case the mean values are significantly zero. The accuracies are somewhat better for the MCFU than the InSAR phase unwrapper. Also, the comparison between the PulSAR software with MCFU and Atlantis in Row 19 in Table 3, shows significant differences between the elevations derived from the two packages.

Given the overall accuracy of the AUSLIG DEM, the tests have shown that elevations can be determined by Atlantis and PulSAR with accuracy of the order of 10-15 metres. It should be stressed that in all comparisons between the computed and existing DEM, the maximum errors were of the order of several hundred metres. Generally these large errors applied to a small number of points in comparison to the total number of elevation points involved. Errors in InSAR DEMs can be due to poor coherence between the image pairs caused by characteristics of the objects being imaged, changes in the objects between the two data takes, radar shadow effects, and atmospheric effects on the transmitted beams. The large differences between elevations computed for the three scenes taken at different times of the same region are indicative of the magnitude of errors that are possibly caused by these effects. The mean of the results from the three sets of data in Row 14 in Table 3 indicate that an improvement in the accuracy of the elevations can be achieved. However, more work is required to investigate the causes of the large errors and a means of correcting them.

4. CONCLUSIONS

Five ERS-1 and ERS-2 Tandem data image pairs have been processed using the Atlantis software and one pair of images has been processed with PulSAR. Uniformly distributed Ground Control Points (GCP) were selected on maps of the areas to correct the DEM to the terrain surface derived by Atlantis. Independent check points were used to estimate the accuracy of produced DEM. PulSAR software did not require the use of GCPs. The computed elevations were also compared with the national 9" DEM. Based on these experiments, the following conclusions can be drawn:

- The accuracies of the elevations derived by Atlantis from full scenes, 110x40 km in size, based on GCPs are of the order of 20-40 metres in most cases. For sub-scenes, 55x20km in size, the accuracies are of the order of the accuracy of the GCPs, that is 10 m or better.
- The comparisons of elevations computed by Altantis with the existing 9" DEM revealed accuracies of the same order as results determined for the full scenes based on the GCPs. From these tests, the use of sub-scenes influences the accuracy of the computed elevations. Overall the comparisons of computed elevations for sub-scenes with the existing DEMs are consistent with the accuracies of the existing 9" DEM.
- The comparison of multiple scenes of the same area indicates that significant differences in computed elevations can occur, which are apparently a function of the InSAR data collection process. Taking the mean of elevations derived from multiple scenes can improve the quality of the computed elevations.
- The elevations computed with PulSAR, although only for one scene, may be more accurate than those computed with the Atlantis software. There is a significant advantage in using PulSAR, since GCPs are not required for this software.
- Overall the tests demonstrate that elevations can be determined by both software packages with an accuracy of 10-15 metres.
- While there are one or two exceptions, the mean differences between the computed elevations and the given 9" DEM are general significantly zero, indicating that there is no bias in the datums of the derived elevations.
- For some lower coherence areas, such as mountains, water areas, and areas of poor details, there is considerable difficulty in finding GCPs. GCPs play a very important role in interferometry applications using the Atlantis software.
- The research requires further work on determining the distribution and reasons for the larger errors in the elevations derived by InSAR.

5. REFERENCES

Gabriel A., Goldstein R., & Zebker H., 1989, "Mapping small elevation changes over large areas: Differential radar interferometry", Journal of Geophysical Research Vol. 94, pp. 9183-9191.

Goldstein R. M., Zebker H. A., and Werner C. L., 1988, "Satellite radar interferometry: two- dimensional phase unwrapping", Radio Science Vol. 23, No. 4, pp. 713- 720.

Graham L. C., 1974, "Synthetic interferometer radar for topographic mapping", Proc. of the IEEE, Vol. 62, No. 6, pp. 763- 68.

Muller J.-P., Morley J. G., Walker A. H., Kitmitto K., Mitchell K. L., Chugani K., Smith A., Barnes J., Kenan R., Cross P. A., Dowman I. J., Quarmby N. (2000) "The LANDMAP project for the automated creation and validation of multi-resolution orthorectified satellite image products and 1" DEM of the British Isles from ERS tandem interferometry", LANDMAP Special Session RSS 2000 Leister University, 12-14 September 2000.

The BIRD Payload Platform

by

I. Walter, K. Brieß, W. Bärwald, W. Skrbek, F. Schrandt

German Aerospace Center, Institute of Space Sensor Technology and Planetary Exploration
Rutherfordstr. 2, D-12489 Berlin, Germany
e-mail. ingo.walter@dlr.de

KEY WORDS

Remote sensing, Hot spot detection, Micro-satellite, Optical payload, Platform technology

ABSTRACT

For hot spot events as forest and vegetation fires, volcanic activity or burning oil spills and coal seams a dedicated space instrumentation does not exist. Respectively missions with a new generation of cooled infrared array sensors are planned for the near future.
According to their objectives the BIRD (**B**ispectral **I**nfra-**R**ed **D**etection) mission will answer several technological questions related to the operation of this infrared sensors in space.
As space segment serves a three-axis stabilised micro-satellite with a mass of 92 kg including a contingent of over 30 % for the payload.

The article focuses on the scientific instruments and special aspects of their adaptation to the satellite platform and shows the spacecraft design status.

1. INTRODUCTION

The growing interest on the investigation of fire as indicators for influences on the natural environment from space is reflected in several mission studies. Starting with a proposal for a fire recognition system *(FIRES, 1994)* at DLR the BIRD concept was established to demonstrate the scientific and technological value and the technical and programmatic feasibility of an appropriate remote sensing satellite mission, following a strict design-to-cost philosophy.

Based on the core activity to design a new generation of imaging infrared detectors the interest to investigate their operational behaviour in space led to a complete micro-satellite development, which is oriented on a set of ambitious scientific tasks of the science community. The build-or-buy decision for the spacecraft bus was also very much influenced by the special functional requirements of the payload.

2. MISSION OBJECTIVES AND REQUIREMENTS

Besides the detection and identification of hot spots, caused by vegetation fires, industrial hazards and burning oil wells a variety of scientific objectives emerges from related natural events - volcanic studies, investigation of clouds and atmospheric properties (pollutant emission) and vegetation analysis (aridness, recultivation). These scientific objectives are completed by technological ones summerised in table 1.

Table 1 – Mission objectives of BIRD

	BIRD - Mission Objectives
Primary objectives	*1. Development, qualification and demonstration in space of small satellite technologies* *2. Test of a new generation of infrared array sensors adapted to Earth remote sensing objectives by means of small satellites* *3. Detection and scientific investigation of hot spots (forest fires, volcanic activities, burning oil wells or coal seams)*
Secondary objectives	*4. Thematic on-board data processing (test of a neural network classificator in orbit)* *5. More precise information about leaf mass and photosynthesis for the early diagnosis of vegetation condition and changes* *6. Real time discrimination between smoke and water clouds*

Table 2 - Functional mission requirements on the BIRD payload *(K. Brieß 1997)*

	BIRD - Payload Requirements				
Task	***Spectral***	***Radiometric***	***Geometric***		***Other***
			GSD	***Swath Width***	
Hot-spot detection hot-spot classification observation of vulcanoes	*3.4-4.2 µm* *8.5-9.3 µm* *1 VIS/NIR channel*	*Temperature estimation within dynamic range >2000, saturation limit at T<1300 K, rad. Resol. within IR >12 bit*	*< 300 m*	*As large as possible, min. >100 km*	*Different visir angles at VIS/NIR*
Determination of Veg. Index 3 and comparison with the Normalized Diff. Veg. Index	*840-890 nm* *600-670 nm* *3.4-4.2 µm*	*≥ 7 bit (VIS/NIR)* *≥ 12 bit (MWIR)*	*100 m – 300 m*	*Small*	*Integer pixel size ratio of VIS/NIR and IR pixels*
Improvement of Leaf Area Index	*840-890 nm*	*≥ 7 bit (VIS/NIR)*	*100 m – 300 m*	*Small*	*Different visir angles*
Realtime detection of clouds, *cloud investigation*	*Min. 3 VIS/NIR channels + 1 TIR*	*Dynamic range >1000*	*≤ 1 km*	*Minimum > 100 km*	*Stereo cabability*
Test and evaluation of multi-sensor-multi-resolution technique, test of on-board neural network classification	*3.4-4.2 µm* *8.5-9.3 µm* *1 or more VIS/NIR channels*	*≥ 7 bit (VIS/NIR)* *≥ 12 bit (IR)*	*100 m – 300 m*	*Small*	*Integer pixel size ratio of VIS/NIR and IR pixels*
Technological experiments concerning IR-system	*3.4-4.2 µm* *8.5-9.3 µm*	*Range-level + drift- and detectivity control,* *vibration isolation, pixel alignment*			

The analysis of scientific objectives leads to several requirements for the scientific instruments, here provided by table 2.

The requirements on orbit and operations are determined by the fact that BIRD is foreseen for a piggy-back launch. That means that the design has to fit in several scenarios. At least a LEO from 450 to 900 km (500 km preferred) with an inclination >53° is required.
The operational lifetime is 1 year with a 10 min duty cycle over land regions. This restriction is coming from the limited data volume which is able to handle in a store-and-forward manner with at least one mission operation centre and another small experimental ground station for payload data receiving. Besides that it underlines the characteristic of the BIRD mission to be a demonstrator and not an operational system.

3. SCIENTIFIC INSTRUMENTS

3.1. Hot Spot Recognition Sensor (HSRS) – Instrument Design in two Steps

Base for the space-proven design of the HSRS was a development of an airborne laboratory model of the two IR cameras for the mid- and thermal infrared spectral range according to figure 1. The detectors characterised in table 3 are cooled to 80 K operating temperature by a separate Stirling cycle cooler.
This system was intensively tested under laboratory and airborne conditions and could prove the scientific concept of the BIRD mission.

Fig. 1 – IR camera - Laboratory Model

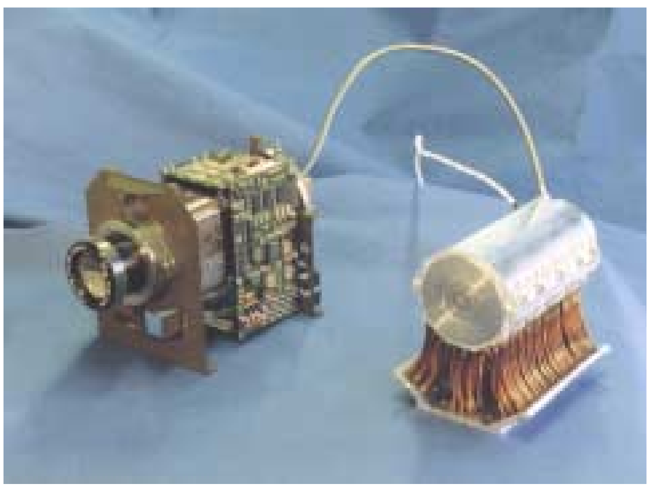

Table 3 – IR-Detector parameters for BIRD

Detector material	*HgCdTe*
Spectral channels	*3.4 – 4.2 µm* *8.5 – 9.3 µm*
Detectivity	*10^{10}cmHz$^{1/2}$/W*
No. of elements	*1024 (2 Arrays available)*
Array format	*2x512 staggered*
Element size	*30 x 30 µm*
Element stagger	*15 µm*
Max. pixel rate	*5 Mhz (4 outputs)*

The system performance allowed the detection of hot spots with a dimension of a tenth of the ground pixel size if the temperature is 800 K or higher. That means from the proposed BIRD orbit fires in the 30 m range are able to identify *(Lorenz, Skrbek 1999).*

However the first results showed that direct detection of hot spots with the required radiometric resolution is not compatible with the limited resources of a micro-satellite. The high power consumption for cooling (40 W cool-down, 32 W operation per channel) and the significant influence of thermal radiation coming from the instruments inner structure were the main disadvantages which desired a design change.

Equipped with the same detector as before an integrated detector/ cooler design was derived from military applications technology and space-qualified (see figure 2). Here the main problem is to provide enough stiffness of the inbound cooling finger beneath the IR-detector chip against dynamical loads during the launch process. A so arising solid structural solution is in contradiction to the demands of thermal de-coupling to minimise power needs. At least a factor of 4 less power could be reached in comparison to a split cooler concept.
Together with a new lens design the inner radiation disturbances could be decreased significantly to improve the temperature measurement accuracy.

Fig. 2 – Miniaturised integrated detector/ cooler assembly
(GMIRL 1998)

Fig. 3 – HSRS with IREU in flight configuration (8.7 + 5.8 kg, 0.22 x 0.21 x 0.45 m³ (right)

The design of the flight configuration of the HSRS (see figure 3) is driven by strong requirements of the co-alignment stability in the line-of-sight of the MWIR to the LWIR channel (±0.2 arcmin at duty cycle). It is characterised by the following attributes:

- Split design in Sensor Head and Electronics Unit (IREU)
- Identical construction of the optical channels (only optical coating of lenses different, figure 4)
- Autonomous thermal control including heat storage and radiator
- Opto-mechanical CFRM-structure with high resonance (> 200 Hz)

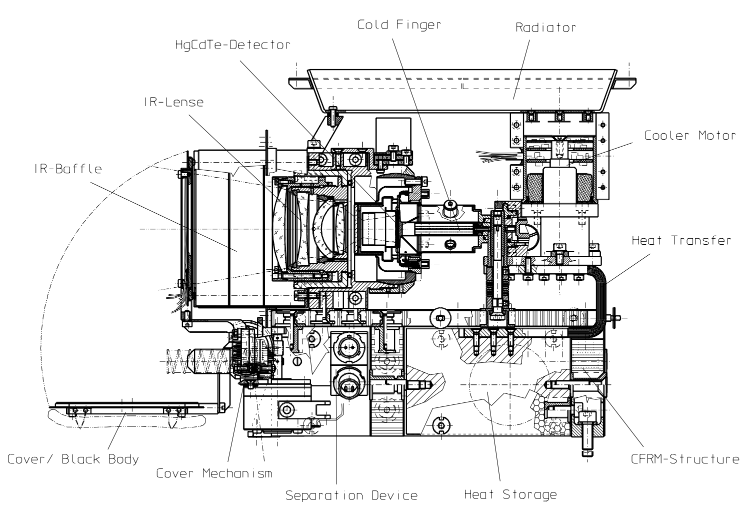

Fig. 4 – Design of HSRS and pre-integrated optical bench and structure (photographs right)

As shown in figure 4 a cover in front of the IR-lenses prevents from contamination – specifically atomic oxygen. It also contains a controllable blackbody for in-flight calibration purpose. The inherent total failure risk is minimised by a separation mechanism that rejects the cover system in emergency cases.

3.2. Wide Angle Optoelectronic Stereo Scanner (WAOSS-B) – an Example of Hardware Reuse

This instrument is the VIS/NIR-sensor of the BIRD payload. Actually developed for the MARS-96 mission a flight spare model was modified slightly.

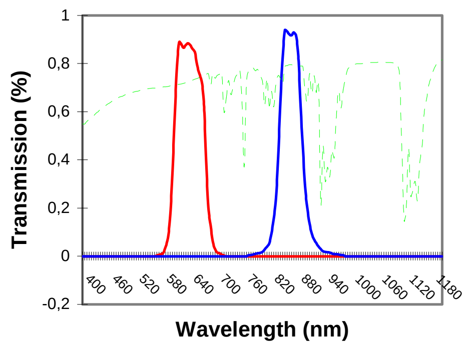

Fig. 5 - Spectral bands of WAOSS-B (NIR doubled)

Fig. 6 - WAOSS-B under integration (8.4 kg, 0.18 x 0.21 x 0.38 m³ (right)

New lenses with integrated filter providing narrow spectral bands over a wide field of view of 50° (see figure 5) adopts the instrument to the tasks of vegetation exploration. On the other hand the in-track stereo capability is an important feature for the cloud investigations.
Due to the modular electronic concept of WAOSS-B almost no hardware modification are needed and the re-configuration is concentrated on the software side, i.e. to provide the master clock function for simultaneous imaging of all BIRD instruments.

3.3. HORUS – Use of an Flight Opportunity

According to the functional requirements the BIRD payload is clearly oriented on medium spatial resolution imagery. However the attractiveness of higher resolution is evident not only for hot spot detection.

So in an advanced project phase close to the final qualifications an panchromatic channel with a focal length of 500 mm was developed – the High Optical Resolution Utility Sensor (HORUS).
It is based on in-house technology and was qualified under optional status and not to drive any requirements of the BIRD spacecraft (power, AOCS etc.). The fit to the WAOSS-B envelope configuration enforced a compact optical design using the Cassegrain principle (figure 7). Containing hybrid electronics (see figure 8) from developments of the ROSETTA mission (*Behnke, Neukum 1999*) HORUS on board of the payload segment besides from its experimental use answers qualification questions.

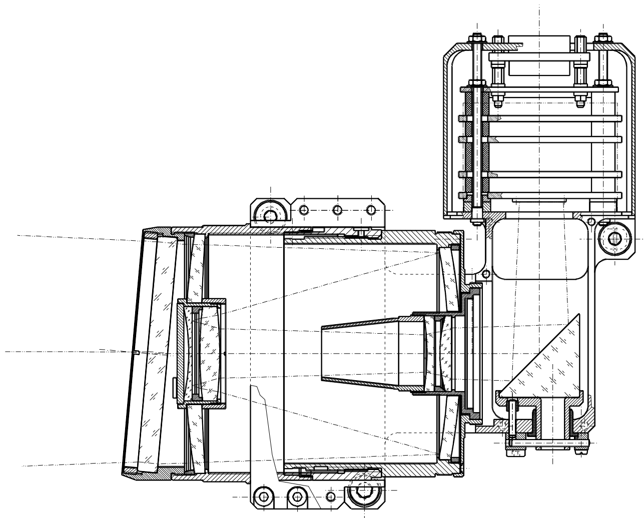

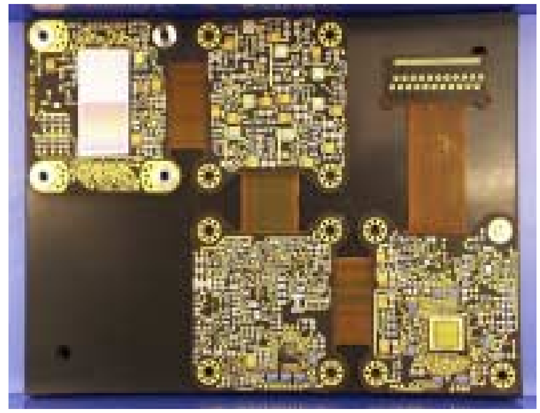

Fig. 8 – Modular CCD hybrid electronics – first use in space on BIRD ahead of the ROSETTA mission

Fig. 7 - HORUS design overview (0.75 kg, 0.14 x 0.15 x 0.07 m³, left)

3.4. Payload Data Handling System (PDH)

The PDH is the functional integrative part of the scientific payload. It has data interfaces to all instruments, the spacecraft bus computer (SBC) and the down-link telemetry channel.
Three kinds of tasks are assigned to the PDH:

- distribution of high level commands and Housekeeping extraction out of the payload data stream
- science data storage, telemetry frame generation and down-link
- on-board thematic data compression

Each of the two functional redundant PDH-subsystems is based on a TMS320C40 digital signal processor equipped with 1 Gbit mass memory. Advanced multi-chip module technology allows to compress the size of the processor module to one standard European Size printed circuit board.
According to this the PDH is stored in the electronics segment of the spacecraft together with the SBC and secondary electronics.

Additional technological experiments are the fibre optic interconnects or on-line real-time parallel processing. Also the tests of the on-board geo-coding facility and different classification algorithms with the neuro-chip NI1000 are of experimental character.

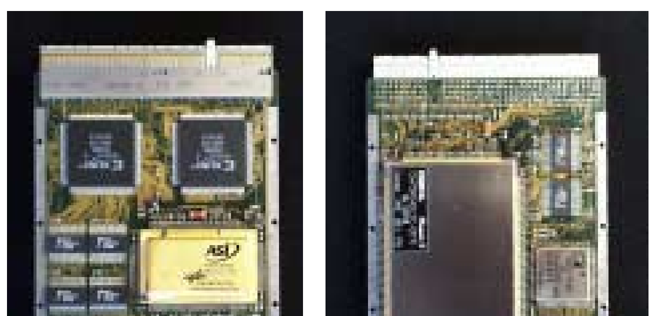

Fig. 9 – Both sides of the PDH processor board, Mass memory (1 of 2 assembled) left, 3D-MCM-processor hybrid right

3.5. Technical Data Overview

To summarise this section Table 3 gives the main technical data of the payload calculated from an altitude of 565 km (piggy-back launch on the indian PSLV in autumn 2001).

Table 3 - Main technical parameters of the BIRD scientific instruments

	HSRS - MWIR	HSRS - LWIR	WAOSS-B	HORUS
Spectral bands	3.4 - 4.2 µm	8.5 - 4.2 µm	forward 600 - 670 nm nadir, backward 840 - 900 nm	450 – 890 nm
F-number	2.0	2.0	2.8	8
Focal length	46.39 mm	46.39 mm	21.65 mm	540 mm
Pixel size	30 x 30 µm	30 x 30 µm	7 x 7 µm	14 x 14 µm
No. of pixels	2 x 512 staggered	2 x 512 staggered	3 x 5184 (2884 illum.)	1024 x1024
Instantaneous FOV	2.22 arcmin	2.22 arcmin	1.11 arcmin	5.35 arcsec
FOV across track	19 deg	19 deg	50 deg	1.6 deg
FOV in track	2.22 arcmin	2.22 arcmin	+25 , 0, -25 deg	1.6 deg
Ground pixel size nadir	365 m	365 m	183 m	14.6 m
Swath width	187 km	187 km	527 km	15 km
Quantization	14 bit	14 bit	11 bit	14 bit
Data rate (aver./ peak)	693/ 4790 kbps	693/ 4790 kbps	597/ 600 kbps	1.8 Mbyte/ image
Power consumption	42 W incl. Electr. Unit	42 W incl. Electr. Unit	18 W	1.7 W
Mass	8.7 kg Camera Head + 5.8 kg Electronic Unit		8.4 kg	0.75 kg

4. BIRD-INSTRUMENTATION AS AN INDEPENDENT MULTI-SENSOR-ASSEMBLY

4.1. Structural Concept

Classical spacecraft designs are oriented on a clear separation of payload which are the scientific instruments and the spacecraft bus containing all sub-system supporting the function of the payload.
Here a strong interaction during the development process requires strict management of interfaces from a very early design phase on. In configurations of small satellites this in addition takes place within a small volume.
Therefore for the BIRD payload and subsystem components had to be developed in a highly iterative process considering the satellite as one complex device. To minimise interface interference the structure design defines a modular system.

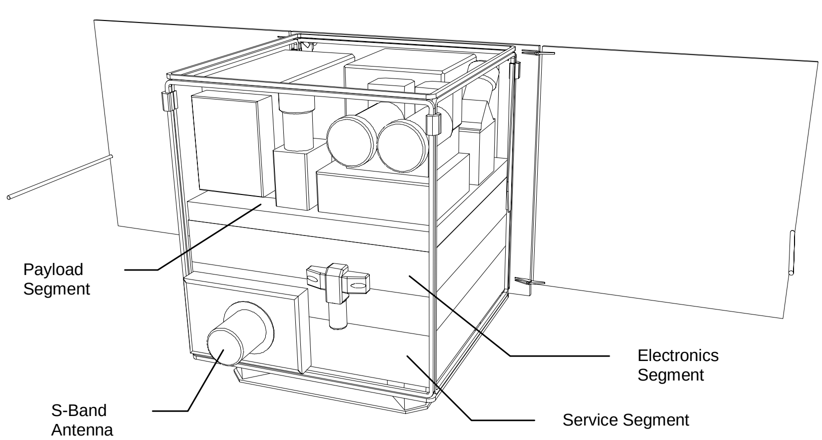

Fig. 10 - Flight configuration of BIRD (0.6 x 0.6 x 1.6 m³)

According to figure 10 the primary structure of the BIRD architecture is a cube-shaped tower of three segments:

1. Service segment as the basic segment with separable launcher interface containing batteries, reaction wheels and gyroscope as well as the GPS system
2. Electronics segment as a container of payload, spacecraft electronics and the communications package
3. Payload segment as a platform for the scientific instruments and the star sensors.

The configuration is completed by a solar cell system of three panels – two of them deployable – the antennas an magnet torquers.

4.2. Payload Segment Requirements

Together with the corresponding part of the electronics segment over 50% of the BIRD- volume is at the payload's disposition – 50 dm³. The mass budget is 30 kg – 30% of the satellite.

According to the functional concept the most pretentious demand is to keep the optical axes of the scientific instruments stable during data acquisition to allow a so-called pixel co-registration for appropriate data processing on ground.
Early analysis showed that the demand for an overlap error of 10% of an infrared pixel between LWIR and MWIR has to be considered in the instrument design itself. All other – the requirements are provided in detail in table 4 - had to be realised by the payload structure.

Instrument	***Function***	***Boresight axis orientation***	***Scientific FOV***	***Instantaneous FOV***	***Stability @ duty cycle****	***Mounting accuracy***
HSRS LWIR	*Hot spot detection 8.5- 9.3 µm*	*Nadir +Z*	*19°*	*2.22 arcmin*	*n.a.*	*n.a.*
HSRS MWIR	*Hot spot detection 3.4- 4.2 µm*	*Nadir +Z*	*19°*	*2.22 arcmin*	*±0.2 arcmin*	*3-4 pixels*
WAOSS-B	*Vegetation/ clouds diagnosis 600-670 nm fw 840-890 nm na 840-890 nm bw*	*Nadir +Z*	*50° x 50°*	*1.11 arcmin*	*±1.0 arcmin*	*8-10 pixels*
HORUS	*High resolution*	*Nadir +Z*	*1.6° x 1.6°*	*0.09 arcmin*	*Not required*	*< FOV*
Star S1	*Star Sensor*	*Cross track -Y*	*17.5° x 13°*	*1.6 arcmin*	*±5.0 arcmin***	*30 pixels*
Star S2	*Star Sensor*	*Cross track -Y +30°*	*17.5° x 13°*	*1.6 arcmin*	*±5.0 arcmin***	*30 pixels*

** Accuracy with respect to the optical axis of HSRS LWIR as reference*
*** Accuracy of ±0.1 arcmin will be measured by in-flight calibration*

Table 4. Overview of BIRD instruments and their optomechanical requirements

Besides the opto-mechanical other constraints influenced the design:

- Highly compact configuration in order to be open for more than one launch opportunity
- Application of instruments with space qualification for other missions (indivisible constructive bodies)
- Instrument placement according to cross-calibration concepts
- Payload as independent module for parallel development and qualification

4.3. Payload Platform Concept and Technology

The overall spacecraft design concept started with an isostatic mounted aluminum plate as a base for the scientific instruments. Besides the great mass of such a solution analysis identified a need to control the temperature within 1K for thermal stability under a 200 W emission of heat during the duty cycle.

Hence CFRM were chosen for a plate material oriented on a target mass of 4 kg. To overcome the difficulties with heat conduction in-plane (measured coefficient 0.55 W m^{-1} K^{-1}), first ideas intended to supply every instrument with a heat pipe. This option was in strong contradiction to the modular character of the structure. The preferred solution is to combine two CF-honeycomb panels on top and below of a 3 mm-thick layer of Carbon Fibre Carbon (CFC). This layer provides heat conduction to the heat pipe interfaces on the front ends of the platform with a coefficient of 155 W m^{-1} K^{-1} – comparable with aluminum.

As Figure 11 shows, the instrument mounting interfaces of this multi-sandwich structure are inserts with an enlarged plate founded in the CFC-layer. All connections with thermal relevance are glued with silver-filled epoxy structure. The heat conduction reaches over 50% of that from aluminum its CTE is a factor of 15 less.
Another effect is the de-coupling of structural loads coming from the spacecraft bus because of separated mounting planes for spacecraft and scientific instruments.

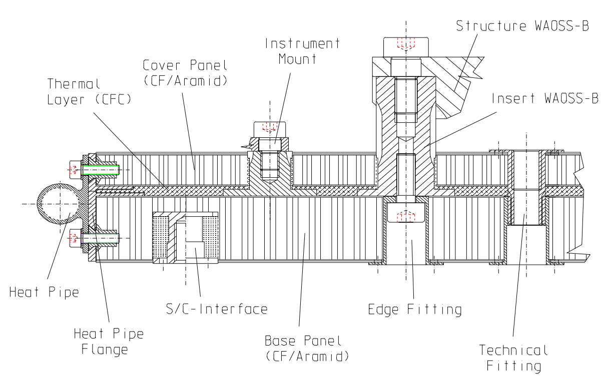

Fig. 11 Design principle of the payload platform (cross section)

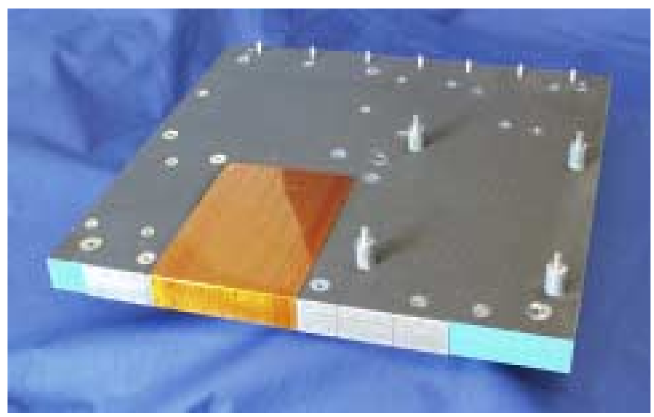

Fig. 12 CFRM platform incl. payload mounting points and thermal control elements

4.4. Payload Platform Test and Performance

During the thermal/ vacuum program of the BIRD Structure- Thermal- Model simulating the pre-defined duty cycles of the complete spacecraft in-situ measurements of the co-alignment of all scientific instruments were implemented.
Because there is no access to the payload situated in the vacuum chamber an optical principle with the help of alignment prisms were installed which allows observation of all instruments from one point without movement of the payload segment or the measuring equipment. The misalignment caused by instrument and platform deformation in cold and warm operational phases is detected by autocollimation.

Figure 13 and 14 shows the principle of measurements and a screen plot of the autocollimator. The precision of this procedure is about 10 arcsec.

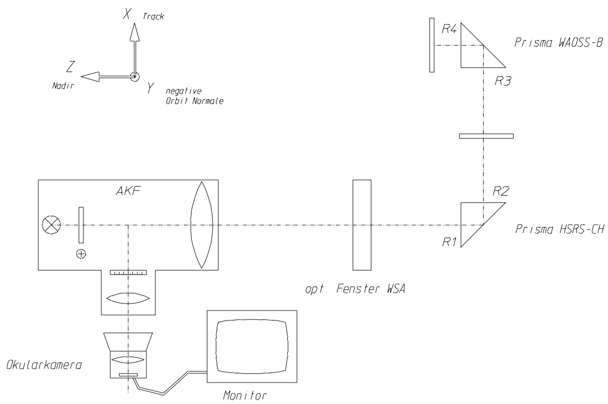

Fig. 13 ***Optical principle for in-situ optical alignment test under vacuum***

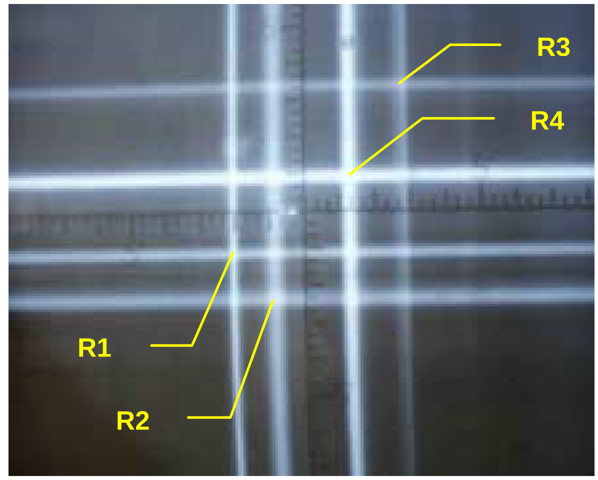

Fig. 14 ***Monitor of Autocollimator with reflexions from Instruments: R1 & R2 - HSRS, R3 & R4 – WAOSS-B***

The test were performed step by step starting with the platform itself to avoid misinterpretations by thermal effects of the test facility (figure 15). Due to the measuring principle the complete payload could be covered with multi-layer-insulation in a flight-like manner (figure 16).

Fig. 15 ***Test preparations inside the vacuum chambers door***

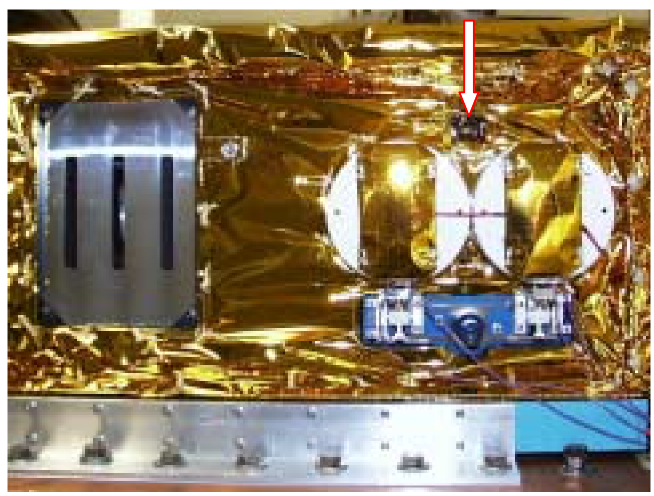

Fig. 16 ***Nadir side of the BIRD payload STM with optical entrance for collimation (arrow)***

As a result it could be stated that the typical alignment deviations due to instrument operations are 1 arcmin and 3 arcmin due to the change of the platform temperature of 30 K representing the shift of orbit conditions over the mission. Here the influence of the spacecraft structures behaviour made from milled aluminum could not be compensated completely.

4.5. Platform Integration and BIRD Spacecraft

According to figure 17 the payload segment is completed by two star sensors, the upper low gain antenna, GPS- antenna and magnetic field sensor. Including the payload specific harness which is not shown at the drawing a very compact configuration is performed.

Fig. 17 BIRD payload segment overview (right, w/o harness)
Fig. 18 Complete calibrated payload segment prior mounting on the S/C (aft view, below)

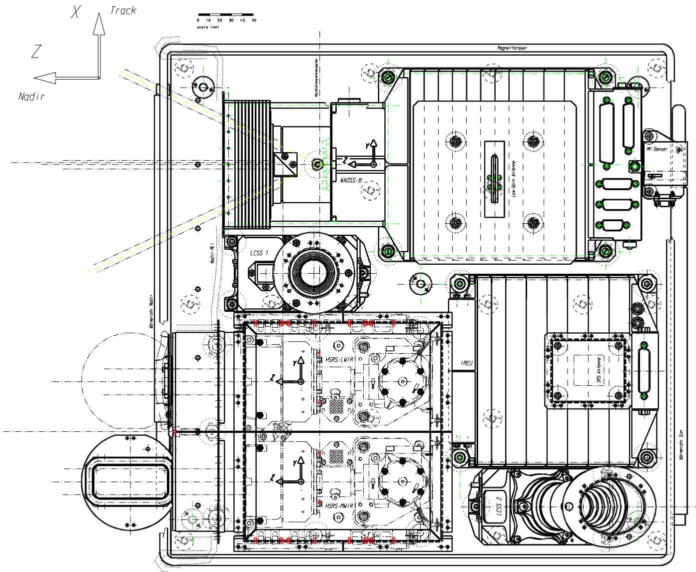

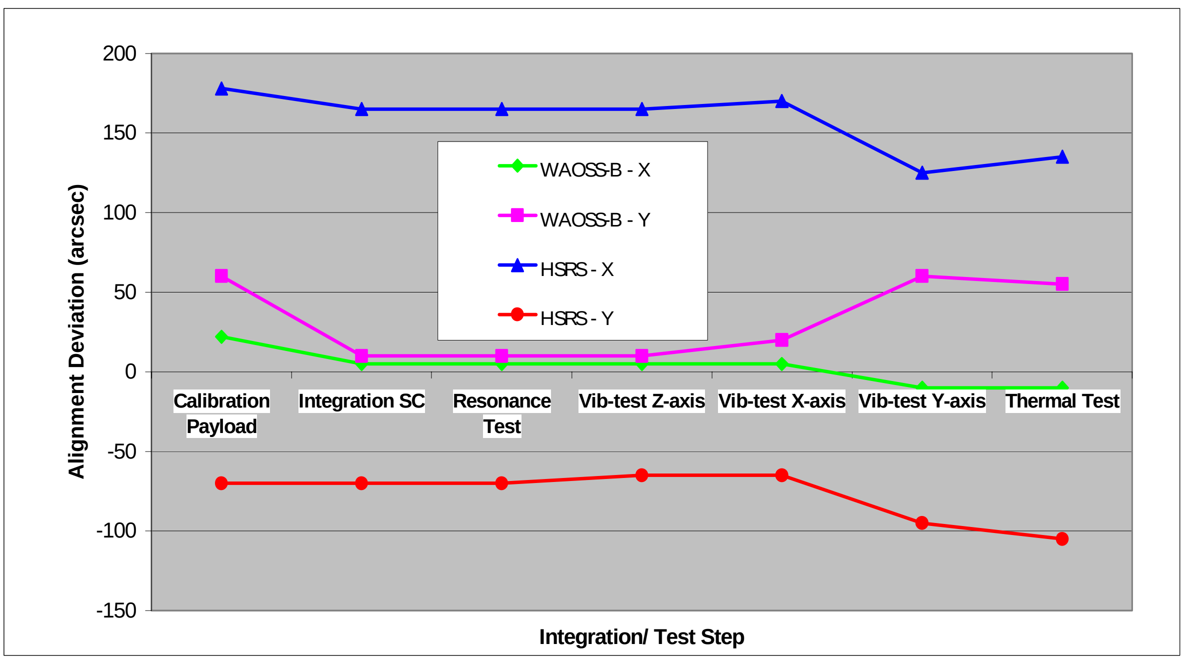

Fig. 19 Co-alignment of the BIRD payload during integration and tests *(BIRD 2001)*

With the help of the principle described it was possible to check the optical orientation during all integration and test steps. Thus the joint calibration of all instruments was realised with the hardware integrated according to figure 18 without intermediate mounting procedures. Co-alignment control as stated in figure 19 secures the up-date of the calibration file. So effects of mounting and settlement caused by dynamical loads can be included.

The advantage of the independent design of the payload segment during integration with the spacecraft results in a quite simple mounting procedure based on minimised interfaces. That also gives flexibility in case of refurbishment of components is needed.

However it could be demonstrated that platform technology should be a part of the payload design for a satellite mission if there are special demands on optical stability and packing density. Accuracy needs in the sub-pixel range are not to be satisfied under low-cost constraints. Here the focus should be on the knowledge of deviations coming from the flight equipment environment.

Fig. 20 - Flight Model BIRD under CoG measurements (right)

Fig. 21 – Pre-resonance test of the flight configuration (below)

5. REFERENCES

(FIRES 1994)	Fire Recognition System for Small Satellites. Phase A Study, DLR Institute of Space Sensor Technology, Berlin and OHB-System, Bremen
(K. Brieß et al 1997)	BIRD, Phase B Report, Technical Plan, DLR Institute of Space Sensor Technology, Berlin, p. 19
(E. Lorenz, W. Skrbek, B. Zhukov)	Airborne testing of a bi-spectral infrared push-broom scanner for hot spot detection, Proc. SPIE, vol. 3759, pp. 97-105
(GMIRL 1997)	The newsletter of GEC Marconi Infrared, Southampton, p. 2
(T. Behnke, G. Neukum 1999)	Super Resolution Channel of the HRSC, Proposal to ESA, DLR Institute for Space Sensor Technology and Planetary Exploration, Berlin 1999, p. 6
(D. Hundertmark, R.Schuster 2001)	BIRD payload alignment, Report, DLR Institute for Space Sensor Technology and Planetary Exploration, Berlin 2001, pp. 10 -11

INDIRECT ORIENTATION OF PUSHBROOM SENSORS WITH 3-D FREE-FORM CURVES

Garry H. Zalmanson and T. Schenk
Dept. of Civil & Environmental Engineering & Geodetic Science
The Ohio State University
Columbus, OH 43210
zalmanson.1@osu.edu, schenk.2@osu.edu

KEY WORDS: Line Photogrammetry, Registration, Line Scanners, Free-Form Curves, Stochastic Processes

ABSTRACT

This paper presents a rigorous mathematical framework for determining the exterior orientation parameters of a pushbroom image from 3-D curves represented parametrically and naturally. The central motivation for utilizing one-dimensional features is to provide continuous control information essential for accommodating high frequency sensor maneuvers that cannot be fully recovered from direct orientation mechanisms of insufficient quality. On the other hand, it is neither theoretically nor practically feasible to completely ignore such auxiliary mechanisms for solving the orientation problem of pushbroom systems. Bearing these two principals in mind, we fist develop a unified model combining any prior information on the EOPs (e.g., from GPS/INS/IMU) with a mathematically rigorous incorporation of 3-D curves. We then demonstrate how the orientation problem of somewhat unstable platforms can highly benefit from incorporation of one-dimensional object space entities. That is done by studying a variety of spatial configurations of such entities and comparing the orientation results obtained with them to those obtained from traditional point-based solutions. We conclude with some current research efforts towards multi-sensor feature-based photogrammetric triangulation.

1 INTRODUCTION

Over the past two decades pushbroom systems based on CCD line sensors have evolved as a mature and viable solution for a wide range of airborne and spaceborne remote sensing applications. From a photogrammetric perspective, this technology significantly differs from the traditional frame cameras, however. The platform motion provides the second dimension of pushbroom images, resulting in a rather unconventional geometry in which each scan-line has a different set of six exterior orientation parameters (EOPs). Consequently, for utilizing these sensors in photogrammetric applications, a full and accurate recovery of these EOPs must be accomplished. Not surprisingly, such a strict demand on the accuracy of the EOPs, coupled with the (problematic) sequential image acquisition lead to the widely accepted consensus that non-frame systems cannot yield sufficiently robust geometric solutions unless accompanied with high-quality GPS/INS systems for direct and continuous sensor orientation. Such integration is still believed to be necessary for accommodating various platform perturbations and instabilities that are likely to occur during image formation. Our paper partly challenges this argument. We show that while it is undoubtedly true for traditional point-based orientation methods, when employing one-dimensional features, such as roads, railways and pipe-lines as ground control, the dependency on extremely accurate and therefore expensive GPS/INS systems becomes less critical. The central motivation for utilizing one-dimensional features is to provide continuous control information in the object space. In analogy, GPS/INS provides continuous information directly on the EO parameters with the notable difference that no relationship between EO and the surface is established. Another advantage of adopting feature-based orientation techniques is the fact that no prior correspondence between individual points describing the features in both domains (image & object) is required. Therefore, there is practically no limitation on the number of image space measurements that can be associated with the corresponding control 3-D features. Whereas for frame images the ability to incorporate more observations results in a just more accurate estimate of the (common) EOPs, for pushbroom sensors it provides an otherwise impossible continuous control essential to address the randomness of the underlying acquisition process.

In this paper we present a unified approach for the recovery of the EOPs of pushbroom sensors combining any prior information on the EOPs (e.g., GPS/INS) with a mathematically rigorous incorporation of 3-D free-form curves. The proposed model does not address any existing imaging system specifically, but rather, it provides a generic framework to solve the orientation problem for a general linear sensor with an arbitrary orientation determination system (ODS). The remainder of this paper consists of six sections and is structured as follows. After formally stating the problem, sections 3 and 4 show, respectively, how parametric and free form curves can be rigorously incorporated to solve for the EOPs of a dynamic image. To make the proposed method more intuitive and at the same time to motivate the advantages of using linear features for geo-referencing dynamic images section 5 presents a specific stochastic error model for the angular orientation elements. In section 6, that specific error model is used to test the feasibility and the performance of our proposed method. In particular, we emphasize on demonstrating its superiority over traditional point-based orientation techniques, especially in terms of the accuracy of the recovered EOPs. Finally, in section 7, concluding remarks are drawn and future activities in this research area are listed.

2 PROBLEM STATEMENT

In this section we briefly summarize the geometric model of image formation with a pushbroom sensor, followed by defining the problem to be solved. Fig 1 depicts a typical imaging scenario of a generic time-dependent linear system.

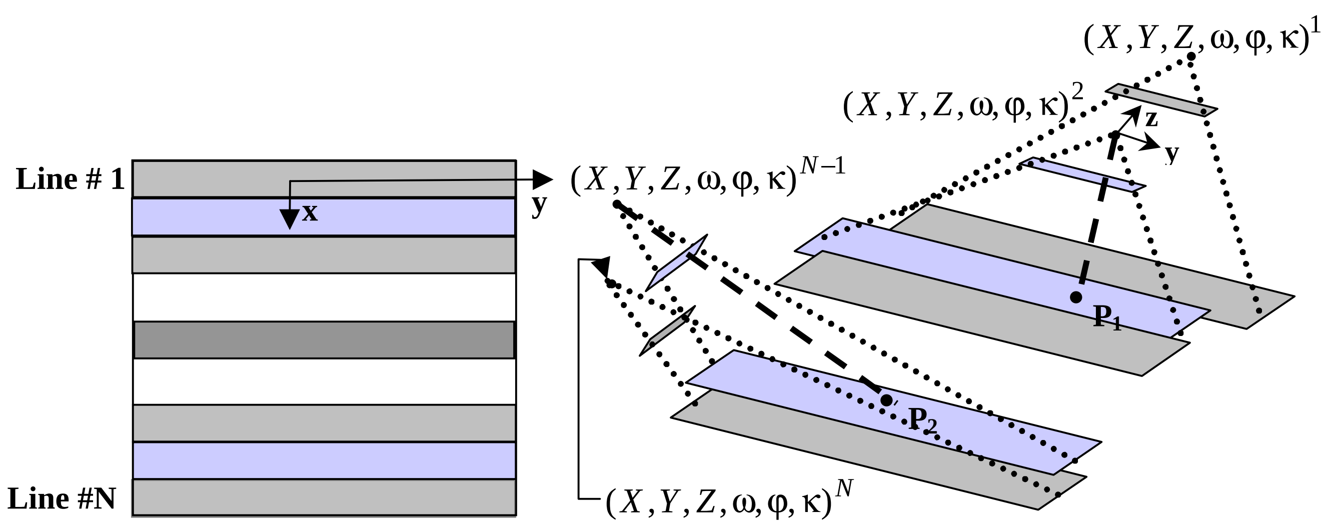

Figure 1: Linear-array image (left) and its corresponding ground swath (right).

Following common photogrammetric notations for time-dependent systems, the Sensor Coordinate Frame (SCF) is defined with the origin at the instantaneous perspective center, z-axis coinciding with the optical axis, y-axis parallel to the linear CCD array, and with x-axis completing a right-handed Cartesian system. The 3-D coordinates (X_p, Y_p, Z_p) of a point P in local reference frame are related to its SCF coordinates (x, y) through the following set of equations, keeping in mind that the sensor position $(X_O^{line}, Y_O^{line}, Z_O^{line})$, and the orientation matrix $R(\omega^{line}, \varphi^{line}, \kappa^{line})$ are now time (scan-line) dependent.

$$\begin{bmatrix} x \\ y \\ -f \end{bmatrix} = \lambda R(\omega^{line}, \varphi^{line}, \kappa^{line}) \begin{bmatrix} X_p - X_O^{line} \\ Y_p - Y_O^{line} \\ Z_p - Z_O^{line} \end{bmatrix} \tag{1}$$

In (1), f is the system's focal length, x denotes a sub-pixel location (ranging from –0.5 and 0.5 times the pixel size), and λ, a scalar that differs from point to point. Under the assumption that the interior orientation of the sensor is perfectly known, what remains to be determined are the EOPs, i.e., the three positional elements and the three angular elements for each scan-line. Altogether we have 6N unknowns to be estimated for an N-line image. These 6N parameters are, essentially, not independent and in fact highly correlated. Thus, not only that their independent recovery is practically impossible (due to an inherently degenerate geometric configuration), but it is also physically incorrect. Therefore, when one comes to estimate the EOPs of a dynamic image, the introduction of some a-priori error model accommodating the evident correlation between the respective parameters is unavoidable. Over the years, many researchers (e.g., [3,4]) used the so-called piecewise polynomials to model the variations in the six exterior orientation parameters. The idea was to introduce low-order spline functions and to recover their free parameters using ground control points and auxiliary data obtained from on-board direct orientation (e.g., GSP/IMU) devices. There is a fundamental problem with such a simplistic description, however. That is since the spline model is just a mathematical tool that only accounts for systematic/deterministic factors, such as positional and angular velocities and accelerations. Physical systems (e.g., GPS, IMU, star-trackers), however, also suffer from random errors, being of course of different nature compared to their deterministic counterparts. Therefore, to faithfully model the dynamics of the orientation parameters both systematic and random factors should be accommodated, with first step in this direction done in [5]. The exact list of these factors primarily depends on the characteristics of the aiding orientation system. In general we can say that systematic errors can be ascribed to calibration misalignments and random-constant-like factors such as IMU drifts and scale-factors, while their random counterparts result from high-frequency platform maneuvers when no IMU component is present or to its control-loop inherent white noise when it is. In any case we claim that in order to accommodate a broad range of system anomalies a physical orientation model, tailored to a specific acquisition control mechanism, must be introduced. While a thorough investigation of dynamic error models of INS systems is not in the scope of this work, a conceptual framework to carry out such an analysis will be presented.

We now turn to describe the second major contribution of this work. Imagine that our aiding direct orientation system is not present or is of non-sufficient accuracy, particularly being unable to resolve high-frequency error factors. In this case an accurate recovery of the EOPs through traditional (point-based) methods would require a large and very densely distributed set of control points. In this paper we propose a practical alternative to this strict demand by introducing one-dimensional control features and their analytically rigorous incorporation for solving the orientation problem.

3 ORIENTATION USING PARAMETRIC CURVES

In this section we derive a rigorous mathematical model for determining the EOPs of a pushbroom image from 3-D analytical curves represented parametrically. In what follows we will assume that our control information is given in the form of a class of 3-D curves, called *regular curves*. A regular curve is defined as the locus of points traced out by the end point of a vector $\Gamma(s) = [X(s) \quad Y(s) \quad Z(s)]^T$ as the curve parameter $s \in \Re$ ranges from a to b. Further, $\Gamma(s)$ must have continuous second derivatives and its first derivatives must not vanish simultaneously anywhere in the interval $a \le t \le b$. We now modify (1) to express that a measured point (line, y) on the image corresponds to $\Gamma(s)$ as follows (see Fig 2). (Note that given a sub-pixel value of the scan-line, its x-coordinate is uniquely determined).

$$\begin{bmatrix} x \\ y \\ -f \end{bmatrix} = \lambda R(\omega^{line}, \varphi^{line}, \kappa^{line}) \begin{bmatrix} X(s) - X_O^{line} \\ Y(s) - Y_O^{line} \\ Z(s) - Z_O^{line} \end{bmatrix} \tag{2}$$

As stressed earlier, at this stage we are just interested to support a generic auxiliary orientation mechanism. Thereby, we model the dynamic EOPs as some implicit vector-valued process of stochastic onboard measurements β (e.g., GPS, gyros, accelerometers, etc.) and non-random factors ξ (e.g., calibration misalignments, gyro drifts, scale-factors, etc.). We now rewrite (2) to result with the following pair of condition equations written for each measured point on the image that corresponds to $\Gamma(s)$:

$$G_x(\mathrm{EOPs}(\beta,\xi), x, s) \equiv x + f\frac{u}{w} = 0 \qquad \text{with} \qquad \begin{bmatrix} u \\ v \\ w \end{bmatrix} = R(\omega^{line}, \varphi^{line}, \kappa^{line}) \begin{bmatrix} X(s) - X_O^{line} \\ Y(s) - Y_O^{line} \\ Z(s) - Z_O^{line} \end{bmatrix} \tag{3}$$
$$G_y(\mathrm{EOPs}(\beta,\xi), y, s) \equiv y + f\frac{v}{w} = 0$$

In G_x, G_y two groups of quantities are identified. The first consists of elements that are "observed". These include image measurements (x/line, y/sample) and auxiliary measurements β, collectively denoted by χ, hereafter. The second group consists of non-random factors including those originating from the auxiliary mechanism, i.e., ξ, and the new parameter s, associated with $\Gamma(s)$. What's interesting is that this, apparently innocent introduction of the curve parameter s, allowing a free motion along the tangent direction $\Gamma'(s) = [X'(s) \quad Y'(s) \quad Z'(s)]^T$ of $\Gamma(s)$ in object space, is, in essence, a central foundation of our feature-based orientation solution.

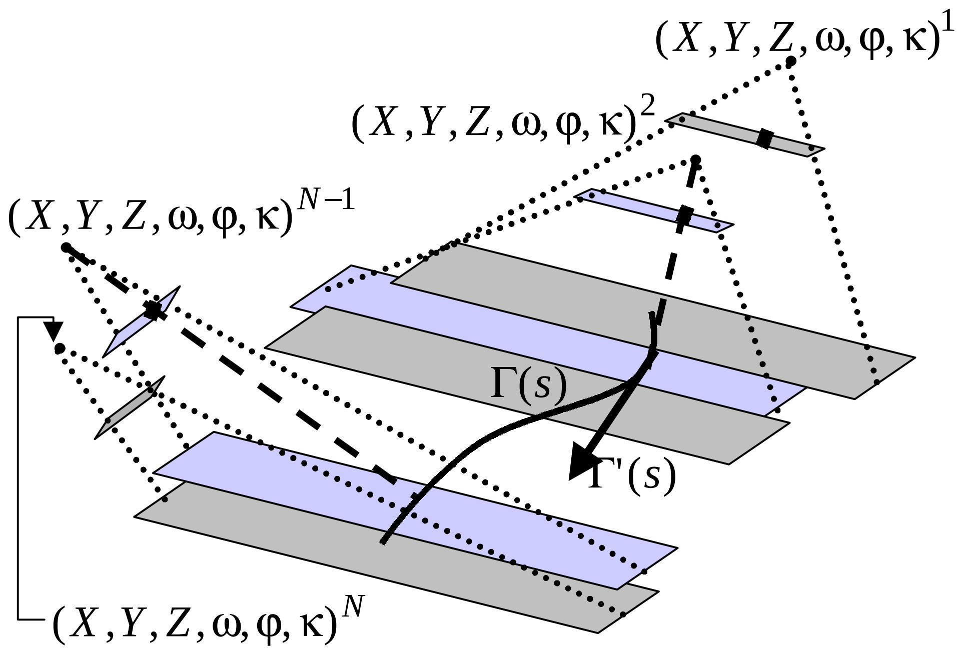

Figure 2: Associating pushbroom imagery points with a parametric 3-D curve.

To arrive at the set of linear equations, (3) must be linearized. Linearization requires initial values ξ_0 for the non-random parameters ξ as well as an estimate s_0 for the curve parameter s. The simplest way to estimate s_0 is to find the closest point on $\Gamma(s)$ to the ray passing through the instantaneous perspective center and image point (line, y). The computation of the closest point and its associated parameter s_0 requires an iterative minimization scheme, such as Newton method. With the initial estimates, system (3) is linearized to yield the following Gauss-Helmert model:

$$G_x^0 + A_x^1 d\xi + a_x^2 ds + B_x e = 0$$
$$G_y^0 + A_y^1 d\xi + a_y^2 ds + B_y e = 0 \tag{4}$$

With G_x^0, G_y^0 we denote the evaluation of G_x, G_y at the measurement vector χ and the initial estimates of the parameters. The partial derivatives of G_x, G_y with respect to the parameter vector ξ are contained in A_x^1, A_y^1, and those with respect to the measurement vector χ in B_x, B_y, respectively. a_x^2 and a_y^2 are the partial derivatives of G_x, G_y with respect to the curve parameter s, requiring a continuous first derivative of $\Gamma(s)$. Finally, $d\xi$, ds, and de are the increments to the parameters ξ, and s, and the "measurements" error vector e, respectively.
For N image measurements, system (4) is generalized to:

$$G^0 + A_1 d\xi + A_2 dS + Be = 0 \tag{5}$$

with

$$G^0 = \begin{bmatrix} (G_y^0)_1 \\ (G_x^0)_1 \\ \vdots \\ (G_x^0)_N \\ (G_y^0)_N \end{bmatrix}, \quad A_1 = \begin{bmatrix} (A_x^1)_1 \\ (A_y^1)_1 \\ \vdots \\ (A_x^1)_N \\ (A_y^1)_N \end{bmatrix}, \quad A_2 = \begin{bmatrix} (a_x^2)_1 & 0 & 0 \\ (a_y^2)_1 & 0 & 0 \\ 0 & \ddots & 0 \\ 0 & 0 & (a_x^2)_N \\ 0 & 0 & (a_y^2)_N \end{bmatrix}, \quad B = \begin{bmatrix} (B_x)_1 \\ (B_y)_1 \\ \vdots \\ (B_x)_N \\ (B_y)_N \end{bmatrix}, \quad dS = \begin{bmatrix} ds_1 \\ \vdots \\ ds_N \end{bmatrix}$$

and with a combined error vector containing both image observation errors and GPS/IMU errors as follows:

$$e = \begin{bmatrix} d\beta \\ (dline)_1 \\ (dy)_1 \\ \vdots \\ (dline)_N \\ (dy)_N \end{bmatrix}, \quad \Sigma_e = \begin{bmatrix} \Sigma_{d\beta} & C(d\beta, line_1) & 0 & \cdots & C(d\beta, line_N) & 0 \\ C(d\beta, line_1) & (\sigma_{line}^2)_1 & 0 & 0 & 0 & 0 \\ 0 & 0 & (\sigma_y^2)_1 & 0 & 0 & 0 \\ \vdots & 0 & 0 & \ddots & 0 & 0 \\ C(d\beta, line_N) & 0 & 0 & 0 & (\sigma_{line}^2)_N & 0 \\ 0 & 0 & 0 & 0 & 0 & (\sigma_y^2)_1 \end{bmatrix}$$

Note that in general there must be a correlation between the x/line-coordinate of a point and other ODS observations. That is true since the line-coordinate actually expresses the time, and almost any ODS observation is time-dependent. Also note that the covariance matrix Σ_β is by no means diagonal. In fact, it is the interplay between its diagonal and off-diagonal elements that determines the amount of flexibility "given" to the orientation parameters to change within the adjustment.

Following [4], the least-squares solution of system (5), minimizing $e^T \Sigma_e^{-1} e$, is given by

$$\begin{bmatrix} d\hat{\xi} \\ d\hat{S} \end{bmatrix} = -\left(A^T (B\Sigma_e B^T)^{-1} A\right)^{-1} A^T (B\Sigma_e B^T)^{-1} G^0 \quad \text{with} \quad A = \begin{bmatrix} A_1 & A_2 \end{bmatrix} \text{ and} \tag{6}$$

$$\tilde{e} = -\Sigma_e B (B\Sigma_e B^T)^{-1} (G^0 + A \begin{bmatrix} d\hat{\xi} & d\hat{S} \end{bmatrix}^T)$$

Since the original system (3) is not linear, the solution (6) requires an iterative approach ultimately yielding the best (in the least-squares sense) estimates for the EOPs. As shown, it rigorously combines prior information (e.g., from GPS/INS) and geometric relations between parametric curves in object space and their partial projection in the image.

4 GENERALIZATION TO FREE-FORM CURVES

In this section we formalize the EOPs determination problem when some elongated objects, represented as free-form curves are known in object space and can be extracted in the image. A 3-D free-form curve Γ_f, is represented by a sequence of vertices $V = \{V_i\}$. The set of vertices V induces an ordered set of line segments $L = \{\vec{l}_i\}$ where segment $\{\vec{l}_i\}$ connects the two vertices $\{V_i\}$ and $\{V_{i+1}\}$. Let $\Omega = \bigcup_{r=1}^{R} \Psi_r$ ($\Psi_r \bigcap \Psi_s = \varnothing$) be a partial projection of Γ_f, represented by a disjoint set of R components $\{\Psi_r\}$, each comprising a connected set of n_r 2-D points $\{line_j, y_j\}$ with $1 \le j \le n_r$. As before, we assume that there is no point-to-point correspondence between features in object space and their (partial) projections in image space. Then, the problem is to come up with the EOPs that would describe the relationships between object and image features in the best (in least-squares sense) way.

First, we select a subset $\Lambda = \{(line_i, y_i) \mid (line_i, y_i) \in \Omega\}$ of image points that belong to the projected control feature. Subsequently, given V and Λ, together with ODS observations, the following steps are performed iteratively until convergence is reached.

a) For each image location $(line_i, y_i) \in \Lambda$, the direction vector q of the ray from the instantaneous perspective center through (x_i, y_i) is determined by $q = R^T p$ where $p = (x_i, y_i, -f)^T$ (Recall, that x is just a sub-pixel component of the line coordinate).

b) The parametric equation of q in the object space reference frame is defined by:

$$\rho(\nu) \equiv \begin{bmatrix} X(\nu) \\ Y(\nu) \\ Z(\nu) \end{bmatrix} = \begin{bmatrix} X_O^{line} \\ Y_O^{line} \\ Z_O^{line} \end{bmatrix}_k + \begin{bmatrix} q_x^{line} \\ q_y^{line} \\ q_z^{line} \end{bmatrix}_k \nu$$ where k denotes the iteration step.

c) The point q_ν on ρ, which is the closest to Γ_f is located (see also Fig 3). This point is always related to a point l_j^t on one of the line segments $\{l_j\}$ to which q_ν is closest. The two points q_ν and l_j^s are determined analytically by minimizing the scalar- valued function $\Phi(\nu, s) \equiv \| \rho(\nu) - l_i(s) \|^2 =$ stationary (ν, s) for every possible segemnt $\{l_i\}$. The one with the global minimum is finally chosen.

This procedure also establishes a temporary association between every image location and the corresponding segment in the object space. Thus, we ca employ the general procedure described in the previous section for the corresponding line segment $\{l_i\}$. In particular, the curve parameter s and the object space tangent of $\{l_i\}$ are used to form (4). Finally, with all image points in Λ, system (5) is formed and solved for the EOPs iteratively. Note, that the correspondence between a given image location and its associated line segment is dynamic, and may change from iteration to iteration.

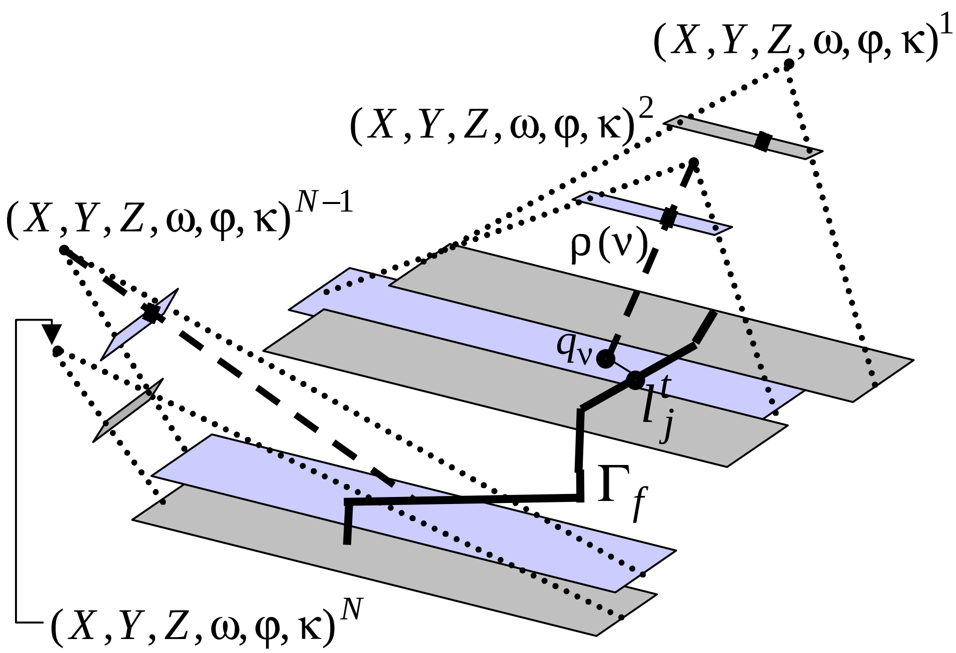

Figure 3: Time-dependent perspective transformation of a 3-D free-form curve.

The proposed orientation method with free-form curves is based on the parametric formalism introduced in the previous section. There are some important differenrces, however. As has been already mentioned the parametric model has been developed for space curves having first order continous derivatives. Clearly, this is not the case for free-form curves with singularities at the vertices of Γ_f. At these singular locations none of the equations of system (5) that require object space derivatives can be formed. Hence, it is important to discuss how to address these singular cases when encountered. A simple way to circumvent this problem is not to estimate the curve parameter s at the vertices. In this case, the closest point l_j^t will be kept fixed, that is, the degree of freedom to move along the otherwise unique tangent direction is removed. This solution is plausible in situations where the object space curve consists of relatively long segments, thus reducing the chance for the closest point to coincide with a vertex (for more details see also [6]). For the opposite case, with many short vertices it is recommended to approximate the set of vertices in the neighborhood of the closest point by an analytical curve, e.g. cubic spline, to eliminate singularities. This strategy will allow us to employ the parametric model developed in the previous section without any change.

5 STOCHASTIC MODELING OF ANGULAR ERRORS

In the previous two sections a generic model for integrating auxiliary navigation solution with one-dimensional control features represented as parametric and free-form curves has been developed. In this section we restrict the modeling problem to the set of angular orientation elements only. Although from a theoretical perspective this restriction indeed affects the generality of the overall problem, it nonetheless serves the primary goal of this paper – to show how the orientation problem of rather unstable platforms can highly benefit from incorporation of one-dimensional entities. Moreover, from a practical point of view, as the GPS technology, with its accurate and at the same time affordable solutions, is quickly penetrating into airborne and spaceborne remote sensing markets, a direct measurement of positional EO elements ceases to be a real problem. On the other hand, while it is true that high-quality attitude determination systems are also available, they are much more expensive and their integration with GPS receivers (only possible when an INS system and not only an IMU is used) and optical sensors is rather complex.

In the remainder of this paper we use the angular error model described by the following set of linear differential equations:

$$\begin{gathered}\dot{e}_\omega = w_1(t),\ \dot{e}_\varphi = w_2(t),\ \dot{e}_\kappa = w_3(t)\\ C(e_\omega, e_\varphi) = C(e_\varphi, e_\kappa) = C(e_\omega, e_\kappa) = 0\end{gathered} \tag{7}$$

with $w_1(t),\ w_2(t),\ w_3(t)$ being zero mean, white noise processes with covariance function $C_{w_i}(t,t') = q_i \delta(t-t')$, where q_i is a constant and $\delta(\tau)$ is the Dirac "delta function". This model may well fit the dynamics of an IMU system with gyros' white noise and initialization biases as the most dominant two error factors. Also note that no cross-correlation between different angular components is assumed.

Integration of (7) leads to

$$e_\omega(t) = b^0_\omega + \int_0^t w_1(\tau)d\tau = b^0_\omega + RW_\omega(t) \quad e_\varphi(t) = b^0_\varphi + \int_0^t w_2(\tau)d\tau = b^0_\varphi + RW_\varphi(t) \quad e_\kappa(t) = b^0_\kappa + \int_0^t w_3(\tau)d\tau = b^0_\kappa + RW_\kappa(t) \tag{8}$$

Here, $b^0_\omega, b^0_\varphi, b^0_\kappa$ denote the three angular biases and $RW_{\omega,\varphi,\kappa}(t)$ the three random walk processes associated with the three angular elements ω, φ, κ, respectively. System (8) clearly demonstrates the heterogeneous nature of the resultant angular error. Unlike traditional solutions for dynamic orientation problem, here, both deterministic (i.e., $b^0_\omega, b^0_\varphi, b^0_\kappa$) and stochastic (i.e., $RW_{\omega,\varphi,\kappa}(t)$) factors are combined. In fact, it is exactly this combination that naturally allows for local line-of-sight perturbations, caused by unexpected platform motion, to be recovered.

We now move to setting up the appropriate equation system for our specific case, giving rise to

$$\begin{gathered}G_x(b^0_{\omega,\varphi,\kappa}, RW_{\omega,\varphi,\kappa}, x, s) \equiv x + f\frac{u}{w} = 0\\ G_y(b^0_{\omega,\varphi,\kappa}, RW_{\omega,\varphi,\kappa}, y, s) \equiv y + f\frac{v}{w} = 0\end{gathered} \quad \text{with} \quad \begin{bmatrix}u\\v\\w\end{bmatrix} = R(\omega^{line} + e_\omega, \varphi^{line} + e_\varphi, \kappa^{line} + e_\kappa)\begin{bmatrix}X(s) - X_O^{line}\\ Y(s) - Y_O^{line}\\ Z(s) - Z_O^{line}\end{bmatrix} \tag{9}$$

or more explicitley, discriminating between the determinisic and stochastic components with

$$\begin{bmatrix}u\\v\\w\end{bmatrix} = R(RW_\omega^{line}, RW_\varphi^{line}, RW_\kappa^{line})\ R(b^0_\omega, b^0_\varphi, b^0_\kappa)\ R(\omega^{line}, \varphi^{line}, \kappa^{line})\begin{bmatrix}X(s) - X_O^{line}\\ Y(s) - Y_O^{line}\\ Z(s) - Z_O^{line}\end{bmatrix} \tag{10}$$

where $R(RW_\omega, RW_\varphi, RW_\kappa),\ R(b^0_\omega, b^0_\varphi, b^0_\kappa)$ are two rotation matrices corresponding to the three random walk processes and the three angular biases respectively. Using the notations set forward for the general case (system (4)), we identify that the three angular biases $b^0_\omega, b^0_\varphi, b^0_\kappa$ can be modeled as a non-random parameter vector, ξ, and the three random walks as an auto-correlated set of observation errors ($d\beta$) with a covariance matrix given by:

$$\Sigma_{d\beta} = \begin{bmatrix} C(\omega_{line1},\omega_{line1}) & 0 & 0 & \cdots & C(\omega_{line1},\omega_{lineN}) & 0 & 0 \\ 0 & C(\varphi_{line1},\varphi_{line1}) & 0 & \cdots & 0 & C(\varphi_{line1},\varphi_{lineN}) & 0 \\ 0 & 0 & C(\kappa_{line1},\kappa_{line1}) & \cdots & 0 & 0 & C(\kappa_{line1},\kappa_{lineN}) \\ \vdots & \vdots & \vdots & \ddots & \vdots & \vdots & \vdots \\ C(\omega_{line1},\omega_{lineN}) & 0 & 0 & \cdots & C(\omega_{lineN},\omega_{lineN}) & 0 & 0 \\ 0 & C(\varphi_{line1},\varphi_{lineN}) & 0 & \cdots & 0 & C(\varphi_{lineN},\varphi_{lineN}) & 0 \\ 0 & 0 & C(\kappa_{line1},\kappa_{lineN}) & \cdots & 0 & 0 & C(\kappa_{lineN},\kappa_{lineN}) \end{bmatrix}$$

with $C(\alpha_{\ln\_k},\alpha_{\ln\_l})$ derived from the covariance function of a random walk process, readily given by

$$C(\alpha_{\ln\_k},\alpha_{\ln\_l}) = E\{\alpha_{\ln\_k},\alpha_{\ln\_l}\} = \int_0^{\ln\_k}\int_0^{\ln\_l} E\{w_\alpha(\tau)w_\alpha(\tau')\}d\tau d\tau' = \int_0^{\ln\_k}\int_0^{\ln\_l} q_\alpha \delta(\tau-\tau')d\tau d\tau' = \begin{cases} q_\alpha \ln\_k & \ln\_l \ge \ln\_k \\ q_\alpha \ln\_k & \ln\_l < \ln\_k \end{cases}$$

with the symbol α referring to each of the three angular elements $\omega, \varphi,$ and κ. To complete the overall covariance matrix Σ_e given in (5), the covariance between the auxiliary angular elements and the corresponding line-coordinate of image space observations must be computed. While in general, such a correlation is present, in our case these two observations are not correlated due to the completely arbitrary nature of the process (white noise) controlling the formation of the angular errors. Finally, the estimated angular biases $\hat{b}^0_\omega, \hat{b}^0_\varphi, \hat{b}^0_\kappa$ along with the filtered stochastic errors $R\tilde{W}_{\omega,\varphi,\kappa}(t)$ are obtained from (6).

6 EXPERIMENTS AND RESULTS

In this section we present several preliminary results from an ongoing R&D research project on the subject, carried out at the OSU. The analysis is based on a simulated high-resolution satellite image consisting of about 6000 scan-lines (of 6000 pixels each) and which is formed within a time frame of 16 seconds. Applying the orientation model developed in the previous section, two cases are examined with a particular emphasis given to the latter. In the first case, three angular biases (i.e., $b^0_\omega, b^0_\varphi, b^0_\kappa$) were applied to the nominal angular EO of the image with the objective to recover them from ground control information given in the form of free-form curves (see Fig 4). This problem, however, is just a special case of a more general problem, thoroughly and successfully addressed in [6], where it was shown how the set of six EOPs of a frame sensor can be recovered from 3-D curves represented parametrically and naturally. Here, in fact, only a subset of the six, namely the three angular parameters are sought. In the second case studied lies the primary contribution of this work. There, three random walk processes, each with the white noise parameter set to $0.05°/\sqrt{hr}$, were “added” to the original angular orientation (see Fig 5). IMUs with similar noise characteristics are classified as medium-quality systems, as reported in [1].

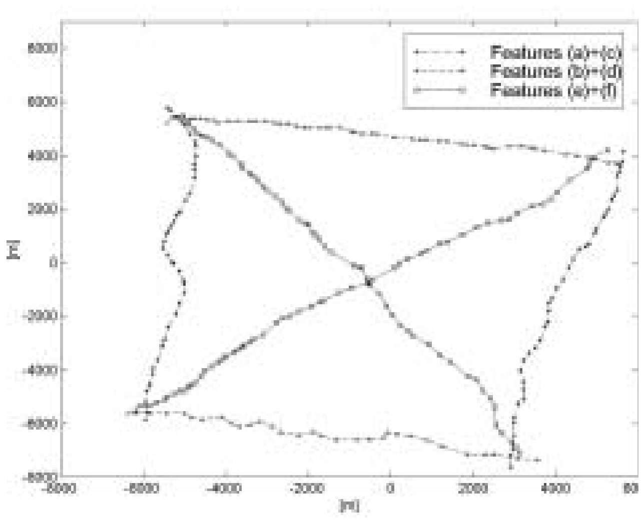

Fig 4: Six free-form curves used as control.

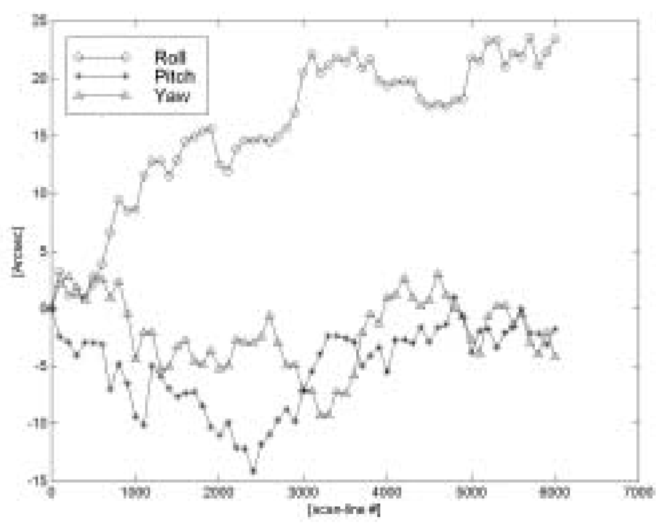

Fig 5: Angular noise (in arcsec) as applied to ω, φ, κ

Now, the objective is to compare the accuracies of the recovered angular perturbations obtained from employing different feature primitives. In particular, it is our main purpose to demonstrate that the reconstruction results using the model presented in (9) are far more superior to traditional techniques based on point primitives. To begin, we use a varying number of equally distributed control points along features (a) and (c) (the western and eastern features in Fig 4, respectively). The incorporation of control points is done within our model (9) but now with the t parameter omitted. The orientation results for point-based filtering are shown in Fig 6., where the accuracies of the recovered angular elements are translated into object space units (i.e., meters).

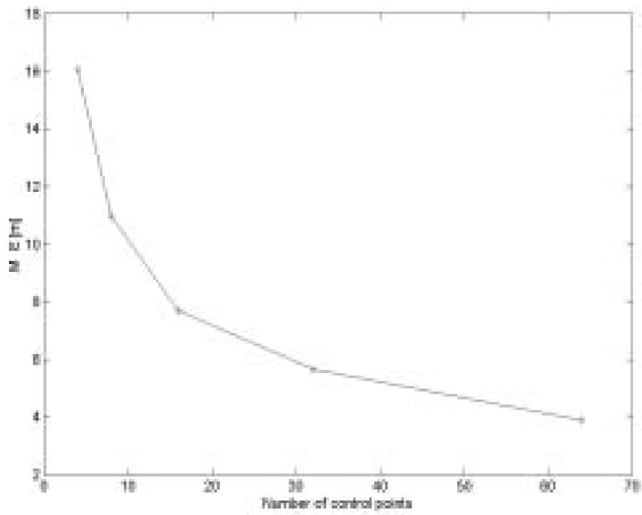

Figure 6: Point-Based Filtering. Mean prediction error (expressed in meters) for the angles ω, φ.

Fig. 6 clearly shows that the recovery of the angular perturbations is only feasible if a considerably large number of control points is used. Moreover, even for about as many as 60 points, the mean prediction error for the roll and pitch angles (the accuracy of the pitch angle is less critical here) results in a ground error of more than 4 meters, which is three-fold the resolution of the image.

Next, we apply model (9) for recovering the angular errors using linear features of Fig. 2, one pair at the time.

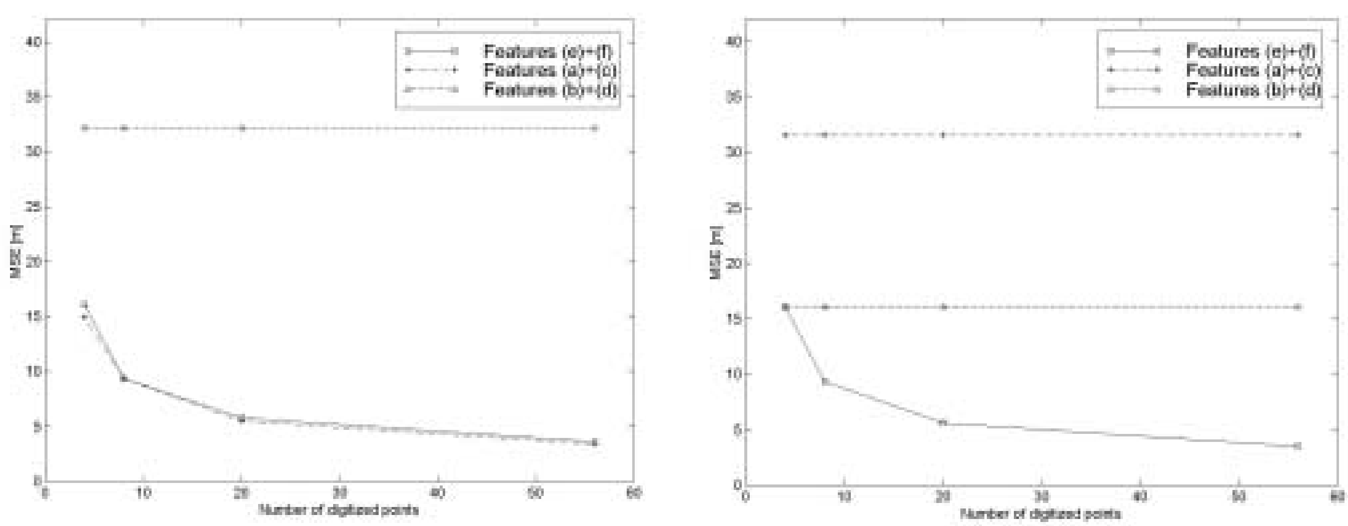

Figure 7: Feature-Based Filtering. Mean prediction error (expressed in meters) for the roll angle (left) and the pitch angle (right).

The first pair consists of elements (a) and (c) coinciding, more or less, with the first and the last columns of the dynamic image. The second pair consists of elements (b) and (d) found at the top and the bottom part of the image, respectively. . The third pair consists of elements (e) and (f), the diagonal features in Fig. 4. A brief analysis of Fig. 7 reveals that the pairs (b)+(d) and (a)+(c) are of no practical use for the recovery problem. As for the pair (b)+(d) none of the two dominant angles (roll and pitch) is improved, regardless of the number of points digitized along the two features. That is, of course, since each of these features is confined to just a few scan-lines of the image, and, hence, does not provide the required continuous coverage. For the second pair, there is no degeneracy in the roll angle, but due to their dominant top-down direction the pitch component can not be accurately resolved. Finally, the pair (e)+(f), with its features distributed in such a way that both the rows and the columns of the image are continuously covered, enables a sufficiently accurate reconstruction of the angular elements.

At first sight, though, the reconstruction results of even the best (in terms of accuracy) configuration (i.e., (e)+(f)) do not seem better than those obtained with control points. However, one extremely important fact should not be forgotten. In line-photogrammetry, there is basically no limitation on the number of image space measurements that can be associated with a control feature. That is since no prior correspondence between individual points describing the features in both domains (image & object) is required. We may, thereby, digitize as many points as necessary on features (e)+(f) in the image to ultimately meet any accuracy requirements, no matter how strict they are. In contrast, for reaching the same accuracy using point-based solutions, each digitized point on the image would require a corresponding ground point with <u>known</u> 3-D coordinates. For example, reaching an accuracy of **one meter** requires about **300 points** in both solutions. However, while in feature-based methods this can be done very easily, and in many cases almost autonomously (using digital photogrammetry techniques), in point-based approaches it entails a time consuming and expensive fieldwork.

7 CONCLUDING REMARKS

A rigorous mathematical model for recovering the EOPs of pushbroom images using parametric and free-form curves has been developed. We've shown its superiority over traditional approaches based on control points, especially for dynamic image undergoing rough perturbations during image acquisition. Future research in this subject will concentrate on developing more specific and detailed IMU calibration models, and will incorporate, in addition to control features, also shape (unknown position) and tie features (unknown position and orientation) occurring in single swath with multiple coverage or in the overlapping area of adjacent swaths. These activities will ultimately pave the way for a development of Multi-Sensor Feature-Based Photogrammetric Triangulation.

REFERENCES

[1] Brown, R. G. and Hwang, P. Y. C., 1997. Introduction to Random Signals and Applied Kalman Filtering. John Wiley & Sons, NY.

[2] Ebner, H., Ohlhof, T., Putz, E., 1996. Orientation of MOMS-02/D2 and MOMS-2P Imagery. In International Archives of Photogrammetry and Remote Sensing, Vol. XXXI Part B3, pp. 158-164.

[3] Habib, A. and Beshah, B. T., 1996. Modeling Panoramic Linear Array Scanner. In International Archives of Photogrammetry and Remote Sensing, Vol. XXXXI Part 3/1, pp. 31-40.

[4] Koch K. R., 1999. Parameter Estimation and Hypothesis Testing in Linear Models (2nd edition). Springer-Verlag Berlin Heidelberg.

[5] Lee, C., Thesis, H. J., Bethel, J. S., and Mikhail, E. D., 2000. Rigorous Mathematical Modeling of Airborne Pushbroom Imaging Systems. Photogrammetric Engineering & Remote Sensing, 66(4), pp. 385-392.

[6] Zalmanson G., 2000. Hierarchical Recovery of Exterior Orientation from Parametric and Natural 3-D Curves. In International Archives of Photogrammetry and Remote Sensing, Vol. XXXIII Part B2, pp. 610-617.

Architecture of "Intelligent" Earth Observation Satellites

Dr. Guoqing Zhou
Department of Civil Engineering and Technology
Kaufman Hall, Rm. 214, Old Dominion University, Norfolk, VA 23529, USA
Tel: (757) 683-3619; Tax: (757) 683-5655; Email: gzhou@odu.edu

(Workshop of ISPRS WG I/2, I/5 and IV/7, **High Resolution Mapping from Space 2001,** University of Hanover) September 19-21-2001

Key Words: Intelligent satellite, Future earth observing, smart sensor, intelligent imaging system

ABSTRACT

This paper presents a revolutionary and advanced satellite imaging concept that could, hopefully, dramatically impact the development of satellite technology in the next 20 to 40 years. The proposed "intelligent" satellite system is a space-based architecture for the dynamic and comprehensive on-board integration of Earth observing sensors, data processors and communication systems to enable simultaneous, global measurement and timely analysis of the Earth's environment for real-time, mobile and common users. The proposed architectures form a seamless integration of diverse components into a smart, adaptable, and robust Earth observation satellite system.

1. INTRODUCTION

1.1 What is the NEXT "new" generation of Earth Observation Satellites?

In 1995, a conference titled *"Land Earth Satellite for Decade"* sponsored by the American Society for Photogrammetry and Remote Sensing (ASPRS), and co-sponsored by the Landsat Management Team (NASA, NOAA, and USGS), NIMA, USDA, EPA, NASA Applications, and others brought together more than 700 experts from the satellite companies, value-added producers and end user communities to study anticipated applications, detect potential problems, and discuss common solutions. It was concluded that the *new generation* of high-resolution, multi (hyper) spectral satellite systems would be widely applied. If as scheduled early, a minimum of 19 satellites will be in polar orbit providing land data at resolutions from 1 to 30 meters in panchromatic, multispectral, and radar formats in the year 2008 (Fritz, 1996). We think this "new generation" of satellites will last until 2010 (see our analysis in Section 1.2). One may ask what is the NEXT "new generation" of land satellite system!

1.2 History of Land Satellite Development

It is quite difficult to absolutely divide the history of earth observation satellite development into different stages. However, to explain the development phases, we will personally distinguish the development into:

The first generation: military satellites (early 1960's thru 1970's). CORONA, ARGON and LANYARD were the first three operational imaging satellite reconnaissance systems. The reconnaissance satellites, which were operated in response to the uncertainties and anxieties created by the early Cold War (McDonald, 1995), appeared at the beginning of the space age. The obvious characteristics is their imaging systems (relative to most recent satellite imaging system), which are basically similar to aerial photogrammetry (Zhou and Jezek, 2001).

The second generation: Experimental period and initial application (1970s thru the middle of 1980s). The typical characteristics are: (1) satellite application from military to civil (Landsat 1, lunched in August 1972), (2) multispectral imagery started to be applied in earth nature resources investigation and management, (3) best ground resolution achieves only 30 m (Landsat 5, TM), (4) imaging systems were basically optical and passive mode.

The third generation: Wide application and technique further developed (1986 thru 1995). Briefly, the characteristics are (1) the first use of linear array push-broom imaging mode in SPOT in 1986, (2) off-nadir viewing enables the acquisition of stereoscopic imagery (capability of stereo mapping); (3) ground resolution in panchromatic channel reaches 10 m in SPOT. (4) active microwave sensor satellite, radar imagery in ERS-1, Europe Space Agency in 1991.

The fourth generation: "new" generation of high-resolution satellite (1996 to ***"2010")***. We think that earth observation satellite has passed the threshold into maturity as a commercial space activity. The characters are briefly summarized in Table 1.

From the history of the satellite development presented above, we conclude that the satellites are updated on an approximate 10-year cycle. Thus we predict the next "new generation" satellite will be intellectualized.

Table 1. Specification of the "new" generation of earth observation systems.

Image mode	Pan	MS	HS	**Orbital altitude**	About 500 ~ 700 km
Resolution	1 m	4 m	8 m	**Inclination**	~ 98°, sun sync.
Bandwidth (microns)	0.45~0.9	8 bands 0.45~0.9	200 bands 0.45~2.5	**Revisit Cycle**	<3 days
Swath	4 to 40 km			**Stereo**	In- & Cross-tracking
Sensor attitude	Digital Star Trackers			**Sensor position**	GPS
Imaging type	Line array Whisk-broom			**On board processor**	No
Countries	Argentine, China/Brazil, Canada, France, Germany, India, Israel, Japan, Korea (South), Ukraine, US government and US commercial companies				

Pan = panchromatic, MS=mutlispectral, HS = hyperspectral.

2. NEW USERS REQUIREMENTS vs. CURRENT SATELLITE SYSTEM

Traditional user's demand is satellite imagery. New societal needs for information, especially mobile GIS and real-time GIS, have migrated from basic imagery to temporal, site specific, update mapping products. These data and information revisions will be requested frequently on an annual to hourly basis; in many ways the requests will be analogous to today's weather updates. In addition, the common consumers will be less concerned with the technical complexities of image processing, and will require the companies to use different strategies, directly providing them with value-added images such as, geo-registration, orthorectification, feature enhancement, radiometric intensification, etc.; and value-added products such as DTMs, orthophotos, image mosaics, fused MS and pan scenes, etc. in order to meet their real-time, mobile GIS's needs. Thus, traditional concepts about satellite system will meet new challenges in the next generation of users in the GIS/mapping community. These challenges include (1) revisit cycle, (2) ordinary users, (3) streaming from acquisition to user, (4) fixed facilities for satellite data downlink, (5) data archival by classification, (6) satellite on-board data processing.

3. ARCHITECTURE OF CONCEPT DESIGN OF "INTELLIGENT" SATELLITE

The architecture of an "intelligent" satellite is illustrated in Figure 1. It integrates the dynamic and comprehensive on-board Earth observing sensors, data processors and communication systems to enable simultaneous, global measurement and timely analysis of the Earth's environment for mobile, real-time, and common users. The major components consist of (1) "intelligent" space segment, (2) "intelligent" control segment, and (3) "intelligent" common end-user.

3.1 Intelligent Space Segment

Concept Design for Imaging System: The imaging instrument applies the push-broom principle. Several hundred CCD line detectors are mounted in parallel at the focal plane of a lens, which is orthogonal to the direction of flight. Multiple superimposed image strips are acquired almost simultaneously by the forward motion of the aircraft over the terrain.

Concept Design of on-board Satellite Data Processor: The "intelligent" on-board data processor is conceptually designed into low "intelligent" and high "intelligent" data processors. The low "intelligent" data processor process on-board data using robust algorithms (less human interaction), such as (all of these can be cost effectively performed on the ground recently), (1) aerial-triangulation of linear array whisk-broom imaging geometry, (2) geo-registration, orthorectification, orthophotos, and image mosaics, (3) data storage, data format transformation, data compression, (4) data fusion of panchromatic and multispectral imagery, and (5) image filtering, enhancement, and radiometric balance. The high "intelligent" data processor contains (1) digital elevation model (DEM), digital terrain model (DTM), (2) classification of multi/hyperspectral imagery, (3) enhancing and extracting spatial information, and (4) satellite image comparison (change detection) so that only specified change data need be transmitted to ground processing information systems,

The available techniques currently and within the next 10 years will make it possible to realize the low *"intelligent"* capability. The implementation of the *high "intelligent"* capability will need several generations because the developments of image processing and computer vision have demonstrated that full-automation of DEM generation, classification, and change detection is quite difficult, particularly in complex areas, like urban secne. This section will briefly discuss how to implement triangulation and orthophoto data processing.

1. *Aerotriangulation on board:* Based on the designed geometric configuration of the imaging system, the rigorous mathematical model of aerotriangulation can be developed using the called *"line central projection"*. The ground control points (GCPs) can be obtained by on-board extracting the conjugate distinctive points from stereo panchromatic pair of satellite images, and 3D coordinates of distinctive points are derived using aerotriangulation (Zhou, *et al*, 2000).

2. *On-board orthophoto generation:* The rigorous, high-precision mathematical model for orthorectification of satellite image can be developed based on the principle of line array push-broom imaging geometry (Zhou and Li, 2000). In this model, all of exterior orientation parameters will be provided by GPS and digital star trackers. The interior orientation parameters will be from in-lab or in-flight calibration. The GCP data should be obtained from the aerotriangulation above.

Concept Design for Revisits Cycle: Real-time and mobile users frequently require collecting spatio-temporal data over very large areas. Therefore, it is apparent that no single satellite can meet such requirement. We conceptually design its architecture that multiple satellites revolve along the same or multiple orbits to guarantee the revisit cycle is within several hours, and even potentially within minutes.

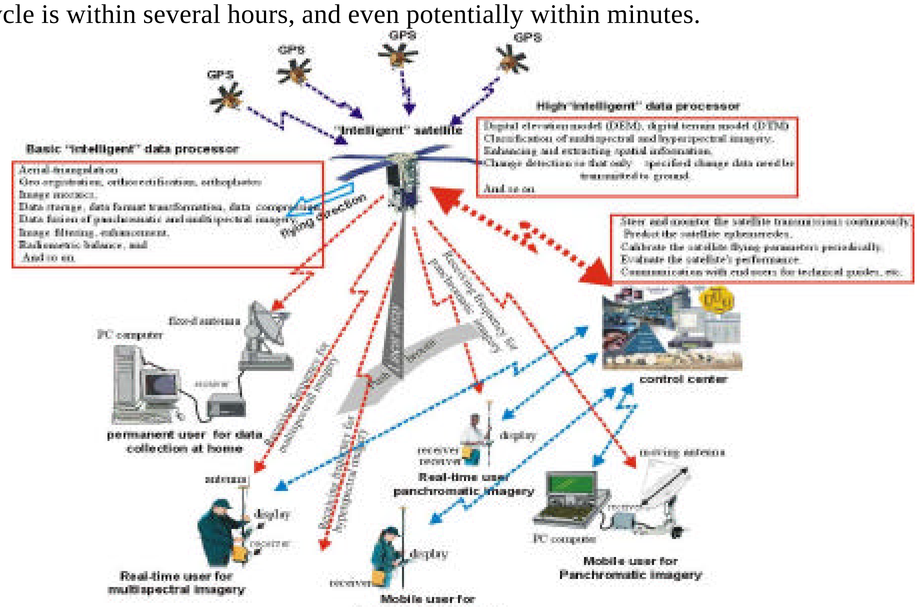

Figure 2. The architecture of "intelligent" earth observation satellite system for 2010-2050.

3.2 Concept Design for Control Segment

This segment contains (1) a master control station and several monitoring stations located around the world; (2) the control station steers and monitors the satellite transmissions continuously, predicts the satellite ephemerides, calibrates the satellite flying parameters and the navigation message periodically, evaluates the satellite's performance; (3) communication with end-users for problem solution, such as receiving frequency, channel, software, technical guides, etc is a function of this segment also.

3.3 Concept Design for the End-User

The end user segment is conceptually designed so that the end users can directly downlink various satellite band imagery according to their needs.This would be as simple as selecting a TV channel for a common user, or a weather update for a real-time user. The examples are (1) A real-time user, e.g. mobile GIS user, requires a real-time downlink for geo-referenced satellite imagery with a portable receiver, small antenna and laptop computer. (2) A mobile user, e.g., search-and-rescue pilot, requires a real-time downlink to geo-referenced panchromatic or multispectral imagery in an airplane. (3) A common user, e.g., farmer, requires receiving their geo-referenced, multispectral imagery at a frequency of 1-3 days for investigation of his harvest. (4) A mineralogist only requires downlink hyperspectral imagery for distinguishing different metals. A professional user, e.g., photogrammetrist, requires a downlink to panchromatic image for stereo mapping. Another strategy is to downlink to the home office where data is rapidly processed and disseminated worldwide to users via low cost web based service or communication providers. The architecture of the end-user design mainly contains:

1. *Antenna and receiver of "intelligent" satellite for end users:* We conceptually design three types of antenna and receiver, (1) Hand-held antenna and receiver for real-time and mobile users, (2) mobile antenna for mobile users, (3) fixed antenna for popular users, professional users or satellite receiving station. The size of mobile and hand-held antennas is much smaller than the current antenna of satellite. We imagine that the end-users connect their (PC) computer to receiver and antenna to real-time downlink and display geo-referenced satellite imagery they require. It appears to the end-users like watching TV using a remote control to select the channels, after the TV dish antenna receives TV signals.

2. *Communication between various users and ground control station:* As described above, different users will need different imagery. For example, a biologist needs hyperspectral imagery for plant species research; an agriculturalists only needs multispectral imagery for their harvest analysis. All of these various users would contact the ground control station to obtain their receiving frequency after payment. The ground control stations communicate real-time with end-users for guidance about receiving frequency, software use, display, and so on.

3. *User Software for "Intelligent" Satellite Data Processing:* We expect the various users to directly receive satellite geo-referenced imagery in the bands that they require, but it does not mean that the transmitted data from the satellite is directly a, such as 8 bit, imagery. It would seem as a TV antenna receives a signal, not direct picture and sound. The signal must be transformed by the TV set into picture and sound. Similarly, the "imagery" in an "intelligent" satellite is a type of *special signal*, (we will call it *special signal* in order to distinguish recent satellite signal and TV signal). However the *special signal* is certainly different from the most recent satellite so-called "raw" or "signal" data because they have to be post-processed by complex procedures. We expect this *special signal* to easily be transformed by only software which is provided by the ground control center so that real-time and common users can easily use it. Of course, application software, e.g., ArcView is necessary because the "imagery" format, display, analysis, further processing, application and management are different with various users.

4. FEASIBILITY ANALYSIS AND CONCLUSION REMARK

International acceptance of this revolutionary concept for "intelligent" satellites will increase with international recognition of the benefits of intellectualized imaging and processing technology. As the spatial information sciences mature, it is time to integrate our technologies into the intellectualizing era so that the burden of educating our consumers to our technology will diminish and various level users, no matter how sophisticated or common, can directly obtain information from satellite at real-time. The future is very bright and promising for the photogrammetry/remote sensing/GIS community.

One may speculate that more realistically the issue is whether sufficient capital will remain available to get the systems developed and launched, especially for the multi-satellite systems. A large outlay of capital is needed for the development to be completed before the companies can begin to realize a revenue stream. It is quite conceivable that these ventures will lead to significant advance in science and technology. On the other hand, a recognized fact is that, in the rush and glamour to utilize outer space, governments have always given the highest priority for funding imagery collection systems and have allocated very limited resources for development of efficient imagery exploitation systems. Even with the high capitalization costs of satellite systems, their advantages of *imaging timeliness, rapid delivery, digital form, simultaneous pan and MS coverage, superior coverage per processing unit, temporal repetitivity, radiometric dynamic range and stereometric fidelity* make them very cost competitive in future.

ACKNOWLEDGMENTS

This research is funded by NASA Institute for Advanced Concepts (NASA-NIAC) at project number 713041I am very grateful to Dr. John T. Neer, who was the founder of SpaceImaging Inc. and its first President and CEO, at Lockheed Martin Space Systems for his guidance and advice. I thank him very much for his review, comments from his 11-year vantage point, and discussion with me. I am grateful to those satellite development scientists who provide mewith helpful advice, encouragement, and relevant materials.

REFERENCES

(1) Fritz L.W., 1996, Commercial earth observation satellites, *International Archives of Photogrammetry and Remote Sensing*, Vol. XXXI, Part B4. Vienna, pp. 273-282.
(2) Lillesand T.M. and R. W., Kiefer, 2000. Remote sensing and image interpretation, Fourth Edition, John Wiley & Sons, Inc. 2000, ISBN: 0-471-25515-7.
(3) McDonald, R.A., 1995, Opening the Cold War Sky to the Public: declassifying satellite reconnaissance imagery, *Photogrammetric Engineering and Remote Sensing*, Vol. 61, No. 4, pp. 380-390.
(4) Stoney, W. E., 1996. The Pecora legacy-land observation satellites in the next century, *in the Pecora 13 Symposium*, Sioux Falls, South Dakota, August 22.
(5) Zhou. G. K. Jezek, 2001, 1960's Satellite mosaic in Greenland, *Int. Journal of Remote Sensing (in press).*
(6) Zhou G. and R. Li, 2000. Accuracy Evaluation of Ground Points from High-Resolution Satellite Imagery IKONOS, *Photogrammetry Engineering & Remote Sensing,* Vol. 66. no. 9, pp. 1103-1112.